Ultrananocrystalline Diamond

Synthesis, Properties, and Applications

Edited by

Olga A. Shenderova
International Technology Center
Research Triangle Park, NC, U.S.A.

Dieter M. Gruen
Argonne National Laboratory
Argonne, IL, U.S.A.

William Andrew Publishing
Norwich, New York, U.S.A.

Copyright © 2006 by William Andrew, Inc.

No part of this book may be reproduced or utilized in any form or by any means, electronic or mechanical, including photocopying, recording, or by any information storage and retrieval system, without permission in writing from the Publisher, with the exception of the following: Chapter 5 of this book, "Electron Transport and the Potential of Ultrananocrystalline Diamond as a Thermoelectric Material," and Chapter 8 of this book, "Theoretical Studies of UNCD Synthesis and Properties," were created by the University of Chicago as Operator of Argonne National Laboratory ("Argonne") under Contract No. W-31-109-ENG-38 with the U.S. Department of Energy. The U.S. Government retains for itself, and others acting on its behalf, a paid-up, nonexclusive, irrevocable worldwide license in said article to reproduce, prepare derivative works, distribute copies to the public, and perform publicly and display publicly, by or on behalf of the Government.

Cover art © 2006 by Brent Beckley / William Andrew, Inc.
Cover photo taken by the Hubble Telescope: "Filaments stream from nebula N44C"
Image Credit: NASA and the Hubble Heritage Team

Library of Congress Cataloging-in-Publication Data

Ultrananocrystalline diamond : synthesis, properties, and applications / edited by Olga A. Shenderova, Dieter M. Gruen.
p. cm. – (Materials science and process technology series)
Includes bibliographical references and index.
ISBN-13: 978-0-8155-1524-1
ISBN-10: 0-8155-1524-3
1. Nanodiamonds – Synthesis. 2. Nanodiamonds – Analysis. 3. Diamond powder – Industrial applications. 4. Diamond thin films – Industrial applications. I. Shenderova, Olga A. II. Gruen, Dieter M. III. Series.

TP873.5.D5U48 2006
666′.88 – dc22

2006004384

Printed in the United States of America
This book is printed on acid-free paper.

10 9 8 7 6 5 4 3 2 1

Published by:
William Andrew Publishing
13 Eaton Avenue
Norwich, NY 13815
1-800-932-7045
www.williamandrew.com

Sina Ebnesajjad, Editor in Chief (External Scientific Advisor)

NOTICE

To the best of our knowledge the information in this publication is accurate; however the Publisher does not assume any responsibility or liability for the accuracy or completeness of, or consequences arising from, such information. This book is intended for informational purposes only. Mention of trade names or commercial products does not constitute endorsement or recommendation for their use by the Publisher. Final determination of the suitability of any information or product for any use, and the manner of that use, is the sole responsibility of the user. Anyone intending to rely upon any recommendation of materials or procedures mentioned in this publication should be independently satisfied as to such suitability, and must meet all applicable safety and health standards.

Contributors

Orlando Auciello
Argonne National Laboratory
Argonne, IL, USA

Amanda S. Barnard
Argonne National Laboratory
Argonne, IL, USA

Fabien Bénédic
Université Paris 13
Villetaeuse, France

Yuriy V. Butenko
Boreskov Institute of Catalysis
Novosibirsk, Russia

John Carlisle
Argonne National Laboratory
Argonne, IL, USA

Larry A. Curtiss
Argonne National Laboratory
Argonne, IL, USA

Vyacheslav V. Danilenko
ALIT Close Joint Stock Company
Kiev, Ukraine

Tyrone L. Daulton
Naval Research Laboratory
Stennis Space Center, MS, USA

Valerii Yu. Dolmatov
JSC Diamond Center
St. Petersburg, Russia

H. D. Espinosa
Northwestern University
Evanston, IL, USA

Alix Gicquel
Université Paris 13
Villetaneuse, France

Irina Gouzman
Soreq Nuclear Research Center
Yavne, Israel

Varvara P. Grichko
International Technology Center
Raleigh, NC, USA

Dieter M. Gruen
Argonne National Laboratory
Argonne, IL, USA

Khaled Hassouni
Université Paris 13
Villetaneuse, France

Alon Hoffman
Technion–Israel Institute of Technology
Haifa, Israel

Vladimir L. Kuznetsov
Boreskov Institute of Catalysis
Novosibirsk, Russia

Guillaume Lombardi
Université Paris 13
Villetaneuse, France

Gary McGuire
International Technology Center
Raleigh, NC, USA

Shaul Michaelson
Technion–Israel Institute of Technology
Haifa, Israel

Francis Mohasseb
Université Paris 13
Villetaneuse, France

Nicolaie Moldovan
Northwestern University
Evanston, IL, USA

Bei Peng
Northwestern University
Evanston, IL, USA

Igor L. Petrov
New Technologies
Chelyabinsk, Russia

Olga A. Shenderova
International Technology Center
Raleigh, NC, USA

Michael Sternberg
Argonne National Laboratory
Argonne, IL, USA

Alexander Ya. Vul'
Ioffe Physico-Technical Institute
St. Petersburg, Russia

Xingcheng Xiao
Argonne National Laboratory
Argonne, IL, USA

Peter Zapol
Argonne National Laboratory
Argonne, IL, USA

Preface

Ultrananocrystalline diamond (UNCD) is one of the important triad of nanostructured carbons which includes fullerenes and nanotubes that have risen to the forefront of materials research over the last two decades. This new kind of diamond composed of 3–5 nm crystallites is an exemplar par excellence of the profound changes in properties that can accompany the reduction in size of a material to low single-digit nanometer dimensions. UNCD occurs in two forms: as a dispersed powder made by detonation techniques and as a chemical vapor-deposited film. Both UNCD particles and UNCD films possess unique properties and different niche applications. For UNCD particles, which were discovered in the 1960s in the former USSR, applications include use in nanocomposites, selective adsorbents, colloidal suspensions, refrigerating fluids, microabrasives, lubricants, quantum dots, cold-cathodes, and many others. UNCD films, discovered in the early 1990s at Argonne National Laboratory are superior in many ways to traditional micro- and nanocrystalline diamond films: they are smooth, dense, pinhole-free, and phase-pure, and can be coated on a wide variety of materials and high-aspect-ratio structures. The set of unique properties include mechanical, tribological (extremely low friction coefficient ~0.01), transport (tunable electrical conductivity combined with low thermal conductivity), electrochemical (wide working potential window), and electron emission (low, stable threshold field). UNCD films have been considered for a variety of applications including MEMS and moving mechanical assembly devices, surface acoustic wave (SAW) devices, electrochemical sensors, coatings for field emission arrays, photonic and RF switching, biosensors and neural prostheses. Recent achievements in n-type doping demonstrate the highest carrier concentrations seen for any n-type diamond material to date resulting in many orders of magnitude increase in UNCD film conductivity that promise applications in high-temperature heterojunction electronic devices. A particularly promising area of active ongoing research is the development of high-efficiency high-temperature thermoelectric materials involving UNCD and UNCD/carbon nanotube composites.

Two communities of scientists, each focused on one of these UNCD fields, have until recently been working independently of each other largely unaware of the vast synergistic relationships existing between them. This book is the first publication addressing in depth and in a

systematic manner the fundamentals of carbon stability at the nanoscale, the mechanisms of UNCD synthesis and phase transformation thus fostering further collaborations between the two existing nanodiamond communities.

The contents of the book are divided into four parts. The first part provides an overview of naturally occurring ultrananocrystalline diamond and its laboratory synthesis including experimental observations of isolated nanodiamonds in the cosmos and so-called diamandoids in petroleum. A summary of numerous synthetic means to produce nanodiamonds that have been reported to date is given. The second part addresses carbon stability at the nanoscale. The third and fourth parts provide in-depth discussions of synthesis, properties, characterization and a wide variety of applications of UNCD films and UNCD particulates of detonation origin. The 15th chapter of the fourth part reviewing current and potential applications of diamond films and particles in the areas of biosensing and medicine emphasizes strong interdisciplinary coupling between nanocarbon-materials science and biology. Nanodiamond particles and their derivatives, diamondoids and their derivatives, and UNCD films, all have high potential in biotechnological and biomedical applications. UNCD films have been suggested to be the ideal platforms for future biochips and biosensors because of their superior mechanical, thermal, and chemical properties as compared to those of glass, silicon, and gold surfaces. UNCD particles have been considered for protein separation, fabrication of integrated biochips and sensors, and anti-tumor activity.

We hope that the present book will attract the attention of scientists working in other areas of nanostructured materials to the opportunities for applications offered by UNCD in its various forms. We believe that there still exist a wide variety of new, unexplored areas of research within carbon nanostructures and particularly, ultrananocrystalline diamond.

Olga Shenderova and Dieter M. Gruen

2006

Contents

Contributors xv

Preface xix

Part I. Overview: Naturally Occurring UNCD and Its Laboratory Synthesis

1. Carbon Family at the Nanoscale 3
   Introduction 3
   1.1 Historical Overview 4
   1.2 Nanocarbon Classification 8
   1.3 Exotic Nanocarbons 12
   1.4 Conclusion 16
   References 16
2. Extraterrestrial Nanodiamonds in the Cosmos 23
   Introduction 23
   2.1 Stellar Nucleosynthesis and Presolar Stardust 24
   2.2 Discovery and Identification of Presolar Minerals 26
   2.3 Origins of Meteoritic Nanodiamonds 27
   2.4 Isotopic Compositions of Meteoritic Nanodiamonds: Stellar Sources 28
      2.4.1 Primary C, Surface Bound H, and Trapped N 30
      2.4.2 Trapped Noble Gases 33
      2.4.3 Trapped Te, Pd, Ba, and Sr 46
      2.4.4 Inferred Stellar Sources 48
   2.5 Microstructure of Meteoritic Nanodiamonds: Formation Mechanisms 50
      2.5.1 Twin Microstructure 50
      2.5.2 Dislocation Microstructure 54

This page has been reformatted by Knovel to provide easier navigation.

2.5.3 Polytypes 55
2.5.4 Inferred Mechanisms of Formation 56
2.6 Noble Gas and N Content in Meteoritic Nanodiamonds: Nebular Processes 58
2.7 Nanodiamonds in Interplanetary Dust Particles: Insights on Solar Nebula Evolution 65
2.8 Summary of Experimental Data 67
2.9 The New Astronomy 68
Acknowledgments 69
References 69
3. Types of Nanocrystalline Diamond 79
Introduction 79
3.1 Nanodiamonds: Shapes 81
3.2 Types of Nanodiamond and Methods of Their Synthesis 82
3.2.1 Zero-dimensional Nanodiamond Structures 84
3.2.2 One-dimensional ND Structures 95
3.2.3 Two-dimensional ND Structures 102
3.2.4 Three-dimensional ND Structures 104
3.3 Conclusion 108
Acknowledgments 109
References 109

Part II. Stability of Nanodiamond

4. Stability of Nanodiamond 117
Introduction: Nanocarbon Phase Stability 117
4.1 Nanocarbon Phase Diagrams 118
4.2 Theoretical Studies of the Relative Phase Stability of Nanocarbons 123
4.2.1 Stability of Large Nanocarbon Particles 124
4.2.2 Stability of Small Nanocarbon Particles 129
4.2.3 Coexistence of Bucky-diamond and Other Nanocarbon Phases 130

This page has been reformatted by Knovel to provide easier navigation.

4.2.4 Stability of Quasi One-dimensional Nanocarbon 132
4.2.5 Summary 134
4.3 Morphologies 134
4.3.1 Morphology of Nanodiamond Particles 134
4.3.2 Morphology of Diamond Nanorods and Nanowires 141
4.3.3 Hybrid Nanocarbon Materials 146
4.4 Conclusions 147
Acknowledgments 149
References 149

Part III. UNCD Films and Related Materials

5. Electron Transport and the Potential of Ultrananocrystalline Diamond as a Thermoelectric Material 157
Introduction 157
5.1 Characterization of n-type Conductivity in UNCD Films 159
5.2 Applications of n-type UNCD Films 165
5.2.1 Field Electron Emission 167
5.2.2 Electrodes for Electrochemistry and Biosensing 168
5.2.3 High-temperature n-type UNCD/p-type All-diamond Heterostructure Diode 169
5.3 Electronic Structure of UNCD Grain Boundaries 170
5.4 UNCD and Carbon Nanotube/UNCD Composites as Potential High-efficiency, High-temperature Thermoelectric Materials 173
5.5 Summary 178
Acknowledgments 179
References 180
6. Plasma-assisted Synthesis: Plasma Experimental Diagnostics and Modeling 185
Introduction 185

This page has been reformatted by Knovel to provide easier navigation.

6.1 Experimental Details 188
6.1.1 MPACVD Reactor and Process Parameters 188
6.1.2 Arrangements for Spectroscopic Diagnostics 190
6.2 Fundamentals of Plasma Diagnostics 191
6.2.1 Optical Emission and Broadband Absorption Spectroscopy 191
6.2.2 Plasma Modeling 199
6.3 Investigations of Typical NCD Deposition Conditions 202
6.3.1 Deposition and Characterization of NCD Films 202
6.3.2 Plasma Diagnostics 207
6.3.3 Conclusion on Plasma Characterization 211
6.4 Investigations of $Ar/H_2/CH_4$ Microwave Discharges with the Plasma Thermochemical Model 211
6.4.1 Parametric Studies 211
6.4.2 Mechanisms of C_2 Formation 220
6.4.3 Conclusion on Plasma Modeling 222
6.5 General Conclusion 223
References 224
7. Nanodiamond Films Deposited from Energetic Species: Material Characterization and Mechanism of Formation 229
Introduction 229
7.1 The Deposition System and Deposition Parameters 231
7.2 Evolution and Properties of the Films Studied by NEXAFS: Coordination and Orientation 235
7.3 Phase Composition of the Films as Reflected by Raman Spectroscopy 240
7.4 Crystalline Structure of the Films by XRD 246
7.5 Morphological Evolution of the Films by AFM 248
7.6 Surface and Grain Boundary Phase Composition Studied by EELS 248
7.7 Hydrogen Content in the Films by SIMS and ERD 251
7.8 Hydrogen Bonding Configuration in the Nanodiamond Films Studied by HREELS 252

This page has been reformatted by Knovel to provide easier navigation.

7.9 Density Evolution of the Films Examined by XRR 257
7.10 Visualization and Evolution of the Films Studied by HR TEM 257
7.11 Formation Mechanism of the Nanodiamond Film Deposited from Energetic Species 260
7.12 Summary 266
Acknowledgments 267
References 267
8. Theoretical Studies of UNCD Synthesis and Properties 273
Introduction 273
8.1 Computational Methodologies 274
8.2 Carbon Dimer Growth Mechanisms on the (110) Face of Diamond 275
8.2.1 The (110) 1 × 1:H Surfaces 275
8.2.2 Clean (110) Diamond Surface 278
8.3 Carbon Dimer Growth Mechanisms on the (100) Surface of Diamond 279
8.3.1 The (100) 2 × 1:H Diamond Surface 280
8.3.2 The (100) 2 × 1 Diamond Surface 281
8.3.3 Nitrogen Addition to (100) 2 × 1 Surface 284
8.3.4 A Model for UNCD Growth Kinetics 285
8.4 Electronic Structure of UNCD 287
8.4.1 Grain Boundaries in UNCD 287
8.4.2 Structure of High-angle Twist GBs in Diamond 288
8.4.3 Electronic Structure of GBs with π Bonding in UNCD 290
8.5 Electronic Structure of Doped UNCD 293
8.5.1 Nitrogen in Diamond and Amorphous Carbon 293
8.5.2 Nitrogen Impurities in the UNCD GBs 294
8.5.3 Other Impurities in the UNCD GBs 298
Acknowledgments 299
References 299

This page has been reformatted by Knovel to provide easier navigation.

9. Mechanical Properties of Undoped and Doped Ultrananocrystalline Diamond: Elasticity, Strength, and Toughness 303
Introduction 303
9.1 The Material 305
9.2 Experimental Technique 308
9.2.1 Elasticity and Strength Experiments 308
9.2.2 Fracture Toughness Experiments 310
9.3 Experimental Results 314
9.3.1 Stress-strain Curves 314
9.3.2 Size Effect and Weibull Analysis 316
9.3.3 Toughness Measurements 319
9.4 Fractographic Analysis 325
9.5 Theoretical Strength 327
9.6 Conclusions 328
Acknowledgments 329
References 329

Part IV. UNCD Particles of Detonation Origin

10. On the Discovery of Detonation Nanodiamond 335
References 344
11. Synthesis and Post-synthesis Treatment of Detonation Nanodiamonds 347
Introduction 347
11.1 Industrial Technologies of Detonation Synthesis of UNCD 349
11.2 Post-synthesis Purification and Modification 354
11.2.1 Chemical Purification 354
11.2.2 UNCD Modification 371
References 375
12. Characterization and Physical Properties of UNCD Particles 379
Introduction 379
12.1 Methods for Characterization of UNCD Particles 380
12.1.1 General Remarks 380

This page has been reformatted by Knovel to provide easier navigation.

12.1.2 X-ray Diffraction 380
12.1.3 Small-angle X-ray Scattering 382
12.1.4 Raman Scattering 383
12.1.5 HRTEM and SEM Studies 386
12.1.6 STM and AFM Studies 387
12.1.7 Visible and Far-infrared Spectroscopic Studies 389
12.1.8 NMR and EPR Studies 390
12.1.9 EELS Characterization of UNCD Powders 391
12.2 The Structure of UNCD Clusters and the Aggregation Problem 391
12.3 Mechanical Properties 396
12.4 Optical Properties 397
12.5 Electronic Properties 397
Summary 398
Acknowledgments 398
References 399
13. Diamond Phase Transitions at Nanoscale 405
Introduction 405
13.1 Stability of Nanocarbons 408
13.2 Surface Chemistry: Stability of Surface Species 411
13.2.1 Surface Groups of NDs 411
13.2.2 Thermal Stability of ND Surface Groups 413
13.2.3 Critical View of the Formation of sp^2-bonded Carbon in Pristine NDs 418
13.2.4 The Onset Temperature of ND Graphitization 420
13.3 Kinetics of Diamond Graphitization 422
13.3.1 Experimental Approaches for the Study of ND Graphitization 423
13.3.2 Kinetic Parameters of ND Graphitization for the Temperature Range of 1370–1860 K 425
13.4 Mechanism of Diamond Graphitization 431
13.4.1 Diamond Surface Reconstruction 431
13.4.2 Cleavage Energies of Diamond Planes 433

This page has been reformatted by Knovel to provide easier navigation.

13.4.3 Shape of Diamond Particles 434
13.4.4 Graphite/Diamond Interfaces 436
13.4.5 Formation of Nanocarbon Species via “Low”-temperature Diamond Graphitization 439
13.4.6 The Formation of the Closed Curved Graphitic Structure on the Surface of Micron-size Diamond 445
13.5 Catalytic Graphitization of NDs in the Presence of Metal Clusters 450
13.6 Graphitization of NDs in the Presence of Oxygen- and Hydrogen-containing Gases 454
13.7 Properties of ND Annealing Products: OLC, sp^2/sp^3 Nanocomposites 457
13.8 Conclusion 461
Acknowledgments 463
References 463
14. Applications of Detonation Nanodiamond 477
14.1 Electrochemical Coatings 477
14.1.1 Chrome Plating 477
14.1.2 Copper Plating 480
14.1.3 Zinc Plating 481
14.1.4 Tin Plating 482
14.1.5 Silvering 482
14.1.6 Gold Plating 483
14.1.7 Nickel Plating 484
14.1.8 Anode Oxidation 484
14.1.9 The Deposition of Alloys along with UNCD 485
14.2 Polymer Compositions and Antifriction Coatings 486
14.2.1 The Polyisoprene and Butadiene–Styrene Copolymer 488
14.2.2 The Polysiloxane Polyblock Cyclolinear Copolymer 491
14.2.3 Polyurethane Foam 492
14.2.4 Frost-resistant Butadiene–Nitrile Rubber 493

This page has been reformatted by Knovel to provide easier navigation.

14.2.5 Rubbers Stable to Explosive Decompression 494
14.2.6 Gas-flame Deposition of Polymer Coatings 495
14.3 Polishing 496
14.4 Oils and Lubricants 504
14.5 Diamond Sinters and Compacts 508
14.6 Bioactivity of UNCD Particles 513
14.7 Other Technological Applications of UNCD Particles 520
References 521
15. Nanodiamond: Designing the Bio-platform 529
Introduction 529
15.1 Functionalization of ND with Heteroatoms and Chemical Groups 531
15.2 Modification with Nucleic Acids 536
15.3 Interaction with Proteins 540
15.4 Application in Biosensors and Medicine 541
15.5 Biocompatibility of ND 547
15.6 Conclusion 549
References 550
16. History of Russian Patents on Detonation Nanodiamonds 559
Introduction 559
16.1 Patents on Methods of DND Synthesis 560
16.2 Patents on Post-synthesis Treatments 563
16.3 Patents on Composition of Matter 570
16.4 Patents on Applications 573
16.5 Conclusion 580
Acknowledgments 581
References 581

Index 589

This page has been reformatted by Knovel to provide easier navigation.

Index

Page numbers in italic, e.g. *29*, refer to figures. Page numbers in bold, e.g. **511**, signify entries in tables.

Index terms		Links	
A			
absorption spectroscopy (AS)	186		
Allende nanodiamonds			
dislocation microstructure	54		
effective diameters and effective shapes	*29*		
alloys, depostion of	485		
ALTAI foundary (Russia)	80		
angle-resolved (AR) NEXAFS	235	239	
anode oxidation	484		
apparent fracture toughness	311		
applications			
bioactivity	513		
biosensors and medicine	541	*542*	
diamond sinters and compacts	508		
characteristics	**511**		
electrochemical coatings	477		
alloy deposition	485		
anode oxidation	484		
chrome plating	477	**479**	**480**
copper plating	480		
gold plating	483		
nickel plating	484	**484**	
silvering	482	**483**	
tin plating	482		
zinc plating	481	**482**	

This page has been reformatted by Knovel to provide easier navigation.

Index terms **Links**

applications *(Continued)*
oils and lubricants 504
polishing 496
polishing compositions **503**
polishing results **503**
polymer and antifriction coatings 486
butadiene–nitrile rubber frost-resistant 493
flame deposition methods 495
physical and mechanical properties of CVPE films **487**
polyisoprene and butadiene–styrene copolymer 488 **489** **490**
polysiloxane polyblock cyclolinear copolymer 491 **492**
polyurethane foam (PUF) 492
rubbers stable to explosive decompression 494
argon
in meteoritic nanodiamonds **34** *35* **38** *44*
astronomy, new 68
asymptotic giant branch (AGB) carbon stars 23 24 27
atomic force microscopy (AFM)
morphological evolution of NCD films 248
characterization of UNCD particles 387 *388*

B

barium
in meteoritic nanodiamonds 46 **47**
Berman–Simon line 117
bias-enhanced nucleation (BEN) of diamond 230
binding energy 124
bioactivity of UNCD particles 513
bioapplication 529 549
biocompatibility 547
functionalization of ND with heteroatoms and chemical groups 531 *533*
interaction with proteins 540 *540*

This page has been reformatted by Knovel to provide easier navigation.

Index terms **Links**

bioapplication *(Continued)*
modification with nucleic acids 536 *538*
size of typical bio-entities *530*
biosensors 541 *542*
electrodes 168
Born–Lande pair interaction potentials 125
boron-doped diamond (BDD) thin films 539
bottom-up approaches to nanodiamond synthesis 101
broadband absorption spectroscopy (BAS) 186
C_2 Mulliken system 194 *195* *196*
C_2 Swan system 196 *197*
CN violet system 198
systems investigated 191 **193**
buckminsterfullerenes (buckyballs) 4
bucky-diamonds 138
coexistence with other nanocarbon phases 130 *131*
shape 82 *83*
bucky-shuttle 14 *15*
butadiene–nitrile rubber, frost-resistant 493
butadiene–styrene copolymer 488

C

C_2 Mulliken system 192 *192* **193** *195* *196*
C_2 Swan system 196 *197*
calcium–aluminum rich inclusions (IDPs) 25
carbolite 3
carbon, amorphous 293
carbon, nanoscale characteristics 3 16
classification 8 *11*
exotic nanocarbons 12 *13* *15*
historical overview 4
timeline **5** **9**

This page has been reformatted by Knovel to provide easier navigation.

Index terms **Links**

carbon, nanoscale characteristics *(Continued)*
stability 408
carbon, prevalence in meteoritic nanodiamonds **47**
carbon dimer growth mechanisms
diamond face 275
clean (110) surface 278 *279*
the (110) 1 × 1:H surface 275 *276* *277*
diamond surface 279 *280*
nitrogen addition to (100) 2 × 1 surface 284 *284*
the (100) 2 × 1:H surface 280 *282* *283*
carbon monoxide (CO) 24
carbon nanotubes (CNTs) 7
carbine *11*
cavity ring down spectroscopy (CRDS) 186
chemical purification of detonation nanodiamond 354
average size of aggregates *367*
industrial process *359*
pH dependence *361*
stratification from suspension *363*
total acidity distribution *362*
chemical vapor deposition (CVD) diamond 4 7 50
dislocation microstructure 54 *55*
extraterrestrial mechanisms 27
hydrogen bonding configuration *254* *255*
surface and grain boundary phase composition *251*
synthesis methods 92
twin microstructure 50 *51* *52* *53*
chemical–mechanical polishing (CMP) 496
chondrites 23 25
nanodiamond abundances **62**
chrome plating 477
microhardness **479**
wear resistance **480**

This page has been reformatted by Knovel to provide easier navigation.

Index terms		Links			
Clausius–Clapeyron equation	127				
closed curved graphitic structures (CCGS)	445	*447*	*449*		
cobalt					
catalytic graphitization of NDs	451	*453*			
compacts	508				
copolymer of vinylidenefluoride with perfluorinepropyl ether (CVPE)	486				
physical and mechanical properties of CVPE films	**487**				
copper plating	480				
D					
density of state (DOS)	174				
density-functional theory (DFT)	274				
density-functional-based tight-binding (DFTB) molecular dynamics	171				
detonation nanodiamond					
see also ultrananocrystalline diamond (UNCD)					
historical perspective	335				
historical outline	**337**				
modification	371	*374*			
phase diagram	340				
surface area	531				
synthesis and post-synthesis treatment	347				
chemical purification	354	*359*	*361*	*362*	*363*
	367				
detonation chamber	*352*	**355**			
incombustable elements	**356**				
industrial technologies	349	*359*			
yield	**352**				
DFTB *see* self-consistent charge density functional-based tightbinding (SCC-DFTB) method					
diamond	*11*				
synthesis from graphite	4	8			

This page has been reformatted by Knovel to provide easier navigation.

Index terms **Links**

diamond blend (DB) 347 350
chemical purification 368
yield **352**
diamond nanorods (DNRs) 96
diamond sinters 508
diamond-like carbon (DLC) 229
diamondoids *13* 84 *85*
commercial production methods 89
diamonds of static synthesis (DSS) 477
differential scanning calorimetry (DSC) 420
differential thermal analysis (DTA) 415
diffuse reflectance Fourier transform infrared spectroscopy (DRIFTS) 414
direct-current glow-discharge (DC-GD) deposition of nanocrystalline diamond (NCD) 230 266
DNA immobilization on diamond surfaces 537 *538*
DuPont Corporation 8 80

E

elastic recoil detection (ERD)
hydrogen content of NCD films 251
electron energy loss spectroscopy (EELS) 31
characterization of UNCD particles 391
formation of sp^2-bonded carbon on NDs 419
surface and grain boundary phase composition of NCD films 248 *249* *250* *251*
electron paramagnetic resonance spectroscopy (EPR)
characterization of UNCD particles 390
electron transport properties of UCND films 157 178
applications of n-type films 165
electrodes for electrochemistry and biosensing 168
field electron emission 167

This page has been reformatted by Knovel to provide easier navigation.

Index terms **Links**

electron transport properties of UCND films *(Continued)*
high-temperature n-type UNCD/p-type all-diamond heterostructure diode 169
composites as potential high-efficiency, high-temperature thermoelectric materials 173
properties **175**
electronic structure of grain boundaries 170 *172* *173*
n-type conductivity 159
Arrhenius plot *161*
Hall effect *163* *164*
electron–heavy-species rate constants 201
extraterrestrial origins of nanodiamonds 23
meteoric nanodiamonds 27
meteoric nanodiamonds, isotopic compositions 28
effective diameters and effective shapes *29*
primary C, surface-bound H, and trapped N 30
presolar minerals, discovery and identification 26
stellar nucleosynthesis and presolar stardust 24

F

Fermi level 296 *298*
Fermi–Dirac distribution 174
filaments **98**
Fourier transform infrared (FTIR) spectroscopy 415 *416*
fullerene nanotubes (buckytubes) 4
fullerenes *11*
full-width half-maximum (FWHM) of a peak 242 243 244

G

generalized tight-binding molecular dynamics scheme (GTBMD) 143
glassy carbon (GC) 235 *236*
gold plating 483

This page has been reformatted by Knovel to provide easier navigation.

Index terms **Links**

grain boundaries (GBs) of UCND films, electronic structure 170 *172* *173*
grain clusters 306
grapheme *13*
graphite *11*
onions *36*
synthesis 4
graphitization of diamond
catalysis by metal clusters 450
experimental approaches 423
estimation of diamond fraction in intermediates 423 **424**
kinetic model 425
in presence of oxygen and hydrogen 454 *456*
kinetic parameters for 1370–1860 K temperature range
absolute rates 429
Arrhenius plot *426*
migration rates **429**
temperature regions 425 *427* *428*
low-temperature diamond graphitization 439
model of ND annealing and OLC formation with holes 439 *441* *442* *443* *444*
mechanism
cleavage energies of diamond planes 433
diamond surface reconstruction 431 *432*
formation of closed curved graphitic structure on diamond surface 445 *447* *449*
graphite/diamond interfaces 436 *437* *438*
shape of diamond particles 434 *435*
OLC and sp^3/sp^2 nanocomposites 457 *457* *458* *460*

H

H/C ratio 199
Hall effect 162 *163* *164*

This page has been reformatted by Knovel to provide easier navigation.

Index terms		Links			
Hartree–Fock (HF) theory	274				
heavy-species–heavy-species rate constants	201				
helium					
in meteoritic nanodiamonds	33	**34**	*35*	**38**	*44*
Helmholtz free energy	124				
high pressure, high temperature (HPHT) synthetic diamond	80				
synthesis methods	90	*91*			
high-energy particle and beam methods for nanodiamond synthesis	93				
highly oriented pyrolitic graphite (HOPG)	235	*236*			
high-resolution electron energy loss spectroscopy (HREELS)					
hydrogen bonding configuration of NCD films	252	*254*	*255*		
HL component of trapped noble gases	35				
hydrogen					
graphitization of NDs	454	*456*			
impurities in UNCD grain boundaries	299				
surface-bound in meteoritic nanodiamonds	31				
I					
ideal strength	328				
infrared (IR) spectroscopy					
characterization of UNCD particles	389				
main bands for surface groups on NDs	**414**				
interplanetary dust particles (IDPs), origin of nanodiamonds	65	*66*			
interstellar medium (ISM)	24	27			
iron					
catalytic graphitization of NDs	451	*451*	*452*		
isotope ratios	30				

This page has been reformatted by Knovel to provide easier navigation.

Index terms **Links**

K

krypton
in meteoritic nanodiamonds **34** *35* **38** *39* 42 *44*

L

Laplace–Young equation 125 127
large nanocarbon particles, stability of 124 *128*
laser-induced fluorescence (LIF) 186
lubricant–cooling liquids (LCLs) 507
lubricants 504

M

mechanical properties of doped and undoped UNCD 303 328
elasticity and strength experiments 308
SEM image and testing setup *308*
experimental results
size effects and Weibull analysis 316 *317* *319* **320**
stress–strain curves 314 *315* *322*
toughness measurements 319 *321* **322** *323* **324** **325**
Young's moduli and fracture strengths **315**
fractographic analysis 325 *326* *327*
fracture toughness experiments *309* 310 *310* *312* *313* *314*
material characterization 305
SEM image *306*
surface roughness *307*
theoretical strength 327
mechanochemical methods for ND dispersion 532
medical applications of NDs 541 *542*

This page has been reformatted by Knovel to provide easier navigation.

Index terms **Links**

meteors, origin of nanodiamonds 27
formation mechanisms 50
dislocation microstructure 54 *55*
inferred mechanisms 56 **58**
polytypes 55 *57*
twin microstructure 50 *51* *52* *53*
interplanetary dust 65 *66*
isotopic compositions 28
effective diameters and effective shapes *29*
inferred stellar sources 48
primary C, surface-bound H, and trapped N 30 **32**
trapped noble gases 33 *37*
trapped Te, Pd, Ba, and Sr 46
nebular processes 58
nanodiamond abundances in chondrites **62**
new astronomy 68
summary of experimental data 67
microelectromechanical systems (MEMS) 303
microfabrication of UNCD 310
micron-diameter filaments 97
microwave plasma-assisted chemical vapor deposition (MPACVD) 187
reactor and process parameters 188 *189*
minerals, presolar 26
modified neglect of diatomic overlap (MNDO) method 134 135
molecular mechanics (MM) simulations 446 *447*
monocrystalline nanodiamond particles 84 *85*
monocrystalline rods **98** *100*
multiply twinned particles (MTPs) 53
multiwall nantotubes (MWNTs) 12 *13*
nanodiamond synthesis methods 94 102

This page has been reformatted by Knovel to provide easier navigation.

Index terms	Links				
Murchison nanodiamonds					
dislocation microstructure	54				
effective diameters and effective shapes	*29*				
Mypolex™	80				
N					
nanobells	14	*15*			
nanocarbon *see* carbon, nanoscale characteristics					
nanocones	14	*15*			
Nanocrystalline diamond films (NCD)					
crystalline structure of NCD films	246	*247*			
density evolution of films	257	*258*			
deposition systems and deposition parameters	231	*232*	*234*		
evolution and properties of films	235	*236*	*238*	*239*	
formation mechanisms of NCD films	260	*262*			
hydrogen bonding configuration of NCD films	252	*254*	*255*		
hydrogen content of NCD films	251	*252*			
morphological evolution of NCD films	248				
phase composition of NCD films	240	*242*	*243*	*244*	*245*
surface and grain boundary phase composition of NCD films	248	*249*	*250*		
visualization and evolution of NCD films	257	*258*	*259*	*261*	
nanocylinders	**99**				
nanodiamond films (NDFs)	229	266	547		
coordination and orientation	235	*236*	*238*	*239*	
crystalline structure	246	*247*			
density evolution	257	*258*			
deposition systems and deposition parameters	231	*232*	*234*		
formation mechanisms	260	*262*			
hydrogen bonding configuration	252	*254*	*255*		
hydrogen content	251	*252*			
morphological evolution	248				
phase composition	240	*242*	*243*	*244*	*245*

This page has been reformatted by Knovel to provide easier navigation.

Index terms	Links			
nanodiamond films (NDFs) *(Continued)*				
surface and grain boundary phase composition	248	*249*	*250*	*251*
visualization and evolution	257	*258*	*259*	*261*
nanodiamond particles	*85*			
morphology	134	*136*	*139*	*141*
nanodiamonds	79			
biocompatibility	547			
biosensors and medicine	541	*542*		
chemical methods for surface modification	532			
fluorination	535			
gas treatment	534			
oxidation	533			
dispersion	532			
interaction with proteins	540	*540*		
modification with nucleic acids	536	*538*		
thermal transformation products	*36*			
nanofibres	**99**			
nanofoams	14	*15*		
nanohorns	14	*15*		
nanopeapods	14	*15*		
nanoplatelets	103	*103*		
nanoporous carbon	14			
nanorods	**99**	*100*		
morphology	141			
nanostructured carbide-derived diamond	106			
nanotubes	**99**			
nanowhiskers	**98**			
nanowires				
morphology	141	*145*		
near-edge X-ray adsorption fine structure (NEXAFS) spectroscopy	231			
evolution and properties of NCD films	235	*236*	*238*	*239*

This page has been reformatted by Knovel to provide easier navigation.

Index terms	Links				
nebulae					
as sources of meteoritic nanodiamonds	58				
nanodiamond abundances in chondrites	**62**				
negatively curved carbon materials	14				
neon					
in meteoritic nanodiamonds	**34**	*35*	**38**		
nickel plating	484				
wearing tests	**484**				
nitrogen					
doping of UNCD	293				
impurities in UNCD grain boundaries	294	*295*	*297*	*298*	
prevalence in meteoritic nanodiamonds	**47**	*60*	64		
trapped in meteoritic nanodiamonds	31	**32**			
N-methyl-D-aspartate (NMDA) receptors	545				
nobel gases, trapped in meteoritic nanodiamonds	33	*37*			
mechanisms	43				
release profiles	*44*				
nuclear magnetic resonance (NMR) spectroscopy					
characterization of UNCD particles	390				

O

oils	504				
one-dimensional nanodiamond structures, synthesis of	95	**98**	*100*		
onion-like carbon (OLC)	121	*122*	127	406	410
coexistence with bucky-diamond	130	*131*			
graphitization of NDs	457	*457*	*458*	*460*	
model of ND annealing and OLC formation with holes	439	*441*	*442*	*443*	*444*
TEM images	*407*				
optical emission spectroscopy (OES)	185	233			
C_2 Mulliken system	192	*192*	*195*		
C_2 Swan system	196	*197*			
CN violet system	198				
deposition systems and deposition parameters	*234*				

This page has been reformatted by Knovel to provide easier navigation.

Index terms **Links**

oxygen
graphitization of NDs 454 *456*

P

P3 component of trapped noble gases 35
P6 component of trapped noble gases 35
palladium
prevalence in meteoritic nanodiamonds 46 **47**
patents on nanodiamonds in Russia 559 580
applications 573 **574**
composition of matter 570 **571**
methods of DND synthesis 560 **564**
post-synthesis treatments 563 **567**
phase diagrams for stability 118 *119* *120* *121* *122*
phase transformation synthesis methods 94
phase transitions of diamond at nanoscale 405 461
catalytic graphitization by metal clusters 450 *451* *452* *453*
graphitization in presence of oxygen and hydrogen 454 *456*
kinetics of diamond graphitization 422
experimental approaches 423
kinetic parameters for 1370–1860 K temperature range 425 *426* *427* *428* **429**
low-temperature diamond graphitization 439
model of ND annealing and OLC formation with holes 439 *441* *442* *443* *444*
mechanism of diamond graphitization
cleavage energies of diamond planes 433
diamond surface reconstruction 431 *432*
formation of closed curved graphitic structure on diamond surface 445 *447* *449*
graphite/diamond interfaces 436 *437* *438*
shape of diamond particles 434 *435*
OLC and sp^3/sp^2 nanocomposites 457 *457* *458* *460*

This page has been reformatted by Knovel to provide easier navigation.

Index terms **Links**

phase transitions of diamond at nanoscale *(Continued)*
stability of nanocarbons 408
stability of surface species 411
formation of sp^2-bonded carbon 418
onset temperature of graphitization 420
surface groups 411
thermal stability of surface groups 413 **414**
TEM images *407* *409*
phonons 384
heat conductivity 174
transport 175
physical properties of UNCD particles 379 398
characterization methods 380
EELS 391
HRTEM and SEM studies 386
NMR and EPR spectroscopic studies 390
Raman scattering 383 *384*
small-angle X-ray scattering (SAXS) 382 *382*
STM and AFM studies 387 *388*
visible and far-infrared spectroscopic studies 389
X-ray diffraction (XRD) 380 *381*
electronic properties 397
mechanical properties 396
optical properties 397
structure of UNCD particles and aggregation 391
P–T phase diagram for carbon *394*
SEM image *393*
planetary nebulae 24
plasma-assisted synthesis 185 223
$Ar/H_2/CH_4$ microwave discharges 222
electrons and power coupling
efficiency 218 *219*
gas temperature 212 *212*

This page has been reformatted by Knovel to provide easier navigation.

Index terms **Links**

plasma-assisted synthesis *(Continued)*
hydrocarbon species 215 *215* *216* *217* *218*
mechanisms of C_2 formation 220
molecular and atomic hydrogen 213 *214*
other charged species 220 *220* *221*
experimental details
MPACVD reactor and process parameters 188 *189*
spectroscopic diagnostics 190 *190*
fundamentals of plasma diagnostics
optical emission spectroscopy (OES) and broadband absorption spectroscopy (BAS) 191 **193**
plasma modeling 199 *200*
plasma diagnostics 211
C_2 density 209 *210*
gas temperature 207 *209*
typical NCD deposition conditions
deposition and characterization of NCD films 202 *203* *204* *205* *206*
plasma-enhanced chemical vapor deposition (PECVD) 185
polishing applications using UNCD 496 **499** **503**
polycrystalline nanodiamond particles 84 *85*
polyisoprene 488
physical and mechanical properties **489** **490**
polysiloxane polyblock cyclolinear copolymer 491
influence of composite modifiers **492**
polyurethane foam (PUF) 492
presolar minerals 26
proteins, interaction with NDs 540 *540*

R

Raman spectroscopy
characterization of UNCD particles 383 *384*
formation of sp^2-bonded carbon on NDs 418
phase composition of NCD films 240 *242* *243* *244* *245*

This page has been reformatted by Knovel to provide easier navigation.

Index terms **Links**

reactive ion etching (RIE) 97
reducing sphere model 425
restricted Hartree–Fock (RHF) calculations 124
rubbers stable to explosive decompression 494

S

scanning electron microscopy (SEM)
characterization of UNCD particles 386 *393*
scanning tunneling microscopy (STM)
characterization of UNCD particles 387
Scherrer formula 248
schwartzite 14 *15*
secondary ion mass spectroscopy (SIMS) 28
hydrogen content of NCD films 251 *252*
self-consistent charge density functional-based tight-binding (SCC-DFTB) method 275
Selyakov–Scherrer expression 380
shapes of nanodiamonds 81
shock wave production of nanocrystalline diamonds 84
silicon 298
silvering 482
wear resistance **483**
single nucleotide polymorphisms (SNPs) 538
single wall nanotubes (SWNTs) 12 *13*
nanodiamond synthesis methods 95
phase diagram for stability 122
sintered ND composites 107
small nanocarbon particles, stability of 129
small-angle X-ray scattering (SAXS)
characterization of UNCD particles 382 *382*
formation of sp^2-bonded carbon on NDs 419

This page has been reformatted by Knovel to provide easier navigation.

Index terms **Links**

small-area electron diffraction (SAED)
visualization and evolution of NCD films 259 *259*
stability of nanodiamond 117 147
morphologies 134
hybrid nanocarbon materials *145* 146
nanodiamond particles 134 *136* *139* *141*
nanorods and nanowires 141 142 *145*
phase diagrams 118 *119* *120* *121* *122*
theoretical studies 123 134
coexistence of bucky-diamond and other nanocarbon phases 130 *131*
large nanocarbon particles 124 *128*
quasi one-dimensional nanocarbon 132
small nanocarbon particles 129
stardust 25
stars
inferred stellar sources of meteoritic nanodiamonds 48
nucleosynthesis 24
stress 312
stress–strain curves 314 *315* *322*
strontium
prevalence in meteoritic nanodiamonds 46 **47**
super grains 306 325
superdiamond 10
supernovae 23 27
inferred stellar sources of meteoritic nanodiamonds 48
nucleosynthesis models *40*
synthesis methods for nanocrystalline diamond 108
chemical vapor deposition (CVD) methods 92
commercial nanodiamond particulate 84
diamondoids 89
shock waves and other methods 84 *86* 88
high pressure, high temperature (HPHT) methods 90 *91*

This page has been reformatted by Knovel to provide easier navigation.

Index terms **Links**

synthesis methods for nanocrystalline diamond *(Continued)*
high-energy particle and beam methods 93
one-dimensional structures 95 **98** *100*
other methods 94
three-dimensional structures 104
nanostructured carbide-derived diamond 106
sintered ND composites 107
UNCD films 105
two-dimensional structures 102 *103*
zero-dimensional structures 84

T

tellurium
prevalence in meteoritic nanodiamonds 46 **47**
temperature-programmed desorption (TPD) 413 414 416 *417*
thermogravimetric analysis (TGA) 415
three-dimensional nanodiamond structures, synthesis of 104
nanostructured carbide-derived diamond 106
sintered ND composites 107
UNCD films 105
tin plating 482
top-down approaches to nanodiamond synthesis 96
total electron yield (TEY) 235 *236*
transmission electron microscopy (TEM) 28
characterization of UNCD particles 386
formation of sp^2-bonded carbon on NDs 419
visualization and evolution of NCD films 257 *258* *261*
triply periodic minimal surface (TPMS) substances 14
two-dimensional nanodiamond structures, synthesis of 102 *103*
types of nanocrystalline diamond 79 108
shapes 81
synthesis methods 82
chemical vapor deposition (CVD) methods 92

This page has been reformatted by Knovel to provide easier navigation.

Index terms **Links**

types of nanocrystalline diamond *(Continued)*
commercial nanodiamond particulate 84 *86*
high pressure, high temperature (HPHT) methods 90 *91*
high-energy particle and beam methods 93
one-dimensional structures 95 **98** *100*
other methods 94
three-dimensional structures 104
two-dimensional structures 102 *103*
zero-dimensional structures 84

U

ultradispersed detonation diamonds (UDDs) 37 45 50 335
ultrananocrystalline diamond (UNCD)
see also detonation nandiamond
films *13* 79 81
electron transport properties *see* electron transport properties of UCND films
synthesis methods 105
historical perspective 7 **9**
particles *13* 79 *85*
characterization and physical properties *see* physical properties of UNCD particles
detonation methods of production *86* 88
synthesis and properties, theoretical studies 273
carbon dimer growth mechanisms 275
computational methodologies 274
electronic structure of doped UNCD 293
electronic structure of grain boundaries with π bonding 290 *291* *292* *293*
electronic structure 287
grain boundaries 287
growth kinetics model 285 *286*
nitrogen impurities in grain boundaries 294 *295* *297* *298*

This page has been reformatted by Knovel to provide easier navigation.

Index terms **Links**

ultrananocrystalline diamond (UNCD) *(Continued)*
nitrogen in diamond and amorphous carbon 293
other impurities in grain boundaries 298
structure of high-angle twist grain boundaries 288 *289* *290*

V

vibrational density of states (VDOS) of graphite 241
visible spectroscopy
characterization of UNCD particles 389

W

Weibull analysis 316 *317* *319* **320**
whiskers **98**
Wiedermann–Franz law 174

X

xenon
prevalence in meteoritic nanodiamonds **34** *35* 37 *37* **38** *39* *41* *44* *60*
X-ray diffraction (XRD)
characterization of UNCD particles 380 *381*
crystalline structure of NCD films 246 *247*
formation of sp^2-bonded carbon on, NDs 418 419
X-ray reflectivity
density evolution of NCD films 257 *258*

Z

zero-dimensional nanodiamond structures, synthesis of
chemical vapor deposition (CVD) methods 92
commercial nanodiamond particulate 84
diamondoids 89
shock waves and other methods 84 *86* 88
high pressure, high temperature (HPHT) methods 90 *91*

This page has been reformatted by Knovel to provide easier navigation.

Index terms **Links**

zero-dimensional nanodiamond structures, synthesis of *(Continued)*
high-energy particle and beam methods 93
other methods 94
zinc plating 481
corrosion resistance **482**

This page has been reformatted by Knovel to provide easier navigation.

PART 1
OVERVIEW: NATURALLY OCCURRING UNCD AND ITS LABORATORY SYNTHESIS

1 Carbon Family at the Nanoscale

Olga A. Shenderova

International Technology Center, Raleigh, NC, USA

Amanda S. Barnard and Dieter M. Gruen

Materials Science Division and Center for Nanoscale Materials, Argonne National Laboratory, Argonne, IL, USA

Introduction

The science of carbon materials is at an important juncture. The historically independent scientific communities studying graphite-based materials, fullerenes, nanotubes and diamond are merging as their interests overlap at the nanoscale. While the current popularity of carbon nanostructures to a large extent is due to fullerenes and nanotubes, other members of the nanocarbon family are also attracting steadily increasing attention. For confirmation we refer to recent reviews[1–3] and books[4–8] on nanodiamond materials. The recent NATO workshop[8] demonstrated that a keen, world-wide interest has developed over the years in the nanostructured diamond materials. Accordingly, structures, properties, and numerous applications of nanostructured graphite, which belongs to a broad group of so-called new carbon materials, have been recently summarized in a book and a review by Inagaki[9,10]. In parallel, new carbon allotropes are being discovered such as, for example, carbolite, an esoteric chain-like crystalline form of carbon.[11]

Understanding properties of carbon entities at the nanoscale within a unified framework, including the conditions under which one form transforms into another, has become an important issue.[3] The relative stability of various carbon structures with characteristic sizes in the nanoscale region will be considered in Chapter 4 of this book.

In the current chapter, we provide brief historical overviews of the discoveries related to sp^2 and sp^3 nanostructured carbon, provide tentative classification of major carbon structures at the nanoscale, as well as summarize exotic nanocarbons observed to date. The word "nanocarbons" used throughout this chapter is defined as carbon materials produced when either their *size* or their *structure* was controlled at the nanometer scale.[10]

1.1 Historical Overview

While the history of synthetic graphite begins in the 19th century,[12] artificial diamonds were not synthesized until the middle of the 20th century. Since then, both graphite- and diamond-related groups of carbon materials have experienced several waves of renewed interest in scientific communities when new types of materials or synthesis techniques had been discovered. Within the graphite-based group, new materials ("new carbon")[9] such as carbon fibers, glass-like carbons, pyrolitic carbons, etc., were developed in the early 1960s, and found broad industrial applications.[9,10] The most significant, relatively recent application of this class of carbon material is probably lithium rechargeable batteries that use nanostructured graphite anodes, which have made possible portable electronic devices.[9] Within this group of "new carbon" materials, texture on a nanometer scale (based on preferred orientation of anistropic hexagonal layers) plays an important role in their properties. Some of the "new" graphitic materials contain nanostructured units within a complex hierarchical structure such as, for example, carbon fibers consisting of carbon nanotubes in their cores. A new era in carbon materials began in the mid-1980s when the family of buckminsterfullerenes ("buckyballs") was discovered,[13] followed by the discovery of fullerene nanotubules ("buckytubes").[14] The discovery of these structures set in motion a new world-wide boom that seems still to be growing. The fullerene nanotubules and graphite-based materials are inherently connected, and researchers who produced carbon filaments had been unknowingly growing nanotubes decades before Iijima's publication.[14] Some of the related topics, predictions, and discoveries of the carbon cage structures are summarized in Table 1.1 in chronological order.

In the history of the diamond-based carbon group, the successful synthesis of diamond from graphite by high-pressure/high-temperature methods was reported in the 1950s.[15] Low-pressure chemical vapor deposition (CVD) of diamond polycrystalline films was first reported as early as 1911 by von Bolton[16] and then again by Ruff[17] in 1917. This avenue of research went almost unnoticed for many decades, until new advances and methods were developed at the beginning of the 1960s.[18–20] Production of CVD diamond thin films then became more widespread in the 1980s.[21–24,54] The area of the CVD of diamond films experienced several shifts of scientific and funding activity. The interest in nanodiamond has increased in the last few years as research activities related to nanotechnology have grown world-wide, and new synthesis methods of

Table 1.1 Related Topics, Predictions and Discoveries of the Carbon Cage Structures*

Year	Event	Comments	Reference
1960	Production of carbon tubes with graphite layer structures	Arc discharge method, 5 μm in diameter tubes	Bacon [45]
1966	A large hollow cage molecule is suggested	Assumed that the molecule can be fashioned out of graphene	Jones [46]
1970	The soccer ball-shaped C_{60} molecule is suggested		Osawa [47]
1973	Prediction that C_{60} would be stable	Huckel calculations; closed shell electronic configuration is predicted	Bochvar and Galperin [48]
1980	First observation of nanotubes**	Arch discharge method	Iijima [49]
1983	Synthesis of dodecahedrane ($C_{20}H_{20}$)	Molecule with the same symmetry (icosahedral) as C_{60}	Paquette et al. [51]
1984	Report on preferential stability of even-atom carbon clusters, especially of a C_{60} species	Mass spectrometry study on laser-ablated carbon plumes. Abundance of C_{60} species in a spectrum is reported, but any special note is not announced	Rohlfling et al. [52]
1985	Discovery of C_{60}	C_{60} and C_{70} are detected in the mass spectrum of laser-evaporated graphite. C_{60} is named Buckminsterfullerene	Kroto et al. [13]
1990	Fullerene synthesis in large quantities	Process of evaporation of graphite electrodes in an arc discharge	Kratschmer et al. [53]

Table 1.1 Related Topics, Predictions and Discoveries of the Carbon Cage Structures* *(cont'd)*

Year	Event	Comments	Reference
1991	Discovery of multiwall carbon nanotubes	Observation of helical multiwall nanotubules of graphite with closed ends deposited on the negative electrode during the DC arcing of graphite	Iijima [14]
1991	Prediction of hyperfullerenes		Curl and Smalley [55]
1992	Observation of carbon onions	Spherical shells of graphite obtained by heating of nanotubes by the electron beam in a microscope	Ugarte [57]
1993	Discovery of single wall nanotubes	Arc process in the presence of Fe or Co catalytic particles	Iijima et al. [58] Bethune [59]
1994	Fullerenes found in meteorites		[63]
1996	Ropes of single-walled nanotubes	Large-scale production of SWNT by laser ablation method	Smalley group [60]
1998	CVD synthesis of aligned nanotube films	MWNT growth in the presence of catalyst	F Ren et al. [61]
2001	Nanotube single crystals	Ordered single crystals of SWNT of micron sizes	Schlittler et al. [62]

* To a large extent, the historical outline is according to a review by Rao et al.[56]

** In principle, after Iijima's publication in 1991,[14] there were several reports indicating that nanotubes had been observed before[50]. We refer above to one of the well-documented publications.

nanocrystalline[25–29] and ultrananocrystalline[1] diamond films have been discovered.

The new nanocarbon science includes, importantly, the fullerenes, nanotubes, and ultrananocrystalline diamond (UNCD) which constitute an energetically very closely related triad. The discovery of the fullerenes and nanotubes has initiated an exciting new chapter in nanoscience and has been fully documented over the years. The history of the discovery and characterization of UNCD films is much less well known. That discovery rests on a radical departure from traditional diamond CVD synthesis. In 1991, D. M. Gruen proposed the use of the carbon dimer molecule, C_2, produced by fragmentation of fullerenes or hydrocarbons as a growth species for diamond CVD synthesis. Gruen theorized that the highly reactive nature of C_2 would allow direct insertion into the carbon dimer rows of the reconstructed (100) surface of diamond and that growth would occur in the virtual absence of atomic hydrogen.[30] When these ideas were put to the test in 1993, it was found that phase-pure diamond films composed of 3–5 nm randomly oriented crystallites were in fact obtained from fullerenes containing argon microwave plasmas.[31] These films were called ultrananocrystalline diamond films so as clearly to distinguish this new diamond material displaying a set of highly unusual properties from nanocrystalline films with crystallite sizes in the 30–300 nm range produced by conventional diamond CVD methods.

Extensive experimental[32] as well as theoretical work[33] has confirmed that C_2 molecules constitute a highly efficient growth species giving rise to ultrananocrystallinity because of very high secondary renucleation rates. The films are strongly bonded by virtue of carbon rehybridization at grain boundaries composed of about 10% of all the carbon atoms in the material. The films can be rendered highly n-type electrically conducting at ambient temperatures by the simple expedient of adding nitrogen to the synthesis gas mixture.[1] Detailed characterization of the electrical,[34] optical,[35] and mechanical[36] properties of UNCD films shows that this material is potentially useful in MEMS devices,[37] high-temperature rectifying diodes,[38] biosensors,[39] thermoelectrics,[40] etc. The strikingly similar free energies of formation of UNCD and carbon nanotubes (CNTs) suggest that in the presence of a catalyst the simultaneous synthesis of UNCD/CNT self-assembled self-composites can be accomplished.[41] The synthesis of dense, thick films of these composites poses considerable experimental challenges and is now being systematically explored. In the C_2-rich plasmas employed in the synthesis procedure, the complex reactions of the C_2 molecule with nanotube walls are crucial to forming cova-

lent bonds with UNCD crystallites. These aspects, as well as the introduction of a variety of nanotube defects, are being treated by using density functional tight-binding (DFTB) theory with results that promise to have potentially far-reaching consequences for the fabrication of "quantum dots" on "graphitic" quantum wires.[42]

Methods for synthesizing diamond powder in the form of single particles with micro- and nanometer sizes were also invented long ago.[43,44] Micro- and nanosized diamond powder had been synthesized by shock waves in the beginning of the 1960s by the DuPont Corporation, a leader in explosive technology previously applied to other materials. DuPont produced diamond using shock wave compression induced by solid explosive detonation of carbon materials (graphite, carbon black) mixed with metal powder (Ni, Cu, Al, Co). Micron- and nanosized particles, tradenamed Mypolex, have been used for high-precision polishing applications for a long time. In 1999, the Mypolex business was acquired by Microdiamant, a Swiss holding company. Another approach for producing diamond powder is the conversion of carbon-containing compounds into diamond during firing of explosives in hermetic tanks.[44] The history of the discovery of this type of nanodiamond, also known as ultradispersed diamond or detonation nanodiamond, will be described in Chapter 10 of this book. This method was initiated in Russia in the earlier 1960s soon after DuPont's work on shock wave synthesis. Publications in this area at that time were very scarce, with some reports appearing decades after the actual discoveries had been made.[44] Some of the related topics and discoveries of the nanodiamond structures are summarized in Table 1.2 in chronological order.

1.2 Nanocarbon Classification

In principle, different approaches can be used to classify carbon nanostructures. The appropriate classification scheme depends on the field of application of the nanostructures. For example, a classification can be based on an analysis of the dimensionalities of the structures, which in turn are connected with the dimensionality of quantum confinement, and thus is related to nanoelectronic applications. The entire range of dimensionalities is represented in the nanocarbon world, beginning with zero-dimension structures (fullerenes, diamond clusters), and including one-dimensional structures (nanotubes, diamond nanorods), two-dimensional structures (graphite sheets, diamond nanoplatelets), and

Table 1.2 **Discoveries and Other Topics Related to "Nanodiamond" Species**

Year	Event	Comments	Reference
1959	Method to synthesize nanodiamond by applying shock waves to carbon material	Graphite-based source material compressed by propelled metallic plate or by placing carbon around high explosives	De Carli and Jameson [43]
Mid-1960s	Commercialization of the shock wave process by DuPont	Mix of carbon (graphite, carbon black, etc.) with copper for cooling and preventing diamond reversion	
1963	Ultradispersed diamond powder produced by detonation of carbon-containing explosives	Ultradispersed diamond (~4 nm primary particles) formation from carbon of explosion products	Volkov et al. [44]
1987	Nanodiamond particles found in meteorites	Size of interstellar diamond particles ~5 nm	[64]
1994	Conversion of nanodiamond to carbon onions upon annealing	Annealing temperature 1300–1800 K, depending on particle size	Kuznetsov et al. [65]
1994	UNCD films	CVD method with microwave-activated carbon/rare gas plasmas (e.g., CH_4/Ar, C_{60}/Ar). Primary particle size 2–5 nm	Gruen [66]
1996	Conversion of carbon onions to nanodiamond under electron beam irradiation	1.2 MeV, >1024 e cm^{-2}; ~100 dpa, T above 900 K	Banhart et al. [67]

three-dimensional structures (nanocrystalline diamond films, agglomerates, fullerite, nanotube ropes). In a different approach, the scale of characteristic sizes can be introduced as the major criterion for classification. This scheme more naturally allows the consideration of complicated hierarchical structures of carbon materials (carbon fibers, carbon polyhedral particles). A summary based on different shapes and spatial arrangements of elemental structural units of carbon cage structures also provides a very useful picture of the numerous forms of carbon structures at the nanoscale.[68]

In terms of a more fundamental basis for the classification of carbon nanostructures, it would be logical to use a classification scheme based on existing carbon allotropes that is inherently connected with the nature of bonding in macroscopic carbon materials. An interesting discussion of carbon allotropy and a scheme for classifying existing carbon forms are provided in ref. [69]. The classification scheme is based on the types of chemical bonds in carbon, with each valence state corresponding to a certain form of a simple substance. Elemental carbon exists in three bonding states corresponding to sp^3, sp^2, and sp^1 hybridization of the atomic orbitals, and the corresponding three carbon allotropes with an integer degree of carbon bond hybridization are diamond, graphite, and carbyne.[69] All other carbon forms constitute so-called *transitional* forms that can be divided into two big groups. The first group comprises mixed short-range-order carbon forms with more or less arranged carbon atoms of different hybridization states, e.g., diamond-like carbon, vitreous carbon, soot, carbon blacks, etc., as well as numerous hypothetical structures like graphynes and "superdiamond". The second group includes intermediate carbon forms with a non-integer degree of carbon bond hybridization, sp^n. The subgroup with $1 < n < 2$ includes various monocyclic carbon structures. For $2 < n < 3$, the intermediate carbon forms comprise closed-shell carbon structures such as fullerenes, carbon onions and nanotubes, hypothetical tori, etc. The fractional degree of hybridization in this group of carbon structures is due to the curvature of the framework. The value of the suggested scheme is that any form of carbon substance is included in the classification.

A hybridization-based scheme for carbon classification was also suggested by Inagaki[9] considering diamond, graphite, fullerenes, and carbyne as four basic carbon forms. In addition, Inagaki's scheme demonstrates interrelations between organic/inorganic carbon substances at the molecular scale and emphasizes the interdisciplinary nature of carbon nanotechnology, which is based on both materials science and chemistry.

The classification schemes outlined above[9,69] have been combined to classify carbon nanostructures within the general hierarchy of carbon materials[3] (Fig. 1.1). The scheme is based on two major characteristics: the type of carbon atom hybridization and the characteristic sizes of nanostructures. Starting with a description of the bonding nature of carbon atoms, the idea is to analyze how different classes of carbon networks are formed with the increasing characteristic size of a carbon structure. Starting with small organic molecules (inner circle), the hierarchy of carbon materials can be described as an extension of organic molecular species to bulk inorganic all-carbon materials through a variety of carbon entities in the nanoscopic size range. If we consider fullerenes, nanotubes, graphene of finite size, and the currently observed smallest nanodiamond clusters as basic structural units in the carbon nanoworld, prototype molecules can be assigned to these units at the scale of molecules (inner circle). It should be noted, however, that this scheme does not mean that these molecules are involved in the synthesis of the units, rather we would

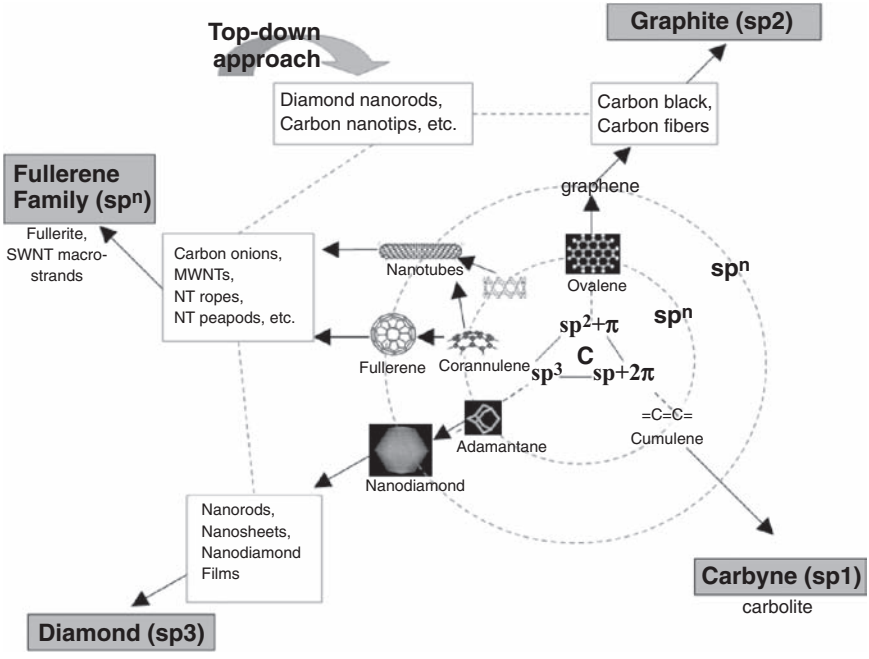

Figure 1.1 Classification of carbon nanostructures. Mark "sp^n" corresponds to intermediate carbon forms with a non-integer degree of carbon bond hybridization.

emphasize topological similarities between organic species and inorganic materials. While the experimentally identified sizes of representative members of sp^2 and sp^n ($2 < n < 3$) families change rather smoothly from the molecular scale (few nanometers) to the scale of nanostructures (tens of nanometers), for sp^3 carbon forms there is currently a gap in sizes between observed molecular forms of the highest diamondoids[70] (~1 nm in size, containing up to 50 carbon atoms) and the smallest nanodiamond particles (~2–3 nm in size, a few thousand carbon atoms). Recently, a hybrid form of nanocarbon with a diamond core and fullerene-like outer shells called bucky-diamond has been suggested and experimentally confirmed in this regime.[71] Typical sizes of basic structural units for nanocarbon are summarized in Table 1.3.

The next structural level in Fig. 1.1, with a corresponding increase of the characteristic sizes, can be considered as consisting of assemblies of the structural units, ranging from simple forms, such as MWNTs or carbon onions (Table 1.3), to more complicated carbon architectures such as carbon black, schwarzites, and agglomerates of nanodiamond particles or UNCD films. An example of a carbon structure with a complex architecture combining two structural units is the recently discovered graphite polyhedral nano- and microcrystals with axial carbon structures having nanotube cores, nanotube-structured tips, and graphitic faces.[76] Finally, at the upper micro/macroscopic scale there is diamond, graphite, carbolite, fullerite, and recently discovered SWNT strands of macroscopic sizes.[77] While the described scheme corresponds to the bottom-up approach of molecular synthesis, it is also necessary to add to the scheme for completeness nanostructures obtained by top-down approaches using different nanopatterning techniques such as, for example, fabrication of diamond nanorods of single crystalline diamond of tens of nanometers in diameter by reactive ion etching combined with microwave plasma treatment of diamond.[78] Obviously, structural units from different families can be combined to form hybrid nanostructures.

Thus one of the comprehensive approaches to classification of carbon nanostructures can be based on combinations of the type of hybridization of carbon bonds within the structure and characteristic size of the structure.

1.3 Exotic Nanocarbons

Beyond the more familiar nanocarbon materials described above, a number of more exotic forms of carbon have also been reported. Exotic

Table 1.3 Range of Geometrical Characteristics of Selected Carbon Entities and Their Simplest Assemblies Observed at the Nanoscale

Schematic view	Entity	Comments, characteristic sizes (experiment)
	Fullerene	Smallest:* C_{20} [72] Most abundant: C_{60} Largest: C_{320} [73]
	Carbon onions	Outer diameter (max): 70 shells [51] Inner diameter: 0.7–1 nm (~C_{60}) [50] From detonation nanodiamond: 5–8 shells [74]
	Single wall nanotubes (SWNTs)	Diameter: typically 1–10 nm [56] Range of diameters: 0.4–100 nm Length: typically 50 nm to 1 μm
	Multiwall nanotubes (MWNTs)	Length: 10 nm to 1 μm Outer diameter: typically 2.5–30 nm [56]
	SWNT ropes SWNT single crystals [62]	Typically 10–100 tubes in a rope (synthesized by laser ablation) Typical length: tens of microns In strands: thousands of NTs
	Single Graphene sheet	Size: 10–15 nm [75] at distance from the substrate: 0.35–0.37 nm
	Diamondoids	Largest molecule currently extracted from crude oil: undecamantane (11 cages) [70]
	UNCD particles	Average size after purification of detonation diamond: 4–5 nm Min size: 1.8 nm [5]
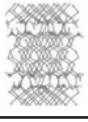	UNCD films	Average grain size: 2–5 nm [1]; sharp grain boundaries (mostly twist GBs)

* The smallest possible fullerene had been produced from dodecahedrane $C_{20}H_{20}$ by replacing the hydrogen atoms with bromine atoms followed by gas-phase debromination.

nanocarbons may adopt a variety of complicated, highly non-spherical shapes. For example, conical shapes such as vertically aligned carbon nanocones (see Fig 1.2c)[79,80] and randomly oriented nanohorns (see Fig 1.2a)[81] have also been observed, as well as aggregates of these structures[82]. These materials typically have a high aspect ratio that is governed by the bonding of the carbon atoms at the tip, although shorter structures have been formed known as nanobells.[83] The structure of the tip has been studied extensively using theoretical and computational methods,[84,85] and may be obtuse due to the inclusion of five-membered rings,[86] or acute with an atom positioned at the apex[87].

This group also contains the so-called nanopeapods,[88,89] in which fullerenes are encapsulated inside a carbon nanotube (see Fig 1.2d)[90]. The nanotube "pod" may contain only one fullerene "pea", forming a bucky-shuttle;[91] or many fullerenes[90] which may even form ordered structures inside[92]. This seemingly straightforward combination of nanocarbon materials also has a number of interesting variations, such as nested nanobells encapsulated along a multi-walled nanotube (see Fig 1.2g),[93] and peapods with many levels of encapsulation such as metallofullerenes inside nanotubes[94].

Another group of exotic nanocarbons are the nanoporous and negatively curved carbon materials. These include the triply periodic minimal surfaces (TPMS)[95] exhibited in schwarzites (see Fig 1.2f),[96–98] carbon nanofoams (see Fig 1.2h),[99] and the theorized hollow diamond[100]. Often compared with zeolites, TPMS structures such as schwarzite are characterized by negative Gaussian curvature (making saddle points necessary in maintaining periodicity) and five- and eight-membered carbon rings.[101] Note that positively curved carbon nanostructures with five- and eight-membered rings are known as haeckelites.[102] Carbon nanofoams, however, are quite different. They are a granular low-density carbon material, with a significant fraction of sp^3 bonding (located on the surface of the clusters) and hyperbolic surfaces akin to schwarzites. Individual clusters are estimated to be 6 nm with a characteristic length of 5.6 ± 0.4 Å; however, at scales >100 nm nanofoam exhibits fractal ordering with an estimated fractal dimension of 2.4.[99]

Although the majority of these exotic nanocarbons are predominantly sp^2 bonded, one exception is the (usually spherical) core–shell hybrid nanocarbon particles known as bucky-diamonds. Although such structures had been observed in one form or another for a number of years, the name bucky-diamond was coined in 2003[71] to describe particles which are characterized by an sp^3-bonded diamond core and a partial or complete sp^2-bonded fullerenic outer shell (see Fig 1.2b)[103].

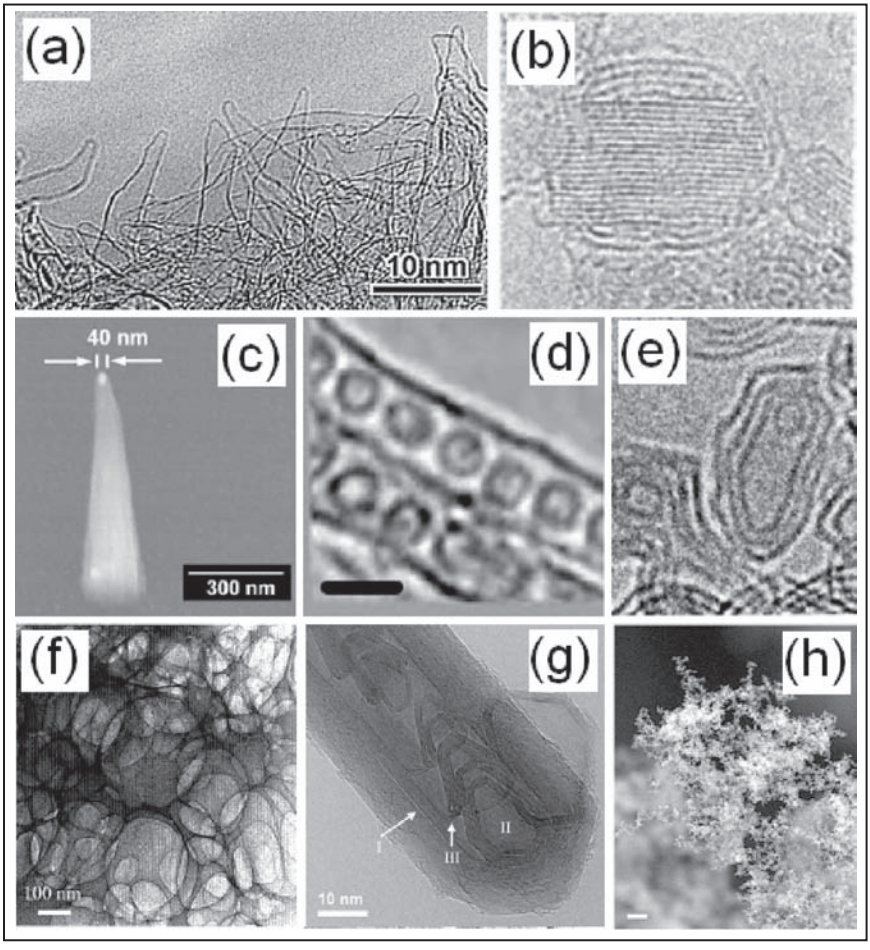

Figure 1.2 Examples of exotic carbon nanomaterials, including (a) nanohorns (reprinted from *Chemical Physics Letters*, **309**, S. Iijima et al., Nano-aggregates of single-walled graphitic carbon nano-horns, 165–170, Copyright (1999), with permission from Elsevier); (b) bucky-diamond with a partial fullerenic shell and a diamond core (reprinted from *Applied Physics A*, in press, A. V. Okotrub et al., Copyright (2004), with permission from Springer-Verlag); (c) a nanocone (reprinted from *Chemical Physics Letters*, **350**, V. I. Merkulov et al., Sharpening of carbon nanocone tips during plasma-enhanced chemical vapor growth, 381–385, Copyright (2001), with permission from Elsevier); (d) nanopeapods (2 nm scale bar) (reprinted from *Chemical Physics Letters*, **390**, A. Gloter et al., Structural evolutions of carbon nano-peapods under electron microscopic observation, 462–466, Copyright (2004), with permission from Elsevier); (e) bucky-shuttle (reprinted figure with permission from Y. K. Kwon et al., *Physical Review Letters*, **92**, 1470, Copyright (1999) by the American Physical Society); (f) carbon schwarzite (reprinted from *Diamond and Related Materials*, **12**, G. Benedek et al., The structure of negatively curved spongy carbon, 768–773, Copyright (2003), with permission from Elsevier); (g) ordered nanobells encapsulated within a multi-walled nanotubes (reprinted from *Chemical Physics Letters*, **367**, Y. A. Kim et al., Cone-type multi-shell in the hollow core of multi-wall carbon nanotube, 537–540, Copyright (2003), with permission from Elsevier); and (h) nanofoam (100nm scale bar) (reprinted from *Applied Physics A*, **69**, A. Rode et al., S755–S758, Copyright (1999), with permission from Springer-Verlag).

Finally, while there have been a number of polytypes of carbon theorized,[104,105] observation of only a handful has been reported in the literature,[106] including the hexagonal 2H (lonsdaleite),[107] 6H,[108] 8H,[109] and rhombohedral 9R[107] and 15R[110]. Some of these structures have been observed as nanoparticles[107,111,106] which are generally imbedded in a matrix. Nanoparticles of n-diamond, i-carbon, and x-diamond have also been observed, where n-diamond is a metallic (fcc) Fm$\underline{3}$m form of carbon with a lattice constant of 3.594 Å,[112–114] i-carbon has the cubic $P2_13$ (or $P4_232$) structure with a lattice constant of 4.32 Å,[112] and x-diamond has the fcc F$\underline{4}$3m structure with a lattice constant of 3.5667 Å[115].

1.4 Conclusion

The new nanocarbon science includes, importantly, the fullerenes, nanotubes, and UNCD which constitute an energetically very closely related triad. This new kind of diamond composed of 2–5 nm crystallites is an exemplar *par excellence* of the profound changes in properties that can accompany the reduction in size of a material to low single-digit nanometer dimensions as will be demonstrated throughout the book. While methods of synthesis of these representative nanocarbons of the triad are well established, the combination of different types of nanocarbons and composites with novel properties is a current experimental challenge and the hybrid carbon nanostructure is one of the major directions in the field. Particularly, the strikingly similar free energies of formation of UNCD and carbon nanotubes suggested that in the presence of a catalyst the simultaneous synthesis of UNCD/CNT self-assembled self-composites can be accomplished. Recently, dense films of UNCD–carbon nanotubes have been synthesized at Argonne Laboratory.

References

1. D. M. Gruen, Nanocrystalline diamond films, *Annu. Rev. Mater. Sci.* **29**, 211–259 (1999).
2. V. Y. Dolmatov, Detonation synthesis ultradispersed diamond: properties and applications, *Russ. Chem. Rev.* **70**, 607–626 (2001).
3. O. Shenderova, V. Zhirnov, and D. Brenner, Carbon materials and nanostructures, *Crit. Rev. Solid State Mater. Sci.* **27**(3/4), 227–356 (2002).
4. V. Yu Dolmatov, *Ultradisperse diamonds of detonation synthesis: production, properties and applications*. St. Petersburg, State Politechnical University, 2003.

5. A. L. Vereschagin, *Detonation Nanodiamonds*, Altai State Technical University, Barnaul, Russian Federation, 2001, in Russian; A. L. Vereschagin, *Properties of Detonation Nanodiamonds*, Barnaul State Technical University Altay Region, 128pp., 2005 (in Russian).
6. V. V. Danilenko, *Synthesis and Sintering of Diamond by Detonation*, Moscow, Energoatomizdat, 2003, in Russian.
7. *Detonation Nanodiamonds and Related Materials*, Bibliography Index, First Issue, Ed. A. Vul, V. Dolmatov, and O. Shenderova, "FIZINTEL", St. Petersburg, 2003.
8. *Ultrananocrystalline Diamond: Synthesis, properties and Applications*, Ed. D. Gruen, A. Vul, and O. Shenderova, NATO Science Series, Dordrecht, Kluwer Academic, 2005.
9. M. Inagaki, *New carbons*, Amsterdam, Elsevier, 2000.
10. M. Inagaki, K. Kaneko, and T. Nishizawa, Nanocarbons – recent research in Japan, *Carbon* **42**, 1401 (2004).
11. *Carbyne and Carbynoid Structures*, Ed. R. B. Heimann, S. E. Evsyukov, and L. Kavan, Dordrecht, Kluwer Academic, 1999.
12. G. Collin, On the history of technical carbon, *CFI – Ceram. Forum Int.* **77**, 28–35 (2000).
13. H. W. Kroto, J. R. Heath, S. C. O'Brien, R. F. Curl, and R. E. Smalley, C-60-buckminsterfullerene, *Nature* **318**, 162–163 (1985).
14. S. Iijima, Helical microtubules of graphitic carbon, *Nature* **354**, 56–58 (1991).
15. See history of the HPHT diamond discovery in: A. S. Barnard, *The Diamond Formula*, Oxford, Butterworth–Heinmann, 2000.
16. W. von Bolton, Uber die Ausscheidung von Kohlenstoft in. Form von Diamant, *Z. Elektrochem.* **17**, 971 (1911).
17. O. Ruff, The production of diamonds. Z. *Anorg. Allgem. Chem.* **99**, 73–104 (1917).
18. A. Rocco, General Electric Memo No. MA-36, Class IV (Aug. 1957).
19. W. G. Eversole, US Patent 3,030,187. Synthesis of diamond, issued 4/17/62 (filed 1958).
20. J. C. Angus, H. A. Will, and W. S. Stanko, Growth of diamond seed crystals by vapor deposition, *J. Appl. Phys.* **39**(29), 15 (1968).
21. B. V. Spitsyn and B. V. Derjaguin, A technique of regrowth of diamond's facet. USSR Patent 339134, filed 10.07.1956, Publ. Bulletin of Inventions, Discoveries and Trade Marks. 1980, No 17. p. 323; B. V. Spitsyn, L. L. Bouilov, and B. V. Deryaguin, Vapor growth of diamond on diamond and another surfaces, *J. Cryst. Growth*, **52**(1), 210–226 (1981).
22. S. Matsumoto, Y. Sato, M. Tsutsumi, and N. Setaka, Growth of diamond particles from methane–hydrogen gas, *J. Mater. Sci.* **17**, 3106 (1982).
23. M. Kamo, Y. Sato, S. Matsumoto, and N. Setaka, Diamond synthesis from gas phase in microwave plasma, *J. Cryst. Growth* **62**, 642 (1983).
24. B. V. Spitsyn, L. L. Bouilov, and B. V. Derjaguin, Diamond and diamond-like films–deposition from the vapor phase, structure and properties, *Prog. Cryst. Growth Charact.* **17**, 79 (1988).
25. S. Sattel, J. Robertson, Z. Tass, M. Scheib, D. Wiescher, and H. Ehrhardt, Formation of nanocrystalline diamond by hydrocarbon plasma beam deposition, *Diamond Relat. Mater.* **6**, 255 (1997).

26. S. S. Proffitt, S. J. Probert, M. D. Whitfield, J. S. Foord, and R. B. Jackman, Growth of nanocrystalline diamond films for low field electron emission, *Diamond Relat. Mater.* **8**, 768 (1999).
27. T. Sharda, T. Soga, T. Jimbo, and M. Umeno, Growth of nanocrystalline diamond films by biased enhanced microwave plasma chemical vapor deposition, *Diamond Relat. Mater.* **10**, 1592 (2001).
28. T. Sharda and T. Soga, A different regime of nanostructured diamond film growth, *J. Nanosci. Nanotech.* **3**, 521 (2003).
29. T. Wang, H. W. Xin, Z. M. Zhang, Y. B. Dai, and H. S. Shen, The fabrication of nanocrystalline diamond films using hot filament CVD, *Diamond Relat. Mater.* **13**, 6 (2004).
30. D. M. Gruen, Conversion of fullerenes to diamond, US Patent 5,209,916 (filed Nov. 25, 1991).
31. D. M. Gruen, S. Liu, A. R. Krauss, and X. Pan, Fullerenes as precursors for diamond film growth without hydrogen or oxygen additions, *Appl. Phys. Lett.* **64**, 1502 (1994).
32. P. Zapol, M. Sternberg, L. A. Curtiss, T. Frauenheim, and D. M. Gruen, Tight-binding molecular-dynamics simulation of impurities in ultrananocrystalline diamond grain boundaries, *Phys. Rev. B* **645**, 454 (2002).
33. S. Bhattacharyya, O. Auciello, J. Birrell, J. A. Carlisle, L. A. Curtiss, A. N. Goyette, D. M. Gruen, A. R. Krauss, J. Schlueter, A. Sumant, and P. Zapol, Synthesis and characterization of highly-conducting nitrogen-doped ultrananocrystaline diamond films, *Appl. Phys. Lett.* **79**, 1441 (2001).
34. O. A. Williams, S. Curat, J. E. Gerbi, D. M. Gruen, and R. B. Jackman, n-type conductivity in ultrananocrystalline diamond films, *Appl. Phys. Lett.* **85**, 1 (2004).
35. P. Achatz, structural, optical and electronic properties of nanocrystalline diamond thin films, Diplomarbeit, Walter Schottky Institute, Techynical University of Munich, May 2005.
36. H. D. Espinosa, B. Peng, B. C. Prorok, N. Moldovan, O. Auciello, J. A. Carlisle, D. M. Gruen, and D. C. Mancini, Fracture strength of ultrananocrystalline diamond thin films – identification of Weibull parameters, *J. Appl. Phys.* **94**, 6076 (2003).
37. H. D. Espinosa, B. C. Prorok, B. Peng, K. H. Kim, N. Moldovan, O. Auciello, J. A. Carlisle, D. M. Gruen, and D. C. Mancini, Mechanical properties of ultrananocrystalline diamond thin films relevant to MEMS/NEMS devices, *Exp. Mech.* **43**, 256 (2003).
38. T. Zimmerman, M. Kubovic, A. Denisenko, K. Janischowsky, O. A. Williams, D. M. Gruen, and E. Kohn, Ultrnanocrystalline/single crystal diamond heterostructure diode, *Diamond Relat. Mater.* **14**, 416 (2005).
39. W. Yang, O. Auciello, J. E. Butler, W. Gai, J. A. Carlisle, J. Gerbi, D. M. Gruen, T. Knickerbocker, T. L. Lasseter, J. N. Russell, Jr., L. M. Smith, and R. J. Hamerts, DNA-modified nanocrystalline diamond thin-films as stable, biologically active substrates, *Nature Mat.* **1** (Nov. 24, 2002).
40. D. M. Gruen, Electron transport and the potential of ultrananocrystalline diamond as a thermoelectric material, Chapter 5 in *Ultrananocrystalline Diamond: Synthesis Properties and Applications*, Ed. O. Shenderova and D. M. Gruen, Norwich, NY, William Andrew, 2006.

41. D. M. Gruen and J. W. Elam, Nanotube-diamond composites, MRS Fall Meeting, Paper Q2.3, December 1–5, 2003.
42. L. A. Curtiss, D. M. Gruen, D. Horner, G. Kedziora, P. Redfern, M. Sternberg, and P. Zapol, Carbon Ad-dimer defects in carbon nanotubes *Phys. Rev. Let.* 96 (7): Art. No. 975506 (2006).
43. P. de Carli and J. Jamieson, Formation of diamond by explosive shock, *Science* **133**, 1821 (1961); P. S. de Carli, US Patent 3,238,019, 1966.
44. K. V. Volkov, V. V. Danilenko, and V. I. Elin, Diamond synthesis from the carbon of detonation products, *Fiz. Goren. Vzriva* **26**, 123–125 (1990) (in Russian).
45. R. Bacon, Growth, structure and properties of graphite whiskers, *J. Appl. Phys.* **31**, 283 (1960).
46. D. E. H. Jones, *The Inventions of Daedalus*, Oxford, W H Freeman, 1982.
47. E. Osawa, Superaromaticity, *Kagaku* **25**, 854 (1970) (in Japanese).
48. D. A. Bochvar and E. G. Galperin, Huckel (4N + 2) rule and some polycondensed systems, *Dokl. Acad. Sci. SSSR* **209**, 610 (1973).
49. S. Iijima, High-resolution electron microscopy of some carbonaceous materials, *J. Microsc.* **119**, 99 (1980).
50. P. Harris, *Carbon nanotubes and related structures*, Cambridge, Cambridge University Press, 1999.
51. L. A. Paquette et al., Total synthesis of dodecahedron, *J. Am. Chem. Soc.* **105**, 5446 (1983).
52. E. A. Rohlfling et al., Production and characterization of supersonic carbon cluster beam, *J. Chem. Phys.* **81**, 3322 (1984).
53. W. Krätschmer, L. D. Lamb, K. Fostiropoulos, and D. R. Huffman, Solid C-60 – a new form of carbon, *Nature* **347**, 354–358 (1990).
54. B. J. Derjaguin and D. V. Fedoseev, Synthesis of diamond at low pressure, *Sci. Am.* **233**, 102 (1975).
55. R. F. Curl and R. E. Smalley, Fullerenes, *Sci. Am.*, 265 (4), 54 (1991).
56. C. N. R. Rao, R. Seshadri, A. Govindaraj, and R. Sen, Fullerenes, nanotubes, onions and related carbon nanostructures, *Mater. Sci. Eng. R* **15**, 209–262 (1995).
57. D. Ugarte, Curling and closure of graphitic networks under electron beam irradiation, *Nature* **359**, 707–709 (1992).
58. S. Iijima and T. Ichihashi, Single-shell carbon nanotube of 1 nm diameter, *Nature* **363**, 603–605 (1993).
59. D. S. Bethune, C. H. Kiang, M. S. DeVries, G. Gorman, R. Savoy, and R. Beyers, Cobalt-catalyzed growth of carbon nanotubes with single-atomic layer walls, *Nature* **365**, 605 (1993).
60. A. Thess, R. Lee, P. Nikolaev et al., Crystalline ropes of metallic carbon nanotubes, *Science* **273**, 483 (1996).
61. Z. F. Ren et al., Synthesis of large arrays of well-aligned carbon nanotubes on glass, *Science* **282**, 1105 (1998).
62. R. R. Schlittler, J. W. Seo, J. K. Gimzewski, C. Durkan, M. S. M. Saifullah, and M. E. Welland, Single crystals of single-walled carbon nanotubes formed by self-assembly, *Science* **292**, 1136–1138 (2001).
63. L. Becker, J. Bada et al., Fullerenes in the 1.85-billion-year-old Sudbury impact structure, *Science* **265**, 642–645 (1994).

64. R. S. Lewis, T. Ming, J. E. Wacker et al., Interstellar diamond in meteorites, *Nature* **326**, 160–162 (1987).
65. V. L. Kuznetsov, A. L. Chuvilin, and Y. V. Butenko, Onion-like carbon from ultra-disperse diamond, *Chem. Phys. Lett.* **209**, 72 (1994).
66. D. M. Gruen, S. Liu, A. Krauss et al., Fullerenes as precursors for diamond film growth without hydrogen or oxygen addition, *Appl. Phys. Lett*. **64**, 1502 (1994).
67. F. Banhart and P. M. Ajayan, Carbon onions as nanoscopic pressure cells for diamond formation, *Nature* **382**, 433 (1996).
68. E. Osawa, M. Yoshida, and M. Fujita, Shape and fantasy of Fullerenes, *MRS Bull*. **19**, 33 (1994).
69. R. B. Heimann, S. E. Evsyukov, and Y. Koga, Carbon allotropes: a suggested classification scheme based on valence orbital hybridization, *Carbon* **35**, 1654 (1997).
70. J. E. Dahl, S. G. Liu, and R. M. K. Carlson, Isolation and structure of higher diamondoids, nanometer-sized diamond molecules, *Science* **299**, 96 (2003).
71. J.-Y. Raty, G. Galli, C. Bostedt, T. W. van Buuren, and L. J. Terminello, Quantum confinement and fullerenelike surface reconstructions in nanodiamonds, *Phys. Rev. Lett.* **90**, 37401 (2003).
72. H. Prinzbach, A. Weiler et al., Gas-phase production and photoelectron spectroscopy of the smallest fullerene, C-20 *Nature* **407**, 60–63 (2000).
73. J. M. Hunter and M. F. Jarrold, Drift tube studies of large carbon clusters: new isomers and the mechanism of giant fullerene formation, *J. Am. Chem. Soc.* **117**, 10317 (1995).
74. V. Kuznetsov and Y. Butenko, Synthesis and properties of nanostructured carbon materials: nanodiamond, onion-like carbon and carbon nanotubes, Ed. Y. G. Gogotsi and I. V. Uvarova, NATO Science Series, Dordrecht, Kluwer Academic, 187, 2003.
75. A. M. Affoune, B. L. V. Prasad, H. Sato, T. Enoki, Y. Kaburagi, and Y. Hishiyama, Experimental evidence of a single nano-graphene, *Chem. Phys. Lett.* **348**, 17–20 (2001).
76. Y. Gogotsi et al., Graphite polyhedral crystals, *Science* **290**, 317 (2000).
77. H. W. Zhu, C. L. Xu, D. H. Wu, B. Q. Wei, R. Vajtai, and P. M. Ajayan, Direct synthesis of long single-walled carbon nanotube strands, *Science* **296**, 884 (2002).
78. E. S. Baik et al., Fabrication of diamond nanowhiskers, *Thin Solid Films* **377**, 295 (2000).
79. Y.-T. Jan, H.-C. Hsieh, and C.-F. Chen, Fabrication of nano-size conic diamond arrays by bias assisted PCVD, *Diamond Relat. Mater.* **8**, 772 (1999).
80. V. I. Merkulov, A. V. Melechko, M. A. Guillorn, D. H. Lowndes, and M. L. Simpson, Sharpening of carbon nanocone tips during plasma-enhanced chemical vapor growth, *Chem. Phys. Lett.* **350**, 381 (2001).
81. S. Iijima, M. Yudasaka, R. Yamada, S. Bandow, K. Suenaga, F. Kokai, and K. Takahashi, Nano-aggregates of single-walled graphitic carbon nanohorns, *Chem. Phys. Lett.* **309**, 165 (1999).
82. D. Kasuya, M. Yudasaka, K. Takahashi, F. Kokai, and S. Iijima, Selective production of single-wall carbon nanohorn aggregates and their formation mechanism, *J. Phys. Chem. B* **106**, 4947 (2002).

83. H.-L. Sun, J.-F. Jia, D. Zhong, Q.-T. Shen, M. Sun, Q.-K. Xue, and E. G. Wang, Scanning tunneling microscopy study of polymerized carbon nanobells: electronic effect and evidence of nitrogen incorporation, *Phys. Rev. B* **66**, 85423 (2002).
84. O. A. Shenderova, B. L. Lawson, D. Areshkin, and D. W. Brenner, Predicted structure and electronic properties of individual carbon nanocones and nanostructures assembled from nanocones, *Nanotechnology* **12**, 191 (2001).
85. S. Berber, Y.-K. Kwon, and D. Tománek, Electronic and structural properties of carbon nanohorns, *Phys. Rev. B* **62**, R2291 (2000).
86. J.-C. Charlier, and G.-M. Rignanese, Electronic structure of carbon nanocones, *Phys. Rev. Lett.* **86**, 5970 (2001).
87. H. Hermann, F. Fugaciu, and G. Seifert, Towards controlled production of specific carbon nanostructures–a theoretical study on structural transformations of graphitic and diamond particles, *Appl. Phys. Lett.* **79**, 63 (2001).
88. B. W. Smith, M. Monthiux, and D. E. Luzzi, Encapsulated C60 in carbon nanotubes, *Nature* **396**, 323 (1998).
89. D. E. Luzzi and B. W. Smith, Carbon cage structures in single wall carbon nanotubes: a new class of materials, *Carbon* **38**, 1751 (2000).
90. B. W. Smith and D. E. Luzzi, Formation mechanism of fullerene peapods and coaxial tubes: a path to large scale synthesis, *Chem. Phys. Lett.* **321**, 169 (2000).
91. Y.-K. Kwon, D. Tománek, and S. Iijima, "Bucky shuttle" memory device: synthetic approach and molecular dynamics simulations, *Phys. Rev. Lett.* **82**, 1470 (1999).
92. A. N. Khlobystov, D. A. Britz, A. Ardavan, G. Andrew, and D. Briggs, Observation of ordered phases of fullerenes in carbon nanotubes, *Phys. Rev. Lett.* **92**, 245507 (2004).
93. Y. A. Kim, T. Hayashi, K. Osawa, M. Endo, and M. S. Dresselhaus, Cone-type multi-shell in the hollow core of multi-wall carbon nanotube, *Chem Phys. Lett.* **367**, 537 (2003).
94. A. Gloter, K. Suenaga, H. Kataura, R. Fujii, T. Kodama, H. Nishikawa, I. Ikemoto, K. Kikuchi, S. Suzuki, Y. Achiba, and S. Iijima, Structural evolutions of carbon nano-peapods under electron microscopic observation, *Chem. Phys. Lett.* **390**, 462 (2004).
95. H. Terrones and A. L. Mackay, From C-60 to negatively curved graphite, *Prog. Cryst. Growth Charact.* **34**, 25 (1997).
96. E. Barborini, P. Piseri, P. Milani, G. Benedek, C. Ducati, and J. Robertson, Negatively curved spongy carbon, *Appl. Phys. Lett.* **81**, 3359 (2002).
97. G. Benedek, H. Vahedi-Tafreshi, E. Barborini, P. Piseri, P. Milani, C. Ducati, and J. Robertson, The structure of negatively curved spongy carbon, *Diamond Relat. Mater.* **12**, 768 (2003).
98. Z. Wang, L. Yu, W. Zhang, J. Han, Z. Zhu, G. He, Y. Chen, and G. Hu, Schwarzite-like carbon entrapped argon bubbles, *Chem. Phys. Lett.* **380**, 78 (2003).
99. A. V. Rode, S. T. Hyde, E. G. Gamaly, R. G. Elliman, D. R. McKenzie, and S. Bulcock, Structural analysis of a carbon foam formed by high pulse-rate laser ablation, *Appl. Phys. A* **69**, 755 (1999).
100. G. Benedek, E. Galvani, S. Sanguinetti, and S. Serra, Hollow diamonds – stability and elastic properties, *Chem. Phys. Lett.* **244**, 339 (1995).

101. H. Terrones and M. Terrones, Curved nanostructured materials, *New J. Phys.* **5**, 126.1–126.37 (2003).
102. H. Terrones, M. Terrones, E. Hernández, N. Grobert, J-C. Charlier, and P. M. Ajayan, New metallic allotropes of planar and tubular carbon, *Phys. Rev. Lett.* **84**, 1716 (2000).
103. A. V. Okotrub, L. G. Bulusheva, V. L. Kuznetsov, A. V. Gusel'nikov, and A. L. Chuvilin, Electronic state of nanodiamond/graphite interfaces, *Eur. Phys. J. D* **34**(1–3), 157 (2005).
104. K. E. Spear, A. W. Phelps, and W. B. White, Diamond polytypes and their vibrational-spectra, *J. Mater. Res.* **5**, 2277 (1996).
105. C. Raffy, J. Furthmüller, and F. Bechstedt, Properties of hexagonal polytypes of group-IV elements from first-principles calculations, *Phys. Rev. B* **66**, 75201 (2002).
106. S. Welz, Y. Gogotsi, and M. J. McNallan, Nucleation, growth, and graphitization of diamond nanocrystals during chlorination of carbides, *J. Appl. Phys.* **93**, 4207 (2003).
107. Y. Lifshitz, X. F. Duan, N. G. Shang, Q. Li, L. Wan, I. Bello, and S. T. Lee, Nanostructure: epitaxial diamond polytypes on silicon, *Nature* **412**, 404 (2001).
108. N. Dubrovinskaia, L. Dubrovinsky, and F. Langenhorst, Synthesis of nanocrystalline diamond and 6H diamond polytype, *Large Meteorite Impacts* 4065 (2003).
109. R. Kapil. B. R. Mehta, and V. D. Vankar, Growth of 8H polytype of diamond using cyclic growth/etch oxy-acetylene flame setup, *Thin Solid Films* **312**,106 (1998).
110. R. Kapil, B. R. Mehta, and V. D. Vankar, Synthesis of 15R polytype of diamond in oxy-acetylene flame grown diamond thin films, *Appl. Phys. Lett.* **68**, 1520 (1996).
111. J. B. Wang, C. Y. Zhang, X. L. Zhong, and G. W. Yang, Cubic and hexagonal structures of diamond nanocrystals formed upon pulsed laser induced liquid-solid interfacial reaction, *Chem. Phys. Lett.* **361**, 86 (2002).
112. J. L. Peng, J. O. Orwa, B. Jiang, S. Prawer, and L. A. Bursill, Nanocrystals of c-diamond, n-diamond and i-carbon grown in carbon-ion implanted fused quartz, *Int. J. Mod. Phys. B* **15**, 3107 (2001).
113. J. O. Orwa, S. Prawer, D. N. Jamieson, J. L. Peng, J. C. McCallum, K. W. Nugent, Y. J. Li, L. A. Bursill, and S. P. Withrow, Diamond nanocrystals formed by direct implantation of fused silica with carbon, *J. Appl. Phys.* **90**, 3007 (2001).
114. B. Wen, T. Li, C. Dong, X. Zhang, S. Yao, Z. Cao, D. Wang, S. Ji, and J. Jin, Study of the stability of n-diamond, *J. Phys.: Condens. Matter* **16**, 2991 (2004).
115. M. Rossi, G. Vitali, M. L. Terranova, and V. Sessa, Experimental evidence of different crystalline forms in chemical-vapor-deposited diamond films, *Appl. Phys. Lett.* **63**, 2765 (1993).

2 Extraterrestrial Nanodiamonds in the Cosmos

Tyrone L. Daulton ‡

Marine Geoscience Division, Naval Research Laboratory, Stennis Space Center, MS, USA

Introduction

Ancient mineral grains of stardust that predate the formation of the solar system are present in the most well-preserved, least altered, and least metamorphosed material that initially formed in our solar system: primitive chondritic meteorites and interplanetary dust particles. Nanometer-sized diamonds are ubiquitous in the matrices of primitive chondrites at up to 1400 ppm of the bulk, often representing a significant component of chondritic carbon. Although the carbon isotopic composition averaged over billions of nanodiamonds is similar to the mean of the solar system, nanodiamonds contain various trapped elements that display isotopic compositions anomalous in comparison to solar compositions. Of these trapped elements, only the isotopically anomalous Xe and Te associated with supernovae provide tenable evidence for a presolar origin for at least a subpopulation of the diamonds. Definitive isotopic evidence of a presolar origin for all or part of the population remains elusive because of the extremely small size of the diamonds. Consequently, the astronomical sources that produced the nanodiamonds and the relative contribution of the sources to the nanodiamond population have not been fully established. Asymptotic giant branch (AGB) carbon stars are a likely source of presolar nanodiamonds based on their pervasive dust production. However, unlike supernovae, the available isotopic evidence can neither support nor eliminate AGB stars as a source. Similarly, the solar nebula should not be neglected as a possible source. Regardless of source, comparative microstructural studies indicate the majority of the nanodiamonds formed by low-pressure vapor condensation. The available data on isotopic compositions, microstructure, and trapped element abundances for

‡ Washington University in St. Louis, Center for Materials Innovation and Department of Physics, St. Louis, MO 63130, USA.

meteoritic nanodiamonds are reviewed in terms of the origin, formation mechanisms, and alteration history of the nanodiamonds.

2.1 Stellar Nucleosynthesis and Presolar Stardust

Nearly all elements heavier then He (collectively considered metals by astronomers) are formed by nucleosynthesis in late-evolutionary-stage stars. The elemental and isotopic compositions of a star depend on the compositions of the star's progenitor protostellar nebula as well as the age and mass of the star. For most of their lives, stars burn H in their core as main sequence stars. When H is depleted in the core, H fusion ceases. At this point, the He-rich core collapses, igniting H burning in a shell surrounding it. Core collapse drives an expansion and cooling of the circumstellar envelope resulting in significant mass loss driven by the solar wind. Stars at this stage of evolution swell as red giants. Strong convective currents transport ("dredge up") nucleosynthesis products from core shells to the outer circumstellar layers, changing the surface composition of these evolving stars. Eventually, the inert He core reaches sufficient temperatures for fusion of He into ^{12}C, and for conversion of some ^{12}C to ^{16}O. Upon depletion of He in the core, fusion ceases in the core and the core–shell structure collapses again. Stellar mass determines the subsequent evolution of stellar nucleosynthesis as well as the depth of the convective envelopes (i.e., dredge-up depth) and consequently the evolution of the elemental/isotopic composition of the outer circumstellar layers. For sufficiently massive stars, core collapse will ignite fusion in the evolving stratified-shell–core structure, ultimately resulting in a further expansion of the circumstellar envelope accompanied by dramatic mass loss. At that point, stars enter the asymptotic giant branch (AGB) phase and form extended ("planetary") nebulae.

Circumstellar envelopes of red giant and AGB stars as well as the ejecta of supernovae become enriched in C, O, and other heavy elements relative to their original main sequence compositions. As circumstellar gases become saturated with heavy elements, expand, and cool, nanometer- to micron-sized particles of stardust condense. The mineral species that condense depend critically on the C/O ratio of the circumstellar gas. This is because the CO molecule readily forms in circumstellar envelopes and is the most strongly bonded diatomic molecule. When the carbon inventory is bound in CO molecules ($C/O < 1$), condensation of silicates dominates. Conversely, when $C/O > 1$, as in carbon stars, condensation of carbonaceous grains dominates.

The death of stars results in the formation of stardust that is transported outward into the interstellar medium (ISM) where it mixes and combines with interstellar gas clouds. Our solar system formed from the collapse of an interstellar gas cloud containing ancient stardust that originated in a variety of stellar environments. During the collapse and evolution of the solar nebula, which began 4.6 billion years ago, a significant fraction of the presolar stardust was reprocessed into new minerals and its original form destroyed. The resulting (solar) material experienced extensive thermal, irradiative, and chemical processing. The most extensive processing occurred in large accreted bodies such as the sun, planets, and their moons where no presolar grains are expected to have survived. However, sufficiently small accreted bodies and those forming in the cold outer solar system would have experienced milder conditions and should contain surviving presolar grains. For instance, asteroidal parent bodies of primitive chondritic meteorites (chondrites) formed early in the evolution of the solar nebula and survived largely unaltered to the present, having experienced only modest thermal alteration since their accretion. Preserved within primitive chondrites are grains of presolar stardust from which the solar system formed, in addition to the first minerals that formed in the solar nebula: chondrules (roughly spherical silicate-rich inclusions); calcium–aluminum-rich inclusions (CAIs); and metal grains. Presolar grains have also been identified in the lesser studied interplanetary dust particles (IDPs) thought to originate from asteroids and comets.

A number of presolar grain species in the form of nanometer- to submicron-sized particles have been isolated from primitive meteorites or observed in IDPs: diamond (3C and 2H polytypes),[1,2] SiC (3C and 2H polytypes),[3–5] graphite,[6] carbide solid solutions of Ti, V, Fe, Zr, Mo, and Ru,[7–11] kamacite (FeNi),[9,11] elemental Fe,[12] titanium oxide,[13] corundum (Al_2O_3),[14] spinel ($MgAl_2O_4$),[15] hibonite ($CaAl_{12}O_{19}$),[16] amorphous silicate glass with embedded metal as well as sulfides,[17,18] pyroxene ($(Mg,Fe)SiO_3$),[18] forsterite (Mg_2SiO_4),[17] olivine ($(Mg,Fe)_2SiO_4$),[18] and silicon nitride.[19,20] Nearly all are high-temperature minerals possessing well-ordered, primary crystal structures consistent with formation within stellar outflows as opposed to low-temperature accretion within the ISM. Stardust is a physical product of distant stellar environments that can be directly studied in the laboratory. Its microstructures provide detailed information on the mechanisms of its formation, the physical conditions at its sources of formation, and the evolution of our solar nebula. Its isotopic compositions identify its sources as well as provide valuable information on stellar nucleosynthesis, stellar evolution, and chemical evolution of our galaxy.

Nanometer-sized diamonds are the most abundant refractory, carbonaceous mineral in chondrites by several orders of magnitude. While there is sufficient evidence to suggest at least some meteoritic nanodiamonds are presolar, the origins of the nanodiamonds remain largely enigmatic because of their nanometer grain size. Although there are a multitude of reviews on presolar grains,[21–41] none discuss nanodiamonds in great depth, except for three short reviews dedicated to that subject[42–44]. The purpose of this chapter is to review the present body of evidence on isotopic compositions, microstructure, and trapped element abundances of meteoritic nanodiamonds in terms of their origins, mechanisms of formation, and alteration history.

2.2 Discovery and Identification of Presolar Minerals

As our protosolar nebula evolved, much of its presolar material, which possessed widely ranging isotopic compositions reflecting particular nucleosynthetic processes that occurred in the different star types at various stages of stellar evolution, was extensively mixed and reprocessed. The resulting solar material became isotopically homogeneous as evident by the uniform isotopic compositions in a large number of elements measured in terrestrial, lunar, Martian, and asteroidal rocks, as well as in the solar photosphere. Mineral grains that have isotopic compositions distinct from the mean compositions of solar system material (i.e., anomalous) in a manner that cannot be produced by physical/chemical mass fractionation, cosmic-ray-induced spallation reactions, or by radioactive decay *in situ* subsequent to the formation of the solar system can be identified as *presolar*. Presolar grains need not have anomalous isotopic compositions in all or any elements, but those that do can be clearly identified as presolar.

In the 1960s, researchers observed that some carbonaceous chondrites contained the noble gases xenon[45] and neon[46] with unusual isotopic compositions that could not be produced from solar isotopic compositions by any known process that occurred in the solar nebula. It was speculated that minerals of presolar origin had astonishingly survived solar system formation as well as the aqueous, thermal, and chemical alteration in asteroidal parent bodies of these primitive meteorites.[47] At that time, the prevailing theory was that material was completely vaporized and homogenized in the hot solar nebula.[48] The discovery of large (4%)

excesses in ^{16}O (an isotope of a major element in CAIs),[49] although later attributed to fractionation effects in the solar nebula,[50] motivated many to seriously consider that the nucleosynthetic record of presolar dust was not completely lost within the first solids that formed in the solar nebula. Subsequent evidence of the survival of presolar dust came from large isotopic anomalies in carbon[51–54] and nitrogen[55]. However, it was the resolute pursuit of the carriers of the isotopically anomalous Ne and Xe noble gas components by a University of Chicago group that ultimately led to the isolation of presolar grains. Because the carrier minerals were unknown, the anomalous noble gases served as tracers in a complicated trial and error sequence of physical and chemical separations. A detailed review is given by Anders (1988).[21] After 20 years of work, the first presolar grains of stardust (diamond, SiC, and graphite) were isolated by chemical dissolution as nearly pure mineral residues (henceforth termed "isolates") and identified.[1,3,4,6] Additional presolar grain species were identified by time-intensive analysis of individual grains in isolates and cross-sectioned specimens.[7–20]

2.3 Origins of Meteoritic Nanodiamonds

Meteoritic nanodiamonds are likely produced in a variety of sources, and several different theories have been put forth for their origins. The important question is what are the actual sources and their relative contribution to the meteoritic nanodiamond population? Supernovae have been suggested as a source based on the presence of isotopically anomalous Xe of supernovae origin, indicating some meteoritic nanodiamonds formed in, or at least were associated with, supernovae. Further, the high abundances of nanodiamonds in chondrites (upwards of 13 to 19% total C inventory, see Section 2.6) suggest a prolific dust source. Although supernovae are the major contributors of gaseous matter to the ISM, they are not the dominant source of condensed dust. This has led to the suggestion that AGB carbon stars may be a dominant source of nanodiamonds based on their pervasive dust production. In addition, the solar nebula has been suggested as a major source of nanodiamonds.[56]

Several mechanisms have been proposed for nanodiamond formation in supernovae. These include: low-pressure condensation, similar to chemical vapor deposition (CVD), in expanding gas ejecta;[57] shock metamorphism of graphite or amorphous-carbon grains driven by high-velocity (grain impact grain) collisions in ejecta shock waves;[58]

annealing of graphite particles by intense UV radiation;[59] and irradiation-induced transformation of carbonaceous grains by energetic ions[60]. In circumstellar atmospheres of carbon stars, nanodiamond condensation by CVD mechanisms has been proposed.[1] Further, CVD would be the likely mechanism for the proposed formation of nanodiamonds in the solar nebula.

2.4 Isotopic Compositions of Meteoritic Nanodiamonds: Stellar Sources

The only physical characteristic that can, in principle, definitively identify the sources of mineral grains (i.e., red giants, AGB stars, supernovae, or solar nebula) is their isotopic composition. Isotopic compositions of individual micron-sized minerals are measured by secondary ion mass spectroscopy (SIMS). In this technique a focused ion beam, incident on a grain, sputters atoms from the surface which are extracted as either individual ions or ionized molecules. The charge/mass ratio of the extracted ions is subsequently measured. The smallest mineral grains that can be isotopically analyzed by the most advanced generation of SIMS instruments, the NanoSIMS, are ~0.1 μm in diameter. This is several orders of magnitude larger than meteoritic nanodiamonds. Meteoritic nanodiamonds have "effective" diameters, defined as the square root of the high resolution (HR)-transmission electron microscopy (TEM) projected cross-sectional area, that range between ≈0.1 and 10 nm with a median of the distribution of 2.58 nm and 2.84 nm for diamonds isolated from the Murchison and Allende carbonaceous chondrites (Fig. 2.1), respectively.[2] This is consistent with earlier, indirect and lower spatial-resolution size measurements by TEM.[61,62]

Presently, there are no instruments capable of measuring the isotopic compositions of an individual nanocrystal. In fact, if such an advanced instrument were developed, the only element in an individual nanodiamond whose isotopic composition could be feasibly measured would be the primary element C. This is because many hundreds of atoms of each element are required for statistically accurate measurements of isotopic compositions, e.g., solar $^{12}C/^{13}C = 89$ and solar $^{14}N/^{15}N = 272$. By comparison, a mean-sized meteoritic nanodiamond contains a mere several thousand C atoms (between 10^3 and 7.5×10^3) and only tens of N atoms (<100), where N is the second most abundant trapped element[63] following surface-bound hydrogen[64]. Since there is only one trapped

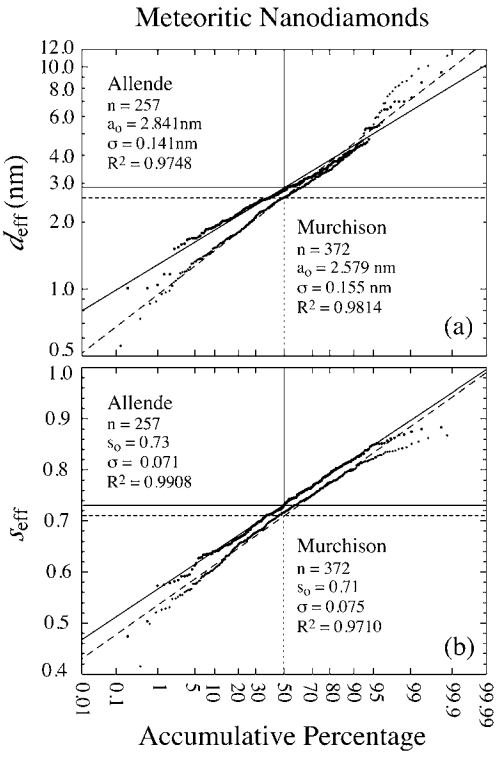

Figure 2.1 Distribution of effective diameters (a) and effective shapes (b) of nanodiamonds isolated from Allende (circles) and Murchison (diamonds) as measured by HR-TEM. Nanodiamonds vary in shape and aspect ratio, therefore an effective diameter was defined as the square root of the projected TEM cross-sectional area and an effective shape was defined as 4π(area/perimeter^2). Least squares fits to log normal, $(2\pi \mathrm{Ln}^2(\sigma))^{-1/2}\exp[-\mathrm{Ln}^2(d_{eff}/a_o)/(2\mathrm{Ln}^2(\sigma))]$, and normal, $(2\pi\sigma^2)^{-1/2}\exp[-(s_{eff} - s_o)^2/(2\sigma^2)]$, distributions are shown: Allende (solid lines) and Murchison (dashed lines). The fitting parameters are given along with the number of measured grains, *n*. Allende nanodiamonds are slightly more spherical, and although their size distributions span the same range, Allende have a factor of ~5 fewer nanodiamonds below 1.5 nm in size than Murchison.

noble gas atom per tens of mean-sized meteoritic nanodiamonds, measurement of isotopic compositions of trapped noble gases in individual nanodiamonds is impossible. Therefore, all isotopic measurements of meteoritic nanodiamonds are of elements/gases extracted from billions of individual diamonds using stepped- combustion and pyrolysis mass spectroscopy.

Although the bulk isotopic composition of C in nanodiamond isolates from acid dissolution residues of chondrites is similar to the solar mean,[63] nanodiamond isolates exhibit various isotopic anomalies in H,[64] N,[63,65,66] Sr,[67] Pd,[68] Te,[68,69] Xe,[1] and Ba[67]. However, only the anomalous Xe and Te associated with supernovae provide tenable evidence for a presolar origin for at least a subpopulation of the diamonds. This is because H is not a reliable indicator of origin because it is loosely bound to diamond surfaces and can be readily altered. Nitrogen isotopic anomalies are problematic, and this will be discussed. Isotopic anomalies in Ba, Sr, and Pd approach marginal levels, being three orders of magnitude smaller than Xe.

2.4.1 Primary C, Surface Bound H, and Trapped N

Isotope ratios are often reported as parts per thousand deviations from a reference standard (stnd) that is chosen to reflect the solar mean, e.g.,

$$\delta({}^{n}X/{}^{m}X) \text{ or } \delta^{n}X = [({}^{n}X/{}^{m}X)/({}^{n}X/{}^{m}X)_{\text{stnd}} - 1] \times 1000‰,$$

where X is the element in question and m is usually the most abundant isotope (or, if not, it is specified when the abbreviated $\delta^{n}X$ notation is used). During stepped combustion of nanodiamond isolates, major release of C (>74% total C) as evolved CO_2 gases is sharply peaked near 500 °C.[63] Bulk ${}^{13}C/{}^{12}C$ compositions of different nanodiamond populations (estimated from the minimum $\delta^{13}C$ measured during major C release) from various carbonaceous, ordinary, and enstatite chondrites are all exceptionally close to the solar mean (Table 2.1), $\delta^{13}C = -32.5‰$ to $-38.8‰$ (${}^{13}C/{}^{12}C = 1/92.0$ to $1/92.6$, where solar ${}^{13}C/{}^{12}C = 1/89$).[63] Although the nearly solar C isotopic composition of meteoritic nanodiamonds is consistent with a solar nebular origin, individual nanodiamonds could possess diverse ${}^{12}C/{}^{13}C$ compositions and their ensemble average from all sources simply mirrors the solar mean. For example, the majority of individually measured presolar SiC grains of AGB origin (>98% SiC population) exhibit a range of C isotopic compositions between $10 \leq {}^{12}C/{}^{13}C \leq 100$, with a mean ${}^{12}C/{}^{13}C \approx 60$ ($\delta^{13}C \approx 483‰$).[20,70,71] The entire SiC population has a mean ${}^{12}C/{}^{13}C \approx 30$ ($\delta^{13}C = 1967‰$) because it includes supernovae-formed SiC which can exhibit strong enrichments in ${}^{13}C$.[20,70,71] These differences suggest that C in nanodiamonds is more rep-

resentative of all the different stellar sources that contributed C to the solar nebula than that of the C in SiC.

The most abundant non-primary element in nanodiamonds is H at concentrations between 10 and 40 at.% as measured for nanodiamonds isolated from the carbonaceous chondrites Allende and Murray.[64] Electron energy loss spectroscopy (EELS) studies of Allende and Murray nanodiamonds suggest H sites are located on the diamond surfaces. Nanodiamonds have a significant fraction of their atoms near the surface (e.g., a 3 nm spherical diamond has 35% of atoms within 0.2 nm of its surface). The plasmon excitation of meteoritic nanodiamonds measured by EELS was shown to fit well with dynamic effective medium analysis models of nanodiamonds with amorphous-C hydrogenated surfaces.[72] In further support, infrared spectra of Allende nanodiamonds exhibit absorption bands attributed to —CH and carboxyl groups (—COOH) on the surface.[62]

Surface-bound H is enriched in deuterium with $\delta^2H = 180 \pm 11‰$ (Allende) and $284 \pm 51‰$ (Murray), corresponding to $^1H/^2H = 5364$ to 4929, respectively, where solar $^1H/^2H = 6420.5$.[64] However, the original deuterium enrichments are likely much higher because a portion of the surface H was altered undoubtedly by nebular and parent-body processes as well as acid dissolution used to isolate the nanodiamonds from the host chondrites. For example, titration experiments indicate several percent of the total H is acidic ($H^+/C = 7 \times 10^{-3}$) presumably in the form of —COOH arising from the acid dissolution treatments.[62] Although surface-bound H can readily be altered and is not a reliable indicator of the source of the carrier grains, the surviving deuterium excess points toward a presolar origin.

The second most abundant trapped element in meteoritic nanodiamonds is N at concentrations an order of magnitude lower than that of H. Nitrogen concentrations vary greatly, ranging between 1800 and 13000 ppm by mass for nanodiamond populations isolated from different chondrites (Table 2.1).[63] During stepped combustion of nanodiamond isolates, a labile C and N component of roughly solar composition is released at low temperature (200–400 °C) prior to the major release of N (Table 2.1).[63] Labile C is marginally more ^{13}C rich and closer to solar composition than that of the bulk nanodiamonds. The labile component varies greatly between nanodiamond populations from different chondrites: ≈3% (Krymka) to 35% (Tieschitz) of the total N released and ≈1% (Murchison) to 26% (Inman) of the total C released (Table 2.1). The labile C and N might reside in the finest grain fraction of the diamonds, on diamond surfaces, or in an impurity present as an amorphous phase.

Table 2.1 C and N Isotopic Compositions of Meteoritic Nanodiamonds (adapted from Russell et al. (1996)[63])

Chondrite Meteorite	Class[a]	Bulk C/N	Lable Component 200–400 °C Release				Bulk Component[b] >400 °C Release	
			% of Total C Released	$\delta^{13}C$ (‰)	% of Total N Released	$\delta^{15}N$ (‰)	$\delta^{13}C$ (‰)	$\delta^{15}N$ (‰)
Orgueil	CI1	130 ± 8	1.3	–28.9	3.7	–75.0	–38.5 ± 0.1	–337.0 ± 0.8
Cold Bokkeveld	CM2	110 ± 8	6.6	–26.1	3.8	–74.3	–37.8 ± 0.1	–350.4 ± 1.0
ALH 83100	CM2	112 ± 9	7.5	–27.2	3.0	–107.2	–38.8 ± 0.1	–346.0 ± 2.2
Murchison	CM2	135 ± 14	1.2	–28.9	14.6	–58.6	–38.2 ± 0.1	–348.4 ± 1.0
Allende	CV3	287 ± 90	10.2	–30.5	13.1	21.8	–35.5 ± 0.1	–359.5 ± 0.8
Vigarano	CV3	290 ± 78	7.0	–26.3	20.1	15.3	–35.1 ± 0.1	–294.1 ± 2.7
Efremovka	CV3	342 ± 97	–	–	10.6	–7.4	–	–305.0 ± 3.0
Krymka	LL3.1	103 ± 23	5.1	–28.3	2.9	–55.0	–37.3 ± 0.1	–347.4 ± 2.8
Adrar 003	LL3.2	75 ± 1	5.8	–24.5	3.4	–18.0	–37.3 ± 0.1	–311.2 ± 3.0
Inman	L3.4	342 ± 83	26.0	–28.7	13.6	–16.0	–32.5 ± 0.1	–342.4 ± 1.2
Tieschitz	H3.6	555 ± 158	–	–	34.6	–5.8	–	–247.4 ± 2.3
Indarch	EH4	242 ± 32	12.3	–25.4	14.4	–20.5	–37.0 ± 0.5	–354.4 ± 0.8

"–" indicates not measured.

[a] For a description of meteorite classes and petrologic type see refs. [121,122].

[b] Minimum value measured during release of main component.

Further, the labile N may be terrestrial, atmospheric N absorbed to grain surfaces. Regardless of its source and carrier, the labile N is not representative of the bulk of the main meteoritic nanodiamond population.

The inferred $\delta^{15}N$ isotopic composition for the main nanodiamond mass (>74% total C) ranges from −247.4‰ (Tieschitz) to −359.5‰ (Allende), corresponding to $^{14}N/^{15}N$ = 361.4 to 424.7, respectively (Table 2.1).[63] These values correspond to the minimum $\delta^{15}N$ measured for evolved N_2 gases during major N release (>65% total N). Solar $^{14}N/^{15}N$ is generally estimated from terrestrial atmospheric N_2 gases ($^{14}N/^{15}N$ = 272).[73] This estimation is consistent with a number of other measurements: N in the solar wind ($^{14}N/^{15}N$ = 200 ± 55) measured by the US Solar and Heliospheric Observatory (SOHO) spacecraft;[74] atmospheric N_2 of Venus ($^{14}N/^{15}N$ = 272 ± 54) measured by the US Pioneer Venus Multiprobe spacecraft;[75] and N extracted from ALH84001 ($^{14}N/^{15}N$ = 276.3 to 276.8) and Chassigny ($^{14}N/^{15}N$ = 270.1 to 272.5) Martian meteorites[76]. However, Martian atmospheric N_2 measured by the US Viking series of spacecraft is distinctly heavy, $^{14}N/^{15}N$ = 165 ± 17.[77] Mass spectrometry measurements of a larger reservoir, the atmosphere of Jupiter, by the US Galileo Probe spacecraft yield $^{14}N/^{15}N$ = 435 (+65, −50), suggesting that solar $^{14}N/^{15}N$ may actually be larger than that estimated from the terrestrial planets[78] and within the range of meteoritic nanodiamonds. This draws into question whether the N isotopic composition of meteoritic nanodiamonds is actually anomalous compared to solar compositions and is of a presolar origin. Analysis of recovered solar wind N that was implanted in collectors of the US Genesis spaceprobe may answer this question. At the very least, N in meteoritic nanodiamonds appears anomalous compared to inner solar system (terrestrial) planetary reservoirs.

2.4.2 Trapped Noble Gases

All five stable noble gases (He, Ne, Ar, Kr, and Xe) are present in meteoritic nanodiamond isolates.[79] Noble gas concentrations are very high and are dominated by He (Table 2.2), ranging between 2.28×10^{-2} and 6.14×10^{-2} ccSTP/g-diamond (or 1.2×10^{-5} and 3.3×10^{-5} noble gas atoms per C) for nanodiamond populations isolated from different chondrites.[80] In comparison, the most gas-rich natural specimens known to date are lunar fines that have solar-wind-implanted He at concentrations of 0.1–1.24 ccSTP/g.[81,82] Nevertheless, despite the high trapped-gas content in meteoritic nanodiamonds, there is only one noble gas atom per tens of diamonds because of the nanometer size of the diamonds.

Table 2.2 Trapped Noble Gas Abundances in Meteoritic Nanodiamond Isolates (adapted from Huss and Lewis (1994)[80])

Chondrite and Class[a]	Reference Isotope													
	^{4}He (10^{-4} cc/g)			^{22}Ne (10^{-8} cc/g)		^{36}Ar (10^{-8} cc/g)			^{84}Kr (10^{-8} cc/g)			^{132}Xe (10^{-8} cc/g)		
	P3	HL[b]	P6[b]	P3	(HL + P6)[c]	P3	HL	P6	P3	HL	P6	P3	HL	P6
Orgueil CI1	179 ± 40	435 ± 43		243 ± 180	830 ± 107	13854 ± 428	1000 ± 289	529 ± 162	100.96 ± 2.46	8.30 ± 0.61	2.11 ± 0.68	34.42 ± 0.96	14.00 ± 0.42	1.31 ± 0.08
Kainsaz CO3.1	30 ± 18	222 ± 19		53 ± 67	981 ± 70	849 ± 69	794 ± 53	962 ± 77	3.49 ± 0.36	8.82 ± 0.24	2.88 ± 0.35	1.39 ± 0.07	19.34 ± 0.41	2.60 ± 0.10
Allende CV3	123 ± 37	175 ± 37		81 ± 248	1089 ± 149	181 ± 18	1014 ± 62	428 ± 60	0.83 ± 0.33	9.52 ± 0.23	0.53 ± 0.30	0.27 ± 0.15	22.15 ± 0.48	2.69 ± 0.16
Leoville CV3	54 ± 22	241 ± 23		111 ± 62	948 ± 66	2032 ± 142	731 ± 69	948 ± 128	9.61 ± 0.53	8.96 ± 0.28	2.96 ± 0.49	3.17 ± 0.12	19.31 ± 0.41	2.67 ± 0.11
Vigarano CV3	16 ± 17	248 ± 19		141 ± 121	830 ± 74	938 ± 76	752 ± 53	952 ± 83	2.78 ± 0.32	7.94 ± 0.22	3.79 ± 0.32	1.56 ± 0.10	16.93 ± 0.37	1.91 ± 0.11
Semarkona LL3.0	126 ± 32	406 ± 33		237 ± 93	775 ± 59	5705 ± 184	801 ± 110	762 ± 110	35.57 ± 0.96	8.18 ± 0.26	3.88 ± 0.56	15.33 ± 0.32	16.00 ± 0.34	1.75 ± 0.07
Bishunpur LL3.1	78 ± 24	211 ± 25		126 ± 31	854 ± 34	2845 ± 126	644 ± 73	870 ± 104	12.79 ± 0.56	7.79 ± 0.20	4.11 ± 0.50	5.59 ± 0.13	17.40 ± 0.36	2.26 ± 0.13
M. Madaras L3.5	21 ± 12	212 ± 18		27 ± 99	934 ± 61	827 ± 72	697 ± 50	1042 ± 81	2.98 ± 0.35	8.35 ± 0.23	3.61 ± 0.35	1.48 ± 0.08	18.06 ± 0.38	2.73 ± 0.11
Tieschitz H3.6	41 ± 13	205 ± 16		13 ± 42	1063 ± 33	736 ± 73	838 ± 43	1263 ± 82	2.32 ± 0.41	9.17 ± 0.22	3.74 ± 0.42	1.23 ± 0.07	20.92 ± 0.43	2.78 ± 0.10
Indarch EH4	15 ± 7	213 ± 9		3.4 ± 1.6	1153 ± 24	112 ± 12	973 ± 53	324 ± 51	0.43 ± 0.13	11.27 ± 0.27	0.33 ± 0.13	0.25 ± 0.05	26.25 ± 0.55	4.23 ± 0.11

All gas concentrations are at standard temperature and pressure (STP) and normalized to 1 gram of diamond.

[a] For a description of meteorite classes and petrologic type see refs. [121,122].

[b] He–P6 isotopic composition is unknown and He–P6 abundance could not be estimated. The measured He–HL component might contain He–P6.

[c] Ne–HL and P6 components could not be separately resolved.

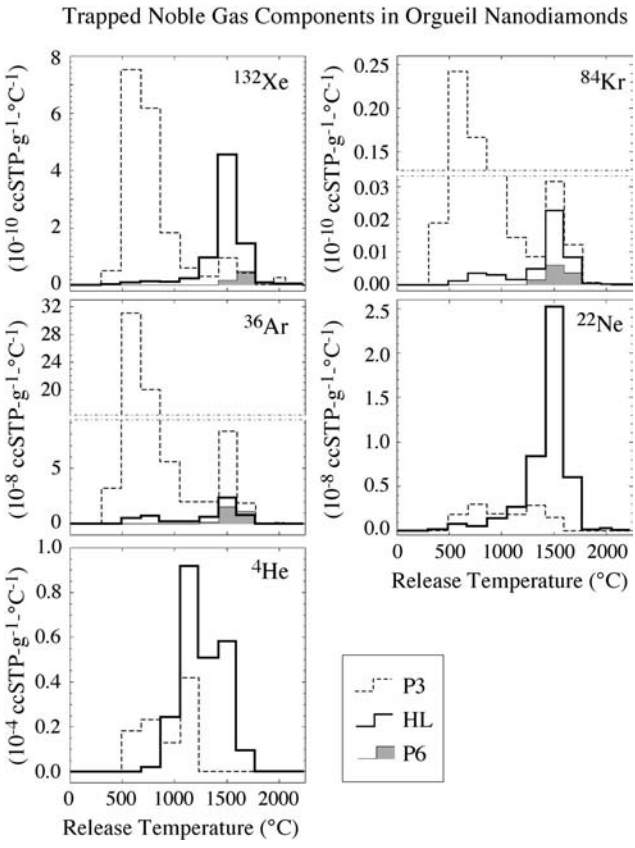

Figure 2.2 Release patterns for the P3, HL, and P6 noble gas components during stepped pyrolysis as a function of temperature for Orgueil nanodiamonds. The plotted Ne–HL component is actually a mixture of Ne–HL and Ne–P6. (Adapted from ref. [80].)

Noble gases occur in three isotopically distinct trapped-gas components (termed P3, HL, and P6) which are released from the meteoritic nanodiamonds at different temperatures during stepped pyrolysis (Fig. 2.2). The P3 component is released only at low temperature (200–900 °C), presumably from surface sites, and the HL component is released only at high temperature (1000–1600 °C), presumably from bulk sites.[79] The P6 component (smaller volumetrically than the P3 component) is not completely separated by stepped pyrolysis from the HL component and is released at slightly higher temperatures than HL gases.

The relative abundances of the P3, HL, and P6 gases in different meteoritic nanodiamond populations vary (Table 2.2). The more labile P3 gases are lost relative to the HL gases in nanodiamonds isolated from chondrites that experienced high levels of thermal metamorphism (see Section 2.6).[80] Further, the HL gas content per gram of diamond increases by up to 50% for the most P3 gas-depleted nanodiamonds isolated from highly metamorphosed chondrites.[79] Such an increase in HL concentration would occur if the P3 carriers lacked exotic HL gases and were preferentially transformed.[23] In laboratory TEM studies, Murchison nanodiamonds heated to 900 °C that lost most of their P3 gas component but still retained their HL component were largely (but not completely) transformed to nanometer-sized, concentric graphite onion structures (Figs. 2.3(a) and (b)).[83] Thermal transformation of ~4 nm diameter nanodia-

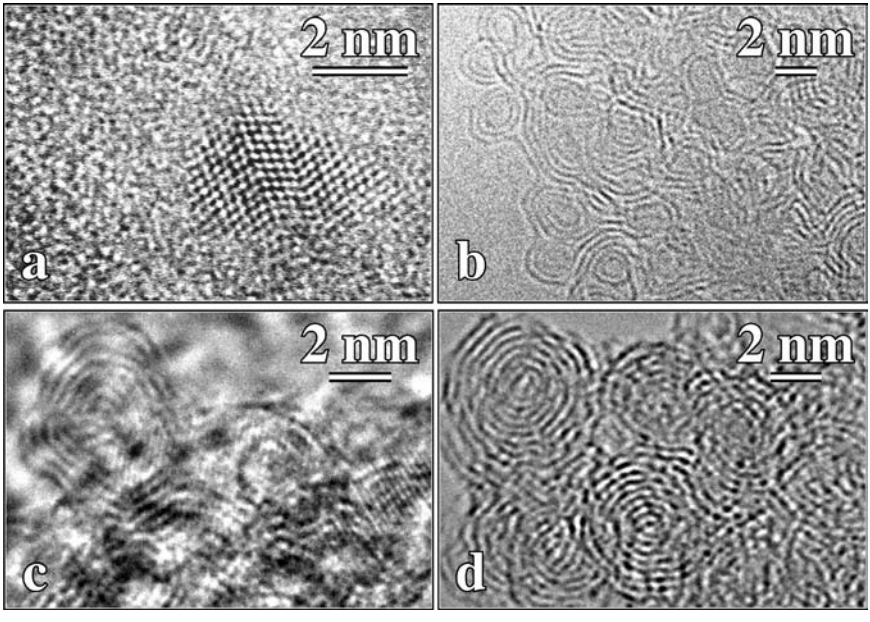

Figure 2.3 Nanodiamonds and their thermal transformation product (graphitic onions): (a) Murchison nanodiamond; (b) transformation product of Murchison nanodiamonds annealed at 900 °C which is below the Xe–HL release temperature; (c) transformation product of shock-synthesized, ultradispersed detonation diamonds (UDDs) annealed at 900 °C; (d) transformation product of UDDs annealed at 1500 °C. In (c), lattice fringes from non-transformed nanodiamonds can be seen superimposed on the lattice fringes of graphitic onions. (Images (a) and (b) courtesy of A. Braatz, F. Banhart, Th. Henning, and U. Ott.)[83]

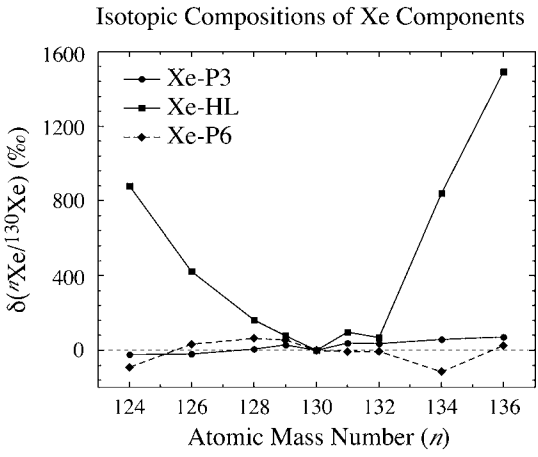

Figure 2.4 Isotopic compositions estimated for the pure Xe–P3, Xe–HL, and Xe–P6 components released from meteoritic nanodiamond isolates (Table 2.3), given as $\delta(^{n}Xe/^{130}Xe)$, where n is the stable isotope mass number. Since ^{130}Xe is shielded and is not produced by *p*- and *r*-processes, it can be assumed to entirely reside in the normal component of HL. Hence, ^{130}Xe is used as the reference isotope. The delta values are normalized such that $\delta(^{n}Xe/^{130}Xe) = 0$ corresponds to the isotopic composition of the solar wind that was implanted into lunar fines (BEOC-12).[82] The Xe–P6 isotopic composition is not well constrained, and the estimation of Xe–P6 that has nearly solar composition is shown.

monds that were formed by shock processes in detonation events (known as ultradispersed detonation diamonds, UDDs) has also been studied. Annealing in vacuum at 700 °C was sufficient to transform some UDDs to graphite onions, perhaps initiated by amorphization, and at 1500 °C most UDDs were transformed (Figs. 2.3(c) and (d)).[84]

Noble gases in the P3 component have isotopic compositions very similar to, but distinct from, the solar wind and the meteoritic P1 component (Fig. 2.4, Table 2.3).[79] The P1 component is associated with solar nebula products and is considered representative of solar gases. The P6 component is believed similar to P3 and P1, although its isotopic composition is poorly constrained and it could be isotopically anomalous ("exotic").[79] In contrast, noble gases in the HL component deviate significantly from solar compositions and are isotopically anomalous (Fig. 2.4, Table 2.3).[79]

The most important noble gas is the isotopically anomalous Xe that occurs in the HL component. Termed Xe-HL, this gas is substantially enriched (by factors of 2) in both its heaviest (Xe–H: ^{134}Xe and ^{136}Xe) and

Table 2.3 Isotopic Compositions of Noble Gas Components in Meteoritic Nanodiamonds (adapted from Huss and Lewis (1994)[79])

Component	Isotopic Composition							
	$^{3}He/^{4}He$							
He–Solar[a]	0.000159 (4)							
He–P3	0.000135 (10)							
He–HL	0.000170 (10)							
	$^{20}Ne/^{22}Ne$	$^{21}Ne/^{22}Ne$						
Ne–Solar[a]	10.7 (2)	0.0294 (10)						
Ne–P3	8.910 (57)	0.029 (1)						
Ne–(HL+P6)	8.500 (57)	0.036 (1)						
	$^{38}Ar/^{36}Ar$	$^{40}Ar/^{36}Ar$						
Ar–Solar[a]	0.1890 (7)							
Ar–P3	0.1900 (10)	<0.03						
Ar–HL	0.2270 (30)	<0.08						
	$^{78}Kr/^{84}Kr$	$^{80}Kr/^{84}Kr$	$^{82}Kr/^{84}Kr$	$^{83}Kr/^{84}Kr$	$^{86}Kr/^{84}Kr$			
Kr–Solar[b]	0.0059 (1)	0.0389 (2)	0.2005 (8)	0.2009 (7)	0.3050 (7)			
Kr–P3	0.0065 (10)	0.0399 (4)	≡0.2035	0.2036 (5)	0.3111 (6)			
Kr–HL	0.0043 (10)	0.0308 (10)	≡0.1600	0.1993 (10)	0.3603 (18)			
Kr–P6[c]	0.0060	0.0385 (8)	≡0.2035	0.2017 (10)	0.3130 (30)			
	$^{124}Xe/^{132}Xe$	$^{126}Xe/^{132}Xe$	$^{128}Xe/^{132}Xe$	$^{129}Xe/^{132}Xe$	$^{130}Xe/^{132}Xe$	$^{131}Xe/^{132}Xe$	$^{134}Xe/^{132}Xe$	$^{136}Xe/^{132}Xe$
Xe–Solar[b]	0.00478 (1)	0.00427 (2)	0.0831 (5)	1.048 (4)	0.1650 (4)	0.8228 (28)	0.3694 (16)	0.2999 (13)
Xe–P3	0.00451 (6)	0.00404 (4)	0.0806 (2)	1.042 (4)	0.1591 (2)	0.8232 (10)	0.3770 (10)	≡0.3100
Xe–HL	0.00842 (9)	0.00569 (8)	0.0905 (6)	1.056 (2)	0.1544 (3)	0.8442 (13)	0.6361 (13)	≡0.7000
Xe–P6[c]	0.00438 (25)	0.00444 (28)	0.0890 (20)	1.114 (8)	0.1660 (11)	0.8214 (47)	0.3291 (50)	≡0.3100

Parentheses represent the errors for the decimal of the least significant digit.

[a] Estimated from meteoritic P1 gas component.

[b] Estimated from the measurement of implanted solar wind in lunar fines, BEOC 12001, ref. [81].

[c] Estimated assuming the component is isotopically normal.

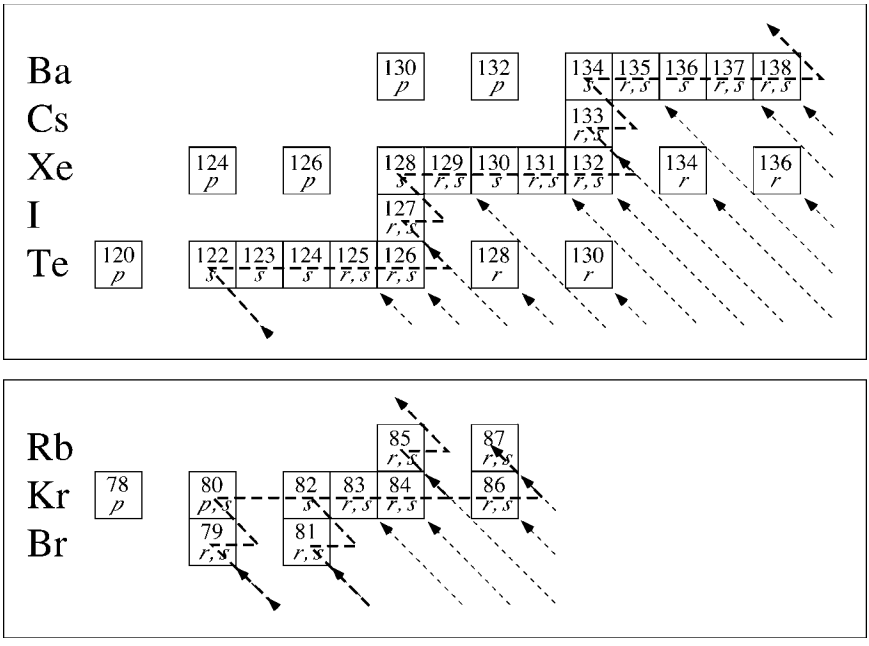

Figure 2.5 Chart of stable isotopes near Xe and Kr. Isotopes are indexed by mass number and the nucleosynthesis process(es) which synthesized the isotope (see text for description) are represented by the letter(s). The *s*-process path through the Xe and Kr regions (zig-zag dashed line) and *r*-process paths (dashed diagonal line) are shown. In the *s*-process, nuclides not on the *s*-process path are destroyed by neutrons and not replenished. The Kr *s*-process path branches at ^{85}Kr. If ^{85}Kr decays (10.8 year half-life) prior to a subsequent neutron capture, ^{85}Rb rather than ^{86}Kr will be produced.

lightest (Xe–L: ^{124}Xe and ^{126}Xe) isotopes with respect to solar Xe.[1,79,80] The light and heavy nuclides are believed to form by explosive nucleosynthesis in supernovae (Fig. 2.5); Xe–L nuclides through the *p*-process (photodisintegration or proton capture) and Xe–H nuclides through the *r*-process (rapid neutron capture) or intermediate to an *r*-process as in a short neutron burst.[85–88] Isotopic compositions predicted by nucleosynthesis models differ from Xe–HL and suggest Xe–HL is an intimate mixture of supernovae ("exotic") Xe with upwards of a factor of 9 greater amount of isotopically solar ("normal") Xe (Fig. 2.6(a)).[79] The Xe–HL component shows little variation in isotopic composition (i.e., Xe–H/Xe–L ratio), either in temperature steps during release (Fig. 2.7(a)) or between nanodiamond populations from different host meteorites (Fig. 2.7(b)).[79]

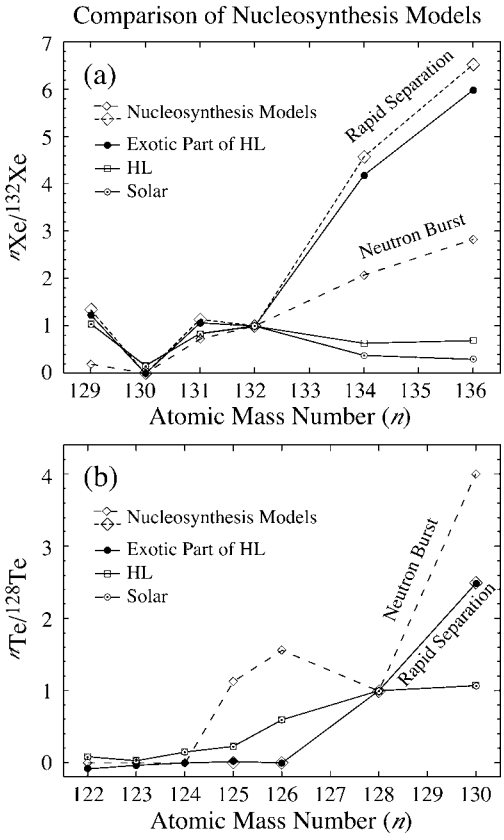

Figure 2.6 Supernovae nucleosynthesis model predictions of (a) Xe and (b) Te isotopic compositions. The neutron burst model[87] (small diamonds) and *r*-process with rapid separation[88] (large diamonds) are compared to the exotic part of (a) Xe–HL and (b) Te–H carried by meteoritic nanodiamond isolates. The exotic part of Xe–HL and Te–H are inferred by assuming all ^{130}Xe and ^{124}Te are in a solar component which is subtracted. Also shown are the as-measured (a) Xe–HL and (b) Te–H (squares), from meteoritic nanodiamonds, which are each an admixture of an exotic and normal component. Solar compositions of Xe and Te (sun symbol) are also shown. The Te model predictions for the *r*-process with rapid separation were provided by B. Meyer and correspond to a separation time of 1544 s which differs somewhat from that predicted by Ott (1996)[88].

Although variations in the amount of Xe–L relative to Xe–H in chondrites have been reported,[89,90] subsequent measurements have failed to confirm these variations.[79,80,91,92] Further, laboratory attempts to isolate the Xe–HL carriers, separate the carriers of Xe–L and Xe–H, and selectively release a particular Xe component from its respective carrier have either failed or

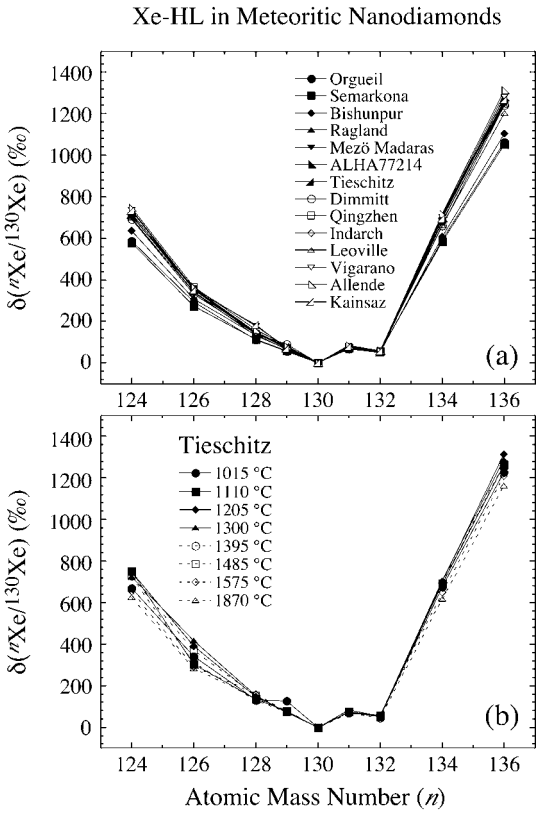

Figure 2.7 Variation in Xe–HL isotopic composition, given as $\delta(^{n}Xe/^{130}Xe)$, where *n* is the stable isotope mass number, for (a) nanodiamonds isolated from different chondrites and (b) as a function of release temperature for Tieschitz nanodiamonds.[79] The delta values are normalized such that $\delta(^{n}Xe/^{130}Xe) = 0$ corresponds to the isotopic composition of the solar wind that was implanted into lunar fines (BEOC-12).[82]

produced tenuous evidence of success at best.[79,93–96] Therefore, nanodiamond populations from different host meteorites contain the *same* Xe–HL composition, i.e., *same* admixture of exotic and normal Xe (shown in Fig. 2.4 and Table 2.3).

One possible explanation for the uniform Xe–HL composition is that all the components (Xe–H, Xe–L, and normal) were acquired together in supernovae. Since Xe–H and Xe–L are produced by different processes in dissimilar environments within supernovae (i.e., neutron rich and neutron

poor, respectively), it has been suggested that Xe–H- and Xe–L-rich regions turbulently mixed (perhaps with normal Xe inherited when the stars initially formed) before the nanodiamonds acquired Xe.[97] However, the grain size and noble gas concentration are such that it improbable for any particular nanodiamond to have more than one noble gas atom. Therefore, one subpopulation of nanodiamonds could have encountered predominantly Xe–L-rich gases while a second subpopulation encountered predominantly Xe–H-rich gases under different supernovae conditions prior to turbulent mixing. Similarly, the normal component of Xe–HL need not have been acquired in supernovae. If correct, the exotic Xe–L and Xe–H carriers (as well as perhaps the carriers of normal Xe) should be separable having originated under (or experienced) different physical conditions.[57,98]

There is no evidence in meteoritic nanodiamond isolates of the presence of *s*-process (slow neutron capture) Xe (Xe–S) in excess to the Xe–S present in the normal Xe component that is mixed with exotic Xe–HL or in excess to Xe–S which can be attributed to trace impurities of presolar SiC. Presolar SiC isolates exhibit clear excesses in Xe–S which is enriched in even-numbered middle isotopes and depleted in odd isotopes.[99] This composition is thought to be produced in AGB stars.[100]

The next most important noble gas after Xe–HL is Kr–HL which exhibits an enrichment in the nuclide with the greatest *r*-process contribution, ^{86}Kr (see Fig. 2.5, Table 2.3).[79] However, unlike the case of Xe–HL, the *p*-process (Kr–L: ^{78}Kr and ^{80}Kr) nuclides exhibit a depletion, not an excess, and there is no evidence of Kr–L (Table 2.3). Furthermore, the excesses in Kr–HL are small enough that they could arise from mass fractionation rather than a nucleosynthetic (i.e., presolar) origin. The anomalies in Ar–Ne– and He–HL are difficult to interpret in terms of nucleosynthesis models and, hence, are not discussed here.

The concentration of Xe-HL in the meteoritic nanodiamond isolates varies by less than a factor of 2 and is upwards of 26×10^{-8} ccSTP ^{132}Xe/g-diamond (see Table 2.2) corresponding to 7.0×10^{12} ^{132}Xe–HL atoms/g-diamond (0.14 ppb Xe/C atoms). Kr–HL concentrations are roughly half that of Xe–HL. With mean diamond diameters ≈2.8 nm,[2] this corresponds to one Xe–HL atom per several million nanodiamonds. This ratio is not equivalent to the actual fraction of the nanodiamond population associated with supernovae. That fraction cannot be readily estimated because the Xe trapping efficiencies, let alone the mechanisms of trapping, are not well known. In other words, the larger fraction of diamonds that encountered supernovae but did not acquire exotic Xe–HL cannot be estimated.

Although the ratio of Xe–HL atoms to nanodiamonds is ~10^{-6} and meteoritic nanodiamond isolates are only ~99.9% pure nanodiamond, it is believed that diamond is the Xe–HL carrier for several reasons. First, graphite and presolar SiC are the major impurities in nanodiamond isolates,[2] and neither show evidence of trapped Xe–HL, in their respective bulk isolates or their individually measured grains. However, nanometer-sized presolar graphite and SiC, as present in the nanodiamond isolates, may differ isotopically from their bulk counterparts. Second, all attempts to isolate the Xe–HL carriers from nanodiamonds that do not carry Xe have failed. Third, the carriers of Xe–HL are inseparable from the carriers of the other HL noble gases. The smooth elemental abundance pattern of extracted noble gases relative to cosmic abundances suggests all HL noble gases are a single component trapped in a single mineral species.[79] The release of HL gases accompanies major release of CO_2 during combustion of the meteoritic nanodiamonds.[101] In particular, the lower release temperatures for HL gases during combustion in oxygen (<500 °C) compared to pyrolysis in vacuum (>1200 °C) implies the carriers of HL gases can be oxidized,[79] precluding trace oxides as the carriers. Together, these points argue that Xe–HL is carried by nanodiamonds.

Two mechanisms have been proposed for the incorporation of noble gases into meteoritic nanodiamonds: entrapment during condensation and ion implantation. A chemical process such as condensation will preferentially trap elements that are reactive (e.g., I) and exclude those that are not (e.g., noble gases). If the trapping mechanism was chemically selective, ^{129}Xe should be greatly enriched over the other Xe–HL isotopes due to trapping of the abundant *r*-process product ^{129}I (16.4 Myr half-life), the radiogenic progenitor of ^{129}Xe.[86,102] One scenario that would circumvent this constraint is for the chemically selective trapping to have occurred only after the ^{129}I had decayed to negligible levels (e.g., 7–10 half-lives or 100–160 Myr). However, since it is implausible that the Xe–HL escaped dilution by non-HL Xe isotopes over such a long time in the ISM, implantation is suggested.[102] Nevertheless, recent nucleosynthesis models speculate that iodine could have been separated from the Xe reservoir on a relatively short time scale (~7500 s) after nucleosynthesis and prior to Xe trapping by the nanodiamonds.[88]

The implantation theory is supported by laboratory ion-irradiation experiments. Low-energy (~700 eV) ion irradiation of ~4 nm diameter UDDs demonstrated implantation of mixed noble gases (He, Ar, Kr, and Xe) at a yield of 0.1 the ion dose (1.5×10^{15} ions cm^{-2}).[103] Thermal release profiles of implanted gases in UDDs exhibited a bimodal release intriguingly similar to those observed in meteoritic nanodiamonds (Fig. 2.8). A

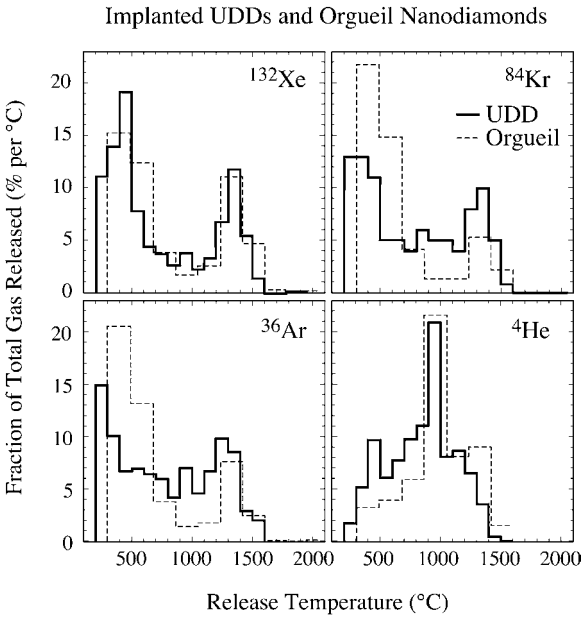

Figure 2.8 Comparison of noble gas release profiles during stepped pyrolysis from Orgueil nanodiamonds (fine dashed line) and nanometer-sized ultradispersed detonation diamonds (UDDs) that were low-energy, ion implanted with mixed noble gases (bold line).[103] (Adapted from ref. 103.)

single irradiation event that can implant two components in nanodiamonds that are released at different temperatures has implications for the interpretation of the P3 and HL gases in meteoritic nanodiamonds. In one proposed scenario,[103] nanodiamonds implanted with HL gases in supernovae ejecta thereafter experienced temperatures sufficient to remove the more labile (low-temperature-released) HL gases while HL gases released only at high temperature were retained. Further, planetary P3 gases were implanted at a later episode; however, many nanodiamonds did not experience sufficient heating to remove the labile (low-temperature-released) gases. In this scenario, the normal component of HL, intimately mixed with the exotic HL component, would actually be planetary P3 gases. If correct, then estimations of the exotic HL composition obtained by subtracting a solar component from HL have been done incorrectly because P3 gases differ subtly in isotopic composition from the solar mean. A recalculation of the isotopic composition of the exotic HL component using the composition of P3 as the normal HL component does not significantly alter the estimated composition of exotic Xe–HL. However, it does convert the deficits in light Kr nuclides to excesses and provides evidence for the presence of the missing Kr–L.[104]

The bimodal release pattern exhibited by irradiated UDDs likely results from ion-range effects and nature of the irradiated target. The UDDs were irradiated as a deposited thin film and the ion ranges were calculated to be of the order of the mean grain radius.[103] However, it is difficult to accurately predict ranges of low-energy ions in bulk solids, let alone in nanocrystals (i.e., 4 nm diameter diamonds have 45% of their C atoms within one unit cell of the surface), and numerically simulated ranges are only an order of magnitude approximation. Thus, it is possible the bimodal release reflects bulk implantation in the topmost UDD layer and near-surface implantation in the underlying layer. Also, an ion with non-center-of-mass incidence into a nanodiamond could implant near the surface of an adjacent crystal. In contrast, presolar diamonds, if implanted, were likely implanted as individual grains suspended in gaseous supernovae outflows, complicating their comparison with ion-irradiated UDDs. However, ion implantation of Xe–HL in presolar nanodiamonds by a wide range of low energies might mirror the range effects mentioned.

Nevertheless, there are problems with the implantation theory for Xe acquisition by nanodiamonds. For implantation to occur in diamond, a large ion like Xe must disrupt many strong carbon sp^3 bonds and displace many lattice atoms along its trajectory, requiring at least several hundred electronvolts of energy. Nearly all of this energy (minus that dissipated by possible sputtered C atoms) would be deposited into a small nanometer system (between 10^3 and 7.5×10^3 C atoms for a mean-diameter grain), substantially heating the diamond. Therefore, Xe implantation should produce heavy lattice damage in nanodiamonds, if not partially or fully transforming the grains. As defect concentrations increase, susceptibility to subsequent thermal transformation should also increase. In contradiction, annealing experiments demonstrated that most Murchison nanodiamonds lost their P3 component and transformed to graphite onions prior to Xe–HL release from the isolates, suggesting the Xe–HL carriers are the most resistant mineral in the isolates to alteration.[83] This deduction is further supported by the decrease of P3 gas abundances and accompanying increase of HL gas abundances in nanodiamonds isolated from meteorites that experienced progressively greater levels of thermal alteration, see Section 2.6. Both gas abundance trends would be expected if P3 carriers and nanodiamonds lacking HL gases were less resistant to alteration than HL carriers. This could argue that the carrier is a more refractory mineral than diamond at the nanometer scale. But if correct, this mineral must have very similar colloidal and chemical properties as nanodiamond to defy any level of separation from the nanodiamonds. If the HL carrier is diamond of high thermal resistance, the HL gases could

reside in the largest size fraction of the population (e.g., as suggested by isotopic measurements of grain size isolates[95]) or in nanodiamonds poor in trapped N and associated defects (see Section 2.6). Thermal spikes from low-energy Xe implantation would be less severe in the largest meteoritic nanodiamonds.

2.4.3 Trapped Te, Pd, Ba, and Sr

Trapped Te, Pd, Ba, and Sr were measured in Allende nanodiamonds by oxidizing the nanodiamonds in an oxygen plasma using radio frequency induction. Combustion products were dissolved in HCl and separated by conventional ion exchange chemistry into two fractions, (Te, Pd, Cd, and Zn) and (Ba and Sr), for analysis.[67,68] Elemental abundances of Te (640 ± 100 ppb), Pd (1900 ± 400 ppb), Cd (14 ± 3 ppb), and Zn (500 ± 70 ppb) were determined by stable isotope dilution mass spectrometry.[68] Elemental abundances correspond to one Pd or Te atom per hundreds of nanodiamonds. Isotopic compositions were measured by thermal ionization mass spectrometry, and small positive anomalies were found in the two *r*-process-only Te–H nuclides (see Fig. 2.5, Table 2.4), $\delta(^{128}Te/^{124}Te) = 4.0 \pm 1.5‰$ and $\delta(^{130}Te/^{124}Te) = 9.3 \pm 2.8‰$, where $^{126}Te/^{124}Te$ was used to correct instrumental fractionation.[68] No evidence of anomalies was observed for the two nuclides (^{125}Te and ^{126}Te) which are produced by both *r*- and *s*-process nucleosynthesis. Analogous to Xe–HL, nucleosynthesis models indicate Te–H is a mixture of a normal and an exotic component, and suggest a presolar origin for some nanodiamonds (Fig. 2.6(b)).[68] The *p*-process-only ^{120}Te nuclide had too low an abundance to yield meaningful statistics for Te–L. Similar to Xe, there is no evidence of excesses in the *s*-process-only (^{122}Te, ^{123}Te, and ^{124}Te) nuclides (see Fig. 2.5, Table 2.4). A small positive anomaly, just outside error, was also observed for Pd, $\delta(^{110}Pd/^{104}Pd) = 9.4 \pm 5.7‰$ (2σ), where $^{106}Pd/^{104}Pd$ was used to correct instrumental fractionation.[68]

Trapped Ba (14 ppb) and Sr (3 ppb) abundances correspond to one Ba or Sr atom per tens of thousand or hundreds of thousand meteoritic nanodiamonds, respectively.[67] The instrumental mass fractionation correction was not well constrained by the Ba and Sr isotopic data. However, regardless of the fractionation correction applied, Ba and Sr exhibited tiny non-radiogenic excesses (>10‰) that were outside the very tight isotopic range exhibited by terrestrial standards.[67] Using $^{134}Ba/^{138}Ba$ for correction of instrumental fractionation, slight excesses in nuclides with significant *r*-process contributions (see Fig. 2.5, Table 2.4) can be exhibited,

Table 2.4 C, N, Sr, Pd, Te, and Ba Isotopic Compositions in Meteoritic Nanodiamonds

Component	Isotopic Composition						
	$^{13}C/^{12}C$						
C–Solar[a]	1/89						
C	1/92.0 to 1/92.6						
δC (‰)	−32.5 to −38.8						
	$^{15}N/^{14}Ne$						
N–Solar[a]	1/272						
N	1/361.4 to 1/424.7						
δN (‰)	−247.4 to −359.5						
	$^{84}Sr/^{88}Sr$	$^{86}Sr/^{88}Sr$	$^{87}Sr/^{88}Sr$				
Sr–Solar[a]	0.006745	0.1194	0.69897				
Sr	0.00674 (1)	0.1204 (2)	0.7829 (7)				
δSr (‰)	0 (1)	8.4 (1.5)	120 (1)[b]				
	$^{102}Pd/^{104}Pd$	$^{105}Pd/^{104}Pd$	$^{106}Pd/^{104}Pd$	$^{108}Pd/^{104}Pd$	$^{110}Pd/^{104}Pd$		
Pd–Solar[a]	0.09133 (7)	2.0092 (19)	≡2.4499	2.3655 (22)	1.0428 (10)		
Pd–H	0.0911 (10)	2.0092 (87)	≡2.4499	2.3683 (126)	1.0526 (59)		
δPd–H (‰)	−3 (11)	0.0 (4.4)	≡0	1.2 (5.4)	9.4 (5.7)		
	$^{120}Te/^{124}Te$	$^{122}Te/^{124}Te$	$^{123}Te/^{124}Te$	$^{125}Te/^{124}Te$	$^{126}Te/^{124}Te$	$^{128}Te/^{124}Te$	$^{130}Te/^{124}Te$
Te–Solar[a]		0.5411 (4)	0.1886 (1)	1.4887 (11)	≡3.9544	6.6249 (48)	7.0753 (50)
Te–H		0.5391 (30)	0.1876 (20)	1.4893 (25)	≡3.9544	6.6514 (90)	7.1411 (190)
δTe–H (‰)		−3.7 (5.5)	−5.4 (10.4)	0.4 (1.8)	≡0	4.0 (1.5)	9.3 (2.8)
	$^{130}Ba/^{138}Ba$	$^{132}Ba/^{138}Ba$	$^{134}Ba/^{138}Ba$	$^{135}Ba/^{138}Ba$	$^{136}Ba/^{138}Ba$	$^{137}Ba/^{138}Ba$	
Ba–Solar[a]	0.001475	0.001413	0.033715	0.091940	0.109543	0.156545	
Ba–H	0.0015 (2)	0.0013 (2)	≡0.033715	0.0931 (4)	0.1095 (3)	0.1575 (2)	
δBa–H (‰)	−14 (116)	−50 (130)	≡0	12.2 (3.8)	−0.6 (2.8)	6.0 (1.5)	

Data from refs. [63,67,68]. Parentheses represent the errors for the decimal of the least significant digit.

[a] Based on terrestrial standards.

[b] Radiogenic component.

$\delta(^{135}Ba/^{138}Ba) = 12.2 \pm 3.8‰$ and $\delta(^{137}Ba/^{138}Ba) = 6.0 \pm 1.5‰$, suggesting supernovae origin for the carriers.[67] The three order-of-magnitude smaller isotopic anomalies in Ba–H over Xe–H, as well as the greater elemental abundances of Ba and Sr relative to Xe and Kr, might suggest the contribution of normal Ba from a trace mineral impurity. The *p*-process (^{130}Ba and ^{132}Ba) nuclides had too low an abundance to yield meaningful statistics for the Ba–L nuclides. Contrary to Xe, Kr, and Ba there was no evidence for an enrichment at the partially *r*-process nuclide ^{88}Sr. Nevertheless, evidence for a slight excess in ^{86}Sr was shown, $\delta(^{86}Sr/^{88}Sr) = 8.4 \pm 1.5‰$.[67]

2.4.4 Inferred Stellar Sources

Since nanodiamond isolates from chondrites exhibit *r*-process-like nuclides (Xe–H, Kr–H, Te–H, and Ba–H)[67,68,79] and *p*-process nuclides (Xe–L and perhaps Kr–L)[79,104] formed by explosive nucleosynthesis, supernovae have been naturally proposed as their sources. In one of the first models, a close binary system consisting of a mass-transferring carbon star and a degenerate white dwarf was proposed. In this model, nanodiamonds were produced in the dusty outflows of the carbon star while HL nuclides were produced by the white dwarf when it accumulated sufficient matter from the carbon star to exceed the Chandrasekhar limit and initiate explosive nucleosynthesis as a type Ia supernova.[105] It was suggested that nanodiamonds formed by the carbon star acquired HL gases by implantation when they encountered HL gases in the supernovae ejecta.

Type II supernovae have also been proposed as sources, and turbulent mixing of different zones within the supernovae ejecta has been modeled to account for the bulk-measured, mean C and N isotopic compositions of meteoritic nanodiamonds.[57,86] The Xe–HL anomalies observed in meteoritic nanodiamonds cannot be explained by a simple mixture of *p*- and *r*-process Xe with solar Xe. This is because such a mixture would produce nearly equal relative excesses in the two *p*-process-only isotopes (Xe–L: ^{124}Xe and ^{126}Xe) as well in the two *r*-process-only isotopes (Xe–H: ^{134}Xe and ^{136}Xe) which is not observed (Fig. 2.4).[88] This is not a severe problem for Xe–H produced in type Ia supernovae models where no true *r*-process is expected.[87] However, it is a problem for type II supernovae and two models have been proposed to account for the observed Xe–H anomaly, each of which has its own difficulties. In one model, Xe–H is made from products of the *s*-process by short neutron bursts, with inter-

mediate neutron densities between those characteristic of *r*- and *s*-processes.[86,87] Neutron bursts are speculated to occur in explosive carbon burning[85] or the outer He-rich shell of a massive star traversed by a supernova shock front[86]. In the second model, Xe–H is synthesized by the standard *r*-process; however, the unstable, neutron-rich precursors of ^{134}Xe (notably the short half-life, ^{134}I and ^{134}Te) are somehow separated from the Xe reservoir to fix the time-evolving ratio of ^{134}Xe/^{136}Xe before it reaches its ultimate *r*-process value.[88] A separation on a time scale of ~7500 s is required to match the pure end-member composition of the exotic component of Xe–HL (Fig. 2.6(a)).[88]

Excesses in ^{128}Te and ^{130}Te, as observed in Te–H, are predicted by both models. However, the neutron burst model[87] predicts large excesses in ^{125}Te and ^{126}Te as well as ^{130}Te/^{128}Te ≈ 4 that are not observed. In comparison, the exotic component of Te–H has inferred ^{130}Te/^{128}Te = 2.5 ± 1.2, obtained by subtracting a normal component which assumes ^{124}Te–H is entirely normal.[68] On the other hand, the rapid separation model can account for the lack of excesses in ^{125}Te and ^{126}Te, provided their long half-life precursors, ^{125}Sb and ^{126}Sb, are separated from the Te reservoir prior to trapping in the diamonds. A separation on a time scale of ~3800 s is required to match the pure end-member composition of the exotic component of Te–H (Fig. 2.6(b)).[68] Similarly, the tiny excesses in Ba–H (^{135}Ba and ^{137}Ba) with respect to the predicted *r*-process yields could be explained by separation of their short half-life precursors, ^{135}I and ^{137}Cs, within these time scales.[88]

The excess observed in Kr–H (^{86}Kr) is difficult to quantitatively interpret in terms of nucleosynthesis models because the contribution to solar Kr from the *s*-process is uncertain, in part because of the branching at ^{85}Kr (Fig. 2.5).[88] However, an excess at ^{86}Kr is expected in both models[87,88] and is observed in Kr–HL. Little can be inferred from Ar–, Ne–, and He–HL compositions because of the inaccuracies in their isotopic measurement, the small anomalies exhibited, and the uncertainties in a number of nucleosynthesis and model parameters.

Although supernovae are undoubtedly sources, the high abundance of nanodiamonds in meteorites (upwards of 13 to 19% total C) suggests prolific sources must have contributed nanodiamonds to the ISM. Additional sources could include AGB carbon stars and the solar nebula. Unfortunately, the elemental abundances and isotopic compositions cannot tightly constrain the different sources and their relative contribution to the meteoritic nanodiamond population. A presolar origin for a large proportion of meteoritic nanodiamonds might be supported by the N isotopic compositions, but the ambiguity in the solar N composition must first be resolved.

Nevertheless, the best conclusion that can be drawn is that there is sufficient evidence to suggest a presolar origin for some fraction of the nanodiamond population.

2.5 Microstructure of Meteoritic Nanodiamonds: Formation Mechanisms

Microstructures of materials are heavily dependent on growth mechanisms, physical conditions during formation, and post-formation alteration mechanisms. In the only detailed microstructural study of meteoritic nanodiamonds to date, several theories for the formation of meteoritic nanodiamonds were evaluated by HR-TEM comparison of nanodiamonds synthesized by shock processes and low-pressure CVD to those isolated from the Allende and Murchison carbonaceous chondrites.[2] Nanodiamonds synthesized by shock processes (termed "shock-synthesized" and also known as UDDs) were produced by detonation of high explosives trinitrotoluene (TNT) $C_7H_5N_3O_6$ and cyclotrimethylene-trinitramine (RDX) $C_3H_6N_6O_6$ in sealed, Ar-filled chambers.[106] Detonation soot was recovered from the chambers and nanodiamonds formed by shock metamorphism of carbonaceous precursors and rapid condensation of vaporized carbonaceous precursors were isolated by acid treatments.[106] The CVD nanodiamonds were synthesized in a substrate-free microwave plasma CVD flow reactor by nucleation and homoepitaxial growth directly from the vapor phase at low pressure.[107] Although changes in experimental conditions can result in a range of growth features and affect the proportion of nanodiamonds synthesized by any given process, microstructural features should exist that are uniquely characteristic of specific formation mechanisms exclusive to either dynamic-shock processes or low-pressure condensation. Daulton et al. (1996)[2] identified such features in the synthesized nanodiamonds, and when compared to the microstructures of nanodiamonds from Allende and Murchison, they indicated that the predominant mechanism for meteoritic nanodiamond formation is low-pressure vapor condensation. The results of that study are primarily described here.

2.5.1 Twin Microstructure

In cubic diamond, twinning along {111} planes is common and results when the stacking sequence of {111} planes is abruptly reversed, e.g.,

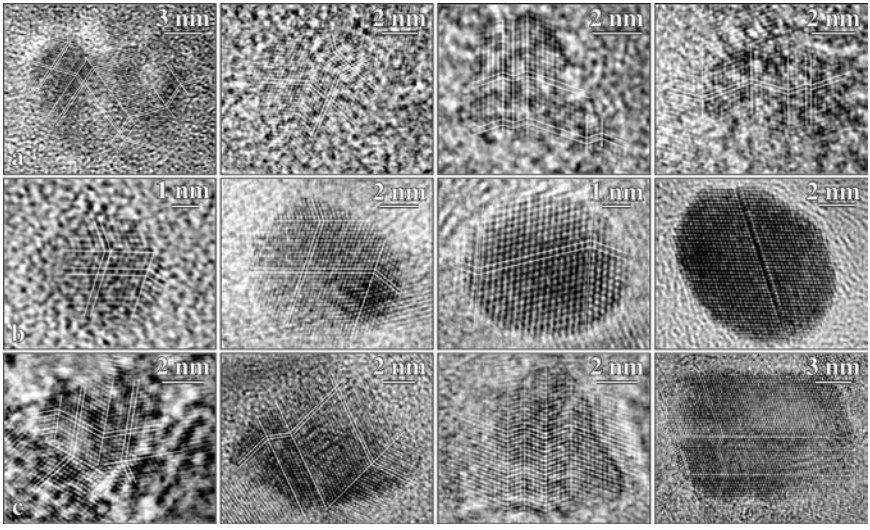

Figure 2.9 Multiply twinned microstructures imaged along the [011] zone axis in meteoritic (row a), CVD-synthesized (row b), and shock-synthesized (row c) nanodiamonds. The two leftmost columns are non-linear multiple twins and the two rightmost columns are linear multiple twins.

{*AaBbCcBbAa*}. In coincident site lattice notation, this twin structure is described as a first-order $\Sigma = 3$ {111} twin. The interface at a $\Sigma = 3$ twin boundary is one of the lowest-energy lattice defects, so cubic nanocrystals can form $\Sigma = 3$ twin structures relatively easily to accommodate growth constraints. Thus, $\Sigma = 3$ twin microstructures can provide a diagnostic indicator for different nanodiamond formation mechanisms.

Multiple $\Sigma = 3$ twins are relatively common microstructures in nanodiamonds and occur in two configurations. The first type (linear) exhibits parallel $\Sigma = 3$ {111} twin boundaries that terminate at the crystal surface (Fig. 2.9). The second type (non-linear) is characterized by oblique $\Sigma = 3$ {111} twin boundaries (Fig. 2.9) that terminate either at crystal surfaces or at twin boundary intersections, or both. Important differences become apparent when the relative abundances of twin microstructures are compared in the synthesized diamonds (Fig. 2.10). First, the ratio of twinned crystals to single crystals in shock-synthesized diamonds (2.48) is a factor of 2 higher than those synthesized by CVD via homoepitaxial growth directly from the vapor phase (1.25). Since re-entrant corners of twinned crystals are associated with increased growth rates over single crystals,[108] this suggests that the mean growth rate for shock-synthesized diamonds is greater than the mean growth rate of CVD-synthesized diamonds.

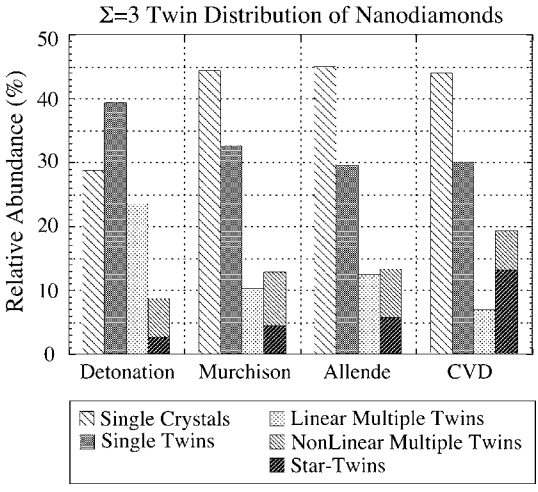

Figure 2.10 Normalized distribution of Σ = 3 twin microstructures for nanodiamonds synthesized by detonation shock[106] and CVD[107] as well as those isolated from the chondrites Murchison and Allende. Unobstructed and isolated nanodiamonds exhibiting clear cross-lattice fringes were classified by their twin type. Statistics are based on 209 (detonation), 372 (Murchison), 257 (Allende), and 130 (CVD) individual nanodiamonds; a total of 968 nanodiamonds.

Nanodiamonds present in the detonation soot residues must have experienced rapid thermal quenching to escape graphitization behind the shock front. Those nanodiamonds that survived must have experienced high growth rates. The ratio of twinned crystals to single crystals in the meteoritic nanodiamonds (1.28) suggests growth rates similar to those of the CVD-synthesized diamonds.

Second, linear twins dominate over non-linear twins in shock-synthesized nanodiamonds. During detonation synthesis of nanodiamonds, large, highly anisotropic shock pressure gradients momentarily exist. Following a shock-induced carbonaceous grain-on-grain collision, partially molten material would rapidly solidify behind planar shock fronts. Further, any nanodiamond condensation behind high-pressure shock fronts would occur within highly anisotropic conditions. In both cases, crystallization should occur along planar growth fronts producing microstructures dominated by parallel twin boundaries. Consistent with this interpretation, the shock-synthesized nanodiamonds display a distribution of multiple twins dominated by parallel twin boundaries. The direction of growth is presumably related to the geometry of the shock front and direction of the pressure gradients. In sharp contrast, CVD-

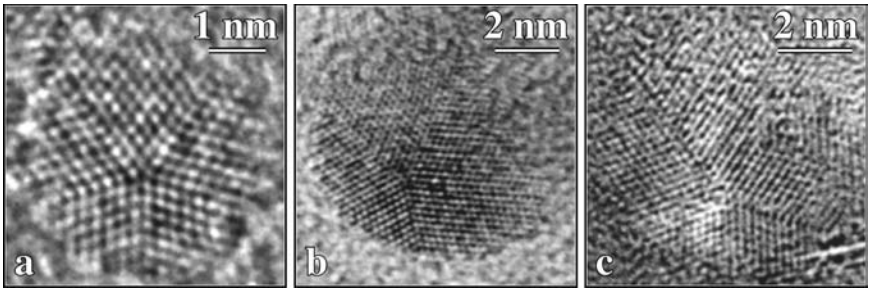

Figure 2.11 Star twin microstructure (i.e. decahedra multiply twinned particle) imaged along a [011] zone axis common to the twin domains in (a) meteoritic (Allende), (b) CVD-synthesized, and (c) shock-synthesized nanodiamonds.

synthesized nanodiamonds are dominated by non-linear multiple twins indicative of isotropic growth.

The most striking non-linear, multiply twinned configurations correspond to multiply twinned particles (MTPs). The most common MTPs are decahedra (termed star twins, five slightly distorted tetrahedra with a common [110] edge with D_{5h} point group symmetry) and icosahedra (20 slightly distorted tetrahedra sharing a common apex with I_h symmetry). The CVD nanodiamonds, synthesized by direct nucleation and homoepitaxial growth from the vapor phase, have a large abundance of star twins (Fig. 2.11(b)). Icosahedra MTPs were also observed. Unlike star twins, icosahedra MTPs do not exhibit well-defined lattice fringes because their arrangement of overlapping tetrahedral twin domains produces complex Moiré patterns. Icosahedra MTPs are excluded in the twin distributions of Fig. 2.10 because the selection criteria used to generate the statistics only accepted nanodiamonds with well-defined <111> cross-lattice fringes.

Although not as abundant as in CVD nanodiamonds by a factor of 2.6, star twins are relatively common growth features in meteoritic nanodiamonds (Fig. 2.11(a)). In contrast, star twins (Fig. 2.11(c)) are relatively rare and least abundant in shock-synthesized nanodiamonds with an abundance a factor of 5.8 less than CVD nanodiamonds (Fig. 2.10). The coherent twin boundaries present in the star twins are indicative of radial (isotropic) growth, as would be possible from the direct nucleation and homoepitaxial growth from a locally uniform supersaturated gas such as in a low-pressure CVD-type process. Although star-twin microstructures would not be expected to form under highly anisotropic conditions, MTPs (as well as non-linear multiple-twin crystals) observed in detonation soot residues might have formed in the rarefaction wave of the expanding

shock front. Vaporization of a fraction of the precursor carbonaceous material in the shock heating event would supersaturate the partially ionized gas in carbon. After passage of the shock front, nanodiamond nucleation and growth might occur with conditions occasionally favorable for limited isotropic growth.

2.5.2 Dislocation Microstructure

In contrast to twin and stacking fault structures, dislocations represent relatively high-energy defects because their cores contain disrupted nearest-neighbor bonds and significant bond distortion. Whereas the formation of twins and stacking faults is influenced by low-energy processes, the formation of dislocations requires relatively high-energy processes. This is especially the case for diamonds, which have strong sp^3 carbon bonds. For example, epitaxial dislocations are common in CVD diamond films and result from strain induced at the substrate interface and at interfaces where two growing crystals impinge at an arbitrary angle. High dislocation densities also develop in natural diamond to accommodate lattice distortions around mineral inclusions and plastic deformation caused by shear stresses in the upper mantle. In contrast, the situation is disparate for nanocrystals, where perhaps only a few mechanisms are available to form high-energy defects. Martensitic-type mechanisms occur behind shock fronts and can leave a high density of residual dislocation defects in the transformation product. This is evident in the shock-synthesized nanodiamonds that exhibit a small population of grains containing dislocations with disorder (Fig. 2.12). In contrast, dislocations are not expected to form in nanometer grains that nucleated directly from the vapor phase, and, indeed, no such defect structures were observed in the CVD-synthesized nanodiamonds.

No analogous dislocations were observed in the Allende and Murchison nanodiamonds. It is unlikely that the acid dissolution used to isolate meteoritic nanodiamonds destroyed those with dislocations. Detonation soot residues were subjected to acid treatments to purify diamond products,[106] although not as extensive as the treatments used to isolate nanodiamonds from chondrites. Nevertheless, the detonation soot residues still retain nanodiamonds with dislocations. Furthermore, thermal processing of the Murchison and Allende parent bodies was likely insufficient to remove dislocations by annealing or destroy dislocation-containing diamonds. Noble gas abundances in nanodiamonds suggest mild thermal processing in Murchison with only minimal loss of nanodi-

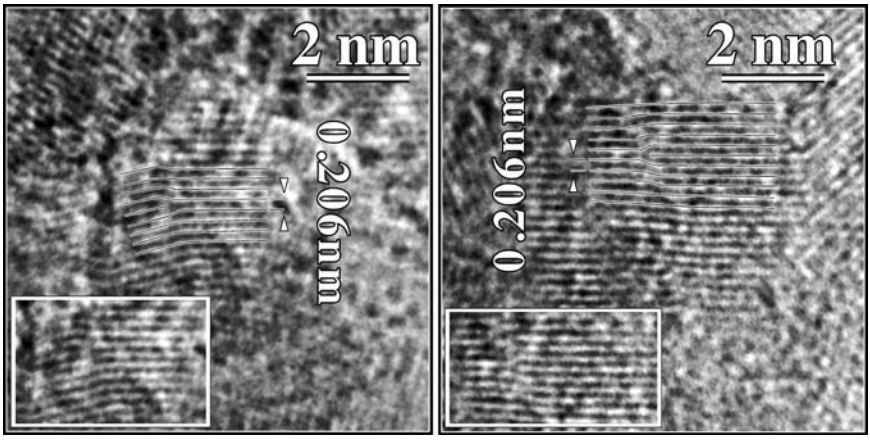

Figure 2.12 Shock-synthesized nanodiamonds containing dislocations. The superimposed lines illustrate the missing <111> half planes. Insets display non-annotated dislocation images.

amonds[109] likely concentrated to the smallest size fraction (see Section 2.6). Although Allende experienced greater thermal processing than Murchison, a significant amount of surface-bound H with deuterium excesses is retained by Allende nanodiamonds.[64,110] Temperatures required to anneal dislocations would be more than sufficient to desorb surface H, resulting in a significant depletion of any deuterium excess. Lack of dislocation microstructures in meteoritic nanodiamonds is likely a primary feature of formation, and therefore suggests that the majority of meteoritic nanodiamonds did not form by shock metamorphism.

2.5.3 Polytypes

In analogy to the twin and dislocation microstructures that correlate with different formation processes, the polytypes present could provide indicators of particular formation mechanisms. For example, the rare 2H polytype of diamond (lonsdaleite) is generally associated with shock processes. Lonsdaleite has been observed together with cubic (3C) diamond in the highly metamorphosed Canyon Diablo iron meteorite and Goalpara achondrite meteorite.[111,112] Analyses of coexisting minerals in these meteorites indicate that they experienced high levels of shock either from parent-body asteroidal collisions or from terrestrial impact.[113,114] Furthermore, macroscopic diamond present in Novo-Urei and Goalpara ureilites have preferred orientations with respect to the meteorite matrix,

indicative of an anisotropic formation process such as shock.[114] Although Greiner et al. (1988)[106] did not report any X-ray diffraction lines of lonsdaleite in the detonation soot residues they examined, HR-TEM images reveal a small amount (< several percent by number) of 2H diamond (Figs. 2.13(a) and (b)).

Meteoritic nanodiamonds contain a very small population of nanocrystals that exhibit cross-lattice fringes consistent with the [100] zone axis of lonsdaleite. Furthermore, a nanodiamond from Allende exhibiting a homoepitaxial intergrowth of the 2H and 3C polytypes was observed (Fig. 2.13(c)). The {111} cubic-diamond plane is identical to the {001} (2H) lonsdaleite plane, and therefore, the interface between the two polytypes is coherent. Shock levels experienced by a meteorite can be gauged from its constituent olivine crystals which have well-characterized responses to shock. Allende is characterized as having suffered negligible shock deformation and Murchison is characterized as a breccia composed of minerals exhibiting slight to moderate shock.[115] Since neither experienced the shock levels necessary to produce lonsdaleite, lonsdaleite must have formed prior to the accretion of those parent bodies.

Synthesized lonsdaleite in the detonation soot residues differs from the meteoritic lonsdaleite in several respects. Shock-synthesized lonsdaleite crystals are generally larger, more ordered, and more numerous than in meteoritic nanodiamonds. These differences might point to a mechanism other than shock for the formation of meteoritic lonsdaleite. For example, low-pressure synthesis of several hexagonal polytypes of diamond, including 2H, have been reported in microwave plasma CVD flow reactors[116] and in thermal plasma CVD reactors.[117] Nanocrystals with cross-lattice fringes similar to those of the [100] zone of lonsdaleite were observed in the CVD residue; however, their small size (<1.2 nm) and low contrast made it difficult to accurately measure their lattice spacings. As such they are only plausible candidates for lonsdaleite.

2.5.4 Inferred Mechanisms of Formation

The microstructures of nanodiamonds isolated from Allende and Murchison, for the most part, are similar to those of CVD-synthesized nanodiamonds and dissimilar to those of the shock-synthesized nanodiamonds. The experimental evidence is summarized in Table 2.5. These observations suggest that the predominant mechanism responsible for the formation of meteoritic nanodiamonds is low-pressure condensation, similar to CVD. This conclusion is based on direct microstructural

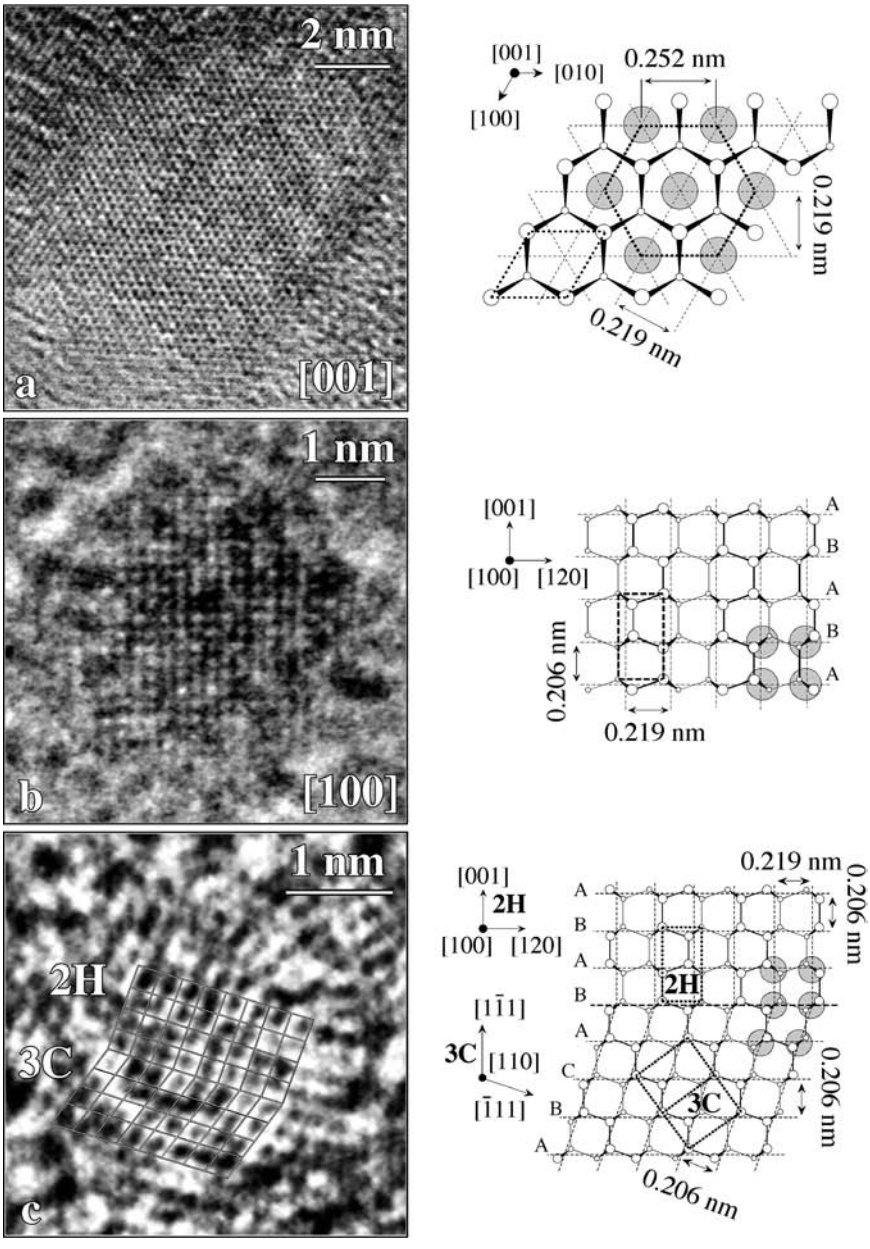

Figure 2.13 Nanodiamonds of the 2H polytype of diamond (lonsdaleite) (a)–(b) synthesized by detonation shock[106] and (c) a 2H/3C intergrowth nanodiamond isolated from Allende. Atomic models of the nanodiamonds along their corresponding crystallographic directions are shown.

Table 2.5 Nanodiamond Microstructures

	Shock	Meteoritic	CVD
Twins/single crystals	2.48	1.28	1.25
Linear twins/non-linear twins	2.72	0.87	0.36
Star twins/all twins	0.04	0.09	0.23
Dislocations	Yes	No[a]	No[a]
2H polytype	Yes	Yes	Maybe

[a] Not observed.

evidence, independent of any models for astrophysical processes or environments (e.g., AGB stars, supernovae, or the solar nebula). Nevertheless, isotopic evidence provides further support. The low-density ($\rho < 2.0\,\mathrm{g\,cm^{-3}}$) variety of presolar graphite is characterized by isotopic compositions similar to those of rare SiC type X grains of established supernova origin.[39,40,118–120] The mean isotopic compositions of graphite from supernovae (individual grain analysis: $3.6 \leq {}^{12}C/{}^{13}C \leq 7223$, mean = 211.15; $28 \leq {}^{14}N/{}^{15}N \leq 306$, mean = 228.38)[118] and meteoritic nanodiamonds (${}^{12}C/{}^{13}C$ = 92.0 to 92.6, ${}^{14}N/{}^{15}N$ = 361.4 to 424.7)[63] differ and this would not be the case if the majority of the nanodiamond population formed by transformation (via shock,[58] UV annealing,[59] or ion irradiation[60]) of graphite in supernovae.

2.6 Noble Gas and N Content in Meteoritic Nanodiamonds: Nebular Processes

The molecular cloud, which collapsed to form our solar nebula, is believed to have contained a homogeneous mixture of presolar grains from multiple sources. As the solar nebula evolved, distinct regions in the nebula would have experienced different thermal histories. Consequently, bodies in the accretion disk would have experienced a range of thermal as well as aqueous processing. This is evident for the meteorite parent bodies by the range of chemical and metamorphic classes in which meteorites are classified.[121,122] Therefore, presolar grains surviving within primitive bodies were witness to both nebular and parent-body processes. A record of those processes would be reflected by the distribution of presolar mineral species present in a primitive body, as well as in the degree to

which primordial trapped elements and gases within the presolar minerals were lost.[63,80,109,123]

As discussed previously, meteoritic nanodiamonds contain three isotopically distinct noble gas components (P3, HL, and P6). The isotopic compositions of Xe–P3 and Xe–HL scarcely vary between nanodiamond populations isolated from different chondrites (e.g., see Fig. 2.7). This suggests that all meteorite parent bodies sampled the same well-mixed reservoir of nanodiamonds during accretion in the solar nebula. Nanodiamonds isolated from different chondrites differ, however, in the abundance of P3 and HL gases. Per gram of diamond, the low-temperature P3 component varies by two orders of magnitude while the high-temperature HL and P6 components vary by a factor of 2–3 with host chondrite (Table 2.2).[80] Considering the HL gas carriers likely originated from many supernovae, variations in gas abundances are difficult to reconcile with the nearly constant isotopic compositions of the P3 and HL components. That is, unless the original gas abundances, resulting from thorough mixing of presolar nanodiamonds in the ISM, were altered by metamorphic processing in the solar nebula.

Nanodiamonds isolated from chondrites of increasing petrologic (metamorphic) type have decreasing abundances of low-temperature-released P3 gases.[80] This is shown in Fig. 2.14(b) for primitive, ordinary chondrites characterized by unaltered chondrules in the matrix (defined type 3). Unlike most classes of carbonaceous chondrites, the levels of thermal alteration experienced by ordinary type 3 chondrites can be semi-quantitatively determined from thermoluminescence sensitivity[122] and other gauges of metamorphic alteration. The correlation between reduced P3 gas content in nanodiamond isolates and markers of thermal alteration suggests the P3 gases were lost during parent-body metamorphism. In contrast to loss of P3 gases, the concentrations of HL and P6 gases (except for labile He) in nanodiamonds increase with increasing petrologic type of the host meteorite (Fig. 2.14(c)).[80] Both gas abundance trends would be expected if nanodiamonds carrying P3 gases and those lacking HL gases were preferentially destroyed over the HL carriers during thermal processing. Recall in Section 2.4.2 that annealing experiments demonstrated that most Murchison nanodiamonds lost P3 gases and transformed to nanometer-scale graphite onions prior to Xe–HL release from the isolates, suggesting Xe–HL carriers are the most resistant minerals in the isolates to alteration.[83]

Destruction of nanodiamonds in meteorite parent bodies by thermal processing is further demonstrated by nanodiamond abundances in the different chondrites. Since nanodiamond is the only known presolar grain

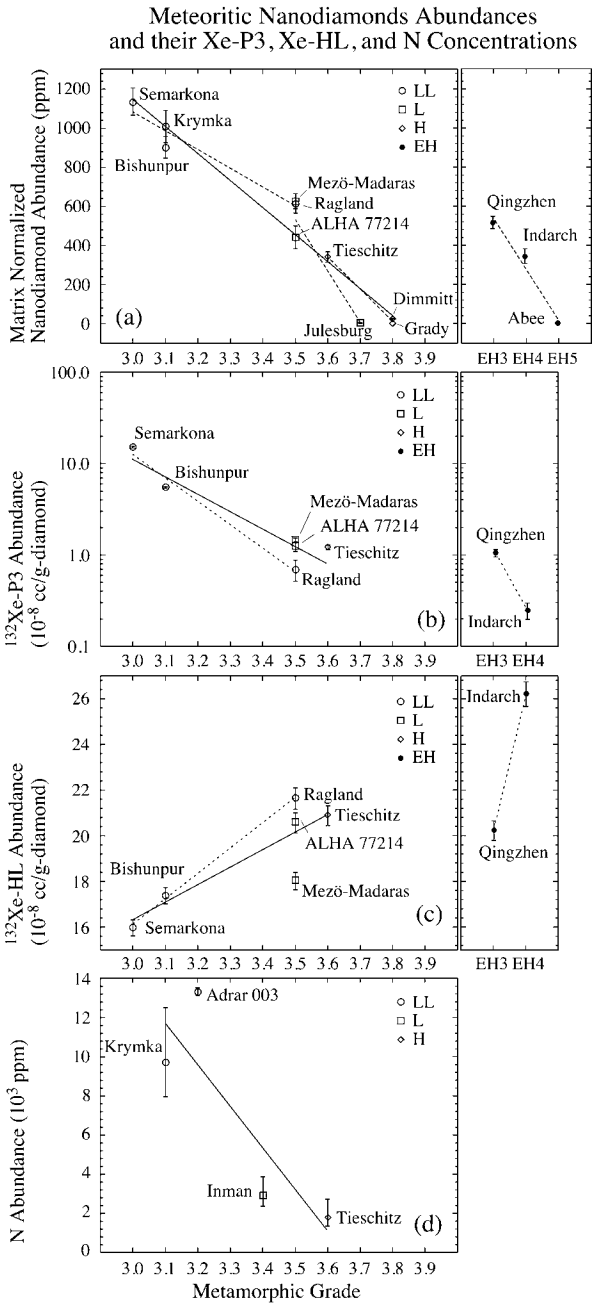
Meteoritic Nanodiamonds Abundances
and their Xe-P3, Xe-HL, and N Concentrations
Matrix Normalized
Nanodiamond Abundance (ppm)
Semarkona
Krymka
Bishunpur
Mezö-Madaras
Ragland
ALHA 77214
Tieschitz
Dimmitt
Julesburg
Grady
Qingzhen
Indarch
Abee
LL
L
H
EH
(a)
EH3 EH4 EH5
^{132}Xe-P3 Abundance
(10^{-8} cc/g-diamond)
(b)
EH3 EH4
^{132}Xe-HL Abundance
(10^{-8} cc/g-diamond)
(c)
N Abundance (10^3 ppm)
Adrar 003
Inman
(d)
Metamorphic Grade

species thought to carry Xe–HL and the Xe–HL isotopic composition is well defined, Xe–HL concentrations in partially digested chondrites can be used as tracers to estimate nanodiamond abundance. Partial chemical digestion of the chondrites is necessary to remove carriers of solar and Xe–P1 gases that would interfere with Xe–HL measurements. Using this technique, nanodiamond abundances (as well as presolar SiC and graphite abundances using other tracers) were shown to decrease with increasing petrologic type of the host chondrite (Table 2.6, Fig. 2.14(a)).[109] The smallest diamond size fraction is likely lost first by metamorphism. This is suggested by the fact that although the nanodiamond size distributions of Murchison and Allende span the same range, the more thermally processed Allende has a factor of ~5 fewer nanodiamonds below 1.5 nm in size than Murchison (Fig. 2.1). No presolar grains are observed in ordinary chondrites with completely recrystallized matrices (e.g., petrologic type >3.8).

This technique was carried one step further to estimate the nanodiamond abundance originally accreted into the parent bodies prior to metamorphic loss. This was accomplished using the most retentive, high-temperature Xe–P6 gases as the tracer. The Xe–P6 content in Orgueil nanodiamonds was used as the calibration reference[109] because Orgueil is considered one of the least thermally processed chondrites.[124] Orgueil experienced a high degree of aqueous alteration (contains ≈ 17% H_2O)[125] and consequently experienced only minimal thermal processing, otherwise the water would have evaporated rapidly and the hydrous phyllosilicates present would have been metamorphosed into other minerals. Chondritic Xe–P6 content was estimated from the measured Xe–HL

Figure 2.14 Abundances of (a) nanodiamonds[109] as well as trapped (b) Xe–P3, (c) Xe–HL, and (d) N concentrations in nanodiamonds[63,80] isolated from type 3 ordinary chondrites in the LL (open circle), L (square), and H (diamond) chemical groups as well as type 3 and 4 EH (solid circle) chondrites. The abscissa is the petrologic grade of type 3 chondrites (left plots) and the petrologic type of EH chondrites (right plots). In both abscissa, increased thermal metamorphism is to the right. The dashed lines are linear least squares fits to exponential (a) or linear (b, c) functions for chondrites within a single chemical group while the solid lines represent fits to all type 3 ordinary chondrites. Chondrites are composed of a fine grain matrix which contains nanodiamonds as well as inclusions of chondrules and CAIs. The proportion of fine grain matrix to matrix inclusions varies in chondrites, therefore the nanodiamond abundances in (a) are normalized to the matrix content.

Table 2.6 **Nanodiamond Abundances in Chondrites (adapted from Huss and Lewis (1995)[109] and Huss et al. (2003)[124])**

Chondrite	Class[a]	Abundance Recovered[b] (ppm bulk)	Abundance Estimated from Xe–HL Content of Meteorite (ppm)		C Content[d] Bulk Meteorite (%)	Fraction Total C as Diamond[e] (%)	References for Chondrite C Content
			Bulk Meteorite	Matrix[c] Normalized			
Orgueil	CI1	1134 ± 35[f]	1436 ± 56	1436 ± 56	3.33 ± 0.16 (*9*)	4.31 ± 0.27	125, 133–140
Murchison	CM2	613	740 ± 76	1164 ± 119	1.90 ± 0.14 (*2*)	3.89 ± 0.49	133, 138
Murray	CM2	560	614 ± 65	1044 ± 111	2.21 ± 0.13 (*6*)	2.78 ± 0.34	133–138
Renazzo	CR2	397	410 ± 63	1318 ± 203	1.50	2.73 ± 0.42	138
ALHA 77307	CO3.0	306	523 ± 74	1551 ± 220	0.28	18.68 ± 2.64	141
Colony	CO3.0	209	303 ± 49	1034 ± 167	0.63	4.81 ± 0.78	142
Kainsaz	CO3.1	149 ± 1[f]	262 ± 90[f]	873 ± 304[f]	0.50 ± 0.11 (*2*)	5.24 ± 2.14[f]	133, 143
Vigarano	CV3	281 ± 18	623 ± 20	1806 ± 107	1.09 ± 0.05 (*3*)	5.72 ± 0.32	133, 139, 143
Leoville	CV3	496 ± 4	545 ± 18	1554 ± 93	0.77	7.08 ± 0.23	143
Mokoia	CV3	430	484 ± 69	1216 ± 173	0.71 ± 0.05 (*6*)	6.82 ± 1.08	133–137, 143
Allende	CV3	250 ± 3[f]	340 ± 45[f]	885 ± 125[f]	0.27 ± 0.02 (*4*)	12.59 ± 1.91[f]	51, 133, 134, 144
Axtell	CV3	238	289 ± 19	826 ± 83			
Acfer 214	CH3	41.2	86.6 ± 9.9	721 ± 110			
Semarkona	LL3.0	142 ± 16[f]	177 ± 6	1134 ± 69	0.57	3.11 ± 0.11	145

Krymka	LL3.1	95 ± 37[f]	137 ± 9	1008 ± 82	0.28 ± 0.01(*2*)	4.89 ± 0.37	145, 146
Bishunpur	LL3.1	115 ± 2	125 ± 4	901 ± 55	0.43 ± 0.11 (*2*)	2.91 ± 0.75	140, 145
Ragland	LL3.5	69.4 ± 2.3[f]	83 ± 5	614 ± 50	0.61	1.36 ± 0.08	147
Mezö-Madaras	L3.5	52 ± 7	62 ± 2	626 ± 38	0.46 (*2*)	1.35 ± 0.04	145, 148
ALHA 77214	L3.5	52 ± 3[f]	61 ± 7[f]	440 ± 58[f]	1.08	0.56 ± 0.06[f]	149
Julesburg	L3.7	<0.01	0.36 ± 0.02	2.6 ± 0.2	0.08	0.05 ± 0.00	150
Tieschitz	H3.6	39 ± 1[f]	46 ± 3[f]	341 ± 27[f]	0.25	1.84 ± 0.12[f]	145
Dimmitt	H3.8	0.3 ± 0.1	3.3 ± 0.3	24 ± 3	0.11 ± 0.02 (*2*)	0.30 ± 0.06	140, 145
Grady	H3.8	<0.02[f]	<0.09	<0.7	0.10 ± 0.01 (*3*)	<0.01	140, 145, 148
Qingzhen	EH3	59 ± 1	73 ± 3	518 ± 31			
Indarch	EH4	29 ± 2[f]	43 ± 2	344 ± 38	0.42 ± 0.01 (*3*)	1.02 ± 0.05	135, 136, 140
Abee	EH5	–	<0.4	<3.2	0.37 ± 0.01 (*2*)	<0.01	134, 140

[a] For a description of meteorite classes and petrologic type see refs. [121, 122].
[b] Not an accurate measure since nanodiamonds were subject to mass loss during isolation.
[c] Chondrites are composed of a fine-grain matrix which contains nanodiamonds as well as inclusions of chondrules and CAIs. The proportion of fine-grain matrix to matrix inclusions varies in chondrites, therefore the nanodiamond abundances are normalized to the matrix content.
[d] Mean and standard error of the mean for (*n*) independent values reported in the literature.
[e] Based on bulk (not matrix normalized) nanodiamond abundance estimated from Xe–HL content in bulk meteorite.
[f] Potentially subject to significant nanodiamond mass loss during meteorite processing.

content in a partially digested chondrite using the corresponding Xe–P6/Xe–HL ratio measured from the nanodiamond isolate. Matrix normalized diamond abundances based on Xe–HL content (Table 2.6) were then adjusted for Xe–P6 gas content using the Orgueil calibration.[109] The difficulty of this technique is that the Xe–P6 component is not well separated from Xe–HL and its isotopic composition is not well constrained. Further, Xe–P6 gases will be lost in the most thermally processed nanodiamonds. Nevertheless, the inferred nanodiamond abundances present prior to parent-body processing vary by a factor of 2 between chondrites and appear to correlate with chemical and physical properties of the host chondrites.[109] This is suggestive that parent bodies accreted dust that experienced a range of thermal processing in the accretion disk.

Nitrogen abundances in different nanodiamond populations vary by over a factor of 7 (Table 2.1) and also correlate with thermal alteration experienced by the host chondrite (Fig. 2.14(d)).[63] However, it has been argued that N, being a substitutional element in the diamond lattice, is not easily degassed from diamond.[63] Diffusion simulations predict significant N isotopic fractionation would result from degassing and this is not observed.[63] Since N substitutionally replaces C in diamond, lattice strain will result from mismatched C—N/C—C bond lengths inducing structural defects, which will reduce the stability of the crystal especially in grains with high N content. The mean N content in meteoritic nanodiamonds is relatively high, a factor of 3 higher than terrestrial kimberlitic diamonds.[66] Considering that meteoritic nanodiamonds originated from many sources, it is reasonable to expect a range of N concentrations in the individual nanodiamonds. Therefore, meteoritic nanodiamonds that possess the greatest amount of N and the highest concentrations of structural defects could be the least stable of the population to metamorphic processing.[126] Preferential destruction of the less stable, N-rich nanodiamonds would explain the decrease in mean N abundance with increased levels of thermal alteration. Since the carriers of Xe–HL appear to be the most stable grains in the meteoritic nanodiamond isolates, Xe–HL carriers may be the most N-poor nanodiamonds.

Presolar grains isolated from meteorites were subjected to processes in the accretion disk of the solar nebula including those of the meteorite parent bodies. Abundances of retained noble gases and of grain species reflect those processes as well as the thermal and chemical conditions the grains experienced. As such, meteoritic nanodiamonds can be used to probe parent-body metamorphism and possibly nebular heating.

2.7 Nanodiamonds in Interplanetary Dust Particles: Insights on Solar Nebula Evolution

In addition to chondrites, presolar grains have also been found in the only other class of primitive specimens of the solar system presently available for laboratory study, IDPs.[17] These are <500 μm diameter, heterogeneous assemblages of diverse, fine-grained (<0.1 μm) minerals that are often unequilibrated.[127] Many have elemental abundances similar to the most primitive chondrites (CI and CM groups). The presence, in some classes of IDPs, of submicron-sized presolar grains,[17] high volatile-element abundances, and a wide range of deuterium abundances ($-420‰ \leq \delta^2H \leq 2.5 \times 10^4‰$) exceeding those exhibited by chondrites[128] demonstrate that some IDPs are among the most primitive material known in the solar system. Although the sources of IDPs are not well determined, they are believed to have been derived from comets, fragmented asteroids, and possibly material that was in the ISM[129].

Since nanodiamonds are relatively abundant in chondrites, and many IDPs appear more primitive than chondrites, it stands to reason that nanodiamonds should be abundant in IDPs. Using the same TEM techniques proven to successfully image nanodiamonds *in situ* within cross-sectioned chondrites (Murchison and Orgueil), Dai et al. (2002) observed nanodiamonds in Antarctic micrometeorites and in large, loose-aggregate (termed "giant cluster") IDPs (Fig. 2.15).[56,130] However, not expected was the lack of nanodiamonds in smaller aggregate (inexactly termed "non-cluster" or "individual") IDPs examined by the same technique.[56,130] Both giant cluster and non-cluster IDPs can have similar mineralogy, petrography, and chondritic-like compositions, but they differ in several respects. First, giant cluster IDPs are fragile assemblages that disintegrate into tens to hundreds of fragments upon impact with collectors in contrast to the smaller (so called "non-cluster") aggregates that often remain intact. Second, N in cluster IDPs is heavier (mean $^{14}N/^{15}N = 238.6$) than non-cluster IDPs (mean $^{14}N/^{15}N = 259$).[128] Most importantly, deuterium enrichments in fragments of cluster IDPs are an order of magnitude larger (approaching that of ISM molecular clouds) and more variable than grains in non-cluster IDPs.[128]

Dai et al. (2002)[56] propose two interpretations of their results, both of which rest on the surmised, but not proven, assumption that the giant cluster IDPs that contained nanodiamonds were derived from asteroids and that the non-cluster IDPs that lacked nanodiamonds were derived from comets. To explain the apparent absence of nanodiamonds in

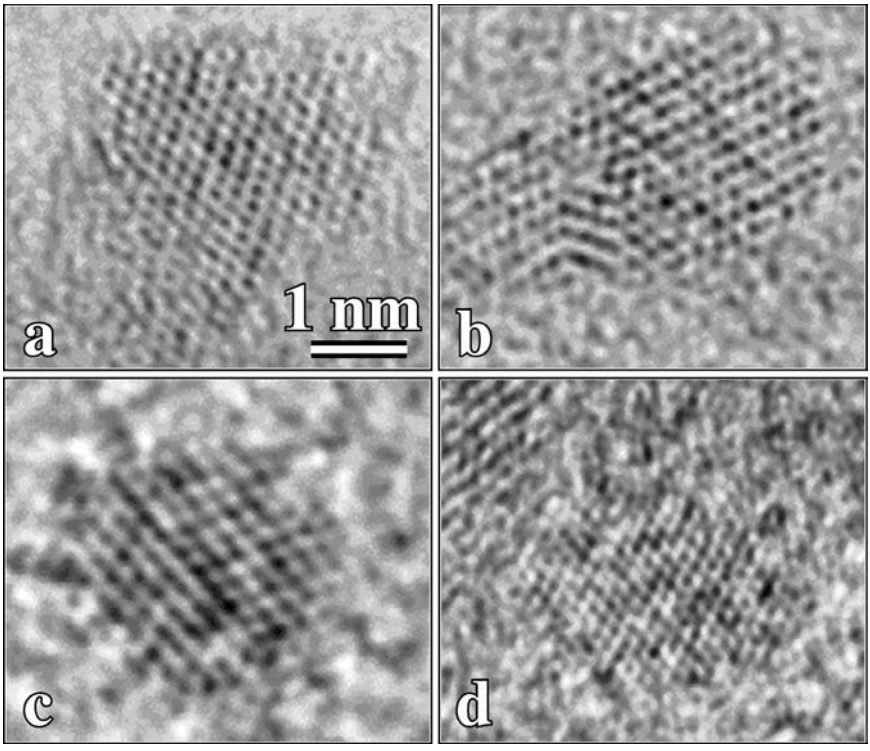

Figure 2.15 Nanodiamonds imaged along the [011] zone axis in etched, cross-sectioned (a) Murchison chondrite, as well as interplanetary dust particles (b) W7110A-2E-D, (c) U2-30C-1G-B, and (d) U2-20GCA-4. (Images courtesy of Z. R. Dai and J. P. Bradley.)[56]

cometary particles, they suggested that the abundance of nanodiamonds in the solar nebula must have decreased with increasing heliocentric distance at the time of asteroid and comet formation. They proposed two scenarios in which that could occur: either some, perhaps most, meteoritic nanodiamonds were formed in the inner solar nebula and are not presolar; or meteoritic nanodiamonds are presolar and the original homogeneous distribution of nanodiamonds was altered by nebular processes.[56] Although the nearly solar C isotopic composition of meteoritic nanodiamonds is consistent with formation in the inner solar nebula, their N isotopic compositions are isotopically anomalous compared to terrestrial planetary reservoirs (see Section 2.4.1). This implies either that turbulent mixing of condensates between the inner and outer solar nebula occurred or that nebular condensates are a minor contribution to the meteoritic nanodiamond population.

There is another possible interpretation of the IDP data. Recall that giant cluster IDPs exhibit deuterium enrichments that are significantly larger and more variable than that exhibited by non-cluster IDPs. This would suggest that giant cluster IDPs are more primitive (i.e., more similar to comet material) than non-cluster IDPs,[128] opposite to the interpretations of Dai et al. (2002)[56,130]. Regardless of the origins of the IDPs that survive atmospheric entry and collection, the isotopic differences in the relatively volatile deuterium and N suggest that non-cluster IDPs experienced more severe thermal histories than giant cluster IDPs. In other words, the main physical difference between IDPs containing nanodiamonds and those lacking nanodiamonds is their thermal history.

Peak atmospheric-entry temperatures of non-cluster IDPs have been estimated between 550 and 950 °C (inferred entry velocities $<14\,\mathrm{km\,s^{-1}}$) and between 653 and 1175 °C (inferred entry velocities $>18\,\mathrm{km\,s^{-1}}$) based on He release curves measured during stepped heating.[131] For giant cluster IDPs, the effects of heating could be greatly minimized for interior grains by volatilization of the outer particles of the cluster.[132] In comparison, meteoritic nanodiamonds are observed to have largely transformed to graphitic onions at 900 °C (see Section 2.4.2). It is possible that nanodiamonds are initially present in both non-cluster and giant cluster IDPs, and that they are transformed preferentially in non-cluster IDPs during atmospheric entry.

Clearly more work is needed to evaluate any of these intriguing possibilities. Microanalysis of comet dust collected from comet Wild 2 by the US Stardust spaceprobe may answer some of these questions, providing insights on the evolution of the solar nebula.

2.8 Summary of Experimental Data

Nanodiamonds, originating from many sources, are present in primitive meteorites at significant concentrations comprising up to 13–18% of the total C inventory in chondrites. Their abundances in chondrites and their retention of trapped gases correlate with the metamorphic history of the chondrite parent bodies, indicating meteoritic nanodiamonds predate the accretion of their parent bodies. Since nanodiamonds are susceptible to alteration in parent bodies, they can be used to probe parent-body and possibly nebular processes.

Nanodiamond isolates from acid dissolution residues of chondrites exhibit various isotopic anomalies, but only the anomalous Xe–HL and

Te–H associated with supernovae provide tenable evidence for a presolar origin for at least a subpopulation, if not all, of the diamonds. Definitive isotopic evidence of a presolar origin for all or part of the population remains elusive because of the extremely small size of the diamonds. Although the rare grains that carry Xe–HL and Te–H have never been isolated as pure isolates and directly identified, sufficient evidence suggests the carrier phase is nanodiamond. This is based on several lines of evidence, the most compelling being the apparent inseparability of the anomalous noble gases from the nanodiamond isolates. While the sources and their relative contribution to the population of meteoritic nanodiamonds remain to be established, microstructural TEM studies indicate that the majority of the meteoritic nanodiamonds formed by low-pressure condensation similar to the CVD process.

2.9 The New Astronomy

Until recently, nearly all of our knowledge about the cosmos was based on the information encoded within the wide spectrum of light reflected or emitted from distant objects. Although astronomical spectroscopy has extracted a wealth of information on temperature, chemical composition and in rare cases some isotopic compositions in astrophysical environments, spectra are often complex, recording a medley of electromagnetic interactions with many mineral and molecular species. While valuable information on ensemble averages of large-scale structures can be obtained, fine details within these structures such as the ranges of isotopic, chemical, and mineral heterogeneity are obscured. Understanding the processes and conditions in astrophysical environments requires information across scale regimes that span a wide range.

Today, the study of the cosmos is no longer restricted to remote observation by gazing up through ground-based and orbital telescopes at stars and galaxies. Physical conditions within dust forming regions of stars, stellar nucleosynthesis, stellar evolution, galactic chemical evolution, and the very evolution of the solar nebula can all be probed in the laboratory by peering down through powerful micro/nanoanalytical microscopes. The study of the microstructure (mineralogy, crystal structure, defect structure) and geochemistry (elemental and isotopic compositions) of presolar stardust, direct specimens from distant stellar environments, has proven to be a vital component of modern astronomy. Laboratory micro/nanocharacterization of presolar and extraterrestrial minerals provides important geochemical information that otherwise would be diffi-

cult, if not impossible, to obtain from traditional astronomical observation of light. Coupled with traditional astronomical observation, micro/nanoanalysis of mineral specimens will certainly reveal much information about the cosmos and our place in it.

Acknowledgments

I thank the following people for valuable comments and discussions: T. J. Bernatowicz (Washington U.), G. R. Huss (U. of Hawaii at Manoa), R. S. Lewis (U. of Chicago), B. S. Meyer (Clemson U.), and S. S. Russell (The Natural History Museum, London). I thank Bradley Meyer (Clemson U.) for providing unpublished calculations for the *r*-process rapid separation nucleosynthesis model. I also thank B. J. Little (NRL) for editorial comments. This chapter is based upon work partially supported by NASA under contract W-10246 issued through the Office of Space Science and NRL through the Office of Naval Research (ONR).

References

1. R. S. Lewis, M. Tang,† J. F. Wacker, E. Anders, and E. Steel, Interstellar diamonds in meteorites, *Nature* **326**, 160–162 (1987).
2. T. L. Daulton, D. D. Eisenhour, T. J. Bernatowicz, R. S. Lewis, and P. R. Buseck, Genesis of presolar diamonds: Comparative high-resolution transmission electron microscopy study of meteoritic and terrestrial nanodiamonds, *Geochimica et Cosmochimica Acta* **60**, 4853–4872 (1996).
3. T. Bernatowicz, G. Fraundorf, M. Tang,† E. Anders, B. Wopenka, E. Zinner, and P. Fraundorf, Evidence for interstellar SiC in the Murray carbonaceous meteorite, *Nature* **330**, 728–730 (1987).
4. M. Tang† and E. Anders, Isotopic anomalies of Ne, Xe, and C in meteorites. II. Interstellar diamond and SiC: Carriers of exotic noble gases, *Geochimica et Cosmochimica Acta* **52**, 1235–1244 (1988).
5. T. L. Daulton, T. J. Bernatowicz, R. S. Lewis, S. Messenger, F. J. Stadermann, and S. Amari, Polytype distribution in circumstellar silicon carbide, *Science* **296**, 1852–1855 (2002).
6. S. Amari, E. Anders, A. Virag, and E. Zinner, Interstellar graphite in meteorites, *Nature* **345**, 238–240 (1990).
7. T. J. Bernatowicz, S. Amari, E. K. Zinner, and R. S. Lewis, Interstellar grains within interstellar grains, *The Astrophysical Journal* **373**, L73–L76 (1991).
8. T. J. Bernatowicz, R. Cowsik, P. C. Gibbons, K. Lodders, B. Fegley Jr., S. Amari, and R. S. Lewis, Constraints on stellar grain formation from preso-

† M. Tang appears as T. Ming in the author list of the cited journals and in publication databases.

lar graphite in the Murchison meteorite, *The Astrophysical Journal* **472**, 760–782 (1996).
9. T. Bernatowicz, J. Bradley, S. Amari, S. Messenger, and R. Lewis, New kinds of massive star condensates in a presolar graphite from Murchison, *Lunar and Planetary Science* **XXX**, 1392 (1999).
10. K. Croat, T. Bernatowicz, F. J. Stadermann, S. Messenger, and S. Amari, Coordinated isotopic and TEM studies of a supernova graphite, *Lunar and Planetary Science* **XXXIII**, 1315 (2002).
11. T. K. Croat, T. Bernatowicz, S. Amari, S. Messenger, and F. J. Stadermann, Structural, chemical, and isotopic microanalytical investigations of graphite from supernovae, *Geochimica et Cosmochimica Acta* **67**, 4705–4725 (2003).
12. T. K. Croat, T. J. Bernatowicz, S. Amari, S. Messenger, and F. J. Stadermann, Metallic iron condensed onto titanium carbides within supernova graphites, *Meteoritics & Planetary Science* **37**, A39 (2002).
13. L. R. Nittler and C. M. O'D. Alexander, Automatic identification of presolar Al- and Ti-rich oxide grains from ordinary chondrites, *Lunar and Planetary Science* **XXX**, 2041 (1999).
14. I. D. Hutcheon, G. R. Huss, A. J. Fahey, and G. J. Wasserburg, Extreme ^{26}Mg and ^{17}O enrichments in an Orgueil corundum: Identification of a presolar oxide grain, *The Astrophysical Journal* **425**, L97–L100 (1994).
15. L. R. Nittler, C. M. O'D. Alexander, X. Gao, R. M. Walker, and E. K. Zinner, Interstellar oxide grains from the Tieschitz ordinary chondrite, *Nature* **370**, 443–446 (1994).
16. B.-G. Choi, G. J. Wasserburg, and G. R. Huss, Circumstellar hibonite and corundum and nucleosynthesis in asymptotic giant branch stars, *The Astrophysical Journal* **522**, L133–L136 (1999).
17. S. Messenger, L. P. Keller, F. J. Stadermann, R. M. Walker, and E. Zinner, Samples of stars beyond the solar system: Silicate grains in interplanetary dust, *Science* **300**, 105–108 (2003).
18. A. N. Nguyen and E. Zinner, Discovery of ancient silicate stardust in a meteorite, *Science* **303**, 1496–1499 (2004).
19. P. Hoppe, R. Strebel, P. Eberhardt, S. Amari, and R. S. Lewis, Evidence for an interstellar nitride grain with highly anomalous isotopic compositions of C, N and Si, *Lunar and Planetary Science* **XXV**, 563–564 (1994).
20. P. Hoppe, R. Strebel, P. Eberhardt, S. Amari, and R. S. Lewis, Small SiC grains and a nitride grain of circumstellar origin from the Murchison meteorite: Implications for stellar evolution and nucleosynthesis, *Geochimica et Cosmochimica Acta* **60**, 883–907 (1996).
21. E. Anders, Circumstellar material in meteorites: Noble gases, carbon and nitrogen, in *Meteorites and the Early Solar System*, edited by J. F. Kerridge and M. S. Matthews (University of Arizona Press, Tucson, 1988), pp. 927–955.
22. E. Anders, R. S. Lewis, M. Tang,† and E. Zinner, Interstellar grains in meteorites: Diamond and silicon carbide, in *Interstellar Dust: Proceedings of the 135th Symposium of the International Astronomical Union*, edited by L. J. Allamandola and A. G. G. M. Tielens (Kluwer Academic Publishers, Dordrecht, 1989), pp. 389–402.

23. E. Anders and E. Zinner, Interstellar grains in primitive meteorites: Diamond, silicon carbide, and graphite, *Meteoritics* **28**, 490–514 (1993).
24. U. Ott, Interstellar grains in meteorites, *Nature* **364**, 25–33 (1993).
25. U. Ott, Physical and isotopic properties of surviving interstellar carbon phases, in *Protostars and Planets III*, edited by E. H. Levy and J.-I. Lunine (University of Arizona Press, Tucson, 1993), pp. 883–902.
26. E. Zinner, Interstellar grains from primitive meteorites: New constraints on nucleosynthesis theory and stellar evolution models, in *Nuclei in the Cosmos III*, edited by M. Busso, C. M. Raiteri, and R. Gallino (American Institute of Physics, New York, 1995), pp. 567–579.
27. E. Zinner, Isotopic abundances in stars as inferred from the study of presolar grains in meteorites, *in Cosmic Abundances*, edited by S. S. Holt and G. Sonneborn (Astronomical Society of the Pacific Conference Series, Vol. 99, 1996), pp. 147–161.
28. T. J. Bernatowicz and R. M. Walker, Ancient stardust in the laboratory, *Physics Today* **50**, 26–32 (1997).
29. T. J. Bernatowicz, Presolar grains from meteorites, in *From Stardust to Planetesimals*, edited by Y. J. Pendleton and A. G. G. M. Tielens (Astronomical Society of the Pacific Conference Series, Vol. 122, 1997), pp. 227–251.
30. S. Amari and E. Zinner, Presolar grains in meteorites: Stardust in the laboratory, *Nuclear Physics A* **621**, 99c–112c (1997).
31. E. Zinner, Presolar material in meteorites: An overview, in *Astrophysical Implications of the Laboratory Study of Presolar Materials*, edited by T. J. Bernatowicz and E. K. Zinner (American Institute of Physics, New York, 1997), pp. 3–26.
32. E. Zinner, Stellar nucleosynthesis and the isotopic composition of presolar grains from primitive meteorites, *Annual Review of Earth and Planetary Science* **26**, 147–188 (1998).
33. E. Zinner, Trends in the study of presolar dust grains from primitive meteorites, *Meteoritics & Planetary Science* **33**, 549–564 (1998).
34. E. Zinner, Errata: Trends in the study of presolar dust grains from primitive meteorites, *Meteoritics & Planetary Science* **33**, 1341 (1998).
35. P. Hoppe and E. Zinner, Presolar dust grains from meteorites and their stellar sources, *Journal of Geophysical Research* **105**, 10371–10385 (2000).
36. U. Ott, Presolar grains in meteorites: An overview and some implications, *Planetary and Space Science* **49**, 763–767 (2001).
37. U. Ott, The most primitive material in meteorites, in *Astromineralogy*, edited by T. K. Henning (Lecture Notes in Physics, Vol. 609, Springer, Berlin, 2003), pp. 236–265.
38. L. R. Nittler, Presolar stardust in meteorites: Recent advances and scientific frontiers, *Earth and Planetary Science Letters* **209**, 259–273 (2003).
39. D. D. Clayton and L. R. Nittler, Astrophysics with presolar stardust, *Annual Review of Astronomy and Astrophysics* **42**, 39–78 (2004).
40. E. K. Zinner, Presolar grains, in *Treatise on Geochemistry*, Vol. 1, edited by K. K. Turekian, H. D. Holland, and A. M. Davis (Elsevier, Amsterdam, 2004), pp. 17–39.

41. T. J. Bernatowicz, T. K. Croat, and T. L. Daulton, Origin and evolution of carbonaceous presolar grains in stellar environments, in *Meteorites and the Early Solar System II*, edited by D. Lauretta, L. A. Leshin, and H. Y. McSween Jr. (University of Arizona Press, Tucson, 2006), in press.
42. T. L. Daulton, Presolar diamonds in Allende, *Meteorite! Magazine* **5**(1), 26–29 (1999).
43. T. L. Daulton, Nanodiamonds in the cosmos. Microstructural and trapped element isotopic data, in *Syntheses*, *Properties*, *and Applications of Ultrananocrystalline Diamond*, edited by D. M. Gruen, O. A. Shenderova, and A. Y. Vul' (Springer, Berlin, 2005), pp. 49–62.
44. G. R. Huss, Meteoritic nanodiamonds: Messengers from the stars, *Elements* **1**, 97–100 (2005).
45. J. H. Reynolds and G. Turner, Rare gases in the chondrite Renazzo, *Journal of Geophysical Research* **69**, 3263–3281 (1964).
46. D. C. Black and R. O. Pepin, Trapped neon in meteorites – II, *Earth and Planetary Science Letters* **6**, 395–405 (1969).
47. D. C. Black, On the origins of trapped helium, neon, and argon isotopic variations in meteorites – II. Carbonaceous meteorites, *Geochimica et Cosmochimica Acta* **36**, 377–394 (1972).
48. A. G. W. Cameron, The formation of the sun and planets, *Icarus* **1**, 13–69 (1962).
49. R. N. Clayton, L. Grossman, and T. K. Mayeda, A component of primitive nuclear composition in carbonaceous meteorites, *Science* **182**, 485–488 (1973).
50. R. N. Clayton, Self-shielding in the solar nebula, *Nature* **415**, 860–861 (2002).
51. P. K. Swart, M. M. Grady, C. T. Pillinger, R. S. Lewis, and E. Anders, Interstellar carbon in meteorites, *Science* **220**, 406–410 (1983).
52. J. Yang and S. Epstein, Relic interstellar grains in Murchison meteorite, *Nature* **311**, 544–547 (1984).
53. F. R. Niederer, P. Eberhardt, J. Geiss, and R. S. Lewis, Carbon isotope abundances in Murchison residue 2C10c, *Meteoritics* **20**, 716–718 (1985).
54. J. Halbout, T. K. Mayeda, and R. N. Clayton, Carbon isotopes and light element abundances in carbonaceous chondrites, *Earth and Planetary Science Letters* **80**, 1–18 (1986).
55. R. S. Lewis, E. Anders, I. P. Wright, S. J. Norris, and C. T. Pillinger, Isotopically anomalous nitrogen in primitive meteorites, *Nature* **305**, 767–771 (1983).
56. Z. R. Dai, J. P. Bradley, D. J. Joswiak, D. E. Brownlee, H. G. M. Hill, and M. J. Genge, Possible *in situ* formation of meteoritic nanodiamonds in the early solar system, *Nature* **418**, 157–159 (2002).
57. D. D. Clayton, B. S. Meyer, C. I. Sanderson, S. S. Russell, and C. T. Pillinger, Carbon and nitrogen isotopes in type II supernova diamonds, *The Astrophysical Journal* **447**, 894–905 (1995).
58. A. G. G. M. Tielens, C. G. Seab, D. J. Hollenbach, and C. F. McKee, Shock processing of interstellar dust: Diamonds in the sky, *The Astrophysical Journal* **319**, L109–L113 (1987).

59. J. A. Nuth III and J. E. Allen Jr., Supernovae as sources of interstellar diamonds, *Astrophysics and Space Science* **196**, 117–123 (1992).
60. M. Ozima and K. Mochizuki, Origin of nanodiamonds in primitive chondrites: (1) Theory, *Meteoritics* **28**, 416–417 (1993).
61. P. Fraundorf, G. Fraundorf, T. Bernatowicz, R. Lewis, and M. Tang, Stardust in the TEM, *Ultramicroscopy* **27**, 401–412 (1989).
62. R. S. Lewis, E. Anders, and B. T. Draine, Properties, detectability and origin of interstellar diamonds in meteorites, *Nature* **339**, 117–121 (1989).
63. S. S. Russell, J. W. Arden, and C. T. Pillinger, A carbon and nitrogen isotope study of diamond from primitive chondrites, *Meteoritics & Planetary Science* **31**, 343–355 (1996).
64. A. Virag, E. Zinner, R. S. Lewis, and M. Tang, Isotopic composition of H, C, and N in Cδ diamonds from the Allende and Murray carbonaceous chondrites, *Lunar and Planetary Science* **XX**, 1158–1159 (1989).
65. J. W. Arden, R. D. Ash, M. M. Grady, I. P. Wright, and C. T. Pillinger, Further studies on the isotopic composition of interstellar grains in Allende: 1. Diamonds, *Lunar and Planetary Science* **XX**, 21–22 (1989).
66. S. S. Russell, J. W. Arden, and C. T. Pillinger, Evidence for multiple sources of diamond from primitive chondrites, *Science* **254**, 1188–1191 (1991).
67. R. S. Lewis, G. R. Huss, and G. Lugmair, Finally, Ba & Sr accompanying Xe-HL in diamonds from Allende, *Lunar and Planetary Science* **XXII**, 807–808 (1991).
68. R. Maas, R. D Loss, K. J. R. Rosman, J. R. De Laeter, R. S. Lewis, G. R. Huss, and G. W. Lugmair, Isotope anomalies in tellurium and palladium from Allende nanodiamonds, *Meteoritics & Planetary Science* **36**, 849–858 (2001).
69. S. Richter, U. Ott, and F. Begemann, Tellurium-H in interstellar diamonds, *Lunar and Planetary Science* **XXVIII**, 1185 (1997).
70. P. Hoppe, S. Amari, E. Zinner, T. Ireland, and R. S. Lewis, Carbon, nitrogen, magnesium, silicon, and titanium isotopic compositions of single interstellar silicon carbide grains from the Murchison carbonaceous chondrite, *The Astrophysical Journal* **430**, 870–890 (1994).
71. S. Amari, C. Jennings, A. Nguyen, F. J. Stadermann, E. Zinner, and R. S. Lewis, NanoSIMS isotopic analysis of small presolar SiC grains from the Murchison and Indarch meteorites, *Lunar and Planetary Science* **XXXIII**, 1205 (2002).
72. T. J. Bernatowicz, P. C. Gibbons, and R. S. Lewis, Electron energy loss spectrometry of interstellar diamonds, *The Astrophysical Journal* **359**, 246–255 (1990).
73. E. Anders and N. Grevesse, Abundances of the elements: Meteoritic and solar, *Geochimica et Cosmochimica Acta* **53**, 197–214 (1989).
74. R. Kallenbach, J. Geiss, F. M. Ipavich, G. Gloeckler, P. Bochsler, F. Gliem, S. Hefti, M. Hilchenbach, and D. Hovestadt, Isotopic composition of solar wind nitrogen: First in situ determination with the CELIAS/MTOF spectrometer on board *SOHO*, *The Astrophysical Journal* **507**, L185–L188 (1998).

75. J. H. Hoffman, R. R. Hodges Jr., M. B. McElroy, T. M. Donahue, and M. Kolpin, Composition and structure of the Venus atmosphere: Results from Pioneer Venus, *Science* **205**, 49–52 (1979).
76. K. J. Mathew and K. Marti, Early evolution of Martian volatiles: Nitrogen and noble gas components in ALH84001 and Chassigny, *Journal of Geophysical Research* **106**, 1401–1422 (2001).
77. T. Owen, K. Biemann, D. R. Rushneck, J. E. Biller, D. W. Howarth, and A. L. Lafleur, The composition of the atmosphere at the surface of Mars, *Journal of Geophysical Research* **82**, 4635–4639 (1977).
78. T. Owen, P. R. Mahaffy, H. B. Niemann, S. Atreya, and M. Wong, Protosolar nitrogen, *The Astrophysical Journal* **553**, L77–L79 (2001).
79. G. R. Huss and R. S. Lewis, Noble gases in presolar diamonds I: Three distinct components and their implications for diamond origins, *Meteoritics* **29**, 791–810 (1994).
80. G. R. Huss and R. S. Lewis, Noble gases in presolar diamonds II: Component abundances reflect thermal processing, *Meteoritics* **29**, 811–829 (1994).
81. P. Eberhardt, J. Geiss, H. Graf, N. Grögler, U. Krähenbühl, H. Schwaller, J. Schwarzmüller, and A. Stettler, Trapped solar wind noble gases, exposure age and K/Ar-age in Apollo 11 lunar fine material, *Proceedings of the Apollo 11 Lunar Science Conference* **2**, 1037–1070 (1970).
82. P. Eberhardt, J. Geiss, H. Graf, N. Grögler, M. D. Mendia, M. Mörgeli, H. Schwaller, A. Stettler, U. Krähenbühl, and H. R. von Gunten, Trapped solar wind noble gases in Apollo 12 lunar fines 12001 and Apollo 11 breccia 10046, *Proceedings of the Third Lunar Science Conference* (Supplement 3), *Geochimica et Cosmochimica Acta* **2**, 1821–1856 (1972).
83. A. Braatz, F. Banhart, Th. Henning, and U. Ott, Transformation of meteoritic diamonds to graphitic onions upon annealing, *Meteoritics & Planetary Science* **34**, A16–A17 (1999).
84. T. L. Daulton, A. P. Koscheev, and R. S. Lewis, Unpublished results (2005).
85. D. Heymann and M. Dziczkaniec, Xenon from intermediate zones of supernovae, *Proceedings of the Lunar and Planetary Science Conference* **X**, 1943–1959 (1979).
86. D. D. Clayton, Origin of heavy xenon in meteoritic diamonds, *The Astrophysical Journal* **340**, 613–619 (1989).
87. W. M. Howard, B. S. Meyer, and D. D. Clayton, Heavy-element abundances from a neutron burst that produces Xe-H, *Meteoritics* **27**, 404–412 (1992).
88. U. Ott, Interstellar diamond xenon and timescales of supernova ejecta, *The Astrophysical Journal* **463**, 344–348 (1996).
89. L. Alaerts, R. S. Lewis, and E. Anders, Isotopic anomalies of noble gases in meteorites and their origins – III. LL-chondrites, *Geochimica et Cosmochimica Acta* **43**, 1399–1415 (1979).
90. R. K. Moniot, Noble-gas-rich separates from ordinary chondrites, *Geochimica et Cosmochimica Acta* **44**, 253–271 (1980).
91. K. L. Levsky, U. Ott, and F. Begemann, Noble gas components in Krymka (LL3.0), *Meteoritics* **24**, 292–293 (1989).
92. N. Schelhaas, U. Ott, and F. Begemann, Trapped noble gases in unequilibrated ordinary chondrites, *Geochimica et Cosmochimica Acta* **54**, 2869–2882 (1990).

93. R. H. Nichols Jr., C. M. Hohenberg, C. M. O'D. Alexander, C. T. Olinger, and J. W. Arden, Xenon and neon from acid-resistant residues of Inman and Tieschitz, *Geochimica et Cosmochimica Acta* **55**, 2921–2936 (1991).
94. R. H. Brazzle, X. Gao, C. M. Hohenberg, and R. H. Nichols Jr., High-precision noble gas analysis of Allende diamond, *Meteoritics* **28**, 327–328 (1993).
95. A. B. Verchovsky, A. V. Fisenko, L. F. Semjonova, I. P. Wright, M. R. Lee, and C. T. Pillinger, C, N, and noble gas isotopes in grain size separates of presolar diamonds from Efremovka, *Science* **281**, 1165–1168 (1998).
96. A. P. Meshik, O. V. Pravdivtseva, and C. M. Hohenberg, Separation of Xe-H and Xe-L by selective laser absorption in Murchison diamonds, *Lunar and Planetary Science* **XXX**, 1621 (1999).
97. O. K. Manuel, E. W. Hennecke, and D. D. Sabu, Xenon in carbonaceous chondrites, *Nature Physical Science* **240**, 99–101 (1972).
98. D. D. Clayton, Spectrum of carbonaceous-chondrite fission xenon, *Geochimica et Cosmochimica Acta* **40**, 563–565 (1976).
99. E. Zinner, M. Tang,† and E. Anders, Interstellar SiC in the Murchison and Murray meteorites: Isotopic composition of Ne, Xe, Si, C, and N, *Geochimica et Cosmochimica Acta* **53**, 3273–3290 (1989).
100. B. Srinivasan and E. Anders, Noble gases in the Murchison meteorite: Possible relics of *s*-process nucleosynthesis, *Science* **201**, 51–56 (1978).
101. A. B. Verchovsky, U. Ott, S. S. Russell, C. T. Pillinger, A. V. Fisenko, and Y. A. Shukolyukov, Carbon, nitrogen, and noble gases in diamond-rich residues of the Efremovka CV3 chondrite, *Lunar and Planetary Science* **XXIII**, 1467–1468 (1992).
102. R. S. Lewis and E. Anders, Isotopically anomalous xenon in meteorites: A new clue to its origin, *The Astrophysical Journal* **247**, 1122–1124 (1981).
103. A. P. Koscheev, M. D. Gromov, R. K. Mohapatra, and U. Ott, History of trace gases in presolar diamonds inferred from ion-implantation experiments, *Nature* **412**, 615–617 (2001).
104. G. R. Huss, U. Ott, and A. P. Koscheev, Implications of ion-implantation experiments for understanding noble gases in presolar diamonds. *Meteoritics & Planetary Science* **35**, A79–A80 (2000).
105. U. G. Jørgensen, Formation of Xe-HL-enriched diamond grains in stellar environments, *Nature* **332**, 702–705 (1988).
106. N. R. Greiner, D. S. Phillips, J. D. Johnson, and F. Volk, Diamonds in detonation soot, *Nature* **333**, 440–442 (1988).
107. M. Frenklach, W. Howard, D. Huang, J. Yuan, K. E. Spear, and R. Koba, Induced nucleation of diamond powder, *Applied Physics Letters* **59**, 546–548 (1991).
108. J. C. Angus, M. Sunkara, S. R. Sahaida, and J. T. Glass, Twinning and faceting in early stages of diamond growth by chemical vapor deposition, *Journal of Materials Research* **7**, 3001–3009 (1992).
109. G. R. Huss and R. S. Lewis, Presolar diamond, SiC, and graphite in primitive chondrites: Abundances as a function of meteorite class and petrologic type, *Geochimica et Cosmochimica Acta* **59**, 115–160 (1995).
110. W. Carey, E. Zinner, P. Fraundorf, and R. S. Lewis, Ion probe and TEM studies of a diamond bearing Allende residue, *Meteoritics* **22**, 349–350 (1987).

111. C. Frondel and U. B. Marvin, Lonsdaleite, a hexagonal polymorph of diamond, *Nature* **214**, 587–589 (1967).
112. R. E. Hanneman, H. M. Strong, and F. P. Bundy, Hexagonal diamonds in meteorites: Implications, *Science* **155**, 995–997 (1967).
113. M. E. Lipschutz and E. Anders, The record in the meteorites – IV Origin of diamonds in iron meteorites, *Geochimica et Cosmochimica Acta* **24**, 83–105 (1961).
114. M. E. Lipschutz, Origin of diamonds in the Ureilites, *Science* **143**, 1431–1434 (1964).
115. E. R. D. Scott, K. Keil, and D. Stöffler, Shock metamorphism of carbonaceous chondrites, *Geochimica et Cosmochimica Acta* **56**, 4281–4293 (1992).
116. M. Frenklach, R. Kematick, D. Huang, W. Howard, K. E. Spear, A. W. Phelps, and R. Koba, Homogeneous nucleation of diamond powder in the gas phase, *Journal of Applied Physics* **66**, 395–399 (1989).
117. K. Maruyama, M. Makino, N. Kikukawa, and M. Shiraishi, Synthesis of hexagonal diamond in a hydrogen plasma jet, *Journal of Materials Science Letters* **11**, 116–118 (1992).
118. C. Travaglio, R. Gallino, S. Amari, E. Zinner, S. Woosley, and R. S. Lewis, Low-density graphite grains and mixing in type II supernovae, *The Astrophysical Journal* **510**, 325–354 (1999).
119. L. R. Nittler, S. Amari, E. Zinner, S. E. Woosley, and R. S. Lewis, Extinct ^{44}Ti in presolar graphite and SiC: Proof of a supernova origin, *The Astrophysical Journal* **462**, L31–L34 (1996).
120. P. Hoppe, R. Strebel, P. Eberhardt, S. Amari, and R. S. Lewis, Isotopic properties of silicon carbide X grains from the Murchison meteorite in the size range 0.5–1.5 μm, *Meteoritics & Planetary Science* **35**, 1157–1176 (2000).
121. A. E. Rubin, Mineralogy of meteorite groups, *Meteoritics & Planetary Science* **32**, 231–247 (1997).
122. D. W. Sears, J. N. Grossman, C. L. Melcher, L. M. Ross, and A. A. Mills, Measuring metamorphic history of unequilibrated ordinary chondrites, *Nature* **287**, 791–795 (1980).
123. G. R. Huss, Ubiquitous interstellar diamond and SiC in primitive chondrites: Abundances reflect metamorphism, *Nature* **347**, 159–162 (1990).
124. G. R. Huss, A. P. Meshik, J. B. Smith, and C. M. Hohenberg, Presolar diamond, silicon carbide, and graphite in carbonaceous chondrites: Implications for thermal processing in the solar nebula, *Geochimica et Cosmochimica Acta* **67**, 4823–4848 (2003).
125. K. Fredriksson and J. F. Kerridge, Carbonates and sulfates in CI chondrites: Formation by aqueous activity on the parent body, *Meteoritics* **23**, 35–44 (1988).
126. A. V. Fisenko, S. S. Russell, R. D. Ash, L. F. Semjenova, A. B. Verchovsky, and C. T. Pillinger, Isotopic composition of carbon and nitrogen in the diamonds from the unequilibrated ordinary chondrite Krymka LL3.0, *Lunar and Planetary Science* **XXIII**, 365–366 (1992).
127. D. E. Brownlee, Cosmic dust: Collection and research, *Annual Review of Earth and Planetary Science* **13**, 147–173 (1985).

128. S. Messenger, Identification of molecular-cloud material in interplanetary dust particles, *Nature* **404**, 968–971 (2000).
129. A. D. Taylor, W. J. Baggaley, and D. I. Steel, Discovery of interstellar dust entering the Earth's atmosphere, *Nature* **380**, 323–325 (1996).
130. Z. R. Dai, J. P. Bradley, D. J. Joswiak, D. E. Brownlee, and M. J. Genge, Nano-diamonds in interplanetary dust particles (IDPs), micrometeorites, and meteorites, *Lunar and Planetary Science* **XXXIII**, 1321 (2002).
131. D. J. Joswiak, D. E. Brownlee, R. O. Pepin, and D. J. Schlutter, Characteristics of asteroidal and cometary IDPs obtained from stratospheric collectors: Summary of measured He release temperatures, velocities and descriptive mineralogy, *Lunar and Planetary Science* **XXXI**, 1500 (2000).
132. W. Klöck, Are all chondritic porous IDPs of cometary origin? *Meteoritics & Planetary Science* **31**, A71–72 (1996).
133. E. K. Gibson, C. B. Moore, and C. F. Lewis, Total nitrogen and carbon abundances in carbonaceous chondrites, *Geochimica et Cosmochimica Acta* **35**, 599–604 (1971).
134. T. Belsky and I. R. Kaplan, Light hydrocarbon gasses, C^{13}, and origin of organic matter in carbonaceous chondrites, *Geochimica et Cosmochimica Acta* **34**, 257–278 (1970).
135. H. B. Wiik, The chemical composition of some stony meteorites, *Geochimica et Cosmochimica Acta* **9**, 279–289 (1956).
136. G. Boato, The isotopic composition of hydrogen and carbon in the carbonaceous chondrites, *Geochimica et Cosmochimica Acta* **6**, 209–220 (1954).
137. J. W. Smith and I. R. Kaplan, Endogenous carbon in carbonaceous meteorites, *Science* **167**, 1367–1370 (1970).
138. F. Robert and S. Epstein, The concentration and isotopic composition of hydrogen, carbon and nitrogen in carbonaceous meteorites, *Geochimica et Cosmochimica Acta* **46**, 81–95 (1982).
139. B. Mason, The carbonaceous chondrites, *Space Science Reviews* **1**, 621–646 (1962–1963).
140. W. Otting and J. Zähringer, Total carbon content and primordial rare gases in chondrites, *Geochimica et Cosmochimica Acta* **31**, 1949–1960 (1967).
141. E. Jarosewich, Chemical analysis of meteorites: A compilation of stony and iron meteorite analyses, *Meteoritics* **25**, 323–337 (1990).
142. A. E. Rubin, J. A. James, B. D. Keck, K. S. Weeks, D. W. G. Sears, and E. Jarosewich, The Colony meteorite and variations in CO3 chondrite properties, *Meteoritics* **20**, 175–196 (1985).
143. J. F. Kerridge, Carbon, hydrogen and nitrogen in carbonaceous chondrites: Abundances and isotopic compositions in bulk samples, *Geochimica et Cosmochimica Acta* **49**, 1707–1714 (1985).
144. R. S. Clarke Jr., E. Jarosewich, B. Mason, J. Nelen, M. Gómez, and J. R. Hyde, The Allende, Mexico, meteorite shower, *Smithsonian Contributions to the Earth Sciences* **5**, 1–53 (1970).
145. C. B. Moore and C. F. Lewis, Total carbon content of ordinary chondrites. *Journal of Geophysical Research* **72**, 6289–6292 (1967).

146. E. Jarosewich and R. T. Dodd, Chemical variations among L-group chondrites, II. Chemical distinctions between L3 and LL3 chondrites, *Meteoritics* **16**, 83–91 (1981).
147. S. I. Recca, E. R. D. Scott, K. Keil, R. N. Clayton, T. K. Mayeda, G. I. Huss, E. Jarosewich, K. S. Weeks, F. A. Hasan, D. W. G. Sears, R. Wieler, and P. Signer, Ragland, an LL3.4 chondrite find from New Mexico, *Meteoritics* **21**, 217–229 (1986).
148. E. Jarosewich, Chemical analysis of seven stony meteorites and one iron with silicate inclusions, *Geochimica et Cosmochimica Acta* **31**, 1103–1106 (1967).
149. E. Jarosewich, Bulk chemical analyses of Antarctic meteorites, with notes on weathering effects on FeO, Fe-metal, FeS, H_2O, and C, *Smithsonian Contributions to the Earth Sciences* **26**, 111–114 (1984).
150. A. L. Graham, The Julesburg (L3) meteorite, *Meteoritics* **28**, 122–125 (1993).

3 Types of Nanocrystalline Diamond

Olga A. Shenderova and Gary McGuire

International Technology Center, Raleigh, NC, USA

Introduction

The term "nanodiamond" is broadly used for a variety of diamond-based materials at the nanoscale (the length scale of approximately 1–100 nanometers) including pure-phase diamond films, diamond particles and their structural assemblies such as loosely bound particle agglomerates, or particles incorporated into other material matrices. Moreover, recently fabricated 1-D diamond nanorods and 2-D diamond nanoplatelets complete the set of possible dimensionalities of the structures. There is a special class of nanodiamond material called "ultrananocrystalline" diamond with the characteristic size of the basic diamond constituents encompassing the range of just a few nanometers to distinguish it from other diamond-based nanostructures with characteristic sizes above ~10 nm. Among ultrananocrystalline diamond (UNCD) materials, the most promising for the nearest future nanotechnological applications are *UNCD particles* produced by detonation of carbon explosive materials (characteristic size of primary particles ~4–5 nm) developed in the former USSR in the 1960s and pure-phase *UNCD films* produced by chemical vapor deposition (CVD) (characteristic size of grains 2–5 nm) recently developed in the USA at Argonne National Laboratory.[1] Moreover, current world consumption of UNCD particulate of detonation origin equals hundreds of kilograms per year. Both UNCD particles and films possess unique properties and different niche applications. These two technologically important materials had been the focus of several recent reviews,[1–4] monographs,[5–7] and proceedings of topical nanodiamond conferences[8–10] and are the major topics of this book. One purpose of the current chapter is to summarize the known methods of synthesis of nanodiamond structures and to provide a more complete picture of the entire nanostructured diamond class of materials. Where appropriate, we also provide a short historical background, the level of commercialization of a particular type of nanodiamond as well as possible applications of nanodiamonds that are not included in other chapters of the book.

Methods for synthesizing diamond powder in the form of single particles with micro- and nanometer sizes were invented in the beginning of the 1960s by E. I. Du Pont de Nemours, USA, and the product has been commercially available since the 1970s (*Mypolex*™). DuPont produced polycrystalline diamond particles up to 50 microns in size using shock wave compression of carbon materials (graphite, carbon black) mixed with catalyst. The size of the primary grains in the polycrystalline particles is about 20–25 nm. Recently, the Mypolex polycrystalline diamond business had been acquired from DuPont, by Microdiamant AG, Switzerland, a company specializing in the micron- and submicron diamond market. The finest diamond fractions produced by micronizing followed by grading encompass the range of 0–50 nm with an average particle size of about 25 nm. Since acquiring the Mypolex product Microdiamant AG now manufactures three size classes smaller than the smallest ever available from DuPont.[30] In addition to Mypolex polycrystalline diamond, Microdiamant AG also provides the finest fractions of particles down to 0–50 nm processed from the starting material high-pressure, high-temperature (HPHT) synthetic diamond (both mono- and polycrystalline) as well as from natural diamond powders. The commercialization of this nanodiamond material has matured and it has been used for high-precision polishing applications for a long time.

An approach for producing UNCD powder with a characteristic size of primary particles of ~4–5 nm is the conversion of carbon-containing explosive compounds into diamond during firing of explosives in hermetic tanks ("detonation UNCD").[11] More details on the fascinating history of the discovery of the UNCD particulate is provided in Chapter 10 of this book. This method was initiated in Russia in the early 1960s soon after DuPont's work on shock wave synthesis. A large-scale production foundry, "ALTAI", was founded in Russia in 1983 to commercialize the process of detonation diamond production in bulk quantities (tonnes of the product per year).[5] According to a USSR government report (1989) on UNCD particulate production, it was planned to increase UNCD production by up to 250 million carats per year.[5] At the present time, however, the production of detonation diamond by "ALTAI" is limited. Currently, there are several commercial centers in the world producing UNCD particulates by explosive detonation and located in Russia, Ukraine, Byelorussia, Germany, Japan, and China. Although discovered several decades ago, UNCD particles became an object of keen interest outside of Russia only in the last few years[8,10] as the field of nanotechnology emerged.

Although developed relatively recently[1] compared to UNCD particles, UNCD films are already close to successful commercialization. The ultrananocrystallinity is the result of a new growth and nucleation mechanism due to using argon-rich plasmas instead of hydrogen-rich plasmas normally used to deposit microcrystalline diamond films. UNCD films are superior in many ways to traditional microcrystalline diamond films: they are smooth, dense, pinhole free, phase pure, and can be deposited conformally on a wide variety of materials and high-aspect-ratio structures.[1]

Diamond with characteristic sizes encompassing several nanometers has also been synthesized by other methods, particularly by the chlorination of carbides,[12] ion irradiation of graphite,[13] electron irradiation of carbon onions,[14] and in the vapor phase in a substrate-free tube flow CVD reactor.[15] Moreover, astronomical observations suggest that as much as 10–20% of interstellar carbon is in the form of nanodiamonds.[16] The questions of when and how does nanodiamond originate in the cosmos remain open, although comparative microstructural analysis of nanodiamonds extracted from meteorites indicates that the majority of cosmic nanodiamonds formed by low-pressure vapor condensation (Chapter 2 of this book).

The chapter will be organized as follows. After a short summary on shapes of experimentally observed nanodiamond structures, the reported methods of synthesis of diamond nanostructures resulting in zero-, one-, two- and three-dimensional structures will be discussed.

3.1 Nanodiamonds: Shapes

Recent *ab initio* simulations demonstrate that within the size range 1 nm to 3 nm for all-carbon diamond clusters the crystal morphology plays a very important role in cluster stability in the sense of preserving diamond structure.[17–19] While the surfaces of the cubic crystals exhibit structures similar to bulk diamond,[17,18] the surfaces of the octahedral, cuboctahedral, and spherical clusters showed a transition from sp^3 to sp^2 bonding.[17–19] The preferential exfoliation of the (111) surfaces for clusters begins in the subnanometer size range and promotes the cluster transition to endo-fullerence for small clusters (~tens of atoms) and onion-like shells with diamond cores (bucky-diamond) for larger clusters[19] (inset in Fig. 3.1(a)). An open question remains about the critical size, above which the bare diamond clusters will have an all-diamond structure

with reconstructed (111) surfaces forming Pandey chains similar to bulk-terminated diamond surfaces.

Ab initio simulations demonstrated that nanodiamond clusters with hydrogenated surface preserve surface structure similar to hydrogenated macroscopic diamond. In order to address the most stable shapes of the hydrogenated nanodiamond particles, heats of formation have been calculated for several nanodiamond series for particles relaxed with the bond order potential.[20] It was concluded that the most stable morphologies for hydrogenated nanodiamond are octahedra, pentaparticles, and groups of spherical particles. Heats of formation of most stable hydrogenated diamond cluster morphologies are lower than those for bucky-diamond and bare reconstructed nanodiamonds. It would be very interesting to perform calculations of heats of formation of nanodiamond clusters with other functional groups on their surfaces rather than hydrogen (for example, hydroxyl, carboxyl, amino groups). Thus according to computational studies, rather diverse stable shapes of nanodiamond particles of several nanometers in size can coexist.

An experimental bucky-diamond shape of UNCD particle is illustrated in Fig. 3.1(a).[21] It is important to emphasize that this shape appears as a result of high-temperature annealing of the initial UNCD particles after surface groups had been desorbed.[22] Until recently, most of the experimental work dealing with nanodiamond produced by means of detonation described the shape of clusters as being spherical.[4] In general, the agglomeration of UNCD particles and the presence of non-diamond coatings on UNCD surfaces seen in many micrographs prevent one from drawing a convincing conclusion on the shape of detonation UNCDs. The perfect spherical shape of a single nanodiamond particle is illustrated in Fig. 3.1(b) for a particle surrounded by carbide material during synthesis by a carbide chlorination process.[23] At the same time, HRTEM images of a single nanodiamond cluster on the surface of a Mo tip clearly indicate the presence of facets on the particle surface, with the cluster resembling a polyhedral shape (Fig. 3.1(c)).[24] More exotic shapes, such as a pentaparticle of nanodiamond, have also been observed (Fig. 3.1(d)). Thus, rather diverse UNCD shapes have been experimentally observed.

3.2 Types of Nanodiamond and Methods of Their Synthesis

There are numerous reports on experimental observations of nanosized diamond, summarized in ref. [3]. Reported methods of nanodiamond syn-

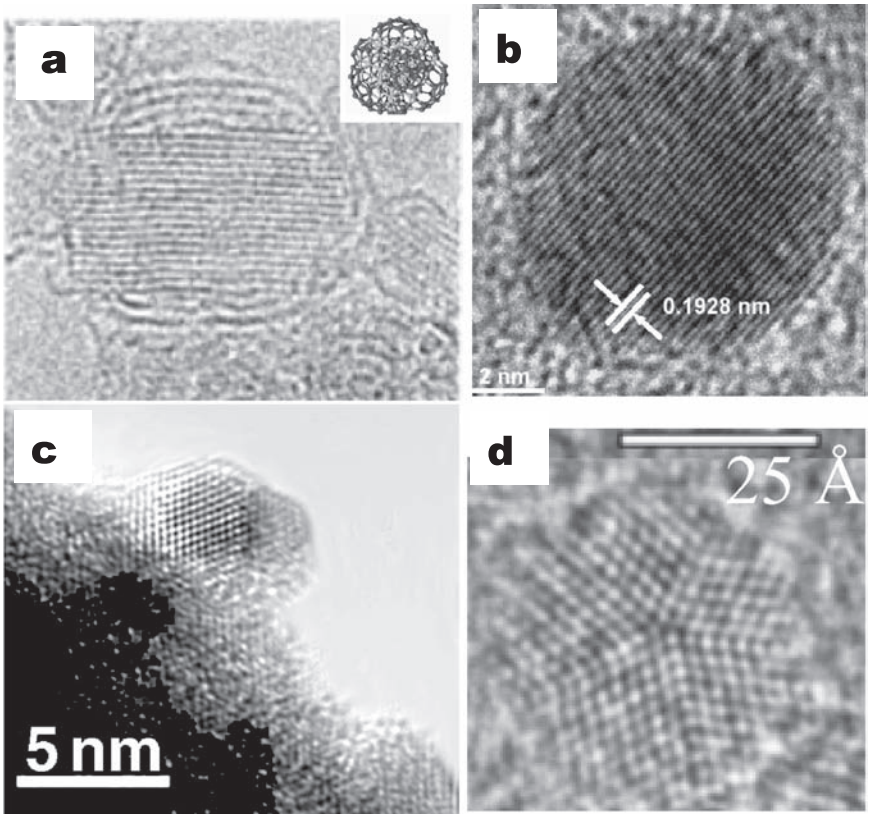

Figure 3.1 HRTEM images of (a) a bucky-diamond formed from a UNCD particle of detonation origin. The inset illustrates an atomic model of a bucky-diamond (courtesy of Guilia Galli, Lawrence Livermore National Laboratory). (b) Spherical diamond in a carbide matrix synthesized by carbide chlorination process. (c) Polyhedral particle of detonation UNCD. (d) A multiple twin particle of a presolar diamond (courtesy of T. L. Daulton, Naval Research Laboratory). (From Kuznetsov, V. L. et al., *J. Appl. Phys.* **86**, 863, 1999 (a); Welz, S., Gogotsi, Y., McNallan, M. J., *J. Appl. Phys.* **93**, 4207, 2003 (b); Tyler, T., Zhirnov, V., Kvit, A., Kang, D., and Hren, J., *Appl. Phys. Lett.* **82**, 2904, 2003 (c). With permission.).

thesis are very diverse, involving methods such as gas-phase nucleation at ambient pressure, chlorination of carbide material at moderate temperatures, HPHT graphite transformation within a shock wave, or carbon condensation during explosive detonation.

The information on types of nanodiamond is arranged below according to the dimensionality of the diamond constituents. We discuss systems of increasing complexity beginning with the zero-dimensional structures in

the form of isolated particles and particles embedded within a matrix of other material, followed by recently synthesized exotic forms of 1-D and 2-D nanodiamond structures. Finally, 3-D assemblies of diamond nanocrystals grown as thin films or compacted from UNCD powder to preformed bulk shapes are reviewed.

3.2.1 Zero-Dimensional Nanodiamond Structures

3.2.1.1 Commercial Nanodiamond Particulate

Below we discuss methods of synthesis of diamond particles at the nanoscale, mostly for the particles that have been commercialized or are close to commercialization, according to the characteristic sizes of the primary particles. We start with *nanocrystalline* particles followed by *ultrananocrystalline* diamond particulate and *diamondoid* molecules (Fig. 3.2). Characteristic sizes of nanocrystalline particles encompass the size range of tens of nanometers, while sizes of primary particles of UNCD are within several nanometers. Diamondoids are well-defined hydrogen-terminated molecular forms consisting of several tens of carbon atoms.

3.2.1.1.1 Nanocrystalline Diamond Particles Synthesized by Shock Waves and by Other Methods

Isolated nanocrystalline diamond particles with characteristic sizes of several tens of nanometers can be monocrystalline or polycrystalline (Fig. 3.2). *Monocrystalline* particles are obtained by processing of micron-sized diamond particles, which are, in turn, a by-product of natural diamond or HPHT diamond synthesis. Synthetic diamond particles with sizes below ~50 microns represent the raw material for making micron and submicron diamond size particles. The processing of micron-sized diamond particles to smaller fractions includes micronizing, purification, and grading of the powder. Monocrystalline diamond particles have rather sharp edges (Fig. 3.2).

Polycrystalline nanodiamond powder (Fig. 3.2) can be processed from micron-sized polycrystalline diamond particles obtained by shock synthesis[25] (Fig. 3.3(a)). Under suitable conditions, explosively produced shock waves can create high-pressure (~140 GPa), high-temperature conditions in confined volumes for a sufficient duration to achieve partial

Nanocrystalline Diamond Particulate

Range of *smallest* fraction sizes: 0-50 nm; average size: ~25nm
other fractions: 0-100nm (average size 50 nm), 0-150nm and up.

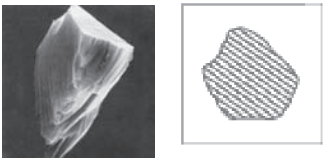

Monocrystalline:
- Natural
- Synthetic HPHT

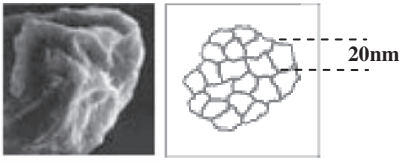

Polycrystalline:
- Shock wave compression of graphite (DuPont process) Grain size ~20nm

Ultrananocrystalline Diamond Particulate

Range of primary particle sizes: 2-10 nm Average size: ~4-5nm

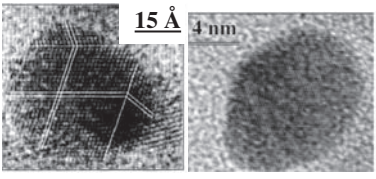

Substantially Monocrystalline; (often with multiple twins)
- Detonation synthesis
- ion irradiation of graphite
- other methods

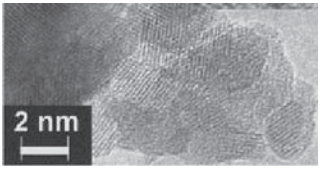

Tend to form agglomerates;
Smallest sizes of agglomerates in stable suspensions obtained by practical ways are ~40-50 nm.

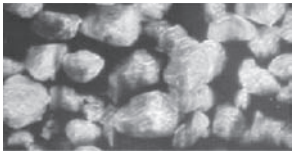

Polycrystalline detonation diamond;
Sintering of detonation UNCD particles by detonation. Fractions: tens/ hundreds of microns.

Highest diamondoids

Hydrogenated molecules with sizes 1-2 nm

- Isolated from petroleum.

Figure 3.2 Summary of nanodiamond particle sizes and structures according to the *primary* particle size (smallest monocrystal). (Pictures of nanocrystalline diamond are courtesy of Microdiamant AG, Switzerland. Pictures of UNCD single particles are courtesy of T. L. Daulton, Naval Research Laboratory. Picture of polycrystalline detonation diamond is courtesy of Alit, Kiev. Examples of higher diamondoids from petroleum, 1 to 2 nm hydrogen-terminated diamond molecules (left to right): rod-shaped [1212] pentamantane $C_{26}H_{32}$, pyramid-shaped [1(2,3)4] pentamantane $C_{26}H_{32}$, irregular disk-shaped [121321] heptamantane $C_{30}H_{34}$, octahedral [1231241(2)3] decamantane $C_{35}H_{36}$. Graphics courtesy of Chevron Texaco Molecular Diamond Technologies.).

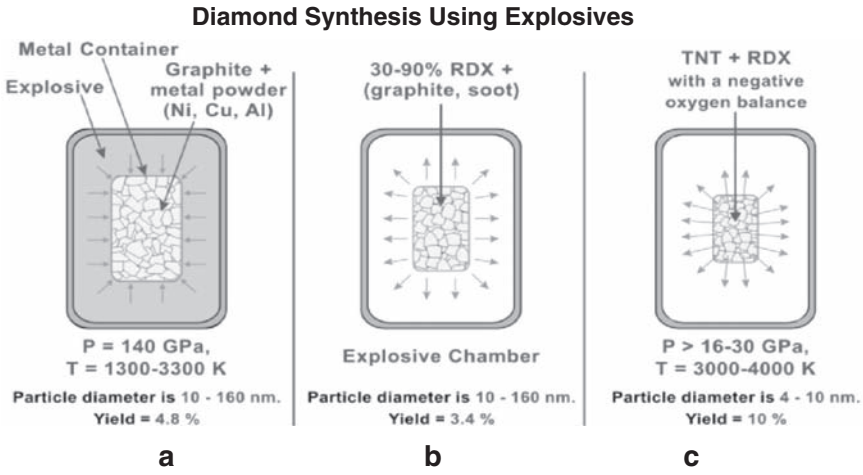

Figure 3.3 Schematic illustration of three different methods of producing nanocrystalline (a, b) and ultrananocrystalline (c) diamond particulate using explosives. Schematics and provided characteristic sizes of primary particles are based on (a) E. I. Du Pont de Nemours & Co. US Patent 3,401,019 (10.09.69); (b) USSR patent 565474 (23.07.76); (c) A. Lyamkin, E. Petrov et al., *Dokl.Acad.Nauk USSR* **302**, 611, 1988. Picture courtesy of Professor Vladimir Kuznetsov, Boreskov Institute of Catalysis SB RAS, Novosibirsk, Russia.

conversion of graphite into nanometer-sized diamond grains (~20 nm) which compact into micron-sized, polycrystalline particles. Copper is mixed with graphite utilized in shock wave synthesis to provide fast heat dissipation at the high temperatures that are reached during the explosion in order to avoid transformation of the diamond back to graphite.[5] Polycrystalline diamond particles of micron size are more friable than monocrystalline diamond microparticles (natural or produced by HPHT) and are widely used in fine polishing applications. It is important to note that agglomerate-free suspensions of nanocrystalline diamond particles (for both monocrystalline and polycrystalline forms) in water and oil have been developed.[26]

Comprehensive characterization of shock-wave-synthesized diamond produced by Beijing Li-Xin Mechanical and Electric High Technology Company was reported in ref. [80]. Shock wave compression of a graphite sample was realized by a flyer steel plate accelerated by a planar shock wave generator. After impact, the shocked graphite was treated with perchloric acid to remove the unconverted graphite phase, purified from metallic impurities, and then oxidized in HF acid to remove impurities like silicon and silicon dioxide. Shock-wave-synthesized diamond was

bulk polycrystalline diamond with a particle size range 0.1–40 mm. The average size of the crystallites of the polycrystalline particles was 10.2 nm. According to Fourier Transform Infrared (FTIR) analysis, the shock-wave-synthesized diamonds (as well as detonation nanodiamonds that also had been studied by the authors[80]) contained surface functional groups such as carbonyl, carboxyl, methyl, and nitryl groups. However, due to the differences in synthesis processes and purification methods, these functional groups appeared with different positions and intensities for the two types of dynamically synthesized nanodiamonds.

Recently, low dynamic pressures up to 15 GPa have been reported to be enough to produce diamond from ordered pyrolytic graphite (with voids between the particles) using planar shock waves parallel to the basal plane of the graphite.[27] Diamond particles consisting of crystallites with grain sizes of several tens of nanometers were observed by HREM in the post-shock sample.[27] Formation of nanocrystalline diamond from polyhedral particles by shock wave synthesis was observed at a dynamic pressure less than 50 GPa.[28]

There are several modifications of the shock wave process for diamond synthesis. In particular, graphite (or other carbonaceous materials such as carbon black, coal, etc.) can be loaded into explosives themselves[29] as against loading in a fixture external to the explosives. The difference between the three major methods of producing nanocrystalline and UNCD particulate using explosives is schematically reemphasized in Fig. 3.3. On a commercial scale nanodiamond synthesized by the loading of graphite into explosives (Fig. 3.3(b)) is produced by Real-Dzerzhinsk, Inc. with nanodiamond yield up to 30% by weight. The major application of the nanodiamond produced by this method is in finishing and superfinishing operations of the polishing process. The product may be used as a free abrasive, in pastes, suspensions, oils, and organosols.

Interestingly, besides the difference in sizes of primary particles in commercial nanodiamonds produced by the shock wave method and those formed from detonated explosives (next section), there is also significant difference in crystallographic forms. Diamond powder from Mypolex and from several vendors producing detonation UNCD was analyzed by Ownby[30,31] using the Rietveld whole-profile powder X-ray diffraction method. This technique determines the percentage of each crystalline phase present. It was shown that Mypolex crystalline diamond powder particles in the size range of 10 to 1000 nanometers formed by explosive shock contain ≤50% 3C, a cubic diamond structure, and ≥50% higher order non-cubic polytype.[30] The single higher order polytype that fits both

the X-ray and neutron diffraction data very well was the 6H polytype[30] (rather than the 2H polytype, named lonsdaleite, that was assumed to be one of the crystalline phases for nanodiamond produced by shock waves[5]). The cubic 3C crystallites appear to be concentrated in the higher size range of each size fraction, while the hexagonal 6H polytypes were concentrated in the smaller size side of each range.[30] The same type of analysis indicated 100% 3C cubic diamond content of crystalline phase in detonation UNCD powder. At the same time, analysis of the microstructure of detonation UNCD by high-resolution microscopy methods performed by Daulton revealed the presence of londsdalite phase in detonation diamonds (Chapter 2 of this book), while X-ray diffraction analysis of the same samples reported by Greiner et al.[78] indicated the presence of only the pure cubic diamond phase.

3.2.1.1.2 UNCD of Detonation Origin

The primary particles of UNCD with characteristic sizes of about 4–5 nm (Figs. 3.1 and 3.2) are obtained by the detonation of solid explosives (Fig. 3.3c) with a negative oxygen balance in a non-oxidizing atmosphere of cooling media (CO_2, water, ice). This class of nanodiamond material is technologically important since detonation UNCD can be produced in bulk quantities. The size of UNCD particles depends on the weight of charge, so, in principle, there is no some specific maximum size, although most vendors produce particles with an average size of 4–5 nm. For example, a primary particle size of UNCD synthesized by Alit, Ukraine in a 100 m^3 detonation chamber is within the range of 2–50 nm.[7] At detonation of explosives of total weight 140 kg, UNCDs with primary particles size up to 60–90 nm have been produced, as well as polycrystals with a size up to 85 μm.[7] Moreover, 10 μm-sized monocrystals of londsdalite (with up to 5 wt.% of the total diamond phase) have been observed as a result of synthesis using 3–140 kg of detonation explosives.[7]

The product obtained by detonation synthesis, called detonation soot, contains the diamond phase, which is separated from soot by chemical treatment. More details on UNCD particle synthesis and purification will be provided in Chapter 11.

While it is possible to isolate the smallest UNCD particles in the range of ~2–5 nm in size (Figs. 3.1 and 3.2) under laboratory conditions, in general agglomeration of the particles remains one of the most serious problems in "true" nanotechnological applications. At the same time there are several very recent reports that suspensions of surface functionalized

detonation UNCD particles of sizes ranging from ten to several tens of nanometers have been developed. Thus, proprietary modified UNCD powder suspended in water has aggregate sizes of 40–50 nm.[32] In another approach, using a stirred-media milling technique, the authors were able to deagglomerate UNCD down to about 10 nanometers.[33] So-called mechanochemical treatment consisting of high-speed shear stirring and high-energy ultrasonic or vibration milling in the presence of dispersants was developed in refs. [81,82]. UNCD slurries in oil with an average particle size of 55 nm were prepared using as a dispersant a block copolymer with —NH_2 as the anchoring group and a polyester chain as the oil-solvatable block.[81] Aqueous suspensions of UNCD with an average particle size of less than 40–60 nm were prepared using sodium oleate as a dispersant.[82]

Another interesting particulate material obtained from UNCD of detonation origin is micron-sized polycrystalline particles obtained at Alit, the Ukrainian company, by detonation sintering using the initial UNCD powder (Fig. 3.2).[7] Due to its more rounded form than Mypolex and monocrystalline diamond particles, this new type of diamond particulate is expected to have different niche applications.[7]

3.2.1.1.3 Diamondoids

Recently, a whole family of hydrogen-terminated diamond species of ~1 to ~2 nm size was discovered, literally filling the gap in sizes between the adamantane molecule that is the smallest specie of H-terminated cubic diamond containing only 10 carbon atoms and the wide plethora of UNCD particles with sizes more than 2 nm described above. These so-called higher diamondoids (whose number of crystal diamond cages is more than three) extracted from petroleum are diamond molecules that are nanometer-sized rods, helices, disks, pyramids, etc.[34,35] (Fig. 3.2). These highly rigid, well-defined, readily derivable structures are valuable molecular building blocks for nanotechnology. Certain higher diamondoids can now be produced in gram quantities and are available through Molecular Diamond Technologies, Inc. on a collaborative basis. The formation mechanisms of the higher diamondoids in petroleum still remain a mystery.[35] So far it has not been possible to synthesize higher diamondoids. Higher diamondoid molecules crystallize into a variety of crystal systems.[34] For example, depending on the isomer type, crystals of pentamantane can be orthorhombic, triclinic, or monoclinic. Rod-shaped [1212] pentamantane molecules form orthorhombic crystals (Fig. 3.4),

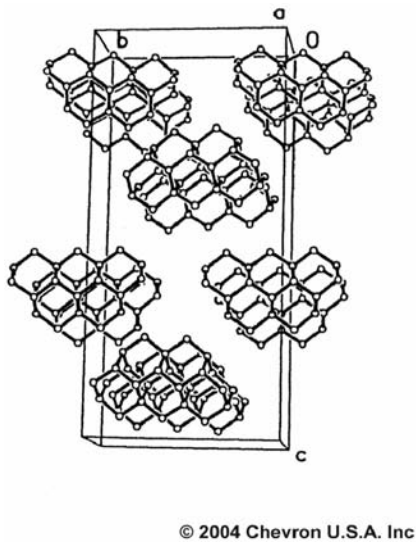

Figure 3.4 Higher diamondoids are diamond molecules that can be isolated to high purity and crystallized. Illustrated is the unit cell of [1212] pentamantane determined by X-ray crystallography on a single orthorhombic crystal (space group $P2_12_12_1$). (Graphics courtesy of Chevron Texaco Molecular Diamond Technologies.).

in which they are aligned parallel to their long axis, perpendicular to their diamond (110) lattice faces.[35]

In the section above different classes of commercially available diamond particles at the nanoscale were discussed. In the following section we will provide a brief overview of nanodiamond particles synthesized on the laboratory scale. Below there is no attempt to separate synthesized diamond particles according to their characteristic sizes; instead the term nanodiamond (ND) is used in a general sense. Figure 3.5 is an attempt to organize the known methods of ND synthesis in a systematic manner.

3.2.1.2 Nanodiamond Synthesized by HPHT

While a particular class of commercial NDs is obtained as a by-product of HPHT synthesis,[26] there are laboratory studies of HPHT conversion of exotic carbon forms to ND. The HPHT process requires approximately 6 GPa pressure and 1500 degrees Celsius to convert graphite powder into diamond in the presence of a catalyst. Using nanocarbon-based materials such as fullerenes[36] and carbon nanotubes[37] as alternative precursor materials to graphite in HPHT synthesis allows much lower temperatures and externally applied pressures in the synthesis of diamond. For example, according to ref. [36], the transformation of buckyballs to diamond at high static pressure can be done at room temperature and does not require a catalyst at all. Another group of authors reported conversion of fullerenes to diamond under "moderate" conditions of 5.0–5.5 GPa and 1400 °C.[38] Recently, bulk samples of nanocrystalline cubic diamond with crystallite sizes of 5–12 nm were synthesized from fullerene C_{60} at 20 GPa and 2000 °C using a multi-anvil apparatus.[75]

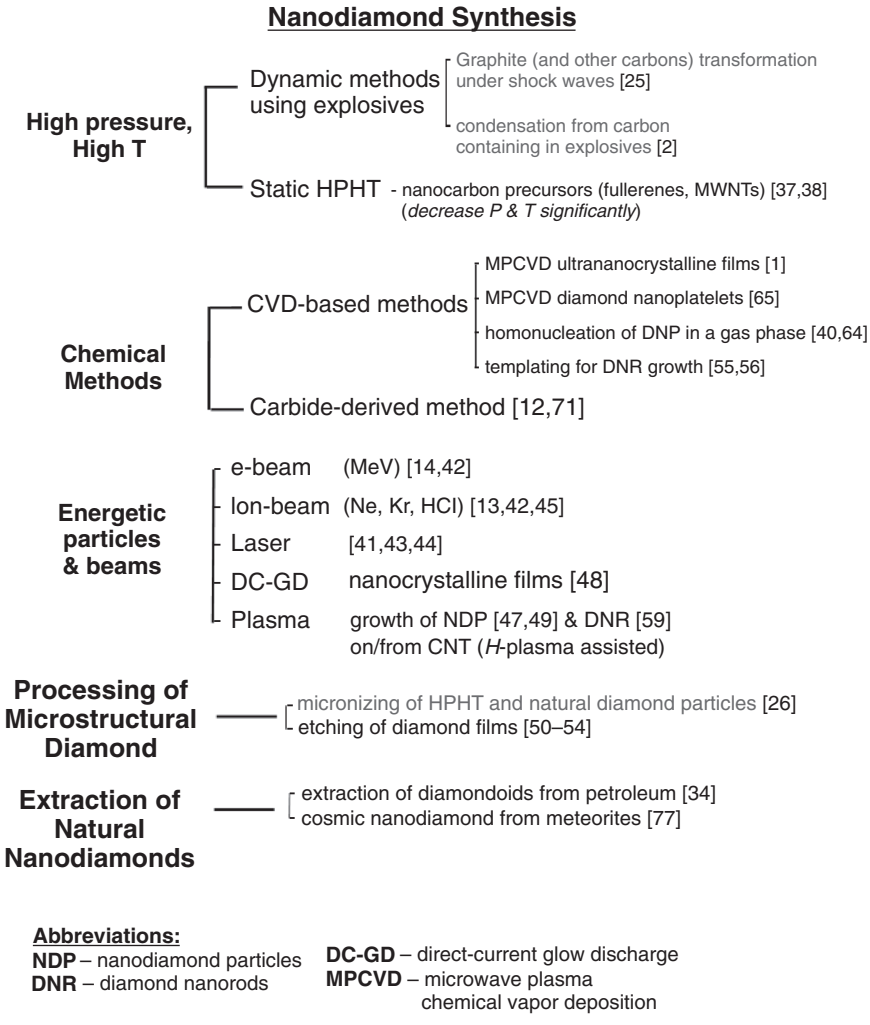

Figure 3.5 Tentative scheme summarizing methods of synthesis of diamond nanostructures. Methods of synthesis of nanodiamond which have been commercialized are highlighted in gray.

Carbon nanotubes have been converted to diamond at 4.5 GPa and 1300 °C using NiMnCo catalyst.[37] Based upon HRTEM observations, the authors suggest that under HPHT conditions the tubular structures collapse and broken graphitic shells curl up and close into spheroidal networks to eliminate the dangling bonds at the edges. The high curvature of the formed nested graphitic shells and cross-links between the layers in

the onion-like structures that are formed lead to an increased fraction of sp^3 bonds which facilitates the formation of diamond. In ref. [39] multi-walled carbon nanotubes were heated in a diamond anvil cell by a laser above 17 GPa and 2500 K. The recovered product consisted of nanometer-sized octahedral crystals (diamond) of less than 50 nm. The tubular structure completely changed to a granular structure with grain sizes corresponding to the diameter of the nanotubes. The grain size of the diamond suggests that the transformation took place by direct conversion of the nanotubes and might provide a means to control diamond crystallite size by the choice of the MWNT size.[39]

3.2.1.3 ND Particles Synthesized by CVD

Frenklach and co-workers[40] studied nucleation and growth of ND powder directly in the vapor phase in a substrate-free low-pressure microwave-plasma CVD reactor. The particles were collected downstream of the reaction zone on a filter within the tubular flow reactor and subjected to wet oxidation to remove non-diamond carbon. The homogeneous diamond nucleation took place when dichloromethane– and trichloroethylene–oxygen mixtures were used as source material. The particles had crystalline shapes with an average particle size of around 50 nm. A mixture of diamond polytypes was observed in the powder.

Frenklach et al.[15] also studied the effects of heteroatom addition on the nucleation of solid carbon in a low-pressure plasma reactor. The addition of diborane (B_2H_6) resulted in substantial production of diamond particles, 5 to 450 nm in diameter, under the same conditions that show no diamond formation without the presence of diborane. The observed yield of the oxidation-resistant powder produced in boron-containing mixtures reached 1.3 mg h^{-1}. It was found that NDs in the CVD residue have an abundance of linear twins and star-twin microstructures consistent with radial (isotropic) gas-phase growth conditions. Studies of diamond nucleation directly from an activated gas phase may provide clues regarding the mechanisms of interstellar dust formation.

Recently, spherical, rather monodispersed diamond particles with diameters of different fractions in the range from 150 to 600 nm have been synthesized in a gas phase by multi-cathode direct-current plasma-activated CVD.[64] The diameters of the spheres varied with the radial distance from the centre of the copper substrate (in particular, particles of 150 nm in size were collected at the circumference area of the substrate). TEM patterns indicated that the internal structure of a spherical particle consists of

nanocrystalline diamond grains ~30 nm in size. Aromatic graphite-like sp^2 carbon had also been detected in the particles.

3.2.1.4 ND Synthesized Using High-Energy Particles and Beams

Another group of methods of ND formation include direct transformation of carbon-based solids to ND. Recent experiments have shown that heavy ion or electron irradiation induces the nucleation of diamond crystallites inside concentric nested carbon fullerenes.[14,42] High-energy electron irradiation (1.2 MeV, $>10^{24}$ e cm^{-2}; ~100 dpa) was successfully used to convert the cores of concentric-shell graphitic onions into nanometer-size diamonds.[14] These experiments were performed in situ in an electron microscope, which allowed continuous observation of the formation process. A strong compression in the interior of the onion was inferred by the observed reduction in the spacing between adjacent concentric shells during irradiation. Ion beam irradiation of carbon solids also resulted in the formation of ND.[42] Irradiation with Ne^+ (3 MeV, 4×10^{19} e cm^{-2}; ~600 dpa) at temperatures between 700 and 1100 °C converted graphitic carbon soot into nanometer-size diamonds.[42] Again the diamonds were found to nucleate in the cores of graphitic onions that developed under irradiation. The increased diamond yield as compared to e-beam irradiation is explained by the higher displacement cross-section, the higher energy transfer, and the higher total beam current on the specimen. ND nucleation occurs inside graphite under ion irradiation at ambient temperature when implanted with Kr^+ ions (350 MeV, 6×10^{12} e cm^{-2}).[13] The residue of the ion-irradiated graphite was found to contain NDs with an average diameter of 7.5 nm. Another example of ND formation includes irradiation of highly oriented pyrolytic graphite surfaces using a highly charged ion (HCI).[45]

There are several reports of ND formation using intense laser radiation of carbonaceous material including fine particles of carbon black[43] and carbon nanotubes.[44] Another example is laser-induced decomposition of C_2H_4 at low pressures and temperatures[41] that results in gas-phase diamond powder formation with grain diameters of 6 nm to 18 μm. According to the authors[41] the high-purity homogeneously nucleated diamond nanoparticles had spherical and faceted morphology. Diamond nanocrystals with cubic and hexagonal structures have also been synthesized by pulsed-laser-induced liquid–solid (acetone–graphite) interfacial reaction at normal temperature and pressure.[76] In the experimental setup, the graphite target was covered by 1–2 mm of acetone and irradiated by

a pulsed laser. The diamond aggregates that were produced consisted of sphere-like particles of about 30 nm in size, with both hexagonal and cubic structures.

3.2.1.5 Other Methods of Synthesis

In contrast to the works described in the previous section, transformation of spherical carbon onions to diamond by low-temperature heat treatment at 500 °C in air without electron or ion irradiation was reported.[46] HRTEM images showed that diamond particles several tens of nanometers in diameter coexist with carbon onions after heat treatment in air. From HRTEM and electron energy-loss spectroscopy studies, the authors[46] suggest that sp^3 sites in the onions and the presence of oxygen during the heat treatment play important roles in the transformation without irradiation.

Phase transformation from multiwalled carbon nanotubes (MWCNTs) to nanocrystalline diamond has recently been achieved by post-treatment of 20–40 nm diameter MWCNT samples in a hydrogen plasma.[47] Nanocrystalline diamond particles with diameters ranging from 5 to 30 nm were embedded in an amorphous matrix (Fig. 3.6(a)). The diamond formation and growth mechanism was proposed to be the consequence of the formation of sp^3-bonded amorphous carbon clusters. As discussed by the authors,[47] the hydrogen chemisorption on the curved graphite network and the energy deposited on the carbon nanotubes by continuous impingement of activated molecular or atomic hydrogen are responsible for the formation of an amorphous carbon matrix. Similar to the role of hydrogen in conventional CVD diamond growth, hydrogen plasma etching prevents graphite formation in the thermally activated processes.

ND nucleation in amorphous carbon films also takes place during the biased enhanced CVD method, in which the substrate is negatively biased and exposed to a CVD plasma. Diamond nuclei of 5–10 nm in diameter have been recently observed in amorphous carbon films grown using bias-enhanced CVD.[48] The authors suggested a general model for diamond nucleation by energetic species (for example, using bias-enhanced CVD or with direct ion beam bombardment). It involves the spontaneous bulk nucleation of a diamond embryo cluster in a dense, amorphous, hydrogenated-carbon matrix; stabilization of the cluster by favorable boundary conditions of nucleation sites and hydrogen termination; and ion-bombardment- induced growth through a preferential displacement mechanism. Formation of a dense, amorphous, hydrogenated-carbon phase occurs via a sub-implantation process, in which energetic carbon, hydro-

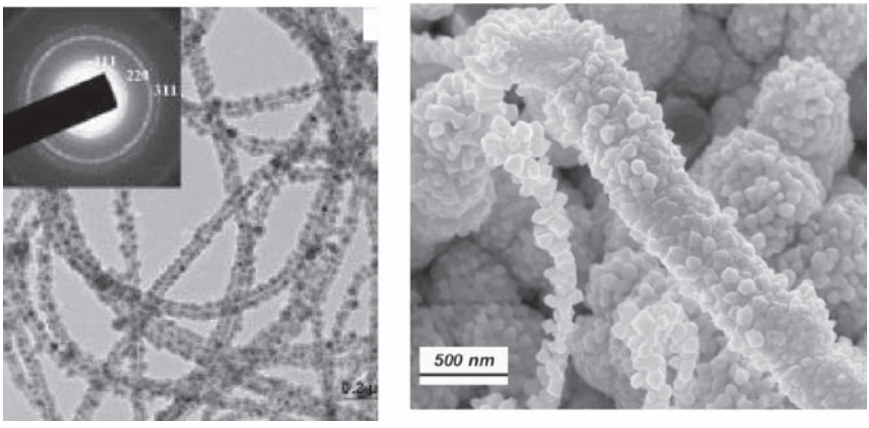

a) b)

Figure 3.6 (a) TEM image showing the diamond crystallites embedded in amorphous carbon clusters and partial reservation of CNT hollow structure after hydrogen-plasma-treated MWCNTs. (b) Nanodiamond–carbon nanotube composites grown by CVD method. ((a) from Sun, L. T., Gong, J. L., Zhu, Z. Y. et al., *Appl. Phys. Lett.* **84**, 2901, 2004; (b) from Terranova, M. L. et al., *Chem. Mater.*, 17(12), 3214, 2005).

carbon, and hydrogen species bombard the surface and incorporate in subsurface layers. More details on the role of energetic species in ND nucleation can be found in Chapter 7 of this book.

Finally, a new class of nanostructured carbon has recently been synthesized where ND particles form hybrid structures with SWNTs.[49] The deposition experiments have been carried out in a hot-filament CVD reactor equipped with apparatus to allow the introduction of powder. The reactants were carbon powder (40 nm in diameter) and atomic H. The Si substrate was coated by submicron catalytic Fe particles that promoted initial growth of SWNTs. At the first stage of the growth sequence, aligned bundles of SWNTs up to 15 μm long were formed followed by synthesis at the outer parts of the SWNTs of well-shaped diamond crystallites with diameters in the 20–100 nm range (Fig. 3.6(b)). The authors[49] attribute the ND nucleation and growth to the presence of an unusually high concentration of atomic H.

3.2.2 One-Dimensional ND Structures

Recently, synthesis of 1-D diamond nanostructures became an object of keen interest and such structures have been fabricated by several

methods, including a top-down approach of etching diamond films,[50–54] bottom-up CVD growth using templates,[55,56] and even growth without spatial confinement.[57–59] Both polycrystalline and single crystal diamond rods/cylinders/whiskers with diameters spanning the range of several tens of nanometers have been synthesized. Based on the chemical inertness and mechanical strength of diamond, appealing applications of diamond nanorods (DNRs) can be envisioned, for example, as fillers in nanocomposites. Comparing nanorods to their related structures, carbon nanotubes (CNTs), for nanocomposite applications highlights desirable material properties of DNRs such as their much larger bending stiffness (they will have longer persistence lengths in composites) and their inherently stable surface bonding when functionalized due to their sp^3-bonding nature. The high thermal conductivity of diamond is well known and that is expected also for DNRs, but the fact that DNRs are insulating (if undoped), compared to the electrically conducting CNTs, suggests other unique niche applications for DNRs.

Methods of synthesis of 1-D diamond structures developed up to date, and related morphological and geometrical characteristics of rods, are summarized in Table 3.1. Interestingly, fabrication by a variety of techniques of diamond rods with diameters as small as 10 μm and lengths of several hundred microns have been reported starting in the 1960s.[60–62] The rods were grown epitaxially from the gas phase under low-pressure conditions on diamond seed crystals wetted with Ni, Fe, or Mn.[60] The diamond phase was confirmed by X-ray diffraction. The growth of single crystal diamond filaments was also reported.[60] Diamond whiskers were also grown in an electron microscope on the sharp edges of diamond or other dielectric crystals (such as mica, garnet) under electron beam irradiation from carbon-containing residual gases at low pressures (10^{-5}–10^{-4} Torr).[61] According to the authors,[61] gas condensate was formed around the sharp edges of the substrate crystals or on the tip of the growing whiskers in the center of the electron beam. Diamond whisker growth in a metal-carbon system at HPHT conditions has also been reported.[62] The whiskers were grown on synthetic seed crystals in an indirectly heated high-pressure chamber with a 1-D thermal gradient. The chamber was charged with a metal powder with diamond seed crystals dispersed in it. At the high-temperature end, a block of carbon was placed in contact with the powder. The chamber was at 40 kbar when heated and the carbon temperature reached ~1300 °C while the temperature of the powder at the far end reached 1160 °C. Whiskers 0.3–0.4 mm long and 30–100 μm thick were obtained with growth rates of 10–20 μm min^{-1}.

Then, over an extended period of time the growth of diamond 1-D structures was beyond the researchers' scope. At the end of the 1990s, growth of diamond structures extended in one direction was accidentally discovered[63] resulting from the self-assembly of UNCD particles of detonation origin to filament microstructures. Micron-diameter filaments were formed by colloidal assemblies of UNCD particles.[63] After extracting and drying, the filaments were similar to glass fibers, but no measurements of mechanical properties have been performed. Koscheev et al. also succeeded in the synthesis of submicron-diameter filaments consisting of UNCD particles obtained by laser ablation of pressed ND pellets.[63] In contrast to the dense filaments in colloids, every laser-ablated fiber is a network of nanoparticle chains. Studies of the elemental composition as well as the IR and Raman spectra of filaments confirmed that they consist of the original nanoparticles retaining diamond structure. After extraction from the vacuum chamber the whole assembly behaved like an aerogel. In both examples of UNCD-based filaments, the filament networks were rather tangled.

At the end of 1990s, deliberate synthesis of 1-D diamond nanostructures started.[50–59] The first work was based on top-down approaches using etching techniques[50–54] or bottom-up template-assisted CVD growth.[55,56] Reactive ion etching of CVD diamond films in oxygen resulted in numerous columnar structures of approximately 300 nm length and 10 nm diameter.[50] Aligned diamond whiskers were formed by air plasma etching of polycrystalline diamond films, particularly of as-grown diamond films and films with molybdenum deposited as an etch-resistant mask.[51] As for the as-grown diamond films, nanowhiskers were found to form preferentially at the grain boundaries of diamond crystals. As a result of dry etching of diamond films with patterned Mo films deposited on the surface, well-aligned whiskers of 60 nm diameter were formed uniformly over the entire film surface with a density of $50\,\mu m^{-2}$. In another approach,[52] microcrystalline or nanocrystalline diamond films were first grown followed by a reactive ion etching (RIE) step accomplished by shutting off the methane supply and feeding only hydrogen into the reactor. Depending on the RIE conditions and morphology of the initial diamond film, low-density or high-density ND cones were fabricated including single-crystal diamond cones. The cone shape is formed due to the faster removal of diamond material in the peripheral regions of the columns. Okuyama et al.[54] used RIE with an oxygen plasma through 2-D SiO_2 ordered arrays as masks. The diameter and length of the diamond cylinders depended on the etching time. Most recently, monocrystalline diamond nanorods have been fabricated by Ando et al.[53] using RIE. They developed a novel

Table 3.1 Summary of Diamond One-Dimensional Structures Synthesized to Date. Terms Rods, Cylinders, anAnd Whiskers Do Not Represent Particular Morphology/Geometry and Are Used According to the Authors' Notation

Morphology	Diameter (*D*), Length (*L*)	Method of Synthesis	Reference
Microcrystalline Structures:			
Monocrystalline rods	*D*: 10–20 μm *L*: 50 μm–2 mm	Grown epitaxially on diamond seed crystals from a gaseous phase under low-pressure conditions and radiation heating of the growth spot in the presence of metal catalyst	[60], 1968
Whiskers	*D*: 10–20 μm *L*: 300 μm	Grown in an electron microscope on the sharp edges of diamond under electron beam irradiation from C-containing residual gases at low pressure	[61], 1975
Whiskers	*D*: 30–100 μm *L*: 400 μm	Grown in the conditions of thermal gradient from C-source material placed in contact with diamond seed crystals mixed with metal powder. High pressures (40 kbar)	[62], 1975
Filaments consisting of nanodiamond particles	*D*: micron and submicron	(a) Nanodiamond particles (4 nm in diameter), assembly in colloids. (b) Laser ablation of pressed nanodiamond pellets	[63], 1999
Nanocrystalline Structures: "Top-Down" Synthesis:			
Nanowhiskers	*D*: 10 nm *L*: 300 nm	Oxygen-plasma etching of CVD diamond films	[50], 1997
Nanowhiskers	*D*: 40–60 nm	Air–plasma etching of (a) as-grown CVD films; (b) films masked with Mo deposits	[51], 2000

Nanocones	*D* at base: hundreds of nm	Bias-assisted reactive ion (H) etching	[52], 2003
Diamond cylinders	*D*: 600 nm–1 µm	Reactive ion etching with oxygen plasma through SiO_2 ordered arrays as masks	[54], 2003
Nanorods: single crystal diamond	D: 50–200 nm *L*: several µm	RIE (CF_4/O_2) of synthetic single crystal (100) and (110) diamond substrate (using micromasks). Post-treatment with microwave plasma (H)	[53], 2004
Nanocrystalline Structures: "Bottom-Up" Synthesis Using Templating:			
Nanocylinders: circular, triangular, or square cross-sections	*D*: up to 300 nm *L*: 5 mm	Deposition through aluminum oxide templates using microwave plasma-assisted CVD	[55,56], 2001
Nanocrystalline Structures: "Bottom-Up" Growth:			
Nanofibres: diamond nanocrystals with $D < 10$ nm	*D*: 0.25–1 µm, at the top: ~50 nm *L*: 2–3 µm	Diamond surfaces treated in microwave *plasma of H* under a *direct-current bias* (–200 V)	[57], 2005
Diamond tubes: single crystal <110>	*D*: 50–160 nm	Grown using MPECVD. *T* of substrate 200 °C. Rugged polycrystalline diamond substrate. Applied *bias voltage* (up to –250 V)	[58], 2004
Nanorods: <011> with (111) side facets	*D*: 8–10 nm *L*: up to 200 nm	DNR formed by prolonged *hydrogen plasma* treatment of MWCNT (>20 h) at 1000 K, 150 Pa	[59], 2004

microfabrication method by combining a microwave plasma treatment with a RIE method. First, the RIE system was used for fabricating whiskers of single crystalline diamond. Then the whiskers were exposed to a microwave plasma of hydrogen gas. As a result, they successfully fabricated a nanometer-scale diamond rod of the single crystal, which has crystalline facets. HPHT synthetic single crystal diamond substrates with (100)- and (110)-oriented surfaces have been etched with oxide impurities acting as micromasks; another mask set consisted of arrays of Al dots. Arrays of DNRs 50–200 nm in diameter and several microns in height (Fig. 3.7(a)) were fabricated.

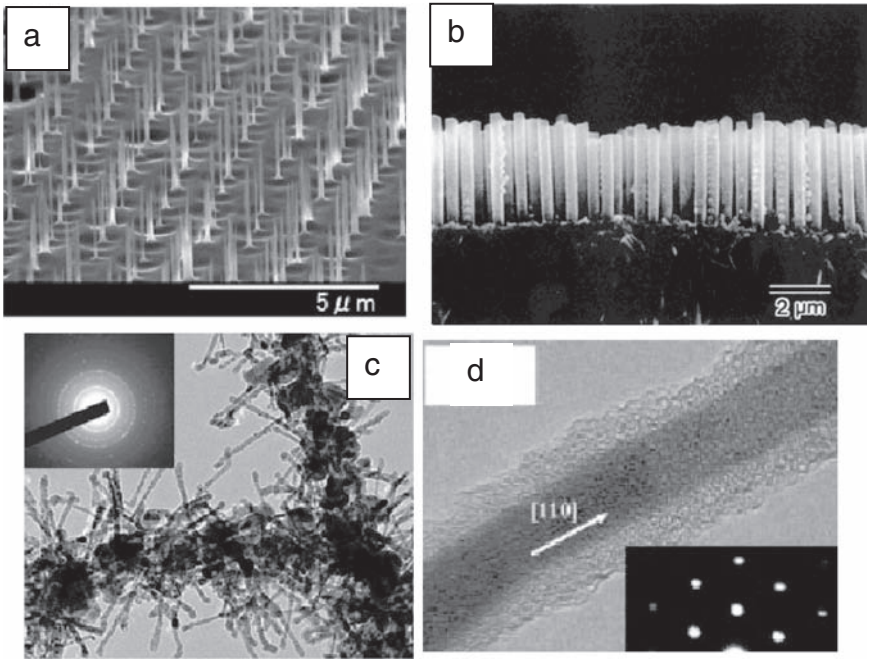

Figure 3.7 (a) SEM micrograph of array of diamond rods fabricated by reactive ion etching. (b) SEM micrograph of nanodiamond cylindrical structure; cross-sectional view of the diamond cylinder membrane after dissolving of the alumina template. (c) TEM image of diamond nanorods grown on the carbon nanotubes during H-plasma treatment. (d) HRTEM image of the nanorod illustrating <011>-oriented diamond core and an amorphous coating. ((a) from Ando, Y., Nishibayashi, Y., and Sawabe, A., Nano-rods of single crystalline diamond, *Diamond Relat. Mater.* **13**, 633, 2004, with permission. (b) from Masuda, H. et al., Synthesis of well aligned diamond nanocylinders, *Adv. Mater.* **13**, 247, 2001, with permission. (c, d) from Sun, L. et al., Diamond nanorods from carbon nanotubes, *Adv. Mater.* **16**, 1849, 2004, with permission.).

In the bottom-up approaches assisted by templating, polycrystalline diamond nanocylinders were grown on anodic aluminum oxide templates using microwave plasma-assisted CVD and 50 nm ND particles as seed materials.[55] Ordered 300 nm diamond nanocylinder arrays with cylinder lengths of about 5 mm are illustrated in Fig. 3.7(b). The same authors synthesized highly ordered arrays of diamond cylinders with square and triangular cross-sections using microwave-enhanced CVD through anodic porous alumina templates with modified pore shapes.[56] By removing the alumina template in concentrated phosphoric acid, an ordered array of cylinders of uniform size and shape was obtained. The authors state that diamond cylinders can be collected from the substrate.

From the discussion above it becomes obvious that it is very difficult to achieve template-less directional growth of 1-D diamond nanostructures and that special approaches are required. Recently it was found that DC bias applied to the diamond substrate can promote directional redeposition of carbon from the substrate into diamond 1-D structures. In the work of Kobashi et al.[57] diamond films and powders were treated in a microwave plasma of hydrogen at 1.6 Torr under a negative DC bias of around −200 V. As a result, a fibrous structure was formed on the diamond surface along the direction normal to the surface. The fiber diameter near the top end was ~50 nm and the fiber lengths were ~2–3 μm. The fibers consisted of diamond nanocrystals (<10 nm in size) covered by an amorphous layer. The authors speculate that hydrogen ions in the vicinity of the specimen are accelerated toward the diamond surface along a uniform electric field forming hydrocarbon fragments with carbon from the substrate. Certain numbers of hydrocarbon species thus generated travel along the side surfaces of the small protuberances under the uniform electric field and redeposit forming fibrous diamond structures.

Chih et al.[58] reported on hollow, vertically aligned, single crystalline nanodiamond tubes (NDTs) grown on a rugged polycrystalline diamond substrate using MPECVD and applied bias voltage (up to −250 V). The tubes' orientation was defined as <110>; their outer and inner diameters were approximately 160 nm and 100 nm, correspondingly. Based on the observations of the morphologies of the NDTs at earlier stages of their nucleation, the authors suggest a model of the formation of single crystalline nanometer-scale diamond tubes based on the coalescence of the diamond nucleus to circular-like structures. As in the previous work,[57] applying a bias voltage to the substrate is the key. The aspect ratio of the nanometer-scale diamond tube can be fine-tuned by the applied bias voltage: with decreasing bias voltage, the diameter and length of a NDT decrease.

Finally, DNRs 8–10 nm in diameter and up to 200 nm in length were grown along the <110> diamond direction by applying prolonged hydrogen plasma post-treatment of MWCNTs[59] (Fig. 3.7(c,d)). MWCNTs were thoroughly purified and no metal catalyst was present in the system. The DNR core was surrounded by an amorphous carbon coating 2–4 nm thick. Depending on the duration of H-plasma treatment, ND particles embedded in the amorphous matrix have been observed (<10 h treatment), or well-defined DNRs (>20 h treatment). The authors suggest that initial diamond nuclei can be formed at the defect sites of MWCNTs due to the presence of hydrogen. Under hydrogen exposure at high temperature (1000 K), MWCNTs themselves transform to amorphous material, where nucleation of the diamond phase can be facilitated. As the next step in DNR formation, the authors speculate on ND crystal growth and faceting, followed by 1-D growth along one of the facets. A role of the particular facet is proposed based on observation of the preferable direction of growth of the DNR. The authors emphasize the role of the amorphous carbon coating that prevents DNR lateral growth as the DNR only grew perpendicular to one of the facets. Thus, a role of MWCNTs in this experiment is to provide a way to achieve a ND nucleus embedded in an amorphous matrix. One role of the amorphous matrix is to provide a carbon source for growth of the DNR. Another factor not considered by the authors that may influence preferable 1-D growth from the ND particles is the specific surface stresses existing in the substrate (MWCNTs) that in turn is nanostructured, prompting energetically preferable growth in the directions perpendicular to the MWCNT axis.

In general, we can conclude that synthesis of DNR has been very successful within the last few years. While all factors prompting 1-D diamond growth are still to be revealed and related growth mechanisms elaborated, it is clear now that the use of H plasma is a very important factor (possible roles are the formation of reactive hydrocarbon species in the substrate from the carbon source as well as the "classical" role of stabilization of the sp^3 C network over sp^2). Another important factor is the substrate bias as in the experiments[57,58] that probably provides directional diffusion of the hydrocarbon radicals along growing diamond protrusions.

3.2.3 Two-Dimensional ND Structures

Single crystalline diamond nanoplatelets have recently been grown on polycrystalline diamond substrates,[65] which were previously coated with a film of nickel 100 nm thick. Deposition was carried out at a temperature

above 1000 °C in a microwave plasma CVD reactor using a 3% CH_4/H_2 gas mixture. SEM and TEM micrographs reveal that the nanoplatelets have regular triangular and parallelogram shapes with well-faceted surfaces; their thickness ranges from 30 to 70 nm and length from several hundred nanometers to a few micrometers (Fig. 3.8). The edges of the platelets are along <110> directions with the top and bottom surfaces parallel to {111} planes. The platelet morphology suggests that it is formed

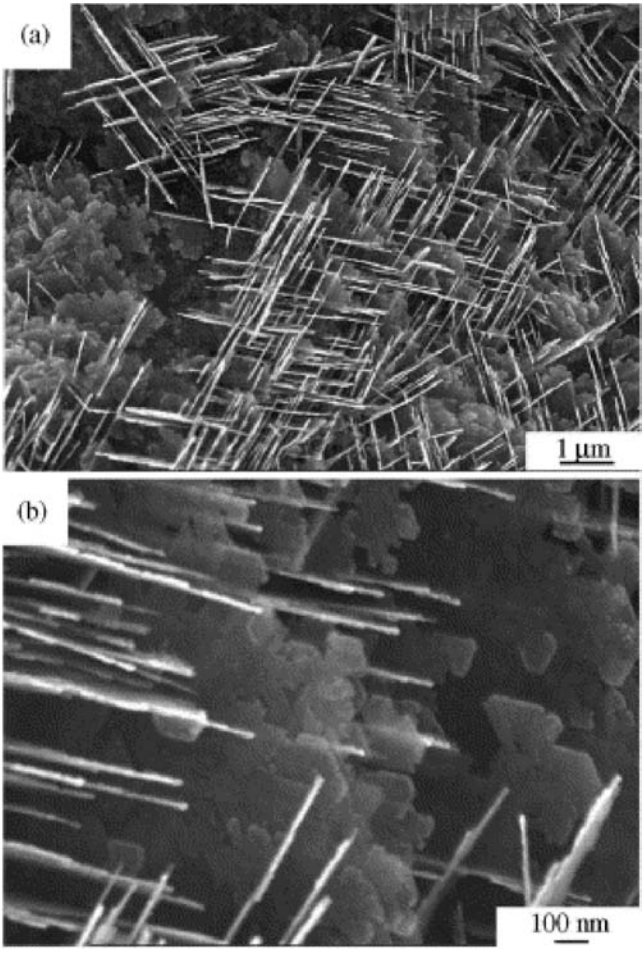

Figure 3.8 SEM micrographs of diamond nanoplatelets at different magnification; (b) demonstrates that the thickness of platelets is approximately 30 nm. (From Chen, H. and Chang, L., Characterization of diamond nanoplatelets, *Diamond Relat. Mater.* **13**, 545, 2004, with permission.).

by lateral growth, although the influence of Ni on the formation of diamond nanoplatelets is unknown.[65]

The same group of authors studied diamond deposition using polycrystalline diamond substrates inserted vertically within the plasma zone of a MPCVD[66] reactor. The substrate was coated with an iron film 30 nm thick before deposition. On the upper area of the specimen near the center of the plasma zone where the temperature was highest (over 1100 °C), <110>-oriented single crystalline diamond nanoplatelets were synthesized. The diamond nanoplatelets had a hexagon-like shape with a thickness about 20 to 60 nm and length of several hundreds of nanometers. Within the bottom region of the substrate near the periphery of the plasma zone, where the temperature was lowest, NDs, Fe nanoparticles, and carbon nanotubes were all produced.

Moreover, catalyst-free MPCVD growth of single crystalline diamond nanoplatelets was also achieved.[67] The (100) silicon substrate was embedded within the plasma zone close to its center where the highest temperature reached greater than 1100 °C during the deposition. SEM and TEM observations clearly show that the diamond nanoplatelets exhibit hexagonal-shaped morphologies, and the thickness and the length are around 20–30 nm and several hundred nanometers, respectively. Both <110> and <111> orientations of the diamond platelets were observed. The authors[65–67] emphasize that, in contrast to diamond growth in a conventional MPCVD process which is in the temperature range from 700 to 900 °C resulting in the formation of diamond crystallites of polyhedral shapes, the high-temperature condition is an important factor for growth of hexagonal-shaped diamond nanoplatelets. The diamond nanoplatelets were synthesized on various substrates only when the substrate temperature was higher than 1000–1200 °C. Regarding the possible role of substrate bias in the growth of lower dimensionality of the product, the only related information is reported in ref. [67]: a substrate bias of −200 V was applied during the nucleation stage. Obviously, a mechanism of growth of the 2-D diamond structures is yet to be revealed.

These results in combination with the results on growth of diamond nanorods discussed above prove that the synthesis of single crystalline ND of desired dimensionality has become a reality.

3.2.4 Three-Dimensional ND Structures

Three types of 3-D UNCD structures that are currently being commercialized are UNCD films, carbide-derived diamond-structured carbon, and bulk-sintered UNCD particles of detonation origin.

3.2.4.1 UNCD Films

UNCD films with 2–5 nm grains have been synthesized in Argonne National Laboratory by Gruen and colleagues[1,68,69] using a new plasma deposition process which utilizes a high content of noble gas. UNCD thin films were synthesized using argon-rich plasmas instead of the hydrogen-rich plasmas normally used to deposit microcrystalline diamond. By adjusting the noble gas/hydrogen ratio in the gas mixture, a continuous transition from micro- to nano- to ultrananocrystallinity was achieved. The controlled continuous transition from the micro- to the nanoscale is a unique capability of the method.[1]

The use of small amounts of carbon-containing source gases (C_{60}, CH_4, C_2H_2) with argon leads to the formation of C_2 dimers, which are the growth species for all UNCD thin films. The nanocrystallinity is the result of a new growth and nucleation mechanism, which involves the insertion of C_2 into the π-bonds of the non-hydrogenated reconstructed (100) surface of diamond. Then, unattached carbon atoms react with other C_2 molecules from the gas phase to nucleate new diamond crystallites.[1] This results in an extremely high heterogeneous nucleation rate ($10^{10}\,cm^{-2}\,s^{-1}$, which is 10^6 times higher than from conventional CH_4/H_2 plasmas). UNCD grown from C_2 precursors consists of ultrasmall (2–5 nm) grains and atomically sharp grain boundaries. Up to 10% of the total carbon in the nanocrystalline films is located within the two- to four-atom-wide grain boundaries. Because the grain boundary carbon is π-bonded, the mechanical, electrical, and optical properties of nanocrystalline diamond are profoundly altered. More subtle control of the properties of UNCD films can be accomplished via the addition of supplementary gasses to the plasma (N_2, H_2, B_2H_6, PH_3) and growth conditions (biasing, power). For instance, the addition of hydrogen leads to highly insulating films with large columnar grains. The added nitrogen leads to the formation of CN in addition to C_2 in the plasma. The presence of CN results in decreased renucleation rates during growth, which leads to larger grains and grain boundary widths.

The scientific and applied aspects of this unique material are discussed in depth in Part 3 of this book. Discovered only very recently, UNCD films have found a surprisingly wide range of niche applications. In many cases, prototype devices had been demonstrated.

In general, ND films may be grown by a number of deposition processes distinctive in the growth species, deposition parameters, and formation mechanisms. Each method results in different types of ND films in terms of grain size, grain boundary nature, hydrogen content, non-diamond phase content, and different chemical and physical properties. For

example, nanocrystalline carbon film consisting of diamond grains 3–5 nm in size surrounded by an amorphous matrix has been synthesized by DC glow discharge CVD from a methane–hydrogen mixture. In this case film deposition occurred from energetic species by a sub-plantation mechanism of diamond grain nucleation and growth. This method is discussed in more detail in Chapter 7 of this book.

3.2.4.2 Nanostructured Carbide-Derived Diamond

Selective etching of carbides is an attractive technique for the synthesis of various carbon structures including nanocrystalline diamond.[12,23,70] Carbon produced by extraction of metals from carbides is called carbide-derived carbon.[70] As summarized in ref. [70], leaching in supercritical water, high-temperature treatment in halogens, vacuum decomposition, and other methods can be used to remove metals from carbides to produce carbon coatings or bulk and powdered carbon. In principle, chlorination of carbides for the production of carbon-based materials and, in particular, nanoporous carbon, is a relatively mature technology that has been commercialized (see, for example, http://www.skeleton-technologies.com). However, the synthesis of nanocrystalline diamond by this technique[12] is a recent achievement.

Particularly during extraction of silicon from silicon carbide or metal carbide using chlorine-containing gases at ambient pressure and temperatures not exceeding 1000 °C,[23] nanocrystalline diamond with an average crystallite size of 5 nm was formed, as illustrated in Fig. 3.3(b). Nanocrystalline diamond is usually surrounded by amorphous carbon. Continued heat treatment of the nanodiamond at about 1000 °C and higher temperatures results in graphitization and the formation of carbon onions within a few micrometers of the SiC/carbon interface. This onion-containing layer can grow to a thickness of more than 100 μm with uniform structure and properties. The diamond-containing interlayer and the saw-like interface toward the metal carbide explains the excellent adhesion of the carbide-derived coatings and the onion-like surface layer provides excellent tribological properties. It has been shown that the presence of hydrogen during chlorination is not required for diamond synthesis.[23] However, hydrogen can stabilize the diamond nanocrystals in carbide-derived carbon and lead to the growth of thick diamond-structured layers. If no hydrogen is added, diamond nanocrystals transform to graphite, forming carbon onions and other curved graphitic nanostructures. The specific

feature of diamond-structured carbon is multiple diamond structures including cubic, hexagonal (londsdalite) structures as well as a variety of other diamond polytypes.[12,23]

The carbide-derived carbon coatings show excellent tribological behavior in both room air and dry nitrogen and are at the stage of commercialization for tribological applications, particularly as coatings for dynamic seals for water pumps made of SiC.[70] The coatings are self-lubricating with remarkably low friction coefficients that can be tailored by altering the reaction parameters; the coatings show no measurable wear. While the role of a nanocrystalline diamond layer in the present applications of carbide-derived carbon coatings is minor, the comprehensive study of the carbide halogenation process[12,23] provided, in principle, the methodology of growth of thick diamond-structured layers.

In a similar way, an amorphous carbon/ND structure has been recently produced by annealing Si-containing carbon films.[71] Carbon and silicon were simultaneously evaporated on amorphous carbon substrates at room temperature in a vacuum of 10^{-4} Pa. ND grains of 1.2 nm in size in the as-deposited Si-containing carbon film were detected. Then the as-deposited films were heated at 400–800 °C in a vacuum. Diamond grains of 5–30 nm in size were grown depending on the annealing temperature. The growth of diamond and β-SiC was controllable by adjusting the heating temperature and the proportion of Si. The role of Si as a catalyst in this process was revealed: when Ge was substituted for Si ND formation was not observed.

3.2.4.3 Sintered ND Composites

Another interesting bulk form of ND particles is so-called ND composite,[72,73] which consists of UNCD particles connected by a pyrocarbon matrix. UNCD powder is placed in a container of predetermined shape and then UNCD agglomerates are bonded together by pyrocarbon formed by means of methane decomposition through the entire volume of the diamond powder.[72] This material is characterized by a high porosity (50–70%) and demonstrates a relatively high Young's modulus of 30 GPa. The reported pore size is not greater than 20–30 nm with an average radius of 4.5 nm. Due to the high density of nanopores, the material possesses a high sorption activity, particularly for large biomolecules (such as tripsin).[74] The production of the material has been realized at Skeleton Technologies, Inc.

3.3 Conclusion

Historically, macroscopic diamond was studied apart from many other materials for industrial applications because of its unique mechanical, thermal and optical properties, chemical inertness, and biological compatibility. Many of its superior properties are preserved at the nanoscale compared to nanostructures fabricated from other materials – the strength of the carbon–carbon bond is not altered at the nanoscale, and chemical inertness and biological compatibility have been demonstrated for both diamond nanoparticles and films. At the same time, nanocrystallinity provides unusual properties such as remarkable tribological properties which can be combined with high-conformality deposition of UNCD films in microelectromechanical systems (MEMS) applications that cannot be achieved with microscopic CVD diamond coatings; UNCD particulate allows superfinish polishing with surface roughnesses in the subnanometer range that cannot be achieved with micron- and even nanometer-sized diamond particles.

Nanocrystalline and UNCD diamond films are currently grown using a variety of CVD methods of synthesis. Ironically, several decades ago understanding the role of hydrogen in CVD diamond film growth resulted in an increase of hydrogen content in the source gas which was a major breakthrough for the successful synthesis of microscopic diamond films,[79] while a couple of decades later an approach using a hydrogen-poor plasma[68] resulted in the growth of UNCD films.

There are three major methods of nanodiamond and UNCD particulate synthesis, resulting in commercial products: two methods using explosives as well as a method of micronizing and grinding of micron-sized natural and artificial (HPHT) diamond. The dynamic HPHT methods of using explosives include transformation of carbonaceous species by external shock waves (DuPont method) and formation of UNCD behind the detonation wave front from the carbon contained in the explosives (detonation UNCD). There is often confusion between the last two types of nanodiamond particulate; besides the difference in the mechanism of synthesis (Fig. 3.3), the size of the primary particles and phase composition of the particles are rather different also (Fig. 3.2).

Recently, higher diamondoid molecules have been extracted from crude oil by researchers from Chevron Texaco; so far it has not been possible to synthesize higher diamondoids. Due to their well-defined molecular composition, interesting optical and other properties, and the very favorable business infrastructure at Molecular Diamond Technologies, Inc., it is believed that they will soon be commercialized too.

A rich plethora of new methods of nanodiamond synthesis have appeared within the last few years, so far at the laboratory scale. A large group of methods based on the use of energetic particles and beams include solid state transformation of carbon precursors under electron and ion beam irradiation as well as the use of lasers and other methods (Fig. 3.5). Static HPHT processing of nanocarbon precursors resulted in the synthesis of nanodiamond at much lower pressure and temperature; chlorination of carbides results in the formation of a nanodiamond layer at the boundary of the carbide–carbon phases. Fascinating 1-D and 2-D diamond nanostructures have also been synthesized by a variety of techniques, opening up new possibilities in applications. Their physical properties have not yet been investigated.

Regarding open questions, synthesis of monocrystalline nanodiamond particles of controllable size is yet to be achieved; development of methods to avoid diamond nanoparticle aggregation is needed; and reliable scaled-up growth of diamond nanorods is desired for applications that are envisioned to be very valuable, such as in nanocomposites.

In conclusion, nanocrystalline diamond with its wide diversity of forms is a rapidly developing material from the point of view of both fundamental research as well as the current perspective of application in many areas of nanotechnology.

Acknowledgments

The authors thank the US Army Research Laboratory for support of a portion of this work under grant W911NF-04-2-0023.

References

1. Gruen, D. M., Nanocrystalline diamond films, *Annu. Rev. Mater. Sci.* **29**, 211, 1999.
2. Dolmatov, V. Y., Detonation synthesis ultradispersed diamonds: properties and applications, *Russ. Chem. Rev.* **70**, 607, 2001.
3. Shenderova, O. A., Zhirnov, V. V., and Brenner, D. W., Carbon nanostructures, *Crit. Rev. Solid State Mater. Sci.* **27**, 227, 2002.
4. Belobrov, P. I., Nature of nanodiamond state and new applications of diamond nanotechnology, Proc. IX Int. Conf. “High-tech for Russian Industry”, Moscow, 11–13 September, vol. 1, pp. 235–269, 2003 (in Russian).
5. Vereschagin, A. L., *Detonation Nanodiamonds*, Altai State Technical University, Barnaul, Russian Federation, 2001 (in Russian); Vereschagin, A. L. *Properties of Detonation Nanodiamonds*, Barnaul State Technical University Altay Region, 128 pp., 2005 (in Russian).

6. Dolmatov, V. Y., *Ultradisperse diamonds of detonation synthesis: production, properties and applications*, St. Petersburg, State Politechnical University, 2003.
7. Danilenko, V. V., *Synthesis and Sintering of Diamond by Detonation*, Energoatomizdat, Moscow, 2003 (in Russian).
8. *Nanostructured Carbon for Advanced Applications*, edited by G. Benedek, P. Milani, and V. G. Ralchenko, NATO Science Series vol. 24, Kluwer Academic, Dordrecht, 2001.
9. *Detonation Nanodiamonds and Related Materials*, Bibliography Index, First Issue, edited by A. Vul, V. Dolmatov, and O. Shenderova, "FIZINTEL", St. Petersburg, Russia, 2003.
10. *Ultrananocrystalline Diamond: Synthesis, Properties and Applications*, edited by D. M. Gruen, A. Vul and O. Shenderova, NATO Science Series, Springer, Berlin, 2005.
11. Danilenko, V. V., On the history of the discovery of nanodiamond synthesis, *Phys. Solid State* **46**, 595, 2004.
12. Gogotsi, Y., Welz, S., Ersoy, D. A., and McNallan, M. J., Conversion of silicon carbide to crystalline diamond-structured carbon at ambient pressure, *Nature* **411**, 283, 2001.
13. Daulton, T. L., Kirk, M. A., Lewis, R. S., and Rehn, L. E., Production of nanodiamonds by high-energy ion irradiation of graphite at room temperature, *Nucl. Instrum. Methods B* **175**, 12, 2001.
14. Banhart, F. and Ajayan, P. M., Carbon onion as nanoscopic pressure cell for diamond formation, *Nature* **382**, 433, 1996.
15. Frenklach, M., Howard, W., Huang, D. et al., Induced nucleation of diamond powder, *Appl. Phys. Lett.* **59**, 546, 1991.
16. Tielens, A., Seab, C., Hollenbach, D. et al., Shock processing of interstellar dust – diamonds in the sky, *Astrophys. J.* **319**, L109, 1987.
17. Barnard, A. S., Russo, S. P., and Snook, I. K., Structural relaxation and relative stability of nanodiamond morphologies, *Diamond Relat. Mater.* **12**, 1867, 2003.
18. Barnard, A. S., Russo, S. P., and Snook, I. K., Ab initio modelling of the stability of nanocrystalline diamond morphologies, *Philos. Mag. Lett.* **83**, 39, 2003.
19. Raty, J. Y., Galli, G., Buren, T. et al., Quantum confinement and fullerene-like surface reconstructions in nanodiamonds, *Phys. Rev. Lett.* **90**, 037401, 2003.
20. Shenderova, O. et al., Carbon family at the nanoscale, in *Ultrananocrystalline Diamond: Synthesis, Properties and Applications*, edited by D. M. Gruen et al., NATO Science Series, p. 1, Springer, Berlin, 2005.
21. Kuznetsov, V. L., Zilberberg, I. L., Butenko, Y. V. et al., Theoretical study of the formation of closed curved graphite-like structures during annealing of diamond surface, *J. Appl. Phys.* **86**, 863, 1999.
22. Kuznetsov, V. L. and Butenko, Y. V., Nanodiamond graphitization and properties of onion-like carbon, in *Ultrananocrystalline Diamond: Synthesis, Properties and Applications*, edited by D. M. Gruen et al., NATO Science Series, Springer, Berlin, 2005.

23. Welz, S., Gogotsi, Y., and McNallan, M. J., Nucleation, growth, and graphitization of diamond nanocrystals during chlorination of carbides, *J. Appl. Phys.* **93**, 4207, 2003.
24. Tyler, T., Zhirnov, V., Kvit, A., Kang, D., and Hren, J., Electron emission from diamond nanoparticles on metal tips, *Appl. Phys. Lett.* **82**, 2904, 2003.
25. DeCarli, P. and Jamieson, J., Formation of diamond by explosive shock, *Science* **133**, 1821, 1961.
26. Website of Microdiamant AG, Lengwil, Switzerland.
27. Yamada, K. and Tanabe, Y., Shock-induced phase transition of oriented pyrolitic graphite to diamond at pressures up to 15 GPa, *Carbon* **40**, 261–269, 2002.
28. Zhu, Y. Q. et al., Collapsing carbon nanotubes and diamond formation under shock waves, *Chem. Phys. Lett.* **287**, 689, 1998.
29. Abadurov, G. A. et al., Method of producing diamond and/or diamond-like modifications of boron nitride, US Patent 4,483,836, 1984.
30. Ownby, P. D., Nano 6H diamond polytype polycrystalline powder, Proc. NSTI Nanotechnology Conf., March 7–11, 2004, Boston, Massachusetts, vol. 3, pp. 210–213, 2004.
31. Ownby, P. D., Private communication. Two types of powder of UNCD of detonation origin analyzed using the Rietveld whole-profile powder X-ray method were produced at VNIINF, Snezinsk and NPO "Altai", Russia. Note that the technique does not quantify non-crystalline phases.
32. Puzur, A. P., Bondar, V. S. et al., Physico-chemical properties of modified nanodiamonds, in *Ultrananocrystalline Diamond: Synthesis, Properties and Applications*, edited by D. M. Gruen et al., NATO Science Series, Springer, Berlin, 2005.
33. Krüger, A., Kataoka, F., Ozawa, M. et al., Unusually tight aggregation in detonation nanodiamond: identification and disintegration, *Carbon* **43**(8), 1722–1730, 2005.
34. Dahl, J. E., Liu, S. G., and Carlson, R. M. K., Isolation and structure of higher diamondoids, nanometer-sized diamond molecules, *Science* **299**, 96, 2003.
35. Carlson, R. M. K., Dahl, J. E. P., and Liu S. G., Diamond molecules found in petroleum, in *Ultrananocrystalline Diamond: Synthesis, Properties and Applications*, edited by D. M. Gruen et al., NATO Science Series, Springer, Berlin, 2005.
36. Núñez-Regueiro, M., Monceau, P., and Hodeau, J.-L., Crushing C60 to diamond at room temperature, *Nature* **355**, 237–239, 1992.
37. Cao, L. M., Gao, C. X., Sun, H. P. et al., Synthesis of diamond from carbon nanotubes under high pressure and high temperature, *Carbon* **39**, 311, 2001.
38. Ma, Y. Z., Zou, G. T., Yang, H. B., and Meng, J. F., Conversion of fullerenes to diamond under high pressure and high temperature, *Appl. Phys. Lett.* **65**, 822, 1994.
39. Yusa, H., Nanocrystalline diamond directly transformed from carbon nanotubes under high pressure, *Diamond Relat. Mater.* **11**, 87, 2002.
40. Frenklach, M., Kematick, R., Huang, D. et al., Homogeneous nucleation of diamond powder in the gas phase, *J. Appl. Phys.* **66**, 395–399, 1989.

41. Buerki, P. R. and Leutwyler, S., Homogeneous nucleation of diamond powder by CO_2 laser-driven reactions, *J. Appl. Phys.* **69**, 3739, 1991.
42. Wesolowski, P., Lyutovich, Y., Banhart, F. et al., Formation of diamond in carbon onions under MeV ion irradiation, *Appl. Phys. Lett.* **71**, 1948, 1997.
43. Fedoseev, V. D., Bukhovets, V. L., Varshavskaya, I. G. et al., Transition of graphite into diamond in a solid state under the atmospheric pressure, *Carbon* **21**, 237, 1983.
44. Wei, B., Zhang, J., Liang, J., and Wu, D., The mechanism of phase transformation from carbon nanotube to diamond, *Carbon* **36**, 997, 1998.
45. Meguro, T. et al., Creation of nanodiamonds by single impacts of highly charged ions upon graphite, *Appl. Phys. Lett*. **79**, 3866, 2001.
46. Tomita, S., Fujii, M., Hayashi, S., and Yamamoto, K., Transformation of carbon onions to diamond by low-temperature heat treatment in air, *Diamond Relat. Mater*. **9**, 856, 2000.
47. Sun, L. T., Gong, J. L., Zhu, Z. Y. et al., Nanocrystalline diamond from carbon nanotubes, *Appl. Phys. Lett.* **84**, 2901, 2004.
48. Lifshitz, Y., Kohler, T., Frauenheim, T. et al., The mechanism of diamond nucleation from energetic species, *Science* **297**, 1531, 2002.
49. Terranova, M. L. et al., Controlled evolution of carbon nanotubes coated by nanodiamond: the realization of a new class of hybrid nanomaterials, *Chem. Mater*. **17**(12), 3214, 2005.
50. Shiomi, H., Reactive ion etching of diamond in O-2 and CF4 plasma, and fabrication of porous diamond for field emitter cathodes, *Jpn. J. Appl. Phys.* **36**(12B), 7745, 1997.
51. Baik, E. S. and Baik, Y. J., Aligned diamond nanowhiskers, *J. Mater. Res.* **15**, 923, 2000.
52. Zhang, W. J. et al., Structuring nanodiamond cone arrays for improved field emission, *Appl. Phys. Lett.* **83**, 3365, 2003.
53. Ando, Y., Nishibayashi, Y., and Sawabe, A., Patterned growth of heteroepitaxial diamond, *Diamond Relat. Mater.* **13**, 633, 2004.
54. Okuyama, D. et al., Periodic submicrocylinder diamond surfaces using two-dimensional fine particle arrays, *Langmuir* **18**, 22, 2002.
55. Masuda, H., Yanagishita, T., Yasui, K., Nishio, K., Yagi, I., Rao, T. N., and Fijishima, A., Fabrication of a nanostructured diamond honeycomb film, *Adv. Mater.* **13**, 247, 2001.
56. Yanagishita, T., Masuda, H. et al., Synthesis of diamond cylinders with triangular and square cross sections using anodic porous alumina templates, *Chem. Lett.* **10**, 976, 2002.
57. Kobashi, K., Tachibana, T., Yokota, Y. et al., Fibrous structures on diamond and carbon surfaces formed by hydrogen plasma under direct-current bias and field electron-emission properties, *J. Mater. Res.* **18**, 305, 2003.
58. Chih, Y. K., Chen, C. H., Hwang, J. et al. Formation of nano-scale tubular structure of single crystal diamond, *Diamond Relet. Mater.* **13**, 1614, 2004.
59. Sun, L. T., Gong, J. L., Zhu, D. Z. et al., Diamond nanorods from carbon nanotubes, *Adv. Mater.* **16**, 1849, 2004.
60. Deryagin, B. V., Fedoseev, D. V., Luk'yanovich, V. M., Spitsin, B. V., Ryabov, V. A. and Lavrent'ev, A. V., Filamentary diamond crystals, *J. Cryst. Growth*, **2**, 380, 1968.

61. Zamozhskii, V. D. and Luzin, A. N., Growth of diamond whiskers observed in an electron microscope, *Dokl. Akad. Nauk SSSR* **224**, 369, 1975 (in Russian).
62. Butuzov, V. P., Laptev, V. A., Dunin, V. P., Zadneprovskii, B. I., and Sanzharlinskii, N. G., Diamond whisker growth in a metal-carbon system at high pressures and temperatures, *Dokl. Akad. Nauk SSSR* **225**, 88, 1975 (in Russian).
63. *Chemistry and Life* (scientific popular journal in Russian), **1**, 14–16, 1999 (about work of A. Koscheev).
64. Lee, J. K., Baik, Y. J., Eun, K. Y. et al., Synthesis of diamond spheres, *Chem. Vapor Deposition* **10**, 133, 2004.
65. Chen, H. and Chang, L., Characterization of diamond nanoplatelets, *Diamond Relat. Mater*. **13**, 590, 2004.
66. Lu, C. A. and Chang, L., Synthesis of diamond hexagonal nanoplatelets by microwave plasma chemical vapor deposition, *Diamond Relat. Mater*. **13**, 2056, 2004.
67. Lu, C. A. and Chang, L., Microstructural investigation of hexagonal-shaped diamond nanoplatelets grown by microwave plasma chemical vapor deposition, *Mater. Chem. Phys.* **92**, 48, 2005.
68. Gruen, D. M., Liu, S., Krauss, A. et al., Buckyball microwave plasmas: fragmentation and diamond-film growth, *J. Appl. Phys.* **75**, 1758, 1994; *Appl. Phys. Lett.* **64**, 1502, 1994.
69. Gruen, D. M., 356350 ultracrystalline diamond in the laboratory and the cosmos, *MRS Bull.* **26**, 771–776, 2001.
70. Nikitin, A. and Gogotsi, Y., Nanostructured carbide-derived carbon, *Encyclopedia of Nanoscience and Nanotechnology*, edited by H. S. Nalwa, American Scientific Publishers, CA, **7**, 553–574, 2004.
71. Kimura, Y. and Kaito, C., Production of nanodiamond from carbon film containing silicon, *J. Cryst. Growth* **255**, 282, 2003.
72. Gordeev, S. K., in *Nanostructured Carbon for Advanced Applications*, edited by G. Benedek, P. Milani, and V. G. Ralchenko, NATO Science Series vol. 24, pp. 71–88, Kluwer Academic, Dordrecht, 2001.
73. Gordeev, S. K., Belobrov, P. I., Kiselev, N. I., Petrakovskaya, E. A., and Ekstrom, T. C., Novel solid nano diamond/pyrocarbon semiconductor materials, *MRS Symp. Proc.* **63**, F14.16.1, 2001.
74. Ostrovidova, G. U., Makeev, A. V., Biryukov, A. V. et al., Carbon nanocomposite materials as medicinal depot, *Mater. Sci. Eng. C* **23**, 377, 2003.
75. Dubrovinskaia, N. et al., Nanocrystalline diamond synthesized from C60, *Diamond Relat. Mater.* **14**, 16, 2005.
76. Wang, J. B., Zhang, C. Y., Zhong, X. L. et al., Cubic and hexagonal structures of diamond nanocrystals formed upon pulsed laser induced liquid–solid interfacial reaction, *Chem. Phys. Lett.* **361**, 86, 2002.
77. Lewis, R. S., Ming, T., Wacker, J. E. et al., Interstellar diamond in meteorites, *Nature* **326**, 160–162, 1987.
78. Greiner, N. Roy, Philips, P. S., and Johnson, J. D., Diamond in detonation soot, *Nature* **333**, 6172, 1988.
79. Spitsyn, B. V., Bouilov, L. L., and Deryaguin, B. V., Vapor growth of diamond on diamond and another surfaces, *J. Cryst. Growth* **52**(1), 210–226, 1981.

80. Chen, P., Huang, F., and Yun, S., Structural analysis of dynamically synthesized diamonds, *Mater. Res. Bull*. **39**, 1589–1597, 2004.
81. Xu, X., Yu, Z., Zhu, Y., and Wang, B., Dispersion and stability of nanodiamond in clean oil, *Mater. Sci. Forum* **471–472**, 779–783, 2004.
82. Xu, X., Yu, Z., Zhu, Y., and Wang, B., Effect of sodium oleate adsorption on the colloidal stability and zeta potential of detonation synthesized diamond particles in aqueous solutions, *Diamond Relat. Mater*. **14**, 206–212, 2005.

PART 2
STABILITY OF NANODIAMOND

4 Stability of Nanodiamond

Amanda S. Barnard

Center for Nanoscale Materials and Materials Science Division, Argonne National Laboratory, Argonne, IL, USA

Introduction: Nanocarbon Phase Stability

In order to discuss the phase diagram of nanocarbon, it is first necessary to review the features of the phase diagram of bulk carbon in the macroscopic regime. A reasonable amount is known regarding the thermodynamics of the elemental carbon phases (graphite, diamond, liquid and vapor) over a wide range of conditions. Numerous studies have been published over past decades (beginning in the 1960s),[1] iteratively improving upon previous versions of the phase diagram as new information, methods and results become available. Much work[2] has focused on the graphite–diamond–liquid triple point at approximately 12 GPa/5000 K,[3] the boundary between the graphite and diamond stable regions[4] (known as the Berman–Simon line),[5] the melting line of graphite, and the diamond melting line that runs to higher pressure and temperature above the triple point.[6]

Early studies have been recently extended, via explicit calculation of the Gibb free energy equation of state, to describe the phase diagram of carbon up to 600 GPa and 15000 K[7] using Hugoniot analysis.[8] As early as 1979 Grover used the equation of state of carbon to predict crystalline metallic carbon as a post diamond phase.[9] More recently, in the regime of 100–250 GPa a six-fold coordinated post-diamond phase of carbon has been predicted,[10] with similar characteristics as the simple-cubic high-pressure form of carbon known as SC4.[11] The stability and equation of state of (transparent) rectangulated carbon has been investigated, which is formed by the linking of buckled layers of graphite when subjected to high pressure at room temperature.[12] Other high-pressure forms of carbon have also been proposed, such as the four-fold coordinated body-centered-cubic BC8[13] predicted to be stable over 1200 GPa.[14]

At higher temperatures it has been found that liquid carbon is metallic,[15] although there is some conjecture regarding the exact structure of liquid carbon. High-pressure studies of first-order liquid–liquid phase transitions in carbon have been undertaken at temperatures of 4000–

6500 K, reporting that liquid clusters are more likely to be graphite-like (three-fold coordinated) than diamond-like (four-fold coordinated).[6] Other studies, however, have predicted principally four-fold coordinated liquid clusters,[15] such as a simple-cubic structure.[16] Even at more moderate pressures and temperatures, due to the high activation energies for solid-state transformations (and the specific effects of reaction paths), a wide spectrum of other metastable forms and complex hybrid carbon materials may be generated. These include the various specific types of graphite.[17]

The currently accepted version[18] of the (thermodynamic) carbon phase diagram (up to 50 GPa and 6000 K) includes regions for the solid phase transformation of diamond to graphite, graphite to diamond, hexagonal graphite to hexagonal diamond, and the shock compression of graphite to hexagonal or cubic diamond (as well as other experimentally observed phase transitions), as shown in Fig. 4.1. Note that this diagram is distinct from the multi-component (ternary)[19–22] and non-equilibrium phase diagrams that are constructed to describe the growth of diamond films from hydrocarbons,[23] the phase of carbon under non-equilibrium conditions (such as under electron irradiation),[24,25] and the salvation of metals in carbon.[26]

4.1 Nanocarbon Phase Diagrams

An excellent review of much of the past work on the all-carbon pressure–temperature phase diagram is given in ref.[18] This article summarizes the underlying basis for the more recent studies extending the carbon phase diagram to include carbon nanoparticles (as a function of size). In general, the thermodynamic properties of nanoscale carbon particles may be calculated by considering the coexistence of several phases of gases, liquids, and solids in chemical equilibrium. For example, a number of equations of state for carbon in detonation products (which promote a smooth transition from an effective graphite phase to an effective diamond phase) were compared by Charlet et al.[27] to determine their reliability in the consideration of the adiabatic gamma.

An alternative approach is to add a surface energy contribution to the bulk Gibbs free energy per atom of a cluster of n atoms in a given phase,[28] and define the phase equilibrium by equating the Gibbs energies for n-atom clusters of each phase. A number of phase diagrams that include nanocarbon have been proposed, each exhibiting displacement of the

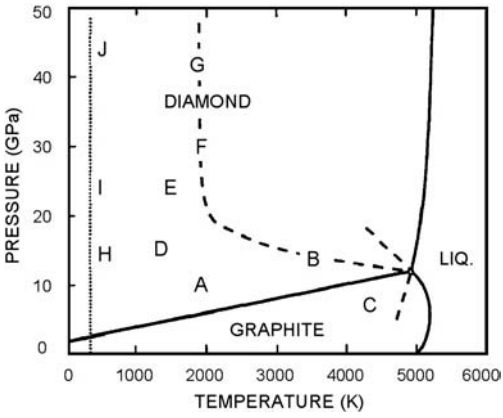

Figure 4.1 P–T phase and transition diagram for carbon. Solid lines represent equilibrium phase boundaries. A: commercial synthesis of diamond from graphite by catalysis; B: *P–T* threshold of very fast (less than 1 ms) solid–solid transformation of graphite to diamond; C: *P–T* threshold of very fast transformation of diamond to graphite; D: single crystal hexagonal graphite transforms to retrievable hexagonal-type diamond; E: upper ends of shock compression/quench cycles that convert hexagonal graphite particles to hexagonal diamond; F: upper ends of shock compression/quench cycles that convert hexagonal graphite to cubic diamond; B, F, G: threshold of fast *P–T* cycles, however generated, that convert either type of graphite or hexagonal diamond into cubic diamond; H, I, J: path along which a single crystal hexagonal graphite compressed in the *c*-direction at room temperature loses some graphite characteristics and acquires properties consistent with a diamond-like polytype, but reverses to graphite upon release of pressure. (Reproduced with permission from F. P. Bundy, W. A. Bassett, M. S, Weathers, R. J. Hemley, H. K. Mao, and A. F. Groncharov, *Carbon*, 34, 141, (1996) © Elsevier 1996.)

phase equilibrium lines for small carbon particles containing from 10^2 to 10^4 atoms.[28–30] Figure 4.2 illustrates the displacement of the phase equilibrium lines for carbon nanoparticles containing 10^3 atoms, where the shadowed region corresponds to estimated uncertainties derived from available experimental data.

Along similar lines, Fig. 4.3[31] (based on the published properties of detonation diamond) depicts the three-dimensional phase diagram for nanocarbon, with the vertical axis providing the size dependence, and the phase diagram for bulk phases shown in the horizontal plane. There are a number of key features of this diagram. Although nanodiamond appears

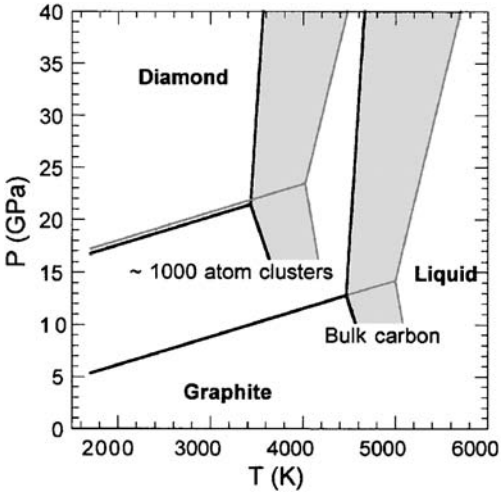

Figure 4.2 Estimated uncertainty in location of carbon particle phase equilibrium lines derived from available experimental data. (Reproduced with permission from J. A. Viecelli, S. Bastea, J. N. Glosli, and F. H. Ree, *J. Chem. Phys.*, 115, 2730 (2001). © American institute of Physics 2001.)

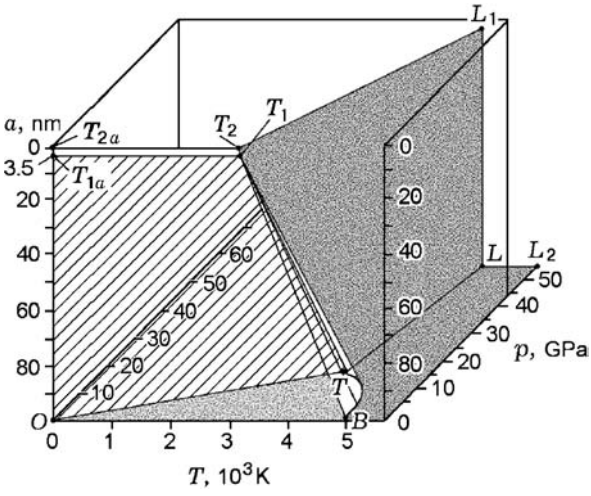

Figure 4.3 Phase diagram of ultrafine carbon: $OBTT_1T_{1a}$ is the existence domain of the graphite phase, OTT_1T_{1a} is the interface between the graphite and diamond phases, BTT_1 is the interface between the liquid carbon and graphite phases, and TT_2L_1L is the interface between the liquid carbon and diamond phases. (Reproduced with permission from A. L. Verechshagin, *Combust. Exp. Shock Waves*, 38, 358 (2002). © Springer 2002.)

as the most stable phase at particle sizes below 3 nm, a lower limit for nanodiamond phase stability is introduced at 1.8 nm (corresponding to the experimentally observed minimum particle size). The striped vertical plane (above the region for graphite) arises from observations of ~4 nm spherical diamond particles in the liquid state at a temperature of 3000 K (lower than that for bulk diamond).[32]

In both diagrams (Figs. 4.2 and 4.3) the position of the triple point is different for small particle sizes than for bulk, although the triple point displaces toward higher pressures in Fig. 4.2 and toward lower pressures in Fig. 4.3. Another variant of the 3-D phase diagram based on the results reported in ref.[28] was suggested by Shenderova et al.,[33] introducing a change of the slope of the diamond/graphite equilibrium line as particle size is decreased (see Fig. 4.4). This change reflects the higher stability of nanodiamond over nanographite observed experimentally under ambient conditions.[33]

In general, a review of the literature regarding the structure of carbon nanoparticles[33] highlights that at sizes below 1.8 nm, other carbon forms are abundant, such as fullerenes and onion-like carbon (OLC). Therefore,

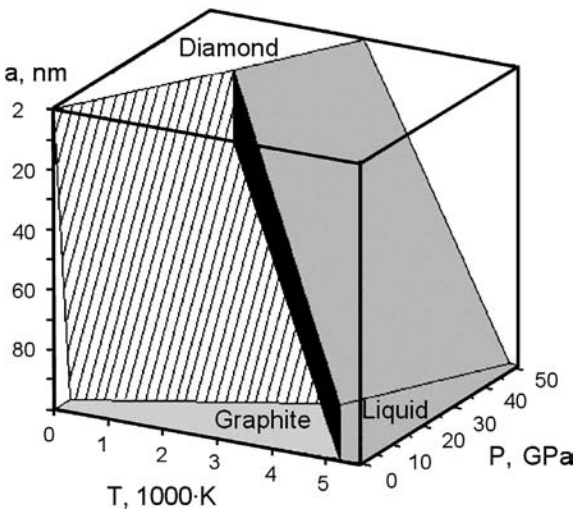

Figure 4.4 Schematic 3-D phase diagram for carbon illustrating the change in position of the triple point as a function of particle size drawn according to ref. [30], illustrating the nanodiamond thermodynamic stability of nanodiamond under ambient conditions. (Reproduced with permission from O. A. Shenderova, V. V. Zhirnov, and D. W. Brenner, *Crit. Rev. Solid State Mater. Sci.*, 27, 227 (2002). © Taylor & Francis 2002.)

it was suggested by Kuznetsov and colleagues[34] to assign a corresponding region of the phase diagram to closed-shell sp^2-bonded nanocarbons. This is shown schematically in Fig. 4.5, where the regions of stability are specifically indicated for fullerenes and OLC for $n = 10$ to 10^3 atoms. The phase diagram for fullerenes was later revisited by other researchers, such as Sundqvist,[35] who examined the polymetric phases of C_{60} and C_{70} fullerenes under pressure, and Korobov et al.,[36] who constructed phase diagrams for pressure-induced solid–solid transformations in polymerized C_{60}. Later, Schöll-Paschinger and Kahl[37] extended the self-consistent Ornstein–Zernike approximation to model the coexistence of fullerenes ($C_{n\geq 60}$) with liquid carbon phases.

In addition to the particles mentioned above, the phase diagrams of other low-dimensional nanocarbon systems have also been examined. These include single-walled carbon nanotubes (SWNTs)[38] and bundles of SWNTs (often referred to as nanotube ropes, or nanoropes);[39] and possibly the smallest nanoscale diamond units of all, the adamantane and

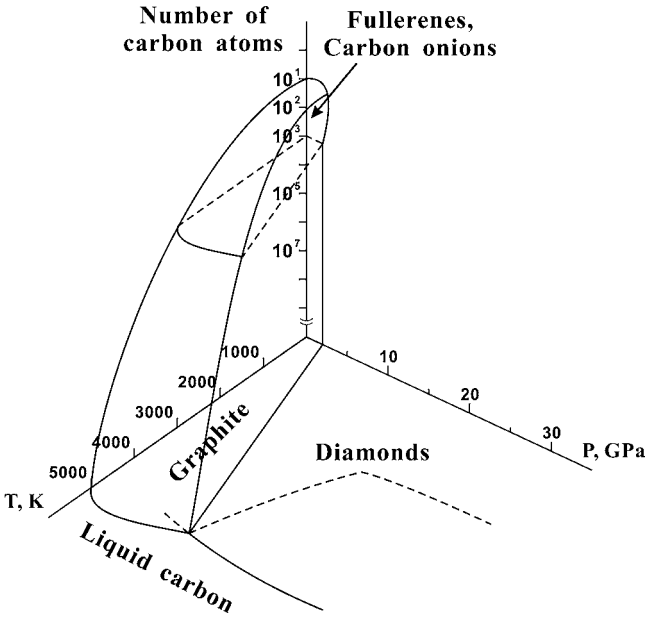

Figure 4.5 Schematic three-dimensional phase diagram for carbon, including fullerenes and OLC. (Reproduced with permission, courtesy of V. L. Kuznetsov, 2005.)

diamantane molecules.[40] These tiny members of the polymantane family are sometimes referred to as diamondoids.[41]

The complete and thorough amalgamation of the phase diagrams of these nanoscale structures (described above) with the phase diagram of bulk "macroscopic" carbon has not yet been realized. There is still a great deal of work to be done in the construction of a complete *P–T–n* phase diagram of carbon. It is likely, however, that knowledge gained from theoretical and computational studies of nanocarbon stability[42] will play an important role in the conception of such a diagram, with thermodynamic treatments of phase equilibrium showing the way.

4.2 Theoretical Studies of the Relative Phase Stability of Nanocarbons

In this section, a summary of the theoretical and computational studies of the relative stability of carbon nanoparticles is provided. The focus will be upon analytical theory and first-principles calculations, with complementary experimental results on this topic being covered in other chapters of this book. In general, the models reviewed here are thermodynamically based, and center around the relationship between graphitic (sp^2-bonded) and diamond-like (sp^3-bonded) carbon at the nanoscale.

To begin, the primary assumption common to most of the studies reviewed here is that (although graphite is the thermodynamically stable phase of carbon macroscopically), because of the small molar volume of diamond compared to that of graphite (for a sufficiently small carbon cluster), nanodiamond can be more stable than nanographite. It should be noted that in analyzing the stability between the clusters of diamond and graphite, the number of carbon atoms in each cluster should be the same, and thus the radius of the diamond cluster is smaller than that of a graphite cluster for the same number of atoms. This is important, because when a cluster becomes smaller, the surface effects dominate the bulk effects.

Due to the relatively large number of studies that have been undertaken in recent years, the results have been broken into two sections, one addressing the phase stability of "large" nanoparticles (in the regime where the relationship between nanodiamond and nanographite is most significant) and the other addressing the phase stability of "small" nanoparticles (in the regime where the relationship between nanodiamond and fullerenes is most significant).

4.2.1 Stability of Large Nanocarbon Particles

In 1987 Almlöf and Lüthi[43] carried out *ab initio* restricted Hartree–Fock (RHF) calculations on the phase stability of planar graphene sheets and cubic diamond clusters. Neglecting the contribution from the cluster zero-point energy, they defined the cohesive energy as the difference between the energy per carbon atom and the energy of the free carbon atom. The results for the cohesive energies of graphene and diamond of –5.416 and –5.395 eV, respectively, were considerably higher than experiment (–7.371 and –7.346 eV at $T = 0$ K), but this was a step in the right direction.[43]

Later, Shaw and Johnson[44] used a diffusion-limited model that assumed that the difference in energy between the carbon clusters and the macroscopic (bulk) carbon, ΔE, was related to the number of surface atoms. Their calculations estimated that ΔE is proportional to $n^{1/3}$ (where n is the total number of atoms).[44]

Building on this foundation, Badziag et al.[45] compared the binding energy of carbon atoms in small sp^3-bonded hydrocarbon molecules and sp^2-bonded polycyclic aromatics (ranging from C_2 to C_{60}). They introduced a simple model to calculate the molecular energies of tetrahedral and hexagonal clusters. In all cases the C—C and C—H bond lengths were optimized prior to the energy calculation, although the geometry was restricted.[45]

The binding energy was plotted as a function of the hydrogen to carbon ratio, with the results forming two approximately linear trends corresponding to the hexagonal and tetrahedral clusters, respectively. Overall, the sign and magnitude of the slopes (obtained from the linear fits) did agree with experimental observation, although explicit values were not reported. By examining the intersection point of the linear fits, their results showed that small hydrogenated nanodiamonds are more stable than graphite, although the actual crossover was found to be very sensitive to the type of clusters included. The crossover of particle stability varied from a hydrogen/carbon ratio of 0.5, corresponding to an octahedral nanodiamond with ~300 atoms (or a diameter of ~1.3 nm), to a hydrogen/carbon ratio of 0.12 which corresponds to an octahedral diamond nanodiamond with approximately 21000 atoms (diameter of ~6.0 nm).[45]

Some years later, Gamarnik[46] reported on the boundaries of the stability regions of diamond and graphite nanoparticles, using a model that began with a statement of the energy of carbon (at low pressure), in terms of the Helmholtz free energy. The lattice energy was determined by summation of

the Born–Lande pair interaction potentials of all the charges in the crystals, and the kinetic energy for the bond electrons in diamond and graphite was derived by relating the Coulomb force acting on a bond electron with the bond electron centripetal force to the neighboring atom. A similar approach was used to calculate the kinetic energy of the graphite bond electron charges. The model also considered atoms located at the particle edges and corners, and the conduction electrons in the graphite model.[46]

By assuming that each inner atom relinquishes one electron charge value to establish a bond (although in the case of diamond this is distributed in four directions, and three directions in the case of graphite), the covalent bond charge value per atom and the conduction electron charge value were established. The results of this model showed that the energy per atom was dependent on the size of the nanodiamond and nanographite particles, as well as the temperature. At $T = 0$, the model predicted that nanodiamond was stable below the point of intersection with graphite at 15 nm, below 10.2 nm at room temperature, below 6.1 nm at 545 °C, below 4.8 nm at 800 °C, and below 4.3 nm at 1100 °C.[46]

In the same year Hwang et al.[47] outlined a chemical potential model to examine the low-pressure synthesis of nanodiamond, in terms of the surface energy of diamond and graphitic clusters. The main advantage of their approach was its applicability to non-equilibrium conditions. They performed thermodynamic calculations using bulk diamond as the reference state and the deposition and etching of carbon during synthesis was analyzed in terms of the activity of carbon. The driving forces for the precipitation of graphite and diamond were evaluated and predicted that, depending on the sign of the driving force, precipitation or etching would occur.[47]

The authors also suggested that the capillary effect (given by the Laplace–Young equation for a small carbon particle) is essential in approaching formation of diamond over graphite, and that the precipitation of diamond and of graphite (from the gas phase) are kinetically equivalent. Assuming that the diamond and graphite particles are spherical, the crossover of phase stability was estimated to be 104 atoms (at 1200 K) for graphitic clusters, and 177–584 atoms for diamond clusters, respectively. This study also went on to examine the nucleation on a substrate, and the model was elaborated to consider the conditions required for nucleation of diamond to dominant during CVD growth.[47]

As an extension of this work Hwang and his colleagues[48] also analyzed in detail the theoretical and experimental aspects of charge on the stability of small diamond and graphite clusters. The charged cluster model surmises that since graphite is conducting, the charge will to be

uniformly distributed over the conducting bulk and the interface; however, in the case of diamond the charge on the diamond cluster will be localized at the interface. Therefore the surface energy of the diamond cluster may be decreased by the presence of charges while that of the graphite cluster cannot.[48]

Experimental evidence[48] suggested that the stability of diamond was favored by a positive bias on the substrate, and the stability of graphite carbon was favored by a negative bias. The implication that the stability of the charged nuclei was affected by the sign of the charge seemed closely related to the well-established fact that the nucleation behavior in the presence of charges depends on the sign of the charge. Unfortunately, the authors admit that the proposed theory (and available data) was not sufficient to make any quantitative prediction on the sign dependence of the stability between diamond and graphite clusters. An extensive and rigorous treatise of this model, outlining the theory and application to appropriate systems, is given in ref.[49]

Around the same time Winter and Ree[28,50] outlined a method for investigating carbon-particle phase stability of graphene sheets and hydrogenated nanodiamonds. They derived an expression for the heat of formation as a function of cluster size and used it to predict the relative stability of the graphite and diamond phases of finite carbon particles. They assumed that each carbon atom in graphite forms three intra-layer sp^2 bonds, and experiences a weak interlayer dispersive interaction between graphene sheets; and in diamond each carbon atom forms four identical sp^3 bonds with the neighbor carbons.[28,50]

Semi-empirical and density functional theory (DFT) methods were used to determine the total energy of sp^2 and sp^3 isolated carbon clusters. To account for the surface effects, the total energy per carbon atom was plotted as a linear function of the hydrogen to carbon ratio. The C—H bond energy was obtained from the coefficients of a least squares fit for both the graphite and diamond clusters, respectively. In agreement with previous results, the model predicted that small nanodiamond clusters are more stable than graphite below approximately 33000–70000 atoms (depending upon the computational method used), corresponding to a particle size of 6–8 nm.[28,50]

In all of the models mentioned above the dependence of the nanodiamond/graphite phase stability on the pressure of the system has not been explicitly accounted for. This was first considered by Jiang et al.[51] using a model of the phase transition between nanodiamond and nanographite (as well as the corresponding thermodynamic functions) based on a pressure–temperature phase diagram of carbon, as a function of size.

The contribution of the size-dependent internal pressure was estimated by assuming spherical, quasi-isotropic nanocrystals, with additional curvature-induced pressure given by the Laplace–Young equation, and using experimental values for the bulk phases. The thermodynamic functions for the diamond-to-graphite transition (in this case) were estimated via the Clausius–Clapeyron equation. The equilibrium size of diamond and graphite was equated (at equilibrium), neglecting the difference of pressure for nanocrystals as a first approximation, and it was shown that the transition size of nanodiamond decreases from approximately 8 nm at 0 K to 3 nm at 1500 K. The authors also point out that the diamond to graphite transition in each direction may follow different kinetics, and the model was used to explain why nanodiamonds are seen to graphitize at the surface, but direct conversion of graphite to nanodiamond is not observed. Such a transition requires a driving force such as that provided by electron irradiation.[24,25]

This model was later extended to include the effects of surface stress on the internal pressure of the nanoparticle.[52] The melting enthalpy was described in terms of the Helmholtz function. The authors plotted the transition interface between nanodiamond (111) and nanographite (0001), to find that the transition size of nanodiamond now decreases from ~11 nm at 0 K to ~4 nm at 1500 K. Furthermore, the transition point at 1300 K was found to provide a transition size between diamond and the OLC, as the transformed product of OLC has a lower Gibbs free energy than the graphite. This indicated that the transition size between the nanodiamond and nanographite should be larger than 2 nm.[52]

Although this study assumes the surface energy is equivalent to surface stress (an approximation that may not be valid in this case) the results clearly show that the effects of surface stress are very important in the description of the phase stability of nanocarbon, since the transition size of nanodiamond without surface stress (above) gave ~8 nm at 0 K to ~3 nm at 1500 K, some 1–3 nm smaller than when surface stress was included.[51,52] These results are shown in Fig. 4.6.

The phase transition between nanodiamond and OLC structures has also been previously addressed by Zaiser and Banhart,[53] who presented a thermodynamic quasi-equilibrium theory to explain this irradiation-induced transformation of OLC to nanodiamond. The model was based on the premise that irradiation of OLC leading to the destabilization of the sp^2 structure was due to the large difference in the cross-sections for irradiation-induced displacements of carbon atoms in diamond and graphite. A non-equilibrium phase diagram was calculated showing the stability of graphite and diamond (as a function of the displacement rate

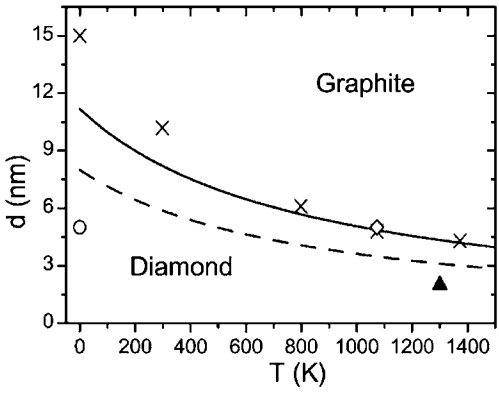

Figure 4.6 The size–temperature transition diagram of carbon at zero pressure, where the solid line shows the model prediction without surface stress and the dashed line denotes the model prediction with surface stress. The theoretical and experimental results are also plotted in the figure. The symbol ○ denotes the theoretical estimation based on the surface energy difference between diamond and graphite. The symbol × gives the theoretical calculation in terms of a charge lattice model. The symbol ◇ is based on the experimental observation at 1073 K that nanodiamonds with $d = 5$ nm are transformed into nanographite, and the symbol ▲ shows an experimental result where nanodiamonds of 2 nm in size transform to OLC at 1300 K. (Reproduced with permission from D. Zhao, M. Zhao, and Q. Jiang, *Diamond Relat. Mater.*, 11, 234 (2002). © Elsevier 2002.)

of atoms), and the results related to experimentally observed results.[53] In this approach the issue of nucleation was excluded in favor of considering the phase transformation as the motion of a phase boundary separating the two (solid) allotropes. The OLC-to-nanodiamond phase transition was attributed to ballistic displacements causing interstitial C atoms (predominantly from sp^2 lattice sites) and a net flux of atoms from the sp^2 to the sp^3 phase. It was shown, however, that if the temperature exceeds an (upper) critical temperature the sp^2 bonding may be stable, even though phase transitions may still occur at lower temperatures.[53]

In addition to these thermodynamic treatments, a small number of kinetic theories have been developed to describe the actual phase transitions that occur at the interface between the sp^2 fullerenic and sp^3 nanodiamond phases. For example, Butenko et al.[54] derived a model to determine a (temperature-dependent) isotropic rate of migration of the interface between the diamond and graphitic regions of spherical nanocarbon particles. They employed a reducing sphere model that assumed that phase conversion begins simultaneously at all interface surface points, and

that (under isothermal conditions) the interface moves with a constant isotropic rate inside the nanoparticle. The reaction rate of the nanodiamond to bucky-diamond (or OLC) transition was treated as a migration rate of the interface between the exfoliated fullerenic shells and the diamond cores. Estimated kinetic parameters in an Arrhenius expression (such as the activation energy) then allowed for quantitative calculations of the diamond graphitization rates in (and around) the critical temperature range.[54]

4.2.2 Stability of Small Nanocarbon Particles

Although all of these models establish the crossover for phase stability of graphite and nanodiamond and model the phase transition in large (~5–6 nm) nanocarbon particles, the question of the phase stability of smaller (<2.5 nm) particles has also been explicitly investigated by Barnard et al.,[55] by extending an established thermodynamic theory to include fullerenes. By treating only dehydrogenated *nanodiamonds* (i.e., nanodiamond structures consisting of mostly sp^3-bonded atoms, as opposed to bucky-diamond), a direct comparison with fullerenes was made.[55]

The method (similar to that derived by Winter and Ree)[50] was based on the enthalpy of formation as a function of size, expressed in terms of the bond energies for diamond-like and fullerenic clusters, the surface dangling bond energy, the number of carbon atoms, the number of dangling bonds on the surface of the particle, and the standard heat of formation of carbon at 298.15 K. In the case of fullerenes, the closed shell eliminates the dependence on the effective surface volume ratio, and therefore the size dependence. Therefore, a term for the strain energy that vanishes in the graphene limit was added, by first making the assumption that a fullerene may be approximated as a homogeneous and isotropic elastic sphere. This was derived by considering the bending and stretching of a suitable elastic sheet, in terms of the bending energy per unit area, the bending modulus of the sheet, and the mean radius of curvature. A spherical model was assumed and an expression for the strain energy per carbon atom was obtained by fitting the calculated energy for all known fullerenes from C_{20} to C_{80} to the inverse of the square of each fullerene radius of curvature.[55]

The cohesive energy and dangling bond energy of nanodiamond was calculated[56] using the linear fit to the spin polarization corrected energy per ion versus number of dangling bonds per ion, and found to be

3.855 eV and 1.619 eV, respectively. Similarly, the strain energy and cohesive energy for fullerenes was 5.19 eV and 7.81 eV, respectively. Using these results the enthalpy of formation for relaxed, dehydrogenated (stable) nanodiamond crystals and fullerenes was then plotted as a function of the number of carbon atoms, and an empirical best fit was applied to find the point of intersection. This intersection was reported at ~1100 atoms, which is approximately equivalent to cubic nanodiamond crystals of 1.9 nm in diameter.[55]

Even below this size, however, still more interesting forms of carbon nanoparticles exist. Therefore it is appropriate to mention here the relationship between these structures and fullerenes, below ~1.5 nm in diameter. Mass spectra data of molecular beams have shown that C_{11}, C_{15}, C_{19}, C_{23}, C_{28}, and C_{36} clusters are in fact more abundant than clusters in the range $C_{29–35}$.[57] In 1991, Tománek and Schluter undertook a study of the stability of "small" carbon clusters using tight-binding methods,[58] examining the growth regimes of various configurations. Other more recent studies using a density function theory[59,60] have identified three regions for the stability of small clusters, including 1-D ring clusters below 20 atoms, an assorted variety of geometries coexisting between 20 and 28 atoms, and fullerenes over 30 atoms. A study of the clusters in the range 24 to 32 atoms was also undertaken by Kent et al.[61] using quantum Monte Carlo methods to compare the energetic stability of bowl, ring, sheet, and cage (fullerene) geometries.[61]

A comparison of the relative stability of fullerenes and closed carbon nanotubes has also been made using first-principles pseudopotential calculations, for clusters between 60 and 540 atoms,[62] based on strain energy contributions due to the curvature effects and the presence of pentagons. The model predicted (in agreement with experimental observations) that a nanotube with a diameter of ~1.3 nm is the energetically preferred one among various SWNTs and fullerenes examined.[62]

4.2.3 Coexistence of Bucky-diamond and Other Nanocarbon Phases

To investigate the cases where carbon nanoparticles may contain both sp^2 and sp^3 bonding, Barnard et al.[63] addressed the stability of multi-shell carbon nanoparticles using the model outlined above for comparing the phase stability of nanodiamonds and fullerenes, and applying it to bucky-diamond and OLC. The onions were treated as nested fullerenes by adding a term for the van der Waals attraction 0.056 eV[64] to the expression used

to describe fullerenes. The bucky-diamonds were treated in the same manner as nanodiamonds, although obviously the dangling bond to carbon atom ratio is different for nanodiamonds and bucky-diamonds (of similar diameter) due to the formation of the delaminated fullerenic outer shells.[63] Note that more information on the structure of bucky-diamonds will be given in the following sections.

The enthalpy of formation (as a function of particle size) for bucky-diamond and OLC was calculated, and the line of best fit extrapolated along with the nanodiamond and fullerene results mentioned in the previous section. There were three main points apparent from this comparison. First, the sp^2-bonded OLC and fullerene results were indistinguishable (within uncertainties) below approximately 2000 atoms. Second, the enthalpy of formation of bucky-diamond is more akin to OLC than the nanodiamonds. Finally, in the region from ~500 to ~1850 atoms the results predicted that a thermodynamic coexistence region was formed, within which bucky-diamond coexists (within uncertainties) with the other nanocarbon nanoparticles.[63]

This region was then further broken into three sub-regions, as indicated in Fig. 4.7. From ~500 to ~900 atoms (~1.4 to 1.7 nm), the enthalpy of formation of bucky-diamond was found to be indistinguishable from that of fullerenes (within uncertainties), although OLC represents the most

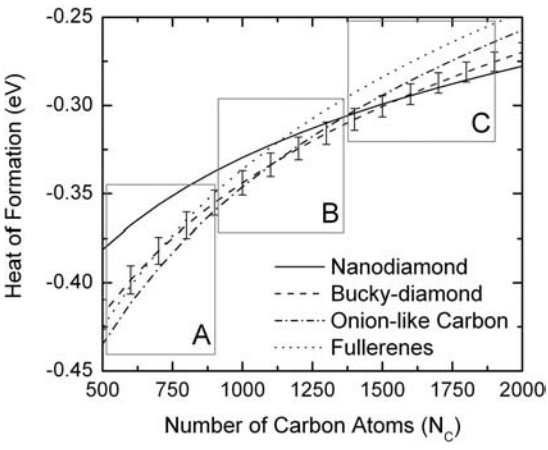

Figure 4.7 Atomic heat of formation of carbon nanoparticles, indicating the relative sub-regions of coexistence of bucky-diamond with other phases. Uncertainties indicated for bucky diamond only. (Reproduced with permission from A. S. Barnard, S. P. Russo, and I. K. Snook, *Phys. Rev. B*, 68, 73406 (2003). © American Physical Society 2003.)

stable form of nanocarbon. Between ~900 and ~1350 atoms (~1.7 and 2.0 nm), bucky-diamond and OLC coexist (within uncertainties), and bucky-diamond was found to coexist with nanodiamond (within uncertainties) between ~1350 and ~1850 atoms (~2.0 and 2.2 nm). Further, the intersection of the bucky-diamond and OLC stability was found to be very close to the intersection for nanodiamonds and fullerenes at ~1100 atoms, suggesting that at approximately 1100 atoms a sp^3-bonded core becomes more favorable than a sp^2-bonded core, irrespective of surface structure.[63]

In this size regime, Raty and Galli[65] used first-principles calculations to examine the relative stability of nanodiamond as a function of surface hydrogenation. Their results indicated that as the size of diamond is reduced to about 3 nm, bucky-diamonds are energetically preferred even over hydrogenated nanodiamonds. The approach was also based on the formation energy, containing terms for the vibrational and the total energy of a nanoparticle obtained using DFT.[65] Their calculations considered five (spherical) particle sizes containing 29, 66, 147, 211, and 275 carbon atoms. By comparing various degrees of hydrogen coverage, the difference in formation energy between particles with hydrogenated surfaces and those with bare surfaces was found to decrease as the size of the nanoparticle increases, but did not depend significantly on the hydrogen chemical potential.[65]

Although the calculations could not establish the exact size at which the crossover between hydrogenated and bare, reconstructed surfaces occurs, the numerical results contained within the paper were used to suggest how varying the hydrogen pressure (and thus its chemical potential) during synthesis may promote different types of thin films. Two ranges for the hydrogen chemical potential corresponding to two different growth conditions of diamond were proposed: one that favors the formation of UNCD and the other that favors the formation of microcrystalline diamond thin films.[65]

4.2.4 Stability of Quasi One-Dimensional Nanocarbon

Finally, the thermodynamic phase stability of diamond nanowires was investigated by Barnard and Snook[66] in an attempt to ascertain if diamond nanowires are energetically stable with respect to carbon nanotubes. They applied the same enthalpy of formation model outlined above for quasi-zero-dimensional carbon nanoparticles[63,67] to the stable diamond

nanowires[68,69] described in later sections. Both zigzag and armchair SWNT structures were investigated, for the cases $m = 3$ to 12.

Once again, the assumption was made that the strain energy of a nanotube contains only two in-plane elastic constants, and that the chiral graphene sheet is homogeneous and elastically isotropic. The nanotube strain was approximated as the bending and stretching of a suitable elastic sheet. Assuming a cylindrical model, the strain energy was obtained by applying a linear fit to the energy per ion versus the inverse square of the mean radius of curvature and extracting the strain energy and cohesive energy from the slope and intercept, respectively.[66]

In similar fashion to their investigation of nanodiamond phase stability, the C—C bond energy and dangling bond energy for the diamond nanowires were also obtained by fitting to the energy per atom versus the number of dangling surface bonds per atom. The slope and intercept of the linear fit gave values for the cohesive energy of –7.55 eV and dangling bond energy of 1.32 eV, respectively. These values (along with those for SWNTs) were used to calculate the enthalpy of formation, which was plotted as a function of the number of carbon atoms per unit length (rather than just the number of carbon atoms).[55] By extrapolating the fits, the intersection of diamond nanowires and carbon nanotubes was found to be ~450 atoms/nm. This corresponds to a diamond nanowire ~2.7 nm in diameter, or an $m = 27$ armchair nanotube.[66]

The intersection of diamond nanowires and nanotubes with graphite was also investigated, although the number of atoms in the graphite model was scaled (per unit length) in two chiral directions, equating to $\theta = 0°$ and $\theta = 30°$ (where θ is the chiral angle) to preserve the correct dimensionality. The intersection of the enthalpy of formation as a function of the number of atoms per unit length for diamond nanowire (averaged over morphologies) and carbon nanotubes with graphite was then obtained (for each "chiral scaling") and found to be 870 and 930 atoms/nm for $\theta = 0°$ and $\theta = 30°$, respectively (~4 nm in diameter).

These results established that, although SWNT represent the most energetically preferred form for ultrafine 1-D carbon nanostructures, a "window" of stability for diamond nanowires exists between approximately 450 and 870–930 atoms per unit length (2.7 to ~4 nm in diameter), beyond which graphite is once again energetically preferred.[66]

In addition to this, there are several studies that investigated the stability of nanotubes relative to graphene. For example, it was determined by Sinnott and colleagues[70] that graphene is the least stable sp^2-bonded structure below ~6000 atoms. Beyond this size graphene sheets become more stable than the (10,0) and (5,5) nanotubes.[70] This is in agreement with the

modified heuristic "bond passivation model" outlined by Rotkin and Suris, and the results comparing nanotubes and nanographene sheets.[71]

4.2.5 Summary

As we can see from the numerous studies outlined above, advances have been made in understanding the relative stability of sp^2- and sp^3-bonded particles at the nanoscale. These studies have clearly identified the two important size regimes, where (depending upon the phases under consideration) $sp^2 \rightarrow sp^3$ or $sp^3 \rightarrow sp^2$ phase transitions may be readily expected. In the case of larger particles, the crossover in stability between nanodiamond and nanographite may be expected at around 5–10 nm in diameter; and for smaller particles the crossover between nanodiamond and fullerenic particles may be expected at 1.5–2 nm.

Focusing upon these two important size regimes, some studies have also sought to elucidate the affects of temperature, pressure, and surface passivation (chemical environment) on the predictions, but there is still much work to be done.

4.3 Morphologies

In addition to the analytical theories that have been used to investigate the stability of nanodiamond, a number of research groups have simulated these transitions, using quantum mechanical methods. Computational studies of the type reviewed in the following sections have proven to be invaluable in clarifying the structural properties that affect nanocarbon stability, and specifically the role in morphology and surface structure.

4.3.1 Morphology of Nanodiamond Particles

In 1998 Winter and Ree[50] used the AMl and PM3 parameterizations of the semi-empirical modified neglect of diatomic overlap (MNDO) method to optimize the geometry of diamond clusters. The results of the optimizations showed varying degree of structural distortion in the model C_{10}, C_{35}, C_{84}, C_{165}, and C_{286} octahedral nanodiamonds. For example, in the small particles the surface atoms of the relaxed diamond clusters altered the positions so as to reduce the number of dangling bonds and causing an elongation of the bonds connecting the surface and core (interior)

atoms. The optimized geometry of the C_{84} nanodiamond exhibited a separation of the 74 surface atoms from the 10 core atoms, with the separation distance increasing to more than 3 Å. This is a consequence of the flattening of the surface corrugation in order to form π-bonds from the dangling orbitals. A similar result was observed in the optimized C_{165} nanodiamond, with the outer 130 atoms separating from the inner 35 atom core.[50]

The exfoliation of the diamond (111) surface was explicitly examined by Kuznetsov et al.[72] The authors used a two-layer cluster model to represent the (111) and (110) surfaces, and carried out calculations using the MNDO method, within RHF theory (including only the valence electrons). The study began with an estimation of the interlayer binding energy for the pairs of (111) and (110) planes, found to be 2.83 eV and 3.93 eV, respectively. This was followed by an examination of the effect of surface relaxation on the interlayer binding energy, by applying a geometry optimization to the upper (111) and (110) surface of each cluster, both of which resulted in surface flattening.[72] The graphitization energies for the (111) and (110) surfaces were also calculated to be 0.003 and 0.24 eV/surface atom (respectively), clearly demonstrating that graphitization of a (111) surface is preferred over that of a (110) surface. The positive graphitization energies were attributable to the small size of the clusters.[72]

The authors proposed that the graphitization mechanism involves the mutual interaction of the exfoliated graphitic sheets and the dehydrogenated diamond surface below, and that the difference between interlayer binding energy along the (111) and (110) directions arises due to different "packing" of the interlayer bonds in the volume between the parallel planes. It was suggested that surface graphitization is initiated by a significant thermal displacement of a single carbon atom at temperatures close to the Debye temperature, and the surface delamination of the (111) surface to form curved graphitic sheets proceeds by a "zipper"-like migration mechanism. A mechanism for the self-assembling formation of a mosaic surface structure on larger (micron size and up) diamond particles was also presented, where the initial diamond surface "blisters" under tensile stress, forming fullerenic "bubbles" that appear as a partial fullerene-like cage structure that is anchored to the remaining stable diamond surfaces around its edges.[72]

To further investigate the importance of surface structure on the nanomorphology of diamond nanoparticles and the relationship between stability and shape, Barnard et al.[56,67,73,74] undertook a broad *ab initio* study of nanodiamond structures of octahedral, cuboctahedral, and cubic morphologies, up to approximately 2 nm in diameter. The calculations

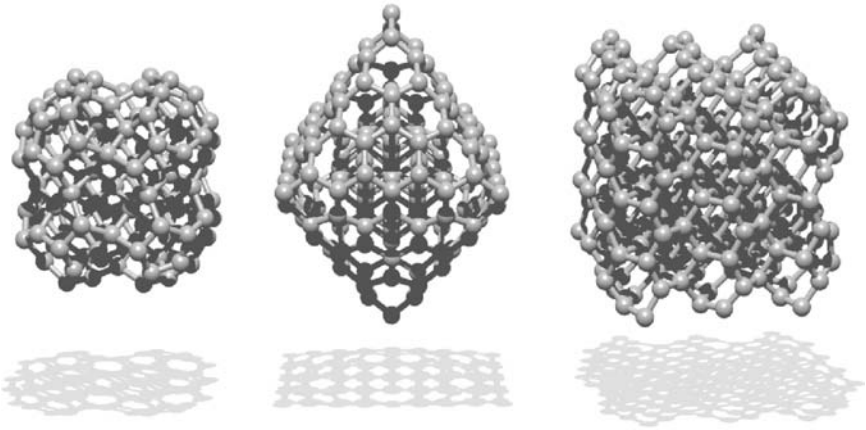

Figure 4.8 The relaxed, dehydrogenated C_{142} (cuboctahedral) and C_{165} (octahedral) bucky-diamonds, and the C_{259} (cubic) nanodiamond of Barnard et al.,[67] left to right. (Courtesy of S. P. Russo (2005).)

were performed with VASP,[75] using DFT within the generalized gradient approximation (GGA) and the exchange-correlation functional of Perdew and Wang (PW91)[76] and ultrasoft, gradient-corrected, Vanderbilt-type pseudopotentials (US-PP).[77] Examples of these structures are shown in Fig. 4.8.

Three cubic nanodiamonds were included in the study (the C_{28}, C_{54}, and C_{259} structures), and in each case the initial step of the relaxation process involved the reconstruction of the (100) surfaces to the (2×1) structure. Upon relaxation the smallest cubic nanodiamond decayed to a tetrahedral amorphous structure, even though the most energetically favorable structure for a 28-atom carbon cluster is known to be the C_{28} fullerene. The two larger cubic nanodiamonds were found to be stable, with surface reconstructions and relaxations comparable to bulk diamond (although a slight "shearing" of the lattice was, however, observed in the case of the C_{54} nanocrystal).[74]

Three octahedral nanodiamonds were also investigated (the C_{35}, C_{84}, and C_{165} structures). In agreement with the previous results of Winter and Ree,[50] the C_{35} crystal adopted of a more rounded appearance, but retained the diamond structure even though the bond lengths altered significantly. The C_{84} octahedral nanodiamond exhibited the 74 surface atoms separating from the 10-atom inner core, forming an octahedral OLC structure, with a shell–core separation distance of ~2.25 Å (smaller than that observed by Winter and Ree).[50] Similarly, the relaxation of the octahedral carbon nanocrystal of the C_{165} atom showed the same transformation in which the 130 surface atoms separate from the 35-atom core cluster,

also forming an octahedral bucky-diamond (with a shell–core distance of ~2.25 Å).[67]

Finally, three structures were considered with cuboctahedral morphology. The smallest cuboctahedral nanodiamond considered, the C_{29} structure, was found to transform into the $C@C_{28}$ endo-fullerene upon relaxation. The larger cuboctahedron with 142 atoms also exhibited a structural transition. In this case, the (100) surfaces reconstructed to the (2×1) structure, followed by the formation of the curved fullerenic "cages" on the (111) surfaces. This reconstruction/delamination was less pronounced in the C_{323} cuboctahedron, where only the central region of the (111) surface and the edges at the intersection of the (111) facets formed fullerenic cages.[67]

Therefore, the *ab initio* relaxations performed by Barnard et al.[56,67] determined that although there is preferential exfoliation of the (111) surfaces over lower index surfaces on isolated clusters, in the absence of (111) surfaces nanodiamond structures may be stable. These findings were supported by a semi-quantitative study of the hybridization of the bonds C—C within the clusters.[73] The technique uses fractional values of the electron charge density in regions localized at the center of bonds in the structure, to provide an easy way of visualizing sp^2 surface bonds in isolation from sp^3 content, thereby highlighting chemical differences between the core and surface of their relaxed nanodiamond structures. The computational details and a complete examination of this visualization method are given in ref. [42].

Around the same time it was shown that similar surface delamination and changes in structure are also observed in relaxed spherical diamond nanoparticles. Raty et al.[78] presented *ab initio* calculations on the effect of quantum confinement and surface reconstructions in nanodiamond, performed with GGA and the time-dependent local density approximation (TDLDA) (using a pseudopotential, plane-wave approach) and semi-empirical tight binding. The GGA calculations were performed for the <1.4 nm cluster sizes, and the tight-binding calculations for the 2–3 nm cluster sizes.[78]

Beginning with (ideal) bulk-diamond terminated spherical particles, the spontaneous low-temperature reconstruction dehydrogenated clusters of 1.4, 2, and 3.0 nm clusters resulted in graphitization of the first atomic layer of the (111) facets. The smaller clusters (studied with GGA) exhibited surface delamination, followed by the formation of five-membered rings linking the delaminated graphene fragments with the remaining core atoms, producing a curved surface the same as the "cages" of Barnard et al.[56,67,73] and the "bubbles" of Kuznetsov et al.[72]. The TB simulations performed on the larger 2 and 3 nm clusters (705 and 2425 atoms,

respectively) also produced the same surface reconstructions. The barrier between the ideal (bulk-diamond) surface structure and the reconstructed surface on a diamond nanocrystal was found to be size dependent (increasing as the size of the nanoparticle is increased). In the larger nanoclusters the barrier was of the order of several tens of electronvolts.[78]

The term bucky-diamonds was proposed by Raty et al.[78] to describe the carbon nanoparticles with a diamond core (of a few nanometers) and a partial or complete fullerenic outer shell observed in this study and the previous work of the other researchers outlined above. Such core–shell structures are distinct from the more OLC-like clusters obtained by Fugaciu et al.[79] in their study of the thermal stability of spherical diamond nanoparticles. They performed molecular dynamics calculations based on density functional tight-binding (DFTB). The simulations were carried out at temperatures in the range of 1400 K to 2800 K, which is comparable to experimental conditions such as laser evaporation. In addition, irradiation effects were taken into account by the random introduction of additional stochastic external momenta. Using this procedure the structural evolution of 50 diamond nanoparticles, ranging from 64 to 275 atoms, was analyzed.[79]

The authors reported[79] that the nanodiamond particles of approximately 1.1 nm size (~120 atoms) underwent fragmentation and formed fullerenic cages, but the nanodiamond particles >1.2 nm (~150 atoms or more) transformed to form two-shell OLC structures. The diamond particles consisting of 159 atoms were shown to transform spontaneously, without simulated irradiation, within a total simulation time of about 10 ps, while the diamond particles with >191 required the applied radiation (or extended simulation times) in order to completely transform. The number of atoms per shell and the structure of the shells fluctuated (with the bond length distribution within individual shells ranging between 1.38 and 1.50 Å), and in some cases the concentric shells were found to be connected by cross-links (atoms belonging to the inner and outer shells connected by sp^3 bonds) with a bond lengths of ~1.54 ± 0.6 Å.[79]

This work[79] was later repeated by Lee et al.[80] who also examined the heat-induced transformation of spherical nanodiamond particles into elongated fullerenes using tight-binding molecular dynamics, as shown in Fig. 4.9. Using the 275-atom spherical cluster examined previously by other authors,[79,78] they confirmed the delamination of the {111} surfaces at low temperature and the transformation of the cluster into a fullerenic structure (with cross-linked atoms between the outer shell and the inner core) at a temperature of 2500 K.[80] Upon cooling (2500 to 2000 K) the cluster was found to completely transform to an elongated, tube-like fullerene via three mechanisms. These include a "flow-out" mechanism

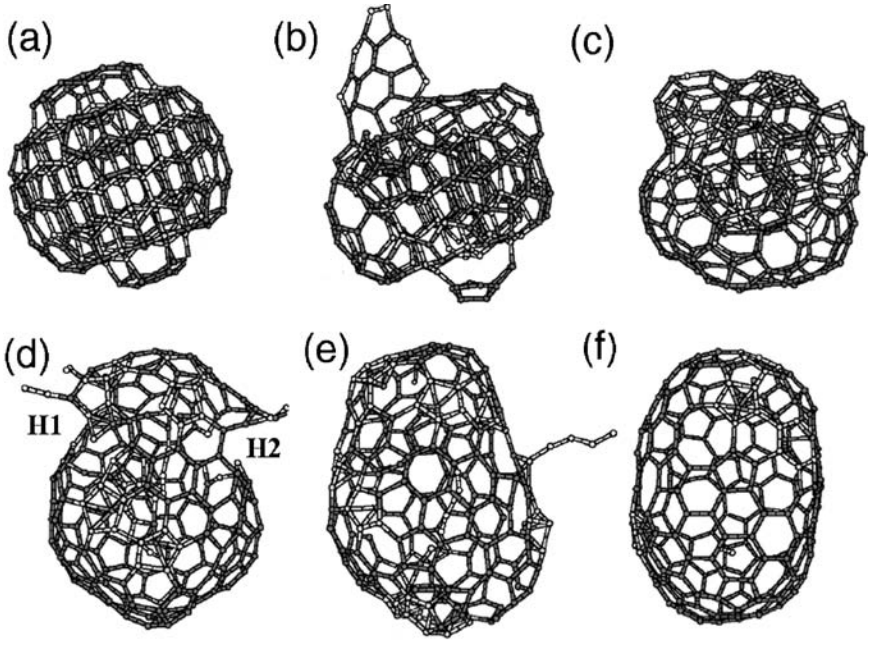

Figure 4.9 Atomic processes of structural transformation of nanodiamond to tube-shaped fullerene by successive annealing. (a) 0 K (at time $t = 0$ ps), (b) ~2500 K ($t = 3$ ps), (c) ~2500 K ($t = 19$ ps), (d) ~2100 K ($t = 35$ ps), (e) ~1900 K ($t = 50$ ps), and (f) ~20 K ($t = 120$ ps). Simulated annealing with temperatures up to 3000 K were performed during the process (e) to (f). Note that two holes H1 and H2 are created in (d). (Reproduced with permission from G.-D. Lee, C. Z. Wang, J. Yu, E. Yoon, and K. M. Ho, *Phys. Rev. Lett.*, 91, 265701 (2003). © American Physical Society 2003.)

where inner atoms exit the core region via holes and defects in the outer shell, a "direct absorption" mechanism where atoms within the shell are adsorbed into the shell structure, and a "push-out" mechanism where inner atoms replace the surface atoms that are pushed into the vacuum.[80]

Another approach to the crystalline stability of dehydrogenated nanodiamonds is to examine the stability and the coalescence of the cores, rather than the instability of the surfaces. As part of a study on the graphitization of diamond surfaces and the diamond/graphite interface using DFTB, Jungnickel et al.[81] examined the equilibrium structure of a sp^3-bonded icosahedral structure of 300 atoms. The structure was found to be stable in a conjugate gradient relaxation, and although the energy was 0.30 eV/atom higher than a C_{300} two-shell carbon onion, the cluster could

not be induced to form the corresponding (lower energy) OLC, even at temperatures of 1200–2700 K.[81]

In a later attempt to model the sp^2 to sp^3 nanocarbon phase transition, Astala et al.[82] reported results that used the DFTB method to model the collision-induced nucleation and growth of nanodiamond inside the same 300 atom OLC structure. The release of atoms due to "knock-on" displacements in outer shells and their transport to the core were simulated by a sequence of random atom additions with zero initial velocities. The evolution of the structures was found to be dependent upon the number of interstitial atoms during the ad hoc injection process. The inner C_{60} fullerene was seeded with a C_{10} cluster, and the irradiation was simulated via the random introduction of varying numbers of additional interstitial carbon atoms. The growing structure was re-relaxed after each addition. These results were then compared with sets of complementary results which use different sampling regimes.[82]

After each simulation, the sets were analyzed and the bonding geometries of the central cores of selected final relaxed systems were compared. The combined results indicated that a critical size for spherical atomic arrangements exists, below which sp^2 structures dominate, and above which sp^3 atoms bond into a diamond-like structure. The confinement by multi-layer carbon fullerenes was suggested to lower this limit and to reduce the capabilities of sp^3-bonded atoms to relax to a graphitic phase. The authors also described the transformation as the percolation of initially dispersed sp^3-bonded regions fusing after a certain threshold, to form one sp^3 core cluster.[82]

It is therefore logical to assume that if confinement by multi-layer carbon fullerenes is responsible for inhibiting relaxation of sp^3-bonded atoms into a graphitic phase, this mechanism may contribute to the stability of diamond-like cores at the center of the bucky-diamond structures.

The mechanism for the stabilization of bucky-diamond surfaces, however, appears to be appropriate passivation. As part of their 1998 study, Winter and Ree[50] also undertook semi-empirical optimization of the geometry of diamond clusters after capping the dangling bonds with hydrogen, using AMl and PM3. In all cases, the surface instability observed following the relaxation of the dehydrogenated clusters was eliminated, and the diamond structure preserved throughout. The optimized (relaxed) diamond clusters capped with hydrogen atoms gave sp^3 C—C bond lengths very close to the experimental value of 1.54 Å.

Similar results were also obtained by Barnard et al.[73,83] using DFT GGA (as described above). By comparing the carbon framework of the relaxed dehydrogenated and hydrogenated versions of the same nanodia-

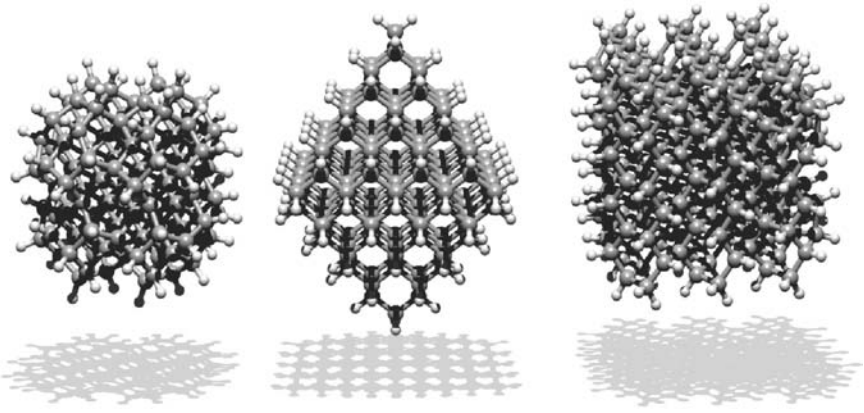

Figure 4.10 The relaxed, hydrogenated $C_{142}H_{80}$ (cuboctahedral), $C_{165}H_{100}$ (octahedral), and the $C_{259}H_{140}$ (cubic) nanodiamonds of Barnard et al.,[83] left to right. (Courtesy of S. P. Russo (2005).)

monds they confirmed that not only was the transformation to bucky-diamond eliminated, but also nanodiamonds were characterized by more bulk-diamond-like properties, such as cohesive energy[83] and surface structure[74]. Examples of these structures are shown in Fig. 4.10.

The retention of the sp^3 bonding was confirmed via calculation of Wannier functions, which are local bond-centered functions (rather than atom-centered ones). The Wannier function calculations confirm that while the dehydrogenated structures contain distorted σ- and π-bonds, the hydrogenated counterparts were found to be entirely σ-bonded.[83,84]

4.3.2 Morphology of Diamond Nanorods and Nanowires

The logical next step in the study of nanocarbon is the investigation of quasi-one-dimensional diamond nanostructures, such as diamond nanorods and nanowires.[85] There have been far fewer studies regarding the stability of these types of materials than there have been regarding quasi-zero-dimensional nanodiamond,[84] leaving many important questions largely unresolved.

The stability of dehydrogenated (111) surfaces on diamond nanowires has been considered by Barnard et al.[86] using two dehydrogenated nanowire morphologies with octahedral and cuboctahedral lateral forms. The computational technique used in this study is the same outlined above

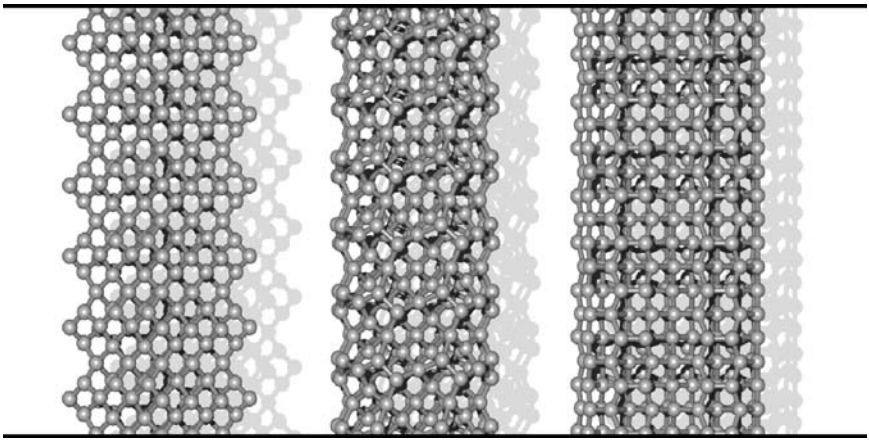

Figure 4.11 Stable dehydrogenated diamond nanowires of Barnard et al.[68] with (left) dodecahedral, (center) "cylindrical", and (right) "cubic" morphology. These structures are 0.72, 0.84, and 0.81 nm in diameter (respectively), with the (periodic) principal axes aligned top to bottom. (Courtesy of I. K. Snook (2005).

in the complementary study of diamond nanocrystals. Three octahedral nanowire structures were examined, bounded by {111} surfaces in all lateral directions (with a rhombohedral cross-section) and principal axis in the [110] direction. A very unusual relaxation was observed in these structures, involving the formation of three-membered rings at the acute edges. This was attributed to the formation of dimers in the [100] direction (denoted as "[100]-dimers") just below the acute nanowire edges, even in the absence of a (100) surface facet.[86]

The larger of the structures, measuring 0.69 nm and 0.90 nm in diameter, exhibited exfoliation of the (111) surfaces to form nanotubular cages in addition to the formation of the unusual three-membered rings and [100]-dimers. The nanotubular cages were oriented parallel to the nanowire principle axis, with chiral structure identical to that of an armchair carbon nanotube. They remained attached to the inner diamond-structured core of the nanowire at the [100]-dimers and at the opposing corner. The inner diamond core also contracted, giving cage–core separation distances of ~2.57 and 2.52 Å, respectively.[86]

Three cuboctahedral diamond nanowires were also examined, bounded by two (100) surfaces and two (111) surfaces in the lateral directions (with an almost circular cross-section), and a principal axis in the [110] direction. In each case the first step of the relaxation involved reconstruction of the (100) surfaces to the (2×1) structure, followed by the exfoliation of the (111) surfaces. In the case of the smallest 0.42 nm cuboctahedral

nanowire, this resulted in the entire nanowire transforming into a "non-classical" nanotube, with the core atoms forming a sp-bonded linear chain along the axis. The authors denoted the final 0.42 nm cuboctahedral structure as a non-classical nanotube, as the armchair structured sections (formed by the exfoliation of the (111) surface) are separated by rows of eight-membered and five-membered rings, which are not present in classical nanotubes.[86]

Similarly the (111) surfaces of the larger 0.63 nm and 0.83 nm cuboctahedral nanowires were found to exfoliate following the (100) reconstruction, forming nanotubular cages running the length of the nanowires (parallel to the principal axis). In these cases, however, the nanotubular cages remained bound to the inner core atoms at the (100) (2 × 1) surfaces. Like the octahedral structures described above, the inner core of the cuboctahedral nanowires was found to contract, resulting in a cage–core separation distance of ~2.42–2.54 Å.[86]

The structures resulting from this study, characterized by (armchair) nanotubular cages along the surface, and diamond-like cores, were denoted as "bucky-wires" (as they represented the 1-D analogue of the bucky-diamonds).[86] The authors did point out, however, that surface hydrogenation has a similar stabilizing effect on bucky-wires, eliminating the nanotubular cages.[86]

One-dimensional carbon nanostructures with a stable sp^3-bonded core were first suggested by Menon et al.[87] who used a generalized tight-binding molecular dynamics scheme (GTBMD) to study quasi-one-dimensional (QOD) carbon nanorods. The structures proposed in this study consisted of four-fold coordinated atoms along the core, and three-fold coordinated atoms at the surface. The authors concluded that the four-fold coordinated (sp^3) atoms at the core were necessary to ensure structural stability following relaxation.[87]

However, it has been found that (like diamond nanocrystals) clean surfaces on diamond nanowires or nanorods may be stable, given the appropriate orientation. In addition to the octahedral and cuboctahedral nanowires, Barnard et al.[68,88] also examined dehydrogenated nanowire morphologies characterized by dodecahedral and cubo-dodecahedral forms. The dodecahedral nanowires were bounded by (110) surfaces in all lateral directions, with a square cross-section and [100] principal axis. One cubo-dodecahedral group (termed "cubic") was bounded by two (100) surfaces and two (110) surfaces, with a square/rectangular cross-section and a [110] principal axis. The other cubo-dodecahedral group (termed "cylindrical") was bounded by four (100) surfaces and four (110) surfaces, with an approximately circular cross-section and a [100] principal axis.

In the case of the dodecahedral nanowires, a mild contraction of the outermost atomic layer was reported, causing the {110} surfaces of the nanowires to become slightly convex in shape.[68] In the case of the cubic nanowires, each structure underwent a two-stage relaxation involving the reconstruction of the (100) surfaces to form the (2×1) surface structure, followed by further relaxation of the entire nanowire. Although the relaxation of the smallest cubic diamond nanowire (with a diameter of <0.5 nm) resulted in a non-classical single-walled nanotube (a transition which involved the dissociation of dicarbon molecules from the surface), the tetrahedral sp^3 structure was preserved throughout the larger 0.60 and 0.81 nm cubic nanowires, with (2×1) surface dimers comparable to bulk-diamond surfaces.[69] Finally, the relaxation of the three cylindrical nanowires also involved the reconstruction of the (100) surfaces to form the (2×1) surface structure, followed by further relaxation of the entire nanowire. In this case, the authors described the final relaxed cylindrical nanowires as twisted rope-like structures, resulting from the (2×1) surface reconstruction and significant contraction of the outermost atomic layer.[68]

Hence (with the exception of the smallest cubic nanowire), the diamond structure was preserved in all of the dodecahedral and cubo-dodecahedral nanowires upon relaxation. None of the surfaces exfoliated as observed in the octahedral and cuboctahedral diamond nanowires. Overall, the relative stability was found to be dependent on both the surface morphology and the crystallographic direction of the principal axis, and dodecahedral nanowires (with [100] axes) were identified as the most structurally stable among all the nanowires considered.[85] Examples of these dehydrogenated and hydrogenated diamond nanowire structures are shown in Fig. 4.11 and 4.12, respectively.

It has also been shown by Shenderova et al.[89] that diamond nanowires with [100] principal axes show increased structural stability and enhanced mechanical properties. The mechanical properties of single-walled nanotubes (SWNTs) and multi-walled nanotubes (MWNTs) were compared to equivalent diamond nanowires with principal axes oriented in the [111], [110], or [100] directions. The study found that at small diameters, SWNTs are stronger than nanowires because of the superior strength of single bonds in graphene over those in diamond. However, as the diameter increases, the load-bearing area increases linearly for SWNTs and as the square of the diameter for nanowires, leading to a larger fracture force for diamond nanowires above a critical diameter of ~1–3 nm (depending on the direction of the axis).[89]

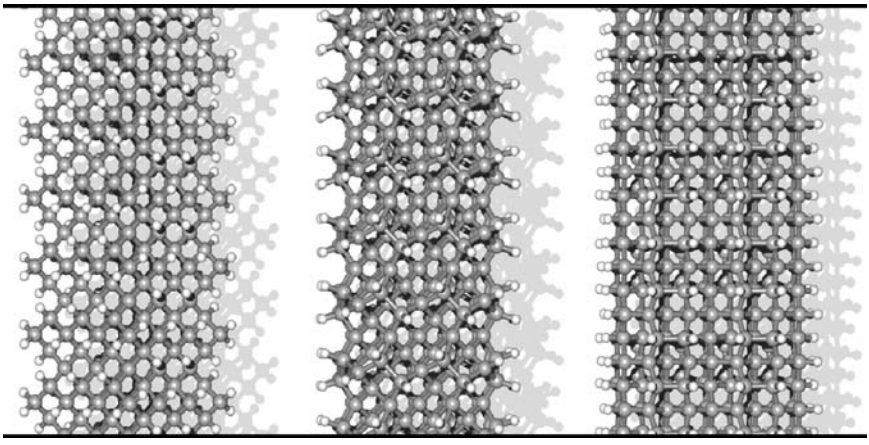

Figure 4.12 Stable hydrogenated diamond nanowires of Barnard et al.[68] with (left) dodecahedral, (center) "cylindrical", and (right) "cubic" morphology. These structures are 0.76, 0.87, and 0.82 nm in diameter (respectively), with the (periodic) principal axes aligned top to bottom. (Courtesy of I. K. Snook (2005).)

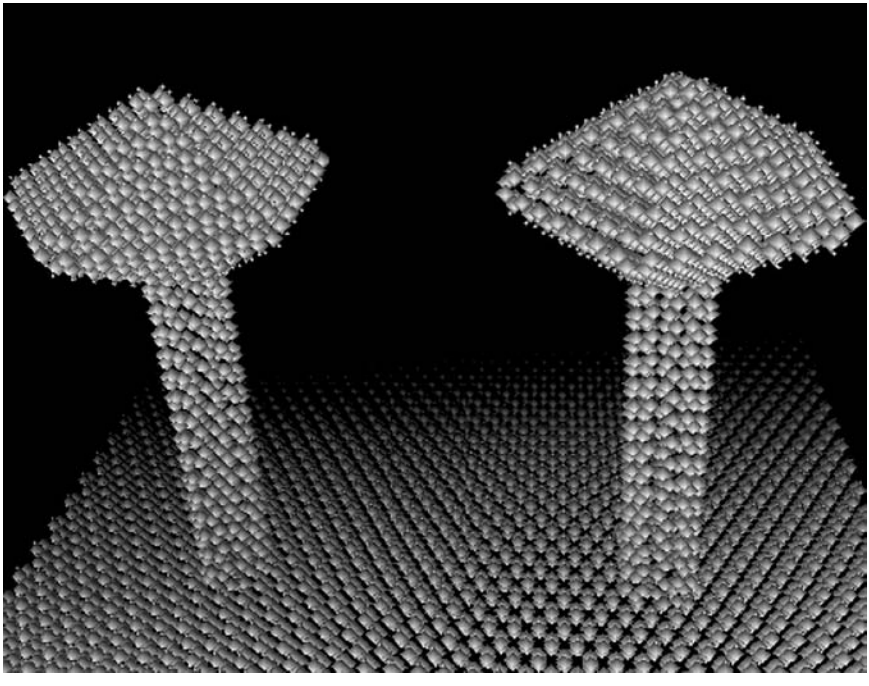

Figure 4.13 Schematic of two "mushroom" nanodiamond–nanotube hybrid structures, formed by attaching a pentagonal nanodiamond to the top of carbon nanotubes bound to a diamond surface. (Courtesy of O. A. Shenderova (2005).)

It was also found that with equal fracture force the weight ratio nanowire/SWNT was a constant 1.47. However, with the requirement of equal weight, the ratio of related fracture forces of nanowire/SWNT was found to be 0.68, indicating that at larger diameters, nanowires are stronger but at the cost of a lower strength-to-weight ratio. The stiffness of diamond nanowires and SWNTs was also compared, using a relation for total force–strain. A "nanostructure stiffness constant" was introduced as a coefficient of proportionality between the applied force and elongation, which was dependent on the diameter of the nanorod (or nanotube). By comparing this stiffness constant as a function of diameter, diamond nanowires were found to be stiffer than SWNTs at diameters exceeding ~1 nm. The study therefore concluded that diamond nanowires are mechanically viable nanostructures.[89]

4.3.3 Hybrid Nanocarbon Materials

To meet the demands of nanotechnologists, the next generation of nanomaterials will need to be robust, complicated architectures such as hybrid nanostructures with controllable structural, electronic, and chemical properties. The well-documented differences in the thermal, mechanical, and electronic properties of the various allotropes of carbon, along with their chemical compatibility, make hybrid nanomaterials that couple nanodiamond and sp^2-bonded nanocarbon an attractive prospect. Currently there are two main synthesis routes in this direction, either the consecutive growth or fabrication of respective phases to form one nanostructure, or the controlled, partial transformation of one phase of nanocarbon into another. Although bucky-diamonds (described above) may be thought of as hybrid carbon nanoparticles (with a core–shell structure), they are not traditionally considered in this way and so far little advantage has been taken of the dual-phase nature of these nanomaterials.

Alternatively, hybrid nanocarbon materials may be either the growth of carbon nanotubes onto nanodiamond or nanodiamond thin films, or the growth of nanodiamond onto carbon nanotubes. Although such materials are now being grown, the formation mechanisms are still largely unknown. So far, there have been formed by far fewer theoretical or computational studies regarding such hybrid nanocarbons than for phase pure carbon nanomaterials (and bucky-diamonds). Two particular studies will be included as examples here.

The first is the study undertaken by Shenderova et al.[90,91] who used many-body classic potential and environment-dependent self-consistent

tight-binding approaches to examine the feasibility of designing composite architectures of nanodiamond and carbon nanotubes. Geometric considerations combined with detailed atomistic simulations were used to investigate bonding and stability of general classes of diamond/carbon nanotube interface structures with low residual stresses and no unsatisfied bonding.[90,91]

The hybrid nanocarbon structures under consideration were formed by bonding carbon nanotubes onto diamond substrates, bonding nanodiamond clusters onto the ends of nanotubes, or both (as shown in Fig. 4.13). It was shown that, depending on nanotube size and morphology, certain chiralities of open nanotubes may be bonded with different facets of diamond clusters or different orientations of diamond surfaces. Particular combinations of nanotubes and diamond surfaces were shown to form chemically and mechanically stable interfaces, since the significant lattice mismatches between a diamond surface and a nanotube may be accommodated due to the high radial flexibility of carbon nanotubes. Possible applications of these systems include use as arrays of field emitters and as nanoscale diodes.[90]

The second is the study undertaken by Barnard et al.[92] who used DFT GGA to investigate the role of atomic hydrogen in creating localized sp^3 hybridized defects on the outer wall of carbon nanotubes. The aim of the study was to elucidate the initial stages of nucleation in the formation of hybrid materials comprising SWNTs coated with faceted diamond nanocrystals all over the outer walls. The results illustrate that certain absorption configurations of hydrogen may produce H-induced defects containing dangling carbon bonds. Such sites were then shown to be favorable adsorption sites for carbon adsorbates (lower in energy than for pristine sites away from the H-induced defect).[92]

Although a number of important problems remain to be addressed to fully understand the formation and growth of hybrid carbon nanomaterials (such as the kinetic processes at the surface and the structure at the nanotube–nanodiamond interface), these studies do address some aspects that are critical to understanding the formation of more complicated carbon nanostructures.

4.4 Conclusions

In summary, the theoretical and computational studies outlined above have focused on the phase transitions between nanodiamond and graphitic and fullerenic forms of nanocarbon. Computationally, these transitions are

well represented by quantum mechanical methods, and the transformations have been modeled using a variety of cluster geometries and sizes.

The numerous analytical theories (the majority of which use thermodynamic arguments) appear to agree as to the upper limit of nanodiamond phase stability. These theories predict nanodiamond to be the stable phase of carbon in the range less than about 5–6 nm. The lower limit of nanodiamond stability has also been estimated to be ~1.4–2.2 nm (again using a thermodynamic approach), along with the phase coexistence of nanodiamond and fullerenic carbon at this lower limit, via the formation of bucky-diamonds.

It is important to note that this range for nanodiamond stability does not by any means represent the only size regime in which nanocrystalline diamond may be formed; it simply indicates that outside of this range the nanodiamonds will be metastable with respect to a transformation to graphitic or fullerenic phases. Further, the identification of a coexistence region indicates that the phase transitions are not entirely thermodynamically driven, and that other factors such as surface energies, surface stress and charge, as well as kinetic considerations, may be instrumental in inducing a change of phase. Therefore a complete examination of nanocarbon phase stability should include not only the use of a sophisticated computational method and large cluster sizes, but also theoretical terms to describe dependencies on a variety of experimentally relevant cluster properties.

One such property, fundamental to the stability of nanodiamond, is the degree of surface hydrogenation. The question of whether (experimentally) particulate nanodiamond can be expected to have hydrogenated (sp^3-bonded) surfaces, or sp^2-bonded "bucky" surfaces under ambient conditions, is currently unresolved. From the review of theoretical and computational studies outlined here it is possible to begin a discussion of this very important question.

Theoretically it was shown by Raty and Galli[65] that a small bucky-diamond may be lower in energy than a hydrogenated nanodiamond, since the sp^2 fullerenic shell is lower in energy than a hydrogenated diamond surface. Unfortunately this study did not adequately account for the difference in chemical potential between "core" atoms and the reconstructed "bucky" surface atoms, and (according to the authors) is applicable to CVD synthesis conditions (far from equilibrium).[65]

However, working on the assumption that bucky-diamonds are energetically preferred, we are confronted with the computational studies that clearly show that hydrogenated nanodiamond surface are stable under ambient conditions. Further, we find experimentally examples of very

small sp^3-bonded hydrogen-terminated carbon particles, such as hydrocarbon molecules and the polymantanes (including the higher diamondoids).[41] A logical explanation is that although H-terminated nanodiamonds may be slightly higher in energy than their dehydrogenated counterparts, they are metastable below the hydrogen desorption temperature, and there will be no spontaneous (size-dependent) hydrogen desorption and recombination without a suitable driving force.

Therefore, until a more rigorous study can be undertaken we must proceed with the assumptions that (experimentally) most small nanodiamonds are in fact bucky-diamonds, but if purified properly (with the shell of a bucky-diamond completely removed) and the clean diamond surfaces are then H-terminated, they should remain that way until suitably perturbed.

Acknowledgments

This work was supported in part by the US Department of Energy, Office of Basic Energy Sciences, under contract no. W-31-109-ENG-38. I would like to greatly acknowledge Salvy Russo and Ian Snook from RMIT University (Australia), O. A. Shenderova from the International Technology Center (USA), A. L. Verechshagin from Byisk Technological Institute (Russia), Q. Jiang from Jinlin University (China), K. M. Ho from Iowa State University (USA), and V. L. Kuznetsov from Boreskov Institute of Catalysis (Russia).

References

1. D. A. Young, *Phase Diagrams of the Elements*, University of California Press, Berkeley (1991).
2. R. C. De Vries, "Synthesis of diamond under metastable conditions", *Annu. Rev. Mater. Sci.*, 17, 161 (1987).
3. S. Prawer, D. N. Jamieson, and R. Kalish, "Investigation of carbon near the graphite-diamond-liquid triple point", *Phys. Rev. Lett.*, 69, 2991 (1992).
4. J. B. Wang and G. W. Yang, "Phase transformation between diamond and graphite in preparation of diamonds by pulsed-laser induced liquid-solid interface reaction", *J. Phys.: Condens. Matter.*, 11, 7089 (1999).
5. R. Berman and F. E. Simon, "The graphite diamond equilibrium", *Z. Elektrochem.*, 55, 333 (1955).
6. M. van Thiel and F. H. Ree, "High-pressure liquid-liquid phase change in carbon", *Phys. Rev. B*, 48, 3591 (1993).

7. L. E. Fried and W. M. Howard, "Explicit Gibbs free energy equation of state applied to the carbon phase diagram", *Phys. Rev. B*, 61, 8734 (2000).
8. W. J. Nellis, A. C. Mitchell, and A. K. McMahan, "Carbon at pressures in the range 0.1–1 TPa (10 Mbar)", *J. Appl. Phys.*, 90, 696 (2001).
9. R. Grover, "Does diamond melt?", *J. Chem. Phys.*, 71, 3824 (1979).
10. T. Sekine, "Six-fold coordinated carbon as a postdiamond phase", *Appl. Phys. Lett.*, 74, 350 (1999).
11. S. Scandolo, G. L. Chiarotti, and E. Tosatti, "SC4: A metallic phase of carbon at terapascal pressures", *Phys. Rev. B*, 53, 5051 (1996).
12. J. V. Badding and T. J. Scheidemantel, "FLAPW investigation of the stability and equation of state of rectangulated carbon", *Solid State Commun.*, 122, 473 (2002).
13. M. T. Yin. "Si-III (BC-8) crystal phase of Si and C: Structural properties, phase stabilities, and phase transitions", *Phys. Rev. B*, 30, 1773 (1984).
14. R. Biswas, R. M. Martin, R. J. Needs, and O. H. Nielsen, "Complex tetrahedral structures of silicon and carbon under pressure", *Phys. Rev. B*, 30, 3210 (1984).
15. G. Galli, R. M. Martin, R. Carr, and M. Parrinello, "Structural and electronic properties of amorphous carbon", *Phys. Rev. Lett.*, 62, 555 (1989).
16. M. P. Grumback and R. M. Martin, "Phase diagram of carbon at high pressure: Analogy to silicon", *Solid State Commun.*, 100, 61 (1996).
17. W. H. Gust, "Phase transitions and shock-compression parameters to 120 GPa for three types of graphite and for amorphous carbon", *Phys. Rev. B*, 22, 4744 (1980).
18. F. P. Bundy, W. A. Bassett, M. S, Weathers, R. J. Hemley, H. K. Mao, and A. F. Groncharov, "The pressure-temperature phase and transformation diagram for carbon; updated through 1994", *Carbon*, 34, 141 (1996).
19. E. G. Rakov, "Calculation of diamond chemical vapor deposition region in C—H—O phase diagram", *Appl. Phys. Lett.*, 69, 2370 (1996).
20. J.-T. Wang, Y.-Z. Wang, Z.-J. Liu, H. Wang, D. W. Zhang, and Z.-Q. Huang, "Phase diagrams for activated CVD diamond growth", *Mater. Lett.*, 33, 311 (1998).
21. Y.-Z. Wan, H.-S. Shen, Z.-M. Zhang, and X.-C. He, "Ternary C—H–halogen phase diagram for CVD diamond", *Mater. Chem. Phys.*, 63, 88 (2000).
22. Z.-J. Liu, D. W. Zhang, P.-F. Wang, S.-J. Ding, J.-Y. Zhang, J.-T. Wang, and K. Kohse-Hoinghaus, "Projective phase diagrams for CVD diamond growth from C—H and C—H—O systems", *Thin Solid Films*, 368, 253 (2000).
23. F. H. Ree, "Systematics of high-pressure and high-temperature behavior of hydrocarbons", *J. Chem. Phys.*, 70, 974 (1979).
24. M. Zaiser, Y. Lyutovich, and F. Banhart, "Irradiation-induced transformation of graphite to diamond: A quantitative study", *Phys. Rev. B*, 62, 3058 (2000).
25. F. Banhart, "Structural transformations in carbon nanoparticles induced by electron irradiation", *Phys. Solid State*, 44, 399 (2002).
26. A. Potemkin and V. Poliakov, "The effect of metal-solvent properties on the alteration of specific zones on a carbon phase diagram", *Diamond Relat. Mater.*, 10, 1597 (2001).
27. F. Charlet, M.-L. Turkel, J.-F. Danel, and L. Kazandjian, "Evaluation of various theoretical equations of state used in calculation of detonation properties", *J. Appl. Phys.*, 84, 4227 (1998).

28. F. H. Ree, N. W. Winter, J. N. Glosli, and J. A. Viecelli, "Kinetics and thermodynamic behavior of carbon clusters under high pressure and high temperature", *Physica B*, 265, 223 (1999).
29. J. A. Viecelli and F. H. Ree, "Carbon particle phase transformation kinetics in detonation waves", *J. Appl. Phys.*, 88, 683 (2000).
30. J. A. Viecelli, S. Bastea, J. N. Glosli, and F. H. Ree, "Phase transformations of nanometer size carbon particles in shocked hydrocarbons and explosives", *J. Chem. Phys.*, 115, 2730 (2001).
31. A. L. Verechshagin, "Phase diagram of ultrafine diamond", *Combust. Exp. Shock Waves*, 38, 358 (2002).
32. A. M. Staver, N. M. Gubareva, A. I. Lyamkin, and E. A. Petrov, Ultrafine diamond powders made by the use of explosion energy, *Fiz. Goreniya Vzriva*, 20, 440 (1984).
33. O. A. Shenderova, V. V. Zhirnov, and D. W. Brenner, "Carbon nanostructures", *Crit. Rev. Solid State Mater. Sci.*, 27, 227 (2002).
34. V. L. Kuznetsov, A. L. Chuvilin, Yu. V. Butenko, I Yu. Mal'kov, A. K. Gutakovskii, S. V. Stankus, and S. R. Khairulin, in *Science and Technology of Fullerene Materials*, edited by P. Bernuer et al. (MRS Proc. 359, Pittsburgh, PA), p. 105 (1995).
35. B. Sunqvist, "Buckyballs under pressure", *Phys. Status Solidi (b)*, 223, 469 (2001).
36. M. V. Korobov, V. M. Senyavin, A. G. Bogachev, E. B. Stukalin, V. A. Davydov, L. S. Kashevarova, A. V. Rakhmanina, V. Agafonov, and A. Szwarc, "Phase transformations in pressure polymerized C_{60}", *Chem. Phys. Lett.*, 381, 410 (2003).
37. E. Schöll-Paschinger and G. Kahl, "Accurate determination of the phase diagrams of model fullerenes", *Europhys. Lett.*, 63, 538 (2003).
38. M. H. F. Sluiter and Y. Kawazoe, "Phase diagram of single-wall carbon nanotube crystals under hydrostatic pressure", *Phys. Rev. B*, 69, 224111 (2004).
39. J. González and J. V. Alvarez, "Phase diagram of carbon nanotube ropes", *Phys. Rev. B*, 70, 045410 (2004).
40. J. Reiser, E. McGregor, J. Jones, R. Enick, and G. Holder, "Adamantane and diamantane: Phase diagrams, solubilities and rates of dissolution", *Fluid Phase Equilib.*, 117, 160 (1996).
41. J. E. Dahl, S. G. Liu, and R. M. K. Carlson. "Isolation and structure of higher diamondoid, nanometer-sized diamond molecules". *Science*, 299, 96 (2003).
42. A. S. Barnard, S. Russo, and I. K. Snook, "Modeling of stability and phase transformations in 0 and 1 dimensional nanocarbon systems", in *Handbook of Theoretical and Computational Nanotechnology*, edited by M. Rieth and W. Schommers, American Scientific Publishers, Stevenson Ranch, CA (2005).
43. J. Almlöf and H. P. Lüthi, in *Supercomputer Research in Chemistry and Chemical Engineering* (ACS Symposium Series, Vol. 353), edited by Klavs F. Jensen and Donald G. Truhlar (1987) pp. 35–48.
44. M. S. Shaw and J. D. Johnson, "Carbon clustering in detonations", *J. Appl. Phys*, 62, 2080 (1987).
45. P. Badziag, W. S. Veowoerd, W. P. Ellis, and N. R. Greiner, "Nanometre-sized diamonds are more stable than graphite", *Nature*, 343, 244 (1990).

46. M. Y. Gamarnik, "Size-related stabilization of diamond nanoparticles", *Nanostruct. Mater.*, 7, 651 (1996); "Energetical preference of diamond nanoparticles", *Phys. Rev. B*, 54, 2150 (1996).
47. N. M. Hwang, J. H. Hahn, and D. Y. Yoon, "Chemical potential of carbon in the low pressure synthesis of diamond", *J. Cryst. Growth*, 160, 87 (1996).
48. N. M. Hwang, J. H. Hahn, and D. Y. Yoon, "Charged cluster model in the low pressure synthesis of diamond", *J. Cryst. Growth*, 162, 55 (1996).
49. H. N. Jang and N. M. Hwang, "Theory of the charged cluster formation in the low pressure synthesis of diamond: Part II. Free energy function and thermodynamic stability", *J. Mater. Res.*, 13, 3536 (1998).
50. N. W. Winter and F. H. Ree, "Carbon particle phase stability as a function of size", *J. Comput.-Aided Mater. Des.*, 5, 279 (1998).
51. Q. Jiang, J. C. Li, and G. Wilde, "The size dependence of the diamond-graphite transition", *J. Phys.: Condes. Matter*, 12, 5623 (2000).
52. D. Zhao, M. Zhao, and Q. Jiang, "Size and temperature dependence of nanodiamond–nanographite transition related with surface stress", *Diamond Relat. Mater.*, 11, 234 (2002).
53. M. Zaiser and F. Banhart, "Radiation-induced transformation of graphite to diamond", *Phys. Rev. Lett.*, 79, 3680 (1997).
54. Yu. V. Butenko, V. L. Kuznetsov, A. L. Chuvilin, V. N. Kolomiichuk, S. V. Stankus, R. A. Khairulin, and B. Segall, "The kinetics of the graphitization of dispersed diamonds at 'low' temperatures", *J. Appl. Phys.*, 88, 4380 (2000).
55. A. S. Barnard, S. P. Russo, and I. K. Snook, "Size dependent phase stability of carbon nanoparticles: Nanodiamond versus fullerenes", *J. Chem. Phys.*, 118, 5094 (2003).
56. A. S. Barnard, S. P. Russo, and I. K. Snook, "Ab initio modelling of stability of nanodiamond morphologies", *Philos. Mag. Lett.*, 83, 39 (2003).
57. P. Harris, *Carbon nanotubes and related structures*, Cambridge University Press, Cambridge (1999).
58. D. Tománek and M. A. Schluter, "Growth regimes of carbon clusters", *Phys. Rev. Lett.*, 67, 2331 (1991).
59. R. O. Jones, "Density functional study of carbon clusters C_{2n} ($2 \leq n \leq 16$). I. Structure and bonding in the neutral clusters", *J. Chem. Phys.*, 110, 5189 (1999).
60. J. L. Martins, F. A. Reuse, and S. N. Khanna, "Growth and formation of fullerene clusters", *J. Cluster Sci.*, 12, 513 (2001).
61. P. R. C. Kent, M. D. Towler, R. J. Needs, and G. Rajagopal, "Carbon clusters near the crossover to fullerene stability", *Phys. Rev. B*, 62, 15394 (2000).
62. N. Park, K. Lee, S. W. Han, J. J. Yu, and J. Ihm, "Energetics of large carbon clusters: Crossover from fullerenes to nanotubes", *Phys. Rev. B*, 65, 121405 (2002).
63. A. S. Barnard, S. P. Russo, and I. K. Snook, "Coexistence of bucky diamond with nanodiamond and fullerene carbon phases", *Phys. Rev. B*, 68, 73406 (2003).
64. Y. Guo, Ph.D. Thesis, California Institute of Technology (1992).
65. J.-Y. Raty and G. Galli, "Ultradispersity of diamond at the nanoscale", *Nature Mater.*, 2, 792 (2003).

66. A. S. Barnard and I. K. Snook, "Phase stability of nanocarbon in one-dimension: Nanotubes versus diamond nanowires", *J. Chem. Phys.*, 120, 3817 (2004).
67. A. S. Barnard, S. P. Russo, and I. K. Snook, "Structural relaxation and relative stability of nanodiamond morphologies", *Diamond Relat. Mater.*, 12, 1867 (2003).
68. A. S. Barnard, S. P. Russo, and I. K. Snook, "Ab initio modelling of diamond nanowire structures", *Nano Lett.*, 3, 1323 (2003).
69. A. S. Barnard, S. P. Russo, and I. K. Snook, "Surface structure of cubic diamond nanowires", *Surf. Sci.*, 538, 204 (2003).
70. S. B. Sinnott, R. Andrews, D. Qian, A. M. Rao, Z. Mao, E. C. Dickey, and F. Derbyshire, "Model of carbon nanotube growth through chemical vapor deposition", *Chem. Phys. Lett.*, 315, 25 (1999).
71. S. V. Rotkin, and R. A. Suris, "Bond passivation model: Diagram of carbon nanoparticle stability", *Phys. Lett. A*, 261, 98 (1999).
72. V. L. Kuznetsov, I. L. Zilberberg, Y. V. Butenko, A. L. Chuvilin, and B. Seagall, "Theoretical study of the formation of closed curved graphite-like structures during annealing of diamond surface", *J. Appl. Phys.*, 86, 863 (1999).
73. A. S. Barnard, S. P. Russo, and I. K. Snook, "First principles investigations of diamond ultrananocrystals", *Int. J. Mod. Phys. B*, 17, 3865 (2003).
74. S. P. Russo, A. S. Barnard, and I. K. Snook, "Hydrogenation of nanodiamond surfaces: Structure and effects on crystalline stability", *Surf. Rev. Lett.*, 10, 233 (2003).
75. G. Kresse and J. Hafner, "*Ab initio* molecular dynamics for open-shell transition metals", *Phys. Rev. B*, 47, R558 (1993).
76. J. Perdew and Y. Wang, "Accurate and simple analytic representation of the electron-gas correlation energy", *Phys. Rev. B*, 45, 13244 (1992).
77. D. Vanderbilt, "Soft self-consistent pseudopotentials in a generalized eigenvalue formalism", *Phys. Rev. B*, 41, 7892 (1990).
78. J. Y. Raty, G. Galli, C. Bostedt, T. W. van Buuren, and L. J. Terminello, "Quantum confinement and fullerene-like surface reconstructions in nanodiamonds", *Phys. Rev. Lett.*, 90, 37402 (2003).
79. F. Fugaciu, H. Hermann, and G. Seifert, "Concentric-shell fullerenes and diamond particles: A molecular-dynamics study", *Phys. Rev. B*, 60, 10711 (1999).
80. G.-D. Lee, C. Z. Wang, J. Yu, E. Yoon, and K. M. Ho, "Heat-induced transformation of nanodiamond into a tube-shaped fullerene: a molecular dynamics simulation", *Phys. Rev. Lett.*, 91, 265701 (2003).
81. G. Jungnickel, D. Porezag, Th. Frauenheim, M. I. Heggie, W. R. L. Lambrecht, B. Segall, and J. C. Angus, "Graphitization effects on diamond surfaces and the diamond/graphite interface", *Phys. Status Solidi (a)*, 154, 109 (1996).
82. R. Astala, M. Kaukonen, R. M. Nieminen, G. Jungnickel, and Th. Frauenheim, "Simulations of diamond nucleation in carbon fullerene cores ", *Phys. Rev. B*, 63, 81402 (2001).
83. A. S. Barnard, N. A. Marks, S. P. Russo, and I. K. Snook, "Hydrogen stabilization of {111} nanodiamond", *MRS Symp. Proc.*, 740, 69 (2003).

84. A. S. Barnard, S. P. Russo, and I. K. Snook, "Modeling of stability and phase transformations in quasi-zero dimensional nanocarbon systems", *J. Comput. Theor. Nanosci.*, 2, 180 (2005).
85. A. S. Barnard, "Structural properties of diamond nanowires: theoretical predications and experimental progress", *Rev. Adv. Mater. Sci.*, 6, 94 (2004).
86. A. S. Barnard, S. P. Russo, and I. K. Snook, "Bucky-wires and the instability of diamond (111) surfaces in one-dimension", *J. Nanosci. Nanotech.*, 4, 151 (2004).
87. M. Menon, E. Richter, P. Raghavan, and K. Teranishi, "Large-scale quantum mechanical simulations of carbon nanowires", *Superlattices Microstruct.*, 27, 577 (2000).
88. A. S. Barnard, S. P. Russo, and I. K. Snook, "From nanodiamond to diamond nanowires: Structural properties affected by dimension", *Philos. Mag.*, 84, 899 (2004).
89. O. A. Shenderova, D. W. Brenner, and R. S. Ruoff, "Would diamond nanorods be stronger than fullerene nanotubes?", *Nano Lett.*, 3, 805 (2003).
90. O. A. Shenderova, D. Areshkin, and D. W. Brenner, "Carbon based nanostructures: diamond clusters structured with nanotubes", *Mater. Res.*, 6, 11 (2002).
91. O. A. Shenderova, D. Areshkin, and D. W. Brenner, "Bonding and stability of hybrid diamond/nanotube structures", *Mol. Simulat.*, 29, 259 (2003).
92. A. S. Barnard, M. L. Terranova, and M. Rossi, "Density functional study of H-induced defects as nucleation sites in hybrid carbon nanomaterials", *Chem. Mater.*, 17, 527 (2005).

PART 3
UNCD FILMS AND RELATED MATERIALS

5 Electron Transport and the Potential of Ultrananocrystalline Diamond as a Thermoelectric Material

Dieter M. Gruen

Materials Science Division, Argonne National Laboratory, Argonne, IL, USA

Introduction

The discovery of ultrananocrystalline diamond (UNCD) films, the third member of the remarkable triad of nanostructured carbons which includes fullerenes and nanotubes, had its conceptual foundation in 1991 when a radically different gas phase chemistry compared to conventional diamond CVD was proposed.[1] In this new process, the carbon dimer molecule, C_2, generated for example in an argon microwave plasma by collisional fragmentation of C_{60} (buckyballs), functions as the growth species rather than the methyl radical which serves this function in the conventional process.[2,3] The fascinating properties of the resultant UNCD films are in part due to the fact that the very high heterogeneous renucleation rates inherent in the C_2 methodology of CVD synthesis produce a microstructure characterized by 3–5 nm randomly oriented crystallites bonded together by high-angle, high-energy twist grain boundaries which are two carbon atoms wide and minimize their free energies by rehybridization rather than by bond bending.[4] Approximately 10% of all carbon atoms in UNCD films partake of the complex bonding situation at the grain boundaries involving a mixture of sp^2, sp^{2+x}, sp^3, and dangling bond configurations. Grain boundary carbons impart a striking set of attributes on UNCD films such as dramatic changes in electron as well as phonon transport properties. Of particular interest for the present discussion is the fact that electron and phonon transport are altered so profoundly that properties such as electrical and thermal conductivities can no longer be considered "intrinsic" but are in fact found to be very strongly "size" dependent. This circumstance enables entirely new frontiers of diamond nanoscience and nanotechnology to be explored.

The C_2 growth process has by now been fully substantiated. It has been put on a firm experimental foundation during the last several years as a result of work in several laboratories using a variety of deposition techniques.[5–8] In addition, C_2 has been found to be a major species even in hydrogen-poor low-methane-content noble gas microwave plasmas, by both optical absorption and theoretical plasma modeling calculations.[8,11] Importantly, extensive tight-binding density functional calculations have elucidated detailed growth and nucleation mechanisms on both (110) and (100) diamond surfaces with C_2 as the growth species and have given insight into the electronic structure of the ubiquitous grain boundaries in this nanostructured material.[12–15] The complex carbon bonding situation at the grain boundaries results in a plethora of states in the 5.5 eV wide band gap of bulk diamond. The quantum chemical calculations give, for example, the location of the Fermi level, participation ratios, electron delocalization information, etc. Addition of nitrogen to the synthesis gas results in incorporation of nitrogen in the grain boundaries leading to substantial electrical conductivity with low activation energy which has by recent Hall and Seebeck coefficient measurements been shown to be n-type.[16–17] Bulk carrier concentrations up to $10^{21}\,cm^{-3}$ are found and mobilities range between 1 and $6\,cm^2\,V^{-1}s^{-1}$. The films which display semi-metallic behavior with electrical conductivities of several hundred per ohm per centimeter represent a breakthrough in diamond science because, for the first time, diamond has been made into an n-type material which conducts electricity at ambient and even at low temperatures.[18] It has been known for a long time that diamond can also be doped p-type with boron; p-type UNCD has been synthesized but not fully characterized as yet. It can be expected to have properties similar in some ways but distinct from n-type material. Clearly, the possibility of having both n- and p-type UNCD opens up potential applications for diamond in electronics as a diode, field-effect transistor, solar cell, thermophotovoltaic device, and biosensor. Of interest for the purpose of the present discussion is the potential for improved performance of thermoelectric materials. The combination of n- and p-type UNCD elements connected in series could lead to the construction of an efficient high-temperature power-generating thermopile.[19,20]

Progress in this field depends on a thoroughgoing investigation of the basic solid state physics and chemistry of n- and p-type UNCD that underlies the use of this material for thermoelectric as well as other novel applications. Fortunately, the experimental and theoretical efforts have been closely linked from the very beginning of the discovery and development

of UNCD and one is now in an excellent position to optimize the intricately interrelated properties of UNCD so as to fashion, for example, a thermoelectric material with a figure of merit high enough to be of interest for practical energy conversion applications.

Experimental and theoretical understanding must go hand-in-hand if the constellation of phenomena that become manifest only at the nanoscale is to fulfill the promise low-dimensional materials offer as new tools for enhancing thermoelectric properties.

5.1 Characterization of n-type Conductivity in UNCD Films

Diamond films grown by low-pressure conventional CVD methods on polycrystalline substrates from synthesis gas mixture whose methane/hydrogen ratio is varied from 0.01 to 0.10 are composed of crystallites whose size decreases from several microns to hundreds of nanometers as the hydrocarbon/hydrogen ratio increases.[21] According to classical nucleation theory, this is the result of an increased heterogeneous renucleation rate as more methane is added to gas mixtures composed primarily of hydrogen. However, very frequently the increase in methane concentration needed to decrease the grain size results in the simultaneous deposition of amorphous carbon so that the films are in fact best described as diamond nanocrystals imbedded in diamond-like amorphous carbon.[9,10]

One of the roles of hydrogen, and in particular atomic hydrogen, in the conventional diamond CVD methodology described above, is to regasify embryonic diamond nuclei and thus to decrease renucleation rates.[4,22] Our recognition of this aspect of conventional diamond CVD led us to investigate the effect of systematically replacing hydrogen by argon in the synthesis gas mixtures.[23] The reasonable expectation that perhaps films could be obtained whose microstructure consists entirely of diamond crystallites so small as to be at the lower limit of diamond stability while still preserving a pure diamond phase was in fact fulfilled. Using gas mixtures consisting of 1% methane and 99% argon, the heterogeneous renucleation rates are of order $10^{10}\,cm^{-2}\,s^{-1}$ resulting in phase pure diamond films composed of 3–5 nm crystallites called ultrananocrystalline diamond (UNCD) films to distinguish them from the nanocrystalline films referred to above. This new form of diamond has properties that set it apart from conventional CVD diamond films.

Molecular dynamics simulations, as already mentioned, show that the ubiquitous grain boundaries present in UNCD films are high-angle, high-energy boundaries that lower their free energies by bond rehybridization rather than by bond bending.[24,25] This leads to a very complex bonding situation for the approximately 10% of carbon atoms in the films that are situated at grain boundaries. Tight-binding density functional calculations detailed in the theoretical section of this chapter have shown that the 5.5 eV band gap of diamond is filled with electronic states whose origin is due to the complex bonding of the carbons at the grain boundaries. A deep understanding of many of the properties of these states is required in order to take full advantage of the electronic properties immanent in UNCD. Suffice it to say at this point that calculations which place a nitrogen atom from infinity into a substitutional site in a grain boundary requires between 3 and 5 eV less energy, depending on which of several grain boundary sites the nitrogen occupies, than to place it in a substitutional site in the diamond lattice.[16] The intriguing possibility therefore arises that nitrogen could be an effective donor and contribute to electrical conductivity by going into grain boundaries. It is, of course, well known that nitrogen in substitutional sites in the diamond lattice occupies a level that is situated 1.7 eV below the conduction band and therefore does not contribute to electrical conductivity. In fact, there has been an intense search for n-type conductivity over an extended period of time so as to have available both n- and p-type diamond, the latter being readily achieved by doping with boron.[26] Among the n-type dopants that have been investigated is phosphorus,[27] but its activation energy is 0.6 eV, still too high for ambient temperature conductivity. Phosphorus substitution occurs most readily into the (111) face of diamond because of size considerations. The pursuit of n-type conductivity has long been seen as a critical area of diamond science where a breakthrough could lead to major advances in making diamond a useful electronic material, and this quest has now taken an important step forward with the development of UNCD.[28]

The effect of sequential additions of nitrogen to the CH_4/Ar synthesis gas on the electrical transport properties of the films is systematically being investigated. Addition of nitrogen leads to the formation of the CN molecule in the microwave discharge by reaction with acetylene to form HCN. This subsequently collisionally ionizes and forms CN by dissociative electron recombination. The addition of nitrogen drastically changes the C_2 as well as the CN concentrations. The ratios between these two radical species determined by emission spectroscopy depend sensitively on the amount of nitrogen added to the plasma, on the total gas pressure,

and on the microwave power. A complete parametric study of this system is now underway including quantitative SIMS measurements on the amount of nitrogen incorporated into the films as well as changes in film microstructure under various deposition conditions.[29–32] SIMS measurements have shown that nitrogen incorporation can reach values of ~10^{20} atoms/cm^3 at plasma nitrogen contents of 10–20% by volume. The detailed mechanistic steps of the reaction of CN with the diamond lattice has been treated theoretically.[16]

Four-point-probe electrical conductivity measurements on UNCD films grown on fused silica substrates at 800 °C using 1% CH_4/Ar/N_2 gas mixtures at a total pressure of 100 Torr and 800 W microwave power are shown as a function of temperature in Fig. 5.1 for 1%, 5%, 10%, and 20% N_2 added to the plasma. Films grown without added nitrogen are highly insulating. The addition of nitrogen can be seen to lead to a dramatic increase in electrical conductivity reaching at least 143 $ohm^{-1} cm^{-1}$ for 20% N_2 at ambient temperatures. In some films (not shown) conductivi-

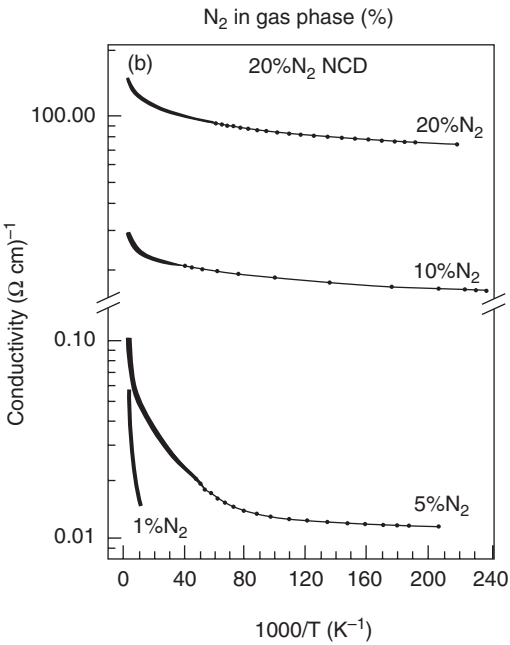

Figure 5.1 Arrhenius plot of conductivity data obtained in the temperature range 300–4.2 K for a series of films synthesized using different nitrogen concentrations in the plasma as shown.

ties as high as 500 $ohm^{-1} cm^{-1}$ have been observed.[18] The conductivity data are remarkable for several reasons. First, it is clear that these films exhibit finite conduction for temperatures even as low as 4.2 K, indicative of semi-metallic behavior which is also seen in heavily boron-doped diamond thin films. These non-linear curves can be interpreted in terms of multiple, thermally activated conduction mechanisms with different activation energies. They can be modeled by a summation of exponential functions as has been done in other studies where "impurity" bands may contribute to the conduction mechanism.

The conductivity data in and of themselves do not reveal the nature of the electrical transport carriers. To determine the sign of the charge carriers, Hall effect measurements were carried out on films deposited on oxidized highly resistive type Ib diamond substrates. Illustrative of the Hall effect data are the measurements depicted in Fig. 5.2.[18] Figure 5.2(a) shows data for a p-type boron-doped polycrystalline diamond control sample. It can be seen that the Hall signal is periodic and 180 ° out of phase with the applied magnetic field. Figure 5.2(b) shows the case for a nitrogenated UNCD sample, giving a similar effect, but with a Hall voltage that is in phase with the applied magnetic field, thus proving the n-type nature of this material. The oscillation amplitude differences between Figs. 5.2(a) and (b) are due to differences in carrier concentrations and excitation currents. For verification of the n-type behavior displayed in the Hall measurements, the n-type nature of the nitrogen-containing UNCD film was also confirmed by Seebeck coefficient measurements.

It is clear that the conductivities and therefore the carrier concentration of n-type UNCD can be controlled by adjusting the nitrogen content of the gas phase. The variation in sheet carrier concentration with temperature of films deposited using plasmas containing 10% and 20% nitrogen are shown in Fig. 5.3. Both films display an extremely low thermal activation energy since their sheet carrier concentrations show only a small variation from 4.8 to $2.2 \times 10^{15} cm^{-2}$ over the range 300–30 K for the 10% and from 1.8 to $1.3 \times 10^{17} cm^{-2}$ over the range 300–15 K for the 20% sample. The films are between 2 and 3 μm in thickness, yielding bulk carrier concentration of 10^{19}–$10^{21} cm^{-3}$, very high values for diamond at ambient temperatures. The variation of mobility with temperature is shown in Fig. 5.4. It can be seen that the room-temperature values are around 1.5 $cm^2 V^{-1} s^{-1}$, and are again rather insensitive to temperature. The 20% N_2 sample varies from 1.565 $cm^2 V^{-1} s^{-1}$ at 300 K to 1.285 $cm^2 V^{-1} s^{-1}$ at 15 K, whereas the 10% N_2 sample varies from 1.485 $cm^2 V^{-1} s^{-1}$ at

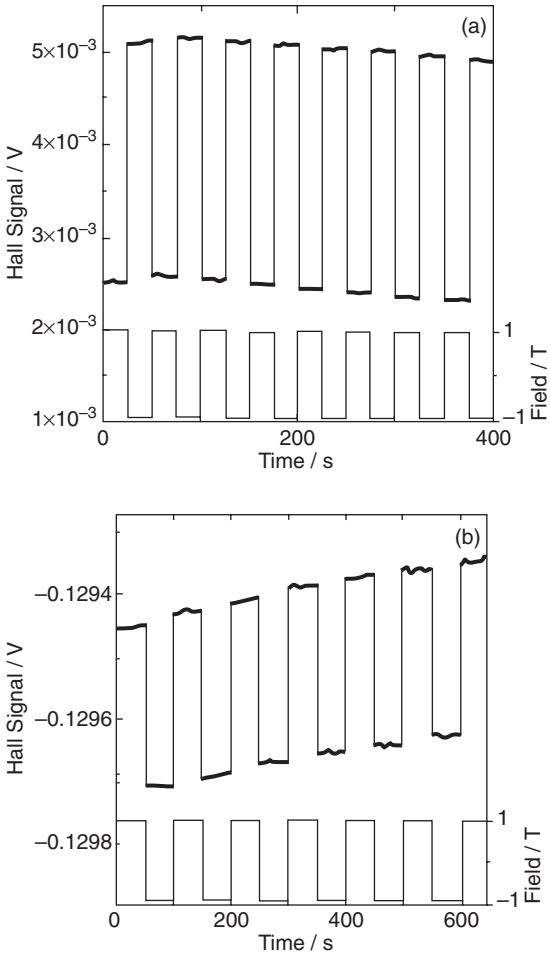

Figure 5.2 (a) Hall effect measurements for boron-doped microcrystalline diamond, where the Hall voltage is plotted as a function of time as the magnetic field is switched in polarity; and (b) similar measurements for UNCD grown with nitrogen added to the gas mixture.

300 K to 1.045 $cm^2 V^{-1} s^{-1}$ at 50 K. These values of mobility were derived from the sheet carrier concentration and the resistivity.

The discovery of ambient temperature n-type UNCD is a breakthrough in that electronic applications of diamond not possible before can now be contemplated. Although nitrogen had been shown to render certain diamond-like carbon (DLC) and tetrahedrally bonded carbon (ta-C) films somewhat electrically conducting, their mobilities are generally in the

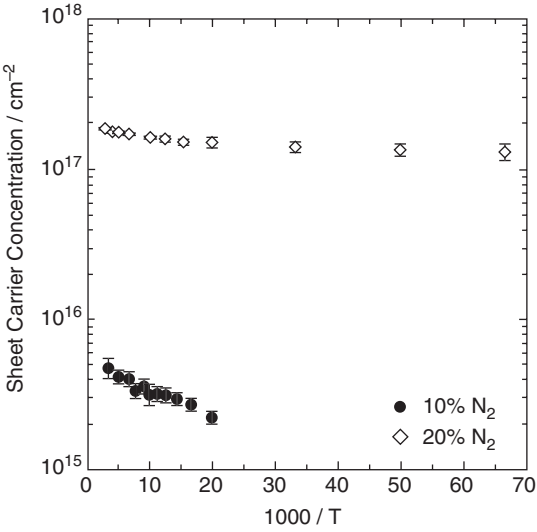

Figure 5.3 Sheet carrier concentrations determined from Hall effect measurements in UNCD grown with nitrogen as a function of temperature.

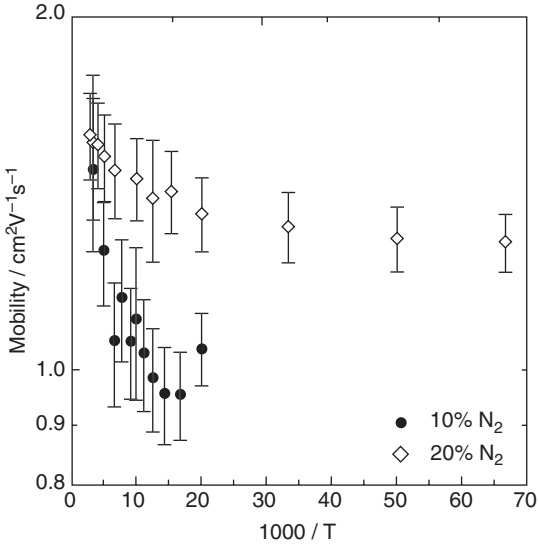

Figure 5.4 Hall mobilities in nitrogen-doped UNCD as a function of temperature.

$10^{-6}\,cm^2\,V^{-1}\,s^{-1}$ range, six orders of magnitude lower than the mobilities of UNCD films and therefore undetectable by Hall measurements. On the other hand, substitutional nitrogen in single crystal and microcrystalline diamond has a level 1.7 eV below the conduction band, too low to make a contribution to conductivity at reasonable temperatures. Thus, type Ib diamond, although containing enough nitrogen to have a yellow color, is very highly resistive.

The unique electrical properties of UNCD presumably are due to the ubiquitous presence of grain boundaries coupled with a high film crystallinity. A more detailed discussion of the electronic structure of the grain boundaries will be given in Section 5.3 of this chapter.

As already pointed out, the n-type conductivity mechanism in nitrogen-containing UNCD is probably not due to a single shallow donor below the conduction band analogous to phosphorous-doped silicon, but rather to states introduced into the band gap of diamond by the complex carbon and nitrogen bonding situation at the grain boundaries leading perhaps to the formation of "impurity" bands. The density of states in the band gap shows a peak near the Fermi level situated about 1 eV above the valence band. There is a shift of the Fermi level toward the conduction band with addition of nitrogen as well as other changes in the energy level structure. In any event, the activation energy for conduction is less than 10 meV for nitrogen gas phase concentrations of 10% and decreases still further with increasing nitrogen content. It is important to keep in mind that near-edge X-ray absorption fine structure, electron energy-loss spectroscopy (EELS), X-ray diffraction, and selective area electron diffraction measurements have shown no evidence of amorphous carbon or crystalline graphite within these films.[4] It is therefore plausible to invoke a conduction mechanism that must involve the grain boundaries in a fundamental way. A detailed elaboration of such a grain boundary mechanism of conduction awaits more extensive theoretical calculations as well as experimental measurements on photoconductivity, impedance, and electron spin resonance spectroscopy, which are currently underway.

5.2 Applications of n-type UNCD Films

Although much has been learned about the properties of n-type UNCD, a great deal of fundamental knowledge needs still to be uncovered in order fully to realize the potential for this material to contribute to the solution

of challenging problems in several areas that depend on the electronic properties of the material. Of particular significance is the fact that one now has at one's disposal both n- and p-type UNCD thus creating a strong incentive to develop an understanding of the theoretical basis for the electronic behavior of these substances. Attention up to now has been focused on n-type UNCD and one must now be equally concerned with p-type UNCD. Substitutional sites in the diamond lattice are energetically more favorable to boron than to nitrogen. However, B and N likely occupy both substitutional as well as grain boundary sites in UNCD with distribution ratios determined by several parameters such as grain size, temperature of deposition, etc. The distribution ratios need to be determined using very high-resolution EELS. Clearly, different conductivity mechanisms will be associated with grain and grain boundary conduction. It is likely that both types of conduction will occur to a greater or lesser extent with both B and N. One possible experimental approach to obtain an answer to this question is impedance spectroscopy. Very preliminary results from Cole–Cole plots indicate that for n-type UNCD in fact even lattice conduction makes a small contribution.[34] Perhaps a "boundary" layer is involved but a better understanding will require considerably more work. Detailed Hall effect, carrier concentration, and mobility measurements must be done on p-type UNCD to complement the n-type data. Tight-binding density functional calculations on p-type UNCD will shed light on the band structure of this material and refined photoconductivity measurements are needed to elucidate the details of the electronic states in the grain boundary. Much theoretical work is required to elaborate an understanding of phonon scattering, phonon transport, electron scattering, electron transport, and electron–phonon interactions in these materials. Only then can one begin to inquire into the parametric optimization of their electronic properties. Finally, UNCD presents one with realistic opportunities for creating entirely new classes of electronic diamond materials by taking advantage of the grain boundary structure uniquely present in UNCD to introduce substituents in addition to nitrogen and boron such as aluminum, phosphorus, sulfur, and others that one would not expect to be electrically active at ambient temperatures except perhaps in this unusual material.

The remainder of this section will deal briefly with several properties of n-type UNCD films that have already been found to be useful. These descriptions are meant to serve as guideposts pointing the way to future, much more extensive utilization of UNCD. Directions are indicated in which further developments are required for progress to be made.

5.2.1 Field Electron Emission

The finding of n-type electrical conductivity in UNCD allows one to explore a variety of research areas where the electronic properties of the films play an important role such as field electron emission. Theoretical calculations and photoemission measurements by Himpsel et al.[35] have demonstrated a negative electron affinity on (111) planes of unreconstructed single crystal diamond and it was thought that electron emission from p-type polycrystalline diamond films might occur in a facile way if the vacuum level indeed lies below the conduction band, as inferred from the work of Himpsel et al.[35] The consensus, however, appears to be that for polycrystalline films a different mechanism must be at work. For example, p-type diamond requires that the film be coated on a tip with a small radius of curvature in order to obtain a field gradient sufficient to measure an emission current at reasonable field strengths. On the other hand, for UNCD, there is the intriguing possibility that a field gradient can be established sufficient to allow electron emission at modest applied fields acting on the two-atom-wide conducting grain boundaries. Such a model implies that quantum-confined electrons bounded by insulating diamond nanocrystallites tunnel through barriers at the narrow grain boundaries aided by a "thermoelectric" effect.[36–38] In the event, the grain boundaries would function in a way different from the emission mechanism associated with sharp tips. We have also investigated n-type UNCD films coated on silicon wafers. To obtain 1×10^{-5} A emission current with a 2.0 mm tungsten probe requires a potential of only 4.5 V μm^{-1}. This result suggests extensions of this research to optimize electron emission even from flat surfaces.

A collaboration with Vanderbilt University has yielded preliminary results on diode and triode field emission devices fabricated with a self-aligning gate formation technique from silicon-on-insulator wafers using well-known silicon micropatterning techniques. This approach has the potential for achieving large-area flat-panel displays and thermionic energy conversion devices. An n-type UNCD layer has been deposited into inverted pyramidal cavities etched into the Si wafer, each cavity being subsequently "filled" with boron-doped microcrystalline diamond. The field emission characteristics of the multi-device assembly from very sharp UNCD tips obtained after a complex multi-step fabrication process were encouraging. Electron transport determines the current density that can be obtained at the diamond tips. Enhancing this property will be key to being able to provide a major improvement over the performance of the state-of-the-art technology available now.[39]

5.2.2 Electrodes for Electrochemistry and Biosensing

Another research area where n-type UNCD plays an important role is in the use of diamond films as electrochemical electrodes.[40] The large potential window of about 4.0 eV in aqueous solutions and extreme resistance to corrosion are two of the reasons diamond electrodes are widely used in electrochemical research and they are beginning to find important applications, for example, in water purification.[41] Conventional boron-doped microcrystalline diamond film electrodes that are in wide use today have a surface roughness of the order of microns because they need to be many microns in thickness so as to be free of pinholes. Electrodes fabricated from n-type UNCD have surface roughness in the low tens of nanometer range without requiring polishing and are pinhole free even at thicknesses of 75 to 100 nm. They have been shown to have very low background currents and a high degree of electrochemical activity for a wide variety of redox systems. Apparent heterogeneous electron transfer rate constants of 10^{-2} to 10^{-1} cm s^{-1} are observed at UNCD electrodes even after repeated use. The electrodes do not require any pretreatment and can be stored in ordinary laboratory air.

Hydrogen-terminated n-type UNCD has been biofunctionalized and can be expected to show considerable promise as an electrode for biosensing applications.[42,43] Covalent modification of the UNCD surface using photochemically or electrochemically induced reactions and subsequent attachment of DNA olignucleotides provide an extremely stable platform for subsequent surface hybridization processes. Comparison of DNA-modified UNCD with other commonly used surfaces for biological modification, such as gold, silicon, glass, and glassy carbon, showed that UNCD is unique in its ability to achieve very high stability and sensitivity while also being compatible with microelectronic processing technologies.[42] These results suggest that n-type UNCD may be a nearly ideal substrate for integration of microelectronics with biological modification and biosensing. The implications for biology of the development of n-type UNCD as an electronic material are increasingly coming to be recognized. For example, it was shown by Haertl et al.[44] that the enzyme catalase can be attached covalently even to n-type nanocrystalline diamond. The enzyme remains fully functional and active, with the n-type diamond film functioning simply as an electrode enabling direct electron transfer to occur from the enzyme's redox center.

5.2.3 High-Temperature n-type UNCD/p-type All-Diamond Heterostructure Diode

Diamond with its high breakdown strength, thermal stability, and chemical inertness would appear to be an ideal candidate for high-power and high-temperature diodes and transistors. However, the lack of a suitable shallow n-type dopant has up to now impeded development of all-diamond electronic devices active at ambient temperatures. Other candidate materials have in fact been explored such as n-type cBN/p-diamond[45] and n-type AIN/p-diamond heterojunctions[46], but an all-diamond structure containing only carbon would offer superior thermal stability allowing reliable operation at very high powers and temperatures. Schottky diodes on oxygen-terminated diamond have barrier heights of 1.7 eV imposing high losses in the forward direction. In the reverse direction, high blocking voltages have in fact been obtained, reflecting the high breakdown strength of diamond, about 10^7 V cm^{-1}, but the refractory metal contacts degrade rapidly due to interfacial carbide formation leading to a catastrophic failure mode.[47] In collaboration with Professor Erhard Kohn at the University of Ulm, Germany we have constructed an all-diamond heterostructure diode consisting of a Ib single crystal of diamond on which is grown epitaxially a heavily B-doped layer, followed by a lightly B-doped depletion layer, followed by a highly n-type conducting layer of UNCD.[28] A detailed analysis of the performance of this diode shows that a pn junction has been formed which displays 7–8 orders of magnitude of rectification. In the forward direction, a characteristic exponential dependence is observed at small potentials which flattens out at higher bias. A model for this behavior has been postulated based on the existence of both grain boundaries and nanocrystallites at the interface with single crystal diamond. A barrier height of 0.72 V can be extracted from the data indicating that the junction potential between the depletion layer and the n-type UNCD is indeed determined by grain boundary states. The temperature stability of this diode is extraordinary, showing no degradation in performance after repeated cycling from ambient temperatures up to 1200 K and back. This appears to be the first time that a semiconductor diode has been operated between ambient temperatures and 1200 K over an extended period of time. This key result makes feasible consideration of the use of n- and p-type UNCDs as high-temperature thermoelectric materials with the possibility of achieving high Carnot efficiencies. Further investigation of this promising diode structure, ideally suited for

high-voltage rectifiers with strongly reduced forward losses at high temperatures and powers, may allow this technology to outperform silicon carbide. For this to occur, reactive ion etching of UNCD needs to be improved. Growth of thin, uniform UNCD layers with accurately known growth rates is essential in order to pass high forward-bias currents. Spectrally resolved photoconductivity and optical transmission measurements are also needed to define the densities of states in the band gap of UNCD. More extensive Hall and electrical conductivity measurements on UNCD are required in order reproducibly to obtain desired carrier concentrations and mobilities in the UNCD layer. Furthermore, high-voltage and high-temperature *I*/*V* and *C*/*V* data need to be obtained and modeled to help establish conditions for large-area device fabrication on polished polycrystalline rather than single crystal diamond. Finally, performance criteria need to be established on such structures.

The all-diamond heterostructure diode described above provides a solid foundation for the development of an all-diamond field effect transistor with n-type UNCD acting as the gate. Genetically engineered antibodies attached to the gate might react with specific proteins in the coats of Class A pathogens resulting in electrical signals that could be measured with extraordinary sensitivity. Such a detector would go a long way toward becoming a real-time sensor needed to minimize exposure to pathogens released for example in a bio-terror attack.

5.3 Electronic Structure of UNCD Grain Boundaries

Approximately 10% of all carbon atoms in UNCD participate in bonding at the grain boundaries (GBs) of the 3–5 nm crystallites that make up the films. It was first shown by Keblinski et al. using molecular dynamics simulations that the structure and bonding of the UNCD GBs is highly complex and unusual.[24,25] As has been pointed out, UNCD is an examplar par excellence of the profound changes in properties manifested by many materials when their sizes are reduced to the single digit nanometer range. In this section, the current knowledge concerning the relationship between the electronic transport and the electronic structure of UNCD GBs will be summarized.

For the most part, the theoretical work on UNCD growth and nucleation[12–15] and the more recent work on UNCD grain boundaries[16,17] have been done by a group of quantum theorists in the Materials Science Division at Argonne National Laboratory headed by Larry A. Curtiss. The first

work, as already mentioned, on the structure of high-angle, high-energy twist GBs in UNCD using Tersoff interatomic potentials showed that (100) GBs are more stable against decohesion than (110) or (111) GBs.[24,25] Furthermore, high-angle (100) GBs are representative of general GBs between randomly oriented crystallites because each carbon at a (100) surface has two broken bonds. All other surfaces also have this feature except the special cases of (111) and (110) planes, where each carbon atom has only one broken bond. Using a model in which the width of the GB is taken to be 0.2 nm, in accord both with HRTEM results and with theoretical values, Cleri et al. found in tight-binding molecular dynamics calculations that about 40% of the GB carbons are three-fold coordinated.[48] The diamond band gap as a consequence is filled with electronic states that arise from dangling and double bonds. Although the states are localized, they could participate in hopping conduction.

The experimental observation that the incorporation of nitrogen in UNCD films leads to ambient temperature n-type conduction has stimulated a detailed investigation using density-functional-based tight-binding (DFTB) molecular dynamics methods to understand this effect on a theoretical basis. Most of the calculations were done on the Σ13 twist (100) GB as a function of the introduction of various amounts of substitutional nitrogen. Incorporation of silicon or interstitial hydrogen was also considered, followed by equilibration, annealing, and relaxation of the resulting structures.

The minimum energy structure for the Σ13 GB is shown in Fig. 5.5.[16] It can be seen that structural disorder is confined to the two GB planes while the rest of the diamond crystal remains ordered, consistent with TEM studies[49] that confirm a GB width of about 0.2 nm. A highly significant and remarkable result of the DFTB calculations is that energy minimization in UNCD is achieved by rehybridization rather than significant atomic displacements, as is the case with ultrananocrystalline silicon. The GB energy is about 7.9 J m^{-2}. While the energy per GB carbon atom is 1.6 eV higher than typical energies of low-angle and special GBs, it is much lower than the value 2.3 eV of a (2 × 1) reconstructed (100) surface carbon atom. The stability of UNCD films may therefore have its origin in the relative stability of the UNCD grain boundaries.[16]

The DFTB method gives a band gap of 6.4 eV which is to be compared to the experimental value of 5.4 eV for bulk diamond. The introduction of topological disorder through GBs in UNCD changes the electronic structure profoundly even in the absence of nitrogen. Substitution of nitrogen for carbon results in different possible bonding positions characterized by sp^2, sp^{2+x} and sp^3 hybridization. The most stable configuration is sp^{2+x} with

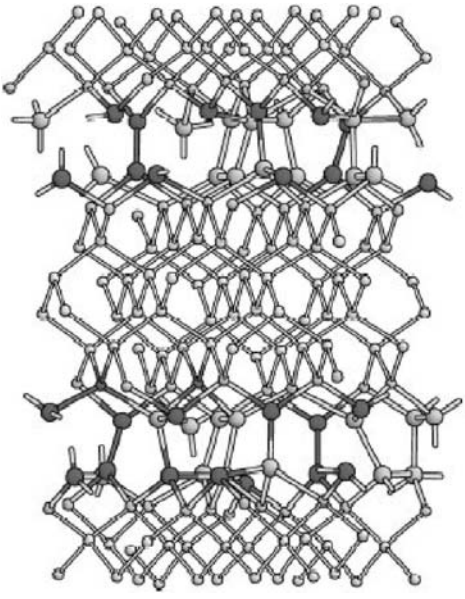

Figure 5.5 Side view of the periodic cell for an optimized diamond Σ13 grain boundary. Two grain boundaries are shown. Black atoms are three coordinated and gray atoms are four coordinated. Atoms in the first layers of the interfaces are shown as larger spheres. Bonds extending across the cell boundary are shown as half bonds.

a formation energy of –0.64 eV compared to a substitutional site in the diamond crystal lattice of 4.9 eV. In view of this large energy difference, it is very likely that nitrogen is concentrated in the GBs. The new electronic states associated with nitrogen in the GB are shown in Fig. 5.6. The carbon dangling bond states hybridized with nitrogen lone pairs are above the Fermi level and donate electrons to the carbon defect states near the Fermi level causing it to shift upward, toward the delocalized π^* carbon bond. Thus, it is reasonable to imagine that variable range hopping or other thermally activated conduction mechanisms can occur in the GBs and result in enhanced electron transport. This mechanism does not require a true doping nitrogen state (four-fold-coordinated nitrogen or three-fold-coordinated nitrogen with a double bond). Furthermore, increase in nitrogen concentration could lead to the observed semi-metallic behavior because of the increase in the connectivity of sp^2-bonded carbon, higher delocalization of the π^* band, and broadening of the π^* band.[16].

A UNCD GB has a much lower local density than the bulk diamond crystal. Therefore, it is more favorable energetically to accommodate larger atoms such as Si and P in the GB than in the diamond lattice position. DFTB calculations show that Si is always three-fold coordinated in a GB site with formation energies of –0.85 eV to 1.45 eV compared to 4.45 eV for a lattice substitutional site. Si substitution in the GB leads to an increase in three-fold-coordinated carbon in the vicinity of Si without the creation of new electronic levels in the band gap. The introduction of Si impurities, therefore, is not expected to influence the electronic properties of UNCD.

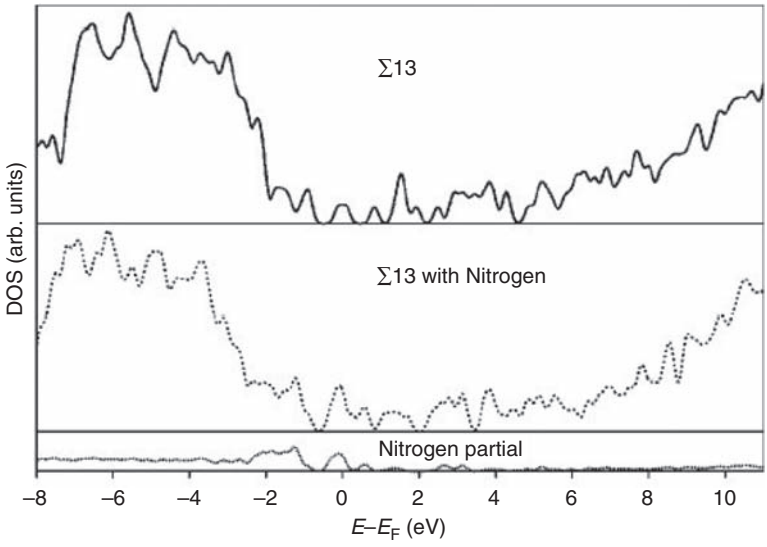

Figure 5.6 Densities of states for a diamond Σ13 grain boundary without and with 30% nitrogen impurities. Local density of states for nitrogen atoms is given in lower panel.

The last statement cannot be made about the introduction of hydrogen into the GBs which DFTB calculations have shown to lead to a reduction in the density of states near the Fermi level. All hydrogen atoms entering the GBs are bound to carbon atoms which become four coordinated. Thus, hydrogen atoms saturate dangling bonds associated with three-fold-coordinated carbon and, as expected, correspondingly decrease the sp^2/sp^3 ratio of the GBs. Molecular dynamics simulations show that thermal motion of hydrogen is restricted to the vicinity of the carbon partner at 1000 K but motion among different carbon sites has its onset at about 1200 K, much lower than the 1700 K temperature characteristic of diffusion of hydrogen in bulk diamond.

5.4 UNCD and Carbon Nanotube/UNCD Composites as Potential High-Efficiency, High-Temperature Thermoelectric Materials

The quest for alternative and renewable sources of energy will increasingly drive much of the global activities in energy-related research in the

coming decades and imbue them with a strong focus and direction. For that quest to be successful, scientific and technological breakthroughs in several challenging areas need to occur. One such area that could have a beneficial impact on power generation technology is the efficient direct conversion of heat to electricity obviating the need for rotating machinery. Such a process would be dependent for its operation on the development of new thermoelectric materials with performance characteristics that far exceed those currently in existence. State-of-the-art thermoelectrics are only about 7% efficient because limits appear to have been reached with bulk materials in maximizing electrical while at the same time minimizing thermal conductivities.

There appears to be no theoretical reason why overall efficiencies of over 40% cannot be achieved. The search for new classes of thermoelectric materials which has been ongoing for over 50 years has received a major new impetus as a result of the emphasis during the last few years on nanoscience. The realization that so-called "intrinsic" properties are in fact size dependent has stimulated investigations of the effects of low dimensionality on thermoelectric behavior leading to predictions of dramatically higher figures of merit, *ZT*, for nanostructured materials.[50–53] The precise physical effects responsible for such improvements are not well understood. However, theoretically it has been shown that the higher interface density in nanomaterials can reduce losses due to phonon heat conductivity while a sharply peaked density of state (DOS) at the Fermi level achievable in nanomaterials can lead to optimal values of thermopower. At the same time the electronic component of the thermal conductivity is reduced because the narrow DOS peaks cut off the high-energy end of the Fermi–Dirac distribution, perhaps resulting in a loss of validity of the Wiedemann–Franz law.[54]

The expression for $ZT = \alpha^2\sigma/\kappa$ (α = Seebeck coefficient, σ = electrical conductivity, κ = thermal conductivity) shows that in order to maximize *ZT*, the electrical conductivity must be increased while the thermal conductivity is held to a minimum. These conflicting requirements are in part responsible for the materials challenges presented by the quest for efficient thermoelectric conversion. Values of *ZT* near unity displayed by Bi_2Te_3 and $Si_{0.8}Ge_{0.2}$ alloys had not been improved upon since their discovery about 50 years ago.[55] In recent years superlattices,[56] PbSeTe/Pb Te quantum dots,[57] as well as nanostructured silver lead chalcogeaides,[58] have made significant gains by reaching *ZT* values in the range 1.5–2.5. Because conversion efficiencies are closely tied to *ZT* values, the increase in *ZT* observed with these nanostructured materials is highly significant and promising.

The discovery and characterization of n-type UNCD presents one with a nanostructured material whose thermoelectric properties are worthy of investigation. Although *ZT* values have not yet been determined, it is worthwhile to discuss the basis for studying the thermoelectric properties of UNCD and UNCD/nanotube composites. Some relevant properties are listed in Table 5.1 where the electrical conductivities, σ, the bulk carrier concentration, the carrier mobilities, and the thermal conductivities, κ, of p-type microcrystalline diamond films[59] are compared to those of n-type UNCD films.[18, 33] Clearly, data of the sort shown in Table 5.1 are also required for p-type UNCD but are currently not available.

It can be seen that the electronic transport properties of n-type UNCD and p-type microcrystalline diamond films are quite similar. For equivalent bulk carrier concentrations, the magnitude and temperature dependence of conductivities for both carrier types in CVD diamond have comparable values. This result needs to be elucidated in detail since the conductivity mechanisms in the two materials are almost certainly very different.

Phonon transport in microcrystalline CVD diamond has been a subject of considerable interest for some time because of the use of this material in heat-spreading applications. The thermal conductivity of MCD has been found to be strongly crystallite-size dependent. Diamond films with crystallite sizes in the range 20–30 μm have thermal conductivities that approach the single crystal diamond value of 25 $W\,cm^{-1}\,K^{-1}$ but decline to a value (extrapolated from Graebner et al.'s data) of ~2 $W\,cm^{-1}\,K^{-1}$ when the crystallite size approaches 300–500 nm.[60] For UNCD with crystallite sizes in the range 3–5 nm, the thermal conductivity at 300 K is 0.02 $W\,cm^{-1}\,K^{-1}$.[61] This remarkable decrease in thermal conductivity can

Table 5.1 Selected Properties of p-type Microcrystalline Diamond (MCD) Films and n-type UNCD Films

	Electrical conductivity ($ohm^{-1}\,cm^{-1}$) (300 K)	Bulk carrier calc. (cm^{-3})	Mobility ($cm^2\,V^{-1}\,s^{-1}$) (300 K)	Thermal cond. ($W\,K^{-1}\,cm^{-1}$)
p-type MCD	500	10^{21}	<0.4	2
n-type UNCD	400	10^{21}	1.5	0.02

be understood on the basis of the theoretical treatment given by Graebner et al.[60] Their calculations show that the strong crystallite-size-dependent thermal conductivity of diamond is primarily due to point and extended defect scattering of phonons. The defected structure of the ubiquitous UNCD GBs characterized by both topological and bond disorder appears to be particularly effective in the scattering of phonons. The unique microstructure of UNCD therefore converts the best thermal conductor, single crystal diamond, into a diamond material having a thermal conductivity close to that of fused quartz. A more detailed understanding of this result awaits deeper insights into thermal transport in nanomaterials which continues to be a subject of ongoing research.[61]

Preliminary Seebeck coefficient measurements at ambient temperatures on n- and p-type UNCD have given values, between 20 and 300 $\mu V\,K^{-1}$, depending on sample preparation.[62] One concludes that n- and p-type UNCD can be regarded as viable thermoelectric materials since they approach the parameters specified by Tritt to reach ZT values near 1 at ambient temperatures.[62]

To realize the potential of nanostructured carbons as high-temperature thermoelectric materials, one must be able to reach ZT values of at least 4 in order to achieve 40% heat to electricity conversion efficiencies with a ΔT of 10^3. As has already been pointed out, this may now be achievable by proper manipulation of parameters that cannot be controlled independently in bulk systems but can in principle be controlled in nanoscale materials.

The remarkable decrease in thermal conductivity due to phonon scattering at the disordered UNCD GBs has been discussed above. Equally important are the narrow peaks in the density of states uncovered by recent tight-binding density-functional calculations on $\Sigma 65$ UNCD GBs which provide a plausible pathway for strongly enhanced electronic conduction to occur in this material.[63] The existence of many electronic states in the band gap of UNCD is due to the complex hybridization of the carbon atoms that constitute the two-atom-wide GBs. The electronic properties of UNCD are illustrations of the dramatic modifications that can occur due to electron confinement in nanostructured materials which exhibit low-, in this case two-, dimensional behavior. It is this insight that forms the basis for attempts now being made in our laboratory to optimize still further the thermoelectric properties of nanostructured carbons. A brief outline of such an attempt will be given here.

The Gibbs free energies of formation of carbon nanotubes (CNTs) and UNCD differ by only 0.1–0.3 eV depending on CNT dimensions and

UNCD crystallite size.[64] Remarkably, the energy difference between these two very different forms of carbon is 15 to 40 times smaller than the carbon–carbon bond energy of about 4 eV which gives rise to the large overall cohesive energies of diamond and graphite. This situation implies that synthesis reactions can in principle be tailored to produce either CNTs or UNCD, or both simultaneously, because the energetics are such as to provide an opportunity for kinetic factors to play a decisive role in determining channel distribution ratios. Clearly, achieving control of reaction kinetics now becomes a powerful tool in the quest for the fabrication of self-assembled nanostructured carbon self-composites with precisely controlled composition.

One potential way of achieving this goal is through manipulation of the fact that CNT synthesis requires the presence of a catalyst while UNCD synthesis does not. Indeed, the judicious introduction of a catalyst in a "distributed" fashion on a substrate prepared for UNCD growth has already resulted in the realization of a UNCD/CNT self-assembled, self-composite.[65] Of particular interest are those transport properties displayed by the new composites that, when optimized, would lead to high thermoelectric figures of merit.

It is important to gain insight into the mechanism of formation of the self-composites which intimately involves the nature of the chemical bonds formed between the nanotubes and the 3–5 nm UNCD crystallites. Direct insertion of C_2, the carbon dimer molecule, has previously been shown to lead to growth as well as to nucleation of UNCD.[12–15] It has now been established by density-functional calculations that C_2 also inserts directly into the C—C bonds constituting the nanotube wall thus providing a fluent mechanism for forming strong covalent bonds between the CNTs and the UNCD crystallites[66] that constitute the microstructural components of these all-carbon self-composites.

HRTEM measurements will be required to elucidate the detailed microstructure of the UNCD/CNT composites. In a model structure in which the CNTs take the place of the GBs in pure UNCD films, the two-dimensional GBs would be replaced by one-dimensional carbon nanotubes with potentially drastic effects on thermoelectric performance. A likely result of such a structure would be that the electronic conductivity of the composite is very much enhanced because the carrier density in CNTs is quite low while the carrier mobility is very high. At the same time, the thermal conductivity can be expected to be held to a minimum because tight covalent bonds to the UNCD crystallites will disrupt the phonon spectrum of the "functionalized" nanotubes. The nanowire CNTs then might

function as one-dimensional conductors of electricity even though they are imbedded in a matrix of UNCD that has a very low thermal conductivity. Furthermore, the inherently large band gap of the diamond host material should aid in providing good carrier quantum confinement and consequently lead to still further enhancement of carrier mobilities.

The possibility of separately controlling electron and phonon transport in nanomaterials has been recognized for some time as already pointed out. More recently, one-dimensional structures such as Bi nanowires have been shown to have Seebeck coefficients in excess of $10^4\,\mu V\,K^{-1}$.[53] This is one of several promising experimental results in the new field of low-dimensional thermoelectrics that have given rise to an interesting theoretical approach to "reversible" electron transport based on a spatially varying chemical potential. A material with a delta function DOS doped in a prescribed way could in principle give thermoelectric performance approaching the Carnot efficiency with *ZT* values of 10 at 300 K.[54]

There clearly is much current interest in using CNTs and CNT composites for thermal management applications. Measurements of thermopower in CNTs have in fact been made.[67–69] Values of the Seebeck coefficient at 300 K are in the range 30–60 $\mu V\,K^{-1}$ and increase with temperature. From the slope of the thermopower curves versus temperature, one extrapolates values of the Seebeck coefficient at 1000 K which lies in the range 100–200 $\mu V\,K^{-1}$ assuming linear behavior. The data up to now do not extend to such high temperatures. It will be of considerable interest to determine the *ZT* values of UNCD/CNT composites at temperatures far above ambient. Such composites might possess many of the desirable properties which enable the "reversible" electron transport behavior postulated in model systems.[54]

5.5 Summary

The fullerenes, carbon nanotubes, and ultrananocrystalline diamond are exemplars par excellence of the profound differences in properties of nanoscale compared to bulk materials. These three nanostructured carbons are closely related energetically in that their free energies of formation differ one from each other by only a few kilocalories per mole. Nonetheless, and surprisingly, even though they are nanoscale materials their distinctive properties are also size determined and very roughly fall into three size categories: 1–2, 2–3, and 3–5 nanometers. The carbon nanostructurers are unstable with respect to graphite and diamond but stable with respect to grapheme sheets containing equivalent numbers of carbon

atoms. They derive their remarkable properties from the ability unique to carbon to rehybridize by virtue of the almost identical energies of the sp^2 and sp^3 electronic configurations. In the case of UNCD films, the rehybridization involves the carbon atoms at the grain boundaries which comprise about 10% all-carbon atoms in the films.

The topological and bond disorders at the ubiquitous grain boundaries in UNCD films impart qualities to this nanoscale material not possessed by bulk diamond which make it suitable for a variety of applications. Among these are microelectromechanical systems (MEMS), tribological coatings, electrochemical electrodes, biological sensors by surface derivatization, field emission devices, surface acoustic wave (SAW) devices, high-temperature all-diamond heterostructural diodes, and many others.

The dramatic effects of nanocrystallinity on electron and phonon transport properties are of particular interest. Bulk diamond is both an excellent electrical insulator and a superb thermal conductor. On the other hand, UNCD films are good electrical conductors, both n-type by virtue of the introduction of nitrogen and p-type by boron substitutions. At the same time, the films are very poor thermal conductors because of effective scattering of phonons at the grain boundaries. Extensive tight-binding density-functional calculations on UNCD and UNCD/CNT composites have given insight into the electronic states introduced into the band gap of diamond by the grain boundary carbons and into the bonding between UNCD and CNT. The calculations reveal a narrow peak in the density of states at the Fermi level due to the low dimensionality of UNCD films as well as the remarkable ability of carbon to rehybridize thereby forming many energetically closely spaced electronic states by linear combinations of atomic orbitals.

Recent developments in the theory of thermoelectric performance enhancement in low-dimensional materials suggest that UNCD and UNCD/CNT composites might fulfill many of the requirements that could lead to high and highly unusual thermoelectric figures of merit. A description of the present state of the art in thermoelectric power conversion is discussed in this chapter and directions are pointed out for achieving potentially significant improvements in conversion efficiencies using nanostructured carbon materials.

Acknowledgments

It is a pleasure to acknowledge the work of Drs. Richard Jackman and Oliver Williams, University College, London who did the Hall measure-

ments and of Professor Erhard Kohn, University of Ulm, who was instrumental in the fabrication of and measurements on the diamond diode. This work was supported by the US Department of Energy, BES-Materials Sciences under Contract W-31-100-ENG-38.

References

1. D. M. Gruen, "Conversion of Fullerenes to Diamond", US Patent 5,209,916 filed November 25, 1991.
2. D. M. Gruen, S. Liu, A. R. Krauss, and X. Pan, "Buckyball Microwave Plasmas: Fragmentation and Diamond-Film Growth", *J. Appl. Phys.*, *75*, 1758 (1994).
3. D. M. Gruen, S. Liu, A. R. Krauss, J. Luo, and X. Pan, "Fullerenes as Precursors for Diamond Film Growth Without Hydrogen or Oxygen Additions", *Appl. Phys. Lett.*, *64*, 1502 (1994).
4. D. M. Gruen, "Nanocrystalline Diamond Films", *Annu. Rev. Mater. Sci.*, *29*, 211–259 (1999); D. M. Gruen, "Ultrananocrystalline Diamond in the Laboratory and the Cosmos", *MRS Bull.*, 771 (October, 2001).
5. F. Benedic, F. Mohasseb, P. Bruno, F. Silva, G. Lombardi, K. Hassouni, and A. Gicquel, "Synthesis of Nanocrystalline Diamond Films in $Ar/H_2/CH_4$ Microwave Discharges", *Synthesis*, *Properties and Applications of Ultrananocrystalline Diamond*, 79–92, ed. D. M. Gruen, O. A. Shenderova, and A. Y. Vul, Springer, Berlin (2005).
6. F. Mohasseb, K. Hassouni, F. Benedic, G. Lombardi, and A. Gicquel, "Modelling of $Ar/H_2/CH_4$ Microwave Discharges Used for Nanocrystalline Diamond Growth", *Synthesis*, *Properties and Applications of Ultrananocrystalline Diamond*, 93–108, ed. D. M. Gruen, O. A. Shenderova, and A. Y. Vul, Springer, Berlin (2005).
7. G. Lombardi, K. Hassouni, F. Benedic, F. Mohasseb, J. Ropcke, and A. Gicquel, "Spectroscopic Diagnostics and Modeling of $Ar/H_2/CH_4$ Microwave Discharges Used for Nanocrystalline Diamond Deposition", *J. Appl. Phys.*, *96*, 6739 (2004).
8. T. Lin, G. Y. Yu, A. T. S. Wee, Z. X. Shen, and K. P. Loh, "Compositional Mapping of the Argon-Methane-Hydrogen System for Polycrystalline to Nanocrystalline Diamond Film Growth in a Hot-Filament Chemical Vapor Deposition System", *Appl. Phys. Lett.*, *77*, 2692 (2000).
9. V. I. Konov, A. A. Smolin, V. G. Ralchenko, S. M. Pimenov, E. D. Obraztsova, E. N. Loubnin, S. M. Metev, and G. Sepold, "D.c. Arc Plasma Deposition of Smooth Nanocrystalline Diamond Films", *Diamond Relat. Mater.*, *4*, 1073–1078 (1995).
10. L. C. Nistor, J. Van Landuyt, V. G. Ralchenko, E. D. Obraztsova, and A. A. Smolin, "Nanocrystalline Diamond Films: Transmission Electron Microscopy and Raman Spectroscopy Characterization", *Diamond Relat. Mater.*, *6*, 159–168 (1997).
11. A. N. Goyette, J. E. Lawler, L. W. Anderson, D. M. Gruen, T. G. McCauley, D. Zhou, and A. R. Krauss, "C_2 Swan Band Emission Intensity as a Function of C_2 Density", *Plasma Sources Sci. Technol.*, *7*, 149–153 (1998).

12. P. Zapol, L. A. Curtiss, H. Tamura, and M. S. Gordon, "Theoretical Studies of Growth Reactions on Diamond Surfaces", *Computational Materials Chemistry: Methods and Applications*, 266–307, eds. L. A. Curtiss and M. S. Gordon, Springer, Berlin (2004).
13. M. Sternberg, P. Zapol, and L. A. Curtiss, "Carbon Dimers on the Diamond (100) Surface: Growth and Nucleation", *Phys. Rev. B.*, *68*, 205330 (2003).
14. M. Sternberg, M. Kaukonen, R. M. Nieminen, and Th. Frauenheim, "Growth of (110) Diamond Using Pure Dicarbon", *Phys. Rev. B.*, *63*, 165414 (2001).
15. M. Sternberg, D. A. Horner, P. C. Redfern, P. Zapol, and L. A. Curtiss, "Theoretical Studies of CN and C_2 Addition to a (100)-(2 × 1) Diamond Surface: Nanocrystalline Diamond Growth Mechanisms", *J. Comput. Theor. Nanosci.*, *2*, 207 (2005).
16. P. Zapol, M. Sternberg, L. A. Curtiss, T. Frauenheim, and D. M. Gruen, "Tight-Binding Molecular-Dynamics Simulation of Impurities in Ultrananocrystalline, Diamond Grain Boundaries", *Phys. Rev. B*, *65*, 045403 (2002).
17. O. A. Williams, T. Zimmermann, M. Kubovic, A. Denisenko, E. Kohn, R. B. Jackman, and D. M. Gruen, "Electronic Properties and Applications of Ultrananocrystalline Diamond", *Synthesis*, *Properties and Applications of Ultrananocrystalline Diamond*, 373–382, ed. D. M. Gruen, O. A. Shenderova, and A. Y. Vul, Springer, Berlin (2005).
18. O. A. Williams, S. Curat, J. E. Gerbi, D. M. Gruen, and R. B. Jackman, "n-type Conductivity in Ultrananocrystalline Diamond Films", *Appl. Phys. Lett.*, *85*, 10 1680 (2004).
19. D. M. Gruen, "The Use of Nanocrystalline Diamond Films for Thermoelectric Energy Conversion", Patent Applied for (Oct. 2005).
20. A. C. Glatz, "Thermoelectric Energy Conversion", *Encyclopedia of Chemical Technology*, Third Edition, *22*, 900, John Wiley & Sons, New York (1983).
21. A. Hoffman, "Mechanism and Properties of Nanodiamond Films Deposited by the DC-GD-CVD Process", *Synthesis*, *Properties and Applications of Ultrananocrystalline Diamond*, 125–144, ed. D. M. Gruen, O. A. Shenderova, and A. Y. Vul, Springer, Berlin (2005).
22. J. E. Butler and H. Windischmann, "Developments in CVD-Diamond Synthesis During the Past Decade", *MRS Bull.*, 22 (September, 1998).
23. D. Zhou, D. M. Gruen, L. C. Qin, T. G. McCauley, and R. R. Krauss, "Control of Diamond Film Microstructure by Ar Additions to CH_4/H_2 Microwave Plasmas", *J. Appl. Phys.*, *84*, 1981 (1998).
24. P. Keblinski, D. Wolf, F. Cleri, S. R. Phillpot, and H. Gleiter, "On the Nature of Grain Boundaries in Nanocrystalline Diamond", *MRS Bull.*, 36 (September, 1998).
25. P. Keblinski, D. Wolf, S. R. Phillpot, and H. Gleiter, "Role of Bonding and Coordination in the Atomic Structure and Energy of Diamond and Silicon Grain Boundaries", *J. Mater. Res.*, *13*, 2077 (1998).
26. R. M. Hazen, *The Diamond Makers*, Cambridge University Press, Cambridge (1999).
27. S. Koizumi, K. Watanabe, M. Hasegawa, and H. Kanda, "Ultraviolet Emission from a Diamond pn Junction", *Science*, *292*, 1899 (2001); M. Nesladek, "Conventional n-type Doping in Diamond: State of the Art and Recent Progress", *Semicond. Sci. Technol.*, *20*, R19–R27 (2005).

28. T. Zimmermann, M. Kubovic, A. Denisenko, K. Janischowsky, O. A. Williams, D. M. Gruen, and E. Kohn, "Ultra-Nano-Crystalline/Single Crystal Diamond Heterostructure Diode", *Diamond Relat. Mater.*, *14*, 416–420 (2005).
29. P. Bruno and D. M. Gruen, Unpublished results.
30. J. Birrell, J. A. Carlisle, O. Auciello, D. M. Gruen, and J. M. Gibson, "Morphology and Electronic Structure in Nitrogen-Doped Ultrananocrystalline Diamond", *Appl. Phys. Lett.*, *81*, 2235 (2002).
31. J. E. Gerbi, O. Auciello, J. M. Gibson, D. M. Gruen, and J. A. Carlisle, "Bonding Structure in Nitrogen Doped Ultrananocrystalline Diamond", *J. Appl. Phys.*, *93*, 5606 (2003).
32. J. E. Gerbi, J. Birrell, M. Sardela, and J. A. Carlisle, "Macrotexture and Growth Chemistry in Ultrananocrystalline Diamond Thin Films", *Thin Solid Films*, *473*, 41–48 (2005).
33. S. Bhattacharyya, O. Auciello, J. Birrell, J. A. Carlisle, L. A. Curtiss, A. N. Goyette, D. M. Gruen, A. R. Krauss, J. Schlueter, A. Sumant, and P. Zapol, "Synthesis and Characterization of Highly-Conducting Nitrogen-doped Ultrananocrystalline Diamond Films", *Appl. Phys. Lett.*, *79*, 1441 (2001).
34. R. B. Jackman, Private communication.
35. F. J. Himpsel, J. A. Knapp, J. A. Van Vechten, and D. E. Eastman, "Quantum Photoyield of Diamond(111) – A Stable Negative-Affinity Emitter", *Phys. Rev. B*, *20*, 624–627 (1979).
36. D. Zhou, A. R. Krauss, T. D. Corrigan, T. G. McCauley, R. P. H. Chang, and D. M. Gruen, "Microstructure and Field Emission of Nanocrystalline Diamond Prepared From C_{60} Precursors", *J. Electrochem. Soc.*, *144*, No. 8 (August, 1997).
37. T. D. Corrigan, D. M. Gruen, A. R. Krauss, P. Zapol, and R. P. H. Chang, "The Effect of Nitrogen Addition to Ar/CH_4 Plasmas on the Growth, Morphology and Field Emission of Ultrananocrystalline Diamond", *Diamond Relat. Mater.*, *11*, 43–48 (2002).
38. A. Ya. Vul, E. D. Eidelman, and A. T. Dideikin, "Thermoelectric Effect in Field Electron Emission From Nanocarbon", *Synthesis*, *Properties and Applications of Ultrananocrystalline Diamond*, 383–394, ed. D. M. Gruen, O. A. Shenderova, and A. Y. Vul, Springer, Berlin (2005).
39. J. Davidson, Private communication.
40. Q. Chen, D. M. Gruen, A. R. Krauss, T. D. Corrigan, M. Witek, and G. M. Swain, "The Structure and Electrochemical Behavior of Nitrogen-Containing Nanocrystalline Diamond Films Deposited from CH_4/N_2/Ar Mixtures", *J. Electrochem. Soc.*, *148*, E44–E51 (2001).
41. Ph. Rychen, Ch. Provent, and L. Papunat, "DiaCell® by Adamant Technologies", 8th Applied Diamond Conference, Argonne National Laboratory (May 15–19, 2005).
42. W. Yang, O. Auciello, J. E. Butler, W. Gai, J. A. Carlisle, J. Gerbi, D. M. Gruen, T. Knickerbocker, T. L. Lasseter, J. N. Russell, Jr., L. M. Smith, and R. J. Hamers, "DNA-modified Nanocrystalline Diamond Thin-films as Stable, Biologically Active Substrates", *Nature Mater.*, 1 (November 24, 2002).
43. J. Wang, M. A. Firestone, O. Auciello, and J. A. Carlisle, "Surface Functionalization of Ultrananocrystalline Diamond Films by Electrochemical Reduction of Aryldiazonium Salts", *Langmuir*, *20*, 11450–11456 (2004).

44. A. Haertl, E. Schmich, J. A. Garrido, J. Hernando, S. C. R. Catharino, S. Walter, P. Feulner, A. Kromka, D. Steinmuller, and M. Stutzmann, "Protein-modified Nanocrystalline Diamond Thin Films for Biosensor Applications", *Nature Mater.*, 1 (August 23, 2004).
45. E. Kohn and W. Ebert, "Electronic Devices on CVD Diamond", *Low-Pressure Synthetic Diamond*, ed. B. Dischler and C. Wild, Springer, Berlin (1998).
46. W. Ebert, A. Vescan, T. H. Borst, and E. Kohn, "High-Current p/p$^+$-diamond Schottky diode", *IEEE Electron Devices Lett.*, *15*, 289 (1994).
47. M. Roser, C. A. Hewett, K. L. Moazed, and J. R. Zeidler, "High Temperature Reliability of Refractory Metal Ohio Contacts to Diamond", *J. Electrochem. Soc.*, *139*, 2001 (1992).
48. F. Cleri, P. Keblinski, L. Colombo, D. Wolf, and S. R. Phillpot, "On the Electrical activity of sp^2-Bonded Grain Boundaries in Nanocrystalline Diamond", *Europhys. Lett.*, *46*, 671–677 (1999).
49. S. Jiao, A. Sumant, M. A. Kirk, D. M. Gruen, A. R. Krauss, and O. Auciello, "Microstructure of Ultrananocrystalline Diamond Films Grown by Microwave Ar-CH_4 Plasma Chemical Vapor Deposition With or Without Added H_2", *J. Appl. Phys.*, *90*, 118 (2001).
50. L. D. Hicks and M. S. Dresselhaus, "Effect of Quantum-Well Structures on the Thermoelectric Figure of Merit", *Phys. Rev. B*, *47*, 12727–12731 (1993).
51. G. D. Mahan and J. O. Sofo, "The Best Thermoelectric", *Proc. Natl Acad. Sci.*, *93*, 7436–7439 (1996).
52. Y. M. Lin and M. S. Dresselbaus "Thermoelectric Properties of Superlattice Nanowires", *Phys. Rev. B*, *68*, 075304 (2003).
53. J. P. Heremans, "Thermoelectric Power, Electrical and Thermal Resistance, and Magnetoresistance of Nanowire Composites", *Proceedings of the Materials Research Society Symposium on Thermoelectric Materials 2003 – Research and Applications*, *Boston*, *MA*, *USA*, *793*, 3, ed. G. S. Nolas, J. Yang, T. P. Hogan, and D. C. Johnson (2003).
54. T. E. Humphrey and H. Linke "Reversible Thermoelectric Nanomaterials", *Phys. Rev. Lett.*, *94*, 096601 (2005).
55. A. C. Glatz, "Thermoelectric Energy Conversion", *Kirk-Othmer Encyclopedia of Chemical Technology*, Third Edition, *22*, 900, John Wiley & Sons, New York (1988).
56. R. Venkatasubramanian, E. Silvona, T. Colpitts, and B. O'Quinn, "Thin-Film Thermoelectric Devices With High Room-Temperature Figures of Merit", *Nature*, *413*, 597–602 (2001).
57. T. C. Harman, P. J. Taylor, M. P. Walsh, and B. E. LaForge, "Quantum Dot Superlattice Thermoelectric Materials and Devices", *Science*, *297*, 2229 (2002).
58. K. F. Hsu, S. Loo, F. Guo, W. Chen, J. S. Dyck, C. Uher, T. Hogan, E. K. Polychroniadis, and M. G. Kanatzidis, "Cubic $AgPb_mSbTe_{2+m}$: Bulk Thermoelectric Materials with High Figure of Merit", *Science*, *303*, 818 (2004).
59. J. Hartmann and M. Reichling, "Thermal Transport in Diamond", *Properties*, *Growth and Applications of Diamond*, 32, EMIS Datareviews Series 26, ed. M. H. Nazare and A. J. Neves (February, 2000).
60. J. E. Graebner, S. Jin, J. A. Herb, and C. F. Gardinier, "Local Thermal Conductivity in Chemical-vapor-deposited Diamond", *J. Appl. Phys.*, *76*, 3 (1994).

61. L. Nanver, DIMES Technical University, Delft, The Netherlands, Private communication; D. G. Cahill, W. K. Ford, K. E. Goodson, G. D. Mahan, A. Majumdar, H. J. Maris, R. Merlin, and S. R. Phillpot, "Nanoscale Thermal Transport", *J. Appl. Phys.*, *93*, 793 (2003).
62. D. M. Gruen, Unpublished results; T. M. Tritt, "Overview of Various Strategies and Promising New *Bulk* Materials for Potential Thermoelectric Applications", *MRS Symp. Proc.*, *691*, 3 (2002).
63. M. Sternberg, P. Zapol, and L. A. Curtis, "Electronic Structure Calculations of Nitrogen and Hydrogen in Diamond Twist Grain Boundaries", Paper given at the 2005 Applied Diamond Conference held at Argonne National Laboratory (May 16–19, 2005).
64. A. S. Barnard, S. P. Russo, and I. K. Snook, "Size Dependent Phase Stability of Carbon Nanoparticles: Nanodiamond Versus Fullerenes", *J. Chem. Phys.*, *118*, 5094, (2003); A. S. Barnard, S. P. Russo, and I. K. Snook, "Coexistence of Bucky Diamond with Nanodiamond and Fullerene Carbon Phases", *Phys. Rev. B*, *68*, 073406-1 (2003); A. S. Barnard, and I. K. Snook, "Phase Stability of Nanocarbon in One Dimension: Nanotubes Versus Diamond Nanowires", *J. Chem. Phys.*, *120*, 3817 (2004).
65. D. M. Gruen and J. W. Elam, "Nanotube-Diamond Composites", MRS Fall Meeting, Paper #Q2.3 (December 1–5, 2003).
66. D. Gruen, L. Curtiss, and P. Zapol, "Synthesis of Ultrananocrystalline Diamond/Nanotube Self-Composites by Direct Insertion of Carbon Dimer Molecules into Carbon Bonds", European Diamond Conference, Toulouse, France (September 11–16, 2005).
67. L. Grigorian, G. U. Sumanasekera, A. L. Loper, S. L. Fank, J. L. Allen, and P. C. Eklund, "Giant Thermopower in Carbon Nanotubes: A One-dimensional Kondo System", *Phys. Rev. B*, *60*, No. 16 (1999).
68. J. Hone, M. C. Liaguno, N. M. Newes, A. T. Johnson, J. E. Fischer, D. Walters, M. J. Casavant, J. Schmidt, and R. E. Smalley, "Electrical and Thermal Transport Properties of Magnetically Aligned Single Wall Carbon Nanotube Films", *Appl. Phys. Lett.*, *77*, No. 5 (2000).
69. L. Shi, D. Li, C. Yu, W. Jang, D. Kim, Z. Yao, P. Kim, and A. Majumdar, "Measuring Thermal and Thermoelectric Properties of One-Dimensional Nanostructures Using a Microfabricated Device", *J. Heat Transfer*, *125*, 881 (2003).

6 Plasma-Assisted Synthesis: Plasma Experimental Diagnostics and Modeling

Fabien Bénédic, Guillaume Lombardi, Khaled Hassouni, Francis Mohasseb, and Alix Gicquel

Laboratoire d'Ingénierie des Matériaux et des Hautes Pressions, UPR 1311 CNRS, Université Paris 13, Villetaneuse, France

Introduction

Low-pressure glow discharges are widely used for material surface processing such as etching, deposition of thin films, or modifications of surface properties. In order to understand and anticipate the properties of the processed material, as well as its performance for specific applications, it is necessary to know the precise composition of the plasma in interaction with the surface of the material during the treatment process. In the field of diamond film synthesis using plasma-enhanced chemical vapor deposition (PECVD) systems, attention should be paid to the absolute density of key species. Among others, the CH_3 radical that is assumed to be the growth precursor of polycrystalline diamond (PCD) films,[1] the C_2 molecule which is generally recognized, in spite of recent discussions,[2] to play a major role in nanocrystalline diamond (NCD) deposition process,[3–5] and the atomic hydrogen H which is an etching agent,[6] should be carefully considered. Besides, some key process parameters, such as the gas temperature which fundamentally acts in the plasma chemistry,[7] should be investigated. These investigations could hopefully help in the control and optimization of the deposition process if they are able to link the local plasma characteristics to the process control parameters (total pressure, feed gas composition, input power, etc.).

These requirements may be achieved at least partly by performing *in situ* plasma diagnostics. Among the different existing techniques, optical diagnostics are particularly suitable because they are non-intrusive, species-selective, and possibly yield good space- and time-resolved information.[8] Optical emission spectroscopy (OES) is the most popular plasma diagnostic technique because it can be easily implemented and is cost effective. It consists in analyzing the plasma radiative emission,

which allows us to reach information relative to the species in electronic excited states. However, this technique suffers from different drawbacks. Especially the information about the species detected in the plasma is not necessarily representative of atoms and molecules in their ground states that form the majority of the medium. This weakness and the resulting lack of knowledge are generally overcome by using an external light source in order to reach data relative to absorbing species. In the case of absorption spectroscopy (AS), the response of the medium is a decrease of the transmitted light intensity, whereas laser-induced fluorescence (LIF) produces a change in the radiative emission of the plasma. Both methods are able to provide information relative to the ground states or low-lying levels of atoms and molecules. Even if laser-based techniques, such as LIF, or cavity ring down spectroscopy (CRDS), are really efficient for monitoring species density and internal energy of molecules, they are costly and often difficult to put into practice. If the purpose is essentially to measure the absolute density of some species without any particular requirements for the spatial resolution, using a simpler and inexpensive technique, a meaningful diagnostic technique could be broadband absorption spectroscopy (BAS).

If optical diagnostics are able to provide the absolute density of some reactive species and the gas temperature, as well, this information remains partial and a more complete characterization of the gas phase is required in order to understand the main phenomena involved in the diamond growth process. Indeed, in this field the studied plasmas are composed of many species, especially carbon-containing species, that are liable to take part in the growth mechanisms. These species, stable or not, radical, aliphatic, or aromatic, are often difficult to detect *in situ* in the operating conditions of the synthesis process. It is even trickier, or impossible, to analyze the chemical composition of the considered discharge at the plasma/substrate interface, where the deposition mechanisms finally occur. Therefore, modeling of the gas phase is required in order to provide a more complete description of the discharges. First, thorough studies aiming to accurately describe the plasma chemistry must be conducted in order to take into account the major species and the most probable thermochemical reactions. More or less sophisticated models can be developed according to the final goals. Numerical schemes able to depict the physical phenomena involved in the discharges must then be developed and may have different degrees of geometry: zero-dimensional, where the plasma is assumed to be quasi-homogeneous; one-dimensional, where the non-uniformity of the plasma is taken into account along a particular

direction; two- or three-dimensional, depending on the plasma symmetry. The highest description level corresponds to self-consistent models, where the equations describing both the plasma and the external energy source are solved together. Generally a suitable compromise between the complexity of the thermochemical reaction scheme and the complexity of the physics has to be adopted. Besides, although the plasma modeling is quite powerful for investigating a plasma discharge, the use of experimental techniques is still essential in order to support and validate theoretical data.

In this chapter we present the investigations carried out in order to improve the understanding and control of nanocrystalline diamond film synthesis using a microwave plasma-assisted chemical vapor deposition (MPACVD) process fed with $Ar/H_2/CH_4$ gas mixtures. The global approach that was followed consists in finding the typical growth conditions of NCD films, developing a thermochemical plasma model able to provide information on the main features of the $Ar/H_2/CH_4$ microwave discharges versus deposition parameters, and performing optical diagnostics in order to support the theoretical results. The first section reports the experimental device employed for NCD deposition along with the materials used for the discharge optical diagnostics using OES and BAS techniques. In the second section, the spectroscopic systems investigated and the methods used are presented, as well as the thermochemical model developed in order to estimate the discharge composition, the gas temperature, and the average electron energy in the frame of a quasi-homogeneous plasma assumption. The third section focuses on the results of film deposition experiments in typical NCD growth conditions and on the characterization of the corresponding microwave discharges by optical diagnostics. The experimental measurements are discussed with respect to results in the literature, and presented along with calculation results in order to partly check the validity of the plasma model. In the last section, parametric studies are completed with the plasma model as a function of some process parameters, so as to draw the main characteristics of the investigated discharges. The calculation results are analyzed and discussed, especially in terms of C_2 production mechanisms and efficiency. Comparisons with the H_2/CH_4 plasmas commonly used for PCD layer deposition are also done, which enables us to infer some conclusions with respect to the NCD deposition process.

6.1 Experimental Details

6.1.1 MPACVD Reactor and Process Parameters

The deposition experiments and plasma diagnostics were performed in a MPACVD device widely used with H_2/CH_4 gas mixtures for PCD film deposition,[9] monocrystalline diamond growth,[10] plasma diagnostics,[11] and plasma modeling[12]. It mainly consists of a quartz bell-jar low-pressure chamber 10 cm in diameter and 17 cm in height, inserted in a resonant cavity of 25 cm diameter and 35 cm height (Fig. 6.1). The dimensions of the microwave cavity have been chosen in order to favor the TM_{023} mode of a 2.45 GHz frequency electromagnetic wave. The plasma discharge is ignited in the microwave cavity in an $Ar/H_2/CH_4$ gas mixture, just above a 5 cm diameter molybdenum substrate holder held in the center of the chamber, with a 1200 W, 2.45 GHz Sairem microwave power supply. An additional heating system composed of a high-current flowing graphite resistor located in the substrate holder allows control of the substrate temperature during growth independently of the other growth parameters. The surface temperature is monitored using an infrared bichromatic pyrometer working at wavelengths of 1.52 and 1.64 μm.

The choice of the deposition conditions was based on results in the literature. According to various anteriority papers, one of the suitable gas mixtures used for NCD deposition is composed of CH_4, employed as a carbon precursor, highly diluted in argon.[13] However, as it is difficult to obtain stable microwave discharges in an Ar/CH_4 mixture when using

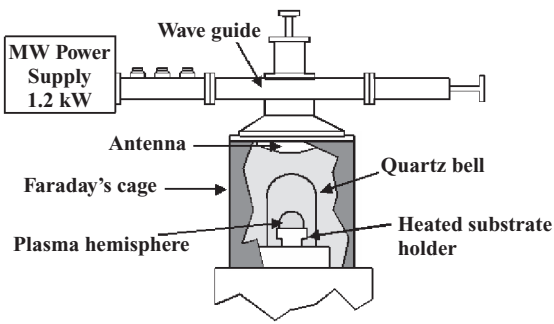

Figure 6.1 Schematic diagram of the MPACVD bell jar reactor used for nanocrystalline diamond deposition and plasma diagnostics.

cavity coupling systems, a small amount of H_2 may be added in the feed gas in order to maintain stable plasmas at relatively high microwave power.[14,15] Therefore, the experimental investigations were performed with a methane percentage in the feed gas set to 1%, while H_2 and Ar concentrations, denoted $\%H_2$ and %Ar respectively, were changed with the input microwave power (MWP). For a given $\%H_2$ in the feed gas, the MWP was set at the maximum value that allowed us to obtain an optimal coupling with a stable hemispherical plasma of 5 cm diameter located just above the substrate surface. Using this procedure the increase of $\%H_2$ was systematically accompanied by a decrease of %Ar so as to keep the CH_4 percentage at 1%, and by the use of a higher value for MWP. Thus, the typical discharge conditions used for NCD deposition and spectroscopic diagnostics were obtained with the four sets of feed gas composition and microwave power ($\%Ar:\%H_2:\%CH_4$-MWP) exhibited in Fig. 6.2: 97 : 2 : 1-500 W, 96 : 3 : 1-600 W, 94 : 5 : 1-700 W, and 92 : 7 : 1-800 W. The total gas pressure was maintained at 20000 Pa (200 mbar) and the total gas flow rate at 250 sccm. For the synthesis experiments the substrate temperature was maintained at approximately 1170 K, while the deposition time was set to 4.0 h.

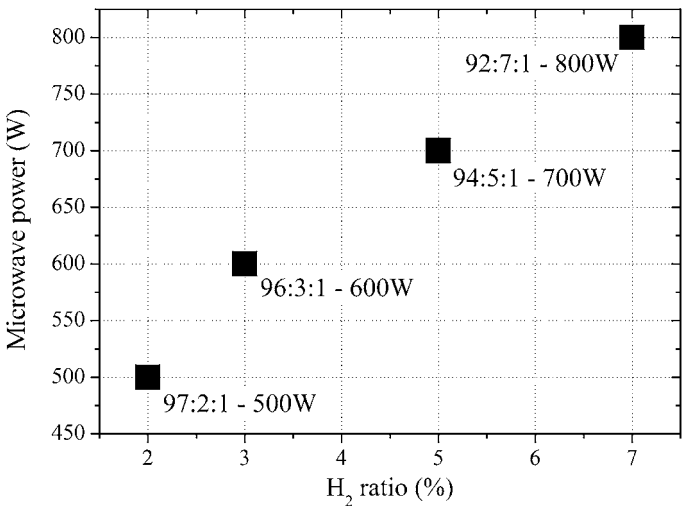

Figure 6.2 Microwave power as a function of H_2 ratio for 200 mbar and 250 sccm, corresponding to the coupled sets of experimental process parameters considered in this work. The gas composition and the microwave power are specified for each dot.

6.1.2 Arrangements for Spectroscopic Diagnostics

The optical arrangement used around the bell jar reactor for OES and BAS diagnostics is shown in Fig. 6.3. A special silica bell with optical arms 25 cm in length and 2 cm in diameter and a modified Faraday's cage were used in order to perform the spectroscopic measurements in the typical growth conditions described above. This particular design of the reaction chamber allows us to avoid any deposition on the optical windows during the measurements, while preventing microwave leaks and maintaining a constant shape of the plasma for the various conditions investigated.[16]

Two monochromators were used, depending on the required spectral resolution. The first one is a high-resolution system and consists of a 1 m focal length Jobin Yvon THR 1000 monochromator, mounted with a 1800 g mm^{-1} grating blazed at 450 nm and equipped with a 1024 × 128 pixel CCD EG&G. The monochromator entrance slit was connected to an optical fiber and set to 10 μm in order to reach a resolution around 0.038 nm. The second system has a lower resolution and consists of a 32 cm focal length Jobin Yvon Spex 320 monochromator, mounted with a 1800 g mm^{-1} grating blazed at 400 nm and equipped with a 1024 × 128 pixel UV-sensitive Jobin Yvon CCD. A resolution of 0.12 nm was measured using the 253.7 nm line of a mercury calibration lamp for an entrance slit of 20 μm.

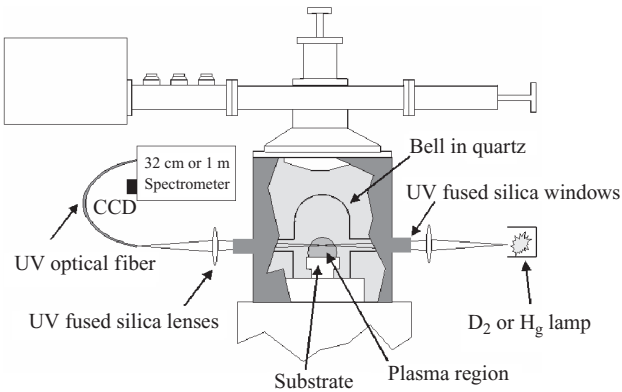

Figure 6.3 Schematic diagram of the optical mount used for optical emission spectroscopy and broadband absorption spectroscopy diagnostics of the $Ar/H_2/CH_4$ microwave discharges.

Two light sources were used for absorption measurements. The first one is a UV Oriel deuterium lamp (30 W, ref. 63163) powered by a stabilized supply (ref. 68840). The second system is a visible light source consisting of an Oriel mercury arc lamp (100 W, ref. 68806) monitored with a stabilized power supply (ref. 6281). Two sets of fused silica lenses focused the light beam coming from the lamps via a collimator in the middle of the discharge and the beam was transmitted through the plasma on the optical fiber linked to the spectrometer. Using this system, the plasma volume probed during absorption measurements was a cylinder of approximately 3 mm diameter. The absorption length, corresponding then to the constant plasma diameter, was estimated to be around $L = 5$ cm.

The transmittance spectrum was obtained for each experimental condition by acquiring four spectra in the following order: an emission spectrum, I_{Plasma}, consisting of the light coming from the microwave discharge with the lamp blocked off, a main spectrum, $I_{Plasma+Lamp}$, corresponding to the light from the lamp after passing through the discharge added to the plasma emission, a lamp spectrum, I_{Lamp}, consisting of the light from the lamp when the plasma was off, and finally a dark spectrum, I_{Dark}, with the lamp blocked off and the plasma off. The transmittance T was then deduced from the following relation:[17]

$$T = \frac{I_{Plasma+Lamp} - I_{Plasma}}{I_{Lamp} - I_{Dark}} \qquad \text{Eq. (6-1)}$$

6.2 Fundamentals of Plasma Diagnostics

6.2.1 Optical Emission and Broadband Absorption Spectroscopy

6.2.1.1 Choice of the Spectroscopic Systems Investigated

Figure 6.4 shows a typical $Ar/H_2/CH_4$ plasma emission spectrum obtained over a large wavelength range from 200 to 700 nm including UV and visible spectral ranges. For the experimental conditions considered in this work, the $Ar/H_2/CH_4$ discharges display an intense green color attributed to the emission of the C_2 dimer ($d^3\Pi_g \rightarrow a^3\Pi_u$) Swan system (0,0) vibrational transitions that occur at 516.5 nm. Four other bands of this system can also be easily distinguished in the visible range: the (1,0), (0,1), (2,0), and (0,2) transitions at 473.7, 563.5, 438.3, and 619.1 nm, respectively. The ($D^1\Sigma_u^+ \rightarrow X^1\Sigma_g^+$) electronic transition of C_2 molecules,

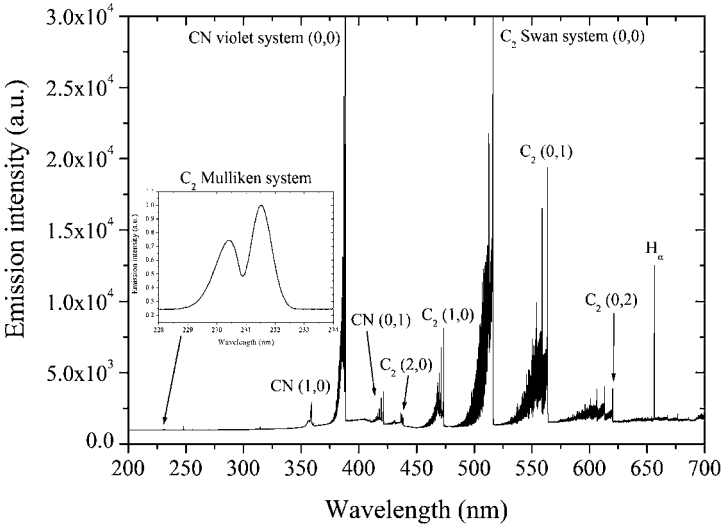

Figure 6.4 Emission spectrum in the UV and visible spectral ranges of a 97 : 2 : 1-500 W $Ar/H_2/CH_4$ microwave discharge containing around 100 ppm N_2 under 200 mbar (line identification after ref. [18]).

known as the Mulliken system, is also noticeable in the UV range at 231.3 nm, whereas the H-atom Balmer transition H_α ($n = 3 \rightarrow n = 2$) is located at 656.3 nm. Besides, around 100 ppm of nitrogen impurities were added to the feed gas in order to produce the CN radical in the discharge as a thermometer species that may be used to estimate some rotational temperatures. Then, the violet system, i.e., the ($B^2\Sigma^+ \rightarrow X^2\Sigma^+$) electronic transition, of the CN radical can be noticed in the spectrum showed in Fig. 6.4 through the (0,0), (0,1), and (1,0) vibrational transitions that appear at 388.3, 421.6, and 359.0 nm, respectively.

Table 6.1 summarizes the characteristics of the species and spectroscopic systems selected among those described above for the investigation of the discharges. The C_2 Mulliken system and the intense C_2 Swan system (0,0) vibrational band were chosen in order to determine the densities of C_2 molecules. These systems were also considered for the estimation of rotational temperatures, as well as the intense CN violet system $\Delta v = 0$ ($v', v'' = 0$–3) vibrational transitions.

6.2.1.2 C_2 Mulliken System

The major interest in studying this system is that the transition occurs between the $D^1\Sigma_u^+$ excited state and the $X^1\Sigma_g^+$ ground level, whereas the

Table 6.1 Species and Spectroscopic Systems Selected in the Visible and UV Ranges for the Investigation of the $Ar/H_2/CH_4$ Microwave Discharges. The Information Obtained Through Emission and Absorption Spectroscopy Is Specified for All the Spectroscopic Systems[19]

Species	Electronic transition	Name	Wavelength (nm)	E (eV)	Ref.	Measurements	
						Emission	Absorption
C_2	$d^3\Pi_g \rightarrow a^3\Pi_u$	Swan (0,0)	516.5	$a^3\Pi_u$: 0.089 $d^3\Pi_g$: 2.59	[20] [21]	$T_{rot}[C_2(d^3\Pi_g)]$	$N[C_2(a^3\Pi_u)]$ $T_{rot}[C_2(a^3\Pi_u)]$
	$D^1\Sigma_u^+ \rightarrow X^1\Sigma_g^+$	Mulliken	231.3	$D^1\Sigma_u^+$: 5.36	[21]	$T_{rot}[C_2(D^1\Sigma_u^+)]$	$N[C_2(X^1\Sigma_g^+)]$ $T_{rot}[C_2(X^1\Sigma_g^+)]$
CN	$B^2\Sigma^+ \rightarrow X^2\Sigma^+$	Violet (0,0)	388.3	$B^2\Sigma^+$: 3.19	[22]	$T_{rot}[CN(B^2\Sigma^+)]$	$T_{rot}[CN(X^2\Sigma^+)]$

Swan system links the $d^3\Pi_g$ and $a^3\Pi_u$ excited levels, the latter lying 0.089 eV above the ground state.[20] The $D^1\Sigma_u^+$ level is 5.36 eV above the $X^1\Sigma_g^+$ ground state[21] and its radiative lifetime is 14 ns[23]. It has been pointed out in several studies that, due to the low energy difference typically lower than the thermal energy of heavy species in microwave discharges, the $X^1\Sigma_g^+$ and $a^3\Pi_u$ states are in thermal equilibrium for the considered moderate pressure.[24,25] This partial equilibrium situation, described by a Boltzmann distribution of the electronic levels, makes possible the determination of the $a^3\Pi_u$ density from the $X^1\Sigma_g^+$ population and the ground state rotational temperature. Moreover, the next electronically excited state of C_2 is the $b^3\Sigma_g^-$ level with an energy 0.8 eV above the ground state. The population of this state and those with greater energy should therefore be negligible with respect to the populations of the $X^1\Sigma_g^+$ and $a^3\Pi_u$ levels. Consequently, it is then possible to determine an accurate estimation of the total C_2 density in the discharge by summing the $a^3\Pi_u$ and $X^1\Sigma_g^+$ populations.

Further, since the energy separation between rotational levels in a given vibrational state is typically smaller than heavy-species translation energy, all "heavy-species–heavy-species" collisions produce a change in the rotational quantum number of diatomic molecules. Consequently, the rotational populations of sufficiently long-lived vibrational states would be characterized by a Boltzmann distribution governed by the gas kinetic temperature. Then, the longer the lifetime is of a considered rovibronic state, the more efficient is the thermalization of the rotational levels with the heavy-species kinetic mode. For this reason, the choice of the $C_2(X^1\Sigma_g^+)$ ground state to estimate the gas temperature through its rotational temperature is particularly relevant compared to all other excited states. Besides, for the considered pressure of 200 mbar, the "heavy-species–heavy-species" high collision rate constant must enhance the thermalization between rotational and translational modes.

The C_2 Mulliken system was thus investigated by both OES and BAS. The former technique allowed us to measure the rotational temperature of the $D^1\Sigma_u^+$ excited state, $T_{rot}[C_2(D^1\Sigma_u^+)]$. The latter enabled us to measure the rotational temperature of the $X^1\Sigma_g^+$ ground state, $T_{rot}[C_2(X^1\Sigma_g^+)]$, that corresponds to the gas temperature, and to estimate the absolute density of the ground state, $N[C_2(X^1\Sigma_g^+)]$. The total C_2 density $N[C2]^{\text{Mull.}}$ within the discharge was then determined following the procedure described in the previous paragraph. Because the Mulliken system is formed of diffuse and smooth R and P rotational branches,[26] a high-wavelength resolution is not required and we used the low-resolution spectroscopic setup. The four spectra needed for estimation of the transmittance function were

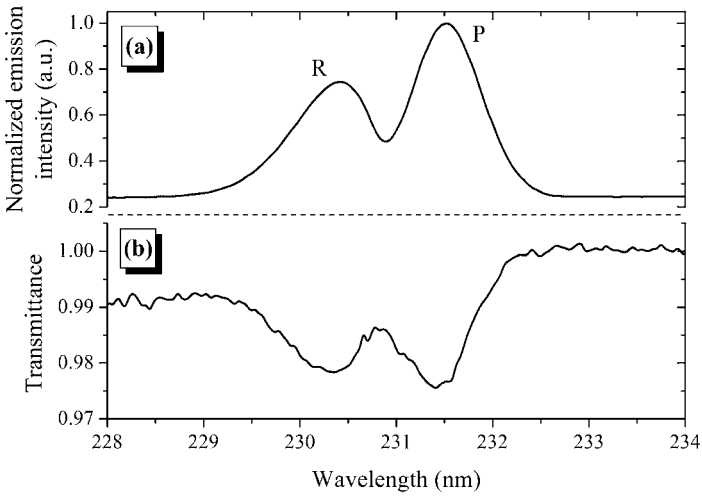

Figure 6.5 Typical examples of spectra obtained around 231 nm for the $C_2(D^1\Sigma_u^+–X^1\Sigma_g^+)$ Mulliken system for a 97 : 2 : 1-500 W $Ar/H_2/CH_4$ plasma. (a) $D^1\Sigma_u^+ \rightarrow X^1\Sigma_g^+$ emission spectrum. (b) $D^1\Sigma_u^+ \leftarrow X^1\Sigma_g^+$ absorption spectrum.[27]

acquired in 30 min by setting the exposure time to 1 s and a number of 300 accumulations. Figure 6.5 shows typical examples of $C_2(D^1\Sigma_u^+–X^1\Sigma_g^+)$ Mulliken system emission and absorption spectra obtained for a 97 : 2 : 1-500 W $Ar/H_2/CH_4$ microwave discharge.

The methods for reaching $T_{rot}[C_2(X^1\Sigma_g^+)]$ and $N[C_2(X^1\Sigma_g^+)]$ from the $D^1\Sigma_u^+ \leftarrow X^1\Sigma_g^+$ absorption and $T_{rot}[C_2(D^1\Sigma_u^+)]$ from the $D^1\Sigma_u^+ \rightarrow X^1\Sigma_g^+$ emission were widely described in ref. [27]. Basically, $T_{rot}[C_2(X^1\Sigma_g^+)]$ and $T_{rot}[C_2(D^1\Sigma_u^+)]$ are first determined from the P–R peak branch separation of the absorption and emission spectra, respectively.[27,28] Then, $N[C_2(X^1\Sigma_g^+)]$ is evaluated by fitting a theoretical absorbance curve to the experimental absorbance using the temperature determined from the P–R branch separation and assuming an equilibrium between the rotational and vibrational temperatures. Figure 6.6 shows an example of the simulated and experimental $C_2(D^1\Sigma_u^+ \leftarrow X^1\Sigma_g^+)$ absorbance curves for a 97 : 2 : 1-500 W $Ar/H_2/CH_4$ microwave discharge. A rotational value of 3600 K was determined from the P–R peak branch separation and a ground state density of $1.6 \times 10^{13}\,cm^{-3}$ was deduced from the best match of both spectra. The total C_2 density was then estimated to be $8.8 \times 10^{13}\,cm^{-3}$. Taking into account various error sources (absorption length, spectroscopic constants, signal weak intensity, etc.), the accuracy of the methods developed to reach $T_{rot}[C_2(X^1\Sigma_g^+)]$, $T_{rot}[C_2(D^1\Sigma_u^+)]$, and $N[C_2]^{exp}$ was evaluated to be around ±500 K, ±300 K, and ±50%, respectively.

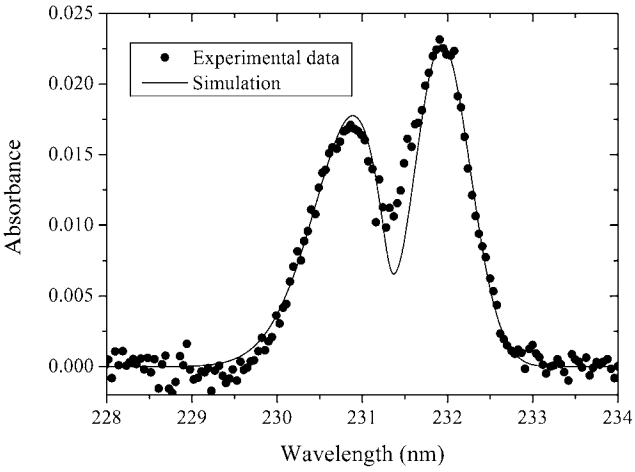

Figure 6.6 $C_2(D^1\Sigma_u^+ \leftarrow X^1\Sigma_g^+)$ simulated absorbance curve compared to experimental data for a 97:2:1-500 W $Ar/H_2/CH_4$ microwave discharge. The C_2 ground state density was estimated at $1.6 \times 10^{13}\,cm^{-3}$ from the theoretical curve, and the rotational temperature at 3600 K from the P–R peak branch separation.[27]

6.2.1.3 C_2 Swan System

The $a^3\Pi_u$ state is metastable while the $d^3\Pi_g$ level, located at energy value of 2.59 eV above the ground state,[21] has a radiative lifetime of 120 ns.[29] For the relatively high gas temperature usually measured in moderate pressure microwave discharges, the $a^3\Pi_u$ level, which is a low-lying level (≈1000 K above the ground state), is significantly populated.[30,31] Moreover, one can take advantage of the metastable $a^3\Pi_u$ state and long radiative lifetime $d^3\Pi_g$ level, in order to determine the gas temperature from the rotational temperature estimated for the $v = 0$ vibrational level of either excited state.

Both emission and absorption of the C_2 Swan system (0,0) band were then investigated in order to get complementary information about the C_2 density and the gas temperature. BAS was used to obtain the density and the rotational temperature of $a^3\Pi_u$ state, $N[C_2(a^3\Pi_u)]$ and $T_{rot}[C_2(a^3\Pi_u)]$, respectively. Knowledge of these values enabled us to estimate the density of the ground state $N[C_2(X^1\Sigma_g^+)]$ and to deduce from the Swan system the total C_2 density, $N[C_2]^{Swan}$, within the plasma by summing the population of the two first states as explained above. OES was used to estimate the rotational temperature of the $d^3\Pi_g$ state, denoted $T_{rot}[C_2(d^3\Pi_g)]$. The high-

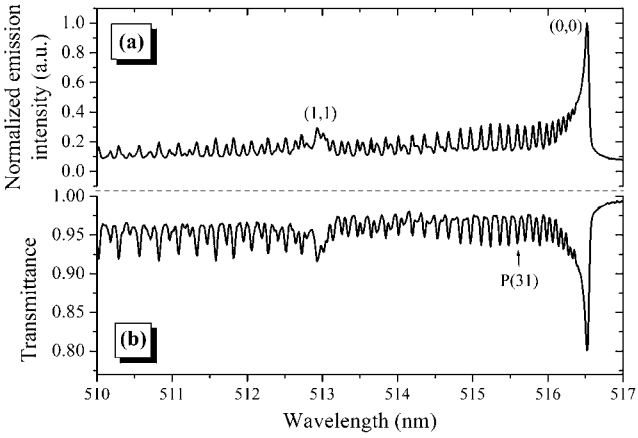

Figure 6.7 Typical examples of spectra obtained at 516.5 nm for the $C_2(d^3\Pi_g–a^3\Pi_u)$ Swan system for a 97 : 2 : 1-500 W $Ar/H_2/CH_4$ plasma. (a) $d^3\Pi_g \rightarrow a^3\Pi_u$ emission spectrum. (b) $d^3\Pi_g \leftarrow a^3\Pi_u$ absorption spectrum.[27]

resolution monochromator was used and due to the strong signal that characterizes the Swan band in $Ar/H_2/CH_4$ microwave discharges, it was possible to reduce the total acquisition time down to 10 min, by setting an exposure time of 16 ms and a number of 8000 accumulations. Figure 6.7 shows typical examples of emission and absorption spectra obtained for the $C_2(d^3\Pi_g–a^3\Pi_u)$ Swan system (0–0) transition in a 97 : 2 : 1-500 W $Ar/H_2/CH_4$ microwave discharge.

The rotational temperatures of lower and upper electronic levels were determined from Boltzmann plots deduced from the absorption and emission spectra, respectively. Details of the method, as well as on rotational lines that are convenient for the determination of the rotational temperature of the Swan system upper and lower states, may be found in refs. [27,32,33]. The accuracy of the temperature values was estimated for both emission and absorption to be around ±300 K. The $N[C_2(a^3\Pi_u)]$ density, corresponding to the number of C_2 molecules on the lower electronic level, was estimated from the absorption intensity of the rotational line P ($J'' = 31$) at 515.7 nm (Fig. 6.7).[27,34] The standard deviation of the values of the density thus obtained was estimated at approximately ±50%. For the example of Fig. 6.7, the density of the $a^3\Pi_u$ electronic state was estimated with this method at $N[C_2(a^3\Pi_u)] = 2 \times 10^{14}\,cm^{-3}$ with a rotational temperature $T_{rot}[C_2(a^3\Pi_u)] = 3320$ K. This led to an estimation of other populations such that $N[C_2(X^1\Sigma_g^+)] = 5 \times 10^{13}\,cm^{-3}$ and $N[C_2]^{Swan} = 2.5 \times 10^{14}\,cm^{-3}$. These values are consistent with those calculated from the Mulliken system.

6.2.1.4 CN Violet System

Both BAS and OES were also performed on the intense $\Delta v = 0$ ($v', v'' = 0$–3) vibrational transitions of the CN violet system located between 385 and 389 nm. The experimental procedure used to acquire the transmittance spectra is similar to the one used in the case of the C_2 Swan band. As far as an efficient thermalization of the translational and rotational modes exists, the choice of the violet system involving the particularly long-lived upper state (390 ns)[35] and the ground state is relevant for the estimation of the gas temperature. Presented in Fig. 6.8 is an example of emission and absorption spectra acquired for the ($B^2\Sigma^+$–$X^2\Sigma^+$) CN violet system in a 97 : 2 : 1-500 W $Ar/H_2/CH_4$ microwave discharge.

For both emission and absorption spectra, the rotational temperatures $T_{rot}[CN(B^2\Sigma^+)]$ and $T_{rot}[CN(X^2\Sigma^+)]$ were estimated from the best fit between simulated and experimental spectra. The fitting procedure makes use of LIFBASE v1.6[36] and assumes a thermal equilibrium between the vibrational and rotational modes. The accuracy of the method was estimated to be the same as that for the C_2 Swan system, i.e., ±300 K. As an example, for a 97 : 2 : 1-500 W $Ar/H_2/CH_4$ microwave discharge, a value of $T_{rot}[CN(X^2\Sigma^+)]$ equal to 3950 K was estimated using the absorption spectrum shown in Fig. 6.8.

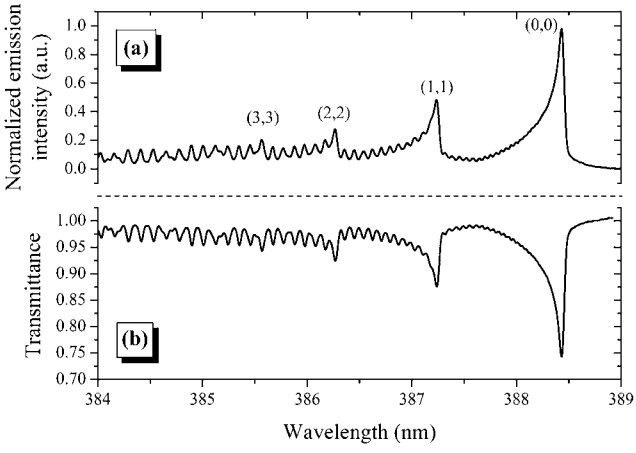

Figure 6.8 Typical examples of spectra obtained between 385 and 389 nm for the ($B^2\Sigma^+$ –$X^2\Sigma^+$) CN violet system for a 97 : 2 : 1-500 W $Ar/H_2/CH_4$ plasma. (a) $B^2\Sigma^+ \rightarrow X^2\Sigma^+$ emission spectrum. (b) $B^2\Sigma^+ \leftarrow X^2\Sigma^+$ absorption spectrum.[19]

6.2.2 Plasma Modeling

The $Ar/H_2/CH_4$ microwave discharges suitable for NCD film deposition are characterized by a strong thermal and chemical non-equilibrium. Consequently, the numerical model developed for investigating such plasmas distinguishes two different energy modes: the heavy-species translation–rotation (t–r) mode, characterized by the gas temperature T_g, and the electron translation mode (e). Due to the relatively high gas pressure, a thermal equilibrium was assumed between the vibrational modes of molecular species and the t–r mode.

As far as chemistry is concerned, the considered discharges are characterized by an H/C ratio which ranges between 8 and 18. For these H/C values, heavy hydrocarbons and soot particles may be formed for some discharge conditions.[37] However, in this chapter we focus only on situations where the formation of these compounds is limited and may be neglected. These situations correspond to gas temperatures higher than 2000 K.[38] Consequently, only species containing up to two carbon atoms were considered in the present model, whereas a more accurate description of the kinetics of these discharges taking into account the possible formation of heavier hydrocarbons and soot particles may be found elsewhere.[39]

Therefore the chemistry of the considered plasmas was described by taking into account neutral and charged hydrogen compounds (H_2, H, H (n = 2), H(n = 3), H^+, H_2^+, and H_3^+), hydrocarbon molecules C_xH_y (x = 1–2, y = 0–6) and their corresponding positive ions (C^+, CH_{3-5}^+, C_2^+, $C_2H_{1-6}^+$), as well as argon-based compounds (Ar, Ar^*, Ar^+, ArH^+, and ArH^{+*}, where * denotes the metastable state) and the singlet state of methylene, $^1CH_2$. These 38 species are involved in a 147 chemical reaction mechanism that is based on the model developed for moderate-pressure H_2/CH_4 plasmas by Hassouni et al.[40,41] The main reactions added to this model are those describing the chemistry of argon compounds.[19] To summarize, the full kinetics model used to describe the chemistry in $Ar/H_2/CH_4$ discharges involves four reaction groups. The first one deals with the chemistry of pure-hydrogen discharge and involves electron impact reactions leading to H_2 dissociation, H_2 and H ionization, and H-atom excitation. It also involves ionization through the quenching of H-atom excited states, ion conversion reactions, and thermal dissociation of H_2. The second reaction group describes the thermal hydrocracking of the H_2/CH_4 mixture. The third group describes the chemistry of hydrocarbon ions. It includes electron impact ionization reactions of hydrocarbon molecules, charge transfer reactions between H_3^+ and hydrocarbon molecules,

charge transfer reactions between hydrocarbon molecules and hydrocarbon ions, and dissociative recombination of hydrocarbon ions. The last reaction group includes all the reactions due to the presence of argon: electron-impact excitation and ionization of argon, charge transfer and ion conversion processes between Ar^+ and ArH^+ ions and hydrogen or hydrocarbon ions, and finally ionization and dissociation of hydrocarbon molecules through collisions with metastable argon.[19]

The thermochemical model discussed above is used to describe the investigated discharges under the assumption of quasi-homogeneity of the plasma. The details of the model based on this hypothesis are extensively described in ref. [41] and we only summarize its main features below. In the quasi-homogeneous plasma approximation the discharge is assumed to be formed of a homogeneous plasma volume, where all the plasma characteristics are constant, and of a thin boundary layer, where species density and plasma temperature vary linearly (Fig. 6.9).

Under this assumption the time evolution of the species density in the bulk of the discharge is governed by a set of ordinary differential equations that may be written:[41]

$$\frac{dy_i}{dt} = \frac{(W_i + R_i)}{\rho} \qquad \text{Eq. (6-2)}$$

where y_i is the mass fraction of species i and ρ is the total plasma density. W_i and R_i are the net production rates of species i by gas phase processes and surface processes, respectively. The method used to estimate W_i and R_i is discussed in detail in ref. [41].

The net production rate W_i depends on the species densities and on the reaction rate constants of the chemical processes involved in the kinetic model. As far as rate constant estimation is concerned, two cases may be distinguished: (i) heavy-species–heavy-species collision rate constants and (ii) electron–heavy-species collision rate constants. In principle,

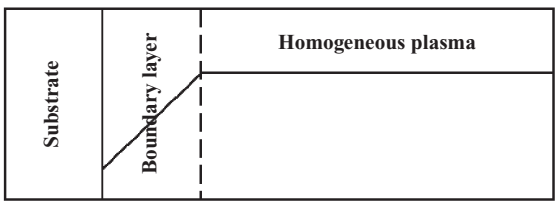

Figure 6.9 Schematic representation of a discharge described in the quasi-homogeneous plasma approximation.

electron–heavy-species rate constants depend on the electron energy distribution function (eedf) which deviates from a Maxwellian distribution for the considered discharges.[42] This means that the solution of the species balance equation (Equation (6-2)) would in principle require coupling the electron Boltzmann equation. However, previous studies have shown that for moderate pressure discharges, the electron–heavy-species reaction rate constants only depend on the average electron energy and that knowledge of the whole electron energy distribution function is not necessary to estimate these rate constants.[40] This brings an important simplification to the model, since instead of coupling the electron Boltzmann equation to the species equation we just need to consider an electron average energy equation. The dependence between the rate constant and the average electron energy can be determined independently by using an offline Boltzmann solver. The average electron energy considered in this model may be written as[41]

$$\frac{d<\varepsilon_e>}{dt} = \frac{\left(MWPD_{av} - Q_{e-t} - Q_{e-v} - Q_{e-\chi} - J_{e-sub}.h_e \frac{S_{sub}}{V_{pl}}\right)}{\rho_e} \qquad \text{Eq. (6-3)}$$

In Equation (6-3), $<\varepsilon_e>$ is the average electron energy; $MWPD_{av}$ is the average microwave power density absorbed by the electrons, which is given by the ratio of the absorbed power to the plasma volume; Q_{e-t} and Q_{e-v} are the rates of the energy dissipated by electrons during energy transfer to the translational and vibrational modes of heavy species; $Q_{e-\chi}$ is the electron energy loss rate due to the activation of chemical processes; J_{e-sub}, h_e, and ρ_e are the electron flux at the substrate surface, the electron enthalpy, and the electron mass density, respectively; and S_{sub} and V_{pl} are the substrate area and the plasma volume, respectively.

The heavy-species–heavy-species reaction rate constants depend on the gas temperature. This is determined by coupling to the species and electron energy equations a total energy equation that may be written[41]

$$\frac{d\langle E\rangle}{dt} = \frac{\left(MWPD_{av} - Q_{rad} - \left[\sum J_{i-sub}h_i + \frac{\lambda(T_g - T_{sub})}{\delta}\right]\cdot\frac{S_{sub}}{V_{pl}}\right)}{\rho} \qquad \text{Eq. (6-4)}$$

where $<E>$ is the total average energy, Q_{rad} is the rate of energy loss by radiation, λ is the thermal conductivity, T_{sub} is the substrate temperature, δ is the thermal boundary layer thickness, ρ is the total mass density, and

J_{i-sub} and h_i are respectively the flux at the substrate surface and the enthalpy of species i.

The surface net production rates R_i depend on the substrate temperature, the boundary layer thickness, as well as the recombination/de-excitation coefficients and the diffusion coefficients of the different species. The way these rates are estimated is extensively discussed in ref. [41], where the values adopted for the recombination/de-excitation coefficients are also given. The species diffusion coefficients and thermal conductivities were estimated from the collision integrals given by Yos[43].

For given discharge conditions, i.e., microwave power density, gas pressure, and feed gas composition, the steady state plasma composition is calculated by time-integrating the coupled set of species and energy balance equations. The integration starts from a plasma composition corresponding to a cold gas with a very small electron density, which is necessary to initiate the ionization process. The absorption of the microwave power induces electron heating that leads to strong ionization and dissociation kinetics, gas heating, and an enhanced thermal chemistry. The resulting change in the gas composition, electron energy, and gas temperature is calculated by time-integrating Equations (6-2–6-4). The numerical algorithm makes use of the fully implicit backward difference formula (BDF). The integration is stopped once the species densities, the electron energy, and the gas temperature reach steady state.

6.3 Investigations of Typical NCD Deposition Conditions

6.3.1 Deposition and Characterization of NCD Films

The growth rate yielded for the various deposition conditions was determined from the estimation of the film thickness through the weight difference of the samples before and after deposition, assuming a constant density of $3.5\,\mathrm{g\,cm^{-3}}$ for diamond. Figure 6.10 shows that growth rates as high as $1\,\mu\mathrm{m\,h^{-1}}$ are reached, which is significantly higher than the values usually reported for microwave processes fed with the same gas mixture.[14,44] This difference could be due in particular to the higher total gas pressure employed in the present work. Besides, a raising of the growth rate is observed for a coupled increase of $\%H_2$-MWP values up to $1.3\,\mu\mathrm{m\,h^{-1}}$ for 7% H_2 and 800 W. This may be due either to the increase of H_2 concentration as discussed in refs. [14,44] or to an increase of the

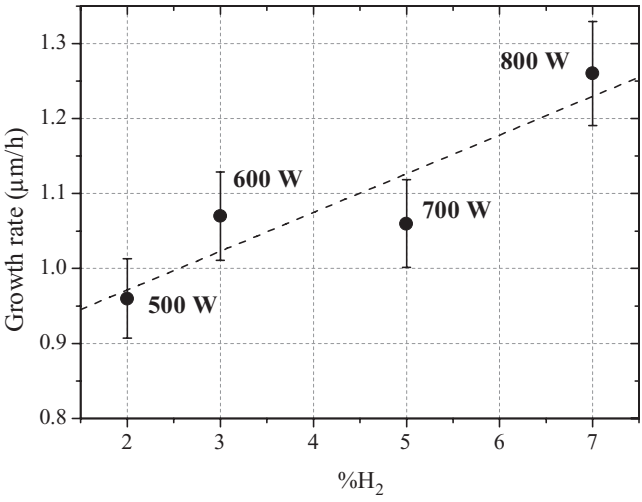

Figure 6.10 Growth rate measured as a function of the couple $\%H_2$–MWP.

MWP density which could lead to an augmentation of the growth key-species density as reported in the case of H_2/CH_4 microwave discharges.[45,46]

The SEM micrographs of the samples are shown in Fig. 6.11. All the films exhibit homogeneous and continuously smooth granular surfaces, typical of NCD layers, where no well-faceted crystallites can be observed. From a qualitative point of view, the surface topography seems to become more important when $\%H_2$ and MWP are raised. This trend was confirmed by AFM measurements performed in tapping mode on a $5 \times 5\,\mu m^2$ area (Fig. 6.12), which point out an appreciable increase of the surface roughness with root mean square (rms) values varying from 24 to 75 nm for $\%H_2$-MWP couples evolving from 2%-500 W to 7%-800 W. A similar behavior has been observed as a function of H_2 concentration in the gas mixture and was associated with a transition toward PCD films resulting in changes of plasma composition and growth mechanisms.[14,44,47] It should be mentioned that, for Figs. 6.11 and 6.12, such a modification of the growth environment could also be attributed to the simultaneous variation of MWP values.

The Raman spectra obtained using a 514.5 nm excitation wavelength are given in Fig. 6.13. The films show typical NCD features: a broad and weak diamond peak at $1332\,cm^{-1}$, the graphite D and G bands at 1350 and $1580\,cm^{-1}$, respectively, and the fingerprint of the nanocrystalline structure at 1140 and $1470\,cm^{-1}$ attributed to transpolyacetylene bands.[48–51]

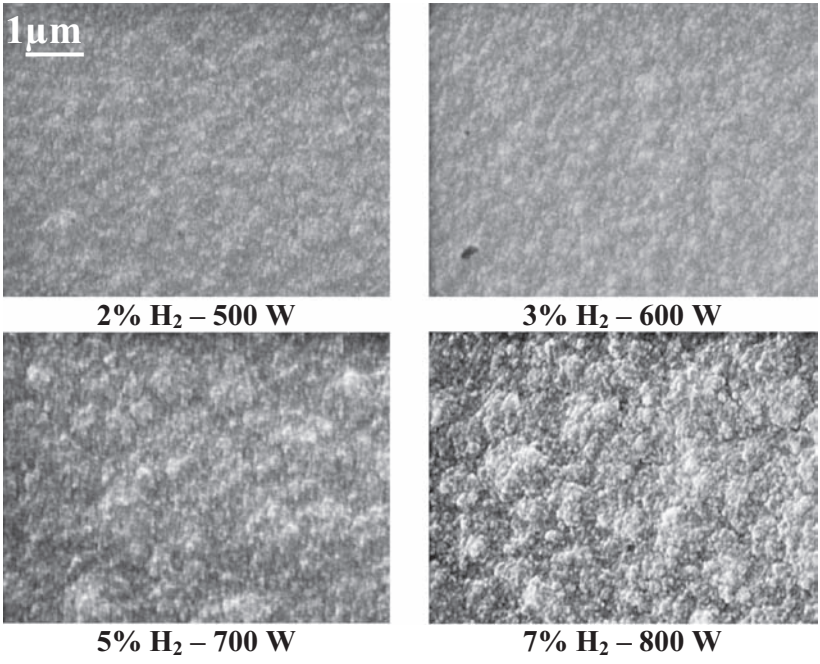

Figure 6.11 SEM micrographs of the NCD samples elaborated for the considered values of $\%H_2$–MWP.

The evolution of the Raman spectra confirms a transition toward more PCD-like characteristics as both $\%H_2$ and MWP are increased, with a noticeable decrease of the transpolyacetylene bands and the emergence of the diamond peak.

Finally XRD characterizations were performed using $CuK_{\alpha 1}$ radiation ($\lambda = 1.54056$ nm) with an incident X-ray angle of 10°. All the XRD spectra of the deposited films are dominated by the <111>, <220>, <311>, and <400> diamond diffraction peaks (Fig. 6.14), which indicates the presence of crystalline diamond within the films whatever the synthesis conditions. The grain size estimated using the Scherrer formula[52] applied to the <111> diffraction peak is shown in Fig. 6.15 as a function of $\%H_2$-MWP values. Although this method provides only a rough prediction of the crystallite average dimensions, satisfactory agreement with TEM measurements has been previously demonstrated.[53] Figure 6.15 emphasizes an increase of the grain size from 15 to 45 nm for the range of $\%H_2$-MWP values investigated, which corresponds to the order of magnitude commonly reported in the literature for NCD layers.[13,14,54–56] This increase of the grain size is consistent with the other characterization results above

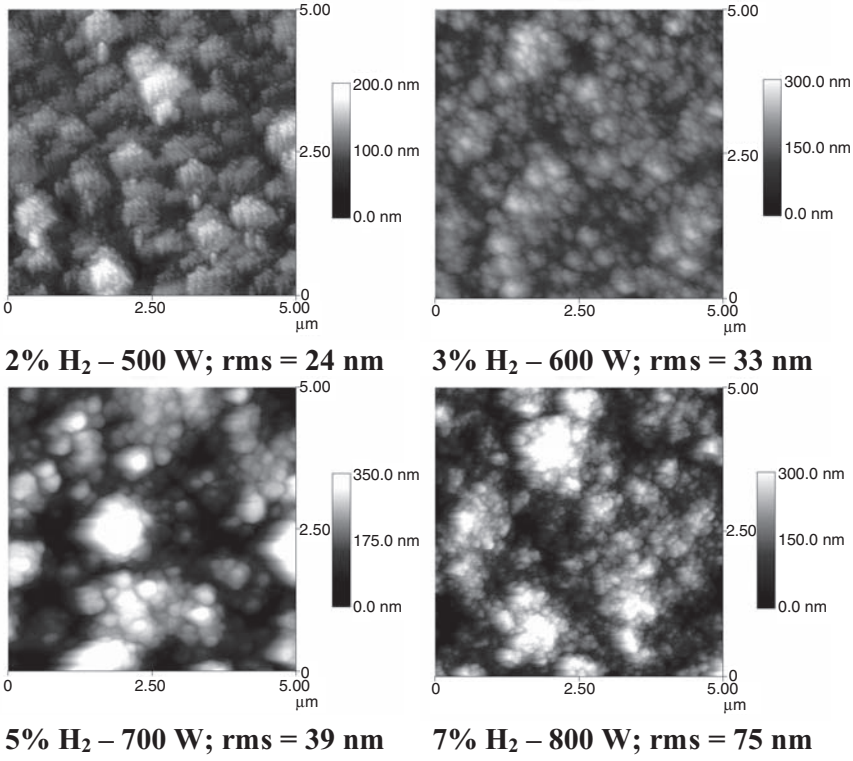

Figure 6.12 AFM micrographs of the NCD samples elaborated for the considered values of %H_2–MWP.

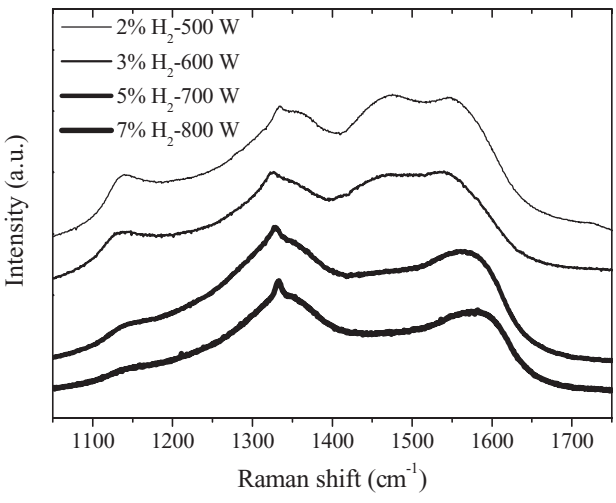

Figure 6.13 Raman spectra of the NCD samples elaborated for the considered values of %H_2–MWP.

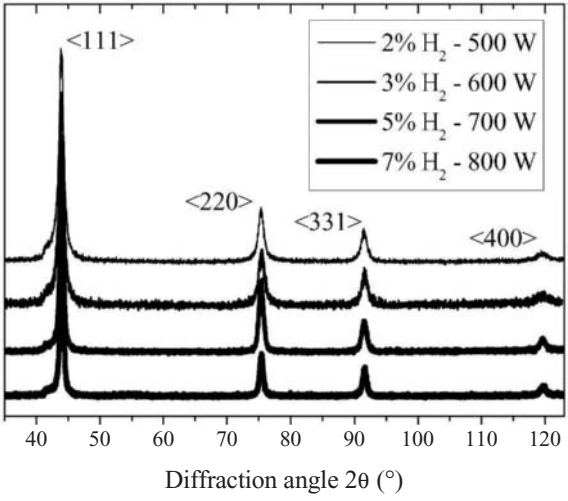

Figure 6.14 XRD patterns of the NCD samples elaborated for the considered values of %H_2–MWP.

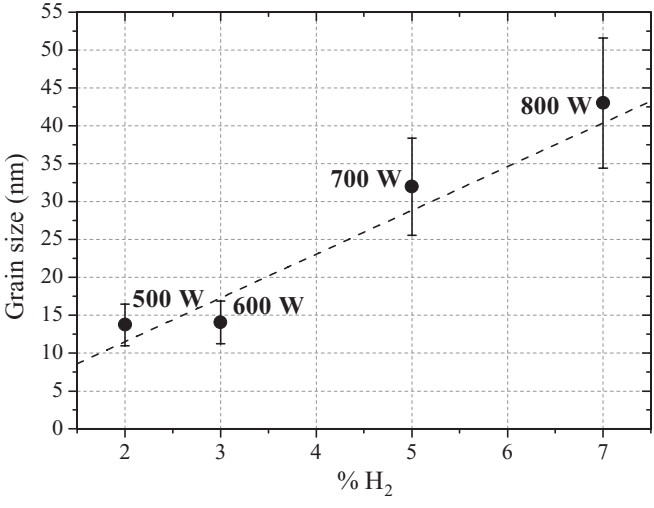

Figure 6.15 Grain size estimated from the Scherrer formula applied to the <111> diffraction peak (Fig. 6.14) of the NCD samples elaborated for the considered values of %H_2–MWP.

and may come from the change in the gas mixture composition[14,44,47] but also from the raising of the MWP density.

The deposition experiments described in this section allowed us to find an experimental window of process parameter values suitable for the synthesis in the bell jar reactor of NCD films with good properties: high growth rate (above $1\,\mu m\,h^{-1}$), weak surface roughness (rms in the range 25–75 nm), small grain size (15–45 nm), and good purity. The best nanocrystalline features are reached at low $\%H_2$ and MWP values, while a simultaneous increase of these parameters leads to a transition toward more microcrystalline structures. However, a more complete understanding and control of the growth process, especially under these conditions, require an analysis of the gas phase. The investigations carried out for this purpose are presented in the following section, the objectives of which are to characterize the microwave discharges in terms of gas temperature and C_2 absolute density and to check partly the validity of the plasma model developed in the frame of this work.

6.3.2 Plasma Diagnostics

6.3.2.1 Gas Temperature

Figure 6.16 presents the different rotational temperatures measured for the four growth conditions considered in this work. Depending on the $\%H_2$-MWP values, the temperature values determined from the C_2 Swan system range from 3200 to 3500 K, those reached through the CN violet system vary from 3400 to 4000 K, and the Mulliken system leads to rotational temperatures in the range 3000–4200 K. Taking into account the error on the experimental values, the temperatures of the upper levels are in relatively good agreement with those of the lower states for the three systems investigated, especially for the C_2 Swan system and CN violet system. This may result from the relatively long radiative lifetimes of the excited levels which insure an efficient thermalization of the rotational levels with the heavy-species translational mode: $C_2(a^3\Pi_u)$ is metastable, and $C_2(d^3\Pi_g)$ and $CN(B^2\Sigma^+)$ have a lifetime of 120 and 390 ns, respectively. Note that the $D^1\Sigma_u^+$ electronic state has a short radiative lifetime of 14 ns. Then the thermalization of the rotational levels of excited and ground states should be caused by quite similar rotational constants, which insures an enhanced rotation–rotation resonance when a transition occurs between both electronic states.[27]

The values of the gas temperature estimated here between 3000 and 4000 K are significantly higher than those reported by other authors for similar discharges. Indeed, Goyette et al. used the BAS technique on the Swan system and reported a gas temperature in the range 1450–1600 K for a 97 : 2 : 1 $Ar/H_2/CH_4$ plasma processed in an ASTeX reactor under pressure and power values in the ranges of 65–133 mbar and 500–1500 W, respectively.[57,58] In another microwave-cavity-based system and for the same gas mixture composition, Huang et al. measured the gas temperature using emission spectroscopy: they reported values ranging between 2100 and 2700 K for a pressure and an input microwave power range between 110 and 210 mbar and 900 and 1500 W, respectively.[59] Such strong differences may come from the higher pressure values adopted in this work. Indeed, higher pressure favors energy transfer to the translational mode of molecules and therefore gas heating. Higher pressures would also lead to a smaller plasma volume, which means greater power density and therefore stronger heating. Another point that may explain the higher temperature values could be the difference in the coupling efficiency between the microwave cavity systems used in these studies and which will be discussed later. Note also that some microwave systems such as ASTeX reactors employed in refs. [57,58] have a water-cooled stainless steel enclosure. These reactors have a near ambient wall temperature, whereas the quartz vessel of the bell jar reactor has a much higher temperature that may reach few hundred kelvin.[60] This appreciable difference in wall temperature could influence the plasma power balance and lead to much higher gas temperature in the case of the bell jar reactor.

The gas temperature calculated with the plasma model is also reported in Fig. 6.16. The values obtained are relatively high and range between 4000 and 4400 K. They increase when both $\%H_2$ and MWP are increased from 2 to 7% and 500 to 800 W, respectively. These high calculated values of T_g are consistent with the experimental results discussed above. One can, however, notice that the calculated values are typically higher than those measured experimentally, and tend to decrease slightly when $\%H_2$ and MWP are raised. One should keep in mind that the zero-dimensional model relies on a *quasi*-homogeneous plasma assumption and is used to describe the plasma bulk, whereas the experimental measurements are integrated along the plasma ball diameter. Thus, taking into account the strong plasma non-homogeneity, the values calculated by the model could be slightly overestimated compared to experimental measurements.

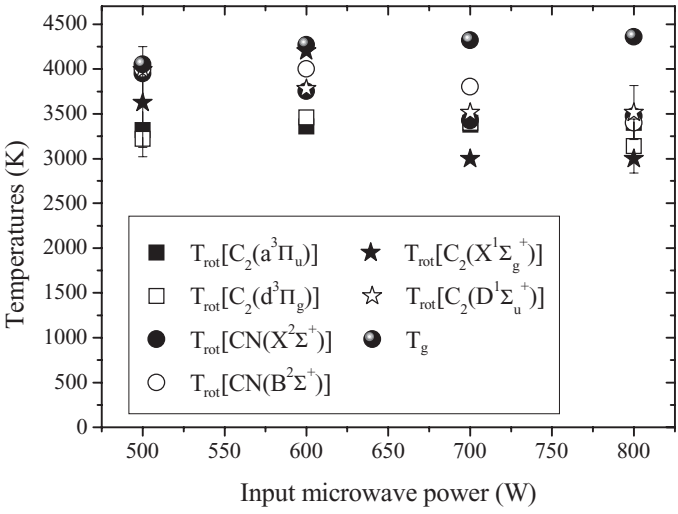

Figure 6.16 Temperatures estimated for $Ar/H_2/CH_4$ microwave discharges under the four growth conditions considered in this work. (i) rotational temperatures determined by BAS and OES: $T_{rot}[C_2(a^3\Pi_u)]$ and $T_{rot}[C_2(d^3\Pi_g)]$ (Swan system), $T_{rot}[CN(X^2\Sigma^+)]$ and $T_{rot}[CN(B^2\Sigma^+)]$ (violet system), and $T_{rot}[C_2(X^1\Sigma_g^+)]$ and $T_{rot}[C_2(D^1\Sigma_u^+)]$ (Mulliken system); (ii) gas temperature T_g calculated with the thermochemical plasma model.

6.3.2.2 C_2 Density

Figure 6.17 presents the absolute density of C_2 in the discharge $N[C_2]^{Mull.}$ deduced from the density of the C_2 ground state $N[C_2(X^1\Sigma_g^+)]$ and the absolute density of C_2 $N[C_2]^{Swan}$ deduced from the density of the C_2 low-lying level $N[C_2(a^3\Pi_g)]$, along with the numerical values $N[C_2]^{model}$ calculated by the thermochemical model. $N[C_2]^{Mull.}$ and $N[C_2]^{model}$ are in satisfactory agreement, with values ranging from 10^{13} to $10^{14}\,cm^{-3}$, depending on the discharge conditions. Both theoretical and experimental data tend to decrease when MWP and $\%H_2$ are simultaneously raised and the values calculated by the model are slightly above the experimental values. The values of $N[C_2]^{Swan}$ estimated from the Swan system absorption are consistent with those of $N[C_2]^{Mull.}$ and $N[C_2]^{model}$ at low MWP and $\%H_2$ (500–600 W and 2–3%), but move significantly away from these densities at higher MWP and $\%H_2$ (700–800 W and 5–7%). As a matter of fact, for the latter values, a deviation of approximately an order of magnitude is noticed between $N[C_2]^{Mull.}$ and $N[C_2]^{Swan}$ that always remains greater. It should be recalled that the method employed for the

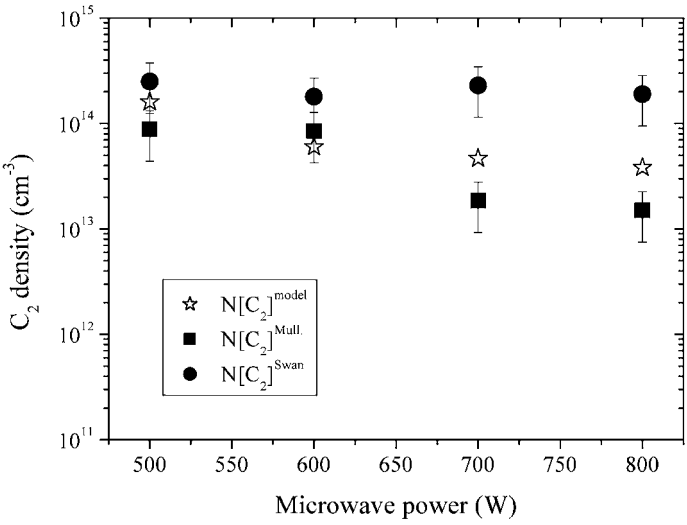

Figure 6.17 Absolute density of C_2 in the $Ar/H_2/CH_4$ discharge under the four growth conditions considered in this work. $N[C_2]^{model}$: theoretical density calculated by the thermochemical model; $N[C_2]^{Mull.}$: total density deduced experimentally from the density of fundamental state $N[C_2(X^1\Sigma_g^+)]$ measured by BAS (Mulliken system); $N[C_2]^{Swan}$: total density deduced experimentally from the density of low-lying level $N[C_2(a^3\Pi_u)]$ measured by BAS (Swan system).[27]

determination of $N[C_2]^{Swan}$ is known to allow only a rough approximation of the C_2 density. Furthermore, some differences between experiment and simulation would be at least partly due to the fact that measurements assume that absorption takes place uniformly over the 5 cm diameter plasma ball, but where density gradients may be present. On the other hand, the model assumes a homogeneous plasma and the calculation results would only reflect what happens in the bulk of the discharge.

The values determined here for the C_2 density, in the range 10^{13}–$10^{14}\,cm^{-3}$, and using three methods, are much greater than those estimated between 10^{10} and $10^{12}\,cm^{-3}$ in other work[57,58] for gas temperatures between 1000 and 1600 K. This difference in C_2 density is consistent with the deviation obtained for the gas temperature. In the investigated discharge conditions and in the bell jar reactor, a strong thermal conversion of CH_4 leading to the formation of the C_2 radical is expected due to the high gas temperature. The C_2 formation mechanisms will be thoroughly discussed in the last section of this chapter.

6.3.3 Conclusion on Plasma Characterization

In this section, NCD growth conditions have been determined and investigated by spectroscopic diagnostics and plasma modeling. The results concerning the gas temperature and the C_2 density show a satisfactory agreement between experimental measurements and theoretical calculations. Therefore, the thermochemical plasma model may confidently be used to analyze the main features of $Ar/H_2/CH_4$ microwave discharges as a function of process parameters. Surprising results are a relatively high gas temperature (3000–4000 K) and C_2 density (10^{13}–10^{14} cm^{-3}) with regard to the moderate input microwave power and results from the literature. Parametric studies are proposed in next section in order to throw some light on the chemical process involved in the considered discharges, especially in the formation of C_2 molecules.

6.4 Investigations of $Ar/H_2/CH_4$ Microwave Discharges with the Plasma Thermochemical Model

6.4.1 Parametric Studies

6.4.1.1 Choice of Investigated Parameters

The model calculations were performed for each $\%H_2$ considered for the growth conditions, i.e., 2, 3, 5 and 7%, by varying the microwave power from 250 W to the maximum values that can be experimentally injected, i.e., 500, 600, 700, and 800 W, respectively. This parametric study was chosen because the input microwave power represents only an upper limit of the power absorbed by the plasma which is actually used in the model. Then, on the computed curves presented afterward, the data corresponding to the greatest MWP for a given $\%H_2$ would correspond to 100% absorption, which is unlikely to happen in the real discharge. The 250 W input power discharge conditions correspond to 50% and 30% absorption yields for the 500 W and 800 W input power cases, respectively. The results will be discussed in terms of either absorbed microwave power or power absorption yield when comparisons with experiment are performed.

6.4.1.2 Gas Temperature

Figure 6.18 shows the variation of the gas temperature T_g as a function of the absorbed microwave power for the different percentages of hydrogen in the gas mixture considered. T_g increases from 3100 K for a discharge containing 2% H_2 for a MWP of 500 W to 4400 K for 7% H_2 and 800 W. The gas temperature increases strongly with the microwave power density and does not depend on the amount of hydrogen in the feed gas. Indeed, the increase of MWP from 250 to 800 W for $\%H_2 = 7$ leads to an increase of 1400 K for T_g. The increase of $\%H_2$ from 2 to 7% leads to a maximum decrease of T_g of about 400 K at 500 W. The values calculated for the discharge conditions simulated in this work always remain higher than 3000 K, although only 30% absorption yields were assumed for some cases (7% H_2 and 250 W MWP). The calculated temperature values are therefore always consistent with those measured using OES and BAS techniques.

It is worth mentioning that the temperature values calculated assuming 100% power absorption are in the range 4000–4400 K and are therefore slightly higher, as previously described, than those determined experimentally in the range 3000–4000 K. This would indicate that the power absorption yield would actually be less than 100%. The simulations show

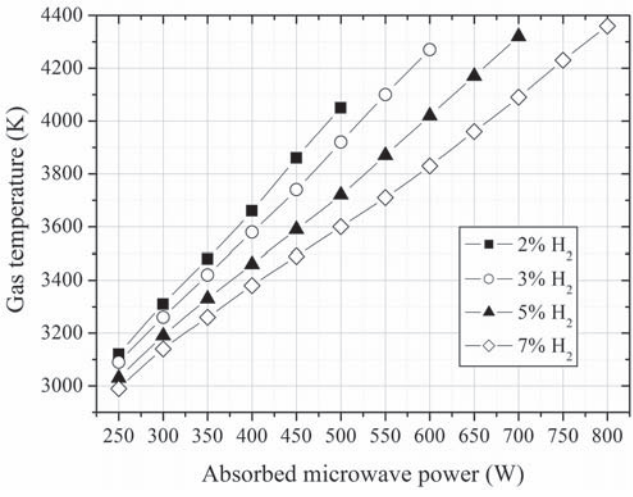

Figure 6.18 Gas temperature T_g calculated in the $Ar/H_2/CH_4$ microwave discharges under 200 mbar as a function of the absorbed MWP and for different $\%H_2$.[19]

that a simultaneous increase of $\%H_2$ and absorbed microwave power, consistent with what is actually performed experimentally, leads to a slight increase of the gas temperature that varies by 200–300 K when $\%H_2$ and MWP are raised from 2%/500 W to 7%/800 W. This slight 200–300 K increase is also observed for smaller power absorption yields. It is not easy to check the validity of this computed 200–300 K variation of T_g using the measured temperature. The experimental error on the rotational temperatures is indeed ±300 or ±500 K, which makes any comparison with respect to this point difficult, although a very slight decrease of T_g may be expected from the observed experimental variations when increasing $\%H_2$ and MWP (Fig. 6.16). The simultaneous increase of $\%H_2$ and MWP seems to have only a slight and negligible effect on this temperature. This result shows that the increase of T_g, which could be suspected when the absorbed power is increased, is in fact limited by the greater energy losses associated with the increase of the thermal conductivity of the gas mixture with the hydrogen amount in the discharge.

A very important result is that the T_g values obtained for the $Ar/H_2/CH_4$ discharges are much higher than those obtained in H_2/CH_4 discharges used for the deposition of PCD films, i.e., around 2200 K for 25 mbar and 600 W.[7] This is caused by the higher thermal conductivity of H_2, which exceeds the thermal conductivity of argon by more than an order of magnitude.[61] As a result, an enhanced thermal transfer to the substrate surface and reactor wall takes place and leads to a lower gas temperature in H_2/CH_4 discharges.

6.4.1.3 Molecular and Atomic Hydrogen

The variation of atomic hydrogen mole fraction as a function of the absorbed MWP and for different $\%H_2$ in the feed gas is given in Fig. 6.19. This shows that the mole fraction of H atoms increases with both MWP and $\%H_2$. For 2% hydrogen in the feed gas, X_H varies from 4×10^{-2} to 7.5×10^{-2}, when MWP increases from 250 to 500 W. For 7% H_2 in the feed gas, the H-atom mole fraction increases from 5×10^{-2} to 0.16 when MWP varies from 250 to 800 W.

For every $\%H_2$, when the efficiency of the power coupling exceeds 50%, the H-atom population exceeds the value that would be obtained assuming a total dissociation of the hydrogen introduced in the feed gas. As a matter of fact, Fig. 6.20 shows that although the H_2 dissociation is very quantitative, the density of H_2 always remains quite significant. This means that methane is also a substantial source of H atoms. The effective

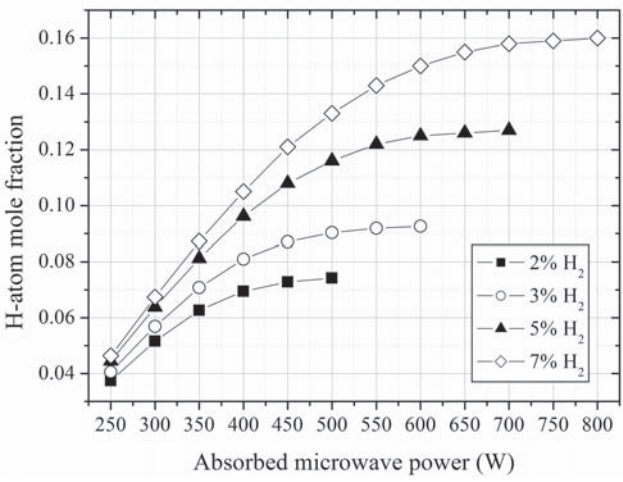

Figure 6.19 H-atom mole fraction calculated in the $Ar/H_2/CH_4$ microwave discharges under 200 mbar as a function of the absorbed MWP and for different $\%H_2$.[19]

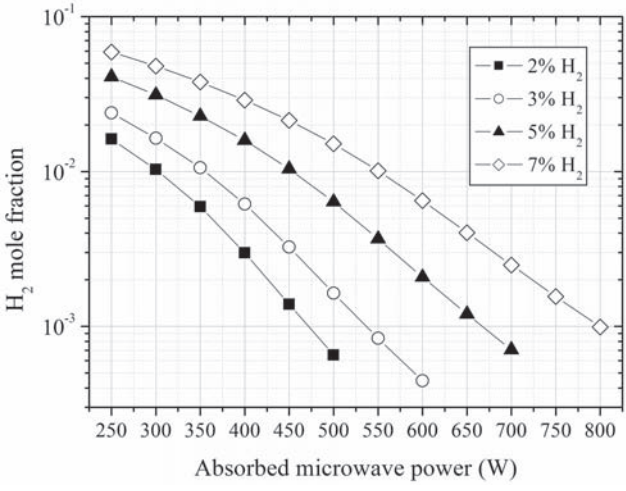

Figure 6.20 H_2 mole fraction calculated in the $Ar/H_2/CH_4$ microwave discharges under 200 mbar as a function of the absorbed MWP and for different $\%H_2$.[19]

dissociation of H_2 and the conversion of CH_4 are mainly due to the thermal cracking processes that are enhanced by the high gas temperature (>3000 K).

The most striking result obtained from these simulations is certainly the very high H-atom density obtained in the investigated $Ar/H_2/CH_4$ dis-

charges when compared to that obtained in H_2/CH_4 discharges used for PCD deposition. As an example, for an absorbed microwave power of 600 W, the deposition of PCD films uses a CH_4/H_2 gas mixture with 99% of hydrogen at 25 mbar. These conditions are characterized by an H-atom mole fraction of approximately 0.01, which yields an H-atom density of $10^{15}\,cm^{-3}$.[40] For the $Ar/H_2/CH_4$ discharges obtained under the same absorbed MWP, the H-atom mole fraction ranges from 0.09 to 0.15 (Fig. 6.19), which corresponds to a density between $3 \times 10^{16}\,cm^{-3}$ and $6 \times 10^{16}\,cm^{-3}$, with only 3 to 7% hydrogen in the feed gas. The $Ar/H_2/CH_4$ discharge conditions corresponding to the NCD film deposition are therefore characterized by a large amount of H atoms. Despite the fact that the NCD synthesis process does not necessarily require hydrogen compounds[54] and is energetically favored by hydrogen-poor plasmas[3,62], discharges used for NCD deposition may be characterized by a relatively high H-atom population compared to H_2/CH_4 plasmas used for PCD deposition. Then, the H atoms could play a key role in the growth process by insuring for instance an enhanced etching of the non-diamond phases.

6.4.1.4 Hydrocarbon Species

As expected, Fig. 6.21 shows an almost complete dissociation of CH_4. It is also essential to point out that the mole fraction of the CH_3 radical,

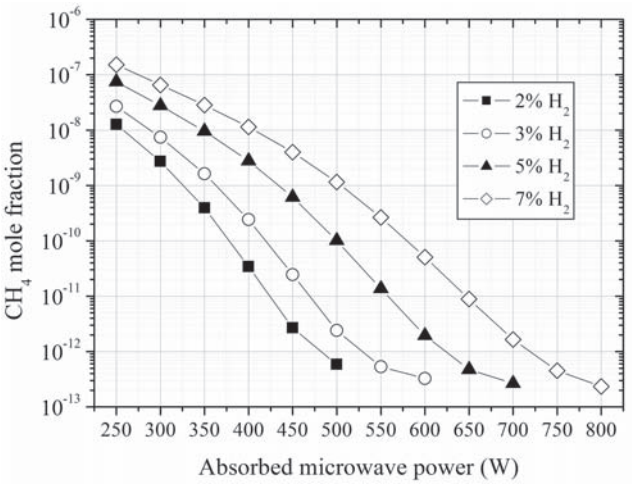

Figure 6.21 CH_4 mole fraction calculated in the $Ar/H_2/CH_4$ microwave discharges under 200 mbar as a function of the absorbed MWP and for different $\%H_2$.[19]

recognized as the growth precursor of PCD films,[1] is very low in the investigated conditions, with values between 10^{-10} and 10^{-6} (Fig. 6.22). Results of simulations demonstrate that CH_4 is almost entirely converted to C_2H_2 at low power (Fig. 6.23), to C_2 at intermediate power (Fig. 6.24), and to C at high power (Fig. 6.25). Indeed, C_2H_2 is the major species at low MWP and its concentration strongly decreases when the MWP increases (Fig. 6.23). This decrease is due to an efficient $C_2H_2 \rightarrow C_2$ conversion which leads to an increase of the C_2 mole fraction up to a maximum value (Fig. 6.24). The value and the position of this maximum depend on the amount of hydrogen in the feed gas. When the MWP is further increased, C_2 is converted to atomic carbon (Fig. 6.25) and its density decreases (Fig. 6.24). The atomic carbon then becomes the major carbon-containing species. This $C_2H_2 \rightarrow C_2 \rightarrow C$ conversion channel is mainly driven by thermal chemistry.

Assuming a 100% power absorption for the four growth conditions, the calculated C_2 mole fraction slightly decreases from 4.5×10^{-4} to 1×10^{-4} (Fig. 6.24), which corresponds to a density variation from 2×10^{14} to $4 \times 10^{13}\,cm^{-3}$, while $\%H_2$ and MWP are simultaneously increased. As previously discussed, these values are in good agreement with those experimentally determined using the C_2 Mulliken system, which also show a decreasing tendency with values varying from 9×10^{13} to $1.5 \times 10^{13}\,cm^{-3}$ (Fig. 6.17). It is essential to stress that the calculated density

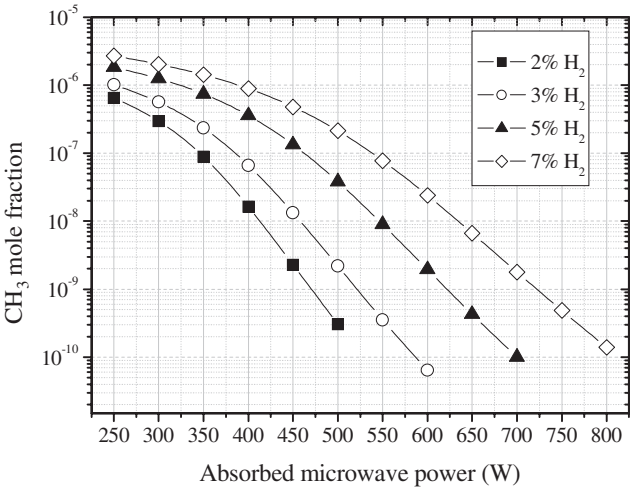

Figure 6.22 CH_3 mole fraction calculated in the $Ar/H_2/CH_4$ microwave discharges under 200 mbar as a function of the absorbed MWP and for different $\%H_2$.

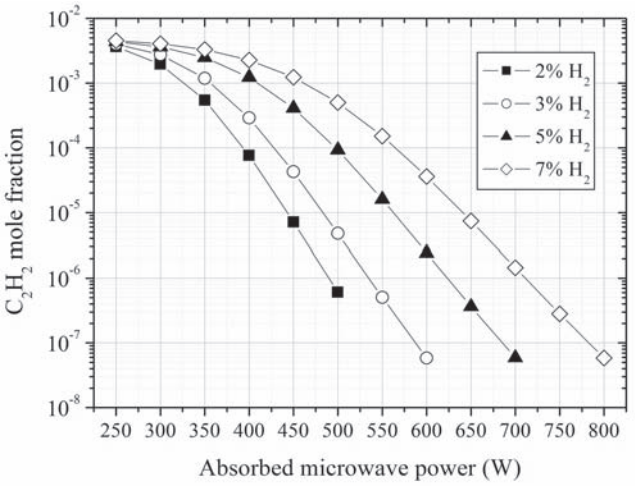

Figure 6.23 C_2H_2 mole fraction calculated in the $Ar/H_2/CH_4$ microwave discharges under 200 mbar as a function of the absorbed MWP and for different $\%H_2$.[19]

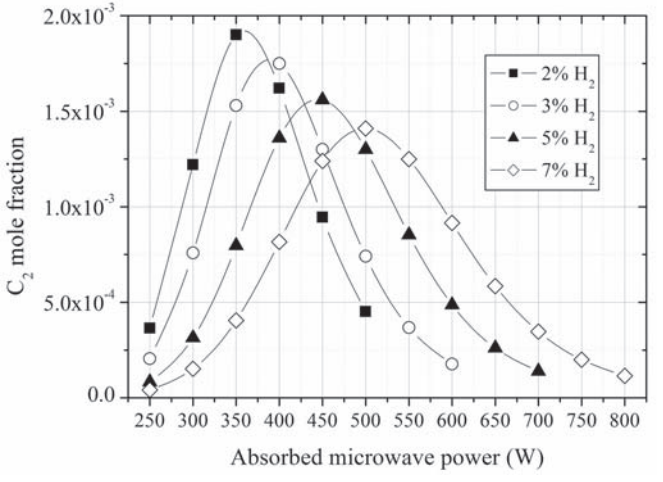

Figure 6.24 C_2 mole fraction calculated in the $Ar/H_2/CH_4$ microwave discharges under 200 mbar as a function of the absorbed MWP and for different $\%H_2$.[19]

strongly depends on the value assumed for the power absorption yielded. If we consider the case with 3% H_2 in the feed gas, assuming 90% instead of 100% for the power absorption efficiency leads to an increase of the C_2 mole fraction by a factor of 2. Taking into account the shape obtained for the variation of X_{C_2} as a function of MWP, the values of C_2

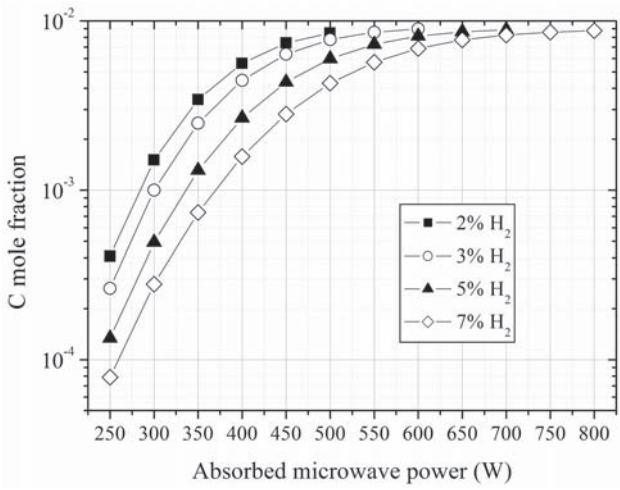

Figure 6.25 C mole fraction calculated in the $Ar/H_2/CH_4$ microwave discharges under 200 mbar as a function of the absorbed MWP and for different $\%H_2$.[19]

density estimated from the present thermochemical model assuming 100% power absorption represents a lower limit of the plasma bulk values.

Finally, concerning carbon-containing species, the predominance of C atoms and C_2 radicals in the investigated discharges represents another significant difference between the presently investigated NCD deposition discharges and the H_2/CH_4 plasmas used for PCD deposition where C_2H_2 is the predominant hydrocarbon species.[40]

6.4.1.5 Electrons and Power Coupling Efficiency

As far as charged species are concerned, the calculated values of electron density in NCD discharges range between 3×10^{11} and $3.5 \times 10^{12}\,cm^{-3}$, depending on the H_2 content in the feed gas and on the power absorbed by the plasma (or the coupling efficiency) (Fig. 6.26). The effect of this last parameter is especially strong, since the increase of the absorbed power by a factor of 2 leads to an increase in the degree of ionization by almost an order of magnitude for discharges with 3% H_2 in the feed gas. The amount of hydrogen also has a significant effect on the electron density that decreases when increasing $\%H_2$ in the $Ar/H_2/CH_4$ gas mixture. The change in the electron density with $\%H_2$ is more significant at high power. This result shows that, despite its low concentration,

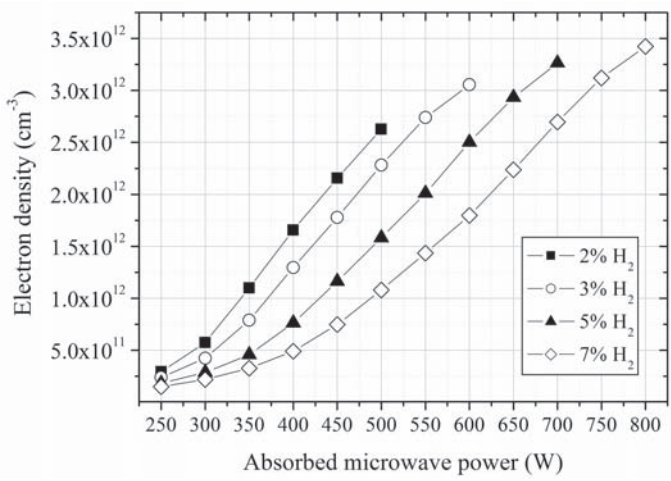

Figure 6.26 Electron density calculated in the $Ar/H_2/CH_4$ microwave discharges under 200 mbar as a function of the absorbed MWP and for different $\%H_2$.[19]

hydrogen insures a significant dissipation of the microwave power coupled to the discharge. Therefore, a NCD discharge with a larger amount of hydrogen requires a smaller electron density to dissipate the power transferred from the high-frequency electric field.

Some of the discharge conditions corresponding to the upper values of the absorbed power lead to an electron density of $3.5 \times 10^{12}\,cm^{-3}$. Such values of the electron density yield a plasma frequency much greater than the cutoff frequency for 2.45 GHz microwave excitation. This means that the wave would not penetrate into the plasma and sustain the discharge at high power. In fact, previous studies on H_2 discharges showed that the electron density in equivalent microwave coupling devices and for the same coupling configuration (hemispherical plasma) cannot exceed $1–2 \times 10^{12}\,cm^{-3}$.[63] Although the present model is not self-consistent and cannot describe this screening effect, the simulation results show that it is unlikely that power values as high as 500, 600, 700, and 800 W may be coupled for $\%H_2$ in the feed gas of 2, 3, 5 and 7, respectively. This means that for these cases, corresponding to the experimental growth conditions, a significant amount of the input microwave power is not dissipated in the plasma and is probably lost in the microwave circuit (wave guide, resonator, metallic wall) or reflected back to the source. This result is consistent with those obtained from the investigation of the energy coupling efficiency in Ar and H_2 pure discharges carried out on the same plasma devices or the same coupling configuration.[60,64] Taking into account

previous discussions on the power coupling efficiency based on the comparison between calculated and measured C_2H_2, C_2, and C densities,[19] the coupling efficiency would be between 70% and 90% for the $Ar/H_2/CH_4$ discharge under conditions corresponding to 3% H_2 in the feed gas. Of course this efficiency may vary with $\%H_2$.

6.4.1.6 Other Charged Species

Concerning other charged species, depending on the discharge conditions the most abundant ions in the studied plasmas may be either ArH^+ at high power density (Fig. 6.27) or C_2^+ (Fig. 6.28) at lower power density. At high power density the increase in the gas temperature is such that the enhanced conversion of C_2 to C leads to a very small C_2 density and ionization rate. At this point, the main ionization channel corresponds to the electron impact ionization of argon followed by an argon–hydrogen ion conversion process.

6.4.2 Mechanisms of C_2 Formation

The kinetics of C_2 formation depends strongly on the gas temperature, i.e., on the absorbed microwave power.

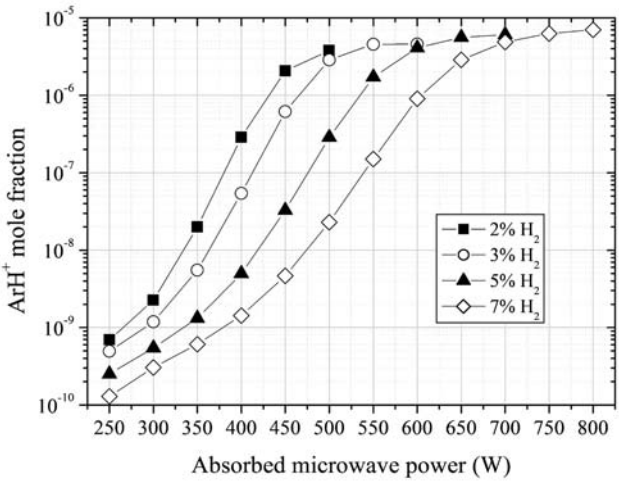

Figure 6.27 ArH^+ mole fraction calculated in the $Ar/H_2/CH_4$ microwave discharges under 200 mbar as a function of the absorbed MWP and for different $\%H_2$.

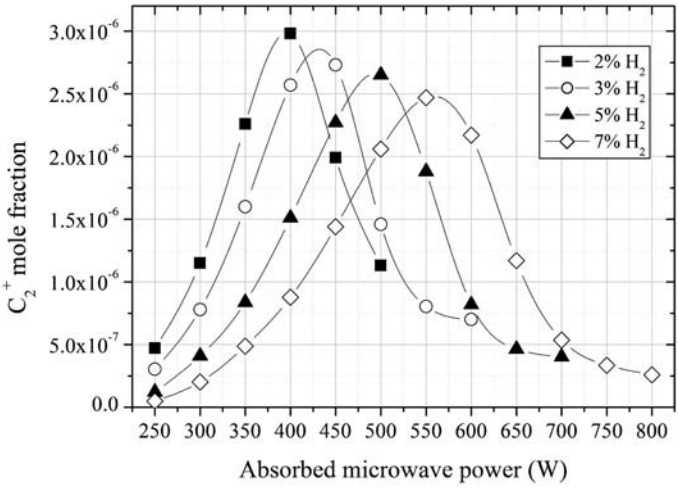

Figure 6.28 C_2^+ mole fraction calculated in the $Ar/H_2/CH_4$ microwave discharges under 200 mbar as a function of the absorbed MWP and for different $\%H_2$.

At low MWP, the major C_2 production reaction involved the dissociative recombination of the C_2H^+ ion. This mechanism is quite different from what is encountered in H_2/CH_4 plasmas used for PCD film deposition. Indeed, the C_2H^+ ion comes principally from the reaction of Ar^+ ion with acetylene and is therefore characteristic of Ar-containing discharges. Thus, the production of C_2 requires the ionization of Ar, followed by the reaction between Ar^+ and C_2H_2 leading to C_2H^+, and finally the dissociative recombination of C_2H^+:

$$Ar^+ + C_2H_2 \Rightarrow C_2H^+ + H + Ar$$
$$C_2H + Ar^+ \Rightarrow C_2H^+ + Ar$$
$$C_2H^+ + e^- \Rightarrow C_2 + H$$

At high MWP, these ionic mechanisms remain identical but another production scheme involving a thermal radical reaction between CH and C gets a comparable weight for C_2 production:

$$C + CH \Rightarrow C_2 + H$$

For discharge conditions with a gas temperature below 2000 K, a thermal conversion of CH_4 cannot be invoked to explain the amount of

C_2 observed, and some authors attribute the C_2 production within the discharge to the dissociative recombination of the acetylene ion:[57]

$$C_2H_2^+ + e^- \Rightarrow C_2 + H_2$$

However, this production mechanism should not be significant since the dissociative recombination of hydrocarbon ions producing only H atoms are much more probable. Besides, in our discharge conditions where the gas temperature was estimated to be higher than 3000 K, the $C_2H_2^+$ mole fraction does indeed not exceed 10^{-8}. Thus, the $C_2H_2 \rightarrow C_2 \rightarrow C$ thermal conversion would be the main source of C_2 production.

If the deposition of NCD films, based on a high secondary nucleation rate, is promoted by C_2 molecules, optimization of the growth process in terms of grain size and growth rate necessitates optimization of the C_2 density. For this purpose, in the case of microwave-assisted processes, we demonstrated that the gas temperature is a key parameter, control of which allows control of C_2 production. As illustrated in this section, optimal values of C_2 density may then be found for instance by changing the input microwave power (Fig. 6.24 for a given $\%H_2$) and/or varying the plasma thermal conductivity by changing the H_2/Ar ratio in the feed gas mixture (Fig. 6.24 for a given MWP).

6.4.3 Conclusion on Plasma Modeling

In this part, a parametric study of $Ar/H_2/CH_4$ microwave discharges was carried out with the thermochemical plasma model as a function of absorbed MWP and for different $\%H_2$. Results indicate that the power coupling efficiency that characterizes the investigated system could be above 70%. Under such conditions, the H-atom density in the investigated discharge is relatively high with a mole fraction ranging between 5 and 15%. This surprising result should be taken into account in the investigation of the surface chemistry leading to NCD formation. Compared to H_2/CH_4 plasmas obtained with the same input microwave power, the $Ar/H_2/CH_4$ discharges are characterized by much higher gas temperatures and H-atom densities, although greater H_2 percentages in the feed gas are used in the H_2/CH_4 PCD deposition plasma. These characteristics lead to a thermal chemistry which is efficient enough to convert quantitatively both CH_4 and C_2H_2 into C_2 and C atoms that become the major carbon-containing species.

From the deposition process point of view, the results obtained here show that the films grown under NCD discharge conditions would be subject to enhanced etching kinetics due to the large amount of H atoms. The hydrocarbon species that would interact with the growing films are probably different from those encountered under PCD discharge conditions. The results obtained indicate that films grown under NCD discharge conditions would probably interact with sp species (C_2 or C_2H_2) or C. Note, however, that sp^3 species may form near the substrate surface in the reacting boundary layer, where the decrease of the temperature from the bulk value (3000–4000 K) to the substrate temperature value (around 1000 K) would lead to a back-conversion from C, C_2, and C_2H_2 to CH_4. However, this back-conversion should remain quite limited and the plasma is probably dominated by the most stable sp species, in particular acetylene, even at the substrate surface.

6.5 General Conclusion

In this chapter we reported on a thorough analysis and description of $Ar/H_2/CH_4$ discharges ignited in microwave cavity systems and employed for nanocrystalline diamond layer deposition. The purpose was to describe the methodology and tools that must be implemented in order to improve the understanding and the control of the synthesis process.

Four steps were considered: (i) the search for an experimental window of process parameter values suitable for the synthesis of NCD films with good properties; (ii) the development of efficient spectroscopic diagnostics and a thermochemical plasma model able to provide information on the deposition process; (iii) the confrontation of experimental and theoretical results obtained in typical NCD growth conditions for highlighting some particularities of the considered discharges and checking the validity of the plasma model; (iv) the theoretical analysis of the plasma kinetics as a function of the process parameters using the plasma model.

Concerning the plasma diagnostics, we focused on the characterization of the plasma bulk with both experimental and theoretical studies, which allowed us to draw important conclusions on the main features and singularities of $Ar/H_2/CH_4$ discharges: relatively high gas temperature, surprisingly high H-atom density, predominance of C_2H_2, C_2, and C depending on the microwave power, evaluation of the coupling efficiency above 70%, etc. These results were compared to those in the literature and to the well-known behavior of H_2/CH_4 microwave discharges used for PCD film synthesis. A first-hand understanding of the deposition process

yielded in the bell jar reactor has then been reached and some suggestions for improving growth in terms of C_2 molecule production were drawn.

We have therefore pointed out that plasma modeling supported by experimental diagnostics is a very efficient tool for probing deposition discharges. However, a global description within the frame of a quasi-homogeneous plasma assumption is quite restricted. To confirm the validity of some conclusions it is necessary to develop at least a one-dimensional model that makes it possible to follow the plasma composition and temperatures in the reacting boundary layer. The development of such a model and its validation through spatially resolved spectroscopic measurements would be of great interest for further understanding of the main phenomena that govern NCD deposition and would be helpful for the development of surface chemistry and growth models. At the moment this work is in progress. Also, a more complete description of the complex chemistry involved in $Ar/H_2/CH_4$ discharges taking into account polycyclic aromatic hydrocarbons (PAHs) and soot particle formation would enable us to improve the process control. This has been accomplished and details will be published elsewhere.[39]

References

1. D.G. Goodwin, Scaling laws for diamond chemical-vapor deposition. I. Diamond surface chemistry, *J. Appl. Phys.* **74**, 6888 (1993).
2. J.R. Rabeau, P. John, J.I.B. Wilson, Y. Fan, The role of C_2 in nanocrystalline diamond growth, *J. Appl. Phys.* **96**, 6724 (2004).
3. P. Redfern, D.A. Horner, L.A. Curtiss, D.M. Gruen, Theoretical studies of growth of diamond (110) from dicarbon, *J. Phys. Chem.* **100**, 11654 (1996).
4. D.M. Gruen, Nanocrystalline diamond films, *Annu. Rev. Mater. Sci.* **29**, 211 (1999).
5. D.M. Gruen, P.C. Redfern, D.A. Horner, P. Zapol, L.A. Curtiss, Theoretical studies on nanocrystalline diamond: nucleation by dicarbon and electronic structure of planar defects, *J. Phys. Chem. B* **103**, 5459 (1999).
6. J.C. Angus, C.C. Hayman, Low pressure, metastable growth of diamond and "diamond like" phases, *Science*. **241**, 913 (1988).
7. A. Gicquel, K. Hassouni, Y. Breton, M. Chenevier, J.C. Cubertafon, Gas temperature measurements by laser spectroscopic techniques and by optical emission spectroscopy, *Diamond Relat. Mater.* **5**, 366 (1996).
8. N. Sadeghi, Molecular spectroscopy techniques applied for processing plasma diagnostics, *J. Plasma Fusion Res.* **80**, 767 (2004).
9. F. Silva, A. Gicquel, A. Tardieu, P. Cledat, Th. Chauveau, Control of an MPACVD reactor for polycrystalline textured diamond films synthesis: role of microwave power density, *Diamond Relat. Mater.* **5**, 338 (1996).

10. C. Findeling-Dufour, A. Gicquel, Study for fabricating large area diamond single-crystal layers, *Thin Solid Films*. **308–309**, 178 (1997).
11. G. Lombardi, K. Hassouni, G.D. Stancu, L. Mechold, J. Röpcke, A. Gicquel, Study of an H_2/CH_4 moderate pressure microwave plasma used for diamond deposition: modelling and IR tuneable diode laser diagnostic, *Plasma Sources Sci. Technol.* **14**, 440 (2005).
12. K. Hassouni, T. Grotjohn, A. Gicquel, Self-consistent microwave field and plasma discharge simulations for a moderate pressure hydrogen discharge reactor, *J. Appl. Phys.* **86**, 134 (1999).
13. D. Zhou, T.G. McCauley, L.C. Qin, A.R. Krauss, D.M. Gruen, Synthesis of nanocrystalline diamond thin films from an Ar-CH_4 microwave plasma, *J. Appl. Phys.* **83**, 540 (1998).
14. D. Zhou, D.M. Gruen, L.C. Qin, T.G. McCauley, A.R. Krauss, Control of diamond film microstructure by Ar additions to CH_4/H_2 microwave plasmas, *J. Appl. Phys.* **84**, 1981 (1998).
15. S. Jiao, A. Sumant, M.A. Kirk, D.M. Gruen, A.R. Krauss, O. Auciello, Microstructure of ultrananocrystalline diamond films grown by microwave Ar-CH_4 plasma chemical vapor deposition with or without added H_2, *J. Appl. Phys.* **90**, 118 (2001).
16. G. Lombardi, G.D. Stancu, F. Hempel, A. Gicquel, J. Röpcke, The quantitative detection of methyl radicals in non-equilibrium plasmas: a comparative study, *Plasma Sources Sci. Technol.* **13**, 27 (2004).
17. K.L. Mennigen, M.A. Childs, H. Toyoda, Y. Ueda, L.W. Anderson, J.E. Lawler, CH_3 and CH densities in a diamond growth DC discharge, *Contrib. Plasma Phys.* **35**, 4 (1995).
18. R.W.B. Pearse, A.G. Gaydon, *The Identification of Molecular Spectra* (London: Chapman and Hall, 1976).
19. G. Lombardi, K. Hassouni, F. Bénédic, F. Mohasseb, J. Röpcke, A. Gicquel, Spectroscopic diagnostics and modeling of $Ar/H_2/CH_4$ microwave discharges used for nanocrystalline diamond deposition, *J. Appl. Phys.* **96**, 6739 (2004).
20. E.A. Ballik, D.A. Ramsay, Ground state of the C_2 molecule, *J. Chem. Phys.* **31**, 1128 (1959).
21. M. Martin, C_2 spectroscopy and kinetics, *J. Photochem. Photobiol. A: Chem.* **66**, 263 (1992).
22. G. Herzberg, *Molecular spectra and molecular structure, volume I – Spectra of diatomic molecules* (Malabar: Krieger, 1989).
23. C.F. Chabalowski, S.D. Peyerimhoff, The Ballik-Ramsay, Mulliken, Deslandre-D'Alambuja and Phillips System in C_2: a theoretical study of their electronic transition moments, *Chem. Phys.* **81**, 57 (1983).
24. A.N. Goyette, T. Matsuda, L.W. Anderson, J.E. Lawler, C_2 column densities in $H_2/Ar/CH_4$ microwave plasmas, *J. Vac. Sci. Technol. A* **16**, 337 (1998).
25. X. Duten, A. Rousseau, A. Gicquel, K. Hassouni, P. Leprince, Time-resolved measurements of the gas temperature in a H_2/CH_4 medium pressure microwave 915 MHz pulsed plasma, *J. Phys. D: Appl. Phys.* **35**, 1939 (2002).
26. R.S. Mulliken, *Z. Electrochem.* **36**, 603 (1930).
27. G. Lombardi, F. Bénédic, F. Mohasseb, K. Hassouni, A. Gicquel, Determination of gas temperature and C_2 absolute density in $Ar/H_2/CH_4$ microwave

discharges used for nanocrystalline diamond deposition from C_2 Mulliken system, *Plasma Sources Sci. Technol.* **13**, 375 (2004).
28. M. Zhao, T.G. Owano, C.H. Kruger, Optical diagnostics of an atmospheric pressure diamond-depositing DC plasma reactor, *Diamond Relat. Mater.* **10**, 1565 (2001).
29. T. Tatarczyk, E.H. Fink, K.H. Becker, Lifetime measurements on single vibrational levels of $C_2(d^3\Pi_g)$ by laser fluorescence excitation, *Chem. Phys. Lett.* **40**, 126 (1976).
30. J. Luque, W. Juchmann, J.B. Jeffries, Spatial distributions of C_2, C_3 and CH radicals by laser-induced fluorescence in a diamond depositing dc-arcjet, *J. Appl. Phys.* **82**, 2072 (1997).
31. J.B. Wills, J.A. Smith, W.E. Boxford, J.M.F. Elks, M.N.R. Ashfold, A.J. Orr-Ewing, Measurements of C_2 and CH concentrations and temperatures in a dc arc jet using cavity ring-down spectroscopy, *J. Appl. Phys.* **92**, 4213 (2002).
32. S. Pellerin, K. Musiol, O. Motret, B. Pokrzywka, J. Chapelle, Application of the (0,0) Swan band spectrum for temperature measurement, *J. Phys. D: Appl. Phys.* **29**, 2850 (1996).
33. M. Heintze, M. Magureanu, Methane conversion into acetylene in a microwave plasma: optimization of the operating parameters, *J. Appl. Phys.* **92**, 2276 (2002).
34. R. Bleekrode, W.C. Nieuwpoort, Absorption and emission measurements of C_2 and CH electronic bands in low-pressure oxyacetylene flames, *J. Chem. Phys.* **43**, 3680 (1965).
35. W.M. Jackson, Laser measurements of the radiative lifetime of the $B^2\Sigma^+$ state of CN, *J. Chem. Phys.* **61**, 4177 (1974).
36. LIFBASE: Database and Spectral Simulation Program (v1.6), J. Luque, D.R. Crosley, SRI International Report MP 99-009 (1999).
37. F. Mohasseb, K. Hassouni, F. Bénédic, G. Lombardi, A. Gicquel, Modelling of $Ar/H_2/CH_4$ microwave discharges used for nanocrystalline diamond growth, *Synthesis, Properties and Applications of Ultrananocrystalline Diamond*, D.M. Gruen, O. Shenderova, and A. Ya. Vul' (Eds.), NATO Science Series, Mathematics, Physics and Chemistry – Vol. 192 (Berlin: Springer, 2005), pp 93–108.
38. S.L. Girshick, C. Li, B.W. Yu, H. Han, Fluid boundary layer effects in atmospheric-pressure plasma diamond film deposition, *Plasma Chem. Plasma Process.* **13**, 169 (1993).
39. F. Mohasseb, K. Hassouni, F. Bénédic, G. Lombardi, A. Gicquel, Formation of soot particles in $Ar/H_2/CH_4$ microwave discharges during nanocrystalline diamond deposition: a modeling approach, *Pure Appl. Chem.*, in press.
40. K. Hassouni, O. Leroy, S. Farhat, A. Gicquel, Modeling of H_2 and H_2/CH_4 moderate-pressure microwave plasma used for diamond deposition, *Plasma Chem. Plasma. Process.* **18**, 325 (1998).
41. K. Hassouni, X. Duten, A. Rousseau, A. Gicquel, Investigation of chemical kinetics and energy transfer in a pulsed microwave H_2/CH_4 plasma, *Plasma Sources Sci. Technol.* **10**, 61 (2001).
42. K. Hassouni, C.D. Scott, S. Farhat, A. Gicquel, M. Capitelli, Non-Maxwellian effect on species and energy transport in moderate pressure H_2 plasmas, *Surf. Coat. Technol.* **97**, 391 (1997).

43. J.M. Yos, Transport properties of nitrogen, hydrogen, oxygen and air to 30000 K, Technical Memorandum RAD-TM-63–7, Avco Corp., Research and Advance Development Div., Wilmington, DE (1963).
44. T.-S. Yang, J.-Y. Lai, C.-L. Cheng, M.-S. Wong, Growth of faceted, ballas-like and nanocrystalline diamond films deposited in $CH_4/H_2/Ar$ MPCVD, *Diamond Relat. Mater.* **10**, 2161 (2001).
45. A. Gicquel, K. Hassouni, G. Lombardi, X. Duten, A. Rousseau, New driving parameters for diamond deposition reactors: pulsed mode versus continuous mode, *Mater. Res.* **6**, 25 (2003).
46. G. Lombardi, K. Hassouni, G.D. Stancu, L. Mechold, J. Röpcke, A. Gicquel, Modeling of microwave discharges of H_2 admixed with CH_4 for diamond deposition, *J. Appl. Phys.* **98**, 053303 (2005).
47. Y. Liu, C. Liu, Y. Chen, Y. Tzeng, P. Tso, I. Lin, Effects of hydrogen additive on microwave plasma CVD of nanocrystalline diamond in mixtures of argon and methane, *Diamond Relat. Mater.* **13**, 671 (2004).
48. A.C. Ferrari, J. Robertson, Origin of the 1150 cm^{-1} Raman mode in nanocrystalline diamond, *Phys. Rev. B* **63**, 121405(R) (2001).
49. R. Pfeiffer, H. Kuzmany, N. Salk, B. Günther, Evidence for trans-polyacetylene in nano-crystalline diamond films from H-D isotopic substitution experiments, *Appl. Phys. Lett.* **82**, 4149 (2003).
50. R. Pfeiffer, H. Kuzmany, P. Knoll, S. Bokova, N. Salk, B. Günther, Evidence for trans-polyacetylene in nano-crystalline diamond films, *Diamond Relat. Mater.* **12**, 268 (2003).
51. A.C. Ferrari, J. Robertson, Raman spectroscopy of amorphous, nanostructured, diamond-like carbon, and nanodiamond, *Philos. Trans. R. Soc. A* **362**, 2477 (2004).
52. H. Klug, L. Alexander, *X-ray diffraction procedures for crystalline and amorphous materials* (New York: Wiley, 1974), pp. 618–708.
53. P. Bruno, F. Bénédic, F. Mohasseb, F. Silva, K. Hassouni, Effects of substrate temperature on nanocrystalline diamond growth: an in-situ optical study using pyrometric interferometry, *Thin Solid Films*. **482**, 50 (2005).
54. D.M. Gruen, X. Pan, A.R. Krauss, S. Liu, J. Luo, C.M. Foster, Deposition and characterization of nanocrystalline diamond films, *J. Vac. Sci. Technol. A* **12**, 1491 (1994).
55. N. Jiang, S. Kujime, I. Ota, T. Inaoka, Y. Shintani, H. Makita, A. Hatta, A. Hiraki, Growth and structural analysis of nano-diamond films deposited on Si substrates pretreated by various methods, *J. Cryst. Growth*. **218**, 265 (2000).
56. Z. Sun, J.R. Shi, B.K. Tay, S.P. Lau, UV Raman characteristics of nanocrystalline diamond films with different grain size, *Diamond Relat. Mater.* **9**, 1979 (2000).
57. A.N. Goyette, J.E. Lawler, L.W. Anderson, D.M. Gruen, T.G. McCauley, D. Zhou, A.R. Krauss, Spectroscopic determination of carbon dimer densities in $Ar—H_2—CH_4$ and $Ar—H_2—C_{60}$ plasmas, *J. Phys. D: Appl. Phys.* **31**, 1975 (1998).
58. A.N. Goyette, J.E. Lawler, L.W. Anderson, D.M. Gruen, T.G. McCauley, D. Zhou, A.R. Krauss, C_2 Swan band emission intensity as a function of C_2 density, *Plasma Sources Sci. Technol.* **7**, 149 (2005).

59. W.S. Huang, T.A. Grotjohn, J. Asmussen, Plasma diagnostic measurements of argon-hydrogen-methane discharges used for ultra-nanocrystalline diamond deposition in a microwave CVD system, *Proceedings of the 27th IEEE International Conference on Plasma Science* (Piscataway, NJ: IEEE), p. 180.
60. M.H. Gordon, X. Duten, K. Hassouni, A. Gicquel, Energy coupling efficiency of a hydrogen microwave plasma reactor, *J. Appl. Phys.* **89**, 1544 (2001).
61. D.R. Lide (Ed.), *Handbook of chemistry and physics*, 81st edition (Boca Raton, FL: CRC Press, 2000).
62. T.G. McCauley, D.M. Gruen, A.R. Krauss, Temperature dependance of the growth rate for nanocrystalline diamond films deposited from an Ar/CH_4 microwave plasma, *Appl. Phys. Lett.* **73**, 1646 (1998).
63. W. Tan, T.A. Grotjohn, Modeling the electromagnetic excitation of a microwave cavity plasma reactor, *J. Vac. Sci. Technol. A* **12**, 1216 (1994).
64. U.M. Kelkar, M.H. Gordon, L.A. Roe, Y. Li, Diagnostics and modeling in pure argon plasma: energy balance study, *J. Vac. Sci Technol. A* **17**, 125 (1999).

7 Nanodiamond Films Deposited from Energetic Species: Material Characterization and Mechanism of Formation

Irina Gouzman

Space Environmental Section, Soreq Nuclear Research Center, Yavne, Israel

Shaul Michaelson and Alon Hoffman

Department of Chemistry, Technion–Israel Institute of Technology, Haifa, Israel

Introduction

Carbon science and technology has developed extensively in the last few decades due to discoveries of various polycrystalline and nanocrystalline diamond film deposition methods, synthesis of nanotubes, fullerenes, and carbon fibers, etc. Nanocrystalline diamond films represent a new remarkable material that is attracting a lot of attention in the scientific world due to its promising potential in many possible applications, such as tribology,[1,2] field emission,[3,4] electrochemistry,[5,6] protective optical windows,[7,8] as well as its unique ability to incorporate n-type dopants[9] compared to polycrystalline and single crystal diamond.

The microstructure and properties of carbon-based thin films depend on the deposition process and conditions used, including pressure, gas phase composition, and substrate temperature, as well as the energy of the reactive species (atoms or ions). One of the most successful examples of using energetic species for synthesis of materials with desirable properties is the deposition of diamond-like carbon (DLC).[10,14] Deposition of films from energetic species within a range of 20 eV to a few kiloelectronvolts has been reviewed recently.[12] In this energy range, the incident ions and atoms can displace surface atoms and adsorbed species and penetrate the substrate surface, which can lead to film growth beneath the surface in the process that has become known as a subplantation.[13] It is currently widely accepted that the subplantation advances through the following stages:

(i) penetration of carbon species to subsurface layers; (2) incorporation of carbon atoms inducing local stresses; (iii) sputtering and dilution of the target atoms until the atoms are identical; and (iv) growth of the pure carbon layer upon successive bombardment.[14] The semi-quantitative subplantation model has been applied to the deposition of carbon nitride, DLC, and homoepitaxy of silicon.[11,15] It has also been used to explain the key steps of the bias-enhanced nucleation (BEN) of diamond.[16] Energetic ions are involved also in the deposition of nanodiamond films, which are described in this chapter.

Nanodiamond films may be deposited by a number of deposition processes which differ in growth species and deposition parameters. In fact, each method results in different types of nanodiamond films. These may differ in terms of the diamond particle size, grain boundary nature, hydrogen content, and defect density, amorphous or graphitic component of the films, morphological properties of the films, and different chemical and physical properties. Also the formation mechanisms of the different films are different: for example, the model of nanodiamond called "ultrananocrystalline" diamond film growth from C_2 dimers onto the film surface,[17] whereas deposition from energetic species is a subsurface or subplantation process.

In this chapter a particular class of nanodiamond films deposited by energetic species are described.[18,19] Deposition is carried out using the direct-current glow-discharge (DC-GD) deposition technique from a methane/hydrogen mixture. In this method film growth occurs from energetic species being accelerated and incorporated into the film surface. At the conditions used in our studies we estimate that the kinetic energy of the ionic species involved in film growth is in the 100–200 eV range. The growth of the nanodiamond film occurs on top of a preferentially oriented graphitic precursor with its basal planes perpendicular to the substrate surface. The nanodiamond films consist of an agglomerate of diamond particles with particle size in the 3–5 nm range with amorphous grain boundaries. The hydrogen concentration in the graphitic precursor is only a few percent, but it increases to ~15–20 at.% in the nanodiamond film. Most likely hydrogen is bonded within the amorphous grain boundaries and saturates the nanodiamond particles. The surface of the films is amorphous in nature. From a microscopic perspective, nanodiamond film growth from energetic species is explained as a subsurface process in terms of a four-step cyclic process [20].

The characterization of the nanodiamond films is very complex and requires the use of a number of microstructural analytical methods. A full

picture of the film properties can only be attained from a combination of characterization methods. These characterization techniques are described below as applied to study nanodiamond films grown by the DC-GD method. However, the approach is more general and may be used to elucidate the phase composition, morphology, evolution, and properties of different materials.

The DC-GD deposited nanodiamond films were comprehensively explored by a number of complementary techniques. The hydrogen content and its role in nanodiamond film formation were assessed. The experimental methods used in our studies comprise near-edge X-ray adsorption fine structure (NEXAFS) to prove the short-range coordination of the carbon films and indirectly their phase composition. These measurements were supported by Raman spectroscopy of the films. X-ray diffraction (XRD) was used to determine the crystalline nature of the films and the diamond particle size. Atomic force microscopy (AFM) was used to measure the morphological evolution of the film surface. The surface and grain boundary phase composition were investigated by a combination of electron energy loss spectroscopy (EELS) measured as a function of incident electron energy and hydrogen etching experiments. Transmission electron microscopy (TEM) allowed the microstructural evolution and its visualization to be achieved. The density evolution of the films was determined by X-ray reflectivity (XRR). The hydrogen content and distribution in the films was studied by secondary ion microscopy spectroscopy (SIMS) and elastic recoil detection (ERD). The hydrogen bonding was investigated by high-resolution electron energy loss spectroscopy (HREELS).

The general structure of this chapter is as follows: the DC-GD deposition method and process used to grow the nanodiamond films are described in detail; then the film characterization and properties are presented. The emphasis is on the different methods applied for the characterization of the films. The advantages and limitations of each method are addressed. Following that, our understanding of the growth mechanism is presented.

7.1 The Deposition System and Deposition Parameters

Carbon films were synthesized by the DC-GD CVD method from a methane–hydrogen mixture in a home-made reactor, shown in Fig. 7.1.

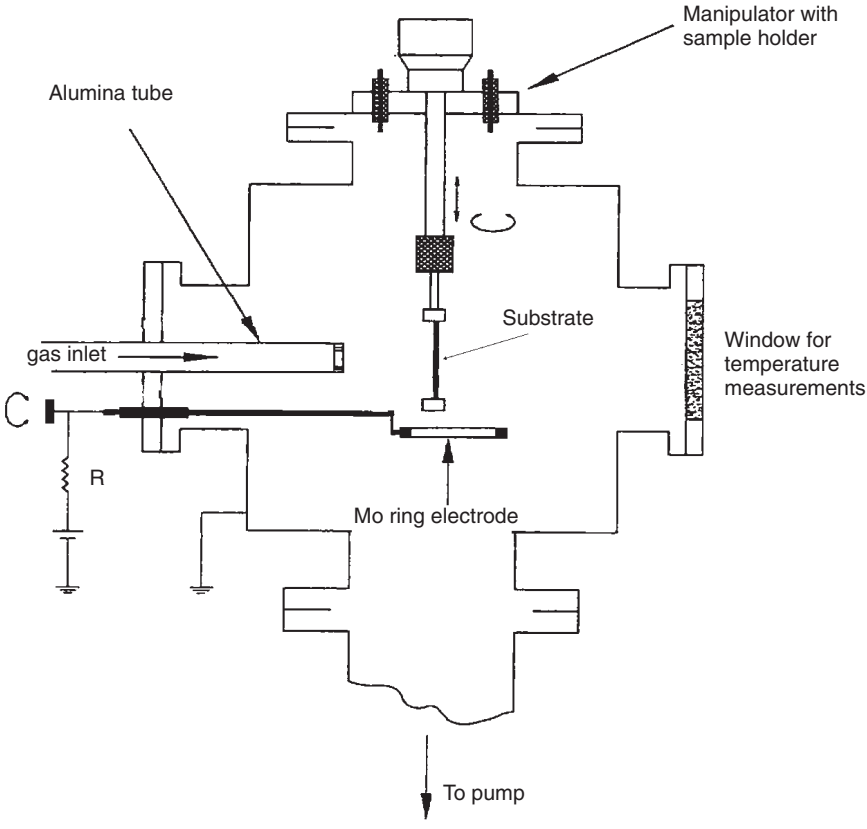

Figure 7.1 Schematic picture of the DC-GD CVD reactor used for nanodiamond film deposition.

The reactor is a deposition chamber with six concentric ports, gas-introduction and gas-activation units, a rotatable XYZ-manipulator, and a mobile molybdenum electrode for sample biasing. Rotary pumps enable a basic pressure of 1×10^{-3} Torr. The sample is heated by resistive heating through the substrates (silicon). The gas-feeding system consists of three independent gas lines, which were used for hydrogen (H_2), methane (CH_4), and argon (Ar). The gas flow is controlled by mass flow controllers. The gaseous mixture is introduced into the chamber through an alumina tube with an orifice of 1 mm, usually at a flow rate of 100 sccm. Gas activation is achieved by DC plasma discharge obtained by biasing the Mo electrode with respect to the sample (grounded). The bias

required for gas activation was about 500 V at a working pressure of 20 Torr. According to our estimations,[20,21] the applied potential difference of 500 V results in a mean energy of ionic species of 100–200 eV at the sample surface.

The following growth parameters were varied in order to determine the optimal deposition conditions for nanodiamond formation: methane concentration (1–20%) and substrate temperature during deposition (800–950 °C). A methane concentration of 9% and substrate temperature of 880 °C were found to be optimal for nanodiamond film deposition. In order to determine the main reactive species involved in the film formation, the plasma composition was examined by optical emission spectroscopy (OES) as a function of methane concentration at a temperature of 880 °C.

The plasma emission was measured by a three-grating assembly spectrometer with a maximal resolution of 0.04 nm and 350–800 nm spectral range. The monochromator was connected to the plasma reactor via an optical fiber ensuring light transmission from the plasma to the entrance slit. In general, plasma emission is observed through a radiative decay of molecules from excited electronic states. However, decay may also occur via collisional quenching and other non-radiative processes. Thus, many of the plasma species that are of interest, for example $CH_3\cdot$ and C_2H_2, cannot be detected by OES measurements.[22] In addition, the relation between excited and ground state populations is not always associated with the change in emission intensity since changes in plasma conditions may affect the excitation rate and competing de-excitation mechanisms. Considering these limitations, a rough estimation of the relative abundance of excited growth species may be obtained.

The OES spectra of DC-GD CH_4/H_2 plasma as a function of methane concentration is shown in Fig. 7.2(a). The spectra are dominated by sharp emission from the hydrogen Balmer H_α line at 656 nm (not shown) and H_β at 486.1 nm as well by less intensive H_γ (434 nm), whereas the introduction of methane results in the CH associated peak at 431.5 nm (corresponding to an $A^2\Delta \rightarrow X^2\Pi$ transition). The intensity of CH peak normalized to the intensity of H_α increases with increasing CH_4 concentration. Figure 7.2(b) shows the high-resolution spectra obtained for different hydrogen/argon/methane concentrations indicated on the plot. For high argon dilutions the presence of the C_2 Swan band (corresponding to the $d^3\Pi_g \rightarrow a^3\Pi_u$ transition with $\Delta\nu = 1$) is observed at 516.5 nm. However, these growth conditions (i.e., Ar concentration of >50%) do not lead to the deposition of nanodiamond films.

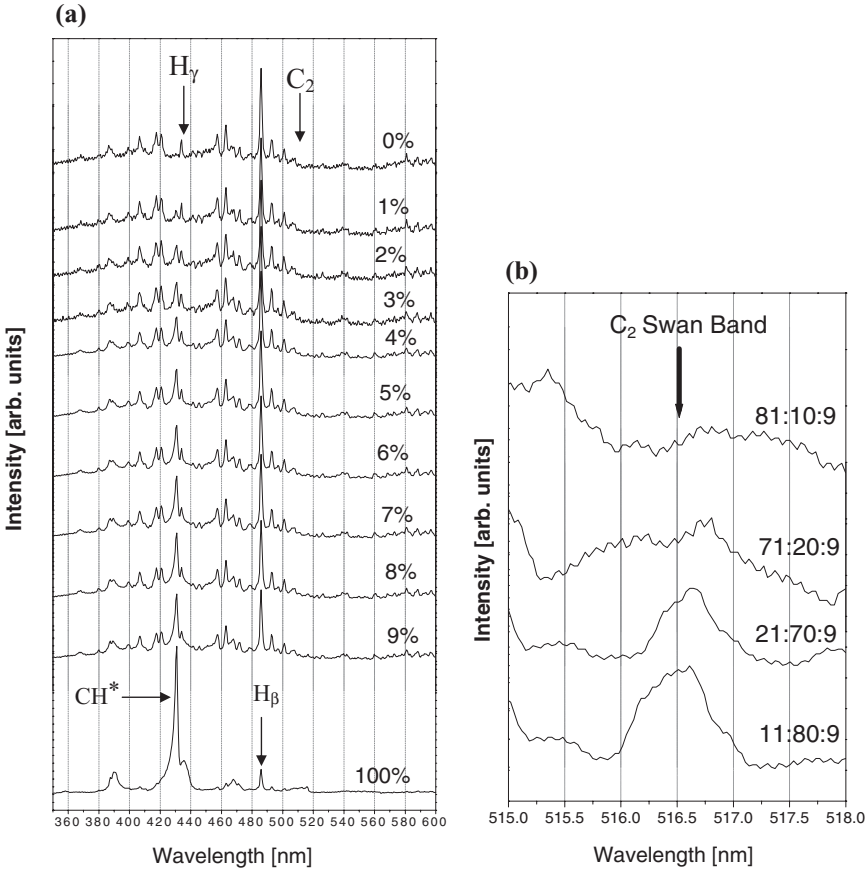

Figure 7.2 OES spectra of DC-GD plasma recorded for 20 Torr gas pressure at growth conditions. (a) OES spectra of hydrogen/methane mixtures as a function of methane concentration: 0% corresponds to pure hydrogen plasma, 100% corresponds to pure methane plasma; (b) High-resolution OES spectra of hydrogen:argon:methane mixtures. The appearance of the C_2 Swan band associated peak at 516.5 nm is apparent only for high argon concentrations.

Compared to microwave (MW) enhanced plasma deposition,[22–24] as well as with DC arc-jet-originated plasma,[25] the C_2 associated peak intensity is much smaller than the CH^* and H^* lines, which may be associated with a small concentration of C_2 species due to interaction with atomic hydrogen. Our main conclusion from these experiments is that the primary growth species in the DC-GD plasma nanodiamond deposition are essentially CH-ionic fragments and not C_2 dimers.

7.2 Evolution and Properties of the Films Studied by NEXAFS: Coordination and Orientation

The films deposited by DC-GD were extensively explored by NEXAFS spectroscopy. This technique is a very powerful spectroscopic method for analysis of the phase composition of the nanocrystalline carbon structures.[26–28] NEXAFS is dominated by multiple scattering of low-energy photoelectrons by nearest neighbors and directly probes unoccupied electron states of the ionized atom.[29] Often one can use a spectral "fingerprint" technique to identify the local bonding environment. With regard to the characterization of carbon-based materials, the NEXAFS technique is extremely useful, as it is not limited by the size of the crystallites, nor affected by any cross-sectional effects between sp^2- and sp^3-bonded carbon, and yields very different spectra for graphite and diamond.[30,31] Furthermore, in the case of anisotropic materials angle-resolved measurements can provide information about preferred growth orientation.[32,33]

NEXAFS measurements of the DC-GD deposited films and well-defined reference materials were carried out on the SA72 beam line (150–600 eV photon energy range, 135 mm spot size) using synchrotron radiation from Super-Aco at LURE, Orsay, France. The monochromator resolution was about 0.1 eV in the region close to the carbon K edge. The spectra were recorded by measuring the intensity of 8 eV and 15 eV secondary electrons. The angle-resolved (AR) NEXAFS measurements were carried out in the total electron yield (TEY) mode recording the sample electron current to the ground. Highly oriented pyrolitc graphite (HOPG), glassy carbon (GC), a high-quality CVD diamond film, and an ion-beam-irradiated CVD diamond were used as reference materials.

Figure 7.3 shows the NEXAFS spectra of the reference materials. Comparison of the near-edge structure of diamond and graphite shows that there are significant differences. These differences are directly related to the bonding structure of diamond (sp^3 hybridization) and graphite (sp^2 hybridization). For graphite the most prominent feature is the C(1s) $\rightarrow \pi^*$ transition at 285.5 eV (fingerprint of sp^2-coordinated carbon). This feature is absent in diamond. Also important is the onset of the σ^* states at 289 eV in diamond (fingerprint of sp^3-bonded carbon), compared to ~291 eV in graphite. The narrow and sharp peak at 289.3 eV, results from a C(1s) bulk core level diamond exciton, lying 0.2 eV below the minimum of the conduction band. The large dip appearing at 302.4 eV reflects the second absolute band gap which is characteristic of the crystalline diamond

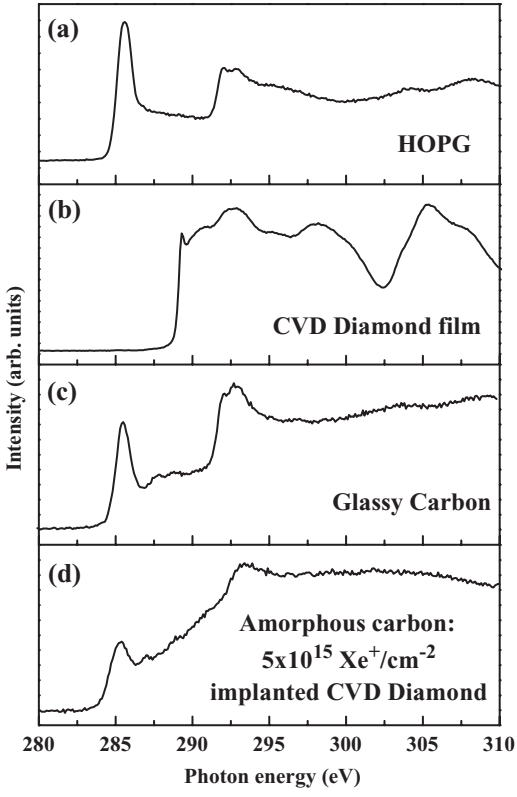

Figure 7.3 NEXAFS spectra recorded in the 280–310 eV photon energy range in the PEY mode collecting 8 eV electrons of HOPG (a), a CVD diamond film (b), glassy carbon (c), and 30 keV Xe^+ ion implanted CVD diamond film (d).

structure. These main spectroscopic features may be used to determine the chemical composition and structure of different carbon films.

The normalized intensity of the C(1s) → π* peak was shown to correlate quantitatively with the sp^2-bonded carbon content.[34] However, in order to separate crystalline size effects from sp^2-coordinated carbon content, glassy carbon, rather then HOPG, was used as a reference material of a predominantly sp^2 character but lacking long-range order. The spectrum of glassy carbon shows the C(1s) → π* and C(1s) → σ* transitions similar to graphite (Fig. 7.3(c)). A small peak observed near 288 eV is most likely due to the C(1*s*) → σ* transition of carbon atoms bonded to hydrogen[35] (the hydrogen concentration in glassy carbon is a few atomic percent)[36]. For quantitative evaluation, the normalization of the C(1s) → π* transition was performed using the intensity of the C(1s)

core level photoemission peak, which is visible if the NEXAFS spectrum is recorded at a partial electron yeild (PEY) mode using 15 eV secondary electrons.[37]

The influence of the defects in the diamond structure on the NEXAFS spectra was studied.[38] For this purpose, a high-quality CVD diamond film was implanted with a Xe^+, 30 keV ion beam at different doses resulting in different degrees of damage in the implanted region from point defects in the overall diamond structure (2×10^{13} Xe^+ cm^{-2}) to full amorphization (graphitization) of the modified region (2×10^{15} Xe^+ cm^{-2}).[36] Figure 7.3(d) shows the NEXAFS spectrum of a fully amorphized CVD diamond film. After high-dose implantation, the only characteristic feature in the spectrum is the transition characteristic of sp^2-bonded carbon at 285.3 eV and other features are smoothed out. This spectrum may be considered as an example of NEXAFS of amorphous carbon and is similar to that reported by Comelli et al.[39] for argon-sputtered amorphous carbon films.

One of the critical parameters determining the phase composition of the films formed by the DC-GD method is substrate temperature. NEXAFS spectra of films deposited at temperatures between 800 and 950 °C and $CH_4:H_2$ of 9 : 91 clearly showed a predominant diamond character of the material deposited at ~880 °C (Fig. 7.4). All NEXAFS spectra display the presence of the C(1s) $\rightarrow \pi^*$ transition at 285.5 eV, characteristic of graphite. However, the intensity of this peak is much lower than that measured for HOPG (see Fig. 7.3(a)). The strength of this feature decreases with increasing substrate temperature from 800 °C up to 900 °C and increases once again for the film deposited at 950 °C. The NEXAFS spectra of the films deposited at 880 and 900 °C show a large dip at 302.4 eV, corresponding to the second absolute gap in the diamond band structure. These two spectra display the "diamond" position of the C(1s) absorption edge at about 289 eV.

The changes in the NEXAFS spectra can be expressed in terms of the π^* parameter defined as the ratio of the intensity of the C(1*s*) $\rightarrow \pi^*$ transition in the studied film with respect to the one in glassy carbon, which was taken to be a graphitic reference (amorphous; no size and polarization effects to be considered). By definition, this parameter is equal to zero for diamond and to unity for glassy carbon. Then, assuming that there are no polarization or crystalline size effects that could result in variations in the X-ray absorption cross-section of the C(1*s*) $\rightarrow \pi^*$ transition, the π^* parameter for each film is expected to represent the sp^2 carbon fraction in the studied films and, consequently, the value of $(1 - \pi^*)$ represents the diamond character of the films. The values of the π^* parameter vary from ~0.8 for the films deposited at 800 and 950 °C to the minimum value of

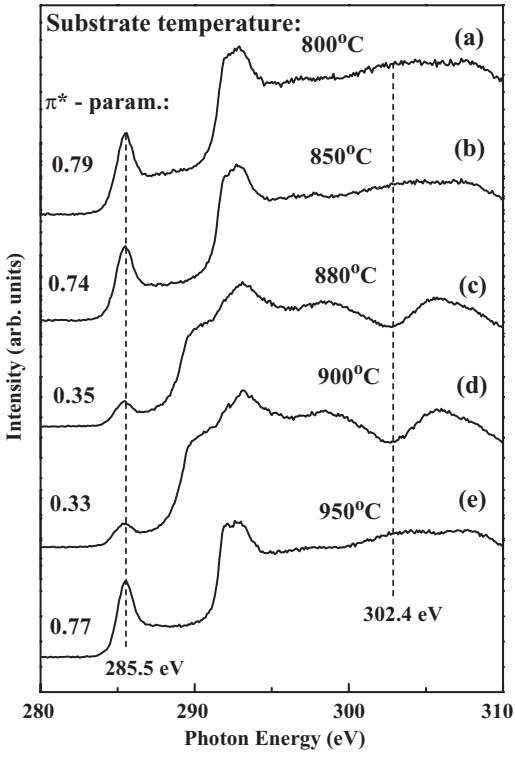

Figure 7.4 NEXAFS spectra recorded in the 280–310 eV photon energy range in the PEY mode collecting 8 eV electrons of DC-GD films deposited for 30 min at a 9 : 91 $CH_4 : H_2$ concentration and different substrate temperatures: 800 °C (a), 850 °C (b), 880 °C (c), 900 °C (d), and 950 °C (e).

~0.3 for the films with maximum diamond character, as shown in Fig. 7.4. These results are proof of the presence of a diamond-bonded carbon in the films deposited at around 880 °C. Along with *diamond*-bonded carbon, a *graphite*-like carbon is formed during the DC-GD process.

The evolution of the films as a function of deposition time was accomplished by carrying out NEXAFS measurements as a function of film thickness. Figure 7.5 shows NEXAFS spectra of the films deposited at 880 °C for different deposition times (5, 15, 30, and 60 min and $CH_4 : H_2$ of 9 : 91). As can be observed in this figure, the DC-GD films are sp^2 bonded up to a deposition time of 15 min. The prominent spectroscopic features of sp^2-coordinated carbon materials include a C(1s)–π^* resonance at about 285.5 eV and the onset of a C(1s)–σ^* transition at 291 eV. However, the films deposited for 30 and 60 min possess a dominant

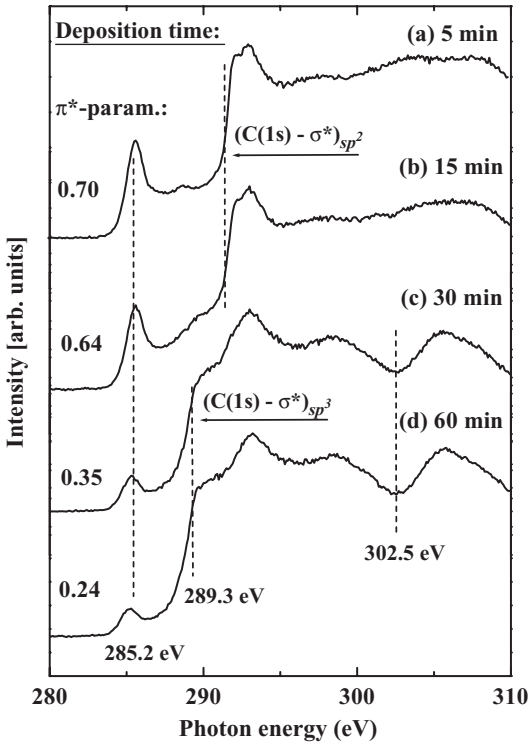

Figure 7.5 NEXAFS spectra recorded in the 280–310 eV photon energy range in the PEY mode collecting 8 eV electrons of DC-GD films deposited at a 9 : 91 CH_4 : H_2 concentration at 880 °C as a function of time: 5 min (a), 15 min (b), 30 (c), and 60 min (d).

diamond character (note the C(1*s*) absorption edge associated with the C(1*s*)–σ^* transition of sp^3-bonded carbon at about 289 eV and the large dip at 302.4 eV). Thus, it can be concluded that the DC-GD nanocrystalline diamond film develops from the graphitic precursor after a deposition time of about half an hour. The presence of the C(1s)–π^* resonance in the films deposited for longer than 30 min demonstrates that this film is actually a composite material. Comparison of the normalized intensity of this peak with the reference spectrum of GC established that the sp^2 phase represents ~20% of the material in the near-surface region (see π^* parameter values in Fig. 7.5).[37]

Additional information regarding the structure and orientation of the material formed during the initial stages of the DC-GD (5–15 min) was derived by angle-resolved NEXAFS (AR-NEAFS). It was shown[40] that

the hydrogenated graphitic layer precursor to nanodiamond formation displays some preferred orientation with respect to the film surface. It is well known that due to the two-dimensional structure of HOPG, π^* electronic states are directed perpendicular to its surface and therefore it is possible to selectively excite final states of this symmetry using polarized light.[32] The σ^* states, on the other hand, have been demonstrated to be insensitive to changes of the incident angle. Based on this analysis the percentage of the orientated basal planes was estimated and it was found that the fraction of alignment of the graphitic carbon in the precursor material is about 42%. A similar percentage of ordered graphitic carbon that reached 50% was estimated to be in the samples grown by MW-activated BEN from a methane/hydrogen mixture.[41] This value is smaller in the 950 °C, 15 min film (about 34%) and is equal to 19% in the 800 °C, 60 min specimen.[37] The main origin of such thermodynamically unstable vertical alignment of the basal planes may be associated with the stresses developing in the film. Moreover, the highest content of the orientated planes was in the films deposited at 880 °C, i.e., in the graphitic precursor to the nanodiamond phase. The consequent conclusion is that the highest stress develops in the film deposited at 880 °C.[42]

7.3 Phase Composition of the Films as Reflected by Raman Spectroscopy

Raman spectroscopy has much to offer as a non-destructive characterization tool. Backscattering geometry, especially with microfocus instruments, allows small regions in the heterogeneous films to be easily examined. Raman spectroscopy is a very powerful technique for the identification of crystalline phases, for studies of defects, structural disorder, and stresses in thin films. Because of its ability to distinguish between the many possible bonding geometries of carbon in carbon-based materials, Raman spectroscopy is a method of choice for characterizing the films formed by most of the deposition methods. However, due to quantum size effects, the use of Raman spectroscopy for the unambiguous phase characterization of films composed of nanosize crystalline particles is complicated.

The Raman spectrum of diamond consists of a single peak at 1332 cm^{-1}, whereas for graphite a single peak is observed at 1580 cm^{-1} (usually labeled the G peak).[36] The diamond peak may be broadened by several wavenumbers by defects and/or small crystalline size. Usually, in the case of CVD diamond films, this peak is accompanied by a broad band centered

around 1500–1550 cm^{-1} believed to be due to the sp^2-bonded carbon, possibly in the grain boundaries.[43] The Raman spectra of polycrystalline graphite and glassy carbon consist of two peaks. The first, located at 1580–1590 cm^{-1} (the G peak), originates from lattice vibrations in the plane of the graphite-like rings.[43] The second peak is located at about 1350 cm^{-1} (the D peak) and occurs in graphitic materials of small crystalline size. This disordered–induced band corresponds to a peak in the vibrational density of states (VDOS) of graphite. The intensity ratio of these peaks (I(D)/I(G)) has been shown to be proportional to $1/L_a$, for 2.5 nm < L_a < 300 nm, where L_a is the in-plane crystallite size.[44] When L_a drops below 2.5 nm, the D-peak intensity decreases (contrary to the trend observed for $L_a > 2.5$ nm), and I(D) approaches zero for fully amorphized films. In amorphous materials, the lack of long-range order leads to a relaxation of the selection rules governing the Raman scattering process, and all vibrational modes can contribute to the Raman spectra.

Because of the very much larger Raman cross-section for graphite sp^2 bonds (5×10^{-5} cm^{-1} sr^{-1}) relative to diamond sp^3 bonds (9×10^{-7} cm^{-1} sr^{-1}), it is very difficult to observe any spectral Raman features associated with a small amount of sp^3 bonding in the presence of sp^2-bonded material.[45] By the same token, the high sensitivity of the Raman spectra to sp^2 bonding allows sensitive detection of small concentrations of sp^2 bonding in a diamond film.

Amorphous, nanostructured, diamond-like, and nanodiamond films were extensively studied by conventional (visible light) Raman, as well as different variations of Raman technique, including surface-enhanced Raman, resonant Raman, and UV Raman. These studies were recently reviewed by Ferrari and Robertson.[46] The published Raman data of carbon materials with similar macroscopic properties show many variations from one spectrum to another with regard to peak positions, linewidths, and lineshapes. This is due to differences in the contributions from diamond-like structures, graphite-like structures, disordered carbon, and the amount of hydrogen in the films, arising from differences in preparation conditions.[46–48]

In the present study, the Raman measurements of the deposited films were performed using a DILOR XY micro-Raman spectrometer, using a 514.5 nm green line from an Ar ion laser in a backscattering geometry. The laser beam spot size was about 0.01 mm^2 and the incident power was 10 mW. The Raman spectra of the films deposited by the DC-GD process at different substrate temperatures in the 800–950 °C range for 60 min and 9% methane concentration are shown in Fig. 7.6. The Raman spectra of the materials deposited at 800, 840, and 950 °C display two broad bands

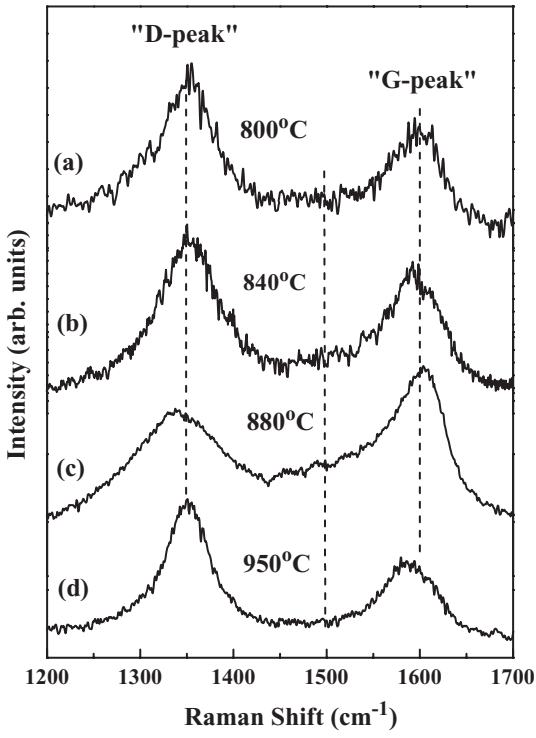

Figure 7.6 Raman spectra of the films after 30 min of DC-GD deposition at different temperatures: 800 °C (a), 840 °C (b), 880 °C (c), and 950 °C (d).

centered at about 1350 and 1595 cm^{-1}. These bands are assigned to the D and G peaks, respectively, and indicate the presence of micro- and/or nanocrystalline carbon phases, predominantly sp^2 in character. For the film deposited at 880 °C, an additional broad band centered at around 1490–1510 cm^{-1} contributes to the observed spectrum. The band in this range is commonly attributed to amorphous carbon. However, it will be shown later that the appearance of this band is accompanied by the appearance of the 1140 cm^{-1} peak, which attribution was discussed intensively in the literature and recently shown by isotopic effects to have originated from C—H bonds.[49]

Besides the appearance of the third band around 1500 cm^{-1}, the Raman spectra as a function of substrate temperature show the variation of: (i) the full-width half-maximum (FWHM) of the D and G peaks; (ii) the position of these peaks; and (iii) the intensity ratio $I(D)/I(G)$. The average values of these parameters, calculated for different sets of samples deposited under identical conditions, are plotted in Fig. 7.7. Only the

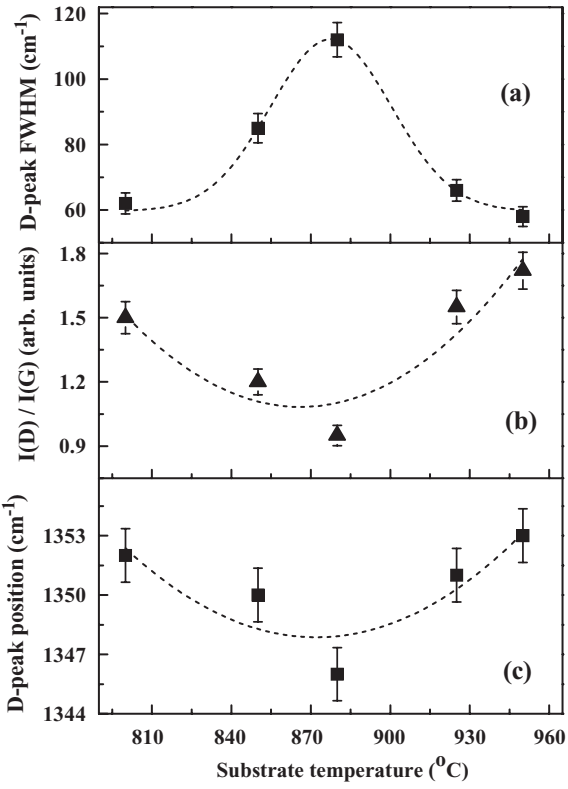

Figure 7.7 The variation of the Raman spectra parameters as a function of substrate temperature: FWHM of the D peak (a), intensity ratio $I(D)/I(G)$ (b), and D-peak position (c).

changes in the D-peak width and position are shown, since the parameters of the G peak are significantly affected by the appearance of the additional third band. It is shown that the FWHM of the D peak possesses a pronounced maximum around 880 °C substrate temperature and decreases toward lower and higher substrate temperatures; in the same temperature range, the intensity ratio $I(D)/I(G)$ and the D-peak position display a minimum, and these parameters increase toward lower and higher substrate temperatures. The Raman parameters (position, width, and relative intensity of the D and G peaks) were shown to vary systematically with deposition conditions and with macroscopic properties of the hydrogenated amorphous carbon films.[50,51] The most conspicuous trend is an increase in the fraction of sp^2-coordinated carbon in the film with decreasing width and increasing D-line intensity and vice versa. Note that the broadening, the decrease in the relative intensity, and the shift toward

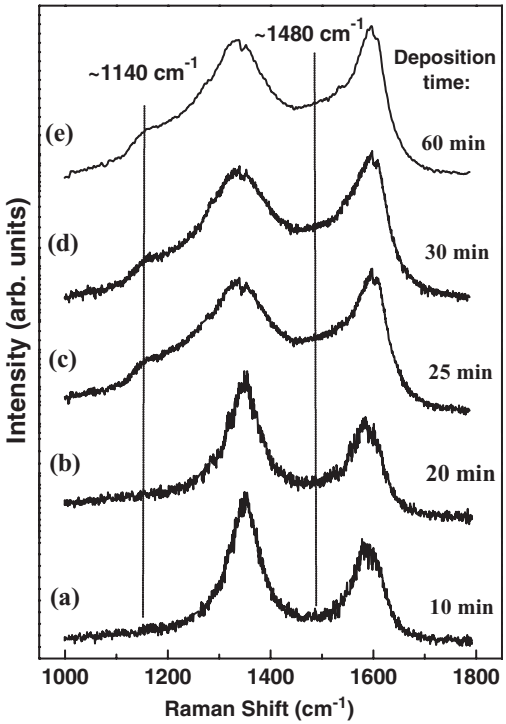

Figure 7.8 Raman spectra of the films after DC-GD deposition at 880 °C substrate temperature as a function of time: 10 min (a), 20 min (b), 25 min (c), 30 min (d), and 60 min (e).

lower wavenumbers of the D peak correspond to a decrease of the relative π^* parameter derived from NEXAFS results. Thus, the results of Raman analysis are consistent with the lowest fraction of the sp^2-bonded carbon deposited under conditions favoring the formation of a predominantly sp^3-bonded film (based on NEXAFS).

The Raman spectra of the films deposited at 880 °C as a function of deposition time are shown in Fig. 7.8. All spectra exhibit the presence of the D and G peaks, which have different widths, relative intensities, and slightly different positions. An additional low-intensity band centered at around 1480–1500 cm^{-1} appears in the spectra of the films deposited after 25, 30, and 60 min of the deposition. This peak is accompanied by an additional band at ~1150 cm^{-1}. The analysis of the FWHM of the D peak, the intensity ratio (I(D)/I(G)), and D-peak position as a function of the DC-GD time shows that the width of the D peak increases significantly, concurrently with the decrease of its relative intensity, and shifts toward lower

wavenumbers with increasing deposition time. It clearly indicates the decrease in the relative fraction of sp^2-coordinated carbon in the films, based on the data published for hydrogenated a:C films[51] and our NEXAFS results.

The peak around 1150 cm^{-1} was often taken as a simple criterion for a nanocrystalline diamond phase.[52] It was also shown that the two modes around 1150 cm^{-1} and 1490 cm^{-1} appear together and show significant dispersion, while the diamond mode does not.[49] However, it was shown by Raman[53,54] and surface-enhanced Raman spectroscopy[55] that these peaks are associated with ν_1 and ν_3 vibration modes of *trans*-polyacetylene co-deposited with diamond phase. We confirm these findings by means of the isotopic effect. Our findings are fully consistent with the recent work of Ferrari and Robertson[46] who used CH_4/H_2, CD_4/H_2, CH_4/D_2, and CD_4/D_2 mixtures and a variety of excitation wavelengths from the visible to UV to demonstrate that these modes are not due to (C—C) sp^3 vibrations.

The nature of the 1150 cm^{-1} peak is elucidated in the present study by depositing films from $^{13}CH_4 + H_2$, $^{12}CD_4 + D_2$, and $^{12}CH_4 + H_2$ gas mixtures (see Raman spectra in Fig. 7.9). In all cases the ratio of hydrocar-

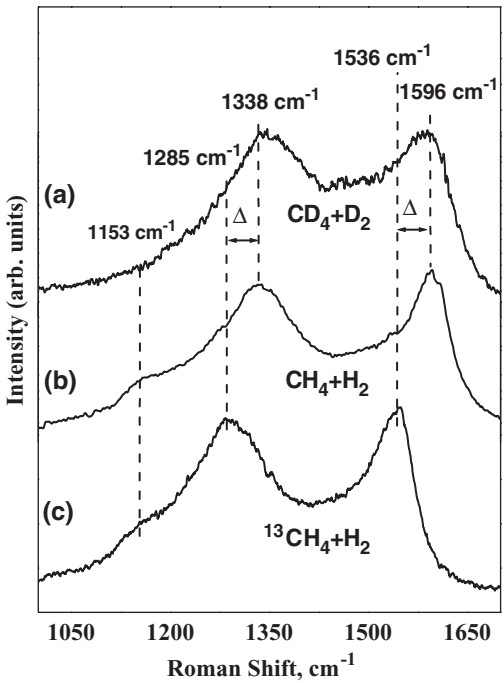

Figure 7.9 Raman spectra of the films deposited for 30 min at 880 °C using CD_4/D_2 (a), CH_4/H_2 (b), and $^{13}CH_4/H_2$ (c) gas mixtures.

bon/hydrogen was maintained as 9/91. The absence of the 1150 cm^{-1} peak is evident in the case of the $^{12}CD_4/D_2$ growth mixture, whereas both carbon peaks centered at 1338 and 1596 cm^{-1} are shifted toward smaller wavenumbers in the case of the ^{13}C isotope: the shift, Δ, equals 53 and 60 cm^{-1} for 1338 and 1596 cm^{-1} peaks correspondingly. Note that the 1150 cm^{-1} peak is positioned at a similar wavenumber for nanodiamond film deposited for $^{13}CH_4$ and $^{12}CH_4$ gas mixtures.

As is shown in Fig. 7.8, only graphitic features dominate the Raman spectra at the initial stages of film formation, whereas nanodiamond phase evolution is coupled with the appearance of peaks at ~1150 and ~1480 cm^{-1}. Whereas the Raman spectrum of the films grown from the $^{12}CD_4/D_2$ mixture displays no evidence of the 1150 cm^{-1} peak, it does exist in the spectrum of $^{13}CH_4/H_2$ and $^{12}CH_4/H_2$. While a very strong and distinct isotopic effect does exist in the carbon-associated peaks of 1338 and 1596 cm^{-1}, the peak of 1150 cm^{-1} is nearly unaffected by the ^{13}C isotope. Indeed, carbon 1338 and 1596 cm^{-1} peaks shift toward lower wavenumbers in perfect agreement with ^{12}C and ^{13}C reduced mass difference:

$$\omega_{^{13}C} = \frac{\omega_{^{12}C}}{\sqrt{\frac{\mu_{^{13}C-^{13}C}}{\mu_{^{12}C-^{12}C}}}} = \omega_{^{12}C} \times 0.9608 \qquad \text{Eq. (7-1)}$$

whereas the same effect much less prominent in the case of ^{13}C—H and ^{12}C—H vibration mode:

$$\omega_{^{13}C-H} = \frac{\omega_{^{12}C-H}}{\sqrt{\frac{\mu_{^{13}C-H}}{\mu_{^{12}C-H}}}} = \omega_{^{12}C-H} \times 0.997 \qquad \text{Eq. (7-2)}$$

This finding further corroborates the fact that the 1150 cm^{-1} mode is associated with a C—H vibration in *trans*-polyacetylene and not with a vibration mode related to a pure carbon phase. Note that this peak was observed even in the nanodiamond films obtained from fullerene-containing hydrogen-poor plasmas, but was initially attributed to nanocrystalline diamond.[17]

7.4 Crystalline Structure of the Films by XRD

Examination of the 880 °C film by NEXAFS clearly shows that the carbon atoms in the films display predominant sp^3 coordination and

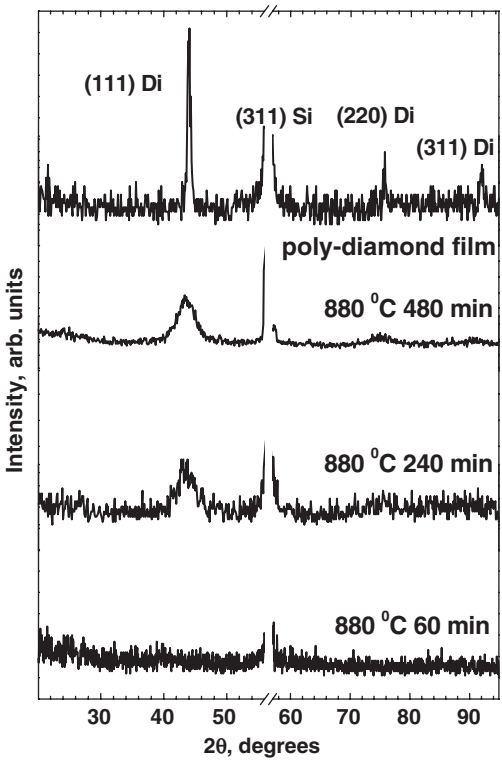

Figure 7.10 XRD patterns of DC-GD carbon films deposited at 880 °C for various deposition times and of reference polycrystalline HF CVD diamond film.

strongly suggests the diamond nature of these films. By XRD we unambiguously determined the nanocrystalline nature of the films. XRD analysis was performed in a Bede D^3 diffractometer combined with 18 kV Rigaku rotating anode generator that produced monochromatized Cu $K_{\alpha 1}$ radiation. The measurements were done under a grazing angle configuration, i.e., the angle between the incident beam and the immobile sample surface was 3.5° while a 2Θ scan of the reflected intensity was performed with a 0.2 mm receiving slit in front of the detector. With this system the X-ray reflectivity were carried out as well.

Figure 7.10 shows diffraction patterns of the DC-GD carbon films deposited at 880 °C as well as of the standard materials. Due to the glancing angle configuration, the (311) Si substrate diffraction peak at 2Θ = 56.12° dominates in all the diffraction patterns. Diffraction patterns of the films grown at 880 °C for 1 h did not exhibit crystalline peaks. The films grown at 880 °C for longer than 1 h deposition demonstrate a diamond structure with a prominent diamond (111) peak at 43.9°. The (111)

diamond peak in the diffraction patterns of the films deposited at 880 °C is broadened as a result of the nanocrystalline structure of these films. The size, D, of diamond particles could be evaluated by the Scherrer formula

$$D = 0.89\lambda/(B\cos\Theta) \qquad \text{Eq. (7-3)}$$

where $\lambda = 1.5406$ Å is the X-ray wavelength, B is the half-width of the diffraction peak, and Θ is the Bragg angle. The instrumental peak width was subtracted from the measured B values. After this correction, the grain size was estimated to be about 5 nm.[42]

7.5 Morphological Evolution of the Films by AFM

AFM was shown to be a powerful technique to accurately measure the surface morphology from which the film growth process may be elucidated.[56] AFM topographic analysis of the nanodiamond film surfaces established a strong roughening effect that accompanies formation of the nanodiamond phase.[37] Non-contact AFM analysis was carried out on a Topometrix 2010 AFM, using pyramidal Si_3N_4 tips with an aspect ratio of 2 : 1. The curvature radii were 10 nm. The average film roughness increased from 2.9 nm in the graphite-like film deposited for 15 min to 33.5 nm in the film deposited for 30 min (more than 10 times). Increase of surface roughness connected with the stress development is a well-known phenomenon in thin-film deposition of semiconductors[57] and metals[58]. Spaepen has demonstrated that an increase of the surface roughness can lead to stress relaxation when the roughness amplitudes approximate the average size of grain sizes on the surface[59] Given the very high values of the measured roughness and the nanosized grain boundaries, stress relaxation via a drastic roughness increase is a plausible mechanism of the stress relaxation for the carbon films deposited by DC-GD.

7.6 Surface and Grain Boundary Phase Composition Studied by EELS

The surface and grain boundary phase composition of the nanodiamond films were explored by EELS measured at different primary electron energies and using the effect of MW hydrogenation on the films.[37]

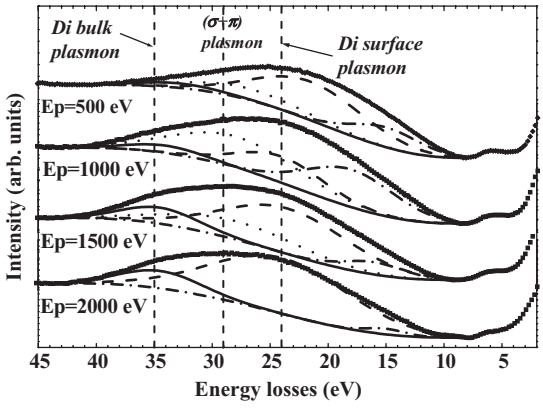

Figure 7.11 EEL spectra of a nanodiamond film (880 °C) for different incident electron energies.

EELS analysis of the samples was carried out in a SPECS ultrahigh vacuum system equipped with a hemispherical electron analyzer. Figure 7.11 shows EELS of a nanodiamond film grown at 880 °C for 60 min using primary electron energies in the 500–2000 eV range. The position of the energy losses used in our analysis was determined by second-order derivatives of the measured EEL spectra.[37]

In EEL spectra recorded using higher primary electron energies, the features in the loss spectrum are outweighed by excitations localized in deeper regions compared to spectra recorded using lower primary energy. For a primary electron energy of 500 eV, loss peaks at 6 and 27 eV are prominent. These losses are characteristic of graphite-like carbon and they are associated with $\pi - \pi^*$ interband transitions and the excitation of the $(\pi + \sigma)$ plasmon, respectively. For primary electron energies higher than 1500 eV, the dominant loss peaks are located at 34 and 23 eV. These losses are assigned to diamond bulk and surface plasmons, respectively. The nature of the peak in the 15–18 eV range is less clear. It is known that an interband transition at about 15 eV appears in EEL spectra of diamond.[60] It can also be represented by a surface plasmon of amorphous carbon that is present in the near-surface area in significant amounts (about 20% by NEXAFS measurements) and its energy will be equal approximately to 19 eV (i.e., 27 eV (the energy of the bulk plasmon of sp^2 carbon)/$\sqrt{2} \approx$ 19 eV). Therefore these results strongly suggest that the *upper surface* of the films is composed of an sp^2-coordinated carbon layer.

To study the nature of the grain boundaries between the nanodiamond particles, the films were exposed to a 30 min treatment in hydrogen MW

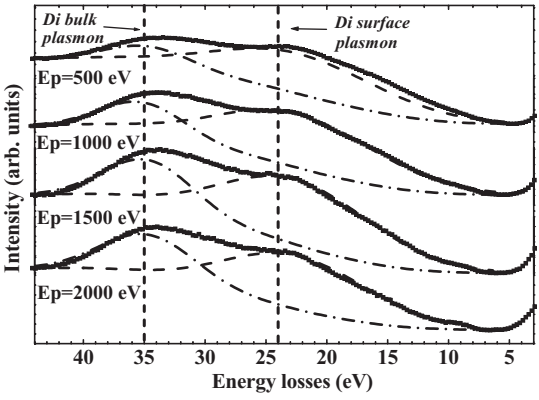

Figure 7.12 EEL spectra for different incident electron energies of a nanodiamond film (880 °C) after 30 min hydrogen MW plasma.

plasma. It is well known that hydrogen MW plasma etches graphite and/or amorphous carbon at a much higher rate than that of diamond. If sp^2-coordinated carbon (whose presence in the films is determined by NEXAFS) is distributed homogeneously throughout the nanodiamond particles, the EEL spectrum is expected to be similar to that measured before hydrogen MW plasma etching. EELS at primary electron energies in the 500–2000 eV range of the film deposited at 880 °C for 60 min followed by its exposure to hydrogen MW plasma for 30 min are shown in Fig. 7.12. As seen in this figure, the EEL spectrum is dominated by diamond features including bulk and surface plasmons at 34 and 23 eV, respectively, for the whole range of the primary energies. Therefore, the sp^2-hybridized carbon is located mostly at the *grain boundaries* between the nanodiamond particles and not within the particles themselves.

MW hydrogen plasma very efficiently etches sp^2-bonded carbon. Under correct conditions (in fact, very similar to those utilized for polycrystalline diamond CVD, but applying pure hydrogen without methane) this treatment was found to produce well-ordered single crystal diamond surfaces as determined by LEED and STM. In a similar manner, the effect of the DC-GD hydrogen plasma on the diamond surface was examined. A polycrystalline diamond film grown by HF CVD underwent a 30 min hydrogen plasma treatment in the DC-GD reactor. Figure 7.13 demonstrates EEL spectra of the sample before and after the hydrogenation. Upon DC-GD plasma hydrogenation, the diamond features at about 33 and 23 eV that belong to diamond bulk and surface plasmons are smeared out. The measured spectrum resembles EEL spectra of hydrogenated DLC films

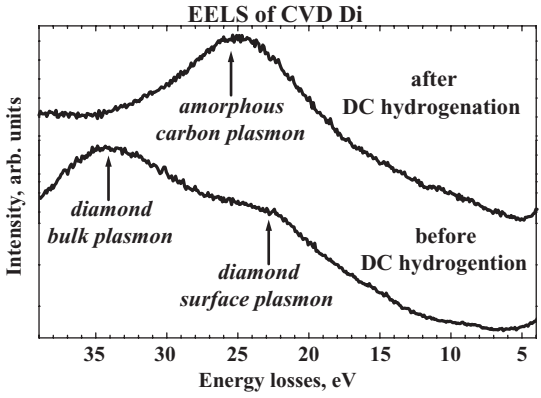

Figure 7.13 EEL spectra of a HF CVD diamond film before and after hydrogenation in the DC-GD plasma. Primary electron energy is equal to 2000 eV.

with a prominent ($\pi + \sigma$) plasmon at 25 eV. It indicates that the role of activated hydrogen in the formation of nanodiamond by the DC-GD method is different from that in the growth of microcrystalline diamonds by CVD. It can be concluded that hydrogen activated by DC-GD has sufficient energy to amorphize the upper surface structure of diamond. This effect has great importance in understanding the mechanism of nanodiamond formation by DC-GD CVD.[61]

7.7 Hydrogen Content in the Films by SIMS and ERD

Hydrogen content in the deposited films was determined by SIMS and ERD.[62] SIMS analysis was performed in a dynamic mode in a Cameca IMS4f ion microscope. The samples were irradiated by a 14.5 keV Cs^+ ion beam. The sampling area was about 64 μm^2. The basic chamber pressure was 8×10^{-10} Torr, while the ion current was about 1×10^{-8} A. As SIMS analysis is complicated by the presence of background hydrogen, the samples were grown from a CD_4/D_2 gaseous mixture for analysis of the deuterium content.[62] Shown in Fig. 7.14 is the deuterium profile of a DC-GD nanodiamond sample grown at 880 °C for 60 min. This figure demonstrates that the hydrogen concentration in the film is not constant; it obtains a maximal value of ~19 at.% in the diamond region and decreases in the graphitic region [62]. Such large concentrations makes accurate

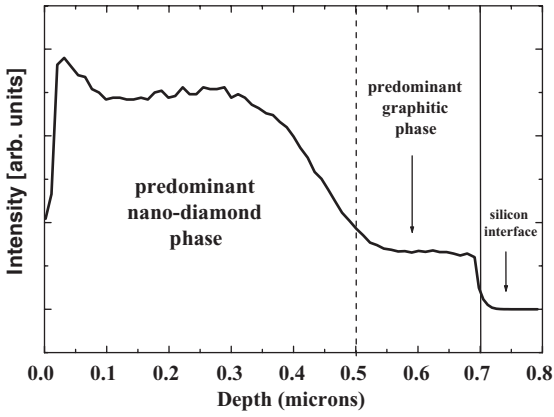

Figure 7.14 SIMS depth profile of deuterium in a nanodiamond film grown from a 9 : 91 CD_4 : D_2 mixture at 880 °C for 60 min.

quantitative analysis of hydrogen by SIMS quite uncertain as the linear calibration of the measured intensity signal is valid up to about 1 at.%. These results clearly show that the nucleation and growth of nanodiamond is accompanied by intensive adsorption of hydrogen in the deposited film. The absolute maximal hydrogen concentration was determined by ERD analysis.[62,63]

7.8 Hydrogen Bonding Configuration in the Nanodiamond Films Studied by HREELS

Quantitative analysis by ERD and SIMS measurements shows enhanced hydrogen retention within the films along with nanodiamond formation (cf. Section 7.7). Using HREELS measurements the hydrogen bonding configuration can be examined. From previous studies characteristic losses were found for hydrogen bonded to different carbon species. The most prominent and agreed-upon features are: the symmetric–asymmetric aliphatic (sp^3) C—H stretching vibration modes which lie in the range of 350–363 meV, whereas the symmetric–asymmetric olefinic (sp^2) stretching modes lie in the 372–381 meV range.[64–67]

We established that the nanodiamond phase has developed onto a preferentially oriented graphitic precursor with a hydrogen concentration of ~5 at%. The formation of the nanodiamond phase is accompanied by the enhancement of hydrogen concentration up to ~15–20 at.%. In this section we examine the different bonding configurations of hydrogen atoms

within nanodiamond films by a combination of HREELS measurement and hydrogen plasma etching. Hydrogen plasma activation was carried out by means of MW and DC-GD at 880 °C.[37] As HREELS is sensitive to the upper atomic layer, the spectra of the as-deposited films do not necessarily reflect the hydrogen bonding to the nanodiamond particles themselves. MW-activated hydrogen plasma preferentially etches the amorphous surface layers and uncovers the nanodiamond crystallites. We compare our results to hydrogen-terminated high-quality polycrystalline diamond film deposited by means of the hot filament (HF) CVD method.

HREELS analysis of the samples was carried out in a SPECS ultrahigh vacuum system equipped with a hemispherical electron analyzer and monochromator. At an incident electron energy of 5 eV the FWHM of the beam was ~5 meV in the straight-through mode.

The HREEL spectra of nanocrystalline diamond films as a function of deposition time are shown in Fig. 7.15 (curves A–C).[68] The HREEL spectrum of high-quality microcrystalline diamond film prepared by the HF CVD method is shown in Fig. 7.15 (curve D). The spectrum of the film deposited for 10 min displays a peak associated with C—H stretch at a loss energy of 362 meV with a FWHM of ~34 meV. For films deposited for longer times this peak shifts to 367 meV and FWHM of ~42 meV. Under similar measuring conditions the C—H vibration of the hydrogenated high-quality polycrystalline CVD diamond film displays a peak position at 360 meV with a FWHM of 19 meV. These results show that the HREELS of the as-deposited nanodiamond films (long deposition times) reflects hydrogen bonded to carbon atoms in predominant sp^2 coordination. This is reasonable considering that our electronic EELS measurements as a function of incident electron energy show that the upper surface of the films is composed of an amorphous sp^2-bonded carbon layer. This important point is discussed further below.

In Fig. 7.16 the HREEL spectra of nanodiamond films deposited for 2 h at optimal growth conditions are shown: namely, as-grown (A) and following exposure for 2 min of MW-activated hydrogen (B). The HREEL spectrum of high-quality HF CVD diamond is shown in Fig. 7.16 (curve C) for comparison. After MW hydrogen plasma etching the HREELS spectrum of the nanodiamond films displays a peak at 140 meV, its overtone at 280 meV, and a third broad peak at ~450 meV. The C—H stretching vibration now appears at a loss energy of 355 meV. Also a small feature may be distinguished close to the elastic peak at ~50 meV loss energy. These results show that MW hydrogen plasma removes the upper amorphous layer of the nanodiamond film and uncovers the hydrogen bonding to the nanodiamond particles themselves.

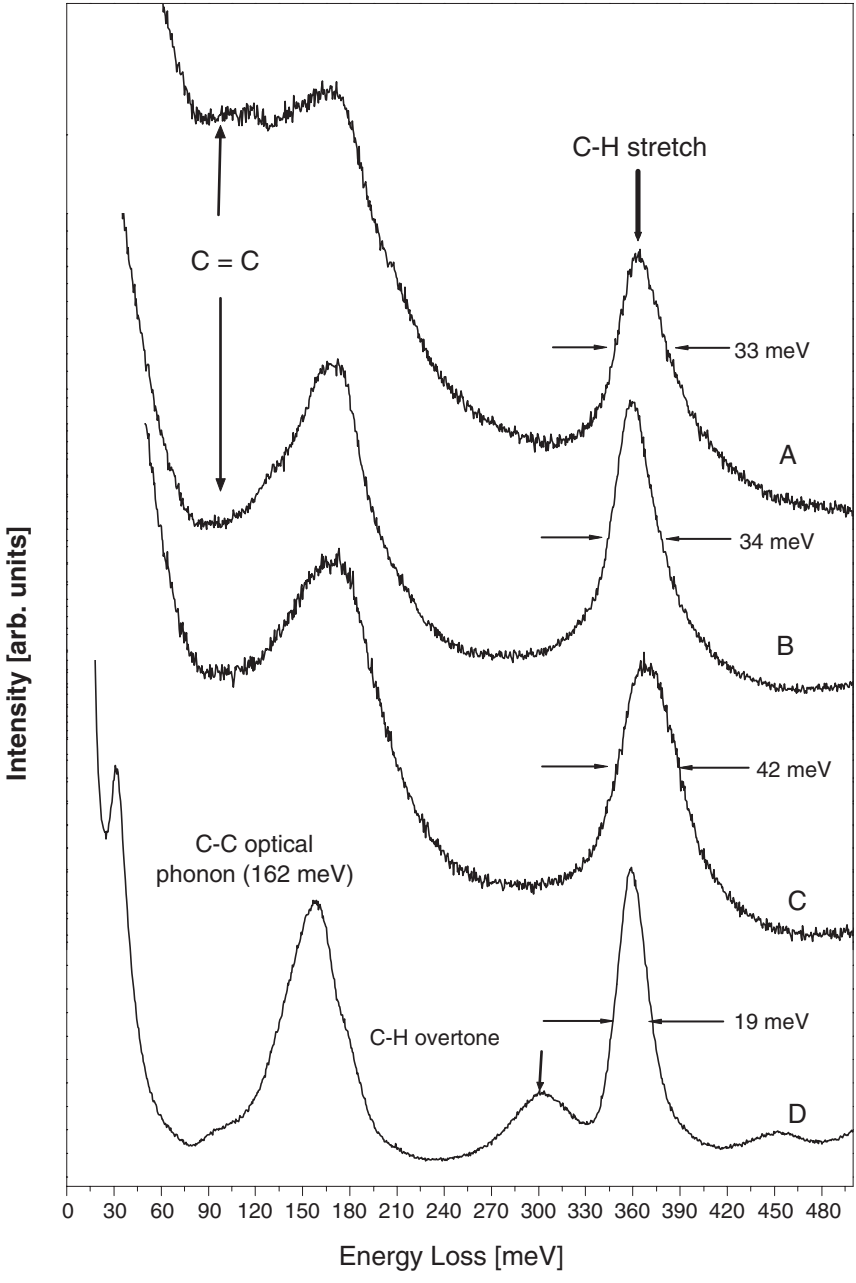

Figure 7.15 HREEL spectra of as-deposited nanodiamond films (A–C) as a function of deposition time. HREEL spectrum of as-deposited HF CVD high-quality diamond film is shown for comparison (D).

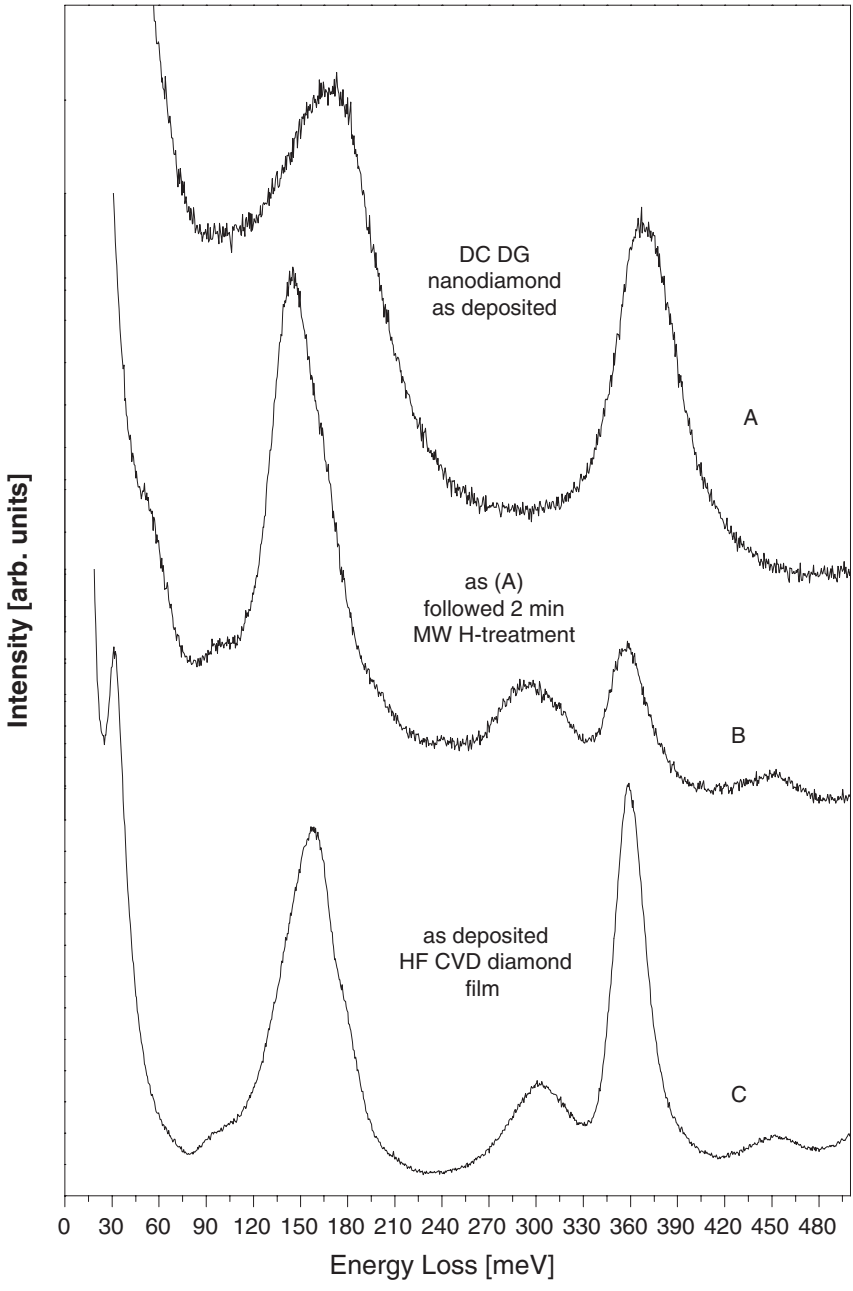

Figure 7.16 HREEL spectra of DC-GD nanodiamond films: (A) as-deposited; (B) following 2 min MW H treatment; (C) HREEL spectrum of as-deposited HF CVD diamond film shown for comparison.

Our experimental results suggest that the hydrogen bonding in the graphic precursor is different from that in nanodiamond film. As is shown in Fig. 7.8 (Section 7.3), only graphitic features dominate the Raman spectra at the initial stages of film formation, whereas nanodiamond phase evolution is coupled with the appearance of peaks at ~1150 and ~1480 cm^{-1}, attributed to ν_1 and ν_3 vibration modes of *trans*-polyacetylene co-deposited with the nanodiamond phase (see Section 7.3 and references therein).

A rigorous interpretation of our HREEL spectra is complicated because of the nanocomposite nature of the nanodiamond films. Here we attempt to interpret the HREEL spectra of the films deposited for different times. As seen in Fig. 7.15, the FWHM of the C—H stretching mode centered at 360–367 meV is ~33–34 meV for films deposited up to ~30 min. Following the development of the nanodiamond phase (90 min deposition) this peak widens and its FWHM has a value of 42 meV. These phenomena may be associated with various contributions of sp^2- and sp^3-bonded carbon, whose C—H bonding configuration is different for the films deposited for more than 30 min.

Another prominent feature is the down-shift of the C—H stretching with deposition time (Fig. 7.15, curve B). The spectra measured for films deposited for 10 and 90 min reflect the bonding of hydrogen in an sp^2-bonded amorphous carbon structure in agreement with our present understanding of the film's surface termination.[37] However, the HREEL spectra of the 30 min films suggest hydrogen bonding in an sp^3 environment (according to back-shift to 360 meV and comparison with the high-quality polycrystalline diamond HREEL spectrum). It may be that after 30 min of deposition during which the primary diamond clusters are formed by stress relaxation or densification (the mechanism for nanodiamond formation from energetic species is discussed in the last section of this chapter), there are some diamond particles positioned also within the surface region, which give rise to a "more sp^3" HREEL spectrum. This hypothesis is supported by our AFM measurements which show a maximal surface roughness for the film deposited for 30 min[37] (cf. Section 7.5).

Now the effect of MW-activated H on the film's surface chemistry is examined. Treatment of as-deposited nanodiamond films by MW-activated hydrogen results in the appearance of pronounced diamond bulk and surface plasmons (at 34 and 23 eV loss energies, correspondingly) (cf. Section 7.6). The HREEL spectra of nanodiamond films seen in Fig. 7.16 (curves A and B) are different in that the spectrum (A) represents loss features mostly associated with the upper amorphous carbon layer whereas

spectrum (B) is mostly associated with nanodiamond crystallites themselves. The two main features of the HREEL spectra of the as-deposited nanodiamond (Fig. 7.16, curve A) are peaks at 367 meV and 170 meV energy loss. The first one is associated with multiple C—H stretching modes whereas the second is associated with contributions from bulk diamond optical phonon, energy losses owing to C—H bending modes, as well as from various surface phonon modes.[64,69,70] Following MW H treatment these two features shift toward 355 meV and 140 meV along with the appearance of broad peaks centered at 280 and 450 meV. The loss at 355 meV is related to the C—H stretching mode associated both with symmetric aliphatic sp^3 carbon and with hydrogen adsorption onto the surfaces of nanodiamond crystallites. The 280 meV broad peak is most likely attributed to overtones of C—C vibrations associated with high-quality diamond surfaces.[71] This loss was also observed in our HREEL spectra of high-quality polycrystalline diamond film deposited by the HF CVD method (Fig. 7.16, curve C).

7.9 Density Evolution of the Films Examined by XRR

Shown in Fig. 7.17 are XRR measurements of a diamond single crystal, a polycrystalline diamond film deposited by HF CVD, and a film grown by DC-GD CVD at 880 °C as a function of deposition time (converted to film thickness). As seen from this figure, the density measured for the polycrystalline diamond was constant with film thickness. However, for the 880 °C DC-GD film the density was found to increase with thickness from ~2.4 to2.5 $g\,cm^{-3}$ in the first two layers, through 2.6 to 2.8 $g\,cm^{-3}$ in the third and fourth layers, to 3 $g\,cm^{-3}$ in the fifth layer. These results are in qualitative agreement with the phase evolution of the films from a graphite-like nature (low density) to a diamond-like one (higher density).

7.10 Visualization and Evolution of the Films Studied by HR TEM

Cross-sectional HR TEM measurements of the films were conducted in a Philips CM200 microscope for structural imaging (point resolution 0.19 nm) and a Gatan parallel electron energy loss (PEEL) spectrometer. The samples were thinned by mechanical grinding, polishing, and ion

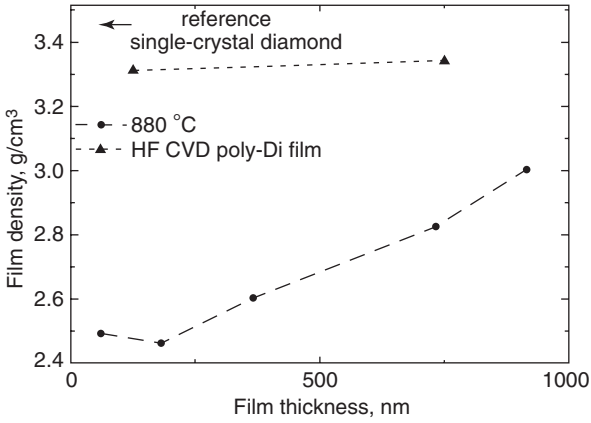

Figure 7.17 X-ray reflectivity measurements of the density of films with different thickness deposited at 880 °C corresponding to the layers indicated in the cross-sectional image of Fig. 7.18. The density increases from 2.4–2.5 g cm^{-3} in the first and second layers, to 2.6 g cm^{-3} in the third layer, 2.8 g cm^{-3} in the fourth layer, and 3 g cm^{-3} in the diamond layer.

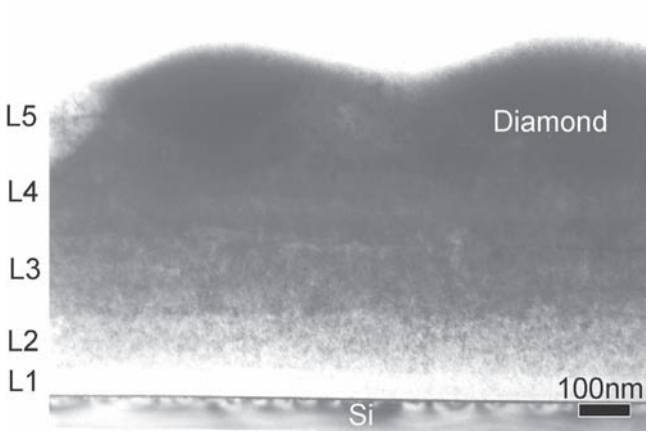

Figure 7.18 Low-magnification cross-sectional TEM image of the nanodiamond (deposited at 880 °C) film. A layered structure consisting of five layers with increasing density (deduced from the darkening of each layer with respect to the previous one) is observed on the Si substrate.

milling (4.5 keV, Ar^+ ion beam in a liquid nitrogen cooling stage) to electron transparency. TEM analysis was carried out on a film grown at 880 °C for 60 min. The low-resolution cross-sectional TEM image of the sample is shown in Fig. 7.18. As seen from this figure, the density of the film increases with film thickness. The higher the density, the darker

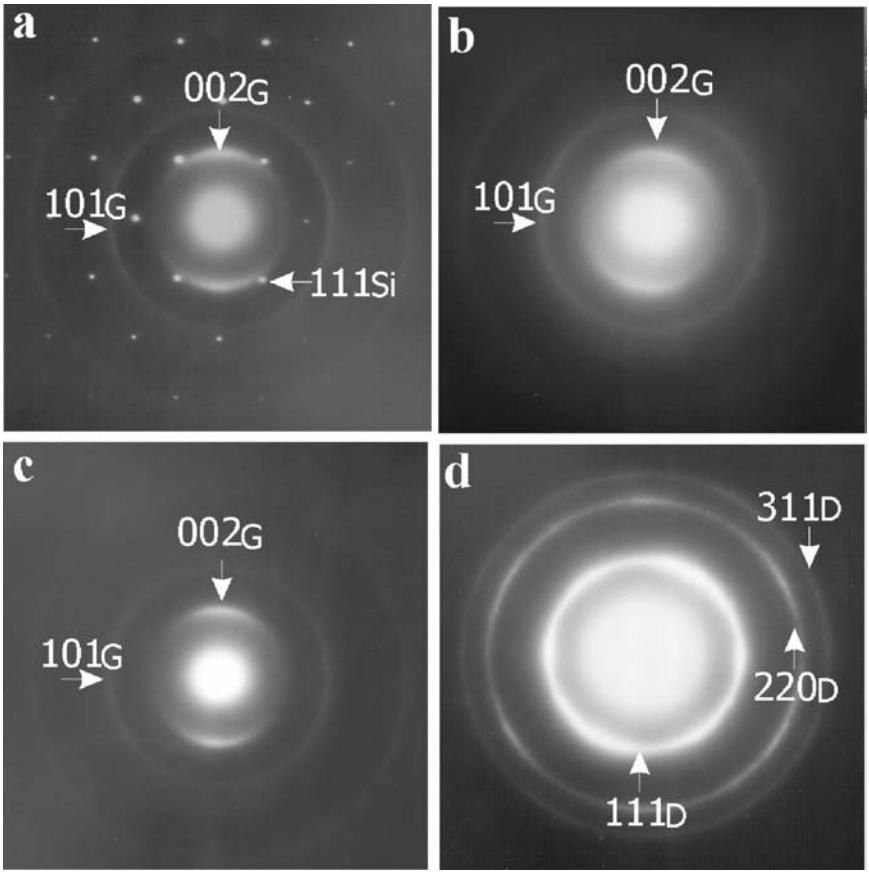

Figure 7.19 Small-area electron diffraction (SAED) pattern of the different layers of the nanodiamond film in Fig. 7.18: (a) interface between Si substrate and first layer; (b) third layer; (c) fourth layer; (d) fifth layer. Layers 1–4 are graphitic with an oriented structure (only partial rings). The relative orientation of the rings with respect to the Si indicates the graphitic basal planes are perpendicular to the Si surface. The rings in the fifth layer are diamond rings which indicate preferred orientation (they are more intense in certain directions with symmetry similar to that of the cubic diamond lattice).

the layer is. To guide the eye the film was divided into five layers and higher resolution examination was carried out on each of these layers. The small-area electron diffraction (SAED) pattern of the first four layers is graphitic (Fig. 7.19). The partial first and third graphitic rings are due to a preferred orientation of the graphitic basal planes in a direction perpendicular to the substrate, as seen from the relative position of the

rings with respect to the silicon substrate spots. This is in agreement with the NEXAFS studies described above (Section 7.2). SAED of the fifth layer shows diamond rings with some preferred orientation (evident by different intensities in different directions) and the first graphitic ring is absent. HR TEM (Fig. 7.20) confirms the previous observations. The first four layers consist of oriented graphitic planes perpendicular to the substrate. The fifth layer is composed of a large number of 2–5 nm sized crystallites with a spacing of 2.06 Å dispersed in a graphitic matrix.

7.11 Formation Mechanism of the Nanodiamond Film Deposited from Energetic Species

As demonstrated throughout the analysis of the films deposited by DC-GD, the mechanism of nanodiamond film formation by this method differs from the one of polycrystalline diamond films growth by other CVD techniques.[20,21] It was also shown that the DC-GD hydrogen plasma severely damages pre-deposited polycrystalline diamond. This shows that the activated hydrogen is sufficiently energetic to induce displacement of sp^3-coordinated carbon atoms in the upper surface region of the films. The strong dependence of the film nature on deposition temperature shows that the hydrogen content in the films has an important role for the stabilization and formation of the nanodiamond particles. There is also no need for any preliminary treatment of the substrate prior to deposition to enhance nucleation or growth. The interface between the nanodiamond films and the silicon substrates consists of a hydrogenated graphite-like precursor with a preferred vertical orientation. Diamond nucleation is accompanied by an increase in density of the films and retention of hydrogen. The increase in density was found to correlate to an increase in stress in the graphitic film.[40] A schematic illustration of the structure of the nanodiamond films produced by the DC-GD CVD method at $CH_4:H_2$ of 9 : 91 and deposition temperature of 880 °C is shown in Fig. 7.21.

From a macroscopic–thermodynamic perspective, nanocrystalline diamond formation can be viewed as associated with a nanographite–nanodiamond phase transformation promoted by stress build-up or densification of the graphitic layers in the presence of hydrogen. The stresses accumulating in the deposited films at 880 °C relax through several processes: (i) nanographite–nanodiamond phase transformation, which is favored by the presence of hydrogen; (ii) surface roughening that accompanies the nanodiamond phase nucleation observed by the AFM meas-

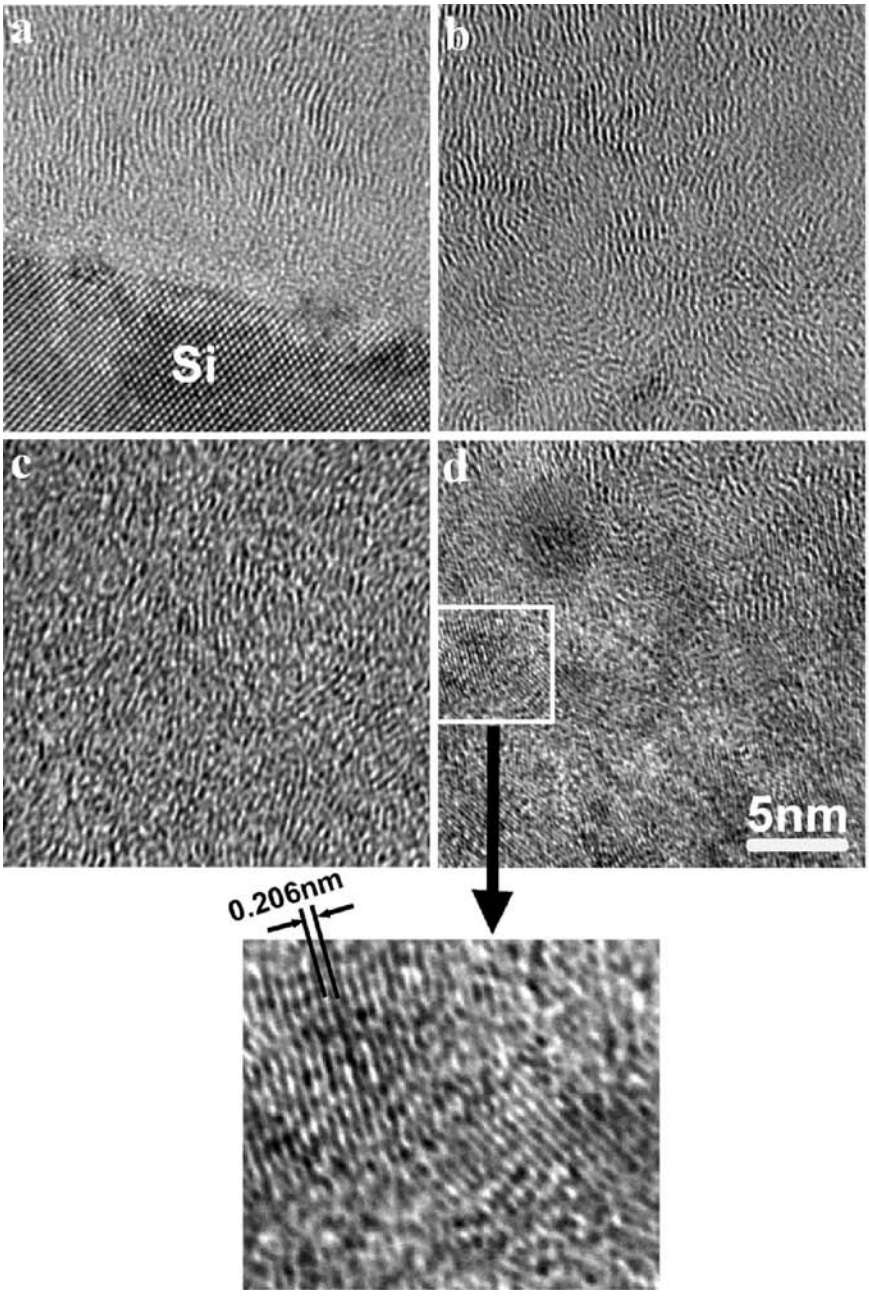

Figure 7.20 Cross-sectional high-resolution TEM (HR TEM) imaging of the layers of the nanodiamond film in Fig. 7.18: (a) interface between Si substrate and first layer; (b) first layer; (c) fourth layer; (d) fifth layer. The graphitic fringes are perpendicular to the Si surface. The films look denser as the layer develops from the first to the fourth. The fifth layer shows 2–5 nm diamond crystallites embedded in a graphitic matrix. The marked region in (d) is enlarged to show the crystallites more clearly.

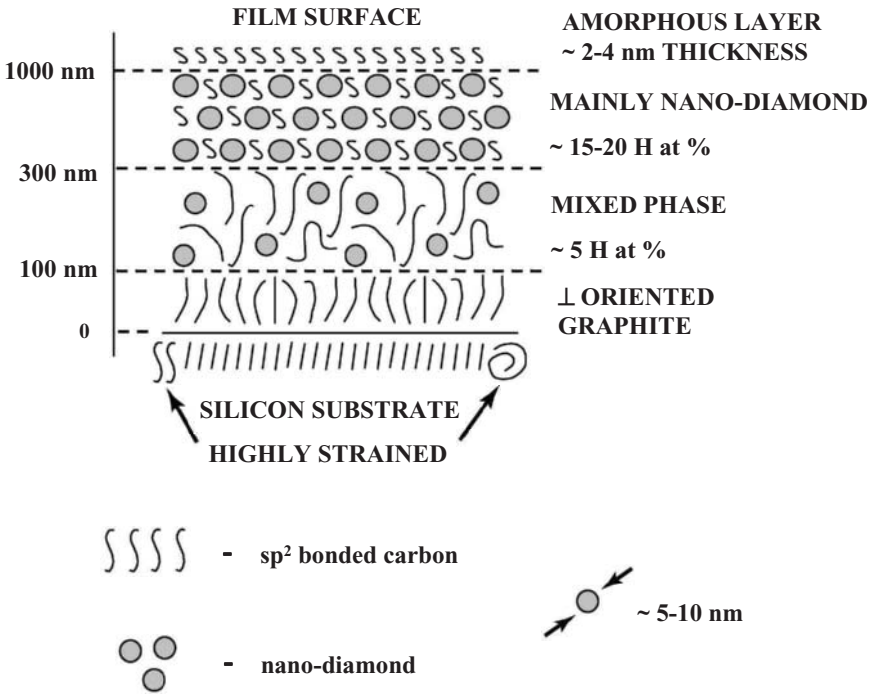

Figure 7.21 Schematic illustration of the nanodiamond film deposited by the DC-GD CVD method.

urements; and (iii) creation of defects in the silicon substrate established by cross-sectional TEM. Badziag et al.[72] demonstrated that hydrogenated nanometer-sized diamonds are energetically favored over graphite, even without requiring the high pressures or extreme kinetic conditions usually associated with diamond growth. Similar conclusions on the thermodynamic stability of nanocrystalline diamond over graphite were obtained by Gamarnik as well.[73]

Hydrogen is expected to influence the stress level in the graphitic layer as well. This occurs due to relaxation of distortions of the interatomic bonds, formation of micro-voids, and termination of dangling bonds. Therefore it can be concluded that for a given methane concentration, temperatures lower than those required for nanodiamond formation lead to higher hydrogen concentration in the deposited films and to the following relaxation of the stresses. Then the films maintain a graphite-like structure. Nucleation of the nanodiamond particles at temperatures above ~920 °C is prevented by a higher rate of hydrogen desorption from the

sample. Such desorption makes the hydrogen content in the deposited film insufficient for the stabilization of the nanodiamond phase.[40]

We have recently suggested a model to explain the mechanism of diamond nucleation from energetic species[21] and nanodiamond film growth.[61] From a microscopic perspective the mechanism of nanodiamond film formation as it occurs in the films deposited at 880 °C may be explained as a subsurface process in terms of a four-step cyclic process [20]:

(1) Formation of a dense, hydrogenated sp^2 carbon coordinated oriented layer.
(2) Precipitation of sp^3 carbon clusters in this graphitic phase.
(3) Growth of nanodiamond particles up to ~5 nm in size by energetic species bombardment of the diamond/hydrogenated carbon interface. It involves preferential displacement of sp^2-coordinated carbon atoms leaving sp^3-coordinated carbon atoms intact, leading to expansion of the diamond phase.
(4) Frustration of growth of the diamond particles.
(5) Growth of the film formed from an agglomerate of nanodiamond particles by a cyclic process which involves processes (2)–(4).

The basic mechanism responsible for the formation of the nanodiamond films by DC-GD is subplantation,[10,13] i.e., a shallow implantation in which the carbon and hydrogen species penetrate to subsurface layers and densification occurs by the balance between trapping (densification) and de-trapping (density relaxation) processes. According to our OES characterization of the DC-GD plasma under deposition conditions (Section 7.1), the main species involved in film growth are CH^* and H^* radicals. The film grows through several concurrent competing processes: (i) penetration of energetic H and C atoms to subsurface layers and trapping at the end of their trajectory; (ii) thermal migration of atoms to the surface; (iii) release of excess hydrogen; (iv) chemical etching of carbon by atomic hydrogen and release of volatile hydrocarbon molecules. The growth thus involves simultaneous deposition and etching. The etching rate of some carbon forms (e.g., sp^2-bonded carbon) might be much larger than that of other carbon forms (e.g., diamond). Most of the hydrogen atoms (more than 90%) are not trapped in the evolving film, since the H atomic concentration is ~0–20% while the H/C atomic ratio in the plasma is 24 (for 9%CH_4/91%H_2).

We now address the evolution of the hydrogenated graphitic layers, characterized by graphitic planes perpendicular to the surface. A similar growth mechanism has already been reported[74,75] for the subplantation of energetic (120–1000 eV) mass-selected carbon ions at elevated temperatures (200–300 °C). The energetic bombardment induces local stress, but the elevated temperature allows for modification of the evolving phase to the most favorable thermodynamic configuration. The basal planes grow perpendicular to the stress (and to the substrate), which is the most compressible way possible. Indeed the first layer is characterized by such orientation with a regular graphitic density. Once the graphitic orientation develops and the amount of amorphous material decreases (second layer), this ordered structure offers channels for the more energetic part of the hydrogen and carbon species to penetrate and be trapped between the planes. This enables a density increase (carbon incorporation) and hydrogen concentration increase observed in the third and fourth layers. The density increase from 2.4–2.5 to 2.8 g cm^{-3} indicates about 15–20% carbon incorporation between the graphitic planes. A similar amount of hydrogen (15–20% of the carbon atom density) is also trapped between the planes. The increased density and hydrogen bonding to the additional carbon atoms account for the higher trapping efficiency of hydrogen in the evolving matrix. Evidence for the formation of *trans*-polyacetylene configurations[46] is provided by Raman, which shows two characteristic peaks around 1490 and 1150 cm^{-1} that are missing in the spectrum of the first two layers.[42]

We now address the diamond nucleation occurring in the fifth layer. Kecent molecular dynamics (MD) calculations showed[21] that once the graphitic phase incorporates ~20% of hydrogen and carbon species and its density reaches a value of ~3 g cm^{-3}, 100% sp^3 hydrogen–carbon clusters precipitate and the hydrogen decorates the surface of these clusters. We suggested that a very small fraction (say 10^{-5}–10^{-6}) of these clusters is made of perfect diamond clusters.[21] Once they are formed they are stabilized by the boundary conditions imposed by the dense matrix. The calculations show that faulty clusters can be annealed by incorporation of carbon interstitials and by hydrogen termination.[21] MD calculations by others showed[76] that graphitic edges may serve as sites for diamond nucleation, enhancing the nucleation probability. This was indeed verified for cubic boron nitride (cBN) nucleation.[77] We did observe the association of oriented graphitic planes with diamond nucleation, but failed to find evidence in our HR TEM images of a preferred nucleation of diamond on graphitic edges with the graphitic basal planes parallel to diamond (111) planes. The SAED pattern nevertheless gives some indication of the

preferred orientation of diamond nanocrystals (the diffraction rings are stronger in certain directions).

The last issue is the growth of the diamond clusters to the dimensions observed in our HR TEM images (~2–5 nm). The experimental conditions leading to diamond growth involve bombardment with energetic species (~100–200 eV) which mostly contain hydrogen. We suggested[21] that the hydrogen atoms preferentially displace the loosely bonded carbon atoms at the a-C:H/diamond interface, leaving the diamond atoms intact. Each loosely bonded carbon atom is preferentially displaced many times, and has a considerable probability of occupying a diamond position. The diamond interface thus expands, consuming a-C:H atoms. This is in accord with the work of Banhart[78] who observed an expansion of the diamond interface when a diamond/graphite interface was bombarded by 1.25 MeV electrons. Then the size of the nanodiamond particles is expected to be determined by the range of the energetic ions and atoms involved in the preferential growth of nanodiamond particles. The displacement energy of carbon atoms in the diamond structure is ~50 eV and that in a graphite-like structure is ~20 eV (approximate values). Whilst the ion energy is larger than the displacement energy of diamond, an amorphous structure is produced. As the ion slows down as it penetrates through the film surface into the subsurface within an energy window between the displacement energy of graphite and diamond, preferential growth of the nanodiamond particles takes place. Frustration of the growth process occurs once the distance between the diamond particle and the surface is larger than the projective range of ions that at such distance do not have sufficient energy to induce preferential displacement of sp^2-coordinated carbon atoms. Nucleation and growth of new diamond particles occurs in a cyclic process resulting in the formation of the nanodiamond film.

Finally, we briefly compare the mechanism leading to the formation of nanodiamond films from energetic CH_x and H species with that deposited from C_2 dimers. The main difference between the mechanism of nanodiamond film growth from energetic particle bombardment and that associated with C_2 species is that the first one occurs in the subsurface region, whereas the second one occurs at the very surface and is associated with particular chemical reactions of highly reactive carbon dimers with the growing film.[17] Nanodiamond film growth from C_2 species requires the *ab initio* existence of a well-defined diamond surface and, therefore, surface pretreatment is necessary in order to introduce primary diamond growth centers. The as-deposited films are characterized by a high sp^3 content of up to 95%.[17] Nanodiamond formation from energetic species

bombardment does not require any substrate pretreatment leading to the formation of nanodiamond grains within a dense carbon matrix and resulting in ~80% film sp^3 content, while a subsurface region a few nanometers thick remains composed of amorphous carbon.

7.12 Summary

Nanocrystalline carbon film of a prevailing diamond character can be deposited by direct-current glow-discharge (DC-GD) chemical vapor deposition (CVD) from a methane–hydrogen mixture. In this case film deposition occurs from energetic species. In this chapter the phase evolution of the films, microstructure, hydrogen content, and bonding in these films were discussed in detail. The surface properties of the films were assessed. The characterization of the nanodiamond films is very complex and requires the use of a number of microstructural analytical methods. A full picture of film properties can only be attained from a combination of characterization methods. The advantages and complementarities of the characterization tools used were discussed. Then our present understanding of the formation mechanism of nanodiamond films deposited from energetic species was presented. It is based on a subsurface process that results in diamond nucleation, growth, frustration of growth, nucleation, etc.

We estimate that the nanodiamond films deposited from energetic species (DC-GD method) display ~80% diamond character and no surface pretreatment is necessary in order to induce their formation. Growth of the nanodiamond film occurs on top of a preferentially oriented graphitic precursor with its basal planes perpendicular to the substrate surface and consists of an agglomerate of diamond particles with particle size in the 3–5 nm range with amorphous grain boundaries. The hydrogen concentration in the graphitic precursor is only a few percent, but it increases to ~15–20 at.% in the nanodiamond film. Most likely hydrogen is bonded within the amorphous grain boundaries and saturates the surface of the nanodiamond particles. The surface of the films is amorphous in nature. From a microscopic perspective nanodiamond film growth from energetic species is explained as a subsurface process in terms of a four-step cyclic process: (i) formation of a dense, hydrogenated sp^2 carbon coordinated oriented layer; (ii) precipitation of sp^3 carbon clusters in this graphitic phase; (iii) growth of nanodiamond particles up to ~5 nm in size by energetic species bombardment of the diamond/hydrogenated carbon interface; (iv) frustration of growth of the diamond particles; and (v) growth

of the film formed of an agglomerate of nanodiamond particles by a cyclic process which involves processes (ii)–(iv).

Acknowledgments

The financial support from the Israeli Academy of Science and the Technion Fund for Promotion of Research for carrying out this work is greatly acknowledged. We would like to thank Prof. Y. Lifshitz with whom we developed and formulated the general mechanism of diamond nucleation from energetic species and nanodiamond deposition.

References

1. Luo, S.Y., Kuo, J.K., Yeh, B., Sung, J.C., Dai, C.W., and Tsai, T.J., "The tribology of nano-crystalline diamond", *Materials Chemistry and Physics*, 2001. **72**(2): 133–135.
2. Huang, L.Y., Xu, K.W., Lu, J., and Guelorget, B., "Analysis of nano-scratch behavior of diamond-like carbon films", *Surface & Coatings Technology*, 2002. **154**(2–3): 232–236.
3. Jiang, N., Sugimoto, K., Nishimura, K., Shintani, Y., and Hiraki, A., "Synthesis and structural study of nano/micro diamond overlayer films", *Journal of Crystal Growth*, 2002. **242**(3–4): 362–366.
4. Wu, K.H., Wang, X.R., Liu, S., and Wang, E.G., "Bistable characteristic and current jumps in field electron emission of nanocrystalline diamond films", *Journal of Applied Physics*, 2001. **90**(9): 4810–4814.
5. Ferreira, N.G., Silva, L.L.G., and Corat, E.J., "Electrochemical activity of boron-doped diamond electrodes grown on carbon fiber cloths", *Diamond and Related Materials*, 2002. **11**(3–6): 657–661.
6. Chen, Q.Y., Gruen, D.M., Krauss, A.R., Corrigan, T.D., Witek, M., and Swain, G.M., "The structure and electrochemical behavior of nitrogen-containing nanocrystalline diamond films deposited from $CH_4/N_2/Ar$ mixtures", *Journal of the Electrochemical Society*, 2001. **148**(1): E44–E51.
7. Li, J.Q., He, D.Y., Guo, W.T., Zhang, J.H., Sun, Y.N., Lei, Q.S., and Gao, X., "Nanocrystalline diamond thin films as infrared optical protective coatings", *International Journal of Modern Physics B*, 2002. **16**(6–7): 1013–1017.
8. Yang, W.B., Lu, F.X., and Cao, Z.X., "Growth of nanocrystalline diamond protective coatings on quartz glass", *Journal of Applied Physics*, 2002. **91**(12): 10068–10073.
9. Bhattacharyya, S., Auciello, O., Birrell, J., Carlisle, J.A., Curtiss, L.A., Goyette, A.N., Gruen, D.M., Krauss, A.R., Schlueter, J., Sumant, A., and Zapol, P., "Synthesis and characterization of highly-conducting nitrogen-doped ultrananocrystalline diamond films", *Applied Physics Letters*, 2001. **79**(10): 1441–1443.

10. Lifshitz, Y., Kasi, S.R., Rabalais, J.W., and Eckstein, W., "Subplantation model for film growth from hyperthermal species", *Physical Review B*, 1990. **41**(15): 10468–10480.
11. Marton, D., Boyd, K.J., Rabalais, J.W., and Lifshitz, Y., "Semiquantitative subplantation model for low energy ion interactions with surfaces. II. Ion beam deposition of carbon and carbon nitride", *Journal of Vacuum Science & Technology A*, 1998. **16**(2): 455–462.
12. Monteiro, O.R., "Thin film synthesis by energetic condensation", *Annual Review of Materials Research*, 2001. **31**: 111–137.
13. Lifshitz, Y., Kasi, S.R., and Rabalais, J.W., "Subplantation model for film growth from hyperthermal species – application to diamond", *Physical Review Letters*, 1989. **62**(11): 1290–1293.
14. Lifshitz, Y., "Diamond-like carbon – present status", *Diamond and Related Materials*, 1999. **8**(8–9): 1659–1676.
15. Boyd, K.J., Marton, D., Rabalais, J.W., Uhlmann, S., and Frauenheim, T., "Semiquantitative subplantation model for low energy ion interactions with solid surfaces. III. Ion beam homoepitaxy of Si", *Journal of Vacuum Science & Technology A – Vacuum Surfaces and Films*, 1998. **16**(2): 463–471.
16. Robertson, J., "Mechanism of bias-enhanced nucleation and heteroepitaxy of diamond on Si", *Diamond and Related Materials*, 1995. **4**(5–6): 549–552.
17. Gruen, D.M., "Nanocrystalline diamond films", *Annual Review of Materials Science*, 1999. **29**: 211–259.
18. Gouzman, I., Hoffman, A., Comtet, G., Hellner, L., Dujardin, G., and Petravic, M., "Nanosize diamond formation promoted by direct current glow discharge process: Synchrotron radiation and high resolution electron microscopy studies", *Applied Physics Letters*, 1998. **72**(20): 2517–2519.
19. Gouzman, I., Lior, I., and Hoffman, A., "Formation of the precursor for diamond growth by in situ direct current glow discharge pretreatment", *Applied Physics Letters*, 1998. **72**(3): 296–298.
20. Lifshitz, Y., Meng, X.M., Lee, S.T., Akhveldiany, R., and Hoffman, A., "Visualization of diamond nucleation and growth from energetic species", Physical Review Letters, 2004. **93**(5): 056101.
21. Lifshitz, Y., Kohler, T., Frauenheim, T., Guzmann, I., Hoffman, A., Zhang, R.Q., Zhou, X.T., and Lee, S.T., "The mechanism of diamond nucleation from energetic species", *Science*, 2002. **297**(5586): 1531–1533.
22. Gruen, D.M., Zuiker, C.D., Krauss, A.R., and Pan, X.Z., "Carbon dimer, C-2 as a growth species for diamond films from methane/hydrogen/argon microwave plasmas", *Journal of Vacuum Science & Technology A – Vacuum Surfaces and Films*, 1995. **13**(3): 1628–1632.
23. Vandevelde, T., Wu, T.D., Quaeyhaegens, C., Vlekken, J., D'Olieslaeger, M., and Stals, L., "Correlation between the OES plasma composition and the diamond film properties during microwave PA-CVD with nitrogen addition", *Thin Solid Films*, 1999. **340**(1–2): 159–163.
24. Heintze, M., Magureanu, M., and Kettlitz, M., "Mechanism of C-2 hydrocarbon formation from methane in a pulsed microwave plasma", *Journal of Applied Physics*, 2002. **92**(12): 7022–7031.
25. Zhao, M.S., Owano, T.G., and Kruger, C.H., "Optical diagnostics of an atmospheric pressure diamond-depositing DC plasma reactor", *Diamond and Related Materials*, 2001. **10**(9–10): 1565–1568.

26. Garcia, M.M., Jimenez, I., Vazquez, L., Gomez-Aleixandre, C., Albella, J.M., Sanchez, O., Terminello, L.J., and Himpsel, F.J., "X-ray absorption spectroscopy and atomic force microscopy study of bias-enhanced nucleation of diamond films", *Applied Physics Letters*, 1998. **72**(17): 2105–2107.
27. Gruen, D.M., Krauss, A.R., Zuiker, C.D., Csencsits, R., Terminello, L.J., Carlisle, J.A., Jimenez, I., Sutherland, D.G.J., Shuh, D.K., Tong, W., and Himpsel, F.J., "Characterization of nanocrystalline diamond films by core-level photoabsorption", *Applied Physics Letters*, 1996. **68**(12): 1640–1642.
28. Coffman, F.L., Cao, R., Pianetta, P.A., Kapoor, S., Kelly, M., and Terminello, L.J., "Near-edge x-ray absorption of carbon materials for determining bond hybridization in mixed sp^2/sp^3 bonded materials", *Applied Physics Letters*, 1996. **69**(4): 568–570.
29. Stöhr, J., *NEXAFS spectroscopy*. Springer Series in Surface Sciences, 25, 1992. Berlin and New York: Springer-Verlag.
30. Morar, J.F., Himpsel, F.J., Hollinger, G., Hughes, G., and Jordan, J.L., "Observation of a C-1s core exciton in diamond", *Physical Review Letters*, 1985. **54**(17): 1960–1963.
31. Batson, P.E., "Carbon-1s near-edge-absorption fine-structure in graphite", *Physical Review B*, 1993. **48**(4): 2608–2610.
32. Rosenberg, R.A., Love, P.J., and Rehn, V., "Polarization-dependent C(K) near-edge X-ray-absorption fine-structure of graphite", *Physical Review B*, 1986. **33**(6): 4034–4037.
33. Jimenez, I., Garcia, M.M., Albella, J.M., and Terminello, L.J., "Orientation of graphitic planes during the bias-enhanced nucleation of diamond on silicon: An x-ray absorption near-edge study", *Applied Physics Letters*, 1998. **73**(20): 2911–2913.
34. Fayette, L., Marcus, B., Mermoux, M., Tourillon, G., Laffon, K., Parent, P., and Le Normand, F., "Local order in CVD diamond films: Comparative Raman, x-ray-diffraction, and x-ray-absorption near-edge studies", *Physical Review B*, 1998. **57**(22): 14123–14132.
35. Hoffman, A., Petravic, M., Comtet, G., Heurtel, A., Hellner, L., and Dujardin, G., "Photon-stimulated desorption of H^+ and H^- ions from diamond surfaces: Evidence for direct and indirect processes", *Physical Review B*, 1999. **59**(4): 3203–3209.
36. Dresselhaus, M.S. and Kalish, R., *Ion implantation in diamond, graphite, and related materials*, 1992. Berlin and New York: Springer-Verlag.
37. Heiman, A., Gouzman, I., Christiansen, S.H., Strunk, H.P., Comtet, G., Hellner, L., Dujardin, G., Edrei, R., and Hoffman, A., "Evolution and properties of nanodiamond films deposited by direct current glow discharge", *Journal of Applied Physics*, 2001. **89**(5): 2622–2630.
38. Laikhtman, A., Gouzman, I., Hoffman, A., Comtet, G., Hellner, L., and Dujardin, G., "Sensitivity of near-edge x-ray absorption fine structure spectroscopy to ion beam damage in diamond films", *Journal of Applied Physics*, 1999. **86**(8): 4192–4198.
39. Comelli, G., Stohr, J., Robinson, C.J., and Jark, W., "Structural studies of argon-sputtered amorphous-carbon films by means of extended x-ray-absorption fine-structure", *Physical Review B*, 1988. **38**(11): 7511–7519.

40. Hoffman, A., Heiman, A., and Christiansen, S.H., "Mechanism of nanodiamond film formation by stress relaxation on a preferentially oriented vertical basal plane graphitic precursor", *Journal of Applied Physics*, 2001. **89**(10): 5769–5773.
41. Garcia, M.M., Jimenez, I., Sanchez, O., Gomez-Aleixandre, C., and Vazquez, L., "Model of the bias-enhanced nucleation of diamond on silicon based on atomic force microscopy and x-ray-absorption studies", *Physical Review B*, 2000. **61**(15): 10383–10387.
42. Heiman, A., Lakin, E., Zolotoyabko, E., and Hoffman, A., "Microstructure and stress in nano-crystalline diamond films deposited by DC glow discharge CVD", *Diamond and Related Materials*, 2002. **11**(3–6): 601–607.
43. Nemanich, R.J. and Solin, S.A., "1st-order and 2nd-order Raman-scattering from finite-size crystals of graphite", *Physical Review B*, 1979. **20**(2): 392–401.
44. Knight, D.S. and White, W.B., "Characterization of diamond films by Raman-spectroscopy", *Journal of Materials Research*, 1989. **4**(2): 385–393.
45. Wada, N., Gaczi, P.J., and Solin, S.A., "Diamond-like 3-fold coordinated amorphous-carbon", *Journal of Non-Crystalline Solids*, 1980. **35–36**(Jan.): 543–548.
46. Ferrari, A.C. and Robertson, J., "Raman spectroscopy of amorphous, nanostructured, diamond-like carbon, and nanodiamond", *Philosophical Transactions of the Royal Society of London Series A – Mathematical, Physical and Engineering Sciences*, 2004. **362**(1824): 2477–2512.
47. Knight, D.S., Weimer, R., Pilione, L., and White, W.B., "Surface-enhanced Raman-spectroscopy of chemical vapor-deposited diamond films", *Applied Physics Letters*, 1990. **56**(14): 1320–1322.
48. Prawer, S. and Nemanich, R.J., "Raman spectroscopy of diamond and doped diamond", *Philosophical Transactions of the Royal Society of London Series A – Mathematical, Physical and Engineering Sciences*, 2004. **362**(1824): 2537–2565.
49. Kuzmany, H., Pfeiffer, R., Salk, N., and Gunther, B., "The mystery of the 1140 cm^{-1} Raman line in nanocrystalline diamond films", *Carbon*, 2004. **42**(5–6): 911–917.
50. Tamor, M.A., Haire, J.A., Wu, C.H., and Hass, K.C., "Correlation of the optical gaps and Raman-spectra of hydrogenated amorphous-carbon films", *Applied Physics Letters*, 1989. **54**(2): 123–125.
51. Tamor, M.A. and Vassell, W.C., "Raman fingerprinting of amorphous-carbon films", *Journal of Applied Physics*, 1994. **76**(6): 3823–3830.
52. Liu, Y., Liu, C., Chen, Y., Tzeng, Y., Tso, P., and Lin, I., "Effects of hydrogen additive on microwave plasma CVD of nanocrystalline diamond in mixtures of argon and methane", *Diamond and Related Materials*, 2004. **13**(4–8): 671–678.
53. Piazza, F., Golanski, A., Schulze, S., and Relihan, G., "Transpolyacetylene chains in hydrogenated amorphous carbon films free of nanocrystalline diamond", *Applied Physics Letters*, 2003. **82**(3): 358–360.
54. Yacoby, Y. and Roth, S., "Resonant Raman-scattering in polyacetylene under hydrostatic-pressure", *Solid State Communications*, 1985. **56**(4): 319–322.

55. Lopez-Rios, T., Mendoza, D., Garcia-Vidal, F.J., Sanchez-Dehesa, J., and Pannetier, B., "Surface shape resonances in lamellar metallic gratings", *Physical Review Letters*, 1998. **81**(3): 665–668.
56. Lifshitz, Y., Lempert, G.D., and Grossman, E., "Substantiation of subplantation model for diamond-like film growth by atomic-force microscopy", *Physical Review Letters*, 1994. **72**(17): 2753–2756.
57. Jesson, D.E., "Morphological evolution of strained semiconductor films", in *Morphological Organization in Epitaxial Growth and Removal*, Z. Zhang and M.G. Lagally, Editors, 1999. Singapore: World Scientific.
58. Warot, B., Snoeck, E., Baules, P., Ousset, J.C., Casanove, M.J., Dubourg, S., and Bobo, J.F., "Growth and stress relaxation of Co/NiO bilayers on MgO(001)", *Journal of Applied Physics*, 2001. **89**(10): 5414–5420.
59. Spaepen, F., "Interfaces and stresses in thin films", *Acta Materialia*, 2000. **48**(1): 31–42.
60. Mcfeely, F.R., Kowalczy, S.P., Ley, L., Cavell, R.G., Pollak, R.A., and Shirley, D.A., "X-ray photoemission studies of diamond, graphite, and glassy carbon valence bands", *Physical Review B*, 1974. **9**(12): 5268–5278.
61. Hoffman, A., Gouzman, I., and Michaelson, Sh., "Formation mechanism of nano-diamond films from energetic species: From experiment to theory", *Thin Solid Films*, 2006, in press.
62. Hoffman, A., Heiman, A., Akhvlediani, R., Lakin, E., Zolotoyabko, E., and Cyterman, C., "Hydrogen content and density in nanocrystalline carbon films of a predominant diamond character", *Journal of Applied Physics*, 2003. **94**(7): 4589–4595.
63. Heiman, A., Gouzman, I., Christiansen, S.H., Strunk, H.P., and Hoffman, A., "Nano-diamond films deposited by direct current glow discharge assisted chemical vapor deposition", *Diamond and Related Materials*, 2000. **9**(3–6): 866–871.
64. Lee, S.T. and Apai, G., "Surface phonons and CH vibrational-modes of diamond (100) and (111) surfaces", *Physical Review B*, 1993. **48**(4): 2684–2693.
65. Ristein, J., Stief, R.T., Ley, L., and Beyer, W., "A comparative analysis of a-C: H by infrared spectroscopy and mass selected thermal effusion", *Journal of Applied Physics*, 1998. **84**(7): 3836–3847.
66. Aizawa, T., Ando, T., Kamo, M., and Sato, Y., "High-resolution electron-energy-loss spectroscopic study of epitaxially grown diamond (111) and (100) surfaces", *Physical Review B*, 1993. **48**(24): 18348–18351.
67. Weiler, M., Sattel, S., Giessen, T., Jung, K., Ehrhardt, H., Veerasamy, V.S., and Robertson, J., "Preparation and properties of highly tetrahedral hydrogenated amorphous carbon", *Physical Review B*, 1996. **53**(3): 1594–1608.
68. Michaelson, S. and Hoffman, A., "Hydrogen in nano-diamond films", *Diamond and Related Materials*, 2005. **14**(3–7): 470–475.
69. Aizawa, T., Ando, T., Yamamoto, K., Kamo, M., and Sato, Y., "Surface vibrational studies of CVD diamond", *Diamond and Related Materials*, 1995. **4**(5–6): 600–606.

70. Thachepan, S., Okuyama, H., Aruga, T., Nishijima, M., Ando, T., Mazur, A., and Pollmann, J., "Surface phonons of C(100)(2X1)-H", *Physical Review B*, 2003. **68**(4): 041401(R).
71. Lafosse, A., Billy, D.T., Guillotin, J.P., Le Coat, Y., Azria, R., Laikhtman, A., and Hoffman, A., "Role of electronic band structure and resonances on electron reflectivity and vibrational excitation functions: The case of hydrogenated diamond", *Physical Review B*, 2003. **68**(23): 235421.
72. Badziag, P., Verwoerd, W.S., Ellis, W.P., and Greiner, N.R., "Nanometre-sized diamonds are more stable than graphite", *Nature*, 1990. **343**(6255): 244–245.
73. Gamarnik, M.Y., "Energetical preference of diamond nanoparticles", *Physical Review B*, 1996. **54**(3): 2150–2156.
74. Kulik, J., Lempert, G.D., Grossman, E., Marton, D., Rabalais, J.W., and Lifshitz, Y., "sp^3 content of mass-selected ion-beam-deposited carbon films determined by inelastic and elastic electron scattering", *Physical Review B*, 1995. **52**(22): 15812–15822.
75. Peng, H.Y., Wang, N., Zheng, Y.F., Lifshitz, Y., Kulik, J., Zhang, R.Q., Lee, C.S., and Lee, S.T., "Smallest diameter carbon nanotubes", *Applied Physics Letters*, 2000. **77**(18): 2831–2833.
76. Lambrecht, W.R.L., Lee, C.H., Segall, B., Angus, J.C., Li, Z.D., and Sunkara, M., "Diamond nucleation by hydrogenation of the edges of graphitic precursors", *Nature*, 1993. **364**(6438): 607–610.
77. Mirkarimi, P.B., Medlin, D.L., McCarty, K.F., Dibble, D.C., Clift, W.M., Knapp, J.A., and Barbour, J.C., "The synthesis, characterization, and mechanical properties of thick, ultrahard cubic boron nitride films deposited by ion-assisted sputtering", *Journal of Applied Physics*, 1997. **82**(4): 1617–1625.
78. Banhart, F., "Irradiation effects in carbon nanostructures", *Reports on Progress in Physics*, 1999. **62**(8): 1181–1221.

8 Theoretical Studies of UNCD Synthesis and Properties

Peter Zapol, Michael Sternberg and Larry A. Curtiss

Argonne National Laboratory, Argonne, IL, USA

Introduction

Diamond films grown from hydrogen-poor argon/fullerene or argon/methane microwave plasmas are characterized by a microstructure consisting of crystallites with an average size of 3–10 nm.[1] These films are called ultrananocrystalline diamond (UNCD). In contrast, diamond films grown by the conventional plasma CVD methods[2] from hydrogen/hydrocarbon mixtures typically have a microstructure with micron-size crystallites. The growth mechanism for diamond films grown from hydrogen-poor microwave plasmas is significantly different than that in hydrogen-rich plasmas since the latter depends on hydrogen abstraction by the hydrogen present in the plasma. The carbon dimer has been proposed as the principal growth species in hydrogen-poor plasmas used to grow diamond.[3] UNCD films have unique properties that have been described in detail in other chapters in this book. Many physical properties such as electrical conductivity, mechanical, and optical properties of UNCD differ from both natural and microcrystalline diamond and offer opportunities for specific applications in tribology, microelectromechanical systems (MEMS), and electronic devices.

In this chapter we review theoretical studies of UNCD including growth mechanisms and electronic properties. These studies have modeled the growth of diamond with the carbon dimer as the growth species. The postulated reaction mechanisms occur by insertion of C_2 into the C—H bonds of the hydrogen-terminated diamond surface or into π-bonded carbon dimers on dehydrogenated diamond surfaces. In Section 8.1 we review some of the computational methodologies that have been used to model growth mechanisms and the grain boundaries in UNCD. In Section 8.2 we discuss the mechanisms for carbon dimer insertion into the (110) face of diamond, while in Section 8.3 we discuss the mechanism for growth on the (100) surface. The electronic properties of UNCD are of great interest due to the large proportion of grain boundaries in the material. In

Section 8.4 we discuss theoretical calculations of the electronic structure of UNCD grain boundaries, while in Section 8.5 we discuss investigations of the effect that addition of N, H, or Si has on the electronic structure of UNCD grain boundaries.

8.1 Computational Methodologies

Most of the methods used in modelling UNCD covered in this chapter fit into one of three general categories: *ab initio* molecular orbital theory, density-functional theory, and density functional-based tight binding. We briefly review these methods here and refer the reader to more detailed descriptions in the literature.

Ab initio molecular orbital methods[4] that have been used to investigate diamond surface reactions include Hartree–Fock (HF) theory and second-order perturbation theory (MP2), which includes correlation effects. While the HF calculations are often reliable for geometries and vibrational frequencies, they are not very good for reaction energies and barriers. Because correlation effects are important, methods such as MP2 theory are more reliable for these quantities. In some cases high-level calculations, such as G2 theory,[5] G3 theory,[6] and CCSD(T),[7] are also used for these energies. These methods can only be used for smaller systems, typically to assess the reliability of MP2 calculations.

Density-functional theory (DFT) is a cost-effective method for studying potential energy surfaces[8] and has frequently been used to study diamond surface reactions. Out of a variety of density functionals available for use, the most popular one is the B3LYP functional.[8] It has been found to give the most accurate results in a number of validation studies when used in combination with large enough basis sets.[9] In the work reviewed in this chapter it is used in combination with a double zeta plus polarization basis set such as 6–31G* for the calculation of equilibrium geometries and barriers and in combination with a larger basis set such as 6–311+G(3df,2p) for energies. While DFT is not as accurate as high-level *ab initio* molecular orbital methods such as G3 theory or CCSD(T), it is the most practical method.

The modeling of materials problems such as growth reactions on diamond surfaces often requires a large number of atoms to be included in the calculations. This is not always possible with the traditional quantum chemical methods such as the *ab initio* and density-functional

methods described in this section. A number of methodologies have been developed and implemented that include quantum mechanics in an approximate way so that a sufficiently large number of atoms can been handled. In some of the work reviewed in this chapter, the tight-binding methodology has been employed to study larger models for UNCD. The specific tight-binding approach that is used is a self-consistent, charge density functional-based tight-binding (SCC-DFTB, denoted DFTB in short) method that is parameterized by fitting to density-functional results for appropriate systems as developed by Frauenheim and coworkers.[10,11] The method is also sufficiently fast that it can be used in molecular dynamics simulations, which include electronic structure. The tight-binding method uses tabulated integrals and the energy is written as a band energy term plus a sum over repulsive pair potentials. The band energy term is the sum of occupied orbital energies obtained with a minimal basis set.

8.2 Carbon Dimer Growth Mechanisms on the (110) Face of Diamond

There have been numerous previous computational studies of diamond growth mechanisms based on hydrogen abstraction and hydrocarbons such as acetylene and methyl radical as the growth species.[12,13,14,15,16,17,18] Carbon dimer growth mechanisms are unique because, compared to previous diamond growth studies, they are not dependent on abstraction of hydrogen from the surface. Studies based on the carbon dimer mechanisms are reviewed here.

8.2.1 The (110) 1 × 1:H Surfaces

There have been several quantum chemical studies of growth mechanisms involving carbon dimer on the hydrogen-covered diamond (110) surface.[19,20,21] The mechanisms for carbon dimer growth are similar to the one that Harris and Belton[22,23] proposed for acetylene addition to the (110) 1 × 1:H surface. This diamond surface is illustrated in Fig. 8.1 and the postulated mechanism for the carbon dimer growth involves the following steps. First, one C_2 unit adds to the surface by inserting itself into one C—H bond (step 1) and then the free end inserts into a second C—H bond

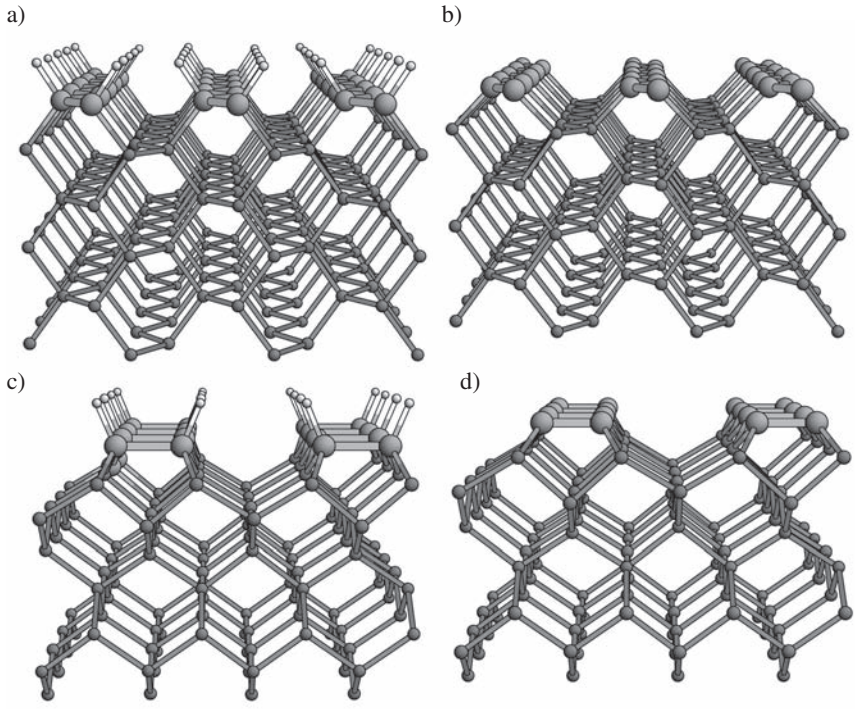

Figure 8.1 Side view of diamond surface structures: (a) (110) 1 × 1:H, (b) (110) 1 × 1, (c) (100) 2 × 1:H, (d) (100) 2 × 1.

(step 2), producing an adsorbed ethylene-like structure across the trough. The third and fourth steps involve a second C_2 inserting itself into two other C—H bonds in a similar manner to produce a surface with two adjacent ethylene-like groups. Formation of a C—C single bond between adjacent ethylene-like groups can produce a new layer on the diamond surface via addition of hydrogen (step 5) or without (steps 6 and 7). An alternative is a concerted addition step (replacing steps 1 and 2), in which the C_2 molecule inserts into two C—H bonds simultaneously.

In an initial study,[19] *ab initio* molecular orbital theory was used to examine the energetics of small-molecule models of the first steps of this growth mechanism, namely, insertion of C_2 into a C—H bond in methane, insertion of CCH into a C—H bond in methane, and the rearrangement of methylvinylidene to methylacetylene. The geometries of equilibrium structures and transition states were determined. At the highest level of theory considered, G2 theory, it was found that C_2 could insert into a C—H bond of methane with no energy barrier, and that insertion of the result-

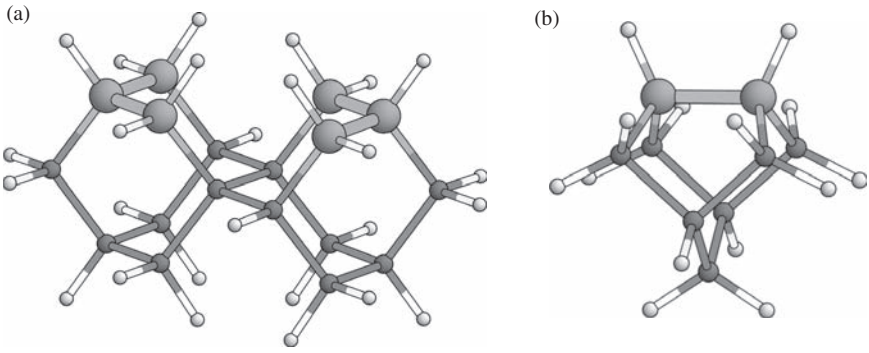

Figure 8.2 Illustration of clusters used for modeling C_2 addition reactions to (a) the (110):H surface ($C_{18}H_{26}$) and (b) the (100):H surface (C_9H_{14}).

ing vinylidene radical, CCH_2, into a C—H bond of methane had a barrier of only 17 kcal/mol.

A more detailed study of C_2 addition to the diamond (110) surface[20] was carried out using DFT. Hydrogen-terminated diamond-like clusters were used to represent the (110) diamond surface. In this study, the (110) surface of diamond was modeled using carbon clusters, with dangling bonds terminated by hydrogens. The $C_{18}H_{26}$ cluster with C_{2h} symmetry, illustrated in Fig. 8.2(a), can accept two added C_2 molecules across the trough of the (110) surface. This structure was fully optimized at the AM1 and HF/6–31G* levels. The AM1 method is a semi-empirical molecular orbital method that was also used to optimize a larger $C_{48}H_{50}$ model of the diamond (110) surface. Reaction energies were calculated with the B3LYP/6–31G* method on these two clusters using the AM1 optimized geometries. The calculations indicated that addition of C_2 to the diamond (110) surface is very favorable, with large energy lowerings of about 150–180 kcal/mol per C_2 (steps 1 and 2). The barriers for addition of C_2 to the (110) surface are small in steps 1 and 2. The two-step addition of C_2 to the C—H bonds on the surface has a barrier of only 5 kcal/mol and a single-step concerted mechanism for C_2 addition has no barrier. Adjacent C_2 moieties on the hydrogen-terminated (110) surface, adsorbed in ethylene-like arrangements, can be connected via a radical mechanism involving initiation by hydrogen atom addition to the double bond of one ethylene-like group (step 5). Investigations of this method indicated that there is little or no energy barrier for this reaction, and that the ethyl-like radical intermediate is stable with respect to β-scission. The other mechanism for linking adjacent surface ethylene-like species directly

(steps 7 and 8) was also investigated. This does not require the assistance of hydrogen addition, and this process was found to have a barrier of about 2 kcal/mol. This corresponds to the linking of the first two ethylene-like units to form a singly bonded diradical structure. Formation of a new surface layer from bonding of radical structures and ethylene-like groups results in an energy lowering of about 20 kcal/mol.

8.2.2 Clean (110) Diamond Surface

A DFTB study of growth steps involving addition of C_2 on a clean diamond (110) surface has been reported by Sternberg et al.[21] This surface is illustrated in Fig. 8.1(b) and in this study it was modeled using a two-dimensional slab geometry with six to eight carbon monolayers. The calculations indicated that initial C_2 adsorption onto a clean (110) surface occurs with small barriers (2–4 kcal/mol) into a surface double bond and the adsorption energy for one C_2 is about 180 kcal/mol. The DFTB results are very similar in magnitude to those found on the hydrogenated surface from the density-functional study described above.[20]

Sternberg et al.[21] also investigated the addition of more carbon dimers. They found that the addition of carbon dimers near the first adsorbed one leads to C_{2n} chains along the [110] direction on the surface. The adsorption energies are in the range 160–230 kcal/mol per C_2 at adsorption sites that lead to chain growth. Sites with smaller adsorption energies of about 115–160 kcal/mol do not result in chain continuation, i.e., defect sites. They also found that the barriers for additional C_2 insertion are small (0–12 kcal/mol). The C_2 chain addition mechanism leads to chain coalescence with broken backbonds on either side. They carried out geometry relaxation studies on a model in which every other trough along the [110] direction was covered with a contiguous chain. The diamond (110) 2×1 reconstruction shown in Fig. 8.3(a) results from this relaxation. Interestingly, it has multiple bent graphene sheets along the [110] direction with a bending direction of a carbon nanotube of the (n,n) type, i.e. the armchair tube. As shown in Fig. 8.3(b), continuing addition of C_2 in the valley between the two arches causes the sp^2-like carbons near the adsorbate to return without barrier to an sp^3 configuration to form the diamond structure.

The diffusion of C_2 on the clean (110) diamond surface was also investigated. The DFTB calculations showed that diffusion of C_2 strongly bonded to the surface is highly unlikely. The diffusion barriers are greater

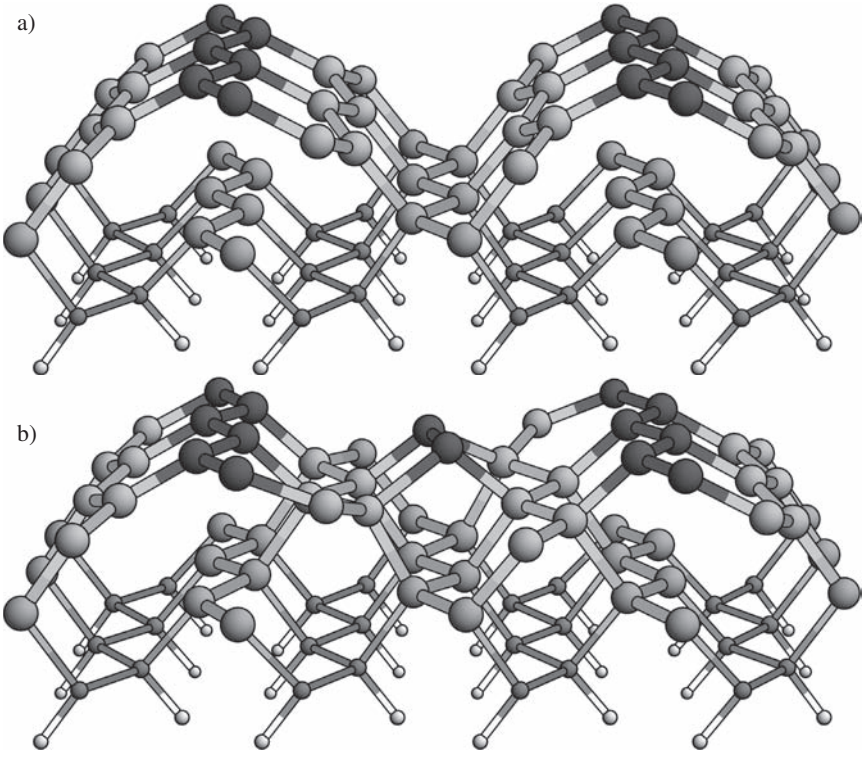

Figure 8.3 Graphitization on a 50% covered diamond (110) 2 × 1 surface (a) and induced rebonding after depostion of additional C_2 (b). (Reprinted with permission from ref. [21]. Copyright (2001) by the American Physical Society.)

than 75 kcal/mol and the only case for which an inter-island diffusion path exists occurs when C_2 is added on top of a C_{2n} chain. The energy barrier along an adsorbate ridge is about 20 kcal/mol. Such a C_2 will diffuse until it reaches the end of the chain and then will be incorporated there.

8.3 Carbon Dimer Growth Mechanisms on the (100) Surface of Diamond

There have been a number of studies of growth on the (100) diamond surface with carbon dimer as the growth species.[24,25,26,27,29] The (100) diamond surface is believed to be the slowest growing surface and thus plays an important role in the growth of UNCD. It is likely that the (100) surface has a substantial fraction (0.1–1%) of sites devoid of hydrogen

under growth conditions used to grow UNCD films and this may play a major role in the growth mechanism. This is because the depositions are carried out with small amounts of hydrogen admixtures (1–2%), while the gas species present in overwhelming quantity is argon. Under the conditions at which the depositions are carried out, particularly at the substrate temperatures of 700–900 °C, some of the surface hydrogen will be missing. Thus, the structures of both the unhydrided (clean) and monohydrided diamond (100) surfaces have been investigated for C_2 growth reactions. The unhydrided diamond surfaces are used to represent the growth mechanisms in the regions with missing hydrogens. In this section we review results for the 2×1:H surface and for the clean surface.

8.3.1 The (100) 2×1:H Diamond Surface

The C_2 insertion reactions on the (100) 2×1:H surface, shown in Fig. 8.1(c), have been investigated by Gruen et al.[24] using DFT. A small cluster, C_9H_{14}, was used to model the initial steps of the reaction of C_2 with the surface. This cluster is shown in Fig. 8.2(b). Several structures resulting from C_2 insertion were investigated. These include (i) a carbene-like structure shown in Fig. 8.4(a) resulting from insertion of one end of

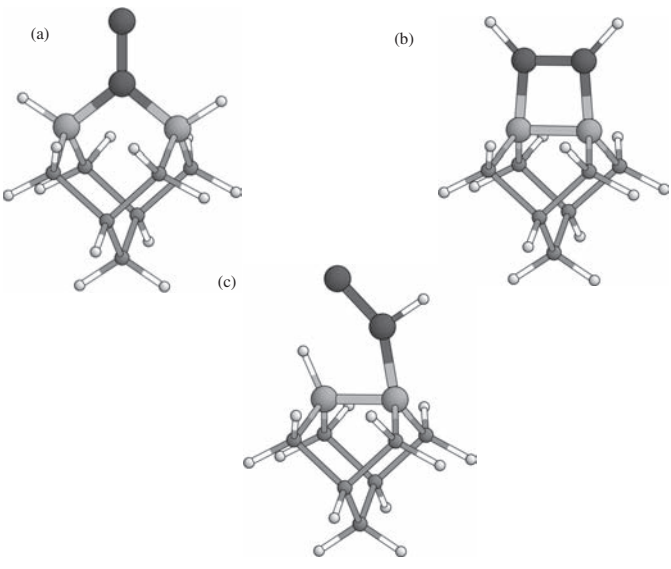

Figure 8.4 Products from addition of C_2 to C_9H_{14}: (a) carbene-like structure, (b) cyclobutene-like structure, (c) vinylidene intermediate.

C_2 into a C—C single bond on the C_9H_{14} cluster and (ii) the cyclobutene-like structure (Fig. 8.4(b)) resulting from insertion of the C_2 into two C—H bonds. The latter is about 32 kcal/mol lower in energy. For both the carbene-like and cyclobutene-like structures, the reaction pathways for the C_2 addition to the cluster C_9H_{14} involves the initial insertion of C_2 into a C—H bond to produce a common, monosubstituted vinylidene intermediate shown in Fig. 8.4(c). However, the energy barrier between this intermediate and the carbene-like structure is about 60 kcal/mol higher than the barrier along the pathway from this intermediate to the cyclobutene-like product. Thus, the density-functional results predict that insertion of C_2 into C—H bonds to form the cyclobutene-like structure (Fig. 8.4(b)) is favored on the monohydrided surface. The cyclobutene-like structure was shown to lead to formation of a new layer of the monohydrided surface.

8.3.2 The (100) 2 × 1 Diamond Surface

The C_2 growth reactions on the clean (100) diamond surface, shown in Fig. 8.1(d), have been modeled with small cluster models using DFT and, subsequently, a more comprehensive investigation was carried out using two-dimensional periodic DFTB calculations.[24,25,26,27,28] In this section we review these studies and discuss the implications for growth on this surface.

The energetics of C_2 insertion reactions in a C_9H_{12} cluster representing the (100) 2 × 1 surface have been studied using DFT to model the initial steps of the C_2 reaction with the surface.[24] The results indicated that insertion of C_2 into a C═C leads to a large energy lowering of about 120 kcal/mol. The insertion of a single end of the C_2 into a C═C bond occurs with no energy barrier. This yields a carbene-like structure as shown in Fig. 8.5(a). Another possible structure is a double insertion cyclobutyne-like structure (Fig. 8.5(b)), but this is 33 kcal/mol more endothermic than the carbene-like structure. These results suggest that the C_2 mechanism of diamond growth on the diamond (100) surface is quite dependent on the degree of hydrogenation of the surface. On the clean surface, the most favorable C_2 addition pathway involves insertion of C_2 into a C═C bond to produce the carbene-like structure, while on the monohydrided surface, insertion of C_2 into C—H bonds to form the cyclobutene-like structure is favored.

The DFTB method was used by Sternberg et al.[25] to carry out a thorough study of diamond growth by C_2 on a clean (100) surface using a peri-

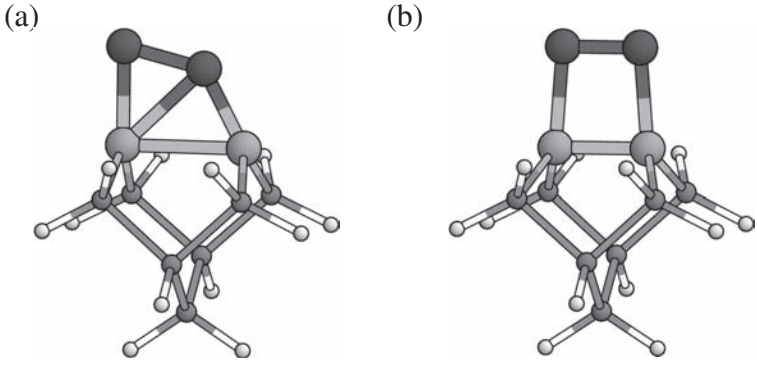

Figure 8.5 Products from addition of C_2 to C_9H_{12}: (a) carbene-like structure, (b) cyclobutyne-like structure.

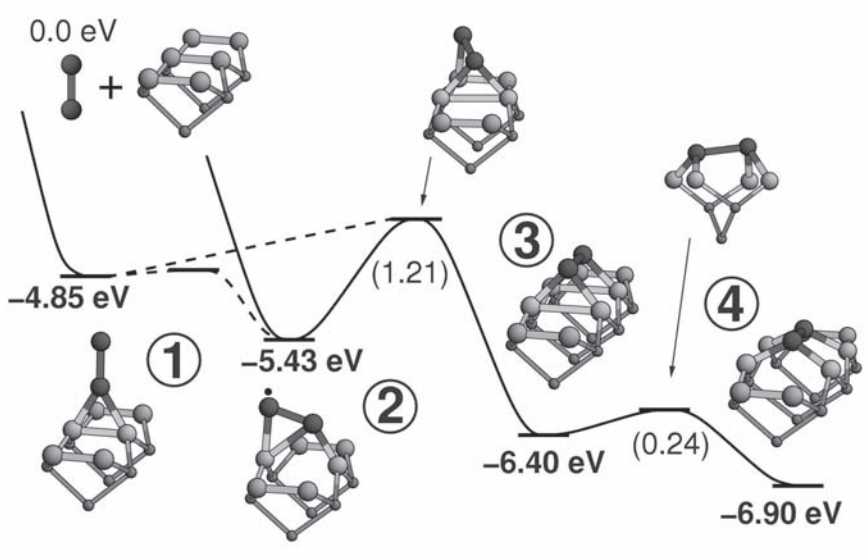

Figure 8.6 Potential energy surface from density functional-based tight-binding study of C_2 addition to a clean diamond (100) 2×1 surface. Energies are in eV. Barrier heights are in parentheses. (Reprinted with permission from ref. [25]. Copyright (2003) by the American Physical Society.)

odic representation of the surface. The unhydrided (100) diamond surface was modeled using a supercell with 16 atoms per monolayer and eight carbon monolayers. The potential energy surface for addition of C_2 to the surface calculated from this investigation is illustrated in Fig. 8.6. The most stable configuration (structure **4** in Fig. 8.6) is a bridge structure

between two adjacent surface dimers along a dimer row. The surface dimers are opened by the insertion and this insertion product has an adsorption energy of 159 kcal/mol (6.90 eV). This structure was not found in the cluster study due to the small cluster size that was used. A barrier of ~28 kcal/mol (1.21 eV) must be overcome to reach it from a higher energy configuration (structure **2** in Fig. 8.6). Other configurations were found in the DFTB investigation with adsorption energies differing by up to 60 kcal/mol and include the structures found in the cluster study. Thus, the results of the study of isolated adsorbates indicate that there are relatively large barriers of >20 kcal/mol to reach the structures leading to growth. A somewhat lower barrier of 12–18 kcal/mol was found if the structure **2** in Fig. 8.6 is neighboring a trough-bridging ad-dimer. Conversely, neighboring adsorbates on a dimer row as shown in Fig. 8.7 were found to have high barriers (~50 kcal/mol) to conversion into growth positions and therefore are likely renucleation sites. The barriers to diffusion were studied and found to be very large, 40–60 kcal/mol, effectively precluding diffusion on the surface at the experimental growth temperatures.

The results of the studies of C_2 addition to the hydrided and unhydrided surfaces suggest a possible explanation for the small grain size that typifies UNCD. First, the clean (100) surface has sites for both growth and renucleation as described above. Second, C_2 addition on the hydrogenated (100) surface was found to lead only to growth and not to nucleation. As a result, since only a small fraction of the (100) surface sites are unhydrided, most C_2 insertion events will lead to growth, with only a few

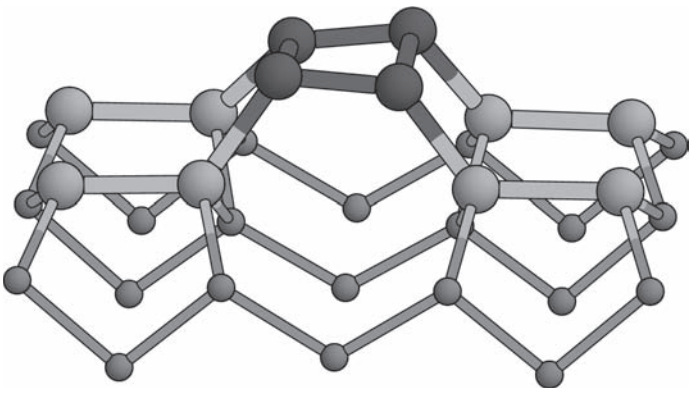

Figure 8.7 Structure resulting from an agglomeration of two adsorbates labeled **2** in Fig. 8.6.

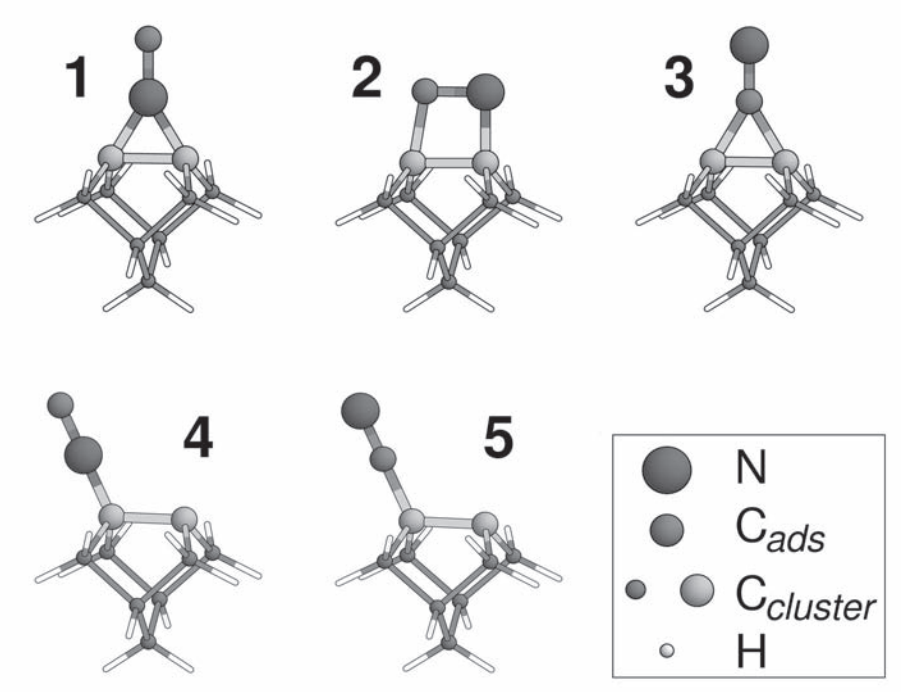

Figure 8.8 Structures of CN adsorbates on a C_9H_{12} cluster. Nitrogen is represented by the large sphere.

leading to renucleation. However, these renucleation sites are likely enough to explain the small grain size observed in UNCD as discussed in Section 8.3.4.

8.3.3 Nitrogen Addition to (100) 2 × 1 Surface

As discussed elsewhere in this book, nitrogen addition dramatically alters the properties of UNCD films. The increase in grain size that accompanies the introduction of nitrogen into the feed gas suggests that a nitrogen-containing species enhances diamond growth or inhibits nucleation. Appreciable amounts of CN radicals and C_2 are found in the microwave plasma, and the concentrations of both increase substantially as N_2 gas is added to the mixture. In order to understand the morphology changes with addition of N_2 to the plasma, we have investigated the binding of a CN radical to a C_9H_{12} model (Fig. 8.8) of the unhydrided, reconstructed diamond (100) 2 × 1 surface.[29] The adsorption structures of CN on this

cluster in various configurations are illustrated in Fig. 8.8. A comparison of the binding energies of different structures shows that when binding is through one end of CN, the carbon end binds more strongly than nitrogen. Further, CN is adsorbed more strongly by binding to only one carbon of the dimer than by inserting into the π bond to form three- or four-membered rings. In the most stable structure, labeled **5** in Fig. 8.8, with a B3LYP/6–31G(d) reaction energy of −103.9 kcal/mol (–4.51 eV), CN is bound through the C to one carbon. The binding of CN across two adjacent dimers is less stable, by about 37 kcal/mol (1.60 eV), than binding to a single dimer through the CN carbon atom. The results of this study suggest that CN addition to the (100) surface will block potential nucleation sites for C_2 addition and is not likely to be a nucleation site itself because the nitrogen site in structure **5** will not be reactive. This provides a possible explanation of the larger grain size observed experimentally in N_2 plasma. A more detailed study of CN adsorption on the (100) surface published elsewhere includes studies of co-adsorption of C_2 and CN and confirms this conclusion.[28]

8.3.4 A Model for UNCD Growth Kinetics

It was shown in previous sections that the dominant chemical reactions involved in growth and nucleation of UNCD are different from those in conventional diamond growth. As a result, a different kinetic mechanism for diamond growth and nucleation will exist. One simple mechanism was suggested by Zapol[30] for hydrogen-poor conditions, assuming that carbon dimers are the only growth and nucleation species. If these dimers arrive at a constant rate, r_d, to the (100) unhydrided surface with surface site density S (~1.4×10^{15}/cm^2), and have a sticking probability of unity, which is not unreasonable since there is no barrier for chemical reaction of carbon dimer with the (100) surface, they can serve as either growth species when the dimer assumes a topologically perfect configuration shown in Fig. 8.6 as structure **4** or nucleation species when it is in a bent vertical configuration shown in Fig. 8.6 as structure **2**. In the model, the nucleation event happens when the arriving dimer interacts with a nucleation site and the growth event is the result of the dimer arrival at the growth site.

Taking into account that there is a barrier for interconversion between the two configurations, which was calculated to be 1.2 eV,[25] one can find a distribution of growth and nucleation species (concentrations [G] and [N], respectively) at the surface as a function of growth rate and substrate

temperature from the transition state theory. The renucleation rate will be simply

$$R = k_d \frac{[N]}{[G]} S$$

or, substituting the ratio by the transition theory equation,

$$R = k_d S \left(\frac{k_d}{\tilde{\nu}} e^{\frac{\Delta E_1}{kT}} + \alpha e^{\frac{\Delta E_2}{kT}} \right),$$

where ΔE_1 and ΔE_2 are the barrier for configuration conversion and the energy difference between growth and nucleation configurations, respectively. Here $\tilde{\nu}$ is approximated by the Debye frequency of diamond and α is a prefactor, which depends on the vibrational frequencies of the two configurations and is close to unity. It was shown by Gruen[1] that the crystallite volume, V, has a simple relation to the renucleation rate, $V = r_d/R$. Thus, the grain size determined as a cubic root of V can be easily derived from the expression for R given above. This simple model gives a surprising result, illustrated in Fig. 8.9, that for an experimentally reasonable growth rate of 1 μm/h, the maximum achievable grain size is about 35 nm. It so happens that at low temperatures the probability of converting nucleation sites into growth sites is not sufficient and at high temperatures conversion back from the growth sites to nucleation sites starts to increase the concentration of nucleation sites. This rather general explanation leads

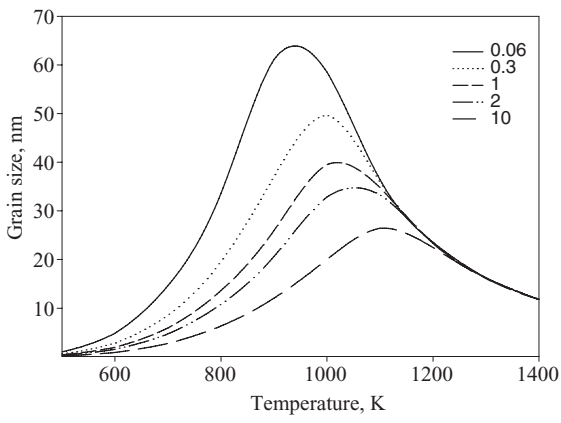

Figure 8.9 Dependence of grain size on growth temperature. Different curves correspond to different growth rates (μ/h).

to the appearance of the maximum in the grain size plot as a function of temperature. In fact, the prediction from this model for a range of temperatures from 700 to 1100 K, and growth rates, is that the grain size of diamond film will vary from 3 to 65 nm, which is in agreement with experimental results of 3 to 10 nm. Taking into account that this is a very crude model and a number of important factors are neglected, one should not expect quantitative agreement with experiment. For quantitative comparisons, the presence of other carbon and hydrocarbon reactions, more sophisticated theoretical approaches, an explicit dependence of growth rate on temperature, influence of gas and surface diffusion at higher temperatures, and other factors should be included into the mechanism. However, at this stage, the predictions resulting from this model can help to design experiments to verify nucleation mechanisms, which are the key to controlling the structure and properties of UNCD.

8.4 Electronic Structure of UNCD

Diamond has a fundamental band gap of 5.45 eV and without doping does not conduct electricity. Both the top valence band and the bottom conduction band have σ character. UNCD, however, exhibits very different electronic properties even without doping.[1,3,31] Since UNCD is formed by diamond crystallites of size 2–10 nm, the interior of the grains has negligible differences in electronic properties as compared to bulk diamond. The crystallites form a continuous film and do not have free surfaces, but rather form interfaces with neighboring crystallites. Therefore, clues to the electronic properties of the nanocrystalline diamond can be found in the structure of these grain boundaries. Indeed, from simple considerations of surface-to-volume ratio, a 3 nm grain will have about 10% of the atoms at its surface. This percentage goes down linearly with an increase in the grain size and one can see that for micrometer-size grains the grain boundary atom fraction is a thousand times smaller, which might explain the difference in properties between microcrystalline diamond and UNCD. Here we review the work on the computational studies of grain boundaries in UNCD.

8.4.1 Grain Boundaries in UNCD

The UNCD films grown in hydrogen-poor plasmas[1,3,31] do not exhibit the columnar morphology typical of polycrystalline diamond films (e.g.,

ref. [32]). If the grains are oriented more or less randomly relative to each other, the majority of the grain boundaries will be high-energy general grain boundaries rather than low-energy coincidence tilt grain boundaries. Such grain boundaries are known to occur in polycrystalline ceramics formed by sintering, e.g., Si_3N_4,[33] where a narrow glassy layer is formed between the grains.

The structure of grain boundaries in diamond has been studied using a variety of methods, including interatomic potentials, tight binding, and DFT.[34,35,36,38] Highly symmetric tilt boundaries exhibit relatively low energies and slightly distorted carbon σ bonds.[37,38] They do not possess dangling bonds. For a general review of theoretical studies of grain boundaries (GBs) in covalent materials see Kohyama.[39]

It was shown by Keblinski et al.[42] that Si nanocrystalline films grown from a melt into which small, randomly oriented crystalline seeds were inserted have a relatively high energy and mostly incommensurate or large-unit-cell GBs on more or less randomly distributed lattice planes. Based on this observation, high-angle, high-energy GBs were proposed to be predominantly present in nanocrystalline diamond as well.[42,43] It was also noted by Kohyama[39] that the idea of "the extended boundary model" was proposed by Ikuhara[40] in order to explain the observed disordered layers at grain boundaries in SiC ceramics.

8.4.2 Structure of High-Angle Twist GBs in Diamond

A study by Wang et al.[41] of (100) twist GBs in diamond using Tersoff interatomic potentials revealed that in the relaxed structures 40–80% of atoms in the two disordered interface planes are threefold coordinated. The GB energies are about 6 J/m^2 with no pronounced dependence on twist angle.

The structure of large-unit-cell twist GBs in diamond was obtained by Keblinski et al.[42,43] in a Monte Carlo simulation using Tersoff potentials. The $\Sigma 9$, $\Sigma 29$, and $\Sigma 35$ (100) and $\Sigma 31$ (111) GBs were considered in these simulations. The structures were kept at 80% of melting temperature for an extensive period of time and then slowly cooled down to zero temperature. The structure of the $\Sigma 29$ (100) GB from this study is shown in Fig. 8.10. The (111) GB was significantly more ordered than (100) and exhibited two peaks in the bond angle distribution, at ~107° and ~116°, corresponding to sp^3 and sp^2 bond angles, respectively. It was shown that the (100) GBs are very narrow, about two atomic layers wide, with about

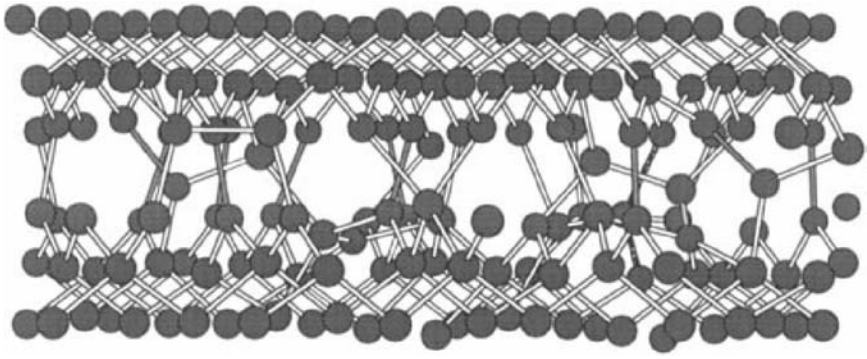

Figure 8.10 Projected bonding structures of the high-temperature relaxed (100) Σ29 twist boundary in diamond. All the bonds between atoms at or near the grain boundary are shown. Approximately 80% of the grain boundary atoms are three coordinated. (Reprinted with permission from ref. [42].)

80% of the carbon atoms at the interface having threefold coordination and only one peak at 116° in the bond angle distribution. This is in contrast to Si, where GBs are wider and atoms at the interface do not exhibit coordination changes.

A tight-binding molecular dynamics study of the Σ29 twist GB of diamond by Cleri et al.[44,45] indicated that about 40% of the GB atoms are threefold coordinated. About 10% of these atoms are not bonded to other threefold-coordinated atoms and represent dangling bonds and the remaining 30% form sp^2 dimers across the GB plane with only a few joining into sp^2 chains of three or more atoms.

DFTB molecular dynamics simulations by Zapol et al.[46] were done on the Σ5, Σ13, and Σ29 twist (100) GBs in diamond. The final minimum energy structures for the Σ13 and Σ29 are shown in Fig. 8.11. About 50% of the atoms in the interface were found to be fourfold coordinated. From 23% to 34% of carbon atoms in the interface were found to have only three neighbors, out of which one-third to two-thirds show a non-planar configuration typical of dangling bonds and surface dimers and the rest were found to form π-bonded pairs across the interface. The remaining atoms had intermediate coordination numbers between 3 and 4, having one of the neighbors at a distance between 1.84 Å and 1.96 Å. The GB energy was calculated to be 7.9 J/m^2. The good agreement among different studies[41,42,43,44,45,46] of the spatial and electronic structure of the twist GBs provides confidence in these models to study different electronic and mechanical properties in nanocrystalline diamond materials.

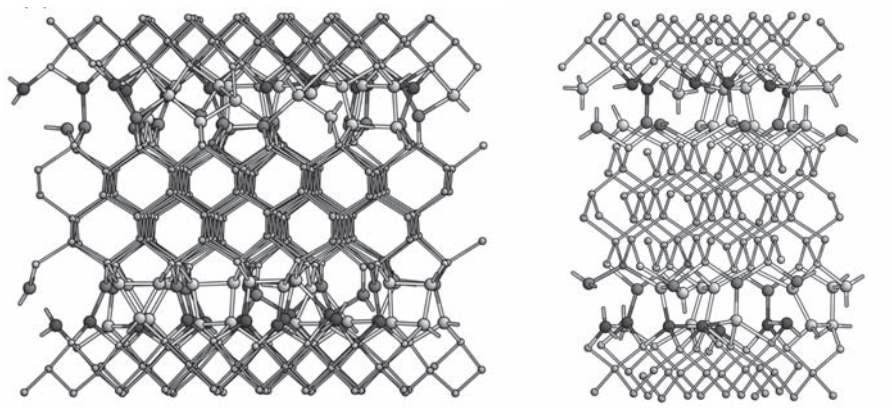

Figure 8.11 Side view of the periodic cell for the optimized structures of diamond Σ29 (left) and Σ13 (right) grain boundaries. Two grain boundaries are shown. Dark (light) shading indicates threefold- (fourfold-)coordinated atoms. Atoms in the first interface monolayers are shown as larger spheres. Bonds extending across the cell boundary are shown as half bonds (interface layer only).

8.4.3 Electronic Structure of GBs with π bonding in UNCD

A high concentration of threefold-coordinated atoms can produce electronic states in the diamond forbidden gap and lead to new electrical properties. A model for the UNCD GB with completely sp^2 bonding across the interface shown in Fig. 8.12 was studied by Gruen et al.[24] using density-functional calculations (BPW91) with periodic boundary conditions. This model is a stacking fault with no dangling bonds and with all sp^2 dimers oriented across the interface. The formation energy of such a π-bonded planar defect was found to be 4.2 J/m^2, which is similar to the energies of twist GBs. The electronic structure of this model was characterized by the presence of π states in the forbidden gap that are localized on the interfacial atoms. The three most prominent peaks in the electronic DOS were found at –0.1, 1.1, and 2.1 eV with respect to the Fermi level.

In a tight-binding molecular dynamics study by Cleri et al.[44] the Σ29 twist GB in diamond was found to have an electronic band structure characterized by a broad spectrum of gap states due to dangling bonds and double bonds. They found that the localized π–π* states always occur in pairs at the same atomic site in the GB region and the average energy separation between two such states is about 2.7 eV. The minimum energy sep-

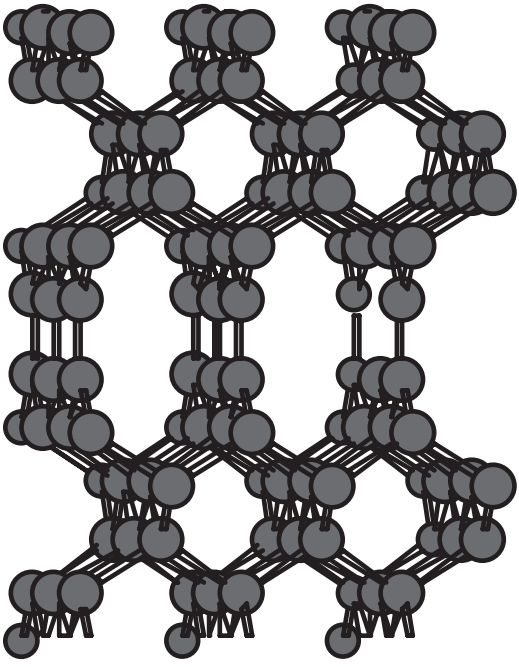

Figure 8.12 Geometry of an sp^2-bonded (100) stacking fault in the diamond structure. Each interface atom has a double bond across the interface.

aration, 2.3 eV, was interpreted as an effective gap. The states in the ranges 3.5–3.6 eV and 5.6–5.7 eV were found to be localized at dangling bonds. The Fermi level in the GB was found at $E_F = 3.05$ eV relative to the top of the diamond valence band. However, metallic conduction was not suggested because of localization of all the electronic states between 0.9 eV and 7.0 eV. It was suggested that the localized states can participate in hopping conduction. An estimate of dc conductivity of the UNCD with a grain size of 10 nm on the basis of a weak-coupling multiphonon model with empirical and calculated parameters gave a value of about $10^{-6}/(\Omega$ cm). The EELS spectrum was constructed from the unoccupied portion of the carbon 2p-orbital-projected DOS calculated using a tight-binding method, convoluted with a Gaussian of FWHM of 1.0 eV and shifted to match the experimental σ^* peak in diamond at 290 eV. The simulated spectra have both σ^* and π^* peaks at 290 eV and 285.5 eV, respectively, as well as two additional peaks originating from GB states at 282.2 eV and 283.7 eV. For comparison, experimental EELS spectra[47] of UNCD show a σ^* peak at 289.5 eV and a π^* peak at ~285 eV.

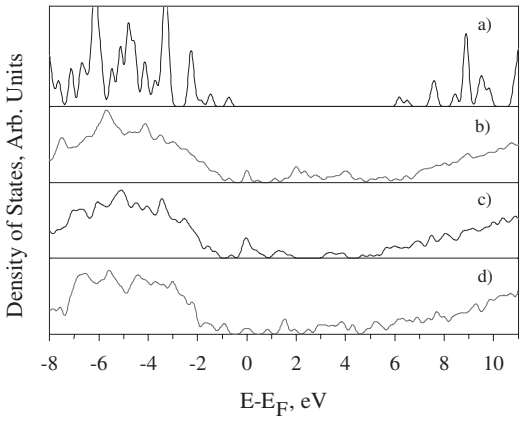

Figure 8.13 Electronic density of states for (a) diamond, (b) Σ13, (c) Σ5(2 × 2) and (d) Σ29 grain boundaries. Energies are given relative to the Fermi energy. Each plot is normalized by the number of atoms in the periodic cell. DOS peaks associated with the grain boundary atoms have higher than expected weight because the fraction of grain boundary atoms is higher in the calculation compared to experimental structures. (Reprinted with permission from ref. [46]. Copyright (2001) by the American Physical Society.)

As part of the computational study of impurities in UNCD, the electronic properties of Σ5, Σ13, and Σ29 GBs were calculated using the DFTB method by Zapol et al.[46] The DOS plots for these structures and diamond are shown in Fig. 8.13. As compared to diamond, new states appear in the band gap: tails near the valence and conduction band edges, a peak at the Fermi level (E_F), and broad features from 0.7 to 2.5 eV and from 3 to 4.5 eV. The local DOSs shown in Fig. 8.14 were calculated for Σ13. The lower mobility edge was found at $E_F - 1.4$ eV. There are π states from 1.2 to 0.8 eV below the Fermi level and π* states from 1.2 to 1.5 eV above the Fermi level that are attributed to sp^2-bonded carbons (see Fig. 8.14). The states near the Fermi level (–0.5 to 0.6 eV) are identified predominantly with dangling bonds. A new σ* peak in DOS from 2.65 to 3.1 eV above the Fermi level arises from the orbitals of the fourfold-coordinated carbon atoms with elongated bonds. The fourfold-coordinated atoms in the GB layers as well as in the adjacent layers contribute to the σ* feature at 3.5 to 4 eV. The states above 5.3 eV are delocalized at the bulk-like atoms and are in the diamond conduction band. As a result, the valence band and conduction band mobility edges are 6.7 eV apart, somewhat similar to the 7.9 eV reported in a previous tight-binding study.[44]

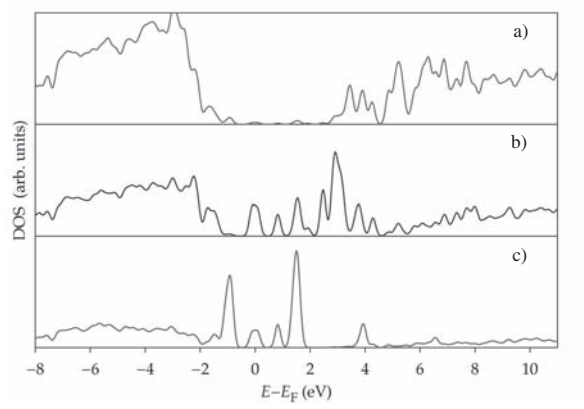

Figure 8.14 Local density of states for a diamond Σ13 twist grain boundary. Contributions from (a) planar (sp^2) and (b) non-planar (sp^{2+x}) three-coordinated atoms and (c) four-coordinated atoms (sp^3) in the grain boundary region are shown. Contributions from bulk atoms are omitted. (Reprinted with permission from ref. [46]. Copyright (2001) by the American Physical Society.)

8.5 Electronic Structure of Doped UNCD

The effects of nitrogen, silicon, and hydrogen on the electronic properties of UNCD are of great interest. Small amounts of hydrogen are present in hydrogen-poor plasmas used for the UNCD growth. Substrate materials such as silicon contribute impurities by diffusion processes. Nitrogen addition to the feed gas leads to a drastic change in electronic properties manifested by an increase in electrical conductivity of several orders of magnitude. Many theoretical studies addressed the structure and electronic properties of the effect of dopants and impurities in bulk CVD and natural diamonds. As compared to the structure and properties of impurities in bulk diamond, impurities in the disordered GBs in UNCD can have different concentrations, geometries, and electronic structure. The distribution of impurities between grains and GBs in the UNCD has not yet been determined experimentally. Here we review theoretical studies of UNCD with impurities.

8.5.1 Nitrogen in Diamond and Amorphous Carbon

The electronic structure of nitrogen defects in diamond has been the subject of many theoretical and experimental studies. It is well established

that a single substitutional nitrogen in diamond (the P1 center) adopts an offsite non-planar configuration with three equivalent neighbors and the fourth neighbor being much farther away.[48] This gives rise to a carbon dangling bond state in the diamond band gap at 1.7 eV below the conduction band[49] and a nitrogen resonance state below the top of the valence band. An anti-bonding combination of the carbon dangling bond and nitrogen orbitals was found at 1.9 eV below the conduction band by Kajihara et al. in their Car–Parinello study.[50] The nitrogen state that Kajihara et al.[50] reported to be at 0.15 eV above the valence band top was ascribed to the nitrogen lone pair with an admixture of valence band states. A bonding combination of the lone pair with the orbitals of the unique carbon neighbor that is strongly hybridized with other carbon states in the valence band was found in the DFTB study.[46] As a result, a number of states with nitrogen participation near the top of the valence band were found; the state with the largest nitrogen contribution was found at 1.5 eV below the valence band maximum, and this state was identified as a lone pair.

A tight-binding study of nitrogen-doped tetrahedral amorphous carbon[51] described several doping and non-doping configurations. It was proposed that nitrogen as a shallow donor in ta-C occurs due to the presence of π^* states below the conduction band. Also, sp^2-bonded nitrogen can dope the π^* states. The overall doping efficiency was estimated to be about 1%. Nitrogen in diamond and amorphous carbon has been investigated using DFTB molecular dynamics.[52] It was found for amorphous carbon that nitrogen is incorporated in a paracyanogen-like manner, having CN double and triple bonding.

8.5.2 Nitrogen Impurities in the UNCD GBs

It was found experimentally that the nitrogen concentration saturates in the UNCD at 0.2% with increasing nitrogen content in the plasma.[31] This concentration is much higher than that in microcrystalline diamond and lower than the nitrogen saturation limit in amorphous carbon. The DFTB calculations by Zapol et al.[46] indicate that some nitrogen substitutions in the $\Sigma 13$ GB give rise to electronic states similar to those for nitrogen defects in diamond. However, the positions and occupancies of the levels in the case of GB substitutions are more diverse and in some cases have no analogy with the bulk substitution. The choice of the substitutional site in the disordered structure is not unique because local disorder creates a number of chemically diverse carbon atom arrangements.

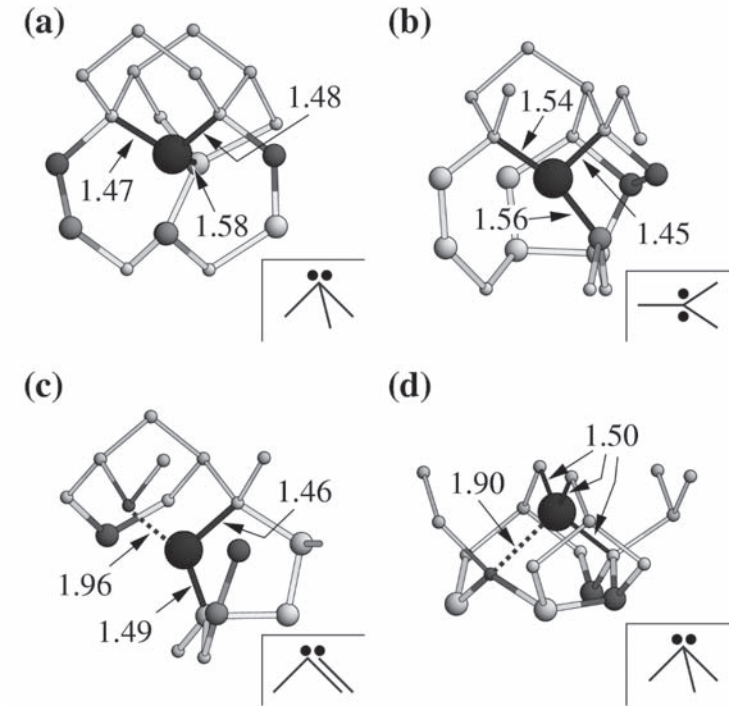

Figure 8.15 Relaxed local structure around a substitutional nitrogen atom at characteristic sites in a Σ13 grain boundary: (a) C3np, (b) C3p, (c) C4 in grain boundary, and (d) C4 in second layer. Bond lengths in Å. The molecular analogies of nitrogen bonding are shown schematically in the insets. (Reprinted with permission from ref. [46]. Copyright (2001) by the American Physical Society.)

Four different initial positions for a single nitrogen atom substitution in the GB were considered: three-coordinated carbon in planar (sp^2) and non-planar (dangling bond) geometries and four-coordinated (sp^3) carbon in the GB layer and in the second layer. The positions of the GB carbon and nitrogen atoms were determined by energy minimization of the structure. The local structure of the optimized nitrogen substituting a carbon with a dangling bond is shown in Fig. 8.15(a). The nitrogen atom is located 0.57 Å out of the plane of its three neighbors. The small changes in the geometry upon relaxation are an expected result considering that the non-planar threefold-coordinated nitrogen configuration is favored for substitutional nitrogen in diamond bulk. As opposed to the bulk case, no bond breaking is required. In the bulk, substitutional nitrogen moves from a T_d position along the <111> direction away from a nearest neighbor to

a threefold-coordinated position of C_{3v} symmetry. Annealed and relaxed local structures for the other three positions are shown in Figs. 8.15(b–d). Substitution in the planar threefold-coordinated site (sp^2 carbon) shown in Fig. 8.15(b) results in a slightly puckered nitrogen configuration with the nitrogen atom located 0.27 Å out of the plane. Its carbon bond partner across the interface moves from a previously planar configuration into a considerably more pyramidal one and the bond to the nitrogen lengthens from 1.42 to 1.56 Å. Both processes indicate a change of the bonding character from a double bond to a single bond and a new dangling bond on the carbon atom. The next substitution site for nitrogen substitution, a fourfold-coordinated site (sp^3) in the GB layer, becomes twofold coordinated upon relaxation and the third nearest neighbor is 1.96 Å away. Finally, the configuration of nitrogen upon substitution in the second layer, shown in Fig. 8.15(d), is non-planar threefold coordinated and the fourth neighbor is 1.90 Å away, quite similar to that in the bulk diamond. Generally, the carbon–nitrogen bond lengths are in the range 1.45–1.56 Å. The distortions of bonds are caused by the geometrical constraints due to the surrounding carbon lattice. These restrictions are weaker for nitrogen in the GB compared to the diamond bulk because of the local disorder. Therefore, it is easier to accommodate nitrogen in the GB.

The states for different nitrogen sites are shown schematically in Fig. 8.16. Substitution into the threefold-coordinated sites in the GB (sites *a* and *b*) gives a nitrogen lone pair state about 1.5 to 2 eV below the Fermi level. If nitrogen is substituted into a fourfold-coordinated site (site *c*), the nitrogen orbitals give contributions to the carbon π states at -1 eV and to the π^* states at 0.5 eV relative to the Fermi level, in addition to the nitrogen lone pair. Finally, the substitution site in the second layer (site *d*) gives rise to an unoccupied level about 0.8 eV above the Fermi level, which has strong carbon participation. In this case, the Mulliken charge on the nitrogen is reduced by about 0.4*e*. This charge is transferred to the state at the Fermi level associated with a carbon dangling bond, forming a carbon lone pair. The formation energies for other nitrogen substitutions are slightly higher: the planar threefold-coordinated site energy is 0.7 eV, the fourfold-coordinated carbon site energy is 1.7 eV, and the energy of the site in the GB second layer is 2.6 eV. All of the GB sites are preferred over the diamond bulk site for nitrogen substitution. Since the substitution energy in the bulk of the grain should be close to that in a diamond crystal, under equilibrium conditions the nitrogen concentration in the GB will be many orders of magnitude higher than that in the grains. Typical growth conditions for UNCD are usually far from equilibrium; however, in view

of the large energy difference it is likely that nitrogen will be concentrated in the GBs.

To investigate the possible shift of the Fermi level due to nitrogen substitution as well as the interaction of nitrogen impurities, a DFTB calculation was performed by Zapol et al.[46] for a higher concentration of nitrogen in the GBs. Of all the GB carbon atoms, 30% were substituted by nitrogen, resulting in an overall nitrogen concentration of about 8 at.%. After annealing and relaxation, the nitrogen distribution by configurations in the GBs is about 50% sp, i.e., nitrogen with two bonds to carbon atoms, and the rest nearly equally divided between sp^2 and sp^{2+x} geometries. The sp configuration appears only at the increased nitrogen concentration and it is similar in bonding to the nitrogen in a pyridine molecule. However, no aromatic rings or pyridine were found in this structure. The electronic states associated with nitrogen are most prominent just above the top of the valence band, near the Fermi level and in the σ* carbon dangling bond region around 3 eV above the Fermi level. This is illustrated schematically in Fig. 8.16, as well as in the DOS plot in Fig. 8.17. The Fermi energy is shifted toward the conduction band by about 0.4 eV. The states near the

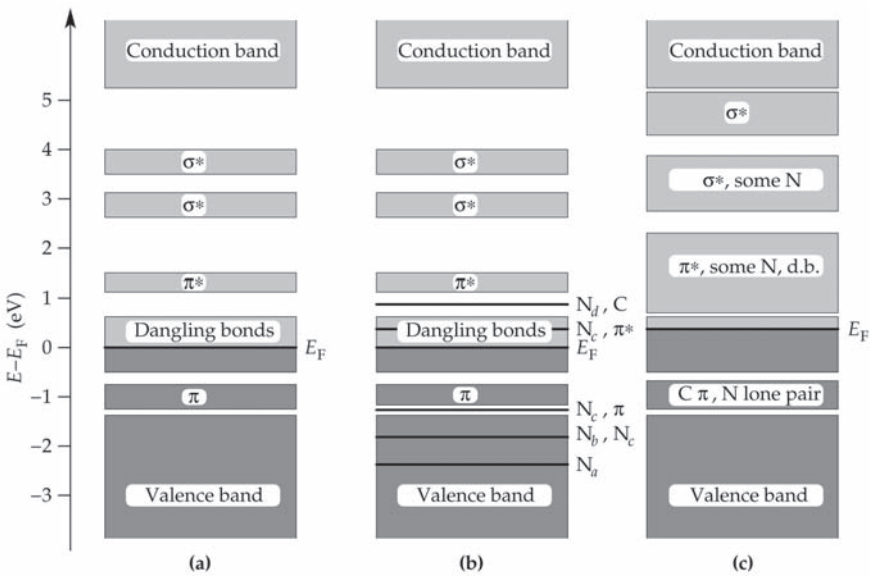

Figure 8.16 Schematic band structure for a diamond Σ13 grain boundary: (a) without nitrogen impurities, (b) with one nitrogen per cell, and (c) with 16 nitrogens per cell. Subscripts on nitrogen levels correspond to different substitution sites. (Reprinted with permission from ref. [46]. Copyright (2001) by the American Physical Society.)

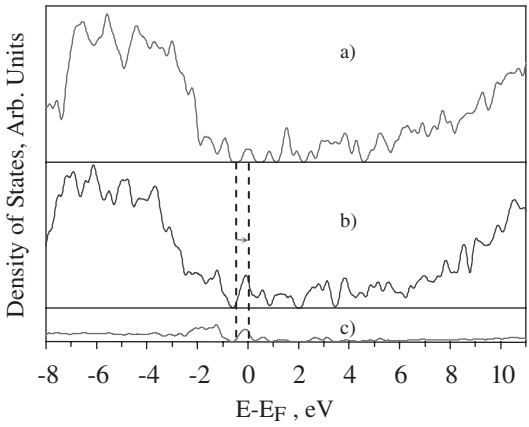

Figure 8.17 Density of electronic states for a diamond Σ13 grain boundary (a) without nitrogens, (b) with 16 nitrogens per cell, (c) partial DOS for nitrogens. An upward shift of Fermi level (0.4 eV) is indicated by the arrow. (Reprinted with permission from ref. [46]. Copyright (2001) by the American Physical Society.)

top of the valence band originate from nitrogen lone pair electrons and they are significantly mixed with carbon π states toward the delocalized π* carbon band.

On the basis of these results, it was proposed that variable range hopping or other thermally activated conduction mechanisms can occur in the GBs and result in enhanced electron transport. This mechanism does not require a true doping nitrogen state (fourfold-coordinated nitrogen or threefold-coordinated nitrogen with a double bond).

8.5.3 Other Impurities in the UNCD GBs

The effect of impurities other than nitrogen on electronic properties of UNCD was investigated by Zapol et al.[46]

Silicon substitution into a GB site always results in the Si atom being fourfold coordinated, independent of the initial configuration. The carbon–silicon bond lengths are typically 1.78 to 2.01 Å. The bond angles are distorted from tetrahedral angles, with values between 84° and 110°. The formation energies of the substitutional Si are 0.85 to 1.45 eV compared to bulk reservoirs as a reference. The energy required to insert Si into the GB is much lower than the 4.45 eV required to insert it into the diamond crystal. A GB has a much lower local density than the ordered diamond structure, and therefore it is easier to accommodate a larger

silicon atom. The number of fourfold-coordinated carbon atoms in the vicinity of Si increases.

In the same study,[46] hydrogen incorporation into UNCD was simulated by adding four hydrogen atoms per GB unit cell at random positions in the interface of the annealed structure. In the final structure, all hydrogen atoms are bonded to carbon atoms, which, as a result, become fourfold coordinated. The average carbon hydrogen bond length is about 1.10 Å. The average hydrogen binding energy is 3.5 eV. The number of carbon atoms with a dangling bond decreased from 21% to 4%. Thus, hydrogen atoms saturate dangling bonds of threefold-coordinated carbons, as expected. Since the total amount of hydrogen used in the calculation was lower than the number of dangling bonds in the initial structure, some dangling bonds are still present. The main change in the electronic structure is the reduction of the DOS near the Fermi level. This finding is consistent with the fact that hydrogen is known to passivate surfaces, GBs, and other lattice imperfections in CVD diamond.

The conclusion from the studies[46] of silicon and hydrogen insertion into the twist GBs in diamond is that these isolated impurities do not lead to improved electrical properties of UNCD. However, more studies are needed to investigate how different hydrogen concentrations and formation of complexes with other impurities and dopants affect the electronic properties of this material.

Acknowledgments

This work is supported by the US Department of Energy, BES-Materials Sciences, under Contract W-31-109-ENG-38.

References

1. Gruen, D. M., "Nanocrystalline Diamond Films", *Annu. Rev. Mater. Sci.*, **29**, 211 (1999).
2. Angus, J. C. and Hayman, C. C., "Low-Pressure Metastable Growth of Diamond and Diamondlike Phases", *Science*, **241**, 913 (1988).
3. Zhou, D., Gruen, D. M., Qin, L.-C., McCauley, T. G., and Krauss, A. R., "Control of Diamond Film Microstructure by Ar Additions to CH_4/H_2 Microwave Plasmas", *J. Appl. Phys.*, **84**, 1981 (1998).
4. Hehre, W. J., Radom, L., Pople, J. A., and Schleyer, P. v. R., *Ab Initio Molecular Orbital Theory* (Wiley, New York, 1987).
5. Curtiss, L. A., Raghavachari, K., Trucks, G. W., and Pople, J. A., "Gaussian-2 Theory for Molecular Energies of First- and Second-Row Compounds", *J. Chem. Phys.*, **94**, 7221 (1991).

6. Curtiss, L. A., Raghavachari, K., Redfern, P. C., Rassolov, V., and Pople, J. A., "Gaussian-3 (G3) Theory for Molecules Containing First- and Second-Row Atoms", *J. Chem. Phys.*, **109**, 7764 (1998).
7. Bartlett, R. J. and Stanton, J. F., "Applications of Post-Hartree-Fock Methods: A Tutorial", *Reviews in Computational Chemistry*, Lipkowitz, K. B. and Boyd, D. B., Eds. (VCH, New York, 1994), Vol. 5, pp. 65–169.
8. Kohn, W., Becke, A. D., and Parr, R. G., "Density Functional Theory of Electronic Structure", *J. Phys. Chem.*, **100**, 12974 (1996).
9. Curtiss, L. A., Raghavachari, K., Redfern, P. C., and Pople, J. A., "Assessment of Gaussian-2 and Density Functional Methods for the Computation of Enthalpies of Formation", *J. Chem. Phys*., **106**, 1063 (1997).
10. Frauenheim, Th., Seifert, G., Elstner, M., Hajnal, Z., Jungnickel, G., Porezag, D., Suhai, S., and Scholz, R. A., "Self-Consistent Charge Density-Functional Based Tight-Binding Method for Predictive Materials Simulations in Physics, Chemistry and Biology", *Phys. Status Solidi B*, **217**, 41 (2000).
11. Porezag, D., Frauenheim, Th., Kohler, Th., Seifert, G., and Kaschner, R., "Construction of Tight-Binding-Like Potentials on the Basis of Density-Functional Theory: Application to Carbon", *Phys. Rev. B*, **51**, 12947 (1995).
12. Huang, D., Frenklach, M., and Maroncelli, M., "Energetics of Acetylene Addition Mechanism of Diamond Growth", *J. Phys. Chem.*, **92**, 6379 (1988).
13. Huang, D. and Frenklach, M., "Energetics of Surface Reactions on (100) Diamond", *J. Phys. Chem.*, **96**, 1868 (1992).
14. Skokov, S., Weiner, B., and Frenklach, M., "Energetics of Surface Reactions on (100) Diamond Plane", *J. Phys. Chem.*, **99**, 5616 (1995).
15. Frenklach, M., Skokov, S., and Weiner, B., "An Atomistic Model for Stepped Diamond Growth," *Nature*, **372**, 535 (1994).
16. Besler, B. H., Hase, W. L., and Hass, K. C., "A Theoretical Study of Growth Mechanisms of the (110) Surface of Diamond from Acetylene and Hydrogen Mixtures," *J. Phys. Chem.*, **96**, 9369 (1992).
17. Latham, C. D., Heggie, M. I., and Jones, R., "Ab Initio Energetics of CVD Growth Reactions on the 3 Low-Index Surfaces of Diamond", *Diamond Relat. Mater.*, **2**, 1493 (1993).
18. Zapol, P., Curtiss, L. A., Tamura, H., and Gordon, M. S., "Theoretical Studies of Growth Reactions on Diamond Surfaces" Chapter 7 of *Computational Materials Chemistry: Methods and Applications* (Kluwer Academic, Dordrecht, 2004).
19. Horner, D. A., Curtiss, L. A., and Gruen, D. M., "A Theoretical Study of the Energetics of Insertion of Dicarbon (C_2) and Vinylidene into Methane C—H Bonds", *Chem. Phys. Lett.*, **233**, 243 (1995).
20. Redfern, P., Horner, D. A., Curtiss, L. A., and Gruen, D. M., "Theoretical Studies of Growth of Diamond (110) from Dicarbon", *J. Phys. Chem.*, **100**, 11654 (1996).
21. Sternberg, M., Kaukonen, M., Nieminen, R. M., and Frauenheim, Th., "Growth of (110) Diamond Using Pure Dicarbon", *Phys. Rev. B*, **63**, 1655414 (2001).
22. Harris, S. J., Belton, D. N., and Blint, R. J., "Thermochemistry on the Hydrogenated Diamond (111) Surface", *J. Appl. Phys.*, **70**, 2654 (1991).
23. Belton, D. N. and Harris, S. J., "A Mechanism for Growth on Diamond (110) from Acetylene", *J. Chem. Phys.*, **96**, 2371 (1992).

24. Gruen, D. M., Redfern, P. C., Horner, D. A., Zapol, P., and Curtiss, L. A., "Theoretical Studies on Nanocrystalline Diamond: Nucleation by Dicarbon and Electronic Structure of Planar Defects", *J. Phys. Chem. B*, **103**, 5459 (1999).
25. Sternberg, M., Zapol, P., and Curtiss, L. A., "Carbon Dimers on the Diamond (100) Surface: Growth and Nucleation", *Phys. Rev. B*, **68**, 205330 (2003).
26. Sternberg, M., Zapol, P., and Curtiss, L. A., "C_2 Adsorption on the (100) Diamond Surface: Cluster and Periodic Calculations", *Mol. Phys.*, **103**, 1017 (2005).
27. Curtiss, L. A., Zapol, P., Sternberg, M., Redfern, P. C., Horner, D. A., and Gruen, D. M., "Quantum Chemical Studies of Growth Mechanisms of Ultrananocrystalline Diamond", in "Synthesis Properties and Application of Ultrananocrystalline Diamond" ed. D.M. Gruen, O. Shenderova, and A.Y. Vul', *Proceedings of the NATO Advanced Research Workshop*, St. Petersburg, Russia, June 7–10, 2004 (Springer, Dordrecht, Netherlands, 2005), NATO Science Series II: Mathematics, Physics and Chemistry, vol. 192, pp. 3948.
28. Sternberg, M., Horner, D. A., Redfern, P. C., Zapol, P., and Curtiss, L. A., "Theoretical Studies of CN and C_2 Addition to a (100) (2×1) Diamond Surface: Nanocrystalline Diamond Growth Mechanisms", *J. Comput. Theor. Nanosci.* 2, 207 (2005).
29. Sternberg, M., Zapol, P., Frauenheim, T., Carlisle, J., Gruen, D. M., and Curtiss, L. A., "Density Functional Based Tight Binding Study of C_2 and CN Deposition on (100) Diamond Surface", *Materials Research Society Proceedings (Nanotubes, Fullerenes, Nanostructured and Disordered Carbon)*, **675**, W12.11.1–W12.11.5 (2001).
30. Zapol, P., Unpublished.
31. Bhattacharyya, S., Auciello, O., Birrell, J., Carlisle, J. A., Curtiss, L. A., Goyette, A. N., Gruen, D. M., Krauss, A. R., Schlueter, J., Sumant, A., and Zapol, P., "Synthesis and Characterization of Highly-Conducting Nitrogen-Doped Ultrananocrystalline Diamond Films", *Appl. Phys. Lett.*, **79**, 1441 (2001).
32. Wild, Ch., Herres, N., and Koidl, P., "Texture Formation in Polycrystalline Diamond Films", *J. Appl. Phys.*, **68**, 973 (1990).
33. Tanaka, I., Kleebe, H. J., Cinibulk, M. K., Bruley, J., Clarke, D. R., and Rühle, M., "Calcium Concentration Dependence of the Intergranular Film Thickness in Silicon-Nitride", *J. Am. Ceram. Soc.*, **77**, 911 (1994).
34. Narayan, J. and Nandedkar, A. S., "Atomic Structure and Energy of Grain Boundaries in Silicon, Germanium and Diamond", *Philos. Mag. B*, **63** 1181 (1991).
35. Shenderova, O. A., Brenner, D. W., and Yang, L. H., "Atomistic Simulations of Structures and Mechanical Properties of Polycrystalline Diamond: Symmetrical <001> Tilt Grain Boundaries", *Phys. Rev. B*, **60**, 7043 (1999).
36. Shenderova, O. A. and Brenner, D. W., "Atomistic Simulations of Structures and Mechanical Properties of <011> Tilt Grain Boundaries and Their Triple Junctions in Diamond", *Phys. Rev. B*, **60**, 7053 (1999).
37. Morris, J. L., Fu, C. L., and Ho, K. M., "Tight-Binding Study of Tilt Grain Boundaries in Diamond", *Phys. Rev. B*, **54**, 132 (1996).
38. Kohyama, M., Ichinose, H., Ishida, Y., and Nakanose, M., "Tight-Binding Calculation of Grain Boundaries in Diamond", *Mater. Sci. Forum*, **207–209**, 261 (1996).

39. Kohyama, M., "Computational Studies of Grain Boundaries in Covalent Materials", *Modelling Simul. Mater. Sci. Eng.*, **10**, R31 (2002).
40. Ikuhara, Y, "Grain Boundary and Interface Structures in Ceramics", *J. Ceram. Soc. Jpn*, **109**, S110–S120 (2001); Tsurekawa, S., Nitta, S, Nakashima, H., and Yoshinaga, H., "Grain Boundary Structures in Silicon Carbide–Verification of the Extended Boundary Concept", *Interface Sci.*, **3**, 75 (1995).
41. Wang, Z. Q., Dregia, S. A., and Stroud, D., "Energy Minimization Studies of Twist Grain-Boundaries in Diamond", *Phys. Rev. B.*, **49**, 8206 (1994).
42. Keblinski, P., Wolf, D., Phillpot, S. R., and Gleiter, H., "Role of Bonding and Coordination in the Atomic Structure and Energy of Diamond and Silicon Grain Boundaries", *J. Mater. Res.*, **13**, 2077 (1998).
43. Keblinski, P., Phillpot, S. R. P., Wolf, D., and Gleiter, H., "On the Nature of Grain Boundaries in Nanocrystalline Diamond", *Nanostruct. Mater.*, 12, 339 (1999).
44. Cleri, F., Keblinski, P., Colombo, L., Wolf, D., and Phillpot, S. R., "On the Electrical Activity of sp^2-Bonded Grain Boundaries in Nanocrystalline Diamond", *Europhys. Lett.*, **46**, 671 (1999).
45. Cleri, F., "Atomic and Electronic Structure of High-Energy Grain Boundaries in Silicon and Carbon", *Comput. Mater. Sci.*, **20**, 351 (2001).
46. Zapol, P., Sternberg, M., Curtiss, L. A., Frauenheim, Th., and Gruen, D. M., "Tight-Binding Molecular Dynamics Simulation of Impurities in Ultrananocrystalline Diamond Grain Boundaries", *Phys. Rev. B*, **65**, 045403 (2001).
47. Birrell, J., Carlisle, J. A., Auciello, O., Gruen, D. M., and Gibson, J. M., "Morphology and Electronic Structure in Nitrogen-Doped Ultrananocrystalline Diamond", *Appl. Phys. Lett.*, **81**, 2235 (2002).
48. Smith, W. V., Sorokin, P. P., Gelles, I. L., and Lasher, G. J., "Electron-Spin Resonance of Nitrogen Donors in Diamond", *Phys. Rev.*, **115**, 1546 (1959).
49. Farrer, R. G., "On the Substitutional Nitrogen Donor in Diamond", *Solid State Commun.*, **7**, 685 (1969).
50. Kajihara, S. A., Antonelli, A., Bernholc, J., and Car, R., "Nitrogen and Potential Normal-Type Dopants in Diamond", *Phys. Rev. Lett.*, **66**, 2010 (1991).
51. Robertson, J. and Davis, C. A., "Nitrogen Doping of Tetrahedral Amorphous Carbon", *Diamond Relat. Mater.*, **4**, 441 (1995).
52. Frauenheim, Th., Jungnickel, G., Sitch, P., Kaukonen, M., Weich, F., Widany, J., and Porezag, D., "A Molecular Dynamics Study of N-Incorporation into Carbon Systems: Doping, Diamond Growth and Nitride Formation", *Diamond Relat. Mater.*, **7**, 348 (1998).

9 Mechanical Properties of Undoped and Doped Ultrananocrystalline Diamond: Elasticity, Strength, and Toughness

H. D. Espinosa, Bei Peng, and Nicolaie Moldovan

Department of Mechanical Engineering, Northwestern University, Evanston, IL, USA

Xingcheng Xiao, Orlando Auciello, John Carlisle

Materials Science Divisions, Argonne National Laboratory, Argonne, IL, USA

Introduction

Failure of brittle materials is caused by the unstable propagation of microcracks that initiate at surface or volume defects. Typically, such defects exhibit a random distribution of size, orientation, and location. At the millimeter or larger size scale, where microstructure details are averaged, material strength does not strongly depend upon the size and shape of the test specimen. Other characteristics of the system such as the size of the process zone ahead of a crack tip become dominant. However, at the micron and submicron scale, where the number of defects can be greatly reduced by decreasing the size of the interrogated volume or surface, fracture strength is strongly size dependent. This size effect can be explained by the statistical theory first proposed by Weibull.[1] This theory describes strength variability in brittle materials by means of well-defined statistical parameters. Hence, knowledge of these material parameters, i.e., Weibull modulus and characteristic strength, is the first step in developing predictive capabilities in applications of interest, for instance, microelectromechanical systems (MEMS).[2]

The existence of size effect in brittle MEMS materials has been reported by LaVan et al.,[3] Sharpe et al.,[5,2] Espinosa et al.,[6,7] Bagdahan et al.,[2] Chasiotis et al.,[8,9] and Chen et al.[10] LaVan et al. arranged a cross-comparison of the strength of Sandia polysilicon as identified by various laboratories.[2] All the samples were fabricated with a thickness of 2.5 μm

while the sample lengths ranged from 15 to 1000 μm. Five laboratories (see LaVan et al.,[4] Tsuchiya et al.,[11] Sharpe et al.,[5,2] Chasiotis and Knauss,[8,9] and Read et al.[12]) tested the same samples with various methodologies. Although the results varied from group to group they all found a strong size effect in the strength of the polysilicon specimens. Weibull analysis predicted a general tendency for strength to increase with decreasing specimen size.

Sharpe et al.[5,2] created a novel specimen design and loading mechanism that permitted testing of polysilicon specimens of various thicknesses, widths, and lengths. The specimens were 1.5, 2.0, and 3.5 μm thick, 6, 20, and 600 μm wide, and 250, 1000, and 4000 μm long. The measured Young's modulus had a value of 158 ± 10 GPa with no evidence of substantial specimen size effects. However, the strength exhibited an increase from 1.2 to 1.6 GPa as the specimen size was decreased.[5] Bagdahn et al.[2] later used Weibull analysis to identify the strength of straight specimens and specimens containing holes or notches leading to stress concentrations. These authors unequivocally demonstrated that Weibull statistics are capable of predicting the strengths of MEMS components. A design methodology was also proposed. In addition, Weibull analysis combined with SEM observations showed that strength scales with sidewall area rather than with total surface area or volume.

Chasiotis and Knauss[8,9] performed micro-tensile tests on elliptically perforated polysilicon specimens. They showed that failure strength at the root of a notch increases with decreasing size of the stressed domain. When the notch radius was made as small as 1 μm the failure stress increased on average by a factor of 2 relative to the stress values derived from unnotched specimens. They also observed that failure initiation was controlled by the sidewall area of the specimens due to micromachining-induced roughness.

Chen et al.[10] tested mesoscale biaxial flexure and radiused hub flexure single-crystal silicon specimens with different surface conditions. The Weibull characteristic strengths of planar biaxial flexure specimens were found to lie in the range of 1.2 to 4.6 GPa. These authors assumed that surface defects instead of bulk defects play a dominant role in determining the strength because of the strong influence of surface finish.

Espinosa et al.[6] found similar results in the investigation of ultra-nanocrystalline diamond (UNCD). The strength of UNCD thin films 1 μm thick decreased from 4.13 to 1.74 GPa when surface roughness increased from 20 to 107 nm (RMS). However, due to the limited number of tested

specimens possessing the same surface finish but different volumes, these researchers were prompted to further examine the validity of Weibull theory in the prediction of UNCD strength.

In this chapter we examine the applicability of the Weibull statistics in prediction of the strength of doped and undoped UNCD thin films. A particular emphasis is placed on assessing the role of volume vs. surface in the prediction of the material strength. We also present the membrane deflection fracture experiment developed by Espinosa and co-workers, and identify the mode I toughness of UNCD. The chapter begins with a description of the investigated materials and a short description of the testing methodologies, followed by the reporting of experimental results including fractographic observations. A statistical analysis of the reported data based on maximum likelihood estimation is used to identify Weibull parameters. The discussion of results and their implication in the design of MEMS/NEMS based on UNCD completes the chapter.

9.1 The Material

UNCD is a material developed at Argonne National Laboratory with unique properties particularly suitable to the development of MEMS/NEMS. UNCD has an extremely small grain size (3–5 nm),[13] outstanding mechanical properties (~97 GPa hardness, 967 GPa Young's modulus, and 4.13 GPa failure strength)[6,7], unique tribological properties (coefficient of friction of the order of ~0.02–0.03)[14], and field-induced electron emission (threshold voltage 2–3 V/μm)[15]. Electrical conductivity measurements of the nitrogen-doped UNCD films showed that the conductivity increases dramatically (up to 143 per Ω cm) with increasing nitrogen content.[16]

In this work, deposition of UNCD films was performed in a 6 inch Cyrannus-IPLAS (Innovative Plasma Systems GmbH) by employing microwave plasma enhanced chemical vapor deposition (MPECVD). This process utilizes argon-rich CH_4/Ar plasma chemistries,[12] where C_2 dimers are the growth species derived from collision-induced fragmentation of CH_4 molecules in an Ar plasma. Before deposition, all cleaned Si substrates were ultrasonically seeded by immersing the wafers in a suspension of nanodiamond powders (~5 nm in diameter) in methanol for 30 minutes, then rinsed with methanol and distilled water sequentially.

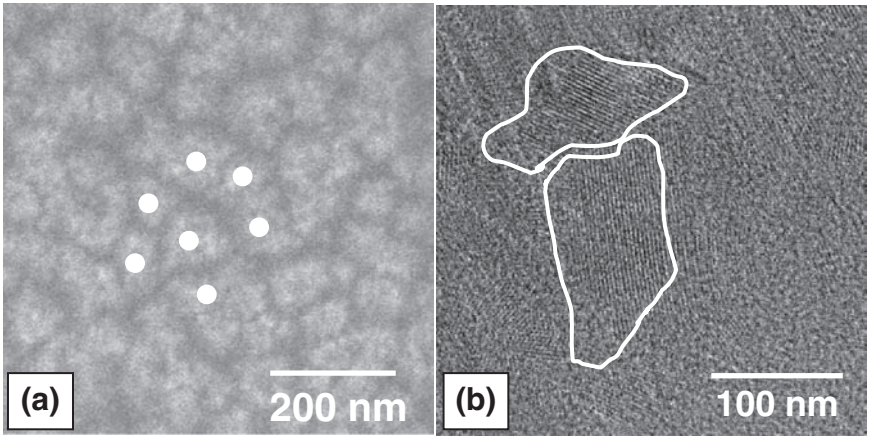

Figure 9.1 (a) SEM image of *super grains* on the film nucleation surface; dots illustrate typical nucleation sites. (b) TEM image shows that each "super grain" is composed of many grains with some instances in which the super grain has nanograins with approximately the same crystal orientation.

Images of the bottom surface, the nucleation surface, obtained by means of high-resolution SEM after the film was released from the substrate by KOH etching, reveal that grains do start to nucleate from discrete seeding domains. Figure 9.1(a) is a SEM image from the bottom surface of the film. It clearly shows domains with an average size of 100 nm and their boundaries. Note that the domains defined by these boundaries are not necessarily single crystals because, from TEM observations, it is known that the average grain size of undoped UNCD is about 3–5 nm;[13] by contrast, the domain size is between 50 and 200 nm. We call these domains *super grains* or *grain clusters*. In each of the super grains there are thousands of grains with various crystal orientations (see Fig. 9.1(b)). We have found that the size of the super grains is not dependent on the N_2 concentration in the films but depends on the density and size of the seeding diamond nanoparticle (dots in Fig. 9.1(a)). Each domain starts growing at the seeding diamond nanoparticle and continues to grow until impinging on other domains. Domain boundaries are defined in the process.

Undoped UNCD films were deposited in 99% Ar and 1% CH_4 mixture at 200 mbar and a total flow rate of 50 standard cubic centimeters per minute. The nitrogen-doped UNCD films were deposited at a pressure of 150 mbar. The CH_4 flow rate was fixed at 1 sccm, but the nitrogen flow rate varied from 5 to 20 sccm and the Ar flux decreased correspondingly

in order to maintain the same total flow rate of 100 sccm. The microwave power was 1.2 kW and the substrate temperature was 800 °C during deposition of both types of films. In this chapter 5% doped UNCD means that during film deposition the percentage of the nitrogen gas is 5% in the total gas flow; similarly for 10% and 20% doped UNCD.

A detailed TEM study of the nanostructure of nitrogen-doped UNCD[17] reveals that nitrogen is being incorporated preferentially at the grain boundaries. High-resolution TEM and nanoprobe-based electron energy-loss spectroscopy indicate that both the grain size and grain-boundary width increase with the increase in nitrogen concentration. The average size of the grains gradually increases from about 4 to 16 nm, as the nitrogen content in the plasma is changed from 0% to 20%. The grain-boundary width increases as well, from about 0.5 to 2.2 nm.

The surface roughness of undoped and doped UNCD films was identified by atomic force microscopy (AFM). The study shows that roughness decreases gradually from 20.3 nm (RMS) to 13.9 nm (RMS) when the N_2 content in the plasma increases from 0% to 20% (see Fig. 9.2). By

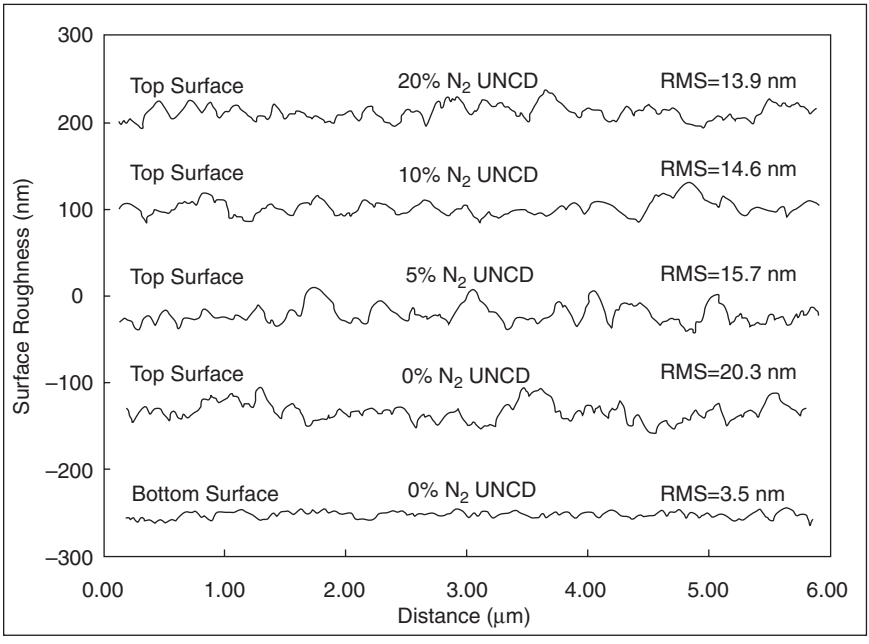

Figure 9.2 Surface roughness of UNCD films synthesized with 0%, 5%, 10%, and 20% N_2 added to the plasma. Bottom surface roughness is unaffected by N_2 content.

contrast, as previously mentioned, the morphology of the grain nucleation layer (bottom layer) is quite different from the surface layer. AFM images reveal a RMS roughness in the range of 3.5–8.4 nm, independently of the N_2 content, which is much lower than that of the film top surface.

9.2 Experimental Technique

9.2.1 Elasticity and Strength Experiments

The mechanical testing methodology involves the tensile testing of microfabricated freestanding thin-film UNCD specimens in a fixed–fixed configuration. The specimens are attached to the substrate at both ends and span a micromachined window beneath (see Fig. 9.3(a)). The geometry of membranes can be described best as a double dog-bone tensile specimen. Undoped and doped (5%, 10%, and 20%) UNCD films were deposited on silicon substrates. Thicknesses were accurately controlled during the deposition process and then measured. Subsequently, the films were patterned using an aluminum masking layer and the structures were released by KOH etching from the back side. The details of the specimen microfabrication are reported in refs. [6,7] and in Section 9.2.2.

The membrane deflection experiment (MDE) developed by Espinosa et al.[18] was used to deform and stress the specimens until failure. A combined nanoindenter and AFM apparatus was used in this investigation (Fig. 9.3(b)). The procedure involves applying a line-load, with the nanoindenter, at the center of the spanning membrane (see Fig. 9.4). Simultaneously, an interferometer focused on the bottom side of the mem-

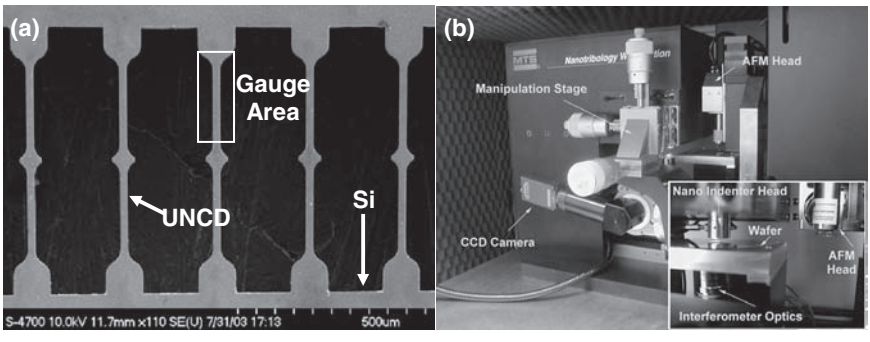

Figure 9.3 (a) SEM image of five UNCD membranes showing characteristic geometries. (b) Photograph of the test setup.

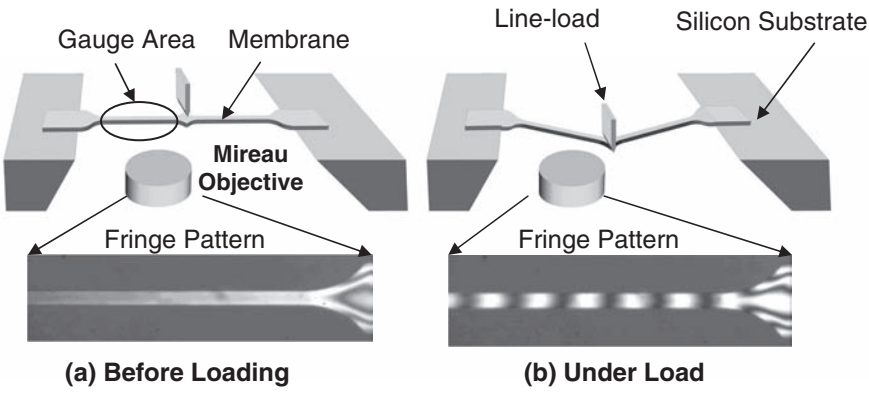

Figure 9.4 Schematic drawing of the MDE setup and monochromatic images of the bottom side of the membranes showing an unloaded membrane (a), and a membrane under load which has developed fringes (b).

brane records the deflection. The result is direct tension with load and deflection being measured independently. A calibration plot and more experimental details can be found in ref. [7], as well as the formulas used to compute stress and strain.

In the present study, peak forces were on the order of 15 mN for the 20 μm wide specimens. The force is estimated to have a relative uncertainty of ±0.6%. The UNCD film thickness was measured by AFM with an uncertainty of ±0.02 μm, and the width was measured by SEM with an uncertainty of ±0.1 μm. The resulting uncertainty in the cross-sectional area calculation is about ±2.5%. The relative uncertainty of the fracture stress is therefore estimated to be about ±3%.

A critical aspect in assessing the applicability of the Weibull theory is the examination of specimens with gauge dimensions spanning a range of volumes and surface areas. For both undoped and doped (5%, 10%, and 20%) UNCD films, specimens with gauge dimensions A (width = 40 μm, length = 400 μm, thickness = 1.0 μm), B (width = 20 μm, length = 200 μm, thickness = 1.0 μm), C (width = 20 μm, length = 200 μm, thickness = 0.5 μm), and D (width = 5 μm, length = 100 μm, thickness = 1.0 μm) were tested to examine the effect of size on strength. Note that gauge volume was varied from 500 to 16,000 μm^3 while the total surface area was varied from 1200 to 32,800 μm^2. Thirty tests were performed for each type of sample exhibiting the same size. Hence, a total of 480 tests were performed.

9.2.2 Fracture Toughness Experiments

The specimen geometry utilized in fracture toughness experiments resembles the typical double dog-bone tensile specimen employed in the standard MDE. However, the specimen contains an atomically sharp crack or a notch as will be described below. The suspended membranes are fixed to the wafer at both ends such that they span a bottom view window (Fig. 9.4). In the areas where the membrane is attached to the wafer and in the central area the width is varied in such a fashion as to minimize boundary effects and to prevent bending failure at these locations. These effects are also minimized through large-specimen gauge lengths. Thus, a load applied in the center of the span results in direct stretching of the membrane in the two areas of constant width in the same manner as in a direct tension test. In this study, membranes with nominal dimensions of length $L_M = 334$ μm, width $W = 20$ μm, and thickness $t = 0.8$ μm were tested.

The film was grown directly onto a Si substrate using a MPECVD technique based on a CH_4/Ar chemistry previously described.[13] Next, the specimens were microfabricated using standard processes. The following is a summary of the steps used in their microfabrication (Fig. 9.5):

Step 1: Growth of UNCD on silicon substrate (~1.0 μm). Deposition of a 300 nm Al film by sputtering. Al is used as mask material due to its resistance to oxygen reactive ion etching (RIE), which is employed to etch UNCD. Depo-

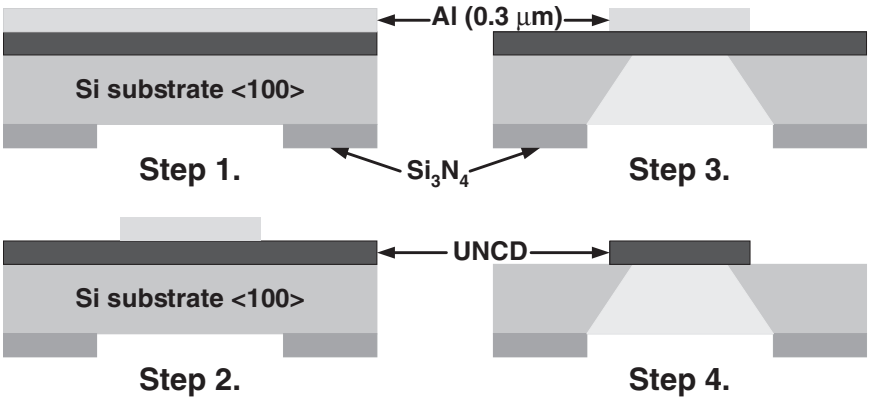

Figure 9.5 Cross-sectional view of the microfabrication steps to obtain freestanding UNCD membranes.

sition and patterning of Si_3N_4 film (~0.5 μm thick) on the other side of the silicon wafer. Si_3N_4 is employed as a mask during KOH etching of <100> silicon.

Step 2: Photoresist, S1805, spin coating, pre-baking, and exposure with mask aligner (Karl Suss MA6). Resist development and post-baking. Wet chemical etching of Al.

Step 3: KOH etching from backside, 9 hours (KOH 30% at 80 °C). The UNCD film is used as an etching stop layer to define windows under the membranes.

Step 4: O_2 RIE, 50 mTorr, 200 W, various times, until the exposed UNCD is etched away. During the RIE etching, the photoresist is also removed.

Step 5: Removal of Al masks using wet etching.

Two techniques were used to produce the pre-existing defects resulting in two types of specimens. The first one used focused ion beam (FIB) micromilling with a beam current density of 15 A/cm^2 and a beam diameter of 10 nm. Two notches with the same length were milled simultaneously. A symmetric edge–cracks configuration was obtained. The geometry of the specimen is shown in Fig. 9.6(a). Blunt notches with tip radii of ~100 nm were produced (see Fig. 9.6(b)). In this configuration, an *apparent* fracture toughness can be computed from the following equations:

$$K_{IC}^{/} = \sigma_f \sqrt{\pi a}\, f(a/W) \qquad \text{Eq. (9-1)}$$

$$f(a/W) = 1.12 + 0.43(a/W) - 4.78(a/W)^2 + 15.44(a/W)^3 \qquad \text{Eq. (9-2)}$$

where σ_f is the failure stress, a is the length of the cracks, and W is the width of the gauge region as shown in Fig. 9.6(a).

The second technique achieved an atomically sharp crack by placing a Vickers indent (with a 200 g load) near the specimen prior to its release by KOH etching. Although the indent was placed on the silicon substrate (see Fig. 9.6(c)), the radial cracks, which initiated at the indent corners, propagated into the UNCD specimens. The length of the crack was measured using high-resolution SEM, see Fig. 9.6(d). In this case, an edge–crack model was used to compute K_I. In this geometry, the function $f(a/W)$is given by

$$f(a/W) = 1.12 - 0.23(a/W) + 10.55(a/W)^2 - 21.72(a/W)^3 \qquad \text{Eq. (9-3)}$$

The data directly obtained from the MDE must then be reduced to arrive at a stress history for the membrane. The load in the plane of the mem-

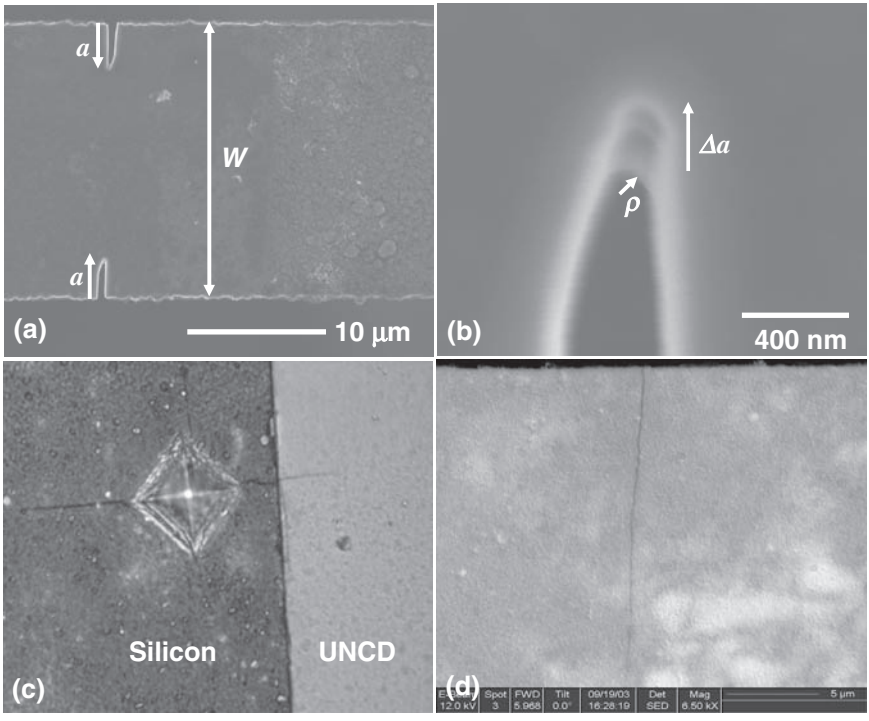

Figure 9.6 (a) SEM micrograph of a pre-notched specimen milled by FIB; (b) magnified view of the notch tip region showing a blunt tip with a root radius of approximately 100 nm and a length uncertainty Δa due to milling errors; (c) optical image showing a sharp crack induced from an indent on the silicon substrate before specimen release; and (d) SEM micrograph of the crack after specimen release. Crack length was measure from SEM images. (Reprinted from ref. [21] with permission from IEEE ©2005.)

brane is found as a component of the vertical nanoindenter load by the following equations:

$$\tan\theta = \frac{\Delta}{L_M} \text{ and } P_M = \frac{P_V}{2\sin\theta} \qquad \text{Eq. (9-4)}$$

where θ is the angle of deflection, Δ is the displacement, L_M is the membrane half-length, P_M is the load in the plane of the membrane, and P_V is the load measured by the nanoindenter. Once P_M is obtained, the nominal stress, $\sigma(t)$, can be computed from

$$\sigma(t) = \frac{P_M}{A} \qquad \text{Eq. (9-5)}$$

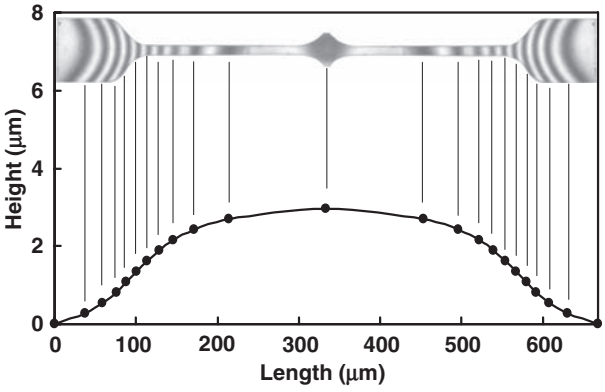

Figure 9.7 Interferometric characterization of freestanding UNCD specimen. Out-of-plane bulging due to residual stresses is observed.

where A is the cross-sectional area of the membrane in the gauge region. The calculation of strain, away from the defects regions, was performed following the procedure given in refs. [7,18]. Note that calculation of material toughness using Equations (9-3) to (9-5) does not require strain measurement.

An important aspect of the UNCD specimens was that each membrane bowed upward as processed, i.e., out of the wafer plane. This is believed to result from the difference in thermal expansion coefficients, between the film and Si wafer, such that cooling down from the deposition temperature, approximately 800 °C, resulted in the Si shrinking more than the UNCD film. Figure 9.7 shows a typical interferometric image and the generated x–z profile. This profile was obtained from the knowledge that the vertical distance between two dark fringes is half the wavelength of the monochromatic green light used in the imaging.

Figure 9.8(a) shows a series of optical images taken at different time intervals during a typical UNCD membrane deflection fracture experiment. A schematic side view of the membrane is shown to the right of each frame. The first frame shows the state of the membrane just before contact is made. The height above the plane of the wafer, Δc, is determined as illustrated in Fig. 9.7. The successive frame shows contact and deflection of the membrane. The process occurs in a smooth manner as seen by the inflection point, denoted by the arrows, moving toward the fixed end of the membrane. The final frame shows the deflection where uniform stretching of the membrane begins. This state can be determined by computing the downward deflection, Δs, such that the membrane

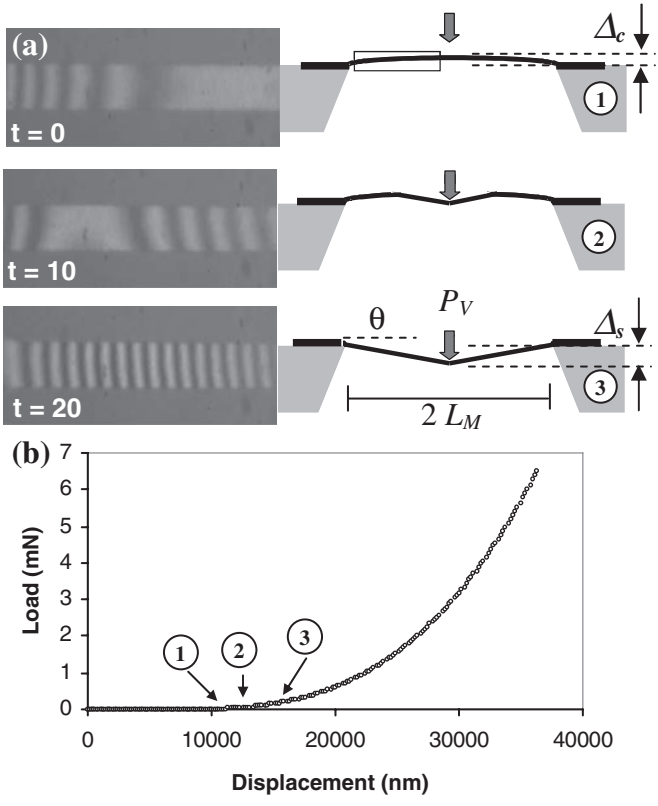

Figure 9.8 (a) Schematic representations of the side view of the MDFE test at three different time intervals. Δ_c is the upward vertical displacement, at the middle of the span, and Δ_s is the deflection at which uniform straining of the membrane begins. (b) Representation of the three states shown in (a) on the load–displacement curve.

becomes straight and uniform straining of the material begins. Figure 9.8(b) shows different time intervals during a typical test with corresponding points on the load–deflection signature. Uniform stretching of the membrane begins at point 3. Note that a non-zero load is needed to achieve this configuration.

9.3 Experimental Results

9.3.1 Stress–Strain Curves

Typical stress–strain curves for undoped and doped (5%, 10%, and 20%) UNCD specimens with the same gauge dimensions (width = 20 μm,

length = 200 μm, thickness = 10 μm) are shown in Fig. 9.9. The slope of the curve in the linear elastic regime represents the material elastic modulus. The curve for each material is representative of the many samples tested to collect statistical information. The values of the Young's modulus and the characteristic strengths, σ_0, are reported in Table 9.1. The characteristic strength is defined as the stress with a 63% failure probability.

Table 9.1 and Fig. 9.9 show that Young's modulus decreases gradually from about 955 GPa to about 849 GPa when the percentage of nitrogen

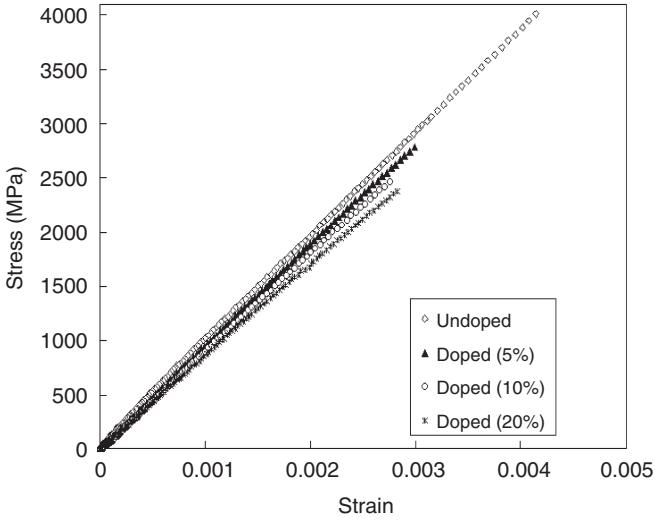

Figure 9.9 Strain–stress curves of typical undoped and doped specimens. The maximum stress in each curve represents the characteristic strength, σ_0, of the various materials.

Table 9.1 Comparison of Young's Moduli and Fracture Strengths of Undoped and Doped UNCD

Sample	Undoped		Doped	
N_2 percentage	0%	5%	10%	20%
No. of tests	30	30	30	30
E (GPa)	955 ± 25	899 ± 22	867 ± 23	849 ± 19
σ_0 (MPa)	4172	2713	2446	2350

increases from 0% to 20% during the UNCD deposition process. This is likely due to the segregation of nitrogen to the grain boundaries and to the fact that C–N bonds have less stiffness than C–C bonds. Also note that the fracture strength drops abruptly from 4172 to 2713 MPa when N_2 increases from 0% to 5%. Then the decline becomes much less pronounced when N_2 increases from 5% to 20%.

Based on Weibull's "weakest link" theory, we infer that by adding nitrogen to the plasma either defects are produced and/or N_2 segregation at the grain boundaries results in a weaker grain/super grain boundary. The presence of nitrogen is enough to produce a major strength drop. Its increase from 5% to 20% does not seem to modify the strength significantly. The exact mechanism leading to this weakening requires further investigation.

9.3.2 Size Effect and Weibull Analysis

As is customary for brittle materials, the strength data is interpreted statistically by assuming that specimen strength obeys a probability density function. In this case, we further assume that the probability function is Weibull's probability function.[1] The experimentally determined probability of failure is defined by ranking the specimen in ascending order of failure stress. Thus, the probability of failure of the *i*th specimen out of a total of *N* is given by

$$P_f = \frac{i - 1/2}{N} \qquad \text{Eq. (9-6)}$$

For specimens with the same shape and size, the cumulative probability of failure, P_f, for uniaxial tensile specimens subjected to a stress, σ, is

$$P_f = 1 - \exp\left[-\left(\frac{\sigma_{\max}}{\sigma_0}\right)^m\right] \qquad \text{Eq. (9-7)}$$

where m is the Weibull modulus and σ_0 is the Weibull characteristic strength. The two Weibull parameters (m and σ_0) are obtained from the slope and intercept of a plot (Fig. 9.10) of $\ln(\ln(1/(1 - P_f)))$ versus the measured failure stress $\sigma_{\max}$. To take into account the effect of volumes or areas the probability of failure can be written as

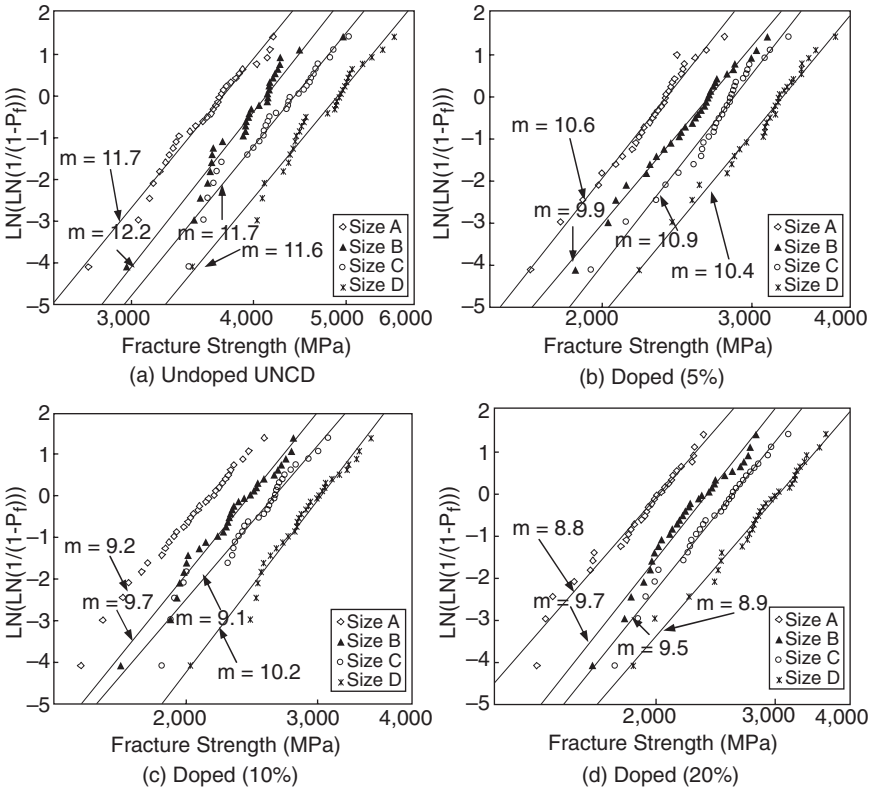

Figure 9.10 Weibull plots for various degrees of doping. The Weibull modulus and the characteristic strength for each set of data are obtained from the straight line fitted to the data.

$$P_f = 1 - \exp\left[-\left(\frac{\sigma_{\max}}{\sigma_{0V}}\right)^m V_e\right] \text{ or } P_f = 1 - \exp\left[-\left(\frac{\sigma_{\max}}{\sigma_{0V}}\right)^m V_e\right] \qquad \text{Eq. (9-8)}$$

where σ_{0V} and σ_{0A} are strengths relative to unit size (Weibull scale parameters), and V_e or A_e is the effective volume or area of the samples subjected to uniform stress. If the uniaxial Weibull model described above is valid, then the two adjustable parameters, m and σ_{0V}, are material constants. However, the estimation of the Weibull parameters is not simply an averaging of the results; the size must be included. The maximum likelihood estimation (MLE) was used to estimate the Weibull parameters by transforming discrete data sets into a single data set with respect to their effective volume, total surface area, or sidewall area.[19] The parameter m

is evaluated by iteratively determining the value of m that satisfies the following equation:

$$0 = \frac{N}{m} + \sum_{i=1}^{N} \ln(\sigma_i) - \frac{N\sum_{i=1}^{N}\left(V_i\sigma_i^m \ln(\sigma_i)\right)}{\sum_{i=1}^{N} V_i\sigma_i^m} \text{ or}$$

$$0 = \frac{N}{m} + \sum_{i=1}^{N} \ln(\sigma_i) - \frac{N\sum_{i=1}^{N}\left(A_i\sigma_i^m \ln(\sigma_i)\right)}{\sum_{i=1}^{N} A_i\sigma_i^m} \qquad \text{Eq. (9-9)}$$

When m is known, the second Weibull parameter can be determined without iteration from

$$0 = N\sigma_{0V}^m - \sum_{i=1}^{N} V_i\sigma_i^m \text{ or } 0 = N\sigma_{0A}^m - \sum_{i=1}^{N} A_i\sigma_i^m \qquad \text{Eq. (9-10)}$$

Figure 9.10 presents the Weibull plots for undoped and doped specimens. For each type of material four sets of data were obtained employing sample sizes A to D. The modulus, m, and the characteristic strength, σ_0, of each data set were obtained from the straight line fitted to the data. The MLE method is used to improve the accuracy of the statistical estimation for the Weibull parameters by transferring the four discrete data sets into a single large data set. Likewise, the data analysis is performed assuming that strength scales with volume, total surface area, or sidewall area, Equation (9-9). Figure 9.11 shows the comparison between experimental results, for undoped samples (size C), with the estimated (or predicted) values using MLE based on volume, total surface area, and sidewall area. By examining these plots, it is clear that the estimation based on volume captures best the trends in the measured data. The estimation based on total surface area or sidewall area is to the left and to the right, respectively, of the experimental results and bound the data in some fashion. This result suggests that the failure of UNCD is controlled by a distribution of volume defects. We will reinforce this finding by examination of features in the fracture surfaces, see Section 9.4.

The Weibull parameters obtained from the tests are summarized in Table 9.2. The scale parameters were determined using MLE based on volume. The last two columns show the predicted characteristic parame-

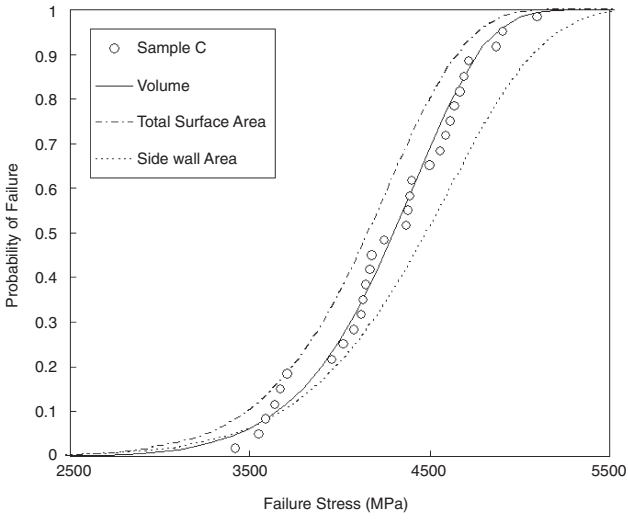

Figure 9.11 Comparison of experimental results with statistically predicted values based on volume, total surface area, and sidewall area.

ters ($\sigma_{0V,\ \mathrm{MLE}}$) and the difference between the predicted values and the measured value. It is shown that the differences are within 2.9%, which means the tests are quite consistent.

Based on the Weibull modulus, the scale parameters and the sample effective volumes, the predicted probability of failure can be calculated from Equation (9-8). The predicted values of strengths coincide fairly well with the experimental results (see Fig. 9.12) indicating that Weibull statistics are indeed capable of predicting the strength of UNCD materials as a function of component size.

9.3.3 Toughness Measurements

Figure 9.13 shows a typical strain–stress signature of a notched UNCD specimen. Both stress and strain are computed away from the notch, i.e., where a homogeneous deformation field develops. The far-field stress is used to compute the material toughness by means of Equation (9-1). The slope of the plot represents the elastic modulus (960 GPa). Failure occurs at a maximum stress of 2.3 GPa in a perfectly brittle fashion.

Fifteen specimens with the FIB-machined notches were tested under the same conditions except that the notch length, a, was varied from 1 to

Table 9.2 **Weibull Modulus Values, Characteristic Strengths, and the Weibull Scale Parameters Determined from Experimental Data**

Sample	Undoped						Doped					
N_2%	0%						5%					
Size	No.	m	σ_0 (MPa)	σ_{0V}*	$\sigma_{0,MLE}$ (MPa)	Error (%)	No.	m	σ_0 (MPa)	σ_{0V}*	$\sigma_{0,MLE}$ (MPa)	Error (%)
A	30	11.7	3714		3725	–0.3	30	10.6	2411		2401	0.4
B	30	12.2	4172		4198	–0.6	30	9.9	2713		2733	–0.7
C	30	11.7	4430		4456	–0.6	30	10.9	2889		2916	–0.9
D	30	11.6	5003		5022	–0.4	30	10.3	3304		3319	–0.5
MLE volume	120	11.6	–	8581			120	10.7	–	5933		
Sample	**Doped**											
N_2%	10%						20%					
Size	No.	m	σ_0 (MPa)	σ_{0V}*	$\sigma_{0,MLE}$ (MPa)	Error (%)	No.	m	σ_0 (MPa)	σ_{0V}*	$\sigma_{0,MLE}$ (MPa)	Error (%)
A	30	9.2	2195		2133	2.9	30	8.8	2034		2020	0.7
B	30	9.7	2446		2461	–0.6	30	9.7	2350		2344	0.3
C	30	9.1	2641		2643	–0.1	30	9.5	2539		2526	0.5
D	30	10.2	3019		3049	–1.0	30	8.9	2922		2932	–0.3
MLE volume	120	9.7	–	5786			120	9.3	–	5719		

* σ_{0V} has the units of MPa × $\mu m^{3/m}$.

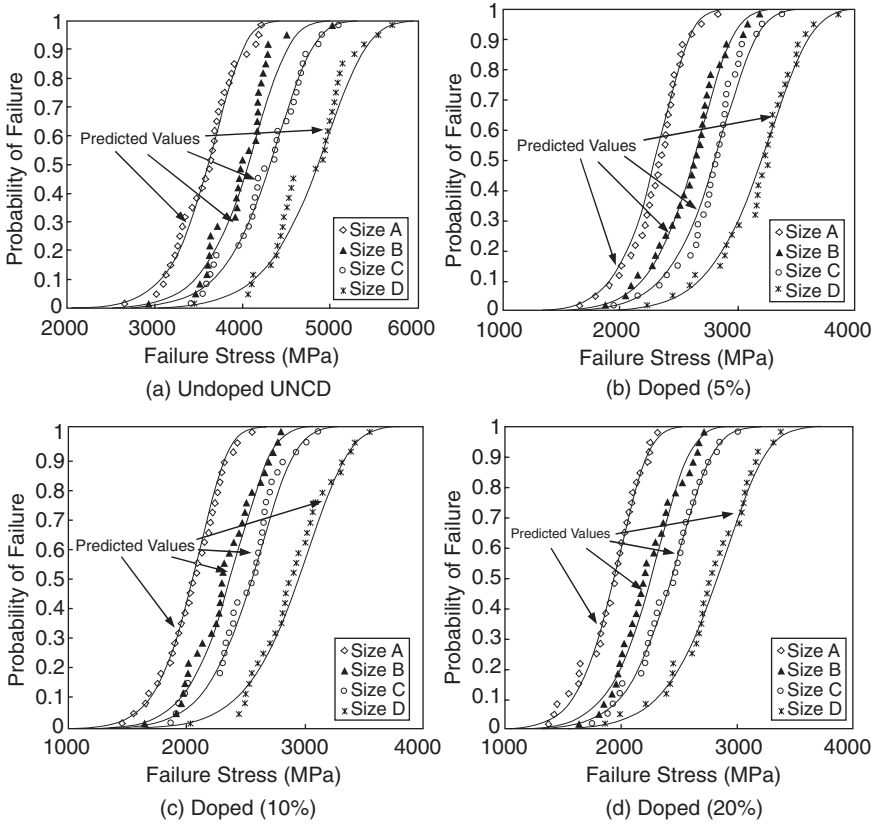

Figure 9.12 Experimental results vs. predicted values.

5 microns. The ratio of the notch length and specimen width, a/W, is in the range of 0.05–0.25. The dimensions a and W were measured using SEM. The *apparent* fracture toughness of the blunt notched specimens was then computed using Equations (9-1) and (9-2).

Values of $K_{IC}^{/} = 6.9 \pm 0.4\,\text{MPa}\,\text{m}^{1/2}$ were obtained (Table 9.3). From Table 9.3 it is clear that the apparent fracture toughness is independent of the notch length. This suggests that only the region of the material immediately in front of the crack-like defect affects the fracture toughness. In all tested specimens, failure occurred from the notch tip. This is illustrated in Fig. 9.14 (a) in which an SEM image of four tested membranes is shown. All the specimens broke at the place where the symmetrically fabricated notches were position. Figure 9.14(b) is a magnified image of a failed region showing that the failure propagated from notch tip to notch

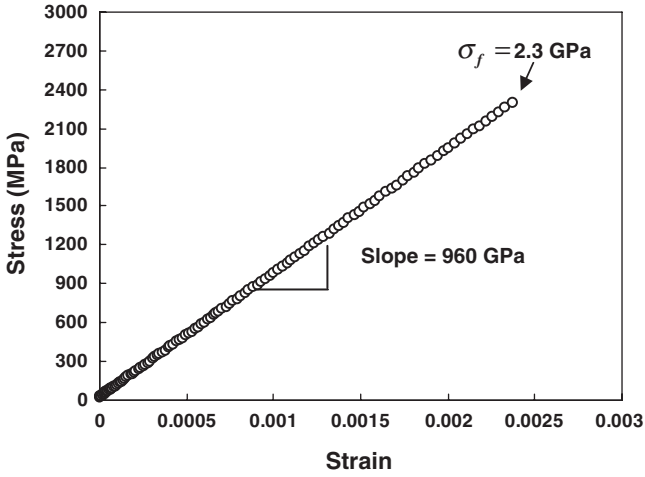

Figure 9.13 Strain–stress curve of a typical fracture test. In this case the fracture stress $\sigma_f = 2.3$ GPa 2.3 GPa corresponds to a specimen with a notch length $a = 2.2\,\mu$m and a root radius of approximately 100 nm. (Reprinted from ref. [21] with permission from IEEE ©2005.)

Table 9.3 Fracture Toughness Measurement on 15 UNCD Specimens with Notches

Sample Number	a (μm)	$\sigma_f^{(exp)}$ (GPa)	K'_{IC} (Eqs. 9-1, 9-2) (MPa m$^{1/2}$)	K_{IC} with Blunt Notch Correction (MPa m$^{1/2}$)
1	1.0	3.23	6.6	4.4
2	1.7	2.69	7.1	4.7
3	1.7	2.46	6.5	4.3
4	2.0	2.27	6.5	4.3
5	2.1	2.41	7.0	4.7
6	2.2	2.28	6.9	4.6
7	2.3	2.19	6.8	4.5
8	2.4	2.14	6.7	4.5
9	2.7	2.08	7.0	4.7
10	3.5	1.78	6.8	4.5
11	3.5	1.88	7.1	4.7
12	3.7	1.68	6.6	4.4
13	4.0	1.67	6.9	4.6
14	4.1	1.73	7.2	4.8
15	4.9	1.53	7.3	4.9
Mean values	–	–	6.9 ± 0.25	4.6 ± 0.18

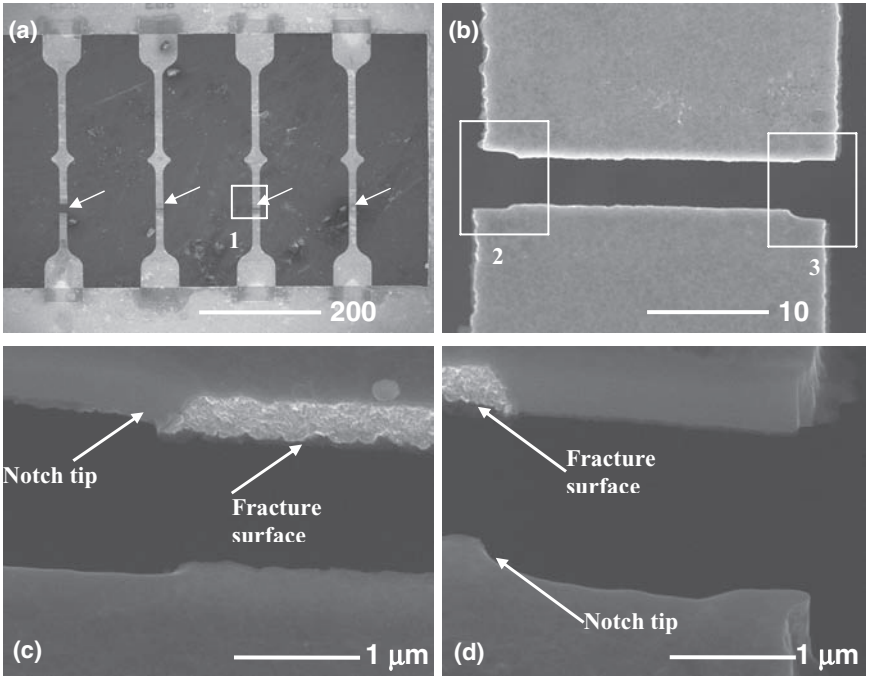

Figure 9.14 SEM image showing four MDFE specimens after testing. The images illustrate that failure indeed occurs in pre-cracked regions (a). Part (b) is an enlarged top view of the fracture region in window 1; (c) and (d) show the fracture surface near the notch tips revealing features of the propagating crack. (Reprinted from ref. [21] with permission from IEEE ©2005.)

tip. The fracture surface exhibits a roughness consistent with the material grain size and microstructure. It is expected that the crack propagation speed would be very high because UNCD has a large elastic modulus and a low density. Figures 9.14(c) and (d) show a magnified view of the fracture plane at both sides of the specimen. The pre-notch and the fracture regions can be easily identified from the surface roughness features.

It is important to note that in the computation of the K'_{IC} values, the notch was replaced by an apparent crack. Hence, corrections must be made because the effect of the blunt notch is to reduce the stress intensity relative to that ahead of a sharp crack. If this effect is not considered, resulting fracture toughness values become erroneously high.

For a blunt tip the asymptotic stress field is given by

$$\sigma_y(x) = \frac{K}{\sqrt{2\pi x}}\left(1 + \frac{\rho}{2x}\right) \qquad \text{Eq. (9-11)}$$

where the origin of the reference system is in the middle between the tip and the center of the circular blunt notch, so that $x > \rho/2$ Comparing this stress field with the corresponding one for a sharp crack ($\rho \rightarrow 0$), Drory et al.[22] proposed the following correction:

$$K_{IC} = \frac{K_{IC}^{/}}{1 + \frac{\rho}{2x}} \qquad \text{Eq. (9-12)}$$

in which $K_{IC}^{/}$ is the measured *apparent* fracture toughness from a blunt notch, ρ is the notch root radius, and x is a radial distance. Since the value of $\rho/2x$ is not determined, Drory et al.[22] assume $\rho/2x$ to be 1, providing a lower bound for K_{IC}. Consequently, they propose a 50% reduction on the measured fracture toughness to take into account the presence of the blunt tip.[22] By measuring the toughness in a specimen containing an indentation induced crack, an assessment of this correction was made. As shown in Fig. 9.6(d), cracks produced by indentation can be assumed atomically sharp, therefore Equations (9-1) and (9-3) can be employed to compute the fracture toughness of the material. Several experiments performed on specimens containing these cracks resulted in an average toughness $K_{IC} = 4.5\,\text{MPa}\,\text{m}^{1/2}$ with a standard deviation of $0.25\,\text{MPa}\,\text{m}^{1/2}$ (see Table 9.4). Therefore, for an average apparent toughness $K_{IC}^{/}$ of $6.9\,\text{MPa}\,\text{m}^{1/2}$, we find that $K_{IC}^{/}$ should be 0.53, which coincides with the mean value of$\rho/2x$, which is 1/2. Consequently we propose to employ a correction factor in Equation (9-12) of 2/3. The corrected toughness values are shown in Table 9.3.

Table 9.4 Fracture Toughness Measurements on Five Specimens Containing Sharp Cracks

a (μm)	W (μm)	$\sigma_f^{(exp)}$ (GPa)	K_{IC} (Eq. 9-3) ($\text{MPa}\,\text{m}^{1/2}$)
2.1	18.1	1.35	4.2
3.9	18.2	0.95	4.4
5.8	18.0	0.80	4.8
6.6	18.2	0.71	4.5
8.2	18.1	0.75	4.4

Average K_{IC} = $4.5\,\text{MPa}\,\text{m}^{1/2}$; standard deviation = $0.25\,\text{MPa}\,\text{m}^{1/2}$.

Table 9.5 Fracture Toughness of MEMS Materials

Material	K_{IC} (MPa m$^{1/2}$)
Si <111>	0.83–0.95 [19]
Glass	~1 [2]
Polysilicon	1.1–1.9 [4–8]
Al_2O_3	3–4 [2]
SiC	3.3 [20]
Si_3N_4	4.1 [21]
Microcrystalline Diamond	5.6 [12]
UNCD	4.6 [This work]

The results obtained in this work shows that the tested UNCD exhibits a fracture toughness larger than that of other MEMS materials such as Si, polysilicon, SiC, Al_2O_3, and Si_3N_4, but slighter smaller than that of microcrystalline diamond (Table 9.5).

9.4 Fractographic Analysis

The specimens and the fracture surfaces were examined with a high-resolution FEG-SEM. We observed that in all the performed strength tests failure occurred in the gauge area. Figure 9.15 shows a typical fracture surface of an undoped sample at various magnifications. Figure 9.15(a) is the overall view of the fracture surface. This image is actually upside down with respect to the loading surface (the grain nucleation layer is on the top). Different patterns are observed containing protrusions all over the fracture surface and a series of grooves between them. These features are consistent with intergranular fracture along cluster boundaries.

In principle, the fracture origin could be on the sidewalls, the top or bottom surfaces, or within the volume. The magnified view of window 1 (Fig. 9.15(b)) shows that the grain nucleation layer is much smoother than the surface layer. As mentioned in Section 9.1 the grain nucleation layer is composed of many "super grains" with dimensions of 50–200 nm. This nucleation layer is so smooth that it is unlikely to be the origin of the failure. Figure 9.15(c) shows the same window but from the perspective of the surface layer. This image clearly reveals that the fracture surface does not follow the valleys of the top and rougher surface. Thorough

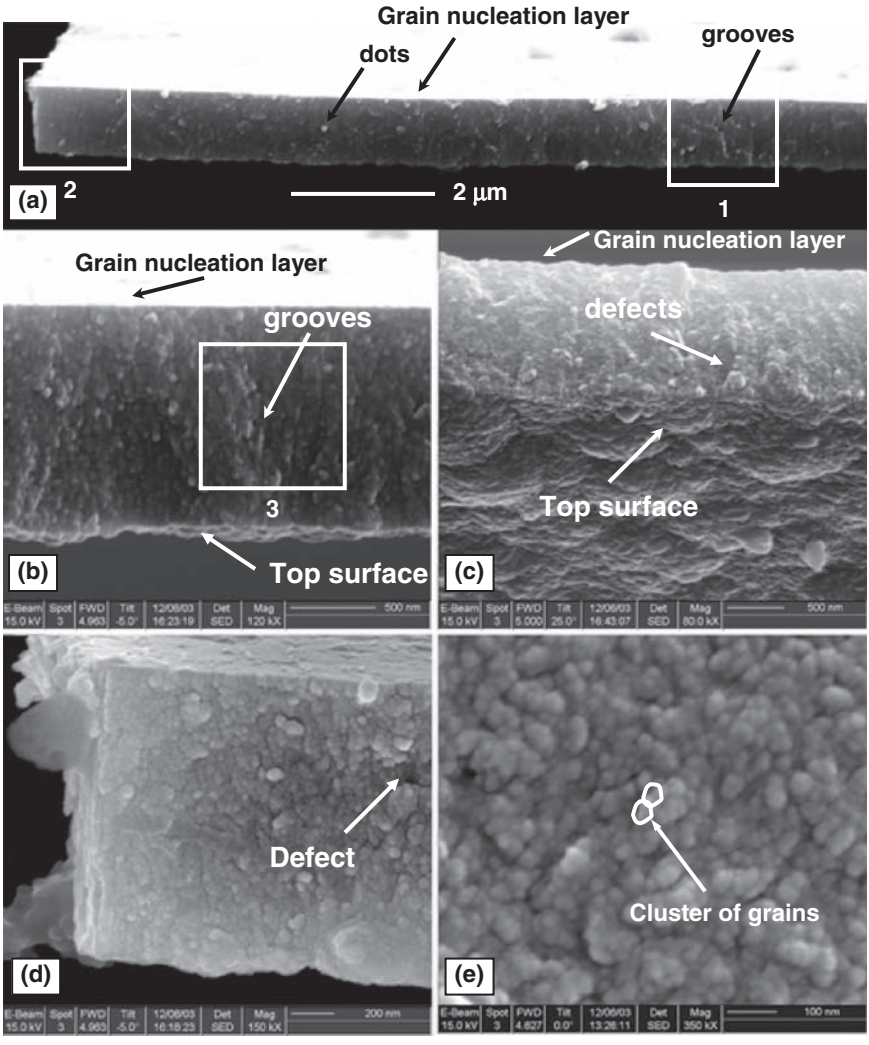

Figure 9.15 Fractographic analysis of undoped UNCD specimen. (a) Overall view of the fracture surface with some fracture features. (b) Magnified view of window 1 imaged from the grain nucleation layer. (c) Window 1 imaged from the top surface layer. (d) Window 2 showing the fracture surface near the sample sidewall. No evidence is observed indicating that failure initiated from the side wall. (e) Window 3 showing clusters of grains. Note that what appears as grooves at a larger scale becomes a well-defined surface fracture feature consisting of clusters of grains.

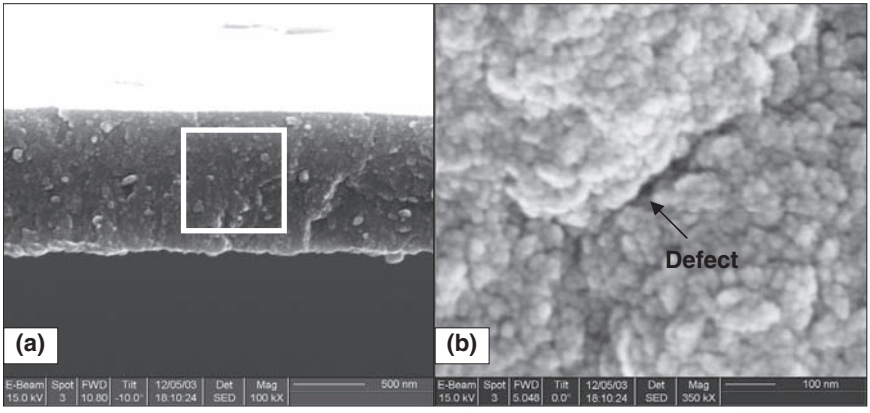

Figure 9.16 (a) Overview of the fracture surface of a 20% N_2 UNCD specimen and (b) magnified view of the area within the white rectangle. The arrow in (b) points to a defect in the bulk of the specimen.

examination did not reveal features consistent with fracture initiation from the top surface. Figure 9.15(d) shows the edge of the fracture surface (window 2) on the left sidewall. Features on this surface are no different from those at the interior. There is no evidence of fracture initiation at the sidewall as was found for polysilicon.[2] Figures 9.15(b–d) show that fracture most likely initiates from interior defects introduced during the film deposition process. Figure 9.15(e) (window 3) further reveals that the grooves observed in Fig. 9.15(a) are actually clusters of grains. It is clear that intergranular failure dominates the failure process in the tested UNCD films. The size of the defects is in the range of 20–30 nm, Fig. 9.15(d).

Observations performed on the doped UNCD samples showed that failure is similar to that of undoped UNCD samples except for slightly more noticeable defects in the fracture surface. Figure 9.16 shows what appear to be small voids approximately 20 nm in size. These voids are likely the remnants of detached carbon regions residing at the boundary between grain clusters.

9.5 Theoretical Strength

The results given in Section 9.3 for undoped and doped UNCD specimens demonstrate a clear effect of specimen size on film strength. Likewise, the analysis confirms the validity of Weibull theory in predicting specimen strength when its volume changes about two orders of magnitude. Since the change in specimen size has limitations, Bagdahn and

co-workers[2] proposed the usage of specimens with stress concentrations, resulting from holes or notches, to achieve a larger variation in effective volume or surface. Our group recently examined experimentally and theoretically the stress field around notches of different radii to obtain an estimate of defect-free size in the film and ideal or theoretical strength, σ_u.[20]

The "ideal strength" of brittle materials such as UNCD can be estimated by measuring the fracture toughness, K_{IC}, and a material characteristic length, d_0, according to

$$\sigma_u = \sqrt{\frac{2}{\pi}\frac{K_{IC}^2}{d_0}} \qquad \text{Eq. (9-13)}$$

The material fracture toughness can be determined by means of the membrane deflection fracture experiment (MDFE) (see Section 9.3.3), while the material's characteristic length can be obtained by matching two different experimental results performed on notches with different root radii, ρ, based on the following equation:

$$K_{IC}^{/} = \sqrt{1+\frac{\rho}{2d_0}}K_{IC} \qquad \text{Eq. (9-14)}$$

In this equation, $K_{IC}^{/}$ is the measured fracture toughness with respect to a finite notch radius.[20,21] Accordingly, for the undoped UNCD we estimate d_0 by employing $K_{IC}^{/}$ (blunt notch with $\rho \approx 100$ nm) of about 6.7 MPa $\sqrt{\text{m}}$ and K_{IC} (sharp crack), of about 4.5 MPa $\sqrt{\text{m}}$.[22] The corresponding d_0 is estimated for undoped UNCD as $d_0^{\text{UNCD}} \approx 35$ nm. Furthermore, from Equation (9-13) we can estimate the *ideal strength* of the material at the characteristic size of d_0 as $\rho_u^{\text{UNCD}} \approx 18$ GPa, which is consistent with the UNCD strength identified in this work based on Weibull theory. Note that this ideal strength is more than four times greater than the value of $\sigma_0 = 4.17$ GPa reported in Table 9.1.

9.6 Conclusions

This chapter investigates the elasticity, toughness, and strength of UNCD and the validity of the Weibull statistical analysis. The fracture strength of UNCD thin films is obtained by testing submicron freestanding films by means of the membrane deflection experiment. The Weibull modulus, m, and the scale parameter, σ_0, are obtained by analyzing the

tensile data. The characteristic strength, σ_0, of undoped and 5%, 10%, and 20% N_2-doped UNCD films was found to be 4172, 2713, 2446, and 2350 GPa, respectively. This significant drop in material strength is connected to the increase in defect size within the film as a result of the addition of N_2 to the plasma. Both undoped and doped UNCD films exhibit a decrease in strength with increase in homogeneously stressed volume. Fractographic observation and data analysis reveal that for ultrasonically seeded films, volume is the *measure* controlling strength size dependence. Our study also shows that Weibull statistics are quite successful in predicting the fracture strength of the tested materials and that this theory can be used with confidence in the design of MEMS devices.

We have also identified the fracture toughness of undoped UNCD. Based on toughness and notch strength measurements we also estimated theoretically the material ultimate strength, $\sigma_u = 18$ GPa, and associated characteristic defect-free size, $d_0 = 35$ nm. While more research is needed to assess the accuracy of this prediction, it constitutes a very valuable tool for assessing deposition techniques and process parameters. Likewise, it provides a means for comparing materials to be employed in micro- and nanodevices.[23]

While in this investigation we have determined that volume is the scaling parameter to be used in the context of Weibull's theory, the reader should keep in mind that process parameters altering surface characteristics may result in a different scaling parameter such as sidewall surface or top surface. In each case, a thorough analysis is required to determine the controlling size scale parameter.

Acknowledgments

The authors would like to acknowledge the contributions of R. Divan and D. C. Mancini in the microfabrication of the UNCD tensile specimens. This work was supported in part by the NSF-Nano Science Interdisciplinary Research Teams (NIRT) under Award Number CMS00304472 and by the National Science Foundation under GOALI Award No. CMS-0120866/001.

References

1. W. Weibull, "A Statistical Theory of the Strength of Materials," *Proceedings of the Royal Swedish Institute Engineering Research*, No. 151, pp. 1–45, 1939.

2. J. Bagdahn, W.N. Sharpe, and O. Jadaan, "Fracture Strength of Polysilicon at Stress Concentrations," *Journal of Microelectromechanical Systems*, Vol. 12, pp. 302–312, 2003.
3. D.A. LaVan, T. Tsuchiya, G. Coles, W.G. Knauss, I. Chasiotis, and D. Read, "Cross Comparison of Direct Strength Testing Techniques on Polysilicon Films," *Mechanical Properties of Structural Films, ASTM STP 1413*, C. Muhlstein and S.B. Brown, Eds., American Society for Testing and Materials, West Conshohocken, PA, 2001.
4. D.A. LaVan, K. Jackson, S.J. Glass, T.A. Friedmann, J.P. Sullivan, and T. Buchheit, "Direct Tension and Fracture Toughness Testing Using the Lateral Force Capabilities of a Nanomechanical Test System," *Mechanical Properties of Structural Films, ASTM STP 1413*, C. Muhlstein and S.B Brown, Eds., American Society for Testing and Materials, West Conshohocken, PA, 2001.
5. W.N. Sharpe, Jr., K.M. Jackson, J.H. Kevin, and Z. Xie, "Effect of Specimen Size on Young's Modulus and Fracture Strength of Polysilicon," *Journal of Microelectromechanical Systems*, Vol. 10, pp. 317–326, 2001.
6. H.D. Espinosa, B. Peng, B.C. Prorok, N. Moldovan, O. Auciello, J.A. Carlisle, D.M. Gruen, and D.C. Mancini, "Fracture Strength of Ultrananocrystalline Diamond Thin Films – Identification of Weibull Parameters," *Journal of Applied Physics*, Vol. 94, pp. 6076–6084, 2003.
7. H.D. Espinosa, B.C. Prorok, B. Peng, K.H. Kim, N. Moldovan, O. Auciello, J.A. Carlisle, D.M. Gruen, and D.C. Mancini, "Mechanical Properties of Ultrananocrystalline Diamond Thin Films Relevant to MEMS/NEMS Devices," *Experimental Mechanics*, Vol. 43, pp. 256–269, 2003.
8. I. Chasiotis and W.G. Knauss, "The Mechanical Strength of Polysilicon Films: Part 1. The Influence of Fabrication Governed Surface Conditions," *Journal of the Mechanics and Physics of Solids*, Vol. 51, pp. 1533–1550, 2003.
9. I. Chasiotis and W.G. Knauss, "The Mechanical Strength of Polysilicon Films: Part 2. Size Effects Associated With Elliptical and Circular Perforations," *Journal of the Mechanics and Physics of Solids*, Vol. 51, pp. 1551–1572, 2003.
10. K.S. Chen, A. Ayon, and S.M. Spearing, "Controlling and Testing the Fracture Strength of Silicon on the Mesoscale," *Journal of American Ceramics Society*, Vol. 83, pp. 1476–1484, 2000.
11. T. Tsuchiya, J. Sakata, and Y. Taga, "Tensile Strength and Fracture Toughness of Surface Micromachined Polycrystalline Silicon Thin Films Prepared Under Various Conditions," *MRS Symposium Proceedings*, Vol. 505, pp. 285–290, Boston, MA, Dec. 1–5, 1997.
12. D.T. Read, J.D. McColskey, R. Geiss, and Y.W. Cheng, "Microtensile Testing of Thin Films in the Optical and Scanning Electron Microscopes," *AIP Conference Proceedings*, Vol. 683, pp. 353–356, 2003.
13. D.M. Gruen, "Nanocrystalline Diamond Films," *Annual Review of Material Science*, Vol. 29, pp. 211–259, 1999.
14. A. Erdemir, G.R. Fenske, A.R. Krauss, D.M. Gruen, T. McCauley, and R.T. Csencsits, "Tribological Properties of Nanocrystalline Diamond Films," *Surface Coating Technology*, Vol. 120, pp. 565–572, 1999.
15. A.R. Krauss, O. Auciello, M.Q. Ding, D.M. Gruen, Y. Huang, V.V. Zhirnov, E.I. Givargizov, A. Breskin, R. Chechen, E. Shefer, V. Konov, S. Pimenov,

A. Karabutov, A. Rakhimov, and N. Suetin, "Electron Field Emissions for Ultrananocrystalline Diamond Films," *Journal of Applied Physics*, Vol. 89, pp. 2958–2967, 2001.

16. B. Bhattacharyya, O. Auciello, J. Birrell, J.A. Carlisle, L.A. Curtiss, A.N. Goyette, D.M. Gruen, A.R. Krauss, J. Schlueter, A. Suman, and P. Zapol, "Synthesis and Characterization of Highly-conducting Nitrogen Doped Ultrananocrystalline Diamond Films," *Applied Physics Letters*, Vol. 79, pp. 1441–1443, 2001.
17. J. Birrell, J.A. Carlisle, O. Auciello, D.M. Gruen, and J.M. Gibson, "Morphology and Electronic Structure in Nitrogen-doped Ultrananocrystalline Diamond," *Applied Physics Letters*, Vol. 81, pp. 2235–2237, 2002.
18. H.D. Espinosa, B.C. Prorok, and M. Fischer, "A Methodology for Determining Mechanical Properties of Freestanding Thin Films and MEMS Materials," *Journal of the Mechanics and Physics of Solids*, Vol. 51, pp. 47–67, 2003.
19. C.A. Johnson and W.T. Tucker, "Advanced Statistical Concepts of Fracture in Brittle Materials," *Engineered Materials Handbook*, *Ceramics and Glasses*, Vol. 4, pp. 709–715, 1991.
20. N. Pugno, B. Peng, and H.D. Espinosa, "Prediction of Strength in MEMS Components with Defects – A Novel Experimental-Theoretical Approach," *International Journal of Solid Structures*, Vol. 42, pp. 647–661, 2005.
21. H.D. Espinosa and B. Peng, "A New Methodology to Investigate Fracture Toughness of Freestanding MEMS and Advanced Materials in Thin Film Form," *Journal of Microelectromechanical Systems*, Vol. 14, No. 1, pp. 153–159, 2005.
22. M.D. Drory, R.H. Dauskardt, A. Kant, and R.O. Ritchie, "Fracture of synthetic diamond," *Journal of Applied Physics*, Vol. 78, pp. 3083–3088, 1995.
23. H.D. Espinosa, B. Peng, N. Moldovan, T.A. Friedmann, X. Xiao, D.C. Mancini, O. Auciello, J. Carlisle, C.A. Zorman, and M. Merhegany, "Elasticity, Strength and Toughness of Three Novel MEMS/NEMS Materials – 3C-SiC, UNCD, ta-C," the Proceedings of the 11th International Conference on Fracture, Turin, Italy, March 20–25, 2005.

PART 4
UNCD PARTICLES OF DETONATION ORIGIN

10 On the Discovery of Detonation Nanodiamond

Vyacheslav V. Danilenko

ALIT Close Joint Stock Company, Kiev, Ukraine

The detonation synthesis of nanodiamonds was discovered about 40 years ago, in July 1963. Within the history of detonation nanodiamonds, also called ultrafine-dispersed diamonds (UDDs), the following three periods can be identified:

(1) The discovery of nanodiamond synthesis in 1963–1982, followed by a prolonged period of low activity in the field.
(2) Rediscovery of the synthesis in 1982–1993, active study, and production of nanodiamonds simultaneously at several research centers in the former USSR. In this period, production potential exceeded the scale of applications.
(3) Unprofitable production of small batches of nanodiamonds in 1993–2004, resulting in the shutting down of a number of research centers and termination of UDD production.

Despite the unfavorable period between 1993 and 2004 in UDD history, the enthusiasts who believed that nanodiamond would find wide industrial applications continued to work hard in the area. And indeed, recently, interest in nanodiamonds has been gradually revived, as demonstrated by the organization of the International Symposia in St. Petersburg, Russia in 2003 and 2004.

Analyzing the history of the discovery of UDD synthesis, it is necessary to consider the following factors:

(1) The history of the discovery of UDD is part of the general history of the development of explosive technologies in the synthesis of superhard materials, and this discovery is a natural result of the extenuation of the previous studies.

(2) The history of the discovery of UDD synthesis is at the same time the history of many years of studies of carbon condensation in the detonation wave, properties, and applications of UDD, and the organization of the commercial production of UDD.
(3) In the history of any discovery, it is important to emphasize priorities. Pioneers always use the experience gained by their predecessors, to whom the appropriate credit should be provided.

The discovery of diamond synthesis under static high pressures at the end of the 1950s stimulated studies aimed at determining the application of explosion energy in diamond synthesis. For the first time, diamond was detected in a shock-compressed graphite sample in the USA in 1961 by P. J. De Carli and A. C. Jamisson. In 1960–1980, a sort of "diamond club" of research centers was formed in the USSR, where dynamic methods for producing superhard materials were major research topics. The "diamond club" included the following institutes: All-Union Research Institute of Technical Physics (VNIITF, Snezhinsk, Chelyabinsk region); Institute of Chemical Physics, Academy of Sciences (IChF, Chernogolovka, Moscow region); Institute of Hydrodynamics, Siberian Academy of Sciences of the USSR (IG, Novosibirsk); Institute of Superhard Materials, Ukraine Academy of Sciences (ISM, Kiev); Institute of Problems of Materials Science, Ukraine Academy of Sciences (IPM, Kiev); and Dnepropetrovsk Institute of Mines (DGI, Dnepropetrovsk, Ukraine).

The general history of the development of dynamic methods for diamond synthesis is outlined in Table 10.1. The history of the discovery of UDD synthesis is unique. UDD was discovered four times over a period of 25 years by scientists from different research centers. Specialists from the VNIITF, a research institute where nuclear weapons were developed, were the first in the USSR to start studies on diamond synthesis in 1960. The merit of these studies is due to Academician E. I. Zababakhin, an outstanding scientist who headed the VNIITF (later the institute was named after him). Owing to his initiative and support, scientists from the gas dynamics group, including K. V. Volkov, V. V. Danilenko, and V. I. Elin, carried out the following pioneering work in diamond synthesis in 1960–1965:[1,2]

(1) Diamonds were obtained by shock compression of graphite and carbon black in spherical and cylindrical storage ampoules (1962).

Table 10.1 Historical Outline of Dynamic Diamond Synthesis

Authors	Year	Subject of Research
B. I. Zababakhin (VNIITP)	1960	Justification of the possibility of diamond synthesis via shock compression of graphite; beginning of experimental research
B. J. Alder and R.H. Christian (USA)	1961	
M. N. Pavlovskii (VNIIEF), K. K. Krupnikov (VNIITP), A. N. Dremin and S. V. Pershin (IchP)	1963 1968	Derivation of the shock adiabate for graphite and confirmation of its conversion into diamond
P. J. De Carli and A. C. Jamisson (USA)	1961	Diamond synthesis with preservation of shock-compressed graphite in a plane ampoule
	1962	As above, but in spherical and cylindrical ampoules (diamond yield 2%)
K. V. Volkov, V. V. Danilenko, and V. I. Elin (VNIITP)	1963	Diamond synthesis by compression of graphite + Me and carbon black + Me mixtures (diamond yield 20%)
	1963	UDD synthesis from carbon of explosion products (diamond yield 8–12% of the charge mass)
G. A. Adadurov (IChP)	1965	Diamond synthesis from graphite
DuPont (USA)	1976	Commercial production of diamond micro-powder *Mypolex* by compressing graphite–copper mixture with a charge mass of 5 t in cylindrical ampoules
G. I. Savvakin (IPM)	1982	UDD synthesis
A. M. Staver, E. A. Petrov, and A. I. Lyamkin (IG)	1982	UDD synthesis

Table 10.1 Historical Outline of Dynamic Diamond Synthesis (cont'd)

Authors	Year	Subject of Research
O. N. Breusov, V. N. Drobyshev, G. A. Adadurov, and A. N. Dremin (IchP)	1983	Pilot-scale production of diamond micro-powders by explosion of pressed 100 g charges of graphite or carbon black mixture with RDX in an explosion chamber
G. V. Sakovich and co-workers (NPO "Altay", Biisk)	1984	Pilot industrial production of UDD (0.6 kg charges from RDX/TNT 40/60%, "dry" cooling)
	1985	Applications of UDD in wear-resistant coating, production of wear-resistant additives with UDD for motor oils
N. R. Greiner, P. S. Philips, and J. D. Jonhson (USA) F. Volk (Germany)	1988	UDD synthesis
Collaborators of the VNIITP and PGUP "Elektrokhimpribor", ZAO "Almazny center", NPO "Sinta" (Minsk) ZAO "ALIT"	1991 – 1995	Pilot-scale production of UDD
V. V. Danilenko, I. A. Petrusha, and A. A. Bothethka (ISM)	1994	Beginning of studies on UDD sintering under static conditions
V. V. Danilenko (ZAO "ALIT")	1995	Ampoule-free sintering of high-density UDD grains by explosion, obtaining diamond single crystals
V. V. Danilenko, P. P. Tolochko, B. A. Vyskubenko, and E. E. Lin (ZAO "ALIT", VNIITF, VNIIEF)	1986–1992	Experiments on UDD synthesis by explosion of large-mass charges (10–140 kg)

(2) Compression of a graphite–metallic coolant mixture was used, which made it possible to increase the diamond yield by an order of magnitude (1963).
(3) The superhard wurtzite modification of boron nitride was obtained using explosions (1963).
(4) Detonation synthesis of nanodiamonds from carbon molecules of explosives was discovered and investigated (1963).

To simplify diamond synthesis, the author proposed and implemented (in 1962) ampoule-free synthesis with explosions in the explosion chamber instead of ampoule synthesis. Graphite was placed directly into a cylindrical charge from a RDX/TNT mix of 60/40%. The charge was encased in a water jacket to suppress graphitization and reduce the unloading rate of detonation products (DPs) and of the synthesized diamond. Even the first experiment with such a setup resulted in a sharp increase in diamond yield. A control experiment, carried out with a graphite-free charge in July 1963, confirmed the hypothesis that diamond was synthesized from the carbon contained in DPs.

Simultaneously, a comparison of the phase diagram for carbon and the parameters at the Jouguet point for the detonation of high-density charges of powerful explosives (the values of pressure and temperature obtained in DPs as a result of detonation-induced decomposition of explosive molecules) proved that the free carbon of DPs must condense in the form of diamond (see Fig. 10.1). It can also be seen that, in order to obtain free carbon in DPs, an explosive with a negative oxygen balance should be used. Such explosive compounds simultaneously serve as sources of energy and carbon. Compared to diamond synthesis from graphite, the advantage of condensation of atomic carbon of DPs into diamond is that neither energy nor time expenditures are required for the destruction or rearrangement of the initial crystal lattice of graphite. Thus, the main problem is not in the formation of UDD but in its storage (i.e., in creating conditions in chamber that prevent oxidation and graphitization of the UDDs obtained). Despite convincing theoretical predictions (Table 10.1), only the experiment carried out in 1963 proved for the first time that diamond is indeed formed in a detonation wave and that the obtained substance can be preserved.

In 1963–1965, about 100 successful experiments were carried out to analyze the effect of explosion conditions, as well as the composition and configuration of charges, on UDD synthesis and the properties of the UDD produced.[1–3] It was shown that DP cooling as a result of conversion of

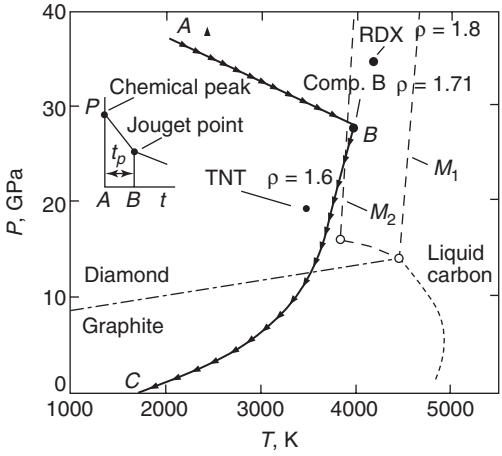

Figure 10.1 Phase diagram of carbon and the detonation parameters. The inset shows the pressure profile in a detonation wave: *A* corresponds to the shock compression of the explosive (chemical peak); *AB* corresponds to the decomposition of explosive molecules with the formation of detonation products (DPs) and condensation of the free carbon (for an explosive with a negative oxygen balance) to UDDs at pressures higher than 20 GPa; *B* corresponds to the termination of the decomposition (the Jouguet point), and t_p is the duration of the decomposition. In the phase diagram, points *A* and *B* are indicated for the composition B (RDX/TNT 64/36%), *BC* corresponds to the isotropic line of DP expansion, M_1 and M_2 are possible melting lines for bulk diamond and for UDDs with particle sizes ~2 nm, correspondingly.[15] ρ is the density in g/cm^3. Owing to the decrease of the nanodiamond melting point it is possible that carbon nanodrops can be formed in the detonation chemical zone, followed by crystallization as UDD or as non-diamond carbon during DP expansion.[15]

the potential energy of DPs into kinetic energy of the envelope surrounding the charge plays a decisive role in the UDD synthesis. It was found that an elongated cylinder is the best shape for charges; the explosion of such a charge from RDX/TNT 60/40% in a water jacket gives a UDD yield of 8–12% of the charge mass and UDD concentration in the detonation soot of up to 75%.

At that time, experiments aimed at developing methods for diamond synthesis were highly classified; for security reasons, the results were initially contained only in secret reports from the VNIITF. Only in 1987 were part of those reports forwarded to the other members of the "diamond club".

UDD synthesis was analogously rediscovered by A. M. Staver, E. A. Petrov, and A. I. Lyamkin under the guidance of Academician V. M. Titov at the Institute of Hydrodynamics, Siberian Division, Academy of Sciences of the USSR (Novosibirsk),[4,5] and by G. I. Savvakin under the guidance of Academician V. I. Trefilov at the Institute of Problems of Materials Science, Ukraine Academy of Sciences (Kiev),[6] who investigated ampoule-free diamond synthesis through shock compression of graphitized carbon and hydrocarbon materials (but without a water jacket). In those experiments, the DP cooling required for UDD storage was attained by shock compression of a noble gas in an explosion chamber ("dry" cooling). The UDD yield was 4–6% of the charge mass for a UDD concentration in the detonation soot of 40–60%. In the USA, UDD synthesis was reported for the first time only in 1988.[7] This fourth UDD discovery took place as a result of the investigation of DPs (gases, soot, etc.) of different explosives during detonation in an argon atmosphere in a chamber 1.5 m^3 in volume. Experiments were conducted at the Fraunhofer Institute of Chemical Technology by Fred Volk (Division Head of the Institute) and by Roy Greiner (from Los Alamos National Laboratory). Detailed investigation of the soot produced by the explosion of RDX mixtures conducted by R. Greiner and co-workers at Los Alamos revealed the presence of UDD in the soot.

In general, the development of this interesting direction in science and technology in the former USSR was hindered by the following circumstances:

(1) The high level of security in the former USSR that had been extended to any research area on diamond synthesis.
(2) The decision of the Soviet government to prioritize research on the production of diamonds by catalytic synthesis under static pressure over developing explosive methods.
(3) The first discovery of UDD synthesis at the VNIITF was a specialization far from diamond production.
(4) Industrial applications of nanoscale materials and nanotechnologies were not developed in the 1960s.

In 1984, a pilot-scale production of UDD was organized for the first time at the "Altay" Research-and-Production Center headed by Academician G. V. Sakovich (0.6 kg charges from RDX/TNT 40/60%, "dry" cooling by inert gases in chamber, UDD yield 4–6%, UDD concentration in soot 40–50%, specific surface 400 m^3/g, UDD particles size 2–4 nm).[10]

Subsequently, a number of new fields of application of UDD that did not traditionally use diamonds were proposed and investigated.[8] It has been proved that small UDD admixtures (0.5–1%) in various materials noticeably improve the properties of these materials and coatings. In all cases, UDD plays a role of an additive that significantly modifies the microstructure. The First Interdisciplinary Scientific Conference on the UDD held at NPO "Altay" in 1986 demonstrated full agreement between the data on UDD synthesis and properties obtained at the VNIITF in 1963–1964 and by other centers in 1982–1986.

UDD purification is an expensive and complex process (see Chapter 13). Different purification methods have been used;[3,9] among them the liquid phase oxidation of detonation soot is considered the most effective (ash content 0.5–1%). More specifically, the following soot oxidation technologies have been used: at VNIITF (1963–1966), a mixture of H_2SO_4 + KNO_3; at VNIITF (1994–2000), ozone (gas); at NPO "Altay", a mixture of H_2SO_4 + HNO_3; at the "ALIT" company (ISM), a mixture of H_2SO_4 + Cr_2O_3. At the end of the 1980s, the technology for UDD purification by using nitric acid under pressure was developed at the Special Technical Design Office (SKTB) "Tekhnolog" (St. Petersburg), where a continuous-operation unit was constructed.[9] The purification method determines the quality and quantity of the UDD surface impurities. It should be noted that for some applications (coatings, lubricants), a mixture of UDD and non-diamond carbon is used (e.g., detonation soot without extraction of UDD).

Detailed studies of the properties and possible areas of application of UDD have been carried out at NPO "Altay", at the ISM and IPM (Kiev), NPO "Sinta" (Minsk), the ZAO "Almaznyi Center" (St. Petersburg), and the VNIITF (Snezhinsk).[9] For the reproducibility of parameters for various UDD powders and suspensions, standard engineering specifications were developed (TU VNIITF, 1994; TU of Ukraine, ISM, 2001). In 1988–1998, extensive studies of carbon condensation in the form of UDD during detonation were performed by A. I. Lyamkin, A. M. Staver, V. F. Anisichkin, I. Yu. Mal'kov, E. A. Petrov, A. P. Ershov, and V. M. Titov at the IG.[4,5] The effect of UDD formation on the detonation parameters was demonstrated in refs. [11–13].

In 1986–1988 at the VNIITF, the author investigated UDD synthesis for the first time using large mass charges (with a mass of up to 20 kg) of various explosives in large explosion chambers with an aim to organize large-scale production of inexpensive, high-quality UDD, which is essential for UDD application at an industrial scale. It was shown that an increase in the mass of charges using a RDX/TNT 60/40% mix does not

change the UDD yield, but UDD grains become coarser (the specific surface of UDD grains is reduced by half, from 400 to 200 m^3/g) and macroscopic lonsdaleite crystals also form.[3] In 1991 at the VNIIEF, a unique experiment on UDD synthesis by exploding a charge with a mass of 140 kg in a water jacket was carried out in a chamber 300 m^3 in volume.[14] In 1992, the author developed large-scale technology for producing UDD (10 kg charges from RDX/TNT 60/40%, water cooling, UDD yield 8–10% and UDD concentration in soot 60–75%, UDD specific surface area 200 m^3/g, particles size 4–6 nm) and implemented it at the commercial plant of the "ALIT" company (Zhitomir, Ukraine). The main part of the plant was an explosion chamber 100 m^3 in volume with water cooling of the UDD (designed by the author)[16]. At present all another manufacturers use small explosion chambers (2–6 m^3) and small charges (0.5–2 kg), which are not effective for UDD industrial production. For example, for the production of 100 kg of UDDs per month, an explosion of ~80 charges of 1 kg mass each day is required, which is unrealistic.

In contrast to the situation in many other UDD application areas, there is a well-developed market for diamond polycrystals with nanostructure (e.g., polishing) and the area of application of such diamond polycrystals is expanding rapidly. In 1994–1998 at the ISM (Kiev), an investigation was conducted on UDD sintering under static pressure.[3,17] It was concluded that the maximum pressure of 10 GPa attainable with conventional compression molds is insufficient for UDD sintering and formation of strong polycrystals. At the same time, the technique of *UDD sintering* at "ALIT" provided a unique "soft" diamond sub-micropowder with polycrystalline particles for superfinish polishing of some electronic devices (produced at "ALITEX", Kiev).[3,18] In 1995, experiments using the big "ALIT" chamber resulted in sintering of high-density UDD grains and diamond single crystals (up to 0.6 mm).[3,19]

It should be mentioned that currently two important application problems for UDDs are awaiting solution: namely, fine UDD dispersion and the stability of UDD suspensions.

In view of the absence of large-scale applications of UDDs in industry, the laboratory and plant at the VNIITF and at the Krasnoyarsk Technical University were closed and production at NPO "Altay" and at the industrial complex "Electrochimpribor" was suspended.

At the beginning of the current century, interest in UDDs, which combine high values of dispersity, chemical resistance, and adsorption activity, has increased owing to the intense development of nanotechnologies around the world. Three scientific international symposia on nanodiamonds took place in 2002–2004,[20–23] and a new Byeloruss-

ian–Chinese joint enterprise "Shandun gold nanodiamond" has been created in China.

Importantly, at present all the conditions for large-scale production of UDDs are available: namely, simple technology of synthesis, production capacities, knowledge of detailed properties, and a number of realistic diverse applications.

References

1. K. V. Volkov, V. V. Danilenko, and V. I. Elin. Diamond synthesis from detonation carbon. *Fiz. Goren. Vzryva*, Vol. 26, No. 3, pp. 123–125 (1990).
2. K. V. Volkov, V. V. Danilenko, V. I. Elin, S. E. Sanina, T. P. Timofeeva, K. K. Krupnikov, and I. V. Sanin. Synthesis of diamond and dense modifications of boron nitrite by dynamic method. *Explosion, Shock, Protection Inf. Bull.*, No. 17, Inst. Geofiz. Sib. Otd. Acad. Nauk USSR, Novosibirsk (1987).
3. V. V. Danilenko. *Synthesis and Sintering of Diamonds by Explosion.* Energoatoizdat, Moscow (2003).
4. A. I. Lyamkin, E. A. Petrov, A. P. Ershov, G. V. Sakovich, A. M. Staver, and V. M. Titov. Production of diamond from explosives. *Dokl. Acad. Nauk USSR*, Vol. 302, No. 3, pp. 611–613 (1988).
5. V. M. Titov, V. P. Anisichkin, and I. Yu. Mal'kov. A study of ultradispersed diamond synthesis by detonation waves. *Fiz. Goren. Vzryva*, Vol. 25, No. 3, pp. 117–126 (1989).
6. G. I. Savvakin and V. I. Trefilov. Formation of the structure and properties of ultradispersed diamonds during detonation of condensed carbon-containing explosives with negative oxygen balance in various media. *Lecture Books of Academy of Sciences of USSR*, Vol. 321, No. 1, pp. 99–103 (1991).
7. N. Roy Greiner, P. S. Philips, and J. D. Johnson. Diamond in detonation soot. *Nature*, Vol. 333, p. 6172 (1988).
8. G. V. Sakovith, V. F. Komarov, E. A. Petrov, P. M. Bryilyakov, M. G. Potapov, and I. G. Idrisov. Ultra dispersed diamond and its practical application. *Proceedings of V All-Union Workshop on Detonation* (Krasnoyarsk), Vol. 2, pp. 272–278 (1991).
9. V. Yu. Dolmatov. Ultradispersed diamonds of detonation synthesis. SPb. (2003).
10. A. L. Vereshchagin. Detonation nanodiamonds. Altai State Technical University, Barnaul (2001).
11. L. N. Akimova, S. A. Gubin, V. D. Odintsov, and V. I. Pepekin. Detonation of explosive with diamond origin. *Proceedings of V All-Union Workshop on Detonation* (Krasnoyarsk), Vol. 1, pp. 14–19 (1991).
12. S. V. Pershin and D. N. Tsaplin. Dynamic research of detonation synthesis of dense phase matter. *Proceedings of V All-Union Workshop on Detonation* (Krasnoyarsk), Vol. 2, pp. 237–243 (1991).

13. C. L. Mader, *Numerical Modeling of Explosives and Propellants*, 2nd ed., CRC Press, Boca Raton, FL (1998).
14. B. A. Vyskubenko, V. V. Danilenko, E. E. Lin, V. A. Mazanov, T. V. Serova, V. I. Suharenko, and A. P. Tolothko. The influence of scale factors on the size and yield of diamond in detonation synthesis. *Fiz. Goren. Vzryva*, Vol. 28, No. 2, pp. 108–109 (1992).
15. V. V. Danilenko. Nanocarbon phase diagram and conditions for detonation nanodiamond formation. *Proceedings of NATO Advanced Research Workshop "Ultrananocrystalline Diamond*", p. 181 (2004).
16. V. V. Danilenko, V. I. Trefilov, and N. V. Danilenko. USSR Patent No. SU 181329 A3, Priority May 12 (1991).
17. V. V. Danilenko, I. A. Petrusha, G. S. Oleinik, and N. V. Danilenko. Evolution of compact structure under high pressure sintering of nanodispersed diamond. *Superhard Mater*, No. 4, pp. 53–61 (1998).
18. K. V. Kirilin and V. V. Padalko. Diamond powder and method for its production. Patent 38541A Ukraine, MPK7 CO1V 31/06. Priority 21.07.01. – Publ. 15.05.01, Byul. No. 4 (2001).
19. V. V. Danilenko. Shock-wave sintering of nanodiamonds. *Phys. Solid State*, Vol. 46, No. 4, pp. 711–715 (2004).
20. *Proceedings of Scientific Seminar on Nanoscale Diamonds* (Kiev). *Superhard Mater.*, No. 6 (2002).
21. *Proceedings of I International Symposium on Detonation Nanodiamonds: Production, properties and application* (St. Petersburg), 2003. *Phys Solid State*, Vol. 46, No. 4 (2004).
22. *Proceedings of NATO Advanced Research Workshop "Ultrananocrystalline Diamond"* (St. Petersburg) (2004).
23. *Bibliography Index: Detonation Nanodiamonds and Related Materials.* First issue, St. Petersburg (2003).

11 Synthesis and Post-Synthesis Treatment of Detonation Nanodiamonds

Valerii Yu. Dolmatov

JSC Diamond Centre, St. Petersburg, Russia

Introduction

Ultrananocrystalline diamonds (UNCDs) occupy an intermediate position between inorganic and organic substances, and this determines their unique properties among other ultradispersed materials, including nanocarbons (fullerenes, nanotubes, carbines). Available UNCD production technologies based on detonation synthesis actually provide only a primary carbon material known as diamond blend (DB) that includes diamond-containing fragments. In addition to these, there are graphite-like structures and amorphous chains of carbon atoms bound to numerous functional groups that form due to an incomplete oxidative destruction of organic products. Naturally, diamond blend contains production-related contaminants like metals, metal carbides, and oxides, as well as some constituents of the medium, like adsorbed gases and liquids. The chemical treatment used for UNCD isolation and purification from the primary detonation soot results practically in a new surface chemistry of the particles.

It would be more appropriate to describe the product of detonation synthesis as a cluster-like material with a complex hierarchy of aggregation states of diamond and non-diamond carbon modifications originating from specific surface relaxations of excess energy gained during the detonation process. The compensation for the excess surface energy occurs at the expense of chemically bonded molecular fragments containing heteroatoms (N, H, O). The excess surface energy is compensated by the formation of more or less stable absorption and/or solvation shells, the composition of which varies with the synthesis medium. Initial detonation soot exhibits a high dispersivity and defect density of carbon structures, which have well-developed active surfaces and, hence, an enhanced reactivity.

Within the detonation soot, the texture changes non-monotonically from the scale of UNCD particles to a larger scale, which is a specific feature of diamond blend as compared to other carbon-containing materials. This is because a diamond blend represents a well-organized spatial structure, due to multistep aggregation of the primary particles, rather than a mechanical mixture of UNCD and non-diamond carbons.[1,2] When etched with nitric acid, the specific area and volume of pores reaches a maximum at ~20% of non-diamond carbon content. Liquid oxidation leads to chemical decomposition of secondary aggregates, producing predictable changes in the powder surface morphology and texture. The residual oxidizable carbon (remaining 18–20%) is, in fact, a diamond-like phase representing the diamond cluster periphery.

A UNCD cluster always contains the following structural elements:

(1) It has a core consisting of sp^3-hybridized carbon atoms with a diamond cubic lattice. The core includes 70–90% of all carbon atoms and has a size of 40–60 Å, as shown by X-ray data.
(2) X-ray analysis also reveals the presence of a transient carbon shell around the core, consisting of amorphous carbon structures 4–10 Å thick. The shell may include from 10 to 30% of sp^2-hybridized carbon atoms and is inhomogeneous. It has been suggested that the inner shell surface adjacent to the core is composed of continuous onion-like carbon sheets, each consisting of six sp^2-hybridized carbon atoms (so called hexagons).[3] This layer is surrounded by fragmentary graphite-like monolayers ("aromatic clusters") that are also part of the shell. This amorphous envelope has a porous texture and contains numerous defects, ruptures in the carbon structures, and, sometimes, a small amount of hetero-atoms incorporated during the detonation synthesis.
(3) There is a surface layer built up from carbon atoms and other hetero-atoms to form a wide spectrum of functional groups. The mass of hetero-atoms may be as large as 10% of the total mass of particles, with oxygen as the major constituent. The functional groups have also been found to contain small amounts of hydrogen and nitrogen atoms, but most of them include oxygen in the form of hydroxyl, carboxyl, ketonic, lactonic, and other groups.

A model UNCD particle should be considered as being a bulk, rigidly structured polymer, rather than a tiny UNCD crystal with a defective surface. Its inner skeleton is formed by saturated carbon bonds and the surface consists of highly polar groups. These cause UNCD particles to actively affect the surrounding environment and to exert their structuring effect.

The major structural feature that makes detonation UNCDs different from natural diamonds or static and dynamic synthetic diamonds is the presence of a transient, mostly carbon-containing shell, rather than the ultradispersed size of the diamond core or the heterogeneous cluster surface. It is the shell that becomes the source of numerous polyheterocyclic nitrogen-containing compounds under the conditions of high-temperature extraction (at 200–400 °C) by organic solvents.[4] This extraction technique reduces the UNCD weight by 5–10%. Moreover, the transient shell supplies a large number of organic substances (carbohydrates, N-containing compounds, bridge alicycles, etc.) when UNCD is subjected to thermosorption at 300 °C in flowing helium. Therefore, a UNCD cluster is not a purely carbon material: the carbon in it represents an ensemble of carbon modifications, with only one of them having the diamond structure. The quantitative characteristics that describe the size and composition of the cluster layers may vary with the conditions of detonation synthesis and, what is most important, with the purification and modification methods used.

Below, the industrial process of detonation nanodiamond synthesis as well as post-synthesis purification and modification treatments are discussed in more detail with an emphasis on different conditions of the processes influencing the structure–property relationships of detonation nanodiamonds.

11.1 Industrial Technologies of Detonation Synthesis of UNCD

The detonation synthesis of UNCD includes four stages.[5] At the first stage, the actual stage of UNCD formation, explosives undergo transformation within the initial volume of the explosive charge itself. Using a coating of condensed matter surrounding the explosive charge confines gaseous and solid detonation products within the charge volume for a few fractions of a microsecond, allowing the “excess” carbon to transform to a larger extent to diamond.

This is followed by the second stage. As soon as the detonation is complete, its product must be cooled quickly via the gas-dynamic mechanism to preserve the UNCD and avoid its transformation to graphite in the reaction zone. The detonation in vacuum, for example, provides the highest cooling rates due to the very fast scattering of the material. But its impact with the detonation chamber walls, where the kinetic energy transforms to thermal energy, creates very high temperatures. After the attenuation of all shock waves in the chamber space, the temperature is ~3500 K, which is close to the detonation temperature. For this reason, there is practically no carbon solid phase left when the detonation is carried out in vacuum. The slowest gas-dynamic cooling of the detonation product is observed if it is surrounded by massive water or ice media; the maximum established temperature of the product is never greater than 500–800 K because water effectively absorbs the energy.[6] An intermediate position between the detonation in vacuum and that in a water (ice) shell is occupied by detonation in a noble gas medium, since the scattering rates in a gas are lower than in vacuum but higher than within a water/ice shell.

The third stage of UNCD synthesis starts with the reflection of the shock wave by the chamber walls, followed by its circulation and a turbulent mixing of the material with the cooling medium. The maximum temperature established in the medium varies with the mass ratio of the explosive and the gas in the chamber, as well as with the medium composition (chemical activity) and the heat capacity of the gases.

The final stage starts when the medium heated by the explosion and confined by a cold shell is cooled rapiply. In addition to various gaseous products (CO_2, CO, O_2, H_2, N_2, CH_4, NO, NO_2, NH_3, H_2O) in the chamber, there are finely dispersed suspended carbon particles possessing a great radiant emittance. As a result, the cooling of the medium represents a combined heat transfer process via convection and radiation. It has been reported in ref. [5] that the diamond blend yield at a temperature below 1500 ± 150 K in the reactor space is greatest, ~12%, if the detonation is carried out in a gas medium. As the temperature rises to 3000–3500 K, the yield drops nearly to zero.

The preservation of the primary diamond blend (DB) and its elemental composition are determined by the heterophase endothermic reactions of the DB gasification by carbon dioxide (reaction 1) and water vapor (reaction 2), which can be represented as a gross reaction (reaction 3):

$$C + CO_2 \rightarrow 2CO - 172.4\,\text{kJ/mol} \qquad \text{Eq. (11-1)}$$

$$C + H_2O \rightarrow CO + H_2 - 130.1\,\text{kJ/mol} \qquad \text{Eq. (11-2)}$$

$$C + CO_2 + H_2O \rightarrow 3CO + H_2 - 151.3\,\text{kJ/mol} \qquad \text{Eq. (11-3)}$$

There are two competing processes occurring in the chamber at high temperature: gasification (primarily of non-diamond carbon due to its high chemical activity) and UNCD graphitization. Not only does the oxidizer (CO) gasify the DB but it affects the particle surface, essentially changing the composition of its functional groups and providing attachment of oxygen-containing groups to the surface. In order to preserve the diamond phase, the cooling rate of the detonation product should be in the range of 3000–4000 K/min, which can be provided by a proper choice of the heat capacity of the gas or water–gas atmosphere in the detonation chamber.

In addition to detonation synthesis, the UNCD production process includes its chemical purification and washing to remove the acid, as well as product conditioning and modification, as discussed in the previous section. The production cycle also involves collection and utilization of acidic vapor and gases, preparation and recycling of nitric acid, and water circulation.

Detonation synthesis is carried out in special chambers (Fig. 11.1), whose volume ranges between 1 and 20 m^3. A detonation chamber is made from slightly or highly doped steel. Preferable reactors are made from a slightly doped steel, for example, "boiler" steel, with an anticorrosion and shock-resistant coating of the inner walls. The chamber is equipped with gas-transport lines and a system of collection and evacuation of condensed products.

The explosive (cast or compacted) is usually a trinitrotoluene/hexogen (T/H) mixture in a ratio from 40/60 to 70/30; the charge weight varies from 0.5 to 2.0 kg. The blasting is performed in one of the three ways shown in Table 11.1. The minimum mass of the explosive is determined by the conditions for the detonation product cooling: volume, pressure and composition of the gases, as well as the strength characteristics of the material of the chamber. In particular, a chamber of 11 m^3 in volume allows a 5 kg charge to be used, but it is possible to use up to 10 kg of explosive in a chamber of 100 m^3. The oxygen content in the working chamber volume, which will not affect the UNCD yield, has been reported to be as high as 2 vol.%[7] or 6 vol.%.[8]

Nanodiamonds can be produced by blasting an explosive in water foam[9] or by spraying water in the chamber space[10]. In the latter case, the mass ratio of the water droplets to the explosive mass is taken to be (3–8) : 1. Both procedures provide a higher heat capacity of the medium, which determines the structural pattern of carbon particles formed via condensation from the plasma, than the heat capacity of a gaseous atmosphere. Besides, the UNCD yield is greater because the detonation products

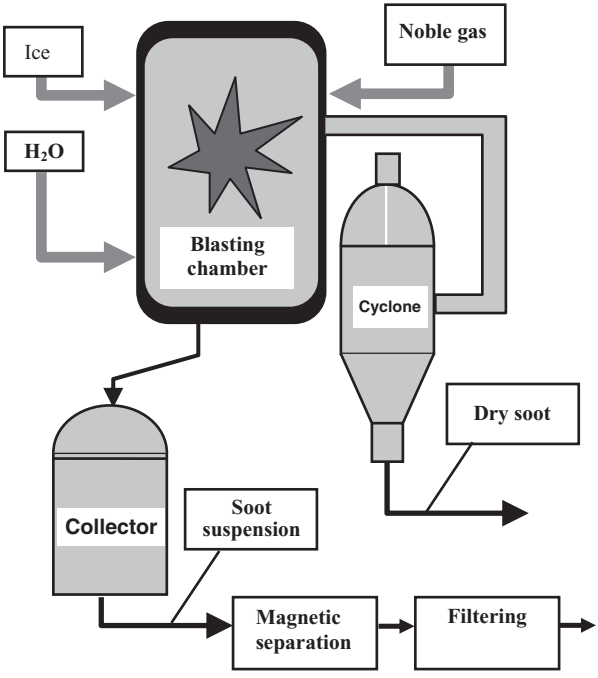

Figure 11.1 Schematic of a detonation chamber.

Table 11.1 Yields of Diamond Blend and UNCD as a Function of the Detonation Conditions

No.	Quality Characteristics of the Final Product	Detonation Conditions		
		Noble Gas[9,28,33,34]	*Water*[12,28,35]	*Ice Shell around the Charge*[6,28]
1	Diamond blend yield, mass %	3–8	6–12	8–18
2	UNCD content in the blend, mass %	20–40	40–63	55–75
3	UNCD yield per explosive mass %	0.6–3.2	2.4–7.6	4.4–13.5
4	Content of incombustible impurities, mass %	3–5	1.5–3.0	1–2

are cooled faster, reducing the amount of UNCD that can transform to graphite. However, the application of these procedures, as described in ref. [10], are poor illustrations of these theoretical considerations: the UNCD yield reported is, at best, 6 mass % per unit weight of the explosive. The reason for the low yield seems to be the improper choice of the explosive and the low density of the blasting charge.

Another UNCD production technique, explosive blasting, is described in ref. [11]. The authors use liquid droplets or jets (distilled water, a 40% aqueous solution of ethanol, kerosene, a 30% aqueous solution of glycerol, and transformer oil). The mass ratio of the liquid droplets or jet and the explosive is (10–50) : 1. The researchers point out that the UNCD content in the DB is larger than 80 mass %.

It is clear from these examples that the maximum DB yield is 9.6–10.0 mass % and the UNCD yield varies from 7.7 to 8.0 mass % per unit weight of the initial explosive. As the explosive charge increases from 0.5 kg (with a T/H ratio of 40/60 and a chamber volume of 0.6 m^3) to 50 kg (the T/H ratio is 50/50 and the chamber volume is 31.4 m^3), the DB and UNCD yields drop 1.5–2.0 times. In addition to a low UNCD yield, this procedure has other disadvantages: namely, a more complex design of the detonation chamber because of the need to spray it with liquid and because most of the mixture constituents are inflammable.

The authors of ref. [12] describe the production of UNCD by blasting an explosive in water. The minimum amount of water required for this should be sufficient to cover the explosive only. The pressure in the chamber is normal or lower. The authors believe that the presence of air is permissible between the water surrounding the explosive and the chamber (autoclave) walls. Under optimal blasting conditions, the UNCD yield is found to be 6.7–10.0 mass % per unit weight of the initial explosive. Trinitrotoluene and hexogen are not mixed, which makes the production process more complex. A major limitation of this technique is a fairly low yield due to three reasons: an ineffective explosive, the presence of air in the chamber, and a reduced pressure in it.

Blasting in water or ice in an optimal gas mixture increases the primary diamond and UNCD yields and essentially changes the hydrophilic/hydrophobic balance of active surface centers.[6] Still, such DB can be used for the same applications as UNCD of "dry" synthesis, provided that it has been pretreated appropriately. The ice-to-explosive ratio should be (4–9) : 1.

A way to raise the diamond yield by enhancing the fraction of explosive detonated has been suggested in ref. [7]. The authors use a special geometry of the explosive charge–a truncated cone, with the angle between its longitudinal sides varying from 50° to 60°.

We blasted 0.5 kg of a T/H mixture in a ratio of 50/50 in water, and the UNCD particle size was found to be 4.3 ± 0.1 nm. When the explosive mass was increased to 10 kg with T/H = 50/50 under the conditions of water spraying (*Alit* Co., Ukraine), the particles had a size of about 6 nm, and for a T/H mass of 150 kg in a water shell of 1500 kg, their size increased to ~8 nm.[13] This result may be attributed to a larger time for the synthesis in the detonation wave which is enhanced with increasing blasting charge diameter. The UNCD yield becomes larger as the mass ratio of the explosive medium and the blasting charge is increased.

The process of industrial detonation synthesis is carried out in time cycles, starting each cycle with a manual loading of the blasting charge equipped with an electric detonator capsule. This is done through the upper porthole of the detonation chamber which is then sealed. Depending on the technology being practiced at a particular plant, a cylinder explosive charge placed in a plastic bag filled with water or ice is suspended by special belts to a hook soldered to the chamber top. The charge is blasted from another explosion-protected room by applying an electric pulse to the detonator capsule. The chamber volume is usually ~2 m^3; the other parameters are given in Table 11.2. More cost-effective is the use of conversion explosives for making explosive mixtures, primarily from trinitrotoluene and hexogen extracted from out-of-date warheads (mines, missiles, shells).[14,15]

11.2 Post-Synthesis Purification and Modification

11.2.1 Chemical Purification

The characteristics of the soot, and more specifically the structure of UNCD clusters surrounded by a non-diamond carbon shell, vary with the conditions of detonation synthesis and, what is most important, with the purification and modification methods used. This fact determines some principal rules for extraction of pure UNCD:

(1) Rather pure UNCD particles can be extracted only by using aggressive methods capable of supplying high energy sufficient to break the chemical bonds.

Table 11.2 Major Parameters of the Detonation Chamber ~2 m^3 in Volume

Parameters	Normalized Value
1 Type of chamber	Vertical cylinder with hemispherical bottoms
2 Inner hemisphere diameter, mm	>1290
3 Hemisphere wall thickness, mm	>40
4 Inner cylinder diameter, mm	>1275
5 Cylinder wall thickness, mm	>60
6 Inner height of chamber, mm	<1910
7 Inner chamber volume, m^3	<2
8 Maximum explosive mass, trinitrotoluol equivalent, kg	<2
9 Advised T/H mass, kg	0.5–1.0
10 Triggering	Applied high voltage
11 Explosive delivery, porthole opening and closing	Hydraulic
12 Working pressure in hydraulic gear, MPa	3.0–6.3
13 Chamber degassing	Forced
14 Detonation product removal	Pneumatic
15 Admissible working temperature of outer chamber surface, °C	<80

(2) The product of chemical purification has an outer shell structure specific to each purification procedure. This may strongly affect the consumer properties of the product.
(3) Because UNCD possesses rich surface chemistry, one should expect high rates of chemical transformation.

Also, it is important to bear in mind that chemical purification is the most costly and sophisticated step in UNCD technology.

Since all methods for separation of non-diamond carbons employ selective oxidation under mild conditions that do not affect the diamond core but only break the unstable surface C—C bonds, the oxygen-containing groups appear to become dominant. The actual technological product may

Table 11.3 Contents of Incombustible Elements in UNCD Samples, Obtained by Atomic Emission Spectroscopy

Element	Contents of Elements in UNCD, mass %		
	Diamond Center		RFNC–VNIITF, (Snezhinsk, Russia)
	UDD-STW aqueous suspension in TU 05121441-275-95	UDD-TAN aqueous suspension in TU 05121441-275-95	Standard UNCD
Iron	0.15	0.1	0.1
Chromium	0.07	0.05	0.5
Silicon	0.3	0.1	0.15
Aluminum	0.005	0.001	0.01
Sodium	0.03	0.003	0.05
Potassium	0.002	0.002	0.002
Copper	0.005	0.002	0.003
Calcium	0.002	0.002	0.01
Magnesium	0.005	0.003	0.005
Manganese	0.001	Not found at sensitivity $5 \cdot 10^{-4}$ mass %	0.001
Titanium	0.01	0.005	0.002
Lead	0.001	0.001	0.001
Σ	0.58	0.27	0.84
Incombustible residue, %	0.95	0.4	1.4

Note: The analysis was made by Chukhaeva (Russian Federal Nuclear Center–VNIITF, Snezhinsk, Russia).

contain foreign impurities unrelated to UNCD but contaminate it during the synthesis, isolation, and purification steps. One can usually identify several groups of impurities: metals, non-diamond carbons, certain inorganic substances (oxides, carbides), technological reagents, and occasional mechanical impurities (Table 11.3).

Nearly all of the available approaches to UNCD purification are based on the fact that diamond and non-diamond carbon have different tolerances to oxidants.[16] There is no doubt that liquid oxidizers have an advantage over gas reagents, because they can be used at high concentrations in the reaction zone to provide high reaction rates. The product of liquid oxidation of UNCD represents a hydrosol which preserves its properties due to its solvate shell. Besides, this purification procedure can be performed as a continuous process.

There is a report of non-diamond carbon oxidation by ozone.[17] An air–ozone flow is blown through detonation soot at a temperature of 120–400 °C. In spite of a fairly good separation of non-diamond carbon, all incombustible impurities remain in the charge, and this necessitates the use of liquid oxidizers (strong acids) at high temperatures to dissolve the impurities, mostly iron oxides and carbides. The amount of incombustible impurities may be as large as 25 mass %.

Liquid oxidation can be performed at acceptable rates only at high temperatures. For this reason, oxidizing mixtures are prepared from acids with a high boiling temperature – $HClO_4$, H_3PO_4, H_2SO_4 – with the addition of an active oxidizer, e.g., HNO_3, nitrogen oxides, H_2O_2, $NaClO_4$, CrO_3, $K_2Cr_2O_7$, and some others. Initially, the application of perchloric was quite popular due to its unique properties as a high-temperature elemental oxidizer. However, its use and storage may be dangerous and quite costly, so it was soon replaced by other oxidizers.

The authors[18] subjected DB to a mechanical filtration, followed by treatment with concentrated sulphuric acid and heating. The non-diamond carbon was removed from the soot–H_2SO_4 mixture by adding to it an aqueous solution of chromium anhydride. The constituents of the final mixture had the following proportions (mass %): sulphuric acid 28–30%, chromium anhydride 14–16%, water – the rest. After the oxidation, the UNCD was washed with water. It was found that the content of metallic impurities in the final product was 0.9 mass % lower, while that of pure UNCD was as high as 98.5 mass %. This purification technology is complex because it involves several stages; further, it is costly and the waste is toxic.

An alternative liquid purification technique was developed in ref. [19]. Its basic principle is to preserve the dispersivity of carbon material at all stages of its treatment. The reactive suspensions of the initial soot in liquid oxidative mixtures are homogeneous, colloid stable, highly dispersed, and possess a low viscosity. During the reaction, there is a free supply of the oxidizer to solid particles, and there is practically no diffusion limit to the

reaction rate. The high reactivity of the DB allows the use of relatively mild oxidative mixtures:

$$\xrightarrow{\qquad\qquad\qquad\qquad}$$

$$HNO_3—H_2SO_4—SO_3;\ HNO_3—H_2SO_4;$$
$$HNO_3—H_2SO_4—H_2O;\ HNO_3—H_2O;$$

$$\xrightarrow{\qquad\qquad\qquad\qquad}$$

$$HNO_3—H_2O—H_2O_2;\ H_2O_2—H_2O + \text{a catalyst};\ O_2—H_2O + \text{a catalyst}$$

The arrows in these reactions indicate a decrease in the following parameters: the total concentration of the acids, the specific flow rates of the reagents, the amount and toxicity of the gaseous products, and the corrosive reactivity of the medium. As a result, the ecological and economic characteristics of the technological operations have been improved.

The major advantages of oxidizers based on nitric and sulphuric acids are their availability, low cost, and relative simplicity of technological operations and equipment designs.[20] This method, however, consumes large amounts of acids (up to 57 kg per kg of soot), and it is difficult to regenerate and utilize the mixture because of its complex composition. Besides, the diamond surface becomes contaminated with sulphuric and nitric compounds. Alternatively, the use of aqueous solutions of nitric acid can resolve these difficulties and improve the purification quality since no sulphur-containing substances are formed on the diamond.[21–23] This process is carried out at high pressure; the reactors are made of corrosion-resistant materials in order to withstand high temperatures.

Chemically, an attractive oxidizer should be hydrogen peroxide because its interaction with carbon produces only carbon dioxide and water.[24] This treatment does not contaminate the diamond surface with sulphuric or nitric derivatives. Mixtures containing hydrogen peroxide considerably simplify the technological cycle and facilitate environmental protection and utilization of wastes. The limitations of this approach include use of equipment not capable of operating reliably at high pressures, incomplete removal of non-diamond carbon, and UNCD contamination with incombustible impurities.

The most effective and productive technology of UNCD purification is the treatment of the initial soot with dilute nitric acid under pressure (up to 100 atm.) at 240–260 °C (Fig. 11.2).[23] This provides ≥99 mass % product purity after treatment of the soot for only 30–40 min. The diamond core structure remains practically unaffected by the treatment but the outer layer of a UNCD particle is completely changed. It is this fact that makes us state that the purification stage is the key step in determining the

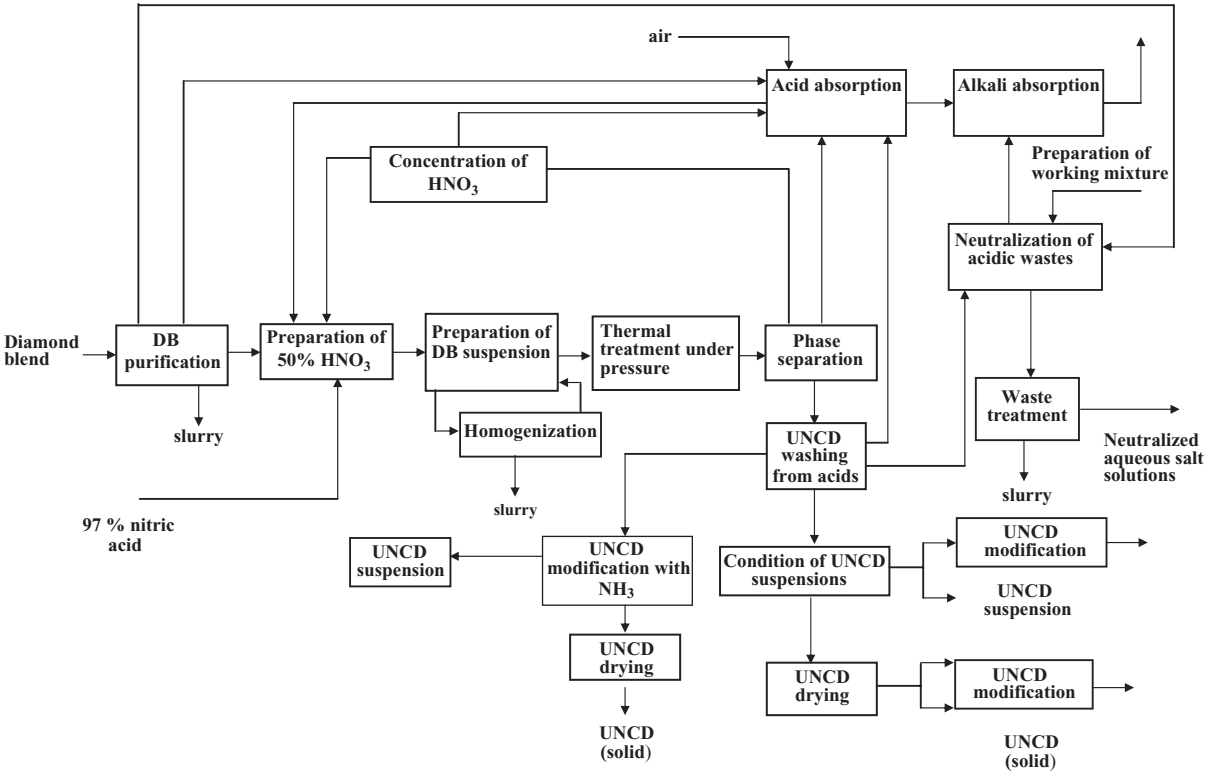

Figure 11.2 Block diagram of the industrial process of UNCD purification and modification.

properties of the product and its diverse modification. This method has been successfully introduced in practice in Russia, as well as in Byelorussia and China. The technology is well developed and tested. One technological cycle includes the entire combination of purification operations and is capable of providing various commercial UNCD modifications.[19,21,23]

High-temperature oxidation by nitric acid under pressure is a complex but effective method of purification that yields only small amounts of hazardous wastes. During the oxidation, nitric acid is reduced to nitric oxides that are completely re-oxidized by air and diluted with water. Then they can be transformed back to nitric acid using standard methods and recycled. Therefore, the major source of the oxidizer is the oxygen in air. Chemically, nitric acid acts only as an oxygen carrier, providing an aggressive oxidation process. An aqueous solution of nitric acid serves simultaneously as the reaction medium and as the carrier agent. The oxidation is combined with the dissolution of metal-containing impurities in the acid to make them water-soluble products.

The UNCD purification involves the following reactions. The oxidation of active carbon starts at relatively low temperatures of 80–180 °C when using nitric acid in a concentration of 50% or more. The primary oxidation occurs even at atmospheric pressure, releasing carbon dioxide and nitric oxides. After the active carbon is oxidized and metal oxides are partially dissolved, further oxidation of inactive non-diamond material requires a higher temperature of up to 220–260 °C. Experimental studies have shown that the addition of 10–40% nitric acid is sufficient for the two processes to be completed. It has been found that the higher is the temperature, the lower may be the concentration of nitric acid.

The product of thermal oxidation under pressure involving all the chemical reactions with UNCD represents a suspension in an aqueous solution of nitric acid. Nearly all impurities are transformed to gases or are dissolved and can be removed by washing the UNCD with distilled water. Nitric acid consumption is determined by the number of steps of the purification process included in a particular process, and may vary over a wide range. Clearly, this requires a cost-effective optimization of the purification process. With the loss due to water washing, the minimum acid consumption may be about 200 kg per tonne of UNCD. A smaller amount of reused nitric acid increases its consumption but may considerably decrease the recycling cost.

Nevertheless, in spite of a high UNCD quality and a high reactor unit productivity, the seemingly simple operation of UNCD washing to remove the acid and soluble impurities proves to be a limiting factor. This process

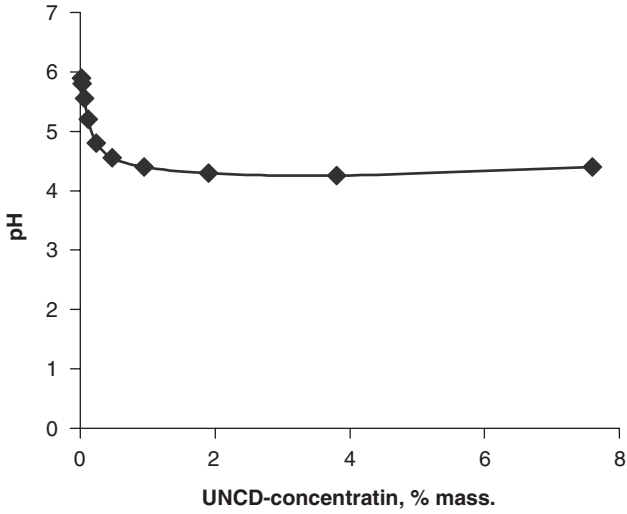

Figure 11.3 Dependence of the pH of the medium on the UNCD concentration in a washed suspension.

may take as along as 4 or 5 days, reducing the productivity of the purification stage as a whole.

When discussing the washing of water-soluble impurities and the control of its efficiency, one should bear in mind that nanodiamonds have their own significant acidity because of the presence of carboxylic groups on the particle surface. An aqueous suspension of pure UNCD cannot be neutral but must show an acidic reaction (Fig. 11.3). During sedimentation, a UNCD suspension forms two layers: a thickened bottom layer with UNCD and a transparent upper layer with no UNCD present. The bottom layer acidity is determined by the total of the effect of the UNCD acidic groups and the dissolved acidic and alkaline reagents. The upper layer acidity is due only to dissolved molecular-level products.

The titration for the total acidity of the transparent layer and of a well-stirred UNCD suspension at different washing stages prior to sedimentation has shown that there is practically no difference between the titration data as long as the acid content in the upper layer remains over 0.5% (pH is ~1). But as the washing is continued (pH > 3), the difference in the acidity values increases rapidly, reaching several orders of magnitude (Fig. 11.4). Therefore, the UNCD particles must behave in water as a poorly soluble, weak organic acid, as is actually observed in practice. For this reason, we can make a UNCD suspension neutral only by using a neutralizing alkaline reagent. Formally, however, the medium pH = 7 may

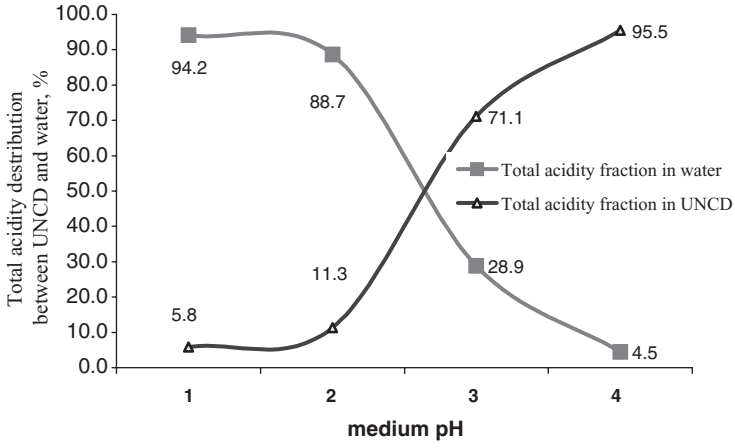

Figure 11.4 The total acidity distribution between the UNCD and the aqueous phase at various pH values in the medium.

give no information about the state of the UNCD particles, since they may be involved in acid–base equilibrium, behaving as an acidic or alkaline reagent, depending on the neutralizing partner reagent acidity.

The acids are removed by water washing. Free sedimentation of nanodiamond particles during the washings to remove the acids or ammonia water (in case of acid neutralization) produces a suspension thickened to 5–7% in UNCD, after which there is no visually observable sedimentation if the concentration of salt-forming impurities is low. The sedimentation rate in diluted suspensions is similar to that for 1 μm particles. The sedimentation of most of the UNCD particles in the presence of a thickened bottom layer takes from 12 to 24 hours at pH < 2. The UNCD concentration is very reproducible at a maximum thickening of ~5–7%. The boundary between the bottom and the upper layer becomes sharp. The thick mass is mobile and can be separated; the addition of water and stirring produces a diluted UNCD suspension, which becomes thickened again to the above degree. So, the value of 5–7 mass % for the thickened layer appears to be a characteristic parameter. Physically, this fact can be interpreted as follows; at this UNCD concentration in the bottom layer, water appears to be in the region where the UNCD particles exert their structuring effect. As a result, water forms hydrospheres that firmly envelope single particles or their aggregates that are held together by their near-range fields. It seems that the crucial role in the transfer of this structuring effect is played by ionic and hydrogen bonds. The mechanism of formation of primary hydrospheres is quite likely to determine the degree of further aggregation of densely enveloped particles into a larger complex

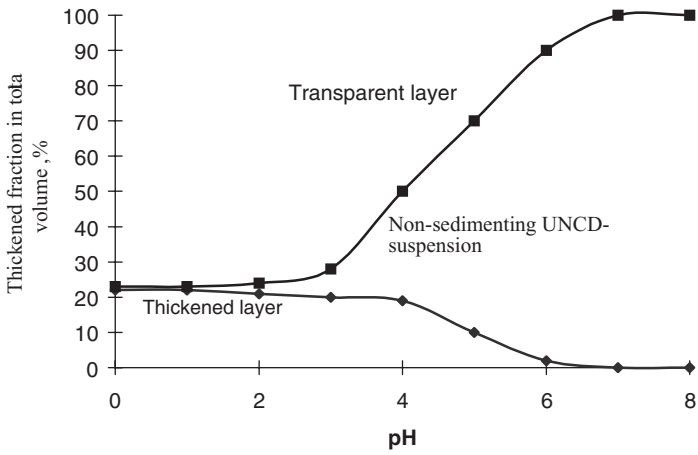

Figure 11.5 The stratification of UNCD suspension during sedimentation as a function of the medium pH. The sedimentation time is 24 hours; the initial UNCD concentration is 1%. Transparent layer is an intermediate layer between the residue and the clear water layer. Clear water volume is the balance in the total volume.

with a common outer hydrosphere, which then behaves as a single large particle. This has been observed in acidic media at pH < 2 and in alkaline media at pH > 8. This process depends insignificantly on the concentration of acids or alkaline reagents at these pH values.

In the absence of foreign impurities, UNCD particles in an aqueous suspension are known to possess a negative surface charge because of a large amount of oxygen-containing polar groups, primarily hydroxylic and carboxylic. But in strong acid solutions, for example, nitric acid, the UNCD surface acquires a positive charge due to the chemical and physical sorption of hydroxonium ions.

As the concentrations of dissolved ammonia or nitric acid become lower with washings, which can be reliably controlled from the pH values, the bottom layer density becomes lower and the interface becomes smeared (Fig. 11.5). The latter effect is due to a decreasing amount of the electrolyte (acid, alkali, or salt) in the suspension during the washing. This results in a partial disintegration of large UNCD associates, with the residual ions being primarily accumulated in the hydrospheres. Visually, this is observed as a smaller degree of thickening and as interface smearing.

As the strong acid or alkali concentration decreases further during washing, the associates nearly totally disintegrate. Eventually, the system returns to the state of water-solvated UNCD aggregates but the penetration of the solvent in the hydrospheres around the aggregates is much less

pronounced. The visually observable effect is known as UNCD "floating" (Fig. 11.5). The use of centrifugation speeds up the process of UNCD aggregation (to 12–14% at pH < 2) but this is effective only for strongly acidic media. At a pH close to 7, the centrifugation efficiency drops, and the floated suspension cannot be clarified completely. The experience of using ultracentrifuges at Russian production plants has demonstrated their low efficiency because of frequent damage to this costly equipment in strongly acidic media, eventually making the UNCD purification process and the final product too costly.

Following the fourth water washing of acidic UNCD (the UNCD layer–pure water ratio is maintained constant at 1 : 4), the nitric acid concentration in the suspension is brought to 0.18–0.25 mass % at pH = 1.8–2.0; after the fifth washing, the acid concentration is in the range 0.07–0.10 mass % at pH = 2.2–3.0. Further washing is considered to be unreasonable because the suspension begins UNCD floating, the precipitation time increases, and the productivity drops. In order to control the floating effect at the pH values of 1.5–2.5, it is better to neutralize the residual acid in the solution and on the UNCD particles by using ammonia water to change abruptly the medium pH from acidic (the residual nitric acid in the suspension is 0.1–0.3 mass %) to slightly alkaline (pH = 9–10). Even at pH = 10, the excess ammonia water in the suspension is only 0.025 mass %.

The treatment of a UNCD suspension with ammonia water has the following advantages:

(1) Ammonium salts of nitric and nitrous acids dissolve well in water and can be easily removed (by one or two washings) together with an upper transparent layer of water.
(2) The excess ammonia water can be easily removed as a gas.
(3) Possessing the smallest ionic radius among alkaline reagents, NH_4^+ readily penetrates into transient pores and micropores of the UNCD aggregates, thereby neutralizing the traces of mineral acids there.

A weakly alkaline reaction in the presence of excess ammonia water and ammonium salts in the suspension (electrolyte) provides fairly fast stratification (with two or three washings) and the UNCD layer thickening to ~8 mass % and, sometimes, even to 12 mass %. Nevertheless, no chemical treatment or even a post-treatment of well-washed UNCD is capable of reducing radically the amount of nitric oxides present in the transient pores and micropores. This can be done, together with a simul-

taneous decrease in the UNCD aggregate size, by heating weakly acidic suspensions of UNCD neutralized with ammonia water, to a temperature range of 200–240 °C for 30 minutes.[25] The following processes occur in such a medium at high temperature and pressure:

(1) The salts produced on the UNCD surface, mostly NH_4NO_3 and NH_4NO_2, readily diffuse into the aqueous solution.
(2) Most of the NH_4NO_3 and NH_4NO_2 decompose at 200–240 °C to produce gaseous products and water, as in reactions (11-4) and (11-5) below. Nitric monoxide formed in reaction (11-4) decomposes further to give molecular nitrogen, as in reaction (11-6); nitric oxides contacting excess ammonia water in reaction (11-7) give nitrogen and water:

$$NH_4NO_3 \rightarrow N_2O + 2H_2O \qquad \text{Eq. (11-4)}$$
$$NH_4NO_2 \rightarrow N_2 + 2H_2O \qquad \text{Eq. (11-5)}$$
$$N_2O \rightarrow N_2 + 0.5O_2 \qquad \text{Eq. (11-6)}$$
$$N_2O_3 + 2NH_3 \rightarrow 2N_2 + 3H_2O \qquad \text{Eq. (11-7)}$$

(3) Due to fast and violent gas release, the UNCD aggregates of 350–500 nm in size break up to give smaller aggregates of 10–100 nm and harmless products – nitrogen and water.
(4) Nitric oxides are desorbed from the UNCD quickly and nearly completely, especially from the inner pores. When hydrolyzed in water, they produce nitrate and ammonium nitrate (in excess ammonia water). We have noted above that nitric oxides adsorbed by the UNCD surface resist removal, especially from micropores, during a conventional water washing even at high temperatures.
(5) After the suspension is cooled down and then washed two or three times in water to remove the residual ammonium salts and ammonia water, the product obtained represents a colloid-stable, highly concentrated, aqueous UNCD suspension. The storage time of such a suspension is practically unlimited, and its properties remain unchanged. Besides, the suspension has a low viscosity and a high mobility in spite of the UNCD concentration of 10–12 mass %, making it suitable for various technological applications.

(6) The increased desorbtion of organic and inorganic impurities from the UNCD surface during the aggregate disintegration in ammonia water at high temperature and pressure raises the nanodiamond purity considerably, sometimes to 99.5 mass %.

For example, the total content of incombustible impurities in a UDD-STW batch washed seven times was found to be 0.95 mass % (Table 11.3). A UDD-TAH batch neutralized with ammonia water to pH = 7.3 and then subjected to thermolysis at 230 °C and two water washings is seen to have twice as low an incombustible element (0.4 mass %) content (Table 11.3). These results were obtained at the *Diamond Center*, St. Petersburg, Russia. Since the UNCD suspension contains excess ammonia water after thermolysis (pH > 7) and there is a certain amount of ammonium salts, it is sedimentationally unstable, which facilitates further water washings (two or three washings).

A disadvantage of this thermolytic procedure is that a complete decomposition of ammonium salts requires the addition of an accurately calculated amount of ammonia water to reach pH = 7.0–7.5. It is this pH range that provides an optimal decomposition of the salts. If the suspension pH is higher than 8, some amount of salts does not decompose to produce gases. It is likely that the UNCD surface containing various functional groups exerts an inhibiting effect on the decomposition of ammonium salts, because they have been found to decompose completely in the absence of UNCD at pH > 8.

However, no matter what thermolytic procedure is used and what amount of ammonium salts is present, the latter can be readily removed together with excess ammonia water by two or three washings until pure UNCD is floated. Such a suspension can be stored for years, but its pH gradually decreases to 4.5, corresponding to the pH value for pure UNCD. Moreover, the UNCD particle size increases from 10–100 nm to 150–300 nm during storage.

To be able to use UNCD in various "subtle" applications, such as superfinish polishing, electronics, oil colloidal composites, etc., it is extremely important to make UNCD aggregates smaller than 100 nm in size. This can be achieved by diluting the suspension considerably, to a UNCD concentration less than 0.1 mass %, which is impractical in an actual industrial application. Ultrasonic treatment is known to reduce the

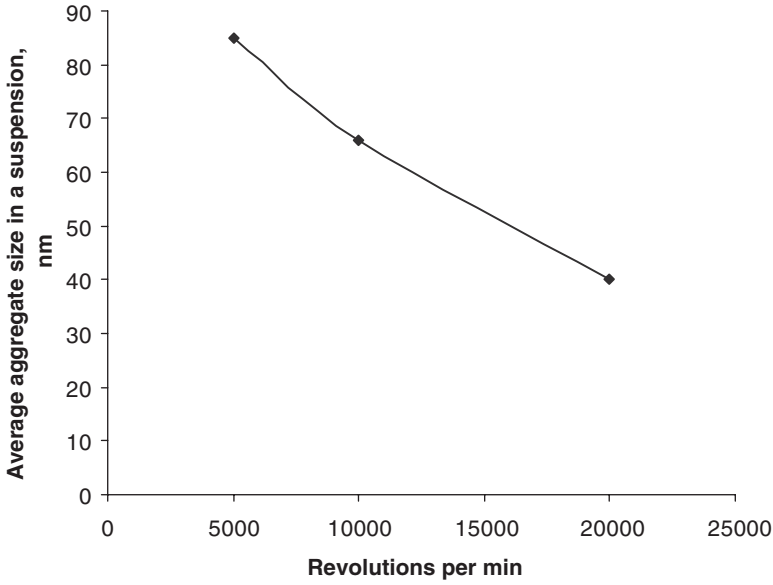

Figure 11.6 The average size of UNCD aggregates in the sedimentation-stable fraction of a suspension (concentration ~0.7 mass %) versus the centrifugation rate.

size of UNCD aggregates but for a short time only, whereas ultracentrifugation can produce a stable unsedimentable suspension in a concentration of about 0.7 mass % by centrifugation of a 3.5 mass % suspension, and the average aggregate size in the 0.7% suspension varies from 40 to 85 nm, depending on the centrifugation rate (Fig. 11.6).

The most effective way of UNCD industrial purification available at present is to treat the initial diamond with an aqueous solution of nitric acid. The procedure involves two stages. The initial DB is first treated with 50–99% nitric acid at 80–180 °C and then with 10–40% nitric acid at 220–280 °C.[23] The purification does not represent a mere mechanical separation but rather involves highly energetic chemical reactions, providing selective breaking of the C—C bonds which are not inherent in diamond. This is normally done by selective oxidation. As a result, the UNCD represents a product essentially different from the initial material. So it can be stated that the purification stage is crucial to the development of consumer properties of nanodiamond. At this stage a variety of UNCD modifications can be created. All problems associated with the designing, management, and maintenance of the whole autoclave reactor unit

continuously operating at high pressure had been solved during pilot production. Although this technology can, in principle, process DB with any UNCD content, the most cost-effective purification process is that with DB containing not less than 30% of UNCD.

Of equal importance is the content of incombustible (mineral) impurities in the DB. The point is that this purification technology allows a reduction of the non-diamond (graphite-like and organic material) content by dozens or even hundreds of times. However, any chemical treatment is capable of reducing the amount of incombustible impurities only by 5–8 times, on the average. Thus, a reasonable amount of incombustible impurities in the DB should not exceed 5%. The amount of incombustible impurities in the DB is proportional to that encapsulated in the primary indestructible UNCD aggregates of 10–60 nm in size, which are hardly accessible, and often just inaccessible, to oxidizing and dissolving reagents.

Thus, apart from DB, the above technology uses industrial nitric acid in a concentration of 50–98%, air, and distilled water. The final product of purification is a thickened, stabilized UNCD suspension in distilled water (a concentrated solution or paste) or a dry powder. The UNCD properties can be modified during the technological cycle to meet the prospective application requirements. This means that the assortment of commercial products can be broadened.

The UNCD purification process described above is illustrated in Fig. 11.2 together with the process flow. Generally, the technology includes the following operations:

(1) *The preparation of DB* includes grinding, averaging, removal of mechanical inclusions, magnetic separation, and drying to a definite humidity. These operations condition the raw material to meet the purification requirements.
(2) *The preparation of aqueous solutions of nitric acid*, which are made from (a) fresh concentrated (about 50%) acid, (b) acid of the absorption stage, (c) circulation acid of the concentration stage. This is done in standard mixers normally used for this purpose. The volume and number of mixers and storage vessels may vary with the nitric acid recycling technology, the amount of material to be processed, and the mixing cycle.
(3) *The preparation of mobile homogenized DB suspensions* in aqueous solutions of nitric acid is an important stage

providing the basis for a continuous process under pressure. Simultaneously, the DB is separated from mechanical inclusions and residual polymers by multistage filtration. The details of these operations depend on the production technology of the initial DB.

(4) *Thermal oxidation of the DB suspension* in a continuous mode under pressure is the key stage. Special equipment and techniques have been designed for triggering, testing, maintenance, emergency shut-down, and scheduled outage. The oxidation is carried out under equilibrium pressure of 8–10 MPa in a reactor cascade under graded temperature conditions up to 240 °C. During the treatment, the carbon matrix is selectively etched due to the involvement of kinetic factors to release unoxidizable UNCD particles, the non-diamond carbon is gasified, the organic fragments of impurities are subjected to destructive decomposition, and the available metals are transformed to water-soluble salts. The necessary temperature conditions are maintained by combining a forced external heating of each reactor and an internal redistribution of heat flow using the phase transition heat and the velocity gradients of the liquid and the gas.

(5) *The separation of oxidation products* is a transient stage from the application of high-pressure reactors to that of normal-pressure reactors. The throttling of the gas–liquid flow coming from the reactor unit is followed by the separation of gaseous products (destruction products and nitric oxides). These are subjected to re-oxidation by air and to acidic absorption of nitric oxides. The gases can be separated in one of two ways: under a pressure of 0.2–0.6 MPa to increase the absorber efficiency or just by rarefaction to simplify the technology.

The acidic UNCD suspension separated from dissolved gases is allowed to sediment and stratify to give a thickened UNCD suspension near the vessel bottom and a layer of transparent nitric acid above. The latter has a concentration of 20–40% and is to be returned for recycling. In this way, from 50 to 75% of the initial nitric acid can be reused. The thickened suspension is further subjected to repeated washing from acids and water-soluble impurities.

(6) *The nitric acid cycle* includes a multistep re-oxidation of nitric oxides by air oxygen to nitric tetraoxide, and absorption of higher oxides by water or diluted nitric acid to produce absorption acid in a 40–50% concentration. Its deficit is compensated by fresh concentrated nitric acid. Generally, the higher is the concentration of the fresh acid, the easier it is to arrange closed cycles of the acid turnover and to support the water balance. It is practically possible to return up to 75% of the initial amount of nitric acid.

(7) *The UNCD washing from the acids* is made by de-ionized water, using a substitutional procedure in a countercurrent cascade mode. This is done at normal and elevated temperatures (up to 80 °C). This procedure can be supplemented with neutralization of the acidic UNCD suspension with aqueous ammonia, followed by thermolysis.

(8) *Wastes processing* includes the following operations. The air flow from the acid absorption columns, containing small amounts of nitric oxides and nitric acid vapor, is washed with aqueous alkali solutions. After the washing, the latter are neutralized. The aqueous solutions of nitric acid containing small amounts of water-soluble metal nitrates, mostly iron nitrates, can be neutralized by any suitable alkali reagents. Besides, one can reuse for this purpose the alkali solutions of the gas purification stage. The neutralized water wastes represent a diluted solution of neutral salts. These wastes can be additionally purified by using the concentration technique to separate the salts, the adsorption methods, etc. The choice of a particular technique is determined by the ecological requirements at the production site and should be optimized in terms of their cost-effectiveness. If one knows the chemical composition of the waste flows, the problem can be dealt with in a conventional way.

(9) *The production of normalized, stabilized UNCD suspensions in distilled water* is to make standard UNCD batches with a fixed composition. The final commercial UNCD product may represent either an aqueous suspension or a water-organic medium.

(10) *The production of dry homogeneous UNCD powders* is practiced widely, although their storage inevitably leads

to UNCD aggregation, due to which some of the active surface is lost. Still, this commercial product is popular because UNCD is largely utilized as powder; further, it is convenient for storage and transportation.

To conclude, the method of high temperature UNCD oxidation in a nitric acid medium is, at present, the most effective method of UNCD purification. It provides the highest and most stable purification parameters, is easily adaptable to a large- or small-scale production, and is well studied.

11.2.2 UNCD Modification

In contrast to classical diamonds, nearly every chemical and, sometimes, physical treatment of UNCD leads to a change in their properties. The reason for such a high sensitivity to external effects lies in the complex structure of a UNCD particle (cluster) and in its ability to form multilayer aggregates, following the laws of fractal physics, in response to practically any effect. Since UNCD manufacturers use various modifications of detonation synthesis and a great variety of chemical treatments, it is natural that the properties of the final product should differ considerably. Moreover, when UNCD is extracted by dry techniques, some of its unique characteristics are irreversibly lost. A subsequent introduction of a dry UNCD powder in a liquid medium and the use of various dispersion methods (ultrasound, cavitation, mechanical disintegration) can provide fairly stable suspensions but the initial UNCD properties cannot be totally recovered. The application of such secondary suspensions has appeared to be ineffective in electrochemical plating in metal–diamond mixtures or for the final polishing of electronic and optical devices.

UNCD modified under different conditions[26–29] has been studied by a differential thermal annealing method. A noticeable increase in the sample mass occurs during heating up to 373 K if the sample was pre-modified by water vapor and methane. However, the sample mass practically did not change if the sample was modified by carbon dioxide or its mixture with methane. The sample mass was found to decrease at the temperatures of 575–752 K if the UNCD was pre-modified by nitrogen and methane, with the decrease being greater for the former. At temperatures above 725 K, the sample mass steadily decreased. The thermograms showing a gradual temperature rise exhibiting a few thermal effects – a broad endothermal peak below 773 K, two broad exothermal peaks at

773–1120 K, and an endothermic peak at 1130–1225 K. The peak shape and the respective temperature markedly vary with the modifying gas used.

These findings indicate that UNCD pre-modification affects its stability in air. After the modification treatment with water vapor, oxidation begins at 675 K, while after the treatment with a mixture of NH_4 and CO_2 it starts only above 775 K. One can conclude from these data that the UNCD surface groups may undergo chemical transformations and even oxidation at 573–773 K.

Some researchers have studied the effect of modified UNCD on heterogeneous (the gas-phase oxidation $CO \rightarrow CO_2$) and electrochemical (H_2 oxidation) catalysis.[30] In the former, the measure of the catalytic activity was the temperature at which CO totally transformed to CO_2. The UNCD surface was modified by thermal and electrochemical treatments, as well as by depositing trace amounts of metallic palladium (Pd). The two-step annealing was performed in a hydrogen atmosphere. The electrochemical treatment was carried out in a 0.1 N solution of sulphuric acid and in a 1 N solution of potassium hydroxide. The surface activation with trace amounts of Pd was made by contact displacement of its salts from the solution. It was found that the oxidation of CO to CO_2 on the initial, unmodified UNCD surface started at 230 °C. The maximum transformation occurred at 380 °C and was as large as 80%. When UNCD was modified electrochemically in sulphuric acid, the oxidation onset shifted from 230 to 80 °C and was 30–40% in this temperature range. On the contrary, the electrochemical modification in an alkaline solution led to the passivation of the diamond surface and an incomplete transformation of CO to CO_2. The deposition of Pd in amounts less than 0.001 mass % remarkably decreased the total transition temperature, from 300 to 180 °C. The authors believe that the CO to CO_2 transition is greatly affected by the ratio of various forms of oxygen present on the diamond. The largest contribution to this process is thought to be made by atomic oxygen. The UNCD treated electrochemically in sulphuric acid at temperatures of 20–100 °C exhibits a peak of atomic oxygen desorption, indicating that the diamond surface can be saturated with atomic oxygen by using this method of treatment. However, the amount of atomic oxygen desorbed by the diamond exposed to an alkaline solution is found to be much smaller. Its amount on Pd-activated UNCD powders is much larger than on the initial samples. So the authors of ref. [30] conclude that palladium catalysis saturates UNCD with atomic oxygen, which, in turn, accelerates the catalytic oxidation of CO to CO_2. A major source of atomic oxygen is likely to be water vapor. It appears that the amount of water actually des-

orbed by the diamond samples electrochemically treated with diluted sulphuric acid is 1.5 times larger than on the initial sample. The activation with trace amounts of Pd increases the content of actually desorbed water by a factor of 6.

Another important result is that the rate of hydrogen oxidation with a diamond catalyst modified in diluted nitric acid is 1.6 times higher than for vanadium and tungsten carbides on the same specific surface. Annealing of UNCD in a hydrogen atmosphere remarkably reduces the amount of physically adsorbed atomic hydrogen, while the amount of chemisorbed atomic hydrogen increases considerably. A two-stage annealing essentially increases the amount of hydrogen chemisorbed by UNCD. The process of hydrogen oxidation seems to be accelerated by both chemisorbed hydrogen and atomic oxygen. It is clear from these data that modified and Pd-promoted nanodiamonds are promising materials for producing catalysts for CO oxidation and electrodes for low-temperature heaters.

Unlike classical diamond, UNCD particles are hydrophilic and can, in principle, produce stable aqueous suspensions. But this ability of UNCD is a natural obstacle to making stable suspensions with non-polar media widely used, for example, in polymer chemistry. Therefore, a chemical modification is necessary to increase the hydrophobic characteristics of nanodiamonds.

An effective way of blocking active functional groups on solids is a sililization reaction. The nature of the resultant surface is determined by the attached tri-methylsililyl groups that make the surface hydrophobic and remove adsorbed water and hydroxyl groups from it. This modification technique makes the UNCD dispersivity in a non-polar organic liquid comparable to that in an aqueous medium.[31] Sometimes, UNCD particles in non-polar media can be stabilized by the attachment of double-bonded groups if tri-methylchlorosilane in a sililizing mixture is replaced by di-methylvinylchlorosilane. This kind of modification produces a paradoxical and poorly predictable phenomenon – a high UNCD dispersivity in polar media. For example, the average diameter of particles decreases from 23 nm in water to 15 nm in ethylacetate. The research into the mechanisms underlying this strange behavior has yielded a model of UNCD particles stabilized by the hydrogen bonds of various functional groups (Fig. 11.7). This model considers a UNCD particle as a fractal aggregate. Provided that an aggregate can be approximated by a spherical particle, the expression for the effective radius of a such particle is written as $R = r_o N^{1/d_f}$, where r_o is the effective radius of a primary UNCD cluster in nanometers, N is the number of primary clusters in the aggre-

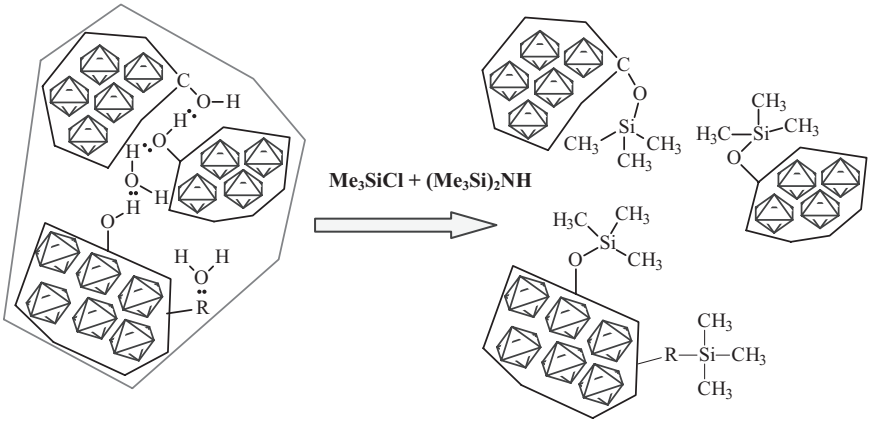

Figure 11.7 Chemical modification of UNCD by sililization: R, a functional group containing an "active" proton (—OH; —NH_2; —COOH, etc.).

gate, and d_f is the fractal dimensionality. The aggregate is stabilized by the hydrogen bonds of different functional groups on the surfaces of the primary clusters forming an aggregate and by zeolite water molecules (Fig. 11.7). Sililization breaks the stabilizing bonds, thereby changing the polydispersity characteristics. The fractal model of a UNCD aggregate implies theoretically the possibility of disintegration into N initial particles. However, the sililization reaction experiences certain steric problems, so that only loosely packed aggregates can disintegrate. Then the system relaxes to a stable state.

An alternative way of making the UNCD surface hydrophobic is to treat a dry UNCD powder with commercial elastomers, such as polydimethyl siloxane or polyisoprene in a benzene solution.[32] It has been suggested that the adsorption of hydrophobic polymer chains by UNCD particles can stabilize the suspension. Indeed, this treatment increases the UNCD dispersivity and the suspension stability in an organic solvent. Polyisoprene has proven to be the most suitable modifier, and the use of this polymer provides a suspension with a predominant particle size of ~300 nm. Such a suspension remains stable to sedimentation for at least 10 days.

The above way of treating purified UNCD with ammonia, followed by heating the suspension to 200–240 °C, is another classical approach to UNCD modification. The nanodiamond surface becomes enriched with amino groups, the suspension stability increases together with improvement of its technological characteristics, and the average aggregate size

decreases to 10 nm. It is this modification procedure that provides suspensions most suitable for electrochemistry, for the production of abrasive and other composites, and for application in medicine and biology. This product (trademark UDD-TAH) is a versatile, high-quality material.

It should be noted that even the way of extracting a dry UNCD powder from an aqueous suspension can affect its quality. To illustrate this, UNCD powder obtained by water evaporation from the suspension at high temperature produces a densely aggregated product which is hard to disperse (trademark UDD-STP). But if its aqueous suspension is allowed to freeze at −15 °C or −18 °C, after defrosting, the UNCD particles aggregate into small porous "balls" of ~5 mm diameter. These balls can be readily separated, dried, and milled into a finely dispersed powder (trademark UDD-SF). Powders of UDD-STP and UDD-SF have been tested by different consumers in several countries. The results indicated that UDD-SF is a preferable material for polishing and creating oil and polymer composites because it is easier to disperse in such media and it is more stable to external effects.

In conclusion, on a practical note, before considering any particular application of detonation nanodiamonds, it is important to figure out details of the method of synthesis by a particular vendor and, most importantly, methods of purification and possible modification.

References

1. Dolmatov V.Yu., Gubarevich T.M., Pyaternikov V.F., Marchukov V.A., and Sushchev V.G. Synthesized diamond-containing material. Patent #2046094, Russian Federation, C 01 B 31/04; 26 July 1995: publ. 20 October 1995, Bull. No. 29.
2. Gubarevich T.M., Kostiukiova N.M., Larionova I.S., and Poleva L.I. Adsorption properties of ultradisperse carbon materials. In: Proceedings of the V All-Union Meeting on Detonation, Krasnoyarsk, 1991, Vol. 1, pp. 112–116 (Russian edition).
3. Aleksensky A.E., Baidakova M.V., Vul' A.Ya., and Siklitzky V.I. The structure of a diamond cluster. *Fizika Tverdogo Tela*, 1999, Vol. 41, No. 4, pp. 740–743 (Russian edition).
4. Dolmatov V.Yu. and Fudjimura T. Nanodiamonds. *Superhard Materials*, 2001, No. 6, pp. 31–37.
5. Mazanov V.A. Macrokinetics of the retention of condensed carbon and detonation diamond in a hermetic explosion chamber. *Physics of the Solid State*, 2004, Vol. 46, 4, pp. 629–635.
6. Dolmatov V.Yu. and Veretennikova M.V. A method of nanodiamond production. Patent #2230702, Russian Federation, C 01 B 31/06: publ. 20 June 2004.

7. Kozyrev N.V., Balyasov S.E., Kazakov A.A., and Likhtetskaya N.G. An explosive charge for detonation diamond synthesis. Patent #1826958, Russian Federation, C 01 B 31/06: publ. 7 July 1993, Bull. No. 25.
8. Kolomichuk V.N. and Malkov I.Yu. A study of ultradisperse diamond synthesis in detonation of explosive mixtures. *Fizika Goreniya i Vzriva*, 1993, Vol. 29, No. 1, pp. 120–128 (Russian edition).
9. Petrov E.A., Sakovich G.V., and Brylakov P.M. Conditions for diamond preservation during detonation synthesis. *Reports of Academy of Sciences of USSR*, 1990, Vol. 313, No. 4, pp. 862–863 (Russian edition).
10. Misonochnikov A.L. and Rumyantsev B.V. A method of ultradispersed diamond production. Patent #2036835, Russian Federation, C 01 B 31/06: publ. 9 July 1995.
11. Korobov D.Yu. and Korobov Yu.A. A disperse diamond-containing composition and its production technique. Patent #2049723, Russian Federation: publ. 10 December 1995, Bull. No. 34.
12. Stavrev S.Y., Lazarov S.B., Stoev K.L., Markov L.G., and Ivanov V.I. Method for production of ultradispersed diamond. US Patent 5,353,708, 1994.
13. Vyskubenko B.A., Danilenko V.V., Lin E.E., Mazanov V.A., Surova T.V., Sukharenko V.I., and Tolochko A.P. The effect of scale factors on the size and yield of detonation diamonds. *Fizika Goreniya i Vzriva*, 1992, Vol. 28, No. 2, pp. 108–109 (Russian edition).
14. Dolmatov V.Yu., Zharkevich V.Yu., and Postnov V.N. Warheads for diamonds. *Double Technologies*, 1998, No. 3, pp. 71–78 (Russian edition).
15. Postnov V.N., Glushchak B.P., Matveev V.N., Trusov Yu.D., Emelyanov G.I., Lunin V.V., Kriukov B.P., and Dolmatov V.Yu. A combined utilization of conventional warheads, weapons, and military machinery by the "FORPOST" technology. *Double Technologies*, 2002, No. 1 (18), pp. 35–48 (Russian edition).
16. Putyatin A.A., Nikolskaya A.V., and Kalashnikov Ya.N. Chemical methods of diamond extraction from the synthesis products. *Superhard Materials*, 1982, No. 2, pp. 2–28.
17. Pavlov E.V. and Skryabin Yu.A. A method and device for non-diamond carbon removal. Patent #2019502, Russian Federation, C 01 B 31/06: publ. 15 September 1994, Bull. No. 17.
18. Filatov L.I., Chukhaeva S.I., and Detkov P.Ya. A method of ultradisperse diamond purification. Patent #2077476, Russian Federation, C 01 B 31/06: publ. 21 March 1991, Bull. No. 11.
19. Gubarevich T.M., Sataev R.R., and Dolmatov V.Yu. Chemical purification of ultradisperse diamonds. In: Proceedings of the V All-Union Meeting on Detonation, Krasnoyarsk, 1991, Vol. 1, pp. 135–139 (Russian edition).
20. Shebalin A.I., Molokeev V.A., and Sakovich G.V. A method of diamond extraction from a diamond-containing charge. International application PCT/SU WO 90/00169, submitted 18 July 1988.
21. Dolmatov V.Yu. and Sushchev V.G. A method of extraction of synthetic ultradisperse diamonds. Patent #1828067, USSR, C 01 B 31/06: publ. 25 March 1986.

22. Dolmatov V.Yu., Sushchev V.G., and Gubarevich T.M. A method of diamond powder purification from surface impurities. Patent #1658558, USSR, C 01 B 31/06: publ. 19 July 1988.
23. Dolmatov V.Yu., Sushchev V.G., Marchukov V.A., Gubarevich T.M., and Korhzenevsky A.P. A method of extraction of synthetic ultradisperse diamonds. Patent #2109683, Russian Federation, C 01 B 31/06: publ. 27 April 1998, Bull. No. 12.
24. Gubarevich T.M., Dolmatov V.Yu., Pyaterikov V.F., and Larionova I.S. Chemical purification of ultradispersed diamonds by hydrogen peroxide. *Journal Prikladnoi Khimii*, 1992, Vol. 65, No. 11, pp. 2512–2516 (Russian edition).
25. Fujimura Tadamasa, Sone Masato, Dolmatov Valeri Yu, and Shiozaki Shigeru. Stable aqueous liquid of finely divided diamond particles. Metallic film containing diamond particles and method of producing the same. Patent #1 288 162 A2 EP. IPC Cl C 01 B 31/06: publ. 5 March 2003, Bull. 2003/10.
26. Dolmatov V.Yu. Ultradisperse diamonds produced by detonation synthesis: properties and applications. *Russian Chemical Reviews*, 2001, Vol. 70(7), pp. 607–626.
27. Kulakova I.I., Dolmatov V.Yu., Gubarevich T.M., and Rudenko A.P., Chemical properties of detonation-synthesized ultradispersed diamonds. *Superhard Materials*, 2000, No. 1, pp. 42–48.
28. Dolmatov V.Yu. *Detonation synthesis ultradispersed diamonds.* St. Petersburg, St. Petersburg State Polytechnic University, 2003 (Russian edition).
29. Kulakova I.I. Surface chemistry of nanodiamonds. *Physics of the Solid State*, 2004, Vol. 46(4), pp. 636–643.
30. Bogatyreva G.P., Marinich M.A., Ishchenko E.V., Gvyazdovskaya V.L., Bazaliy G.A., and Oleinik N.A. Application of modified nanodiamonds as catalysts of heterogeneous and electrochemical catalyses. *Physics of the Solid State*, 2004, Vol. 46(4), pp. 738–741.
31. Neverovskaya A.Yu., Voznyakovsky A.P., and Dolmatov V.Yu. Structure of the dispersive medium and sedimentation resistance suspensions of detonation nanodiamonds. *Physics of the Solid State*, 2004, Vol. 46(4), pp. 662–664.
32. Voznyakovsky A.P., Dolmatov V.Yu., Klubin V.V., and Agibalova L.V. Structure and sedimentation stability of suspensions of detonation-synthesized nanodiamonds in nonaqueous liquids. *Superhard Materials*, 2000, No. 2, pp. 58–65.
33. Lyamkin A.I., Petrov E.A., Ershov A.P., Sakovich G.V., Staver A.M., and Titov V.M. Diamond production from explosives. *Reports of Academy of Sciences of USSR*, 1988, Vol. 302, No. 3, pp. 611–613 (Russian edition).
34. Istomin Yu.A. and Istomin V.Yu. A way of diamond production. Patent #1644996, USSR, MKH C 01 B 31/06: publ. 30 April 1991.
35. Savvakin G.I. Structural defects formed in UDD in detonation of carbon-containing explosives and their effect on diamond caking under pressure. In: Proceedings of the V All-Union Meeting on Detonation, Krasnoyarsk, 1991, Vol. 2, pp. 254–258 (Russian edition).

12 Characterization and Physical Properties of UNCD Particles

Alexander Ya. Vul'

Ioffe Physico-Technical Institute, St. Petersburg, Russia

Introduction

Detonation synthesis of diamond nanoparticles was discovered in the 1960s but the first reports of laboratory production became available only in 1988 (see, e.g., ref. [1]). In that year, the Russian journal *Transactions of the USSR Academy of Sciences*[2] and the journal *Nature*[3] published papers later cited by many researchers in the area of detonation nanodiamonds. It is quite natural that the focus during the next decade was largely on the details of the production and purification technologies.[1] It was at that time that a group of researchers at the Ioffe Physico-Technical Institute (St. Petersburg, Russia), the author of this chapter among them, reported their first results on nanodiamonds.[4] We believe that a substantial breakthrough in both the production and realization of potential applications of nanodiamonds, beyond their obvious use as a polishing material, was made at the turn of the century. Reports on detonation diamonds became quite common at international meetings, and the first specialized workshops were held in 2003 and 2004,[5,6] followed by the publication of the *Bibliography Index* of this subject.[1] The term *ultra-nanocrystalline diamond* (UNCD) suggested by Dieter Gruen for particles with a characteristic size of a few nanometers was coined during the preparation for the NATO Workshop in 2004.[6]

At present, interest in UNCD is mostly due to the general interest in the development of nanotechnologies, because UNCD can be fully explained by theories in these technologies. This chapter provides an overview of work on the structure and physical properties of UNCD, but it starts with a brief survey of common methods used to characterize this material.

12.1 Methods for Characterization of UNCD Particles

12.1.1 General Remarks

The choice of methods for characterization of UNCD particles is based on the need to know: (1) the average size of a single UNCD cluster and the size distribution of UNCD clusters; (2) the sp^2/sp^3 ratio of hybridized carbon atoms in a cluster, or the degree of chemical purification of diamond from the graphite phase; (3) the types of impurities present in the cluster bulk and on its surface.

Most of the studies of these problems have been performed on powders and very few on layers grown by particle deposition from a suspension, using evaporation or electrophoretic techniques.[7,8] An essential obstacle to this approach is that any ultradispersed powder, including that of UNCD, is made up of aggregates of about 1 micron in size, rather than of individual nanoparticles which tend to cluster due to their high surface energy. In an aqueous suspension, UNCD particles form aggregates varying from a few hundred to several thousand nanometers, depending on the pH value. A dry UNCD powder contains clusters hundreds of nanometers in size.[9–11] We will discuss the problem of aggregation in more detail at the end of this chapter.

The problems outlined above and the characteristic size of a UNCD cluster have determined the types of methods used for their analysis, methods which are applicable to nanoclusters in general. We will briefly describe these methods and the results obtained.

12.1.2 X-ray Diffraction

A typical diffraction pattern of a UNCD powder based on the data from refs. [12] and [13] is presented in Fig. 12.1. At large Bragg angles, all UNCD samples produce the same diffraction patterns, and some differences can be observed only in the small-angle region. This observation favors identical long-range order of the crystal structure of the nanoclusters. The broad, symmetric diffraction peaks at the angles $2\theta_{Br} = 43.9°$, 75.3°, and 91.5° well fitted by the Lorentzians are due to the (111), (220), and (311) reflections from a diamond-type lattice with $a_0 = (3.565 \pm 0.005)$ Å. The average cluster size defined by the Selyakov–Scherrer expression

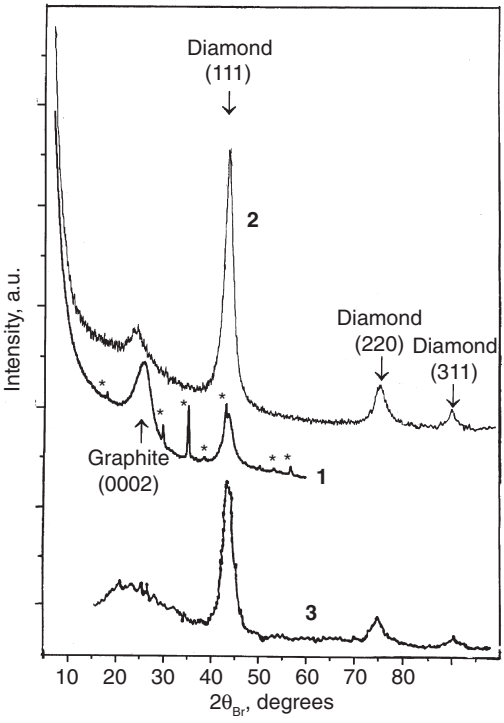

Figure 12.1 X-ray diffractogram of detonation soot (1) and detonation nanodiamond (2,3) after chemical purification of the soot. (1) and (2) are produced by "dry" synthesis from a mixture of TNT and hexogene (60/40) in CO_2,[68] (3) produced by "dry" synthesis in N_2 from a mixture of TNT and hexogene (50/50).[13] (2) chemical purification in nitric acid, (3) chemical purification in perchloric acid. The asterisks identify the Fe_3O_4 diffraction maxima.

from the line half-widths of the three diffraction maxima is found to be $L = (45 \pm 5)$ Å. The coincidence of the average cluster size derived from different diffraction peaks implies that the line broadening is primarily due to small size rather than to internal strains.

Our experiments on various groups of UNCD samples, produced under somewhat different conditions of sp^2 purification and at different times, have shown that the large-angle diffraction patterns are practically identical and that the coherent scattering region is close to 4 nm. This fact is important for creating a UNCD cluster model.

12.1.3 Small-Angle X-ray Scattering

It seems that the fractal character of UNCD clusters was first pointed out in ref. [14]. This was followed by a detailed analysis of the clusters' fractal structure and the effects of various technological conditions on the structure in refs. [15] and [16].

The fractal structure of nanoclusters was studied by conventional techniques in ref. [17]. The authors analyzed the dependence of the small-angle X-ray scattering (SAXS) amplitude I on the wave vector q. In the range $0.036 < q < 0.8\,\text{Å}^{-1}$, corresponding to scattering angles $0.5° < 2\theta_{Br} < 10°$, the peak position in the $I(q)$ curve allows determination of the typical size L of a scatterer, and the slope of the curve provides its fractal dimensionality D. In the classical theory,[18] assuming the scatterer to have a smooth surface, the scattering amplitude $I(q)$ is defined by the power dependence on the wave vector q with an integer power index:

$$I(q) \sim q^{-\alpha}$$

where $q = 4\pi/\lambda \sin\theta_{Br}$ and λ is the wavelength of the scattered radiation. For a scatterer with a smooth spherical surface, the power index α is equal to 4, while for a scattering sphere it is 3.[18,19] Therefore, $\log I(q)$ must be a linear function, $\log(q)$. One can see from Fig. 12.2, which shows the typical dependence for UNCD, that the curves are well approximated by a power function in the range $0.2\,\text{A}^{-1} < q < 0.8\,\text{Å}^{-1}$ but that there is a peak at $q \leq 0.2\,\text{Å}$.

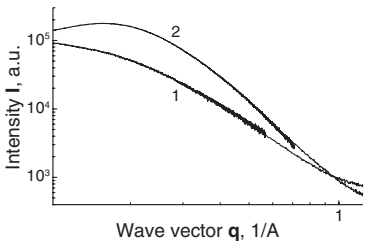

Figure 12.2 Small-angle X-ray scattering curves for detonation nanodiamonds of "dry" and (1) "wet" (2) syntheses after chemical purification in nitric acid. (2) after annealing at 720°C in Ar.

Generally, a fractional value of α may be due to a certain cluster size distribution[20] and not only to the fractal nature of the scatter. However, it has been pointed out in refs. [21] and [22] and experimentally observed in ref. [23] that UNCD clusters exhibit a δ-shaped size distribution function with a maximum at 43 Å, which means that fractional α unambiguously indicates the fractal nature of a UNCD cluster. It is known that the power index α for fractal clusters indicates the type of scatterer. If α is in the range 3 to 4, the scatterer is a cluster with a fractal surface, while for α in the range 0 to 3 it

is a "bulk" fractal. For the former, the fractal size is defined by $D = 6 - \alpha$ and for the latter by $D = \alpha$. Nevertheless, the peak position in the $I(q)$ curve does determine the characteristic size of the scatterer, $L \approx \pi/q_{max}$.[24]

The analysis made in refs. [15] and [16] has shown that the $I(q)$ curves become well smoothed in the logarithmic coordinates, allowing the identification of the UNCD fractal type and the fractal dimensionality of its cluster. These data were further used to design a model UNCD cluster (see below 12.2).

12.1.4 Raman Scattering

There are three major features of UNCD Raman spectra that deserve special attention.[4,12,25] First, there is a strong luminescence background produced by the laser radiation. Second, the photon energy of the laser commonly used in Raman spectroscopy ($\lambda = 488$ nm) is close to the resonance energy π–π^* of sp^2-hybridized electrons, so the amplitude of the Raman signal due to the sp^2-phase is significantly higher than that of the sp^3-phase for the same amount of each phase. Finally, owing to the uncertainty relation, the small size of a crystallite removes the restrictions on the involvement of phonons with the wave vector $q \neq 0$ in the scattering process. Let us consider the last two points at length.

It is common knowledge that the Raman spectrum of crystalline graphite has a single narrow band at 1575 cm^{-1}, which is attributed to the plane E_{2g} mode from the Brillouin zone center.[26] On the other hand, sp^3-hybridized carbon representing single-crystal diamond demonstrates a narrow symmetric line at 1332.5 cm^{-1} with a half-width of about 2.0 cm^{-1},[27] which corresponds to the transverse phonon of the F_{2g} symmetry.

The changes in the structure and size of the sp^2-phase are manifested as changes in the Raman spectrum in the vicinity of 1600 cm^{-1}.[28] In particular, microcrystalline graphite shows a broadening and shift of the 1600 cm^{-1} band toward higher frequencies and the appearance of a new band at 1620 cm^{-1}. Moreover, an additional band emerges at 1350 cm^{-1}. The Raman spectrum was also reported to exhibit a broadening and frequency shift of the "diamond" mode (1332.5 cm^{-1}) at the transition from bulk to nanocrystalline diamond.[29]

Figure 12.3 compares a typical Raman spectrum of UNCD powder with those of microcrystalline diamond powder (grain size of 200 μm) and

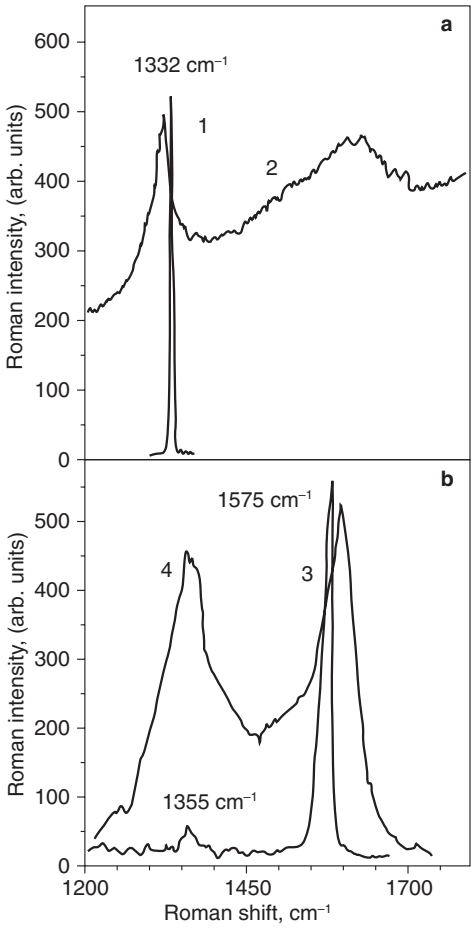

Figure 12.3 Raman spectra of different types of diamond (a) and different types of sp^2-hybridized carbon (b): (1) microcrystalline diamond powder, (2) detonation nanodiamond, (3) pyrolite and (4) activated charcoal ((3) and (4) from ref. [26]).

microcrystalline graphite. One can clearly see the features mentioned above, the broadening and frequency shift of the "diamond" mode, as well as a new band due to microcrystalline graphite. These changes have been interpreted in terms of the violation of the selection rules, arising from the finite size of the crystallites. This fact allows the phonons at high symmetry points located at the Brillouin zone boundary to make their contribution to the Raman spectra.[30]

Indeed, the phonons with wave vector $q > 0$ in bulk (large) crystallites cannot be involved in the photon–phonon interaction because of momentum conservation, $q + \Delta k = 0$.[25] The phonons present in a small crystallite can be considered as a damping wave with a certain effective damping coefficient g. The phonon excitation length (the correlation vibration length) is proportional to g^{-1}. According to the uncertainty principle, the uncertainty in the phonon momentum conservation can be taken to be L^{-1}, where L is the characteristic length limiting the phonon propagation (the phonon correlation length), which is the crystallite size. Therefore, the appearance in the Raman spectra of vibrations with frequencies $\nu(q)$ corresponding to the phonon vectors $0 < q < L^{-1}$ is a manifestation of the size quantization effect also known as phonon confinement.

If translational symmetry is violated further (in nanocrystalline or amorphous graphite), the quasi-momentum conservation principle no longer holds, and the phonons from the Brillouin zone with any wave vector make their contribution to the first-order Raman scattering. For this reason, the Raman spectra of amorphous materials exhibit a vibrational density of states similar to the one-phonon density of states of the crystal.

It seems that a phenomenological evaluation of the correlation length was first suggested in ref. [31]. In this work, the amplitude of the Raman scattering by phonon excitations attenuating along the length L and having dispersion dependence $\nu(q)$ is defined as

$$I(\nu) = \int \frac{|C(0,q)|^2 d^3q}{[\nu - \nu(q)]^2 + (\Gamma_0/2)^2} \qquad \text{Eq. (12-1)}$$

where

$$|C(0,q)|^2 \ \exp\left(-\frac{q^2L^2}{16\pi^2}\right) \qquad \text{Eq. (12-2)}$$

is the squared Fourier coefficient for the weighting function

$$W(r,L) = \exp\left(-\frac{8\pi^2 r^2}{L^2}\right). \qquad \text{Eq. (12-3)}$$

Equation (12-3) describes the case when the phonon amplitude shows a Gaussian slope closer to the crystallite boundary and its boundary value is $\exp(-4\pi^2)$. The choice of the weighting function was substantiated in ref. [31]**.** For practical calculations, Equation (12-1) is usually rewritten as

$$I(\omega) = \int_0^1 \frac{dq \exp(-q^2L^2/4)4\pi q^2}{[\omega - \omega(q)]^2 + (G_0/2)^2} \qquad \text{Eq. (12-4)}$$

where q is expressed as $2\pi/a_0$, $a_0 = 3.5667$ Å is the lattice constant of bulk diamond, and L is the crystallite diameter; G_0 is the line width for an optical phonon in crystalline diamond, otherwise one can account for the instrumental noise of the spectrometer. The dispersion relation $\omega(q)$ is normally expressed analytically:

$$\omega(q) = A + B\cos(q\pi) \qquad \text{Eq. (12-5)}$$

For example, the authors of refs. [32] and [33] used the following parameters for diamond in this relation: $A = 1241.25\,\text{cm}^{-1}$ and $B = 91.25\,\text{cm}^{-1}$;[32] $A = 1193.75\,\text{cm}^{-1}$ and $B = 139.25\,\text{cm}^{-1}$.[33] Equation (12-1) was repeatedly used in ref. [34] to calculate the size of a diamond crystallite in UNCD powder.

A consistent application of the phonon confinement model to describe the Raman spectra of detonation nanodiamond powder in ref. [12] allowed the calculation of the nanocrystallite size and the identification of small amounts of the amorphized sp^2- and sp^3-phases. The validity of the model based on the relationship between the Raman spectra of ultrananocrystalline materials and the spectra of the density of phonon states was experimentally supported in ref. [34]. The authors showed that the Raman spectrum of an amorphous carbon network with sp^3-atoms was in good agreement with the calculated phonon density of states in diamond.

Because of the presence of several bands in the diamond and graphite spectra of the phonon density of states (some of which have frequency overlaps), the analysis of Raman spectra to determine the percentage of the sp^2-phase is an extremely hard matter. This task is also complicated by the above circumstance, the influence of the π–π^* resonance on the spectral amplitude, determined by the sp^2-phase. This was clearly demonstrated in ref. [35] by measuring the Raman spectra of the same nanocrystalline diamond film using lasers with different quantum energies from 2.18 to 4.82 eV. When one goes to a higher excitation energy, the spectral band due to the sp^2-phase (at $1600\,\text{cm}^{-1}$) becomes indistinguishable from that of the sp^3-phase (at $1332\,\text{cm}^{-1}$). Obviously, the application of at least two lasers with energies about 3 and 5 eV might prove very effective for characterization of UNCD by Raman spectral analysis.

12.1.5 HRTEM and SEM Studies

High-resolution transmission electron microscopy (HRTEM) has been widely used to study individual clusters in a UNCD powder.[36] Among these investigations, there are reports by Kuznetsov's research group[37] on the structural changes in clusters during the detonation nanodiamond–graphite transition. The small size of examined area (10–

100 nm) at experiments with high resolution imposes certain restrictions for HRTEM characterization of UNCD powder. The difficulties that arise concern identification of structure of the powder, whether the structure being observed is inherent to that area of the powder being examined or to the powder as a whole. Generally, a detonation powder may exhibit some inhomogeneity and structural non-uniformity, so HRTEM studies are often combined with other techniques, say, X-ray diffraction applied to the same type of sample in order to get more detailed information. Another difficulty involved in HRTEM as well as in SEM experiments is a possible UNCD–onion carbon transition induced by a high-energy electron beam, as demonstrated by the excellent work of Banhart (see ref. [38] and references there).

A general difficulty for characterization of nanoclusters is their small size that reduces parameters for any structural phase transition and as a result experimentalists have to detect and analyze small signals. For example, the laser excitation power used in a Raman spectroscopic experiment must be minimized and the powder should be placed in a helium atmosphere of high thermal conductivity to avoid diamond–graphite transformation during measurements.[12,25] In spite of these difficulties, HRTEM data have provided unambiguous indications of the presence of 4–5 nm diamond crystallites in nanodiamond powders, having a narrow size distribution with possible defective onion carbon sheets on the surface. The number of available UNCD studies made by the SEM technique is much smaller.[11] The fractal (self-similar) structure of UNCD powders has been clearly demonstrated in the work discussed in ref. [39].

12.1.6 STM and AFM Studies

The complexity of using scanning tunnelling and atomic-force microscopy (STM and AFM) in the analysis of nanopowders is primarily due to the need to mount and fix UNCD particles on an atomically smooth surface. Besides, it is very hard to measure the real size of a cluster when it is much smaller than the probe used.[40]

An AFM investigation has been undertaken to reveal the structure of UNCD clusters, the type of cluster packing, and the possible presence of a regular packing mode.[10] It should be noted that the earlier attempts to apply AFM to nanodiamond powders were unsuccessful because of high particle mobility relative to the substrate. The use of organic

fixatives also failed because the cluster aggregation mode changed radically during the fixation. The samples used to obtain AFM images were prepared by deposition onto a silicon wafer by evaporating an aqueous nanodiamond suspension. The silicon wafer had the (100) orientation and the surface roughness was less than 1 nm. The nanodiamond concentration in the suspension was about 0.05% by weight, and the deposited diamonds formed a continuous thin layer on a horizontal wafer; they were subsequently dried in a thermostat at a temperature of 120 °C for 1 hour. The average weighted layer thickness measured ellipsometrically at the wavelength $\lambda = 632.8$ nm varied from 120 to 350 nm.

To increase the contrast and resolution of AFM images, the samples were subjected to pretreatment by ultraviolet light in air for several hours. Ultraviolet light seems to be able to etch off the residual amorphous carbon and C—H groups from the cluster surface. One can see from Fig. 12.4 that AFM reveals the presence of aggregates and that the nanodiamond layer on silicon represents individual islands of 20 nm height. The length of the aggregates is of the order of a few hundred nanometers and they show no signs of symmetry, regular packing, or preferred arrangements. The AFM images at higher resolution presented in ref. [10] show that the smaller particles making up an aggregate range widely in size from hundreds of nanometers to a few nanometers. These data supported an earlier assumption of a fractal structure of a UNCD powder consisting of self-similar particles ranging in size from several hundreds of nanometers to a few nanometers.

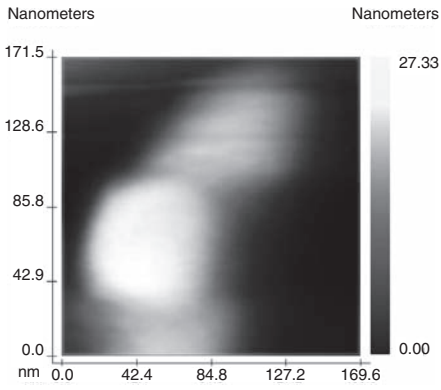

Figure 12.4 Typical AFM image of detonation nanodiamond cluster on silicon substrate.

The authors of ref. [41] have obtained STM images of aggregates made up of several 4 nm clusters. A specific feature of the method used in this work was that the aggregates were preliminarily destroyed by shock wave and that the wafer was made from graphite with an atomically smooth surface (HOPG); further, the authors used electrophoretic deposition from a nanodiamond suspension.

12.1.7 Visible and Far-Infrared Spectroscopic Studies

There are few reports of using light absorption by nanodiamond powders in the visible or far-infrared regions. This is not surprising since coating technologies deal with continuous diamond and diamond-like films rather than with layers consisting of individual particles. The production of coatings by chemical vapor deposition (CVD), including the application of nanodiamond powders as precursors, has been described in much detail (see, e.g., refs. [42,43]). Still, it is worth mentioning here some of the reports important in the determination of nanodiamond structure.

The authors of refs. [44,45] studied layers about 200 nm thick on fused quartz wafers, deposited from an aqueous suspension of nanodiamond powder. It was found that the absolute values of the absorption coefficient α ranged between $10^3\,cm^{-1}$ and $10^4\,cm^{-1}$ at wavelengths in the range $\lambda = 0.2–1.0\,\mu m$. These values are several orders of magnitude larger than the absorption coefficients of natural single crystal diamonds for the same spectral range. On the other hand, both the $\alpha(\lambda)$ dependence and the absolute value of the absorption coefficient nearly coincide with those for amorphous diamond-like films.[46] However, an attempt to find the band gap of diamond powder using plots of $(\alpha h\nu)^{1/2} = f(h\nu)$, by analogy with amorphous materials, failed because the absorption spectrum could not be interpolated by a linear function. The latter fact is not surprising since it has also been observed in amorphous materials. In that case, the optical band gap is often assumed to be the energy at which the absorption coefficient is equal to $10^4\,cm^{-1}$.[47] When that criterion was used, authors took the energy to be 2.06 eV. One should recall that the band gap of natural single crystal diamond is $\varepsilon_g = 5.5\,eV$; therefore, the optical absorption edge lies at 225 nm. Depending on the sp^2/sp^3-bond ratio, the band gap in amorphous diamond-like films may be much smaller. For example, it was shown in ref. [48] that a tetrahedral network of amorphous carbon with 86% of atoms having sp^3-bonds and 14% of atoms having sp^2-bonds possessed a band gap of about 2 eV and that decreasing the number of sp^2-bonds increased the optical band gap.

Therefore, a strong absorption in the visible spectrum of nanodiamond powders and the difference between the optical band gap of a powder and natural diamond can be attributed to the presence of some amount of the amorphous sp^2-phase. The available Raman scattering and X-ray diffraction data[4,12] suggest that the sp^2-phase is located on the surface of

nanodiamond clusters. We will make use of this conclusion when discussing the structure of UNCD particles and their aggregation.

It is common knowledge that the attempt to understand the nature of interstellar dust absorption in the ultraviolet region with a peak at 217.5 nm (4.6 μm^{-1}; 5.7 eV) entailed, together with other facts, the discovery of fullerenes[49] and the arc-discharge method of their production.[50] Recently, an attempt has been made to relate the observable absorption to the presence of onion carbon.[51–53] Since detonation nanodiamonds were used in refs. [51,52] as the initial material for producing onion carbon, these workers also analyzed the absorption spectra of nanodiamond aqueous suspensions in the range of 0.5–0.2 μm. They found a monotonically increasing absorption with decreasing wavelength in this spectral range but they failed to offer a clear interpretation of this fact. However, a theoretical analysis of the experimental data showed that the resonant absorption of π-electrons by the plasma in multishell carbon onions perfectly fitted the interstellar absorption peak at 4.6 μm^{-1}.

The large specific surface of clusters in a UNCD powder, usually reported to be 200–300 $m^2 g^{-1}$, determines their high absorptive capacity. Infrared spectroscopy has often been employed to identify the surface state, primarily the surface functional groups.[54] It has been shown in ref. [55] that nanodiamond readily absorbs water when exposed to the ambient conditions. Following the absorption, the O—H vibrations are found to dominate the infrared spectrum which also indicates the presence of different C—H and C—O groups. The IR spectra are reported to be similar to those published in ref. [55]. In all the samples studied, the dominant absorption band was centered at 3400 cm^{-1} with a width of 500 cm^{-1}, accompanied by a sharper peak at 1630 cm^{-1}. These peaks were suggested to be due to the O—H vibrations.[55] We also observed absorption bands at 2950, 1750, 1300, and 1100 cm^{-1} attributed to C—H, C—C, C—O, and C—O—C groups.[56,57]

12.1.8 NMR and EPR Studies

Although nuclear magnetic and electron paramagnetic resonance (NMR and EPR) data on nanodiamonds are reported only in a few publications, they have considerably added to our knowledge of the surface structure of nanodamond clusters and the defects present there. For example, the NMR technique revealed the presence of CH, CH_3, and CH_2 groups in

various configurations, namely C═CH_2, C—CH_3, O═CH_2, O—CH, depending on the degree of chemical purification of the initial detonation soot.[57] The same authors also detected O—H groups.

The EPR technique was used for a detailed investigation of electronic properties of nanographite powders produced by high-temperature annealing of nanodiamonds. Its application together with ^{13}C NMR, X-ray diffraction, and TEM methods to study the electronic properties of nanodiamonds[58] has shown that a high concentration of paramagnetic centers (up to 10^{20} spin g^{-1}) is due to structural defects, namely dangling C—C bonds, on the diamond cluster core. Impurities have also been found on the cluster surface. As a result, the EPR technique has been demonstrated to be a useful tool for estimating the degree of nanodiamond powder purification.

12.1.9 EELS Characterization of UNCD Powders

It is well known that electron energy loss spectroscopy (EELS) allows an accurate identification of sp-hybridization of carbon atoms. It was this method that provided the sp^2/sp^3-bond ratio in diamond-like films (see, e.g., ref. [59]). Especially effective is the combination of EELS with the other methods discussed above, in particular with HRTEM.[60] These have revealed the transformation of onion carbon to crystalline diamond under the action of a high-energy electron beam (1.25 MeV) at high temperature ($T = 700\,°C$).[61] We will later use the EELS data[62] to describe the structure of nanodiamond powders (see page 393).

12.2 The Structure of UNCD Clusters and the Aggregation Problem

Let us consider the current concepts of the structure of UNCD powders, based on the analysis of data obtained by the methods mentioned above and on theoretical treatments.[63–66]

It may be considered to be an established fact that a nanodiamond powder produced by detonation synthesis (usually of trinitrotoluene and hexogene) contains particles having a diamond crystal lattice and a characteristic size of 4.5 nm. In the detonation soot, these particles appear to be covered with a shell of carbon atoms with various types of sp-bonds. The unusually narrow range of the size distribution of diamond

nanocrystals (4–5 nm) has been emphasized by many workers. The reason for this is that it is diamond, rather than graphite, which appears to be a thermodynamically stable form of nanocarbon when the particle size lies in the above range. This hypothesis was offered in refs. [21] and [63] and has been supported recently by the results of numerical simulation of a stable carbon cluster.[66]

The simulation has shown that the free surface of a diamond nanocluster, if it has no radical groups attached to it, transforms to a quasi-spherical surface consisting of a mixed pentagon/hexagon network. This kind of transformation which minimizes the surface energy was supported by the calculations made in ref. [65]. A temporary reconstruction of the cluster surface which did not affect its core was observed in small-angle X-ray scattering experiments with nanodiamond powders made with a time interval of two years.[67]

We would like to emphasize again that the surface structure and shell thickness of a nanodiamond cluster are determined by the cooling kinetics of the detonation product and by the purification method used,[68] whereas the cluster core is always present and can be detected by conventional X-ray diffraction (Fig. 12.1). This obscures the fact that both a detonation powder and its suspension consist of much larger particles, of about 100 nm. In reality, therefore, the researcher deals with submicron particles rather than with nanoclusters. A common diamond powder has a typical fractal structure which preserves its self-similarity when the size scale changes (Fig. 12.5). The fact that nanoclusters aggregate to form submicron and micron particles due to a high surface energy is not surprising. What is surprising is the high stability of 100 nm aggregates, which were termed core aggregates in ref. [69]. They cannot be broken into primary 4 nm particles by a conventional ultrasonic treatment of the suspension but require the application of shock waves in a railgun to disaggregate them into 40–60 nm aggregates.[8] It was only recently that core aggregates could be disaggregated into single UNCDs by using so-called stirred medium milling in which a nanodiamond powder is vigorously mixed with zirconium dioxide microbeads.[69] The suspension obtained proves quite unique in at least two of its characteristics: it is black and has an unusually high viscosity.[70]

In order to understand the reason for the high stability of core aggregates and their specific structure, let us consider qualitatively the mechanism of detonation nanodiamond formation (Fig. 12.6). A primary UNCD particle represents a perfect diamond lattice, which is manifested as an X-ray coherent scattering region of about 4 nm. Such particles are formed at the shock wave front at P = 20–30 GPa and T = 3000–4000 K

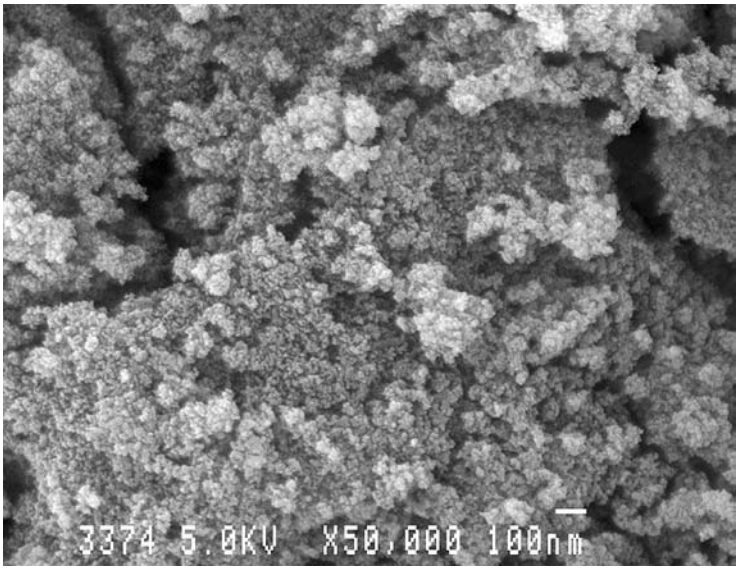

Figure 12.5 Typical high-resolution SEM image of detonation nanodiamond powder produced from a mixture of TNT and hexogen (60/40) with purification in nitric acid.

and produce polycrystals with a mean size of 100 nm at decreased temperature and pressure, but still remaining in the region of diamond thermodynamic stability. The most important feature of these polycrystals, or core aggregates, is the nearly total absence of the sp^2-phase inside them. This phase is detectable only at the aggregate interfaces because the primary particles are disoriented relative to one another, resulting in the formation of dislocations and other defects at the interface.

The polycrystalline nature of UNCD aggregates was reported in ref. [62]. The lattice disorientation of the primary particles leads to the fact that X-ray diffraction and Raman scattering reveal only 4 nm particles, the size of a perfect crystal lattice. The stability of the core aggregates is determined by the same factor as in common polycrystallites, namely, by the chemical bonds between the contacting primary 4 nm particles, which seem to be covalent in this case.

As the temperature and pressure decrease further (still within the region of diamond thermodynamic stability), the core aggregates group together to form secondary aggregates containing numerous defects, such as dislocations and even microcracks, at the interface with the core aggregates. The secondary aggregates, in turn, form larger but less stable particles since the number of dislocations and other defects increases with particle

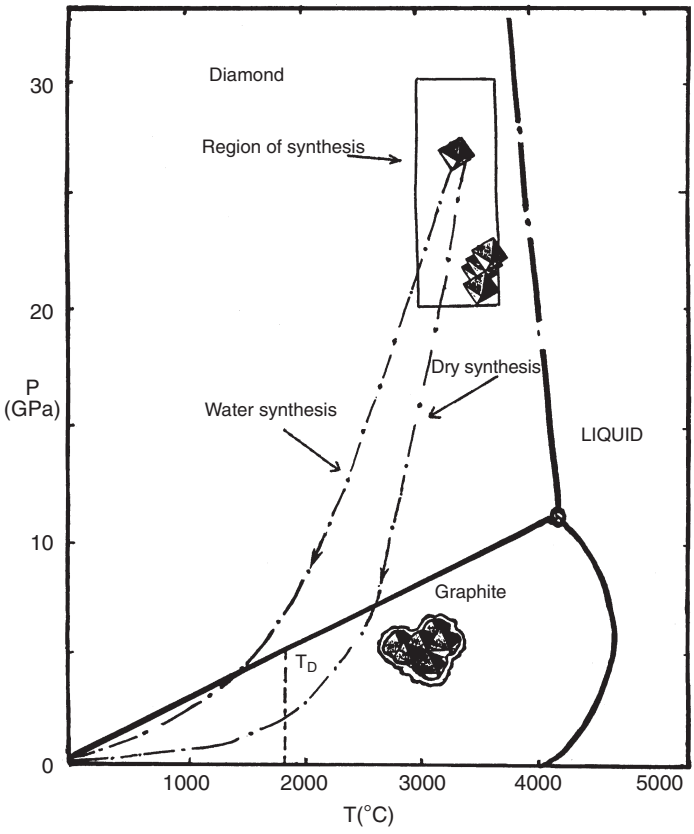

Figure 12.6 *P–T* phase diagram for carbon, showing the region for detonation nanodiamond synthesis from explosives and kinetic of cooling of detonation products in the case of "water" and "dry" synthesis (T_D – Debye temperature).

size. This is due to the fact that the particle density decreases as its radius becomes larger, like in any other fractal structure.

It is common knowledge that the key factor in the crystallization of various forms of carbon is the kinetics of this process. The kinetics of detonation synthesis is an especially important parameter because the pressure and temperature go through the region of kinetic instability of diamond. Indeed, these parameters drop sharply after the detonation and appear to be in the region where diamond is thermodynamically unstable. If the temperature is still high enough (above the Debye temperature of diamond $T_D \sim 1800\,K$) to support a high mobility of carbon atoms, the reverse transition from diamond to graphite will be more pronounced than at $T < T_D$ when the transition to graphite thermodynamic stability occurs.

The higher the cooling rate, the shorter the time for the detonation product to be found in the region of diamond kinetic instability and, hence, the smaller the probability of the reverse transition to graphite during the synthesis.

The reverse diamond–graphite transition leads to the formation of a sp^2-hybridized carbon shell around the free (unoccupied) surface of the core and secondary aggregates. The presence of weakly bonded π-electrons is attributed to this shell. The sp^2/sp^3 ratio in the detonation soot is found to vary with the conditions of the synthesis (the dP/dt and dT/dt ratios) and with the medium used in the detonation chamber.

Nanodiamonds produced by dry and wet syntheses differ in the thickness of the onion-like shell. This is because the carbon produced in dry synthesis goes more slowly through the region of diamond kinetic instability, so the thickness of a closed onion shell appears to be greater than in wet synthesis. It is quite natural that with an equal degree of purification from the detonation soot, the nanodiamond samples obtained by dry and wet syntheses should differ only in the scatterer size, as we found earlier.[68] The kinetics of the dry and wet processes are illustrated qualitatively in Fig. 12.6. The experimental support of this, at least qualitative, interpretation is that the proportion of diamond in the detonation carbon produced by wet synthesis is much larger. This is why wet synthesis should prove to be more effective for commercial production of nanodiamonds. Subsequent chemical purification removes most of the sp^2-carbon from the detonation soot, so commercial detonation nanodiamonds represent a powder or suspension largely composed of secondary aggregates. The ordinary color of a suspension is light gray due to Rayleigh light scattering by the aggregates because their size is about the wavelength of light in the visible spectrum.

The observation of Raman spectral features coinciding with the peaks of the phonon density of states for diamond and graphite[12] indicates the presence of some amount of amorphous diamond and graphite, which seem to be deposited on core aggregates. One may suggest[70] that the milling of the aggregates is accompanied by surface graphitization of the primary 4 nm particles because of the local heating due to inelastic collisions between zirconium dioxide balls and the aggregates. The black color of the aqueous UNCD suspension that is observed during this process could be attributed to light absorption by the sp^2-phase.

The hypothesis of surface graphitization during the milling is based on the fact that the diamond–graphite transition begins with the cluster surface.[12,37] The analysis of X-ray diffraction data has shown that the

initial graphite represents a set of equidistant graphite sheets of less than 4 nm size and that the major source of this phase is the diamond core heat annealing at temperatures $T_a > 1200$ K. The temperature of the transition onset found in this work, $T_a \sim 1000$ K, correlates well with the electron microscopic data of ref. [37] indicating that the diamond core begins to shrink in size only at temperatures above $T_a = 1300$ K, when onion carbon is formed. A sharp peak at 1575 cm^{-1} in the Raman spectrum, which is clearly detectable at $T = 1400$ K and is interpreted as being due to the formation of onion carbon, supports the validity of the phase transition temperature hypothesis.

It is essential to note that the onset of the diamond–graphite transition in nanodiamond powder has been observed at much lower temperatures than in single bulk diamond crystals with $T > 1900$ K.

We can conclude from this analysis that commercial detonation nanodiamond powders consist of particles making up a fractal hierarchy, namely, 4 nm diamond cores which coalesce to form stable core aggregates which, in turn, aggregate to produce larger but less stable clusters of the second and third order. These can be disintegrated by a common ultrasonic treatment, whereas first-order aggregates (core aggregates) can be broken only by shock waves or a milling process.

12.3 Mechanical Properties

The obvious application of nanodiamond powders, determined by their mechanical properties, is their use as abrasives or constituents of coating materials. This subject was briefly discussed in the book by V. Dolmatov.[71] Unfortunately, there has been little experimental work on this issue so far (see, e.g., ref. [1]). The advantages of detonation nanodiamonds as components of metal-containing composites for making electroplated coatings were demonstrated in ref. [71]. The experimental data showed an increased durability and microhardness of such coatings. It was found, in particular, that detonation nanodiamond appeared to be a preferable component of chromium–diamond coatings as compared with conventional synthetic diamonds of the same size.[72] Besides, a recent study showed that metals, molybdenum in particular, coated with detonation nanodiamond also exhibited a higher surface durability.[73]

An application of the abrasive properties of nanodiamond is nanodiamond's use as a starting material to produce polycrystalline powders of the *Mypolex* type.[74] We believe, however, that boron, silicon, and nitrogen are more promising for creating novel nanodiamond-

based composites, and the first steps have already been taken along this line.[75]

12.4 Optical Properties

We briefly described some optical properties of nanodiamond films in Section 12.1.7. Here we would like to mention what is apparently the first work on the nonlinear optical properties of nanodiamond suspensions.[76] It was shown that the nonlinear optical response of onion-like carbon was stronger than that of diamond nanoparticles. This was largely due to nonlinear absorption which produced a strong limiting optical effect. The researchers also found that the absorption coefficient in the visible and near-UV spectral regions of an onion carbon suspension was much larger than that of a UNCD suspension.

12.5 Electronic Properties

We would like to draw the reader's attention to some experimentally observable electronic characteristics of detonation nanodiamonds, leaving aside the results of numerical simulation (see, e.g., ref. [65]) and the data on UNCD films.[77]

The fact that the diamond core of a detonation particle has a nanoscale size raises the question of quantum-size effects in the electronic behavior of these particles. Such effects were indeed registered experimentally at least in two studies.[58,78] The first study revealed the variation of the *g*-factor of the unpaired electron associated with the size effect. The other study combined X-ray absorption and emission experiments with *ab initio* calculations, which showed that the core size has to decrease to less than 2 nm for the researcher to be able to detect an increase in the optical band gap due to the quantum-size effect. For comparison, classical semiconductors, such as germanium and silicon, show this kind of band gap increase in 6–7 nm crystallites.

Transport properties in UNCD clusters are still poorly understood for at least two reasons. First, the specific electrical conductivity of diamond is known to be very high and, second, it is very hard to obtain reliable experimental data on these characteristics when using pressure contacts. For example, the electrical conductivity of powders is largely determined by the interface conductivity of the contacting particles and, hence, by the pressure applied to the contacts. Nevertheless, the authors of ref. [79]

found the lower limit of the specific conductivity of UNCD powders to be ($\rho > 10^9\,\Omega\,\mathrm{cm}$) and demonstrated that a high-temperature annealing, causing surface graphitization of diamond clusters (see above), decreases the resistivity by several orders of magnitude, making it as low as a few fractions of $1\,\Omega\,\mathrm{cm}$ at 1800 K.

There has been much interest in autoelectron (field electron) emission from UNCD-based structures (see, e.g., ref. [80]), which is explained as follows. It has been found experimentally that autoelectron emission is most effective in sp^2/sp^3-carbon mixtures.[81] Further, detonation nanodiamond is a unique material in that the sp^2/sp^3 ratio can be readily varied by using a high-temperature annealing. Three models have been suggested to explain the key role of the sp^2/sp^3 ratio in autoelectron emission by nanocarbon materials.[82–84] The first two models assume that the field emission in nanomaterials is associated with a special band structure of the emission center consisting of sp^2-hybridized carbon. The last of the three models accounts for the electron drag by phonons in carbon nanocomposites, and this suggests an explanation that does without additional assumptions. But only further efforts can show which of the models can adequately describe the field emission process. A proof of the model's validity would be the design and implementation of a field electron emitter based on nanocarbon structures.

Summary

To conclude, it would be useful to outline some practical measures that might improve the characterization and study of UNCD physical properties. We believe that such measures might include the development of methods for:

- detection and identification of impurities and defects in nanodiamonds, alongside technologies for intercalation and doping of UNCD and onion carbons;
- identification of functional groups on the UNCD cluster surface;
- the creation of composites based on nanodiamonds and the study of electron and phonon processes occurring in them.

Acknowledgments

I would like to thank A. E. Aleksenskii, A. T. Dideikin, E. D. Eidelman, V. I. Siklitsky, and E. Osawa for numerous fruitful discussions

of the above issues, V. Davydov for Raman characterization of nanodiamonds and useful discussion, and Y. Ohki for SEM characterization.

References

1. Vul', A. Ya, Dolmatov, V. Yu., Shendorova, O. (eds). *Bibliography Index: Detonation Nanodiamonds and Related Materials*, First issue. Ioffe Institute, St. Petersburg (2003).
2. Lymkin, A. I., Petrov, E. A., Ershov, A. P., Sakovitch, G. V., Staver, A. M., Titov, V. M. Production of diamonds from explosives. *Dokl. Akad. Nauk USSR,* 1988, 302, 611–613.
3. Greiner, N. R., Philips, D. S., Johnson, J. D., Volk, F. Diamonds in detonation soot. *Nature*, 1988, 333, 440–442.
4. Aleksensky, A. E., Baidakova, M. L., Boiko, M. E., Davydov, V. Yu., Vul', A. Ya., Diamond–graphite transition in ultradispersed diamond. X-ray and Raman characterization of diamond clusters. In: *Application of Diamond and Related Materials: Third International Conference*, Gaithersburg, Maryland, USA, August 21–24, 1995. NIST Special Publication Issue 885, 457–460.
5. Collection of Papers of the First International Symposium "Detonation Nanodiamonds: Fabrication, Properties and Applications". St. Petersburg, Russia, July 7–9, 2003. *Phys. Solid State* 2004, 4, 595–769.
6. Gruen, D., Shendorova, O., Vul', A. (eds.). *Proceedings of the NATO Advanced Research Workshop on the Synthesis, Properties and Application of Ultrananocrystalline Diamond*, Springer, The Netherlands (2005).
7. Affoune, A. M., Prasad, B. L. V., Sato, H., Enoki, T. Electrophoretic Deposition of Nanosized Diamond Particles, *Langmuir*, 2001, 17, 547–551.
8. Vul', A. Ya., Dideykin, A. T., Tsareva, Z. G., Brunkov, P. N., Korytov, M. N., Zhukov, B. G., Rozov, S. I., Nashchekin, A. V. Direct STM observation of single nanodiamond clusters. *Abstracts of NATO Advanced Research Workshop "Synthesis, Properties and Application of Ultrananocrystalline Diamond"*, Ioffe Institute, St. Petersburg, Russia (2004), p. 44.
9. Kuznetsov, V. L., Aleksandrov, M. N., Zagoruiko, I. V., Chuvilin, A. L., Moroz, E. M., Kolomiichuk, V. N., Likholobov, V. A., Brylyakov, V. A., Sakovitch, G. V, Study of ultra disperse diamond obtained using explosion energy. *Carbon*, 1991, 29, 665–668.
10. Aleksenskii, A. E., Osipov, V. Y., Dideykin, A. T., Vul', A. Y., Adreaenssens, G. J., Afanasev, V. V. Ultradisperse diamond cluster aggregation studied by atomic force microscopy. *Tech. Phys. Lett.*, 2000, 26, 819–821.
11. Vul', A. Ya., Golubev, V. G., Grudinkin, S. A., Krüger, A., Naramoto, H. Diamond films: initial CVD growth stage using nanodiamonds as nucleation centers. *Tech. Phys. Lett.*, 2002, 28, 787–789.
12. Alexenskii, A. E., Baidakova, M. V., Vul', A. Ya., Davydov, V. Yu., Pevtsova, Yu. A. Diamond–graphite phase transition in ultradisperse-diamond clusters. *Phys. Solid State*, 1997, 39, 1007–1015.
13. Chen, Pengwan, Huang, Fenglei, Yun, Shourong. Characterization of the condensed carbon in detonation soot. *Carbon*, 2003, 41, 2093–2099.

14. Ershov, A. P., Kupershtokh, A. L. Formation of fractal structures at explosion. *Combustion, Explosion and Shock Waves*, 1991, 27, 111–117 [in Russian].
15. Baidakova, M. V., Vul', A. Ya., Siklitski, V. I., Faleev, N. N., Fractal structure of ultradisperse-diamond clusters. *Phys. Solid State*, 1998, 40, 715–718.
16. Baidakova, M. V., Vul', A. Ya., Siklitski, V. I., Ultradisperse-diamond nanoclusters. Fractal structure and diamond–graphite phase transition. *Chaos Solitons Fractals,* 1999, 10, 2153–2163.
17. Glatter, O. The interpretation of real-space information from small-angle scattering experiments. *J. Appl. Cryst.*, 1979, 12, 166–175.
18. Guinier, A., Fournet, C., Walker, C. B., Yudowitch, K. L. *Small-Angle Scattering of X-Rays*. Wiley, New York (1955).
19. Siklitsky, V. I., Ivanov-Omskii, V. I., Baidakova, M. V. Fractal structure of copper clusters embedded in DLC. In: *Diamond-Based Composites and Related Materials*, ed. M. Prelas. Kluwer, London (1997), pp. 197–202.
20. Pfefer, P., Avnir, D. Chemistry in noninteger dimensions between two and three. I. Fractal theory of heterogeneous surfaces. *J. Chem. Phys.*, 1983, 79, 3558–3566.
21. Badziag, P., Verwoerd, W. S., Ellis, W. P., Greiner, N. R. Nanometre-sized diamonds are more stable than graphite. *Nature*, 1990, 343, 244–245.
22. Kuznetsov, V. L., Malkov, I. Yu., Chuvilin, A. L., Moroz, E. M., Kolomiichuk, V. N., Shaichutdinov, Sh. K., Butenko, Yu. V. Effect of explosion conditions on the structure of detonation soots: ultradisperse diamonds and onion carbon. *Carbon*, 1994, 32, 873–882.
23. Osawa, E. Disintegration and purification of Crude Aggregates of Detonation Nanodiamond. A few remarks on nano methodology. In: *Proceedings of the NATO Advanced Research Workshop on the Synthesis, Properties and Application of Ultrananocrystalline Diamond*, Springer, The Netherlands (2005), pp. 231–240.
24. Bohren, C. F., Huffman, D. R. *Absorption and Scattering of Light by Small Particles*. Wiley, Chichester and New York (1983).
25. Mikov, S. N., Igo, A. V., Gorelik, V. S., Raman scattering of light on diamond quantum dots in a matrix of potassium bromide. *Phys. Solid State*, 1995, 37, 1671–1673.
26. Tuinstra, F., Konig, J. L. Raman spectra of graphite. *J. Chem. Phys.,* 1970, 53, 1126–1131; Nemanich, R. J., Solin, S. A. First- and second-order Raman scattering from finite size crystals of graphite. *Phys. Rev.*, 1979, 20, 392–401.
27. Solin, S. A., Ramdas, A. K. Raman spectrum of diamond. *Phys. Rev B.*, 1970, 1, 1687–1698.
28. Yoshikawa, M., Nagai, M., Matsuki, M., Fukuda, H., Katagiri, H., Isida, H., Ishitani, A. Raman scattering from sp^2 carbon clusters, *Phys. Rev. B*, 1992, 46, 7169–7174.
29. Yoshikawa, M., Mori, Y., Maegawa, M., Katagiri, G., Ishida, H., Ishitani, A. Raman scattering from nanometer-sized diamond. *Appl. Phys. Lett.*, 1993, 62 (24), 3114–3116; Obraztsov, A. N., Timofeev, M. A., Guseva, M. B., Babaev, V. G., Valullova, Z. Kh., Babina, V. M. Comparative study of microcrystalline diamond. *Diamond Relat. Mater.*, 1995, 4, 968–971.
30. Cardona, M. (ed.). *Light Scattering in Solids*. Spinger, Berlin, Heidelberg, and New York (1975).

31. Campbell, I. H., Fauchet, P. M. The effect of microcrystal size and shape on the one phonon Raman spectra of crystalline semiconductors. *Solid State Commun.*, 1986, 58, 739–741; Richter, H., Wang, Z. P., Ley, L. The one phonon Raman spectrum in microcrystalline silicon. *Solid State Commun.*, 1981, 39, 625–629.
32. Ager III, J. W., Veirs, D., Rosenblat, G. Spatially resolved Raman studies of diamond films grown by chemical vapor deposition, *Phys. Rev. B*, 1991, 43, 6491–6499.
33. Yoshikawa, M., Mori, Y., Obata, H., Maegaw, M., Katagiri, G., Ishida, H., Ishitani, A. Raman scattering from nanometer-sized diamond. *Appl. Phys. Lett.*, 1995, 67, 694–696.
34. Lipp, M. J., Baonza, V. G., Evans, W. J., Lorenzana, H. E. Nanocrystalline diamond: effect of confinement, pressure, and heating on phonon modes. *Phys. Rev. B*, 1997, 56, 5978–5984.
35. Leeds, S. M., Davis, T. J., May, P. W., Pickard, C. D. O., Ashfold, M. N. R. Use of different excitation wavelengths for the analysis of CVD diamond by laser Raman spectroscopy. *Diamond Relat. Mater.*, 1998, 7, 233–237.
36. Tao, X., Kang, X., Jiazheng, Z. TEM and HRTEM studies on ultradispersed diamonds containing soot formed by explosive detonation, *Mater. Sci. Eng. B*, 1996, 38, L1–L4.
37. Kuznetsov, V. L., Malkov, I. Yu., Chuvilin, A. L., Moroz, E. M., Kolomiichuk, V. N., Shaichutdinov, Sh. K., Butenko, Yu. V. Effect of explosion conditions on the structure of detonation soots: ultradisperse diamonds and onion carbon. *Carbon*, 1994, 32, 873–882; Butenko, Yu. V., Kuznetsov, V. L., Chuvilin, A. L., Kolomiichuk, V. N., Stankus, S. V., Khairulin, R. A., Segall, B. The kinetics of the graphitization of dispersed diamonds at "low" temperatures. *J. Appl. Phys.*, 2000, 88, 4380–4388.
38. Banhart, F., Ajayan, P. M. Carbon onion as nanoscopic pressure cell for diamond formation, *Nature*, 1996, 382, 433–435; Banhart, F. Structural transformations in carbon nanoparticles induced by electron irradiation. *Phys. Solid State*, 2002, 44 (3), 399–404.
39. Baidakova, M. V., Siklitsky, V. I., Vul', A. Ya. Small angle X-ray study of nanostructure of ultradisperse diamond. In *Proceedings of International Symposium "Nanostructures: Physics and Technology"*, St. Petersburg, June 23–27, 1997, Ioffe Institute, St. Petersburg, Russia (1997), pp. 227–230.
40. Schirach, R.-J., Kolbesen, B. O., Aderhold, D. D., Comes, F. J. Characterization of crystal faces of polycrystalline HFCVD diamond films by STM/STS. *Fresenius J. Anal. Chem.*, 1997, 358, 335–338.
41. Vul', A. Ya., Dideykin, A. T., Tsaryova, Z. G., Brunkov, P. N., Korytov, M. N., Zhukov, B. G., Rozov, S. I., Nashchekin, A. V. Direct STM observation of single nanodiamond clusters. In *Program and Abstracts NATO ARW "Synthesis, Properties and Applications of Ultrananocrystalline Diamond"*, June 7–4, 2004, Ioffe Institute, St. Petersburg. p. 44.
42. Baidakova, M. V., Vul', A. Ya., Golubev, V. G., Grudinkin, S. A., Melekhin, V. G., Feoktistov, N. A., Kruger, A. Growth of diamond films on silicon substrates by hot-filament CVD. *Semiconductors*, 2002, 36, 651–657.
43. Yanchuk, I. B., Valakh, M. Ya. Vul', A. Ya., Golubev, V. G. Grudinkin, S. A., Feoktistov, N. A., Richter, A., Wolf, B. Raman scattering, AFM and nano-

indentation characterisation of diamond films obtained by hot filament CVD. *Diamond Relat. Mater.,* 2004, 13, 266–269.
44. Alexenskii, A. E., Osipov, V. Yu., Kryukov, N. A., Adamchuk, V. K., Abaev, M. I., Vul', S. P., Vul', A. Ya. Optical properties of layers of ultradisperse diamond clusters obtained from an aqueous suspension. *Tech. Phys. Lett.*, 1997, 23, 874–876.
45. Alexenskii, A. E., Osipov, V. Yu., Vul', A. Ya., Ber, B. Ya., Smirnov, A. B., Melekhin, V. G., Adriaenssens, G. J., Yakubovskii, K. Optical properties of layers of nanodiamonds. *Phys. Solid State*, 2001, 43, 145–150.
46. Vasiliev, V. A., Volkov, A. C., Musabekov, E., Terukov, E. I., Features of photoluminescence in amorphous hydrogenated carbon *a* —C:H, *Tech. Phys. Lett.*, 1988, 14, 1675–1679 [in Russian]; Ivanov-Omskii, V. I., Tolmatchev, A. V., Yastrebov, S. G. Optical absorption of amorphous carbon doped with copper. *Philos. Mag. B*, 1996, 73, 715–722.
47. Chu, V., Conde, J. P., Jarego, J., Brogueira, P., Rodriguez, J., Barradas, N., Soares, J. C. Transport and photoluminescence of hydrogenated amorphous silicon–carbon alloys. *J. Appl. Phys.*, 1995, 78, 3164–3173.
48. Stumm, P., Drabold, D. A. Structural and electronic properties of nitrogen doped fourfold amorphous carbon. *Solid State Commun.*, 1995, 93, 617–621.
49. Kroto, H. W., Heath, J. R., Brien, S. C., Curl, R. F., Smalley, R. E. C60: Buckminsterfullerene. *Nature*, 1985, 318, 162–163.
50. Krätschmer, W., Lamb, L. D., Fostiropoulos, K., Huffman, D. R., Solid C60: a new form of carbon. *Nature*, 1990, 347, 354–358.
51. Tomita, S., Hayashi, S., Tsukuda, Y., Fuiji, M. Ultraviolet–visible absorption spectroscopy of carbon onions. *Phys. Solid State*, 2002, 44, 450–453.
52. Tomita, S., Fujii, M., Hayashi, S. Optical extinction properties of carbon onions prepared from diamond nanoparticles. *Phys. Rev. B*, 2002, 66, 245424.
53. Chhowalla, M., Wang, H., Sano, N., Teo, K. B. K., Lee, S. B., Amaratunga, G. A. J. Carbon onions: carriers of the 217.5 nm interstellar absorption feature. *Phys. Rev. Lett.*, 2003, 90, 155504.
54. Mironov, E., Koretz, A., Petrov, E. Detonation synthesis ultradispersed diamond: structural properties investigation by infrared absorption. *Diamond Relat. Mater.*, 2002, 11, 872–876.
55. Ji, S., Jiang, T., Xu, K., Li, S. FTIR study of the adsorption of water on ultradispersed diamond powder surface. *Appl. Surf. Sci.*, 1998, 133, 231–238.
56. Iakoubovskii, K., Baidakova, M. V., Wouters, B. H., Stesmans, A., Adriaenssens, G. J., Vul', A. Ya., Grobet, P. J., Structure and defects of detonation synthesis nanodiamond, *Diamond Relat. Mater.*, 2000, 9, 861–865.
57. Simons, W. W. (ed.). *The Sadtler Handbook of Infrared Spectra*. Sadtler Research Laboratories, Philadelphia, US (1978).
58. Shames, A. I., Panich, A. M., Kempiński, W., Alexenskii, A. E., Baidakova, M. V., Dideikin, A. T., Osipov, V. Yu., Siklitski, V. I., Osawa, E., Ozawa, M., Vul', A. Ya. Defects and impurities in nanodiamonds: EPR, NMR and TEM study. *J. Phys. Chem. Solids*, 2002, 63, 1993–2001.
59. Pomsonnet, L., Donnet, C., Varlot, K., Martin, J. M., Grill, A., Patel, V. EELS analysis of hydrogenated diamond-like carbon films. *Thin Solid Films*, 1998, 319, 97–100.

60. Ichinose, H., Nakanose, M. Atomic and electronic structure of diamond grain boundaries analyzed by HRTEM and EELS. *Thin Solid Films*, 1998, 319, 87–91; Huang, J. Y. HRTEM and EELS studies of defects structure and amorphous-like graphite induced by ball-milling. *Acta Mater.*, 1999, 47, 1801–1808.
61. Redlich, Ph., Banhart, F., Lyutovich, Y., Ajayan, P. M. EELS study of the irradiation-induced compression of carbon onions and their transformation to diamond. *Carbon*, 1998, 36, 561–563.
62. Bursill, L. A., Peng, J. L., Prawer, S. Plasmon response and structure of nanocrystalline diamond powder. *Philos. Mag. A*, 1997, 74, 769–781.
63. Gamarnik, M. Y., Energetical preference of diamond nanoparticles, *Phys. Rev. B*, 1996, 54, 2150–2156.
64. Shenderova, O. A., Zhirnov, V. V., Brenner, D. W., Carbon nanostructures. *Crit. Rev. Solid State Mater. Sci.*, 2002, 27, 227–356.
65. Barnard, A. S., Russo, S. P., Snook, I. K., Ab initio modelling of stability of nanodiamond morphologies, *Philos. Mag. Lett.*, 2003, 83, 39–45.
66. Raty, J.-Y., Galli, G., Bostedt, C., van Buuren, T. W., Terminello, L. J. Quantum confinement and fullerene-like surface reconstructions in nanodiamonds. *Phys. Rev. Lett.*, 2003, 90, 037401.
67. Baidakova, M. V., Siklitsky, V. I., Dideikin, A. T., Vul', A. Ya., Surface reconstruction in diamond nanoparticles. In *Book of Abstracts of the First International Symposium "Detonation Nanodiamonds: Technology, Properties and Applications"*, Ioffe Institute. St. Petersburg (2003), p. 76.
68. Aleksenskii, A. E., Baidakova, M. V., Vul', A. Ya., Siklitskii, V. I. The structure of diamond nanoclusters. *Phys. Solid State*, 1999, 41, 668–671.
69. Krüger, A., Kataoka, F., Ozawa, M., Fujino, T., Suzuki, Y., Aleksenskii, A. E., Vul', A. Ya., Osawa, E. Unusually tight aggregation in detonation nanodiamond: identification and disintegration. *Carbon*, 2005, 4, 1722–1730.
70. Eidelman, E. D., Siklitsky, V. I., Sharonova, L. V., Yagovkina, M. A., Vul', A. Ya. A stable suspension of single ultrananocrystalline diamond particles. *Diamond Relat. Mater.*, 2005, 14, 1765–1769.
71. Dolmatov, V. Yu. *Ultradisperse Diamonds of Detonation Synthesis: Production, Properties and Applications.* State Politechnical University, St. Petersburg (2003).
72. Dolmatov, V. Yu., Fujimura, T., Burkat, G. K., Orlova, E. A., Veretenikova, M. V. Preparation of wear-resistant chromium coatings using different types of nanodiamonds. *Powder Metall. Met. Ceram.*, 2003, 42, 587–591.
73. Patrusheva, T., Letunovsky, V., Goryacheva, L., Gorschkov, A., Sergienko, V., Jakovleva, E. Protective coatings ultra fine diamond. *Carbon*, 2002, 40, 125–135.
74. Danilenko, N. V. *Synthesizing and Sintering of Diamond by Explosion*. Energoatomizdat, Moscow (2003).
75. Shulzhenko A. A., Gargin V. G., Bochechka A. A., Oleinik G. S., and Danilenko N. V. Diamond nanopowders used to improve strength of diamond- and silicon carbide-based composites. *Superhard Mater.*, 2000, 3, 3–15.
76. Koudoumas, E., Kokkinaki, O., Konstantaki, M., Couris, S., Korovin, S., Detkov, P., Kuznetsov, V., Pimenov, S., Pustovoi, V. Onion-like carbon and

diamond nanoparticles for optical limiting. *Chem. Phys. Lett.*, 2002, 357, 336–340.

77. Williams, O. A., Zimmermann, T., Kubovic, M., Denisenko, A., Kohn, E., Jackman, R. B., Gruen, D. M. Electronic properties and applications of ultrananocrystalline diamond. In: *Proceedings of the NATO Advanced Research Workshop on the Synthesis, Properties and Application of Ultrananocrystalline Diamond,* Springer, The Netherlands (2005), pp. 373–382.
78. Raty, J.-Y., Galli, G., Bostedt, C., van Buuren, T. W., Terminello, L. J. Quantum confinement and fullerenelike surface reconstructions in nanodiamonds. *Phys. Rev. Lett.*, 2003, 90, 037401.
79. Kuznetsov, V. L., Butenko, Yu. V., Chuvilin, A. L., Romanenko, A. I., Okotrub, A. V. Electrical resistivity of graphitized ultra-disperse diamond and onion-like carbon. *Chem. Phys. Lett.*, 2001, 336, 397–404.
80. He Deyan, Shaoa Lexi, Gonga Weibin, Xie Erqing, Xu Kang, Chen Guanghua. Electron transport and electron field emission of nanodiamond synthesized by explosive detonation. *Diamond Relat. Mater.*, 2000, 9, 1600–1603.
81. Krauss, R., Auciello, O., Ding, M. Q., Gruen, D. M., Huang, Y., Zhirnov, V. V., Givargizov, E. I., Breskin, A., Chechen, R., Shefer, E., Konov, V., Pimenov, S., Karabutov, A., Rakhimov, A., Suetin, N. Electron field emission for ultrananocrystalline diamond films. *J. Appl. Phys.*, 2001, 89, 2958–2067.
82. Obraztsov, A. N., Volkov, A. P., Pavlovsky, I. Yu., Chuvilin, A. L., Rudina, N. A., Kuznetsov, V. L. Role of the curvature of atomic layers in electron field emission from graphitic nanostructured carbon. *JETP Lett.*, 1999, 69, 411–417.
83. Karabutov, A. V., Frolov, V. D., Konov, V. I. Diamond/sp^2-bonded carbon structures: quantum well field electron emission? *Diamond Relat. Mater.*, 2001, 10, 840–846.
84. Dideykin, A. T., Edelman, E. D., Vul', A. Ya. The mechanism of autoelectron emission in carbon nanostrucrures. *Solid State Commun.*, 1993, 126, 495–498; Dideikin, A. T., Edelman, E. D., Vul', A. Ya. Thermoelectric effect in field electron emission from nanocarbon. In: *Proceedings of the NATO Advanced Research Workshop on the Synthesis, Properties and Application of Ultrananocrystalline Diamond*. Springer, The Netherlands (2005), pp. 383–394.

13 Diamond Phase Transitions at Nanoscale

Vladimir L. Kuznetsov and Yuriy V. Butenko

Boreskov Institute of Catalysis, Novosibirsk, Russia

Introduction

The graphitization and oxidation of diamond is a crucial issue for practical applications. These processes limit the performance of diamond used in cutting tools, optical windows, and electronic devices when the diamond surface is exposed to high temperatures and reactive gases (O_2, CO_2, H_2O, etc.).[1–4] Graphitization of diamond particles is a complicated process consisting of several steps, which unite in different combination and lead to different final structures due to a variation of number of atoms on a diamond particle. First steps include diamond structure transformation into graphene-like fragments, while further steps include the transformation of these primary fragments via joining and rearrangement and defect annealing into final products. In some cases the significant difference in the rates of these elementary steps allows us to distinguish them very clearly. At the same time this difference in the rates of elementary steps allows us to get a rather diverse family of nanocarbon materials (see later).

Experimental data analysis available in the scientific literature leads to the conclusion that the mechanism of diamond graphitization depends on reaction conditions and factors causing graphitization. Thus one can distinguish several principal independent processes resulting in diamond graphitization, namely:

(1) Thermal graphitization under vacuum, which occurs due to thermally activated movements of carbon atoms.
(2) Reactive graphitization caused by reactive gases in ambient atmosphere.[5–7]
(3) Graphitization catalyzed by metals.[1]
(4) Irradiation-induced graphitization (caused by laser or gamma-ray irradiation and by particle (electron, neutron, ion) beams).[8–10]

Recently diamond graphitization under high contact compression was observed as a result of pressing a sharp diamond indenter against its surface.[11]

In this chapter we mainly consider the first three types of graphitization leading to nanoscale objects while the basic mechanisms of radiation effects in carbon nanostructures with particular emphasis on atom displacements by knock-on collisions-induced diamond graphitization was described in detail by Banhart.[10] Furthermore Banhart et al.[12–15] have observed an interesting aspect of carbon transformation at nanoscale concerning the mutual transformation of onion-like carbon (OLC) to diamond and vice versa under electron or ion irradiation of dispersed carbon materials. Using the assumption that changes of atomic positions in irradiated phases are governed by thermally activated jumps (equilibrium diffusion) on the one hand, and, on the other hand, by ballistic knock-out displacements (non-equilibrium contribution), Zaiser and Banhart[16] developed a non-equilibrium phase diagram showing the stability of the phases (dynamical phase equilibrium) as a function of atom displacement rate and temperature.

The surface of atomically pure diamond is very active both physically and chemically, providing the chemical modification of the diamond surface with oxygen- and hydrogen-containing surface groups.[17] Decreasing diamond particle size leads to an increase in the ratio of surface and bulk carbon atoms. It determines the higher concentration of surface atoms and the higher concentration of surface defects. Finally, it provides higher reactivity and some specific properties of small diamond particles.

Synthesis of nanodiamonds (NDs) of medium size ~3–5 nm by the detonation of explosives was developed over the last four decades. The history of discovery of detonation NDs, the development of the detonation synthesis method and purification procedures of NDs, properties, and application fields of NDs are described in detail in recent books and reviews[18–24] and in this book. The technology is based on the detonation transformation of carbon-containing explosives with negative oxygen balance.[25–33] Knowledge of the reactivity of NDs to graphitization and oxidation can be even more important than that for bulk diamond crystals. At the same time, the small size of NDs provides additional features of the structure of graphitization products and a new approach in the production of new types of nanocarbons: the nanosize form of sp^2 carbon, namely, OLC, consists of closed graphene shells enclosed in each other; closed polygonized nanographite particles; sp^2/sp^3 nanocomposites with diamond cores, etc. Thus, we demonstrated that high-temperature anneal-

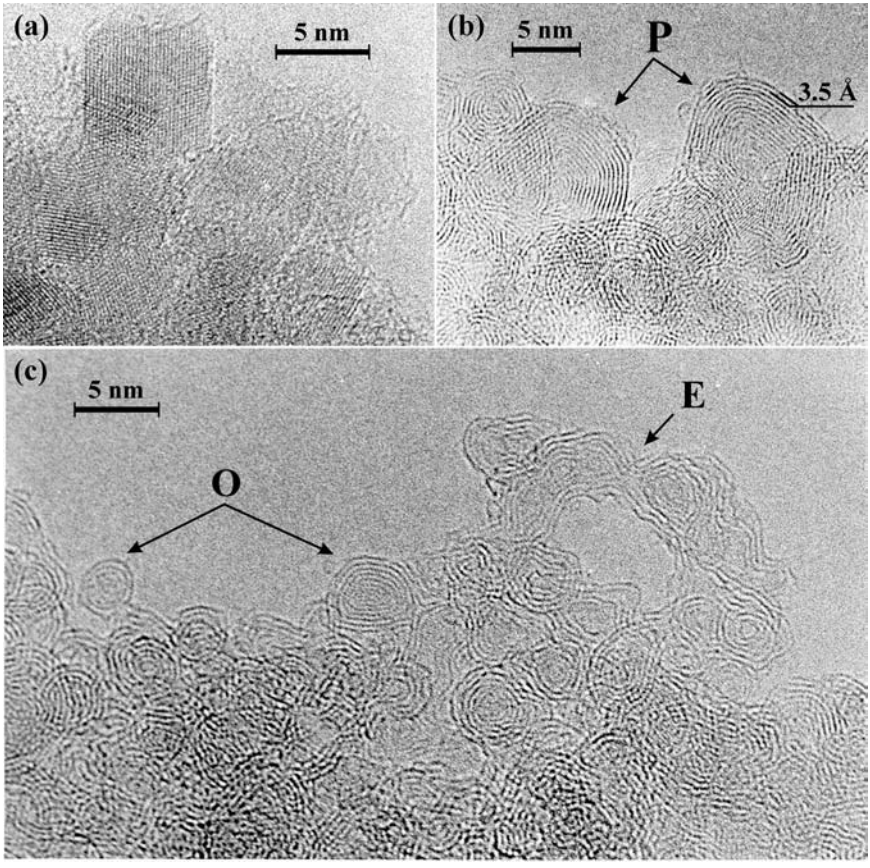

Figure 13.1 High-resolution TEM images of pristine NDs (a), and their annealing products produced at 1200–1800 K (b) and (c). Dark contrast lines (a) and curves ((b) and (c)) correspond to diamond crystal planes and graphite-like shells, respectively. The distances between lines correspond to the (111) lattice parameter of ND (a) (d_{111} = 0.2063 nm) and those between rings (b) and (c) to the distance between the graphite-like shells 0.34–0.35 nm (d_{002} = 0.3354 nm for hexagonal graphite). OLC particles are marked **O** (see (c)), polyhedron particles (b) are marked **P**, elongated particles with linked external graphite-like layers and closed quasi-spherical internal shells (c) are marked **E**.[34]

ing (~1200–1800 K) of NDs in vacuum produces OLC.[34,35] Figure 13.1 shows the annealing products produced by ND annealing at these temperatures. One can clearly see the formation of OLC and polyhedral particles with closed graphitic shells.

While one could predict the formation of nanosized products of ND annealing because of the low self-diffusion of carbon atoms up to high

temperatures (2000–2200 K), it was rather surprising to observe the self-organized formation of closed, curved graphite nanostructures (multilayer nanotubes and nanofolds) during annealing of micron-sized diamond.[36] Thus, Fig. 13.2 demonstrates the initial stage of surface transformation of micron-sized diamond particles after heating in vacuum at 1890 K.[36] One can see the formation of fullerene-like semi-spheres bonded with the diamond surface. The same results were obtained in experiments with synthetic and natural diamonds.

The detection of intermediate products of the annealing of the diamond surfaces[34–36] provides the most informative features of these studies. In this chapter we attempt to provide explanations of these and other observations concerning diamond graphitization using experimental and theoretical data available in the literature. We present the data concerning features of nanoscale diamond transformation, and discuss the mechanism of graphitization and properties of diamond annealing products.

13.1 Stability of Nanocarbons

The relative stability of nanocarbons became a major issue following the discovery of NDs in detonation soot, fullerenes, and nanotubes, nanocarbons in interstellar dust, etc. This problem was carefully considered in numerous papers and reviews[19,37] and in Part 2 of this book. Here we present only the main conclusions, which follow from those considerations. Different approaches were used for estimation of the stability of nanocarbons, which is necessary for comparison with experimental data.

First of all we refer to the traditional *P–T* phase diagram of carbon,[38] which contains two allotropic forms of carbon: graphite and diamond. Diamond at atmospheric pressure is the unstable form of carbon at all temperatures, despite the rather small energy difference between the two phases (~0.02 eV/atom). Thus the existence of NDs at temperatures up to 1200 K can be explained in terms of the high activation barrier for a phase transition. Thus, high temperatures (>1200 K), radiation, and/or the use of a catalyst are required to realize the phase transformation. It is obvious that when dealing with nanoscale objects the traditional phase diagrams should be modified. The downsizing of a material particle increases its surface energy and inflects an aspect of the phase diagrams of disperse systems in comparison with those for bulk single crystals. Thus the boundaries of a liquid phase and pressure-dependent regions of polymorphic transformations are inflected.

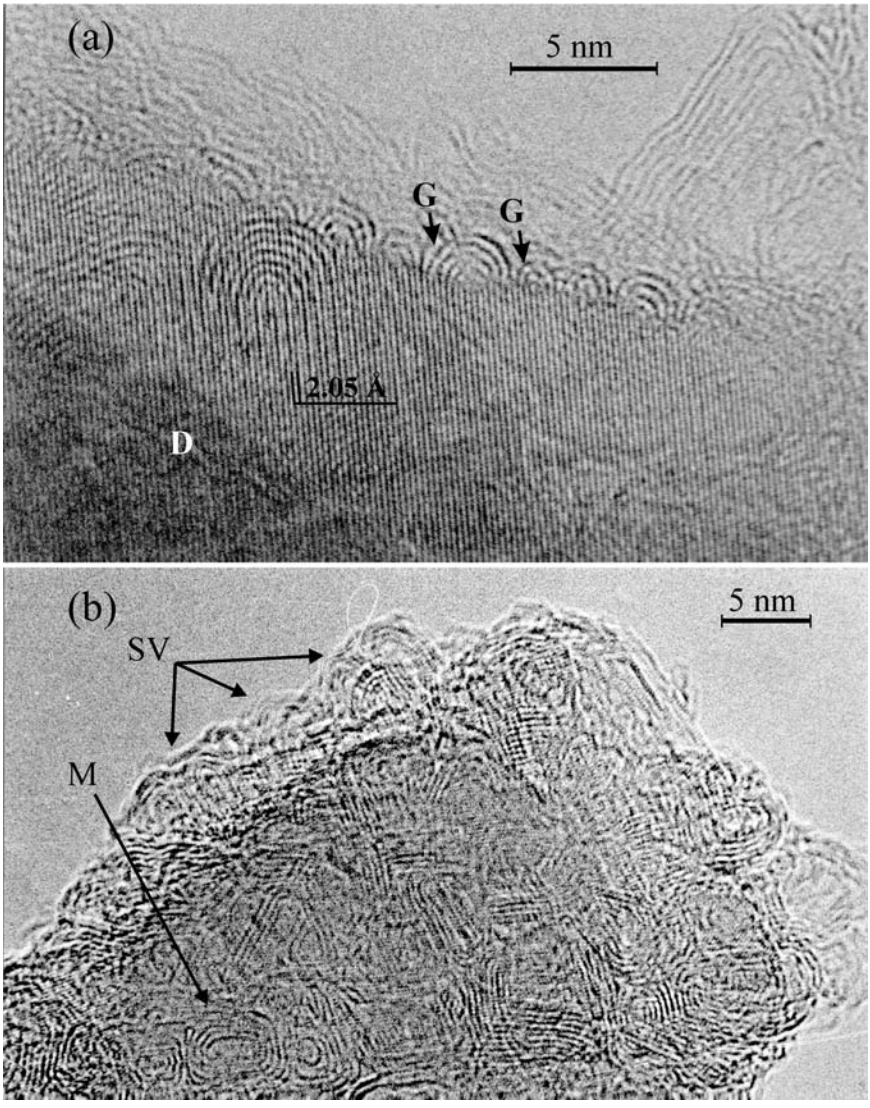

Figure 13.2 High-resolution TEM images of the surface intermediates of micron-sized diamond transformation to nanosized curved graphite-like carbon; diamond heated at 1890 K for 1 hour. (a) One can see the formation of two graphitic sheets (**G**) from three diamond planes (111) (**D**) on the interface of diamond with growing graphitic species (arrows show 3–2 transformation). (b) Mosaic (**M**) of closed curved graphitic structures on diamond core (dark region). A variation of focus gave the possibility of seeing (111) diamond planes of the core. **SV** indicates the side view of the closed curved graphite-like structures.[36]

Independently Viecelli et al.[39] and Danilenko[40] demonstrated that coordinates of triple points on the phase diagram for NDs shift to lower temperatures and higher pressures in comparison with those of bulk diamond crystals. This means that the region of thermodynamically stable diamond particles shifted to higher pressures. These data allow us to propose a three-dimensional phase diagram of carbon, where the number of carbon atoms in a particle is an additional parameter besides pressure and temperature.[19,41]

However, traditional thermodynamic considerations can hardly be used for the estimation of the stability of particles consisting of a few hundred atoms, because significant changes occur in the macroscopic parameters, which had been traditionally used for the description of nanoscale objects. Computational methods can provide data on the relative stability of carbon systems with a limited number of carbon atoms. Summarizing the results on the stability of different carbon clusters,[42–45] one can conclude that three regions for the stability of small carbon clusters can be distinguished: below 20 atoms the most stable geometries are one-dimensional ring clusters; between 20 and 28 atoms, clusters with quite different types of geometry have similar energies; and for larger clusters fullerenes would be more stable. OLC seems to be the most stable structure for carbon clusters containing up to 1000–2000 atoms. At least the OLC is a final product of ND annealing when carbon atoms cannot migrate from one OLC particle to another. The conversion of diamond clusters containing up to 275 atoms into concentric-shell fullerene structures with cross-links between the two concentric shells was observed by means of molecular dynamics simulations (at temperatures from 1400 to 2800 K) based on approximate Kohn–Sham equations.[46]

It should be mentioned that the stability of small carbon clusters significantly depends on the surface group composition and charge of the cluster. It was demonstrated that hydrogenated carbon diamond clusters are more stable than graphitic clusters with the same number of carbon atoms and possess negative enthalpy of formation in respect to bulk graphite used as the standard state.[47,48] This coincides with the discovery of higher diamondoids, hydrocarbons resembling hydrogenated nanometer-sized diamond molecules, which demonstrate exceptional thermal stability.[49,50] Furthermore it was mentioned[2] that in a hydrogen atmosphere diamond is stable up to 2000 °C. Thus, it is essential to consider the composition and thermal stability of surface groups so as to eliminate diamond dangling bonds and stabilize the diamond structure.

13.2 Surface Chemistry: Stability of Surface Species

The earlier work devoted to the surface states and surface chemistry of macroscopic diamonds was reviewed by Evans.[51] It was specifically mentioned that the hydrogen-containing groups (≥CH, >CH_2, —CH_3) are formed on oil-polishing diamond surfaces or treated by hydrogen; oxygen-containing groups such as >C═O, —COOH, ≥C—OH, ≥C—O—C≤ can be formed on diamond surfaces polished in an aqueous media or oxidized by heating in an oxygen atmosphere; and the fluorination of diamond results in the formation of ≥CF, >CF_2, —CF_3 groups. In contrast to macroscopic diamonds, due to the high surface-to-volume ratio of carbon atoms in a nanoparticle the influence of surface structures and surface groups on the physical and chemical properties of ND particles becomes crucial. In this chapter we mainly consider the thermal stability of surface groups of detonation NDs. It is considered that the decomposition of surface groups is followed by the surface graphitization of NDs. The fields of applications of detonation NDs and methods of investigation of ND surface chemistry are briefly reviewed.

13.2.1 Surface Groups of NDs

Detonation ND particles as produced are encapsulated in amorphous carbon and mixed with other non-diamond forms of carbon. Partial graphitization of ND particles during detonation synthesis results in the formation of graphite-like curved layers on the surfaces of diamond particles.[36] ND content in explosive soot can be up to 80% depending on the synthesis conditions.[20,35] The average size of ND particles is 4–5 nm while the majority of particles are within the size range 2 to 20 nm.[18,19,35]

To isolate NDs from explosive soot, purification techniques based on chemical treatments with different oxidative agents ($HClO_4$, HNO_3, nitrogen oxides, H_2O_2, O_3, CrO_3, $K_2Cr_2O_7$, etc.) are applied.[18,19,21] (See also chapters in this book.) The purification procedure results in the oxidation of non-diamond forms of carbon and leaves more stable ND particles. However, the surfaces of ND particles that are exposed to strong oxidative agents also undergo oxidation. Depending on the temperature of the purification process and the oxidizing agent, various chemical groups are formed on diamond surfaces. Investigations of the surface chemistry of NDs started in the early 1980s with the development of synthesis tech-

niques and the purification of detonation NDs in the USSR. This work is widely reviewed in the recent monographs of Vereschagin[18] and Dolmatov[21] (and in this book).

Diamond nanoparticles of size 4–5 nm have a significant number of surface atoms (~15%).[19] The chemical groups of ND bonded to its surfaces eliminate the highly reactive dangling bonds of these surface atoms. This provides a relatively high content of surface groups in ND considered as a material. Thus, the elemental analysis of the as-prepared ND revealed the following elemental composition of detonation ND: 85–87% of carbon, 0.1–2.5% nitrogen, and 0.5–2.5% hydrogen; the rest is oxygen.[18–21,52–54] All oxygen and hydrogen atoms belong to surface groups of ND.[18,52,53,55,56] Nitrogen is incorporated in nitrogen-containing groups such as amide groups[53] and nitro-groups.[55,57] It is also incorporated in the diamond lattice. An X-ray photoelectron spectroscopy (XPS) study of a partially graphitized ND sample at 1100 °C showed the presence of nitrogen; thus it was concluded that nitrogen is included within the diamond structure.[58] However, the nature of nitrogen centers in detonation NDs is still under discussion.[18,53,57,59]

One can see that the contribution to the total weight of surface groups in diamond nanoparticles is 10–14%.[18] The estimations given in ref. [18] showed that each surface carbon atom of a ND particle forms a bond to at least one heteroatom (H, O, N); the authors of ref. [55] concluded that one oxygen atom present in oxygen-containing surface groups falls on two surface carbon atoms of ND treated in strong oxidative reagents ($HClO_4$ or a mixture of HNO_3 and /H_2SO_4). It can be concluded that the chemical surface groups of ND form a dense "coat" on its surface.

Surface group of ND are important not just from the point of view concerning diamond particle stability and graphitization. They also have attracted great interest from different research groups as a way to the controlled functionalization of the ND surface. It was proposed that surface groups of ND are responsible for some of the IR absorption features observed in spectra of the interstellar medium[60–63] (see also Chapter 2). ND surfaces can be rendered as either hydrophobic or hydrophilic by adjusting the surface chemistry and, thus, ND particles can be prepared in the form of stable colloidal solutions in different media, which is necessary for different applications.[18,19,21,64–67] It was shown that ND particles suspended in a solution can be electrophoretically deposited on a substrate.[18,19,21,68–74] The high surface area of ND particles (250–420 m^2/g) provides improved integration in composite materials with metal and polymers.[18–21] This also opens up possibilities for chemical reactions on ND surfaces[75] and the wide potential for surface functionalization of

ND.[52,53,55,56,76,77] Specific surface functionalization of ND powders enables a variety of biomedical applications of ND derivatives: for example, for the separation, purification, and immobilization of nucleic acids and proteins,[21,64,78–83] application as a luminescent biochip,[80,84] biosensors,[19] and as antigen delivery vehicles.[85] The influence of NDs on human blood cells was studied in refs. [86,87]. Oxidized ND can generate interest as an efficient support for different catalysts as was found for larger diamond crystals.[88–94]

The surface chemistry of detonation NDs has been intensively investigated in a number of papers: IR spectroscopy,[53,55–57,60–63,66,76,77,82,95–99] temperature-programmed desorption (TPD),[55,100,101] chemical titration[18,98] polarography,[18] and XPS.[77] It was found that oxygen-containing groups, such as ≥C—OH (hydroxyl), ≥C—O—C≤ (ether group or bridge oxygen), >C═O (ketonic group), —COOH (carboxyl), —C(O)—O—C≤ (ester or lactone group), and —C(O)—O—(O)C— cyclic acid anhydride group, are formed on the surfaces of the ND starting material during oxidative treatments. The relative concentration of these groups depends on the type of oxidative agent used.[52,53,55,56] Table 13.1 summarizes the main characteristic frequencies of surface groups observed in IR adsorption spectra of NDs. The spectral features of ND surface groups mainly correspond to those for larger diamond crystals or graphite materials.[102] For their primary identification one can also use the spectral characteristic of functional groups found, for example, in ref. [103]. It should be noted that besides the spectral features of surface groups, lattice vibrations of diamond are also observed in IR spectra. Jiang and Xu[53] proposed that the presence of impurities such as nitrogen and/or defects in the structure of NDs cause the forbidden single phonon modes to become IR active. This makes a partial contribution to the broad bands at 1500–1000 cm^{-1}, which are greatly superimposed on the functional group modes.[53]

13.2.2 Thermal Stability of ND Surface Groups

Thermal stability of ND surface groups has been studied in refs. [53,56,95]. Thermal decomposition of the oxygen-containing groups results in the formation mainly of CO and CO_2. Both these gases are normally detected by a mass spectrometer or a chromatograph in TPD spectra upon heating a sample. However, it is difficult to unequivocally identify the surface groups from which the desorbing species originate. The com-

Table 13.1 Infrared Assignments of Main Bands for Surface Groups Observed on Nanodiamonds. Some Frequencies Were Related to Characteristics for Functional Groups Found in Ref. [103]

Frequency range (cm^{-1})	Assignment	References
3200–3600	**ν O—H** in water, hydroxyl groups in carboxylic or tertiary alcohol	53,56,57,82, 95,99,102
3360–3320	**ν N—H** amide groups	53
2800–3000	**ν-as** and **ν-s C—H** vibrations in hydrogen-containing groups: ≥CH, >CH_2, —CH_3	53,57,66,77, 95,102
1700–1865	**ν C═O** in ketonic, carboxylic, acid anhydrides groups, ester (lactones)	53,56,57,66, 77,82,95, 102
1620–1640	**δ O—H** in absorbed water	53,56,66,95
1460 (weak) 1458 (weak) 1300–1400 1300–1450	**δ-as C—H** in ≥CH, >CH_2, —CH_3 groups **δ C—H** for sp^3-bonded carbon	53, 95 57 103
~1260	**ν C—C, ν C—N** N-induced one-phonon process and/or defect structure in diamonds	53,57
1100–1370	**ν C—O—C** in ether, acid anhydride, lactones, epoxy groups	53,56,57,82, 102
1120–1200	**δ O—H** in carboxylic groups	53,56,102
1100–1350 1000–1100 1200–1350 1100–1200	**ν-as** and **ν-s C—F** vibrations **ν-s C—F** in C—F group **ν-as C—F** in CF_2 and CF_3 groups **ν-s C—F** in CF_2 and CF_3 groups	77 103

Abbreviations as in ref. [103]: as, antisymmetric; s, symmetric; ν, stretch; δ, bend or deformation.

bination of Fourier transform infrared (FTIR) spectroscopy, XPS, and TPD is useful in the identification of the surface groups and gives additional information about their decomposition temperatures.

Dandekar et al. combined TPD and diffuse reflectance Fourier transform infrared spectroscopy (DRIFTS) to study the nature of surface groups of differently treated carbon materials including diamond powder

with an average size of 1 μm.[102] The authors of this work reviewed work devoted to applications of the TPD technique for the characterization of carbon surface groups. It was shown that CO_2-yielding complexes like carboxylic acids, anhydrides, and lactones are mainly responsible for the acidic character of carbon rather than CO-yielding complexes like the phenolic and quinonic groups.[102,104] For sp^3-bonded carbon these groups correspond to hydroxyl groups in tertiary alcohol (weak acid) and ketonic groups (non-acidic group). The CO_2-yielding complexes were shown to decompose typically over a temperature range starting at 500 K and exhibiting desorption maxima at 600 and 900 K.[102,104] It was also proposed that carboxylic groups are responsible for the low-temperature peak; the high-temperature CO_2 evolution was attributed to acid anhydride groups.[102,104] The CO-yielding groups were divided into distinct groups, which have CO evolution maxima at 900 and 1100 K.[102,104]

Cataldo and Koscheev[56] studied the thermal stability of ND samples treated with ozone using thermogravimetric analysis (TGA-DTG) combined with differential thermal analysis (DTA). They found that a ND sample treated with ozone loses 3% of its weight at 550 °C (in an inert atmosphere); in contrast to this behaviour, the weight loss of bulk diamond was zero at this temperature. It was proposed that, due to the large concentration of oxygen-containing groups on ND surfaces and high surface area of ND powder, the weight loss was related to the desorption of different absorbed molecules, and to the condensation processes of adjacent chemical groups: for example, two neighbouring carboxylic groups form an anhydride group; carboxylic and hydroxyl groups form a lactone group.[56] This process results in the release of water molecules. Raising the temperature to 900 °C in an inert atmosphere resulted in the decomposition of all oxygen-containing groups and in a total weight loss of 11.5% (for bulk diamond the weight loss was found to be only 1% at the same temperature).[56] This result agrees well with the values of 10–14% for the weight of ND surface groups found in other work.[18]

Figure 13.3 presents the FTIR spectra of a ND sample annealed in a vacuum at different temperatures. Figure 13.4 presents the TPD spectra of ND and submicron diamond (ASM1 0.1/0).[97] All diamond samples were treated in similar conditions with a mixture of $HClO_4$ and H_2SO_4 (1 : 1) at 200 °C.[35,95] One can see that there is a correspondence between features in the spectra of ND and submicron diamond. However, the spectrum of submicron diamond is better resolved, while the peaks of the TPD spectrum of ND are broad and overlap each other. This can be understood if we take into account that a chemical group on defective surfaces of ND particles has a larger number of possible locations. Therefore, the tem-

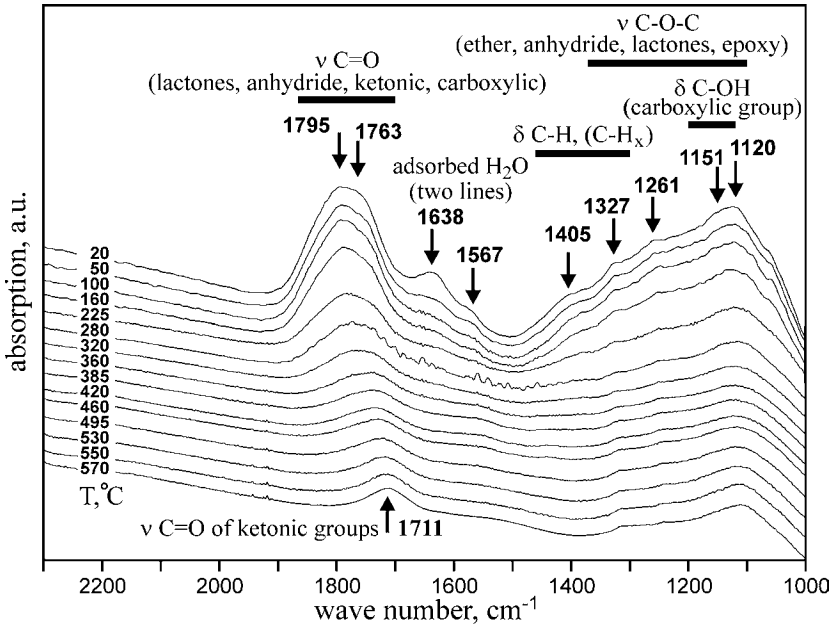

Figure 13.3 FTIR spectra of surface groups of a ND sample heated at different temperatures (as shown on the figure). The initial ND sample was purified in a mixture of $HClO_4$ and H_2SO_4 (1 : 1) at 200 °C. The characteristic ranges of vibrations of the surface groups are presented (FTIR spectra were recorded by Prof. E. A. Paukshtis).[100]

perature range of the thermal decomposition of a surface group depends on its surrounding and the crystallographic plane on which this group is attached.

The decomposition of oxygen-containing surface groups of a ND sample treated in a mixture of $HClO_4$ and H_2SO_4 starts at approximately 500 K and finishes approximately at a temperature of 1150 K. Hydrogen-containing groups decompose in a temperature range of 1050–1400 K releasing hydrogen (Fig. 13.4). We believe that at a low-temperature region of 500–920 K two processes occur: (1) the condensation of different oxygen-containing groups releasing water molecules and corresponding oxygen-containing groups;[56] and (2) the decomposition of acidic groups (carboxyl, anhydride, and lactone groups) releasing CO_2 and CO gases. It should be noted that partial decomposition of CO_2 resulting in CO formation occurs in the electron ionizer of our mass spectrometer, which can be a reason for the observed correspondence in the positions of CO_2 and CO peaks. We registered the maximum of gas evolution of all

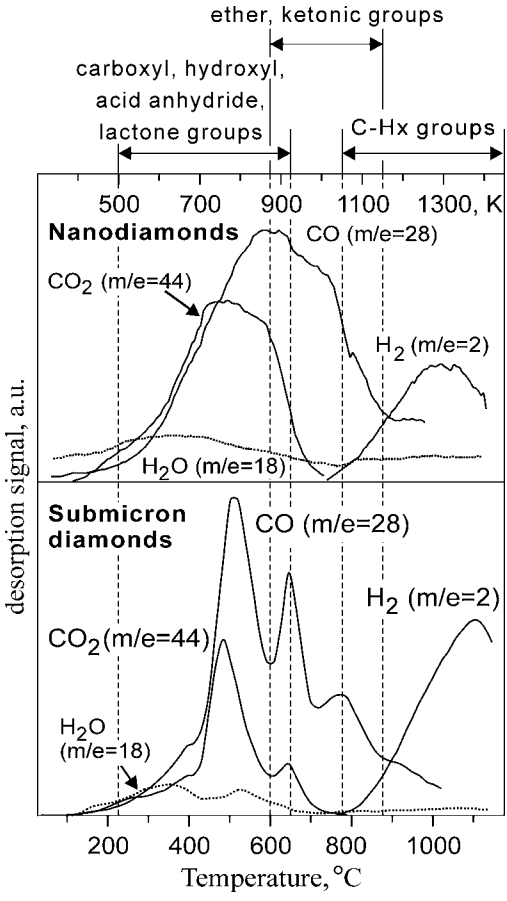

Figure 13.4 TPD curves of CO, CO_2, H_2O, and H_2 gases originating from decomposition of the surface functional groups of pristine ND and submicron diamonds purified in a mixture of $HClO_4$ and H_2SO_4 (1 : 1) at 200 °C. The temperature regions of decomposition of different oxygen- and hydrogen-containing surface groups of diamonds are presented.[100]

gases (pressure abruptly increased) from the diamond samples over a temperature range of 720–850 K. We attribute the evolution of CO at the temperature region of 870–1150 K to the decomposition of ether (bridging oxygen) and ketonic groups. The TPD data allow us to attribute observed changes in the FTIR spectra of the ND sample (Fig. 13.3) at a temperature range of 290–840 K. Thus, decreasing the bands at 1700–1865 cm^{-1} corresponds to the disappearance of C═O stretching modes in carboxylic groups, anhydrides, lactones, while the remaining peak at maximum

heating temperature with a maximum at 1711 cm^{-1} (Fig. 13.3) belongs to C═O stretches in ketonic groups of the ND sample.

The thermal decomposition of surface groups provides an additional way for the regulation of their composition and modification of surface properties.[53,97,105] The full decomposition of surface groups in a vacuum or inert atmosphere results in the formation of bare diamond surfaces, which can reconstruct decreasing surface energy due to the closing of dangling bonds of surface atoms (see Section 13.4.1). However, for ND particles the situation can be different. Barnard et al.[106] and Raty et al.[107] showed theoretically that bare {111} surfaces of a ND particle undergo deeper graphitization. A bare ND particle transforms to a more stable bucky-diamond particle that appears as a ND particle covered with nanometer-sized fullerene-like shells.[106,107] It was shown that further graphitization progresses from the surfaces of ND particles and leads to the formation of OLC.[34,41,108–112] The bucky-diamonds appear as intermediates of the ND transformation to OLC.

13.2.3 Critical View of the Formation of sp^2-Bonded Carbon in Pristine NDs

There is no a commonly accepted view on the nature of sp^2-bonded carbon on the surface of ND particles. Since different authors used NDs from different vendors using different purification procedures and no uniform standard method of purification exists, experimental results on the presence of sp^2 carbon in pristine NDs differ significantly. Here we briefly demonstrate the results obtained by different research techniques which can be found in the literature:

- *XRD*. The XRD analysis of ND samples performed in refs. [111,113–115] revealed the presence of a small amount of disordered carbon. Tomita et al.[111] and Xu et al.[113] clearly showed in an XRD spectrum of an initial ND sample the presence of the (002) peak of graphite corresponding to small quantities of sp^2-bonded carbon in pristine samples. However, Prasad et al.,[116] Mykhaylyk et al.,[112] and Qian et al.[117] did not observe features belonging to sp^2-bonded carbon in XRD spectra of pristine ND samples.
- *Raman spectroscopy*. The sp^2-bonded carbon in initial ND samples was observed by Yoshikawa et al.[118] (excitation at 514.5 nm); Tabata et al.[75] (excitation at 514.5 nm);

Mykhaylyk et al.[112] (excitation at 244 nm); Aleksenskii et al.[114] (excitation at 488 nm); and Prasad et al.[116] (excitation at 514.5 nm). Obraztsova et al.[119] found no graphite features in the Raman spectrum of a ND sample (excitation at 457.9 nm).

- *Electron energy loss spectroscopy (EELS), small-angle X-ray scattering (SAXS), and high-resolution transmission electron microscopy (HRTEM).* An EELS study undertaken in ref. [112] revealed about 40% of sp^2-bonded carbon in an initial ND sample. SAXS modeling performed in this work also confirmed the presence of outer, less dense shells surrounding ND particles, which were attributed to amorphous carbon with mixed sp^2/sp^3 bonding. The presence of disordered graphite-like species on ND surfaces can also by observed by HRTEM.[109–112,116]

These contradictory results, on the other hand, can be understood if we consider limitations of these methods:

(1) XRD is more sensitive to the presence of well-ordered materials (with a particle size more than 2–3 nm) and less sensitive to amorphous materials; thus the disordered sp^2-bonded carbon cannot be observed if its concentration is less than 5–7%.
(2) The Raman scattering cross-section of diamond and graphite carbon strongly depends on the excitation wavelength used.[118,120] The Raman scattering cross-section of diamond is about one-sixtieth that of graphite at an excitation wavelength of 514.5 nm,[118] therefore the presence of even a negligible amount of sp^2-bonded carbon significantly contributes to the Raman bands of graphite-like species. If Raman spectra of a carbon sample are measured by shorter excitation wavelength close to the band gap of diamond (~5.5 eV, 225.8 nm), the detection sensitivity for the Raman band of diamond might become higher than that for graphite. It should also be considered that the laser radiation in a Raman spectrometer can result in local overheating of a specimen and can cause oxidation (in air) and even graphitization of a ND sample.
(3) As mentioned above, the surfaces of ND particles after a purification procedure with oxidative agents are covered

by a dense "coat" composed of various chemical groups. These groups stabilize ND surfaces and prevent them from graphitization. However, under electron bombardment (EELS, HRTEM) the decomposition of surface groups[121–124] resulting in surface graphitization occurs. The transformation of diamond particles to carbon onions under electron irradiation was demonstrated by Qin and Iijima[125]. Later Roddatis et al.[126] also demonstrated that OLC formation from NDs can be activated by high-energy electron irradiation. Zaiser and Banhart[16] showed that irradiation at low temperatures (<580 K) and high temperatures (>1100 K) promotes the transformation from diamond to graphite, but at intermediate temperatures the reverse process can occur. Thus, conclusions from TEM data concerning the nature of graphite-like carbon on the surface of NDs should be accepted with care.

It can be concluded that the disordered sp^2-bonded carbon can appear on surfaces of initial ND particles, but its presence and quantity evidently depend on the conditions of synthesis and purification of ND samples. The formation of sp^2 species on ND surfaces can be avoided by the hydrogenation of ND particles.[127–129]

13.2.4 The Onset Temperature of ND Graphitization

The thermal graphitization of detonation NDs has been studied by a number of authors. It has been carried out in: vacuum;[34,41,108–112] argon[73,113–116,130,131] and hydrogen ambient;[132] and under high pressure.[117] The registered low-temperature onset of ND graphitization differs in different papers depending on experimental conditions and the research technique used. Thus, when graphitization was performed in argon ambient the changes in XRD spectra related to the appearance of sp^2 carbon were observed between 800 and 1000 °C.[113,131] Raman spectroscopy used in these two papers reveled that features originating from graphitic carbon become significant after annealing at 800 °C. Xu et al.[113] used differential scanning calorimetry (DSC) in argon to find the temperature onset of ND graphitization. The onset of an exothermic peak at 670 °C on a DSC curve was related to the initiation of ND graphitization. Qian et al.[117] studied the graphitization of diamond powders of different sizes at high

pressures from 2 to 8 GPa. The onset temperature of 730 °C for graphitization of 5 nm ND powder was estimated at 2 GPa with Raman spectroscopy data. However, Prasad et al.[116] did not observe features belonging to sp^2-bonded carbon in the XRD spectra of a ND sample annealed at 900 °C in argon.

It is difficult to explain the variation of the onset temperature of ND graphitization from 670 to 1000 °C found in these works. However, we should emphasize the removal of oxygen-containing reactive gases (O_2, H_2O, CO_2, CO, etc.) from a reaction vessel (reactor). The decomposition of oxygen-containing groups at a temperature range of 500–923 K results in a large evolution of CO and CO_2 (Fig. 13.4),[95] which can affect the graphitization process. Thus, even small concentrations of these reactive gases can cause a decrease in the graphitization onset temperature, increase the graphitization rate, and affect the structure of graphitization products (see Section 13.6).

Pristine ND nanoparticles often have a gray color. It should be noted that the color of a pristine ND sample can vary depending on the size of ND particles and their aggregates. Osawa[133] has observed the change of color of a ND colloidal solution (from gray to black) during milling of ND suspensions in water or organic solvents, which leads to a decrease in the size of ND particle aggregates. We observed a change of color of ND particles to black from the gray color of pristine ND particles after heating at 900 °C in a vacuum of 10^{-5} Torr for 1 hour. HRTEM studies of this sample did not reveal the presence of well-ordered graphitic structures on its surfaces (see Section 13.4.5 and ref. [108]). The surfaces of annealed ND particles mostly look uncovered after annealing in vacuum at this temperature. Note that TEM irradiation promotes ND graphitization (see Section 13.2.3); however, a short time registration can help to avoid significant surface graphitization of diamond. Prasad et al.[116] observed the change of color of a ND sample to black from the brownish appearance of the pristine particles after heating at 900 °C in argon ambient for 3 hours. However, these authors mentioned that HRTEM images after this heat treatment show large portions of unconverted diamond particles, while the surface seems to have been covered with portions of amorphous carbon with no clear long-range order. Thus, it can be concluded that the black color of ND samples does not necessarily portray their significant graphitization.

The absence of a pronounced sp^2 component at lower binding energy in the C1s photoemission spectrum (see ref. [134]) of a ND sample annealed at 900 °C in vacuum for 1 hour also indicates that the annealing of NDs at these conditions is insufficient to produce appreciable graphi-

tization. The sample remains as an insulator.[135] Partial graphitization of the sample, nevertheless, according to Raman spectroscopy and XRD data,[136] occurs. The graphitization can proceed only on bare ND surfaces. As the annealing temperature increases up to 1150 °C (for 1 hour), the HRTEM images reveal the formation of 2–4 curved graphite layers on surfaces of ND particles with sizes more than 2 nm[41,108] (see Section 13.7). The images demonstrate well-resolved interfaces between diamond cores and curved graphite layers adjacent to the diamond surfaces[41,108] (see Section 13.7). The HRTEM images show that the full graphitization of ND particles with sizes less than 2 nm occurs at these conditions, indicating significantly higher graphitization rates for small ND particles.

The experimental data discussed above allow us to conclude that the temperature of full decomposition of oxygen-containing groups (about 900 °C) results in the reconstruction and only partial graphitization of ND surfaces in vacuum; however, at this temperature no well-ordered graphite-like structures can be formed on ND surfaces. The full unveiling of ND surfaces occurs at 900–1150 °C with decomposition of hydrogen-containing groups resulting in the formation of several curved graphite-like shells on the surfaces of large ND particles (>2 nm), and full graphitization of small ND particles (<2 nm) with the formation of OLC particles containing 2–3 fullerene-like shells (see Section 13.4.5). We believe that surface groups of NDs stabilize the ND particles. Upon complete removal of the surface groups, the surface carbon atoms become more mobile, which inevitably leads to the graphitization of NDs.

13.3 Kinetics of Diamond Graphitization

As mentioned earlier, in general large diamond transforms into graphite at appreciable rates only at high temperatures ($T > 2000$ K). Classic quantitative studies of the graphitization of macroscopic size diamonds by Davies and Evans[137] were carried out in the temperature range 2150–2300 K. These researchers determined the rates of graphitization for the (111) and (110) faces as well as the kinetic parameters describing the rates. Under high vacuum conditions, the first steps of diamond graphitization are preceded by a rearrangement of diamond surfaces.[138] Because of the relatively low graphitization rates involved, Hoffman et al.[139] obtained quantitative data for the range 1500–1800 K only for a (100) surface exposed to ion etching. In this chapter we consider the kinetics of ND graphitization in a low-temperature region (1370–2150 K). A detailed

explanation of the experimental procedure and calculations can be found elsewhere.[108] In this section we outline some of the main steps and results of this work in comparison with results of other work devoted to diamond graphitization.

13.3.1 Experimental Approaches for the Study of ND Graphitization

It is essential to note that investigations of the graphitization of diamond nanoparticles with sizes of 2–20 nm allowed us to carefully examine the structure of the starting material and products of their graphitization by HRTEM. A study of macroscopic objects (more than 1 μm in size) demands a special preparation procedure for the samples, while HRTEM was successfully applied for study of the graphitization of NDs[34,41,108] and submicron diamonds.[36,140] Another advantage of the use of nanoparticles is their high surface area compared to the surface area of macroscopic particles. Thus, graphitization starts from the surface of diamond particles, and even slight graphitization can be quantitatively measured, though it is difficult to perform in the case of macroscopic diamond crystals due to their low surface area. This allowed us to investigate ND graphitization in the lower temperature region (1370–1870 K) and to register directly the extent of graphitization.

13.3.1.1 Estimation of the Diamond Fraction in the Intermediates of ND Graphitization

The estimation of diamond fractions was performed by determining the densities of pristine NDs, partially graphitized samples, and fully graphitized samples.[108] This is facilitated by the rather large difference in the density of carbon in its diamond and graphite forms. Since, as noted earlier, graphitization proceeds from the surface to the bulk, larger percentage changes in the density are observed in smaller particles than in larger ones. In small ND samples, a significant conversion from diamond to graphite-like carbon occurs within experimentally reasonable times in the temperature range of interest. The intermediates of ND graphitization are composed of two phases (sp^3- and sp^2-bonded carbon), in which both have the same molecular weight. Thus the ratios of sp^3/sp^2 carbon can be calculated as

$$\frac{1}{\rho} = \frac{x_1}{\rho_1} + \frac{x_2}{\rho_2}, \qquad \text{Eq. (13-1)}$$

where x_1 and x_2 are the weight fractions of the diamond and graphite-like carbon, respectively, ρ_1 and ρ_2 are their densities, and ρ is the average density of a sample, which is defined from the values of the volume and weight of the sample. The volume of samples was measured by a helium pycnometer (the measured ND density (ρ_1) was 3.07 ± 0.02 g/cm^3 and the density of OLC (ρ_2) was 2.03 ± 0.02 g/cm^3).[108] The weight fractions x_1 and x_2 are related as

$$x_1 = 1 - x_2. \qquad \text{Eq. (13-2)}$$

Taking into account experimental errors arising from density measurements, one can only estimate the sp^3/sp^2 ratio within experimental error. However, according to the literature, the estimation of this ratio based on the density of a carbon material is often used and becomes useful when compared with results of other methods. For example, the authors of refs. [141,142] used the following relation between the diamond fraction in amorphous carbon films and the sample's density:

$$x_{\text{diamond}}(\%) = (\rho \text{ g/cm}^3 - 1.92)/0.0137, \qquad \text{Eq. (13-3)}$$

where ρ is determined by EELS.

A comparison of the results obtained by (13-3) and (13-1) is given Table 13.2. The small difference in the values obtained by different approaches

Table 13.2 A Comparison of Values of Diamond Fractions in Partially Graphitized Nd Samples Obtained by Different Approaches

Annealing temp. (K)	1420	1600	1800
Density (g/cm^3) (ref. [108] and this work)	2.90 ± 0.02	2.53 ± 0.02	2.14 ± 0.02
Diamond fraction (ref. [108] and Eq. (13-1))	0.86 ± 0.05	0.57 ± 0.05	0.15 ± 0.05
Diamond fraction (refs. [141,142], Eq. (13-3))	0.72 ± 0.02	0.45 ± 0.02	0.16 ± 0.02

can be explained by the differences of carbon materials: namely, amorphous carbon in refs. [141,142] and OLC ND in ref. [108].

13.3.1.2 The Kinetic Model; the Reducing Sphere Model

Since the graphitization of diamond starts from its surface and proceeds to the bulk, one goal was to determine a temperature-dependent isotropic rate of migration of the interface between the diamond and graphite regions of the particles.[108] For the study of ND particle graphitization the orientational effects of diamond graphitization were averaged. To achieve the goal we employed the reducing sphere model. The model assumes that the phase conversion begins simultaneously at all surface points and that under isothermal conditions the interface moves with *a constant isotropic rate (k) inside the bulk of the particle*. We also made the simplifying assumption that the particles are spherical. In the simplest case the initial diamond particles all have the same radius r_0 and weight M_0. Then the graphitization of the surface diamond layers leads to a change in the diamond core radius, Δr, and a new weight of diamond M. The weight fraction x of the non-graphitized diamond can be expressed as

$$x_{\text{diamond}} = \frac{M}{M_0} = \frac{(r_0 - \Delta r)^3}{r_0^3}. \qquad \text{Eq. (13-4)}$$

Thus, if the weight fraction x of the diamond at the end of the heating is known, the change in radius can be calculated. Further, to the extent that the sample was heated isothermally, one could relate the corresponding Δr to the rate of interface motion k and the time interval Δt by $\Delta r/k\Delta t$, and thereby determine k.

Finally the size distribution of initial ND particles (determined by SAXS) was taken into account. The detailed calculations of the graphitization rates for this realistic case are presented elsewhere.[108]

13.3.2 Kinetic Parameters of ND Graphitization for the Temperature Range of 1370–1860 K

13.3.2.1 Two Temperature Regions for Diamond Graphitization (1370–1860 K and above 1900 K)

Figure 13.5 presents an Arrhenius plot of the obtained ND graphitization rates (triangles in the figure) as a function of $1/T$, where T is the

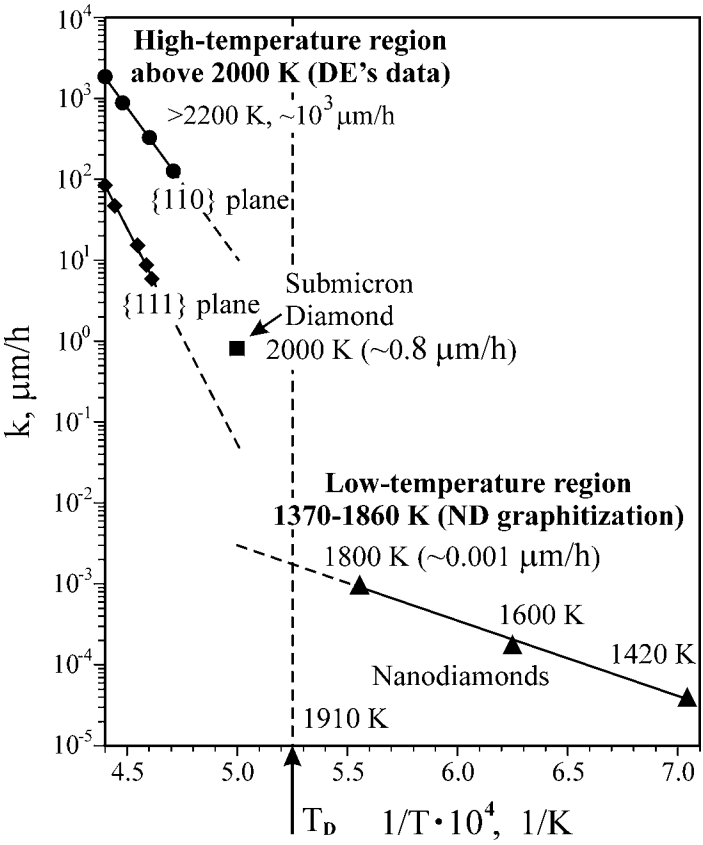

Figure 13.5 The rates of interface migration for the ND and submicron size particles (see ref. [108]) and for the {111} and {110} faces of macroscopic diamonds determined by Davies and Evans (DE's data; see refs. [5,137]). The dashed lines are extrapolations of the Arrhenius expression fits to the low- and high-temperature rates. The Debye temperature for diamond, T_D = 1910 K, appears to serve as the boundary between the low- and high-temperature regions of diamond graphitization where the graphitization occurs by different mechanisms.

annealing temperature. We found the activation energy, 45 kcal/mol, in the lower temperature region (1370–1860 K), to be only roughly one-half the energy of one C—C bond in diamond, 87.3 kcal/mol. That suggests a graphitization mechanism in which the atoms do not completely separate from the surface but in which the outer diamond planes transform progressively into graphite planes. Our estimate of the graphitization activation energy is very close to that found for a (100) face which had been

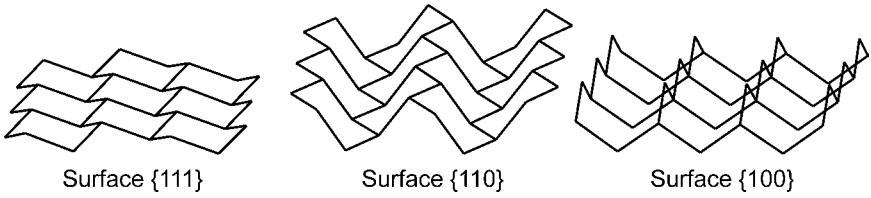

Figure 13.6 Fragments of different diamond surfaces.

amorphitized by Ar ions (42 kcal/mol).[139] The obtained activation energy for NDs agrees well with results presented in ref. [117], which are 202, 206, and 214 kJ/mol (48.3, 49,2, and 51.2 kcal/mol, respectively) for diamond powders of average grain sizes of 5, 50, and 250 nm, respectively for the temperature range of 1073–1673 K at a pressure of 2 GPa.

It was interesting to compare our data with those obtained by Davies and Evans (hereafter DE) for temperatures ranging from 2150 to 2300 K.[5,137] DE determined the rates of graphitization of the {110} and {111} faces of macroscopic samples of diamond (mass ~0.02 g). Fitting those rates to the Arrhenius expression, DE found the activation energies for the {110} and {111} faces to be 176 kcal/mol (736 kJ/mol or 7.6 eV/atom) and 252 kcal/mol (1054 kJ/mol or 10.9 eV/atom), respectively. From measurements of the rates at elevated pressures, DE determined that the "activation volumes" for both surfaces are about 10 cm^3/mol. In the DE model it is taken in the account that the activation energies are high (close to the energy for the vaporization of diamond) and correspond to the breaking of the two C—C bonds for the {110} surface and the three C—C bonds for the {111} surface (see Fig. 13.6), and that the activation volume is approximately equal to that for a single carbon atom in diamond. Based on these assumptions it was concluded that the process defining the rate of graphitization is the detachment of a single atom from the diamond surface.

We estimated the rate of the migration of the diamond/graphite interface to be 0.8 ± 0.4 μm/h at 2000 K for submicron diamonds.[108] To relate our results for the rates, k, for the ND and submicron size particles to those of the DE model[5,137] we display both sets of results in Fig. 13.5 over the extended temperature range of 1400–2400 K. The results of both models have been extrapolated up to temperatures around 2000 K using the Arrhenius fits at higher and lower T, respectively. It is seen that while the rate for the submicron diamonds lies well above the extrapolated rate for the NDs, it is within the range of values extrapolated from DE's rates for the {110} and {111} surfaces. This supports the conclusion that different

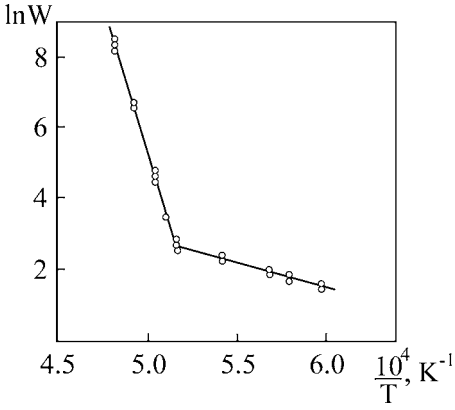

Figure 13.7 Dependence of the specific graphitization rate (*W*) on temperature in Arrhenius coordinates for diamond powder with a mean particle size of about 4 μm. The specific graphitization rate was determined from the dependence of the amount of the graphite formed on time. (Reprinted from Surf. Coat. Technol, 28(2), D.V. Fedoseev, S.P. Vnukov, V.L. Bukhovets, and B.A. Anikin, "Surface graphitization of diamond at high temperatures", 207–214, Copyright (1986) with permission from Elsevier.)

graphitization mechanisms are operative at and above 2000 K and below 1800 K. The Debye temperature, $T_D \cong 1910$ K, can be taken as the boundary between the two regimes. We recall that at and above T_D, all modes of vibrations are excited.[108]

Fedoseev et al.[7] studied graphitization kinetics on synthetic and natural diamond powders with particle size in the range 0.5–120 μm in a vacuum of 10^{-4} Torr. The authors found the existence of two temperature regions for graphitization, which have substantially different activation energies. It was shown that in the low-temperature region, up to 1900 K, the graphitization activation energy is 200 kJ/mol (47.8 kcal/mol), whereas in the high-temperature region it is 1200 kJ/mol (287 kcal/mol). Therefore the mechanisms of the graphitization process in these regions are expected to be different.[7] Figure 13.7 shows the dependence of the specific graphitization rate on temperature in Arrhenius coordinates found in ref. [7]. The temperature boundary of 1900 K between the two regions coincides fairly well with that found by us for NDs.[108] The graphitization activation energy for the high-temperature region approximately coincides with the activation energies found using the DE model. For the low-temperature region (below 1900 K) the activation energy of 200 kJ/mol (47.8 kcal/mol) is close to that of 230 kJ/mol (55 kcal/mol) for the oxidation of diamond found by Evans[5] and Uspenskaya et al.[6] (see Section 13.6). Therefore, Fedoseev et al.[7] concluded that there seems to be an influence of oxygen-containing compounds on the graphitization process in the low-temperature region.

Such an influence is discussed in Section 13.6. It is shown that oxygen- and hydrogen-containing gases participate in the carbon redistribution processes. These processes influence not only the observed graphitization rates, but also the graphitization products. Enoki et al.[73,116,130] conducted

graphitization of NDs in argon flow and found the formation of graphite nanoparticles, while graphitization of NDs at the same conditions but in a vacuum of 10^{-5} Torr resulted in the formation of OLC.[34,41,108–112] It is likely that argon, which was used in refs. [73,116,130], could contain some impurities of oxygen-containing gases, causing graphitization to occur by a different mechanism (see Section 13.6). HRTEM images of ND graphitization products produced at different temperatures in vacuum[41,108,135] (see Section 13.7) with clearly observed intermediates of the ND transformation allow us to conclude that the derived activation energy of $E = 45 \pm 4$ kcal/mol (188 kJ/mol) for the low-temperature region (1370–1870 K) corresponds to the activation energy of the graphitization process occurring through the direct transformation of sp^3-bonded carbon to graphite-like carbon.

13.3.2.2 Absolute Rates of ND Graphitization

Rates of the diamond–graphite interface movement calculated from the derived kinetic parameters for various temperatures are presented in Table 13.3. One can see that at the onset of the low-temperature region (1370–1860 K) the rates of graphitization are very low, while small diamond particles 1–2 nm in size are easily graphitized even at 1420 K by a 1 hour treatment to produce 3–4 curved defective graphite shells, whereas only 1–2 graphite layers are formed on the surface of larger diamond particles. However, the contribution of the small particles to the kinetic results is negligible because, according to the SAXS data,[108] the amount of small particles with radii below 1.0 nm in the ultradispersed diamond sample is about 0.5% by weight. Thus, the estimated rates of graphitization are also average rates. Obviously, there is a dependence of graphitization rates on sizes of diamond particles, and smaller ND particles graphitize at significantly higher rates. Qian et al.[117] observed

Table 13.3 Migration Rates of the Diamond/Graphite Interface at Various Temperatures Calculated from the Kinetic Parameters for the Temperature Range of 1370–1860 K (Activation Energy of E = 45 ± 4 kcal/mol and Pre-exponential Factor A = 74 ± 5 nm/s) in Ref. [108]

T (°C)	1373	1473	1573	1673	1773	1873
k (Å/h)	0.2	0.6	1.6	3.8	8.2	16.2

differences in graphitization rates among nano, submicron, and micron diamonds.

Raising the annealing temperature to 1800 K for about 1 hour results in almost full graphitization of ND. The XPS study revealed the absence of sp^3 carbon in the sample and is consistent with our previous HRTEM data, which showed the absence of diamond structures in samples heated above 1800 K.[134] However, the data on the true densities and, thus, calculated graphitization rates of the ND annealing products indicate that this sample still consists of 15% diamond.[108] This discrepancy is explained by the presence of sp^3-bonded carbon only in the core of the largest particles (of size up to 20 nm). The "screening" of these diamond cores by the surrounding graphite-like shells is the reason for the absence of the sp^3-bonded carbon component in the C1s XPS spectra of the sample annealed at 1800 K (photoelectrons from the cores have a mean free path shorter than the thickness of the outer graphitic shells). Some particles may contain a small diamond core, which cannot be seen in the HRTEM micrographs because of their low contrast. It is probable that such cores are retained as a result of the high pressures existing inside the OLC particles. The existence of high pressure inside a graphitized particle at temperatures below the Debye temperature can be explained in the following way. As the graphitization proceeds from the surface and the outer graphite shells close, the OLC particle formed retains an excess of carbon atoms that could ultimately convert into graphite-like structures. Since at this temperature the external carbon layers cannot easily be rearranged and thus relieve stress, a pressure develops which is capable of stabilizing the diamond core. Banhart and Ajayan[12] reported on the formation of a diamond core inside the OLC when their samples were heated to 1270 K and radiated with an electron beam. Even annealing at higher temperature is sometimes not enough to convert all ND particles to OLC; Tomita et al.,[111] using the XRD technique, revealed the presence of traces of sp^3-bonded carbon in a ND sample annealed at 1700 °C for 30 min at a pressure less than 2×10^{-3} Pa.[110]

The HRTEM data indicate that the annealing of synthetic micron-size diamonds at 1890 K (see Fig. 13.2(b)) in a vacuum for 1 hour results in the formation of a graphite-like carbon layer 30–50 Å thick. This corresponds to the graphitization of a diamond surface layer 17–30 Å thick. The thickness of the diamond layer calculated with the kinetic parameters is equal to 18 Å (Table 13.3). The experimental and calculated rates of graphitization thus agree within experimental error.

The direct measurement of sample density appears to be a reliable method for estimating the diamond fraction in a sample composed from

two phases: sp^2- and sp^3-bonded carbon. This method allows estimation only of an average value of the diamond fraction; therefore derived values of graphitization rates do not reflect the dependence of the rates on sizes of diamond particles. However, the determined kinetic parameters yield graphitization rates which agree well with the HRTEM data related to the graphitization of submicron diamond. This suggests that the kinetic parameters of the ND graphitization can be used to estimate rates for the graphitization of larger diamonds. These parameters can help one control the modification of the diamond surface by the formation of fullerene-like carbon states on this surface.

13.4 Mechanism of Diamond Graphitization

13.4.1 Diamond Surface Reconstruction

The reconstruction of diamond surfaces has been the subject of numerous theoretical and experimental studies.[3] Interest in this field is motivated by the apparent importance of reconstruction steps in the chemical vapor deposition (CVD) synthesis of diamond and in the diamond graphitization processes. The surface of any diamond (synthetic or natural) is regularly covered with chemical groups, the composition of which depends on the history and procedures of the diamond treatment. Surface reconstruction starts after the decomposition of surface groups. The motive force for the reconstruction of diamond surfaces is the saturation of the dangling bonds, which is induced by partial rehybridization of the surface atoms towards sp^2.[138] Below we will briefly summarize findings on diamond surface reconstruction. The simple crystallographic planes (100), (110), and (111) correspond to the faces of the three major crystal forms of diamond: the {100} cubic, the {110} dodecahedral, and the {111} octahedral (see Fig. 13.8). Both cubic and octahedral surfaces are predominant in high-pressure synthetic diamond and in CVD films. Twinning occurs frequently on the (111) planes. The diamond planes with different crystallographic indexes have different ability for further transformation after surface group elimination. Among the ideal dehydrogenated and reconstructed diamond {100} surfaces, the most energetically favorable are dimers in two principal arrangements: namely, row and zigzag. The energies of the two are close to each other. The row dimer reconstruction has been observed experimentally[127,143–145] as well as zigzag steps,[146] and confirmed theoretically.[147]

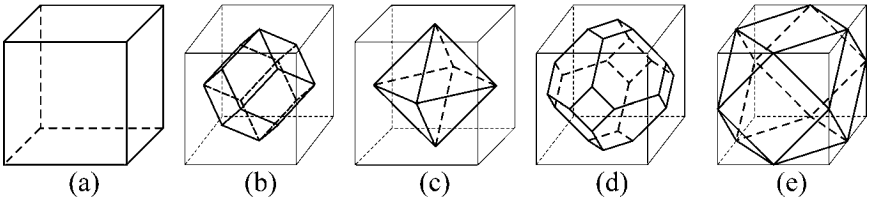

Figure 13.8 Shapes of diamond crystals and their surface planes: (a) cubic form {100}; (b) dodecahedral form {110}; (c) octahedral form {111}; (d) and (e) mixed forms with surface planes {111} and {100}.

There are some differences in the descriptions of the nature of C—C bonds of the reconstructed {100} surface. On the one hand, the minimum energy of a dehydrogenated {100} diamond surface was found to consist of dimers having bi-radical structures (2 × 1 reconstruction). The reason for the dimers to have a single C—C bond as opposed to a double bond is the strain characteristic to other C—C bonds of the surface.[147] On the other hand, the {100} surface reconstruction, as was proposed, is achieved by the formation of rows of π-bonded dimers giving a 2 × 1 reconstruction[148] with a bond length of d = 1.37 Å comparable to that of a C═C double bond in a hydrocarbon molecule.[149]

It is known that clean reconstructed diamond {111} surface has a π-bonded chain structure, denoted as 2 × 1.[148,150–152] Unlike Si or Ge, long-range reconstruction is absent in diamond {111}.[153] Pate[127] confirmed the results of other researchers that upon annealing (up to ~1270 K) a diamond (111) surface reconstructs to a 2 × 2/2 × 1 surface structure which is accompanied by the formation of intrinsic surface states. Photon-stimulated ion desorption and EELS results indicate that very little, if any, hydrogen-bonded carbon exists on this reconstructed surface. The 2 × 2/2 × 1 surface is therefore thought to be hydrogen free.[127] At complete or near-complete monolayer hydrogen coverage, the diamond (111) surface transforms to a bulk-like structure,[154–156] denoted as 1 × 1. The hydrogen coverage has been found to control the transition between the two distinct structures.[157] The 1 × 1 structure readily reconstructs back to the 2 × 1 structure after complete removal of hydrogen by thermal desorption.[127,158] At intermediate hydrogen coverage, a transition state exists.[156]

On the {110} and {111} surfaces, reconstructions lead to the formation of π-bonded chains with bond lengths of d ~ 1.43 Å comparable to those in graphite. This requires a 2 × 1 reconstruction on (111), while no reconstruction on (110) is necessary.[148] The important difference is that for the (110) surface, chain formation is compatible with the topology of the

underlying lattice, whereas on the C (111) surface the six-ring topology of the ideal diamond structure has to be replaced by alternating five- and seven-membered rings.[159,160]

13.4.2 Cleavage Energies of Diamond Planes

To consider the graphitization ability of different diamond surfaces it is reasonable to compare it to the cleavage energy of different planes because of the similarities of these processes. Theoretical cleavage energies along different planes were calculated using the fixed energy of a single C—C bond and a number of C—C bonds per square of specific plane necessary to cleave along this plane.[161] This provides a rather small energetic difference for the planes. However, cleavage of diamond occurs mostly along {111} planes and significantly less frequently along the other planes. Quantum chemistry calculations allow better understanding of the preferential cleavage of diamond along {111} diamond planes.

Kern et al.[162] and Shenderova et al.[163] estimated the cleavage energies of the low-index surfaces of diamond. It was found that the {110} surface has the lowest cleavage energy. On the {111} surface with one dangling bond (1db), where also only one bond per surface atom has to be broken, the cleavage energy is 0.66 eV higher. However, these authors showed that, as already emphasized in ref. [160], simple bond-scission arguments are not appropriate for a reliable estimation of the cleavage energies. For the {111} and {110} 1db surfaces, even a simple relaxation of the surface layer reduces the surface energy by an important amount, whereas for the multiple dangling surfaces a relaxation is energetically quite ineffective.[162] A reconstruction reduces the energies of the {100} and {111} surfaces by almost 50% so that finally the reconstructed {111} 1db surface has the lowest energy and the {100} 2db surface is only 0.46 eV/atom higher in energy than the {110}) surface (which is stable in an unreconstructed state), in spite of a much larger cleavage energy.

Kuznetsov et al.,[140] using the standard semi-empirical method (MNDO), demonstrated that the binding energy between two layers in the {111} cluster is lower than that in {110} clusters (2.83 eV for the {111} surface and 3.93 eV for the {110} surface, respectively). They also studied the effect of surface relaxation on the interlayer binding energy. For this the top layers were allowed to relax during optimization of the geometry. For both the {111} and {110} surfaces, some flattening of the surface layer takes place. Despite the latter, the 1×1 periodicity of the top {111} layer remains unchanged. These authors[140] obtained a relaxation energy

of 0.20 eV/surface atom for the {111} surface and 0.27 eV/surface atom for the {110} surface. The relaxation energy for {111} is gratifyingly close to the value of 0.17 eV/surface atom obtained by Jungnickel et al.[164] in a first-principles molecular dynamics study. The very small difference between the two relaxation energies indicates that relaxation does not significantly alter the previously calculated difference between the binding energies for the {111} and {110} surfaces.

A difference between interlayer binding energies along the [111] and [110] directions seems to arise from the different "packing" of the interlayer bonds in the volume between the "parallel" planes.[140] For the {111} planes all such bonds are parallel, in contrast to those of the {110} planes. Thus, despite the fact that each "isolated" sp^3 C—C bond has the same energy in all diamond lattice directions, the interbond interactions depend on the orientations of the bonds with respect to each other. This interaction should be mainly repulsive in character, taking into account the relatively small average distances of about 0.25 nm between bonds and the fact that each bond is occupied by two electrons.

13.4.3 Shape of Diamond Particles

Due to the different abilities of diamond crystallographic planes for reconstruction and graphitization, the shape of diamond crystals determines the reaction path of graphitization. Diamond crystal forms are considered elsewhere.[2,4,19] Diamond occurs in several crystal habits, which include the octahedron, the dodecahedron, cube, and other more complicated forms (see Fig. 13.8). However, there is no commonly accepted view in the literature on the shape of ND crystals.

Shenderova et al.[19] discussed the shape of ND particles. The shape of ND particles from 3 to 5 nm in size is often assumed to be spherical.[165,166] This led to speculation that the diamond nanoparticles are formed from liquid drops.[167] However, one should mention that the statements about the spherical shape of diamond nanoparticles are usually based on TEM pictures at low magnification, where the particles are seen as so small that it is impossible to make any assessment about their shapes. After more detailed investigations of TEM images, it was found that the spherical shape of ND particles is rather rare. Figure 13.9 illustrates the shape of ND crystals produced in explosive conditions. This shape is similar to that of microscopically sized diamond particles formed in the gas phase during a CVD process, as was first described in ref. [168]. The typical habit of these clusters was regularly shaped cuboctahedral and twinned crystals,

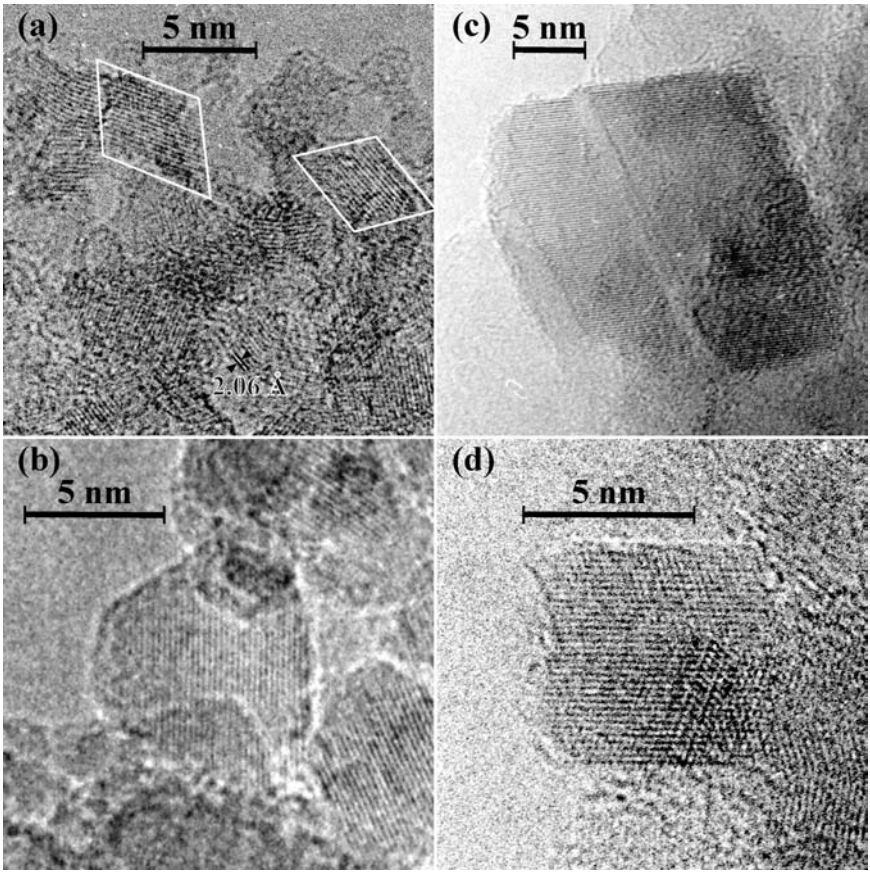

Figure 13.9 HRTEM micrographs of initial ND particles with different shapes and sizes (a)–(d). The straight dark contrast lines in the micrographs correspond to the (111) crystallographic diamond planes. The distance between these lines is 2.06 Å. The frames in micrograph (a) outline the forms of two ND particles.

that is, a twinned cuboctahedron, an icosahedron, and a decahedral Wulffpolyhedron.

The shape of a diamond crystal is inherently related to the ability of different crystallographic planes to reconstruct, to graphitize, and to react with the environmental gases. As was observed by Evans,[5] the graphitization rates of diamond crystallographic planes (GR_{hkl}) depend on the reaction conditions. For the high-temperature range (higher that 2000 K)[5]

$$GR_{110} > GR_{111} > GR_{100},$$

while for the low-temperature range (1370–1860 K, see Section 13.4.2)

$$GR_{111} > GR_{110} > GR_{100}.$$

It is necessary to mention that the oxidation rates (OR) of diamond planes also differ significantly and decrease in the following sequence:[5]

$$OR_{111} > OR_{110} > OR_{100}.$$

Thus, taking into account the different chemical reactivity and graphitization ability of the different crystallographic planes of diamond, the spherical form of NDs produced in explosive conditions can hardly be proposed. Due to the possibility of partial graphitization of primary diamond particles in such explosions during decreasing pressure and temperature, the faceting of the primary particles can occur. Furthermore oxidative treatments used for ND elimination from explosive soot usually partially oxidize the diamond particles and lead to additional faceting of the particles with the most reactive faces in these conditions. An example of the usage of the different graphitization ability of diamond crystallographic planes was used by Evans[5] to produce diamond crystals faceted with {110} surfaces.

13.4.4 Graphite/Diamond Interfaces

Two different types of graphite/diamond interfaces were registered by HRTEM.[34,36] The first type occurs when the diamond surface contains {111} faces. It is well known that a (111) layer of diamond consists of buckled hexagons and that their projected size on a (111) plane is very close to that of the hexagons in graphite. The resemblance of the (111) diamond planes to (0001) graphite planes and, as noted earlier, the low cleavage energy of the (111) surface lead to exfoliation of graphitic layers during graphitization from diamond {111} surfaces. Figure 13.10 presents the exfoliated graphitic scales oriented parallel to (111) diamond planes, while their edges merge to the diamond surface.

Another type of graphite/diamond interface occurs if less reactive planes facet diamond surfaces. In this case the transformation of (111) diamond planes is nevertheless the most reactive to graphitization. Using multi-body potential calculations, Lambrecht et al.[169] demonstrated that the interface strain energy is minimized when three (111) diamond planes match up with two (0001) planes of graphite. A key idea behind this

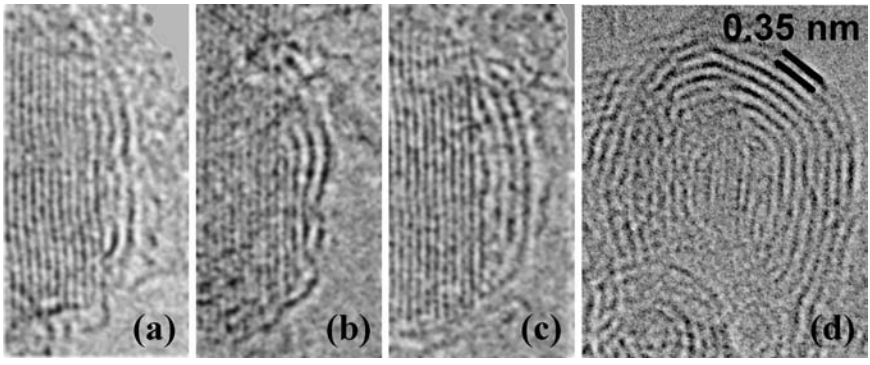

Figure 13.10 HRTEM micrographs of three different ND particles (a, b, c) at a very early stage of the transformation. Dark contrast parallel lines correspond to diamond (111) crystal planes (the distance between the lines is 0.206 nm). Other curved lines correspond to graphite-like shells with the distance between them equal to 0.34–0.35 nm (d_{002} = 0.3354 nm for hexagonal graphite). The exfoliation occurs preferentially from the diamond {111} surfaces. The exfoliated planes are seen to merge with the diamond surface and sometimes with each other to avoid dangling bond formation. (d) The formation of semi-closed graphite-like shells; a diamond core (4–5 diamond (111) planes) is seen within nested nearly spherical shells.[140]

graphite/diamond interface model is that there is a 2/3 correspondence between the density of graphite and diamond. This points to a 2/3 relationship between the number of layers that meet at the interface between a {1100} graphite and a {121} diamond surface.[164] We have in fact found direct experimental evidence for the formation of the 2/3 interface[36,140] during the graphitization of micron-size diamond and nanodiamond (see Figs. 13.2(a) and 13.11). Detailed quantum mechanical or molecular dynamics (MD) calculations of the migration of the graphite/diamond interface into a diamond crystal for a cluster of adequate size are difficult. Consequently, we restrict our considerations here to geometrical aspects alone. As shown in Fig. 13.12, we propose that as the 2/3 graphite/diamond interfaces migrate into the bulk of a diamond crystal, the atoms of the inner diamond layer should take part equally in the formation of both graphite sheets. Only in this way can one obtain the same lengths for the two growing graphitic sheets. Figure 13.12 shows that the process somewhat resembles the opening of a zipper. Each of the marked groups of atoms provides for the formation of an additional row of graphite six-fold rings. The process probably proceeds via successive insertion of two carbon atoms per two six-fold rings of a growing sheet

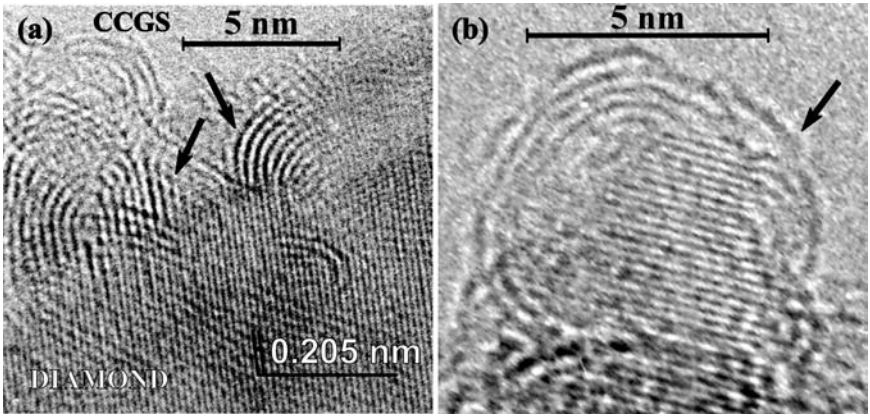

Figure 13.11 HRTEM micrographs of the "diamond/graphite-like species" interfaces of diamond annealing products (vacuum of 10^{-5} Torr) on (a) a submicron diamond particle annealed at 1890 K for 1 h, hour [140] (b) a ND particle annealed at 1420 K for 1.44 h.[41,108] The formation of two graphitic sheets (arrows) from three (111) diamond planes are clearly seen.

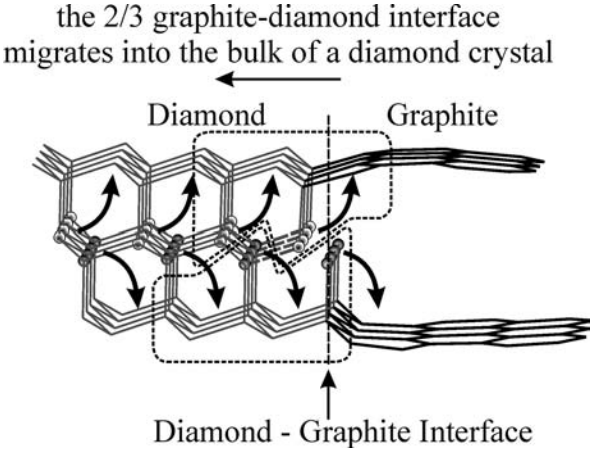

Figure 13.12 Zipper-like scheme in which three (111) diamond planes transform into two graphitic sheets (2/3 interface) as the graphite/diamond interface migrates into the bulk of the diamond crystal. Each of the groups of atoms marked contains two rows of six-fold rings and one additional carbon atom per ring provides for the formation of an additional row of graphite six-fold rings.[140]

with the intermediate formation and subsequent reconstruction of eight-fold rings. However this simple consideration does not take into account the shrinkage of graphene sheets along the 3/2 interface line as compared to the projection of a (111) diamond plane. It results in the formation of a rounded interface line, which could avoid the structural strain along the interface line.

It should be mentioned that the 2/3 graphite/diamond interface can be developed via primary exfoliation of several (111) planes with the formation of fullerene-like caps because the bonds of the edges of their exfoliated graphene sheets merge with the diamond surface. Thus, successive exfoliations of several (111) planes lead to the progressive decrease of the diameter of the internal contacting (111) diamond plane and the formation of multi-cap structures. Further development of these structures produces mosaic-like structures consisting of multi-wall carbon nanotubes (see Section 13.4.6).

13.4.5 Formation of Nanocarbon Species via "Low"-Temperature Diamond Graphitization

Previously we have demonstrated that thermal diamond graphitization is initiated after the removal of oxygen- and hydrogen-containing surface groups stabilizing the diamond surface. Surface reconstructions follow the elimination of the surface groups. Further graphitization depends on the diamond particle size and indexes of a surface crystallographic plane. Thus, the formation of OLC is observed from the NDs with a size less than 5–6 nm; closed polyhedral particles can be produced from the NDs with a size of 7–15 nm, while closed curved graphite-like structures form on the surface of micron-sized diamond.

Initially we consider the graphitization of NDs leading to the formation of OLC and then the formation of closed curved graphitic structure on the surface of micron-sized diamond.

13.4.5.1 Model of ND Annealing and Formation of OLC Structure with Holes

Figures 13.1 and 13.10 present HRTEM images of intermediates of ND annealing products, providing the following conclusions on the most significant features of ND annealing:

- ND graphitization under annealing moves from the surface toward the crystal bulk.
- The transformation rate of the (111) diamond planes to graphite-like sheets is higher than that of other planes.
- The edges of exfoliated graphite-like sheets merge with the upper untransformed diamond planes.
- The distance between the inner graphite-like sheet and the upper untransformed diamond layer does not exceed 0.35 nm, indicating an interaction between the diamond and graphite layers.
- Closure of the fullerene-like shell occurs generally after complete transformation of the diamond core of the particle (Fig. 13.10(d)).

The graphitization of diamond particles depends on the size of the particles. Specifically, the graphitization of very small particles ($d \sim 2$ nm), which have a higher surface energy and contain many surface defects, starts at lower temperatures (1150–1300 K) than those for larger particles. In the case of the annealing of NDs ($d \sim 5$ nm), the curling and closure of nanometric graphite shells and the formation of OLC are explained in terms of elimination of dangling bonds (relating to the difference in the surface energies of the graphite basal plane, 0.135 J/m^2, and of the high-index (101) and (112) planes located on the edges of the basal planes, 4.8 J/m^2).[170] Closure of the graphite shells thus provides a significant decrease in the surface energy of the carbon particles. It is necessary to mention that ND graphitization at relatively low temperatures (1400–1600 K) results in a highly defective OLC structure. This means that ND graphitization and the closure of graphite-like shells proceed independently. Several examples of possible defects in the OLC structure are presented in Fig. 13.13.

Another principal fact concerns the formation of holes in fullerene-like shells (confirmed by X-ray emission spectroscopic characterization of NDs produced at temperatures lower than 1900 K,[171] see Fig. 13.14). At the same time Raman spectroscopy studies allow us to conclude that some portion of the OLC has the structure of ideal carbon onions.[119] Using higher annealing temperatures (higher than 1900–2000 K) leads to the formation of material consisting of closed, polyhedral, hollow nanographite particles, which have no hole defects and do not contain ideal onion-like structures.

Based on these results, a mechanism of OLC formation via ND annealing can be suggested as follows. At the first steps of ND annealing curved

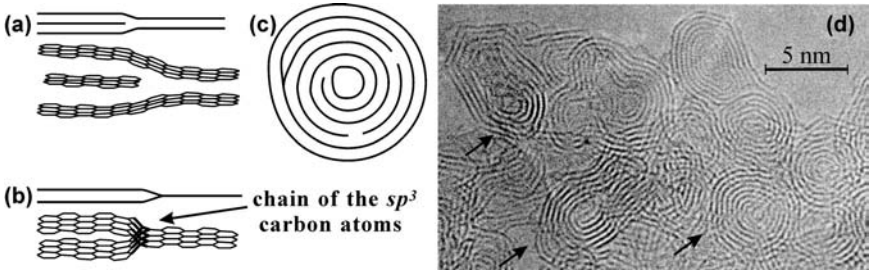

Figure 13.13 Defects in OLC particles produced by annealing of ND: (a) an interstitial plane between two basal planes [10]; (b) "Y" junction of two basal planes into one plane; (c) a schematic of a spiral-like structure having an interstitial plane between two basal planes, (d) a HRTEM image of OLC produced from ND[34]; curved lines correspond to graphite-like shells with the distance between them equal to 0.34–0.35 nm. The arrows on the figure show the proposed locations of the "Y" junctions. The interstitial planes and holes are difficult to observe due to their low contrast on HRTEM images.

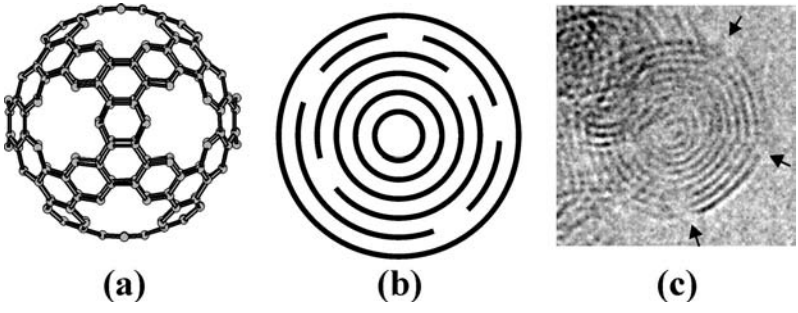

Figure 13.14 (a) Spherical cage C_{180} with holes obtained by removing 12 pentagons from C_{240};[171] (b) scheme of a holed OLC particle;[171] (c) an HRTEM image of a OLC particle produced by annealing of ND at 1900 K for 1 h in vacuum of 10^{-5} Torr; curved lines correspond to graphite-like shells with the distance between them equal to 0.34–0.35 nm. Irregularities in the micrograph of the OLC particle (shown by the arrows) are likely caused by holes in the fullerene-like shells or spiral-like structure of the OLC particle.

graphite-like sheets are formed and exfoliated from the diamond particles (Fig. 13.10). Merging of these sheets leads to the formation of spiral-like multi-shell particles (Fig. 13.15) and finally OLC forms.

Preliminary consideration provides an understanding that the transformation of the most tightly packed diamond (111) plane to the (0001) graphite one is accomplished by shrinkage along the graphitic network.

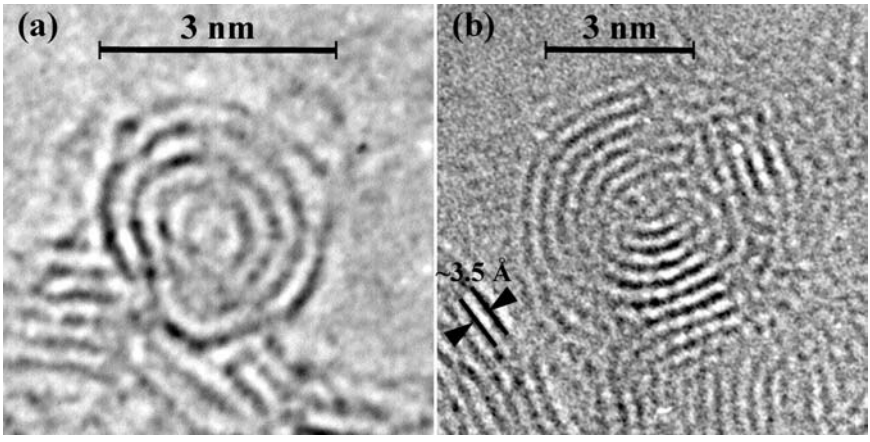

Figure 13.15 HRTEM micrographs of spiral graphite-like particles produced by the annealing of ND (a, b). The dark lines in the micrographs correspond to the (0002) crystallographic graphite planes. The distance between these lines is ~3.5 Å.

At the same time, transformation of ND to OLC leads to a dramatic increase in particle volume (compare the densities of graphite and diamonds, 2.265 and 3.515 g/cm^3, respectively). Thus, one can conclude that the number of surface carbon atoms of the pristine diamond particle is not sufficient to form the perfect closed fullerene-like shell. Thus, the cuboctahedral diamond crystal (2.14 nm between (n00) planes), composed of 1683 carbon atoms, has 530 surface atoms. The cubic diamond particle of the same size, having 1963 atoms, has 434 surface atoms. At the same time, a perfect OLC particle (of size 2.814 nm) composed of four fullerene shells, containing 1800 carbon atoms, has 960 surface atoms. Thus the luck of carbon atoms should be compensated by the capture of carbon atoms from the edges of the inner layers or lead to the formation of hole defects in the graphite-like shells.

To elucidate the reasons leading to the formation of holed OLC structure, modeling of ND annealing has been performed. A DFT study of annealing small ND clusters has been undertaken.[172,173] However, in these papers, due to the limitation on the numbers of atoms in a model, the size of diamond clusters was not large enough to understand the mechanism of defect formation. We have used a combination of MD calculations, which use forces computed by standard semi-empirical quantum mechanics (MNDO, AM1, PM3), to model the surface reconstruction of small diamond clusters followed by molecular mechanics (MM) modeling of

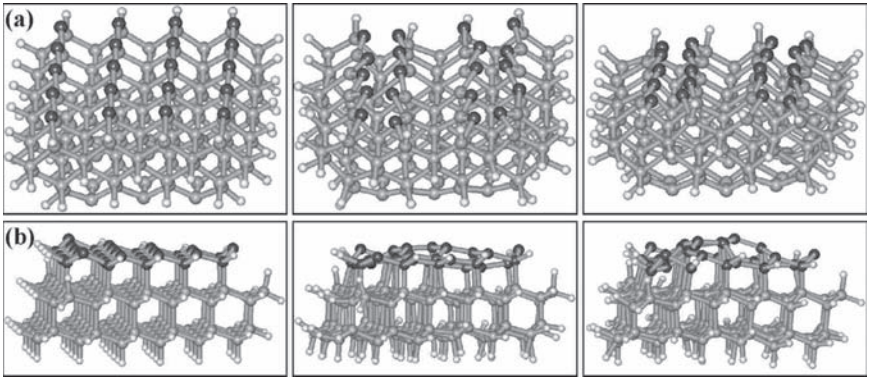

Figure 13.16 Results of molecular dynamics simulations using standard semi-empirical method PM3 for the study of annealing of diamond clusters with bare surfaces of different crystallographic planes. Surface carbon atoms are marked in black, white atoms are hydrogens stabilizing the diamond framework. (a) Reconstruction of (100) planes (2×1 structure observed even at 0 K, stable up to 1500 K); (b) successive graphitization of (111) planes with exfoliation of (0002) graphitic planes (graphitization begins after 0.4 ps and 150 K).[96]

intermediate products of annealing large diamond clusters. In the latter case the initial ND cuboctahedral cluster contained 4490 carbon atoms. Figure 13.16 shows the principal results of the MD study of the annealing of bare (100) and (111) diamond planes. One can see that annealing of the (100) plane results in a 2×1 surface reconstruction stable up to very high temperatures (1500 K), while in the case of a cluster with (111) planes, graphitization occurs at low temperatures. This is in good agreement with experimental results[127] and computer simulations of diamond cluster annealing. Thus for the cuboctahedral cluster surface the reconstruction of the (100) surface and "buckification" of the (111) surfaces was proposed.[174]

We have used results on the relative stability of different diamond planes to construct a sequence of MM models reflecting the successive steps of graphitization of a ND particle. In agreement with our experimental data and MD simulation, the diamond transformation occurs mainly via graphitization of (111) planes. At the same time, reconstructed (100) planes graphitize only at the cross-sections with transformed (111) planes (see Fig. 13.17). One can see the deficit of carbon atoms required for the formation of perfect closed fullerene-like shells at the interface of reconstructed (100) planes where the produced graphene shells merged with each other.

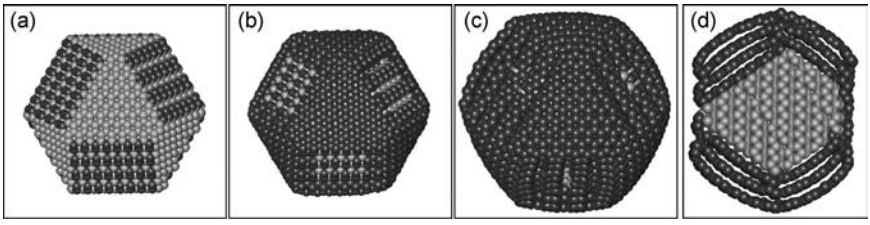

Figure 13.17 Molecular mechanics models of the successive graphitization of a cuboctahedral diamond cluster. Black atoms correspond to carbon atoms involved in graphitic shells and reconstructed diamond planes. (a) (100) planes only reconstructed into 2×1 structures; (b) and (c) graphitization occurs via the transformation of (111) planes: one in the case (b) and three in the case (c), respectively; (d) a cross-section of the particles (c): one can see three graphitic layers around the diamond core. The particle volume is increased due to formation of graphitic scales with decreased density.[96]

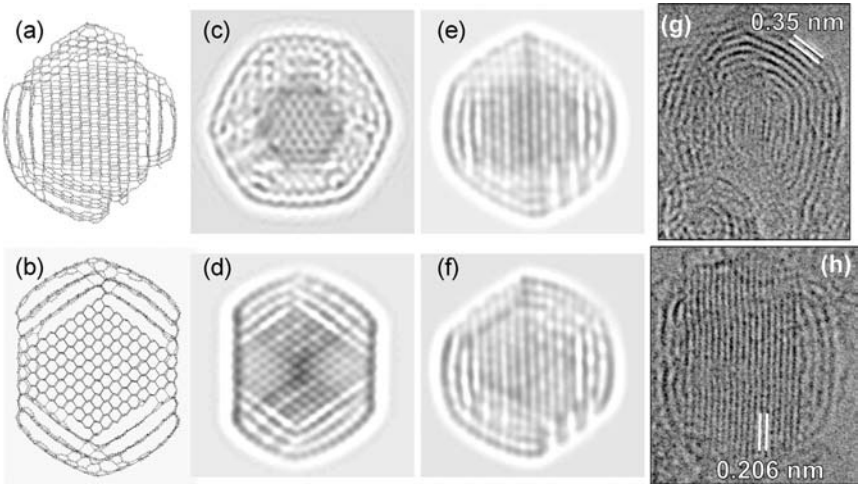

Figure 13.18 The comparison of the molecular mechanics models (a, b) of the partially graphitized diamond particle previously presented in Fig. 13.17 and their electron microscopy images (c–f) calculated after the orientation of the model at different angles of the electronic beam. HRTEM micrographs (g, h) of intermediates of ND annealing products.[96] (The electron microscopy images were obtained and calculated by Dr. A. L. Chuvilin.)

The comparison of the model electron microscopy images calculated using the MM model provide very reasonable agreement with experimental ones (see Fig. 13.18). Thus one can see that graphene-like sheets initially form after transformation of (111) planes. The merging of graphene sheets leading to OLC formation experiences a high deficit of

carbon atoms in the regions of pristine (100) planes and likely leads to the formation of hole defects in OLC shells. Annealing of these holes starts only at temperature higher than 1800–2000 K due to the higher mobility of carbon atoms at these temperatures. In fact, we have observed the formation of hollow onions and annealing defects after heating OLC at temperatures higher 1900–2000 K. Thus, the origin of defects accompanying OLC formation can be explained in terms of the deficit of diamond carbon atoms in the graphite/diamond interface to form perfect fullerene-like shells. However, it should be mentioned that a detailed mechanism of merging local graphitic flakes into closed fullerene-like shells is not clear. It can be assumed that such a mechanism would be similar to that of defect annealing in graphitic materials. So far two mechanisms of defect annealing have been discussed in the literature,[10] namely a migration of carbon interstitials and a vacancy healing through the dangling bond saturation effect resulting in the formation of non-hexagonal rings and Stone–Wales defects.[175]

13.4.6 The Formation of the Closed Curved Graphitic Structure on the Surface of Micron-Size Diamond

By varying the temperature of the annealing process of submicron diamonds (synthetic submicron diamond ASM 0/1),[36] we have succeeded in preparing samples in which the intermediates of the diamond to graphite transformation are detectable.[36,140] Figures 13.2(a) and 13.11 show the interface between the diamond and the growing graphite-like structures. One can see that the direction of (0002) graphite planes coincides with that of the (001) diamond plane with the 2/3 relationship between the number of layers of graphite and diamond, respectively. At the interface between the diamond and the evolving graphite, the formation of two curved graphitic sheets from three diamond planes occurs. Sometimes, on the edges of the diamond particles, we could observe that the images of the closed graphite-like structures overlap each other (Fig. 13.2(a)). The latter indicates that these structures have a limited thickness. So the observed curved graphitic sheets presumably form closed structures, e.g., caps, folds. Actually, a top view of the closed structures shows that they form a mosaic structure on the diamond core (Fig. 13.2(b)). The lengths of the growing folds do not exceed 5–7 nm and short folds appear to form closed multilayered caps. The annealing of diamond in the multi-cap

regions can lead to splitting of the particle surface and the formation of divergent tubular-like or fold structures.

Graphitization can be initiated at the surface defects. It was found that stepped (111) surfaces are graphitized spontaneously.[176] Spontaneous graphitization near a twin core has also been proposed in ref. [164]. MD studies[164,169] lead to the conclusion that graphitization is strongly facilitated by any kind of surface perturbation or roughness such as step-like adsorbates. We found that diamond annealing leads to the formation of closed curved graphitic structures (CCGS) such as OLC (for ND)[34,41,108] and nanofolds, nanotubes (for micron-sized diamond).[36,140] A partial explanation of the self-assembling formation of these structures is discussed below. The most difficult problem concerns the formation of CCGS on samples with dimensions larger than 20–40 nm. Additional factors rather than those for the small particles are involved. We first consider how the "blistering" of a single graphitic segment leads to a saucer-like structure on a diamond surface. As noted above, graphitization is expected to be initiated at a surface imperfection (e.g., at a step or defect). One essential point to note is that the graphite segment is in a state of tension. This is because the width of the six-fold graphite ring is 0.006 nm less than the projection of a diamond six-fold ring on the graphite basal surface (Fig. 13.19(a)). Thus, 10 graphite rings are characterized by a 0.06 nm "shrinkage", an amount which, if concentrated in a single bond, is more than enough to break it. Additional stretching is produced by the formation of curvature at the contacts between the diamond surface and the exfoliated graphite sheet due to the increased distance between the diamond surface and the delaminated graphite shell. To obtain fairly detailed and quantitative information about the exfoliation of a graphite sheet from a diamond surface, we have performed MM simulations (MM force field)[140] on several model structures. The results for one of them are presented in Fig. 13.19(b). It is found that the average carbon–carbon bond length along the exfoliated network is 0.146 nm. This should be compared to the 0.140 nm bond length given by a MM simulation of a relaxed separated graphite sheet, the value of which is somewhat lower than the measured value of 0.142 nm. At the same time, the calculated distance between the diamond surface and the graphite sheet is found to be ~0.32 nm, which is slightly lower than (but still reasonably close to) that found experimentally (0.34–0.35 nm).[34] We note also that when the tension is reduced by detaching one side of the graphite sheet, the calculated distance between the sheet and the diamond surface rose to a value of 0.34–0.35 nm. These results together show that an attached exfoliated graphite network is appreciably stretched. As we will see, this stretching

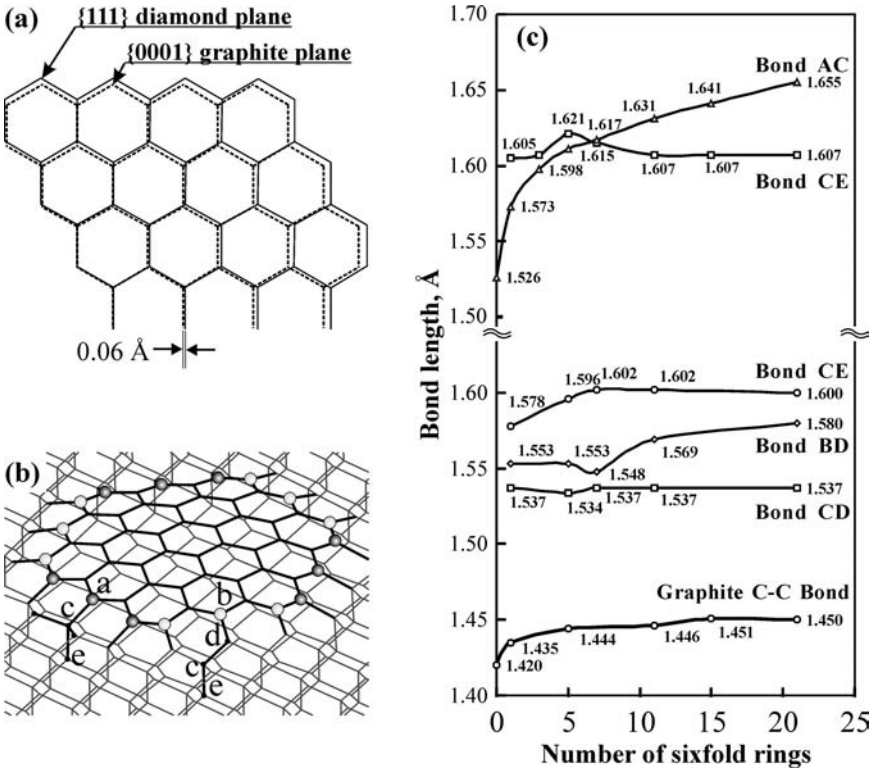

Figure 13.19 Molecular mechanics (MM+ force field) modeling of the initial stage of the formation of a graphitic structure on a diamond surface. (a) Comparison of the projections of the (111) diamond and (0001) graphite planes. (b) Model of an exfoliated {111} plane as a symmetric six-angle sheet. There are two different types of bonding of the sheet to the diamond surface as indicated by the bondings of the atoms labeled **a** and **b** on the edges of the sheet. (c) Dependence of the lengths of the relevant bonds indicated in (b) on the size of the exfoliated graphite sheet (number of six-fold ring across). The lowest curve is a typical bond length well within the free graphene sheets of different size.[140]

can lead to the breaking of a bond between neighboring surface carbon atoms (not the breaking of a bond between the surface layer and diamond bulk) and to the formation of a saucer-like structure. These breaks tend to create mono-atomic steps on the diamond surface. Graphitization is then initiated at these steps. This process ultimately leads to the formation of a mosaic of plates separated by interatomic distances.

To provide more detailed insight into the behavior of the exfoliated graphitic sheets, we focus on the nature of the C—C bonds at the edges

of the sheets. In our model, in accordance with our experimental data, we keep the graphitic sheet merged with the diamond surface. In our simulations, we consider a symmetric six-angle sheet (Fig. 13.19(b)). It turns out to have two different types of interfaces. In the first, each edge graphite atom (a) is directly bonded to a surface diamond atom (c), which in turn is attached to the internal diamond atom (e). In the second type, each edge graphite atom (b) is attached to a border atom (d) which is bonded with two surface diamond atoms (c) which in turn are attached to the internal diamond layer. We have carried out MM studies of a number of such sheets of various sizes, which are characterized by the number of six-fold rings across the structure at its widest extent. In Fig. 13.19(b), for example, the number of rings across the structure is five. These calculations yielded the lengths of the various bonds involved as a function of the size of the sheet. The results are displayed in Fig. 13.19(c), where the results for the bonds along the edges in the *A* and *B* "directions" are separated for clarity. Also shown, for reference, is the bond length for a six-fold ring well within the sheet. The most relevant feature of these results for our purpose is the monotonic growth of the "*ac*" bond and the fact that for *eight or more rings* this bond becomes significantly longer than the others. This indicates that the bond is clearly the one most likely to rupture. Breaking of the bond will be followed by the bonding of the "*a*" graphite atom to an internal diamond atom under the graphitic sheet to eliminate its dangling bond. This process will lead to the formation of a closed plate-like structure, and, in addition, to a mono-atomic step. It seems reasonable that the rupture of the atomic surface layer will occur roughly around 8–10 rings or so, i.e., for sizes of about 2.0–2.5 nm. This is in reasonable accord with our experimental work, where structures ranging from 1 to 4 nm have been observed.[36,140] This agreement, along with that for the distance between the graphitic sheet and the diamond, suggests that the model and calculations are reasonable.

Above, only the initiation of CCGS formation has been simulated. The HRTEM results in Figs. 13.2(b) and 13.20 show that the structures are generally multi-walled (or "multi-capped") and grow to heights significantly greater than ~0.3 nm. Further surface graphitization results in the formation of mosaic-like structures consisting of tightly packed multi-walled nanotubes. This is shown schematically in Fig. 13.21. The exfoliation of succeeding layers is expected to proceed with the formation of the 2/3 graphite/diamond interface discussed above. The "extra" atoms provided to the two graphitic layers by the third diamond layer allow for the extension of the caps. Ultimately, the multi-cap structures can, in turn, grow into nanotubes attached to the diamond surface.

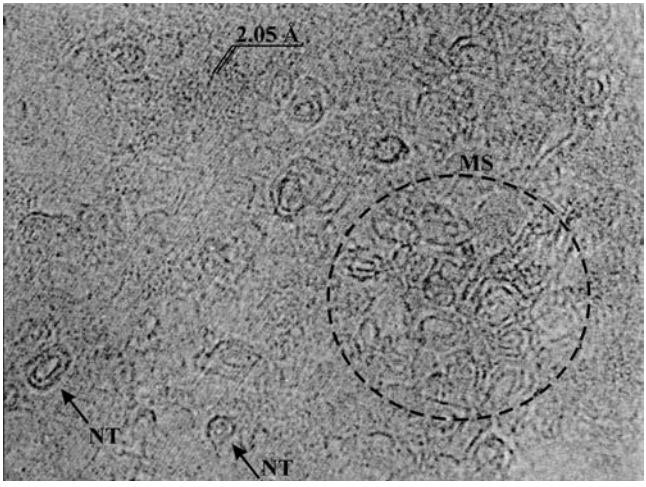

Figure 13.20 HRTEM micrograph of annealing products on a ~1 μm diamond particle ($T = 1500$ K, 3 h, $P = 10^{-5}$ Torr). Top view of several surface carbon nanotubes (**NT**) and the mosaic structure (**MS**) of carbon nanotubes. The straight dark contrast lines, which can be seen in the micrograph, correspond to the (111) crystallographic diamond planes with a distance between them of 2.05 Å.[140]

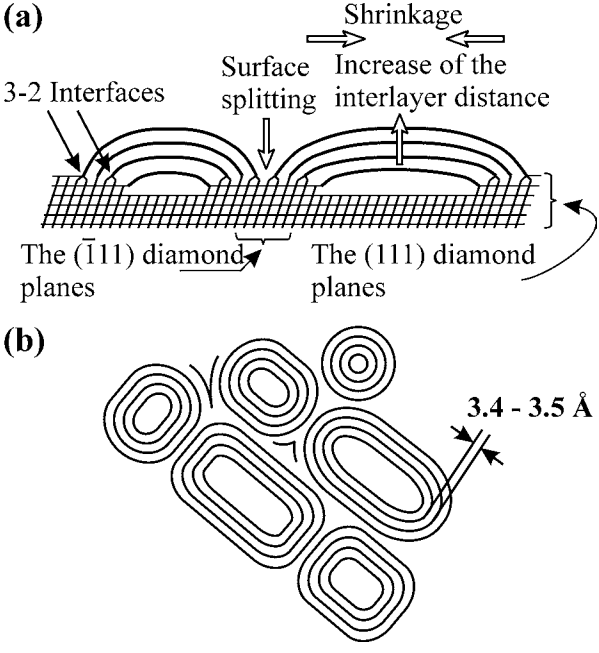

Figure 13.21 (a) The scheme of closed, curved graphite structure formation. The shrinkage along the graphite network and simultaneous increase of the distance between graphite sheets results in the surface splitting and formation of nanotubes. The arrows show the 2/3 graphite/diamond interfaces migrating into the bulk of a diamond crystal. (b) Top view nanotubes. The closed packing of nanotubes results in the formation of mosaic structure.[36]

13.5 Catalytic Graphitization of NDs in the Presence of Metal Clusters

It is not surprising that metals interact with carbon presenting in diamonds. Earlier work devoted to the interactions of macroscopic diamond with metal and metal oxides was reviewed by Evans.[51] Characterization structure and electron properties of diamond–metal interfaces are important, since differently doped diamonds substrates are p- and n-type semiconductors and are of interest for diamond-based electronics.[177] Evans distinguished the following types of chemical interactions of diamond with metals: carbide formation, redox processes involving diamond carbon, and catalytic graphitization. Chemical interaction of metals with diamond occurs at sufficiently high temperature, so that carbon from diamond can migrate into the metal and, according to the metal–carbon phase diagram, form metal carbide phases (e.g., with the following metals: Al, Fe, Mo, Ta, Cr, Ti, Mn, V)[51] or metal–carbon solid solutions (Ni, Co)[4]. We believe that metal–carbon interactions can be generally described in terms of metal–carbon phase diagrams, which reflect the principal possibility of a specific metal dissolving carbon in its volume with the formation of metal–carbon solid solutions or metal carbides. Carbon presenting in diamond reduces partially or completely metal oxide films deposited on its surfaces.[51] Evans described the catalytic graphitization of diamonds involving first detachment of carbon atoms from diamond surfaces, then their transport through the metal film in interstitial sites, and finally their re-precipitation at the interface with a vacuum as the thermodynamically more stable graphite.[51] The temperature of the onset of catalytic graphitization decreases compared to one of uncatalyzed graphitization.[51] Thus catalytic graphitization in internal diamond surfaces surrounding nickel inclusions in synthetic diamond was described.[51] Onset of this process occurred at about 800 °C. Other interesting examples of catalytic diamond graphitization were reported by Pantea et al.,[178] who observed internal graphitization of synthetic diamonds also caused by metal inclusions. Another example of the interaction of metals with condensed carbon was manifested by the Ni- and Fe-catalyzed hydrogen etching of the diamond. These reactions can be used for different kinds of diamond treatment such as polishing, drilling, etc.[179]

In this chapter we consider the catalytic graphitization of NDs in the presence of metal nanoparticles of iron and cobalt. The purpose of this work was to explore the influence of the metal particles on the ND graphitization process, especially in those cases when the sizes of metal particles were less tahn, comparable to, or more than the sizes of ND particles.

A detailed explanation of the experimental procedure for the preparation of metal particles on ND surfaces and the investigation of the catalytic graphitization effect can be found elsewhere.[180] In this section we describe only the main results of this work. The iron particles were deposited on ND particles from the vaporization of iron pentacarbonyl ($Fe(CO)_5$); cobalt particles were also deposited on diamond surfaces from solutions of cobalt acetates. These approaches allowed us to deposit metal particles with a variety of sizes on ND surfaces.

Figure 13.22 presents the HRTEM images of products of the ND annealing in the presence of the deposited iron nanoparticles. The formation of small "caps" (less than 1 nm) (marked by arrows on Fig. 13.22) on the surfaces of OLC is clearly seen. We also observed the formation of short multi-wall carbon nanotubes presented in Fig. 13.23.

Figure 13.24 illustrates the HRTEM images of the ND graphitization products in the presence of cobalt particles with sizes up to 100 nm. The products are presented only for the cobalt particles with sizes less than 5 nm. One can see the formation of curved graphite-like shells (a) and cones ((b) and (c) in the marked region).

Such carbon structures are not formed under the same conditions of ND graphitization in the absence of metal particles. Therefore metal particles

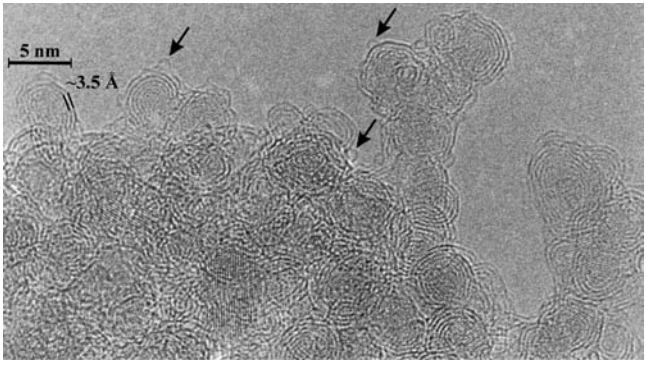

Figure 13.22 HRTEM images of ND particles annealed at 1420 K for 1 h in a vacuum of 10^{-5} Torr in the presence of iron nanoparticles (1–1.5 nm, mass % 1.2).[180] Iron nanoparticles are not seen on the image due to their small size and, therefore, low contrast. Dark contrast parallel lines and curved lines correspond to diamond crystal planes and graphite-like shells, respectively. The distance between lines corresponds to the (111) lattice parameter of ND (d_{111} = 0.2063 nm) and between curved lines to the distance between the graphite-like shells (0.34–0.35 nm). The arrows demonstrate small graphitic "caps" appearing only during annealing in the presence of the iron nanoparticles.

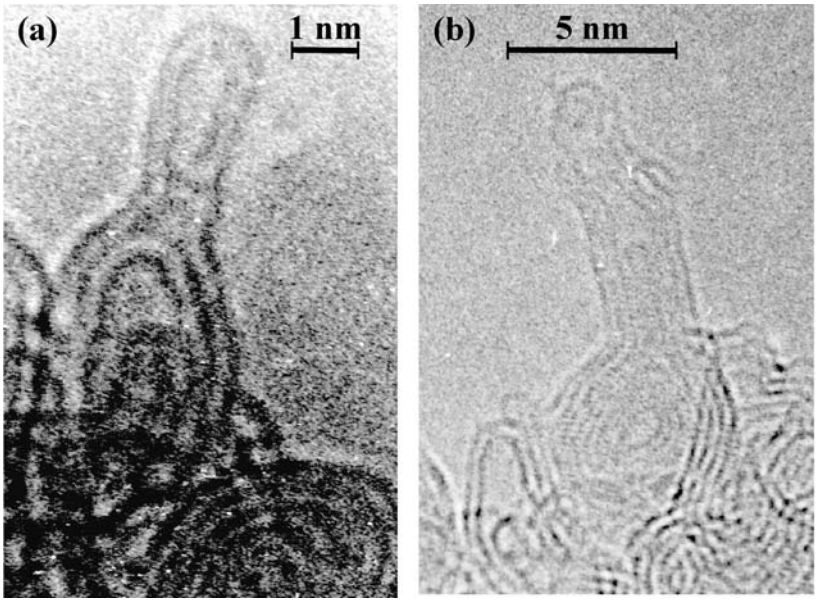

Figure 13.23 HRTEM images of short multi-wall nanotubes (1–2 nm) produced by the ND annealing at 1420 K for 1 h in a vacuum of 10^{-5} Torr in the presence of iron nanoparticles (a, b).[180] Iron nanoparticles are not seen on the image due to their small size and, therefore, low contrast. Dark curved lines correspond to diamond crystal planes and graphite-like shells. The distance between lines corresponds to the distance between the graphite-like shells, 0.34–0.35 nm (d_{002} = 0.3354 nm for hexagonal graphite).

catalyze the ND graphitization and formation of these products. The mechanism for the catalytic graphitization of ND probably consists of successive stages: dissolving of carbon in the metal particles; diffusion of carbon through these particles from the carbon/metal contact regions to the opposite side of the metal particles; and then precipitation of carbon resulting in the formation of different graphitic forms of carbon. At high temperature this process results in the metal particles melting and starting to move in a direction opposite to the formation of graphite-like deposits. The process of catalytic graphitization is schematically presented in the left part of Fig. 13.24. Krivoruchko et al.[181] observed *in situ* a similar catalytic graphitization of amorphous carbon caused by moving liquid-like iron particles with sizes mainly ranging from 20 to 40 nm at 920–1170 K in a TEM microscope.

One can also see the similarities between the catalytic ND graphitization and the catalytic formation of carbon filaments and nanotubes.[182–187]

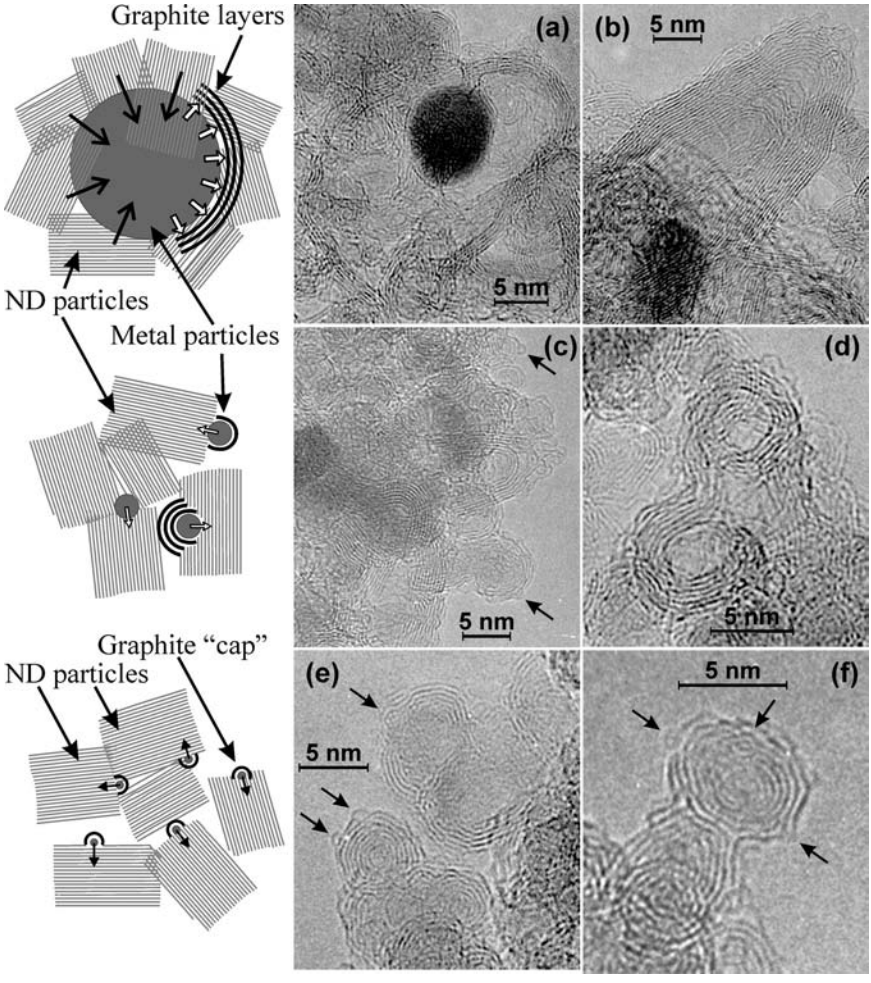

Figure 13.24 HRTEM images (right side of the figure) of the ND graphitization products in the presence of cobalt particles at 1500 K for 3 h in a vacuum of 10^{-6} Torr.[180] Curved solid lines correspond to (0002) graphite-like layers with an interplanar distance of approximately 3.4–3.6 Å. Structures of these products depend on the metal particle size: large metal particles (dark spots on images (a) and (b)) participate in the formation of curved graphite shells and cones, images (a)–(d). The interaction of small metal clusters consisting of only several metal atoms with diamond surfaces initiates the graphitization leading to the formation of graphite "caps" with sizes less than 1 nm on surfaces of larger graphitization products. On images (c), (e), and (f) these "caps" are marked by short arrows. Schemes (left side) illustrate the interaction of metal particles having different sizes of ND particles. Metal particle size influences the type of graphitization products.

The diameter of carbon nanotubes produced by the catalytic decomposition of carbon-containing gases is believed to be determined by the size of the catalyst particles.[182,184] The types of carbon deposits presented in Fig. 13.24 also depend on the sizes of metal particles. The movement of large metal particles (dark sports on Figs. 13.24(a) and (b)) results in the formation of prolonged graphite shells consisting of several curved graphite layers. The cooling down to room temperature of these particles leads to their cessation of movement and encapsulation in graphite layers. One such encapsulated cobalt particle surrounded by graphite layers can be clearly seen in Fig. 13.24(a). The observed graphite cones and shells (Figs. 13.24(b)–(d)) are formed by metal particles which left the graphitization products and are not seen on the images. The interaction of small metal clusters consisting of only several metal atoms with diamond surfaces initiates graphitization leading to the formation of graphite "caps" with sizes less than 1 nm on the surfaces of large carbon particles (see Figs. 13.24(c) and (f)).

Thus we can summarize that metal particles catalyze the ND graphitization. The mechanism of this graphitization consists of successive stages: dissolving of carbon in the metal particles; diffusion of carbon through these particles from the carbon/metal contact regions to the opposite side of the metal particles; and precipitation of carbon resulting in the formation of different graphite forms of carbon. At high temperature this process results in the movement of metal particles leading to the formation of different forms of graphite-like deposits. Structures of these products depend on the metal particle size. Large metal particles participate in the formation of curved graphite shells and cones. Metal clusters consisting of several atoms are inserted into diamond particles. This results in the formation of carbon "caps" (less than 1 nm in sizes) on the surfaces of larger graphitization products.

13.6 Graphitization of NDs in the Presence of Oxygen- and Hydrogen-Containing Gases

Evans[5] showed that oxidation of macroscopic diamond crystals in oxygen (0.4 Torr) promotes the production of a black graphite layer on diamond surfaces. Specifically it was found that the {111} and {110} faces start to graphitize at a temperature of 970 K, whereas the appearance of a graphite layer on the {100} face was registered at 1120 K. The activation energy of 230 ± 10 kJ/mol was found for all diamond surfaces at temper-

atures where no graphitization was detected. Later, Uspenskaya et al.[6] also observed the formation of graphite layers on the surfaces of diamond powders (5–7 μm) at a temperature of 1120 K and above in the presence of oxygen (0.05–0.5 Torr). These authors recorded an activation energy of 230 ± 30 kJ/mol for diamond oxidation, which coincides with the one found by Evans[5].

Evans also demonstrated that a surface graphite layer is formed on the surfaces of diamond by oxidation in oxygen, while no graphitization occurs under the same conditions, but in a good vacuum or in the atmosphere of a purified inert gas. It was shown that diamond heating at 1700 K with a pressure of 10^{-4} Torr for 1 hour results in a black surface coating, whereas doing the same experiment at 10^{-6} Torr results in the diamond remaining clear and unchanged.[5] It was concluded that a study of true graphitization should be done at conditions preventing oxidation.[5] Thus, it was shown that even negligible concentrations of oxygen-containing gases can accelerate the diamond graphitization process, decrease the temperature of graphitization, and, as shown in ref. [188], effect the structure of graphitization products. The catalytic effect on diamond graphitization of oxygen-containing gases was mentioned by Palosz et al.[189] and Qian et al.[190]

The catalytic effect of oxygen on diamond graphitization can be explained by the emergence of a new pathway for the reaction of the conversion of diamond to graphitic forms of carbon. We believe that carbon redistribution processes[188] underlie the mechanism of formation of graphite layers on diamond surfaces in hydrogen- and/or oxygen-containing media. As shown in ref. [188], the carbon redistribution processes result in the formation of macroscopic graphitic carbon particles from initial nanosized diamond particles when graphitization was performed in a closed chamber filled with argon at 1870 °C for 1 hour (see Fig. 13.25); however, the graphitization of the ND sample under the same conditions, but in a vacuum of 10^{-5} Torr, resulted in the formation of OLC.[34,41,108–112] The thermal decomposition of surface groups provides (see Section 13.2) evolution of CO, CO_2, H_2O, and H_2, which are involved in reversible reactions with carbon:

$$C + CO_2 \Leftrightarrow 2CO \qquad \text{Eq. (13-5)}$$

$$C + H_2O \Leftrightarrow CO + H_2 \qquad \text{Eq. (13-6)}$$

$$C + 2H_2 \Leftrightarrow CH_4. \qquad \text{Eq. (13-7)}$$

Thus, the presence of oxygen- and hydrogen-containing gases results in carbon atom redistribution processes, which occur via etching and dep-

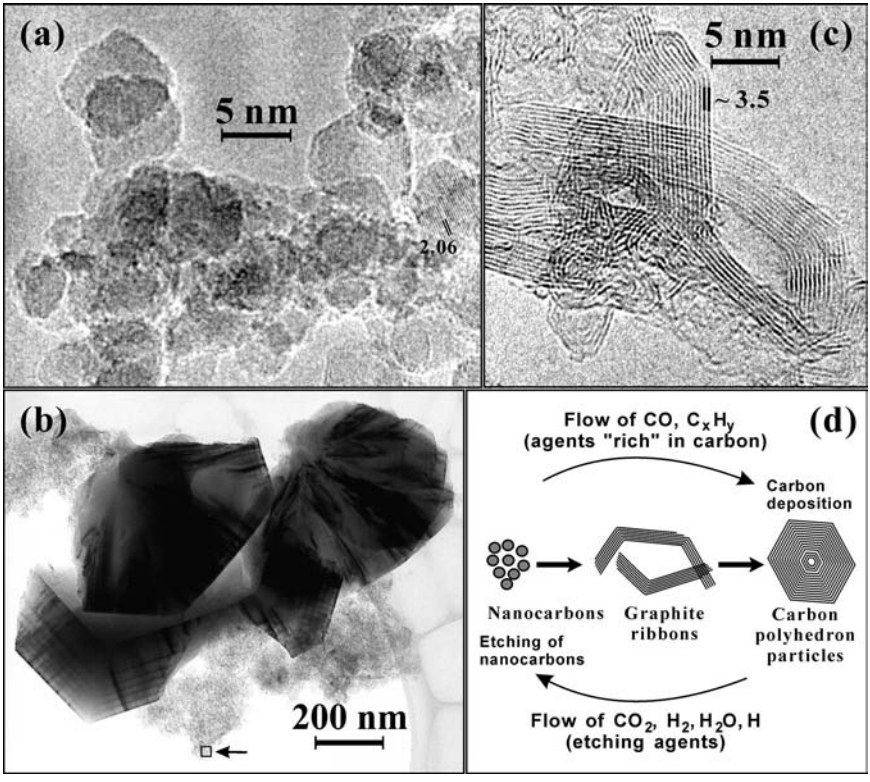

Figure 13.25 HRTEM images of (a) pristine ND before thermal treatment, (b) graphite ribbons, and (c) polyhedron graphite particles observed in the sample prepared by annealing at 2140 K of the pristine ND in a closed chamber filled by argon containing admixtures of CO, CO_2, H_2O, and H_2 gases.[188] Image (c) is a higher resolution image of the marked region of micrograph (b). (d) Scheme of the carbon redistribution process via carbon transport reactions leading to etching of nanocarbons characterized by high surface area and formation of low surface graphitic particles. The graphite ribbons are most likely the primary structures. Carbon deposition preferentially occurs on their surface. A further growth of the ribbons leads to the formation of graphitic polyhedron particles.[188]

osition steps due to the reversible reactions (13-1) to (13-3) of carbon with the reactive gases. These reactions can be considered as carbon transport reactions. These processes result in the etching of carbon nanostructures (ND, OLC, etc.) with a high surface energy and the formation of large-scale graphitic structures. The redistribution process is schematically shown in Fig. 13.25(d). The thermodynamic calculations suggest that at temperatures exceeding 1500 K, redistribution of carbon is mostly caused

by the reactions that involve hydrogen and hydrogen-containing gases, while at temperatures below 1500 K the carbon redistribution processes mainly involve oxygen-containing gases (CO_2, CO, H_2O).

13.7 Properties of ND Annealing Products: OLC, sp^2/sp^3 Nanocomposites

Knowledge of the kinetics of ND graphitization provides one with the opportunity of producing diamond/nanographite nanocomposites with variable ratios of diamond carbon (diamond cores) and defective curved graphitic shells. A desirable extent of graphitization can be achieved at different annealing temperatures by using corresponding heating durations. However, due to the different rates of defect annealing, the defect concentration and their nature can be significantly different. Figure 13.26 presents a general scheme of production of OLC and nanocomposites with different fractions of diamond and nanosized graphitic sheets.[135] The scheme demonstrates that ND annealing at moderate temperatures of 1400–1800 K makes it possible to produce carbon nanocomposites with a controlled ratio of sp^2/sp^3 states in which ND particles are covered with nanosized fullerene-like shells, which are similar to bucky-diamonds.[106,107] Figure 13.27 presents the HRTEM images of the ND

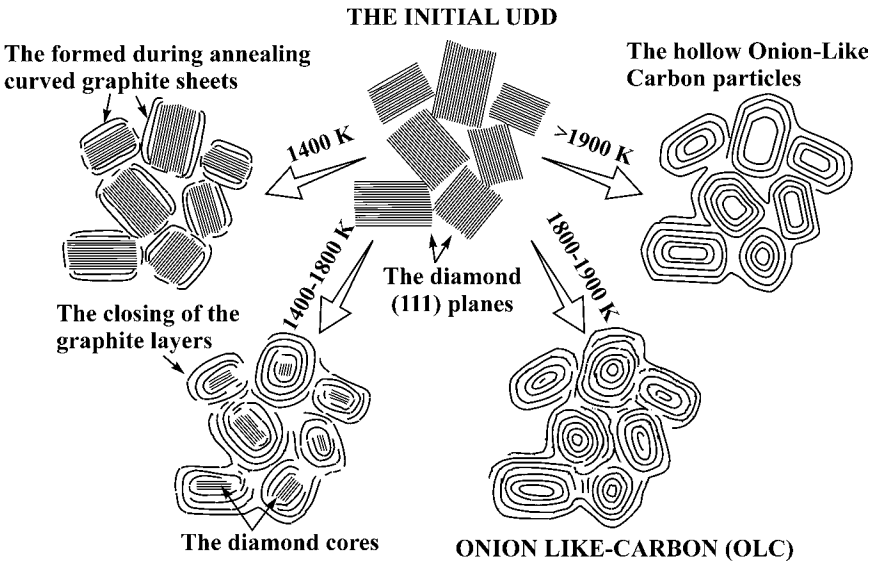

Figure 13.26 Scheme of sp^2/sp^3 nanocomposites and OLC formation.[135]

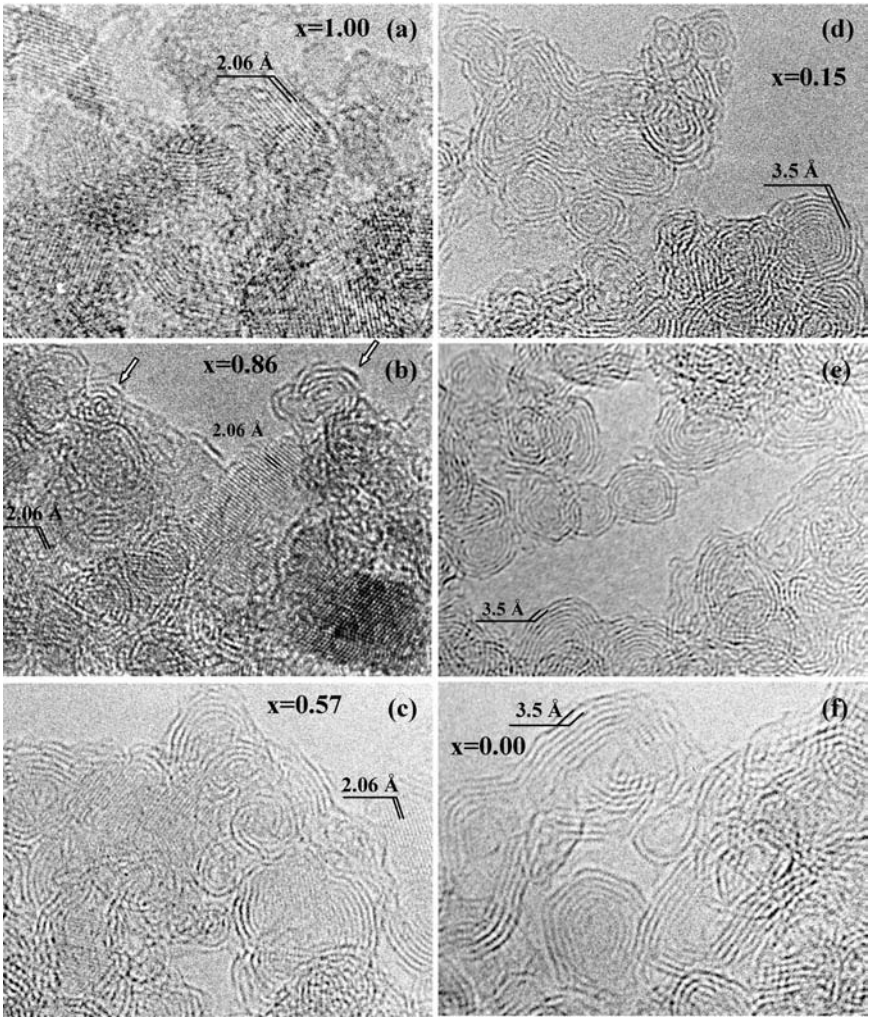

Figure 13.27 HRTEM micrographs of ND samples annealed under a vacuum of 10^{-5} Torr for 1–1.5 h at (a) 1170, (b) 1420, (c) 1600, (d) 1800, (e) 1900, (f) 2140 K.[108,135] The straight dark contrast lines in micrographs (a), (b), and (c) correspond to the (111) crystallographic diamond planes. The distance between these lines is 2.06 Å. The curved dark lines in (d), (e), and (f) correspond to the (0002) crystallographic graphite planes. The distance between these lines is ~3.5 Å. The diamond weight fractions (x) of the samples are also presented within each image. The arrows in (b) show OLC particles containing 2–3 graphite-like shells that were produced by the graphitization of small ND particles (<2 nm) at 1420 K.

annealing products at different temperatures. It should be mentioned that the durations of annealing experiments did not exceed 1.5 hour, therefore more prolonged heating can result in full graphitization of all ND particles even at low temperatures of 1400–1600 K (see Section 13.3). Annealing at 1800–1900 K leads to the formation of OLC containing the carbon onions with 3–8 fullerene-like spherical shells and aggregates of onions. Heating at higher temperatures leads to the formation of hollow OLC with a structure similar to that which was observed when fullerene-containing soot was annealed at temperatures above 2300 K.[191,192]

Products of ND graphitization were characterized with HRTEM,[34,35,108–112,140] Raman spectroscopy,[110,119,136] XRD,[111,112,114,115,132,136,193] XPS,[134,194] EELS[109,112,126] electron spin resonance (ESR),[110] X-ray emission spectroscopy,[171] ultraviolet–visible absorption spectroscopy,[195,196] and electro- and magnetoresistivity measurements.[135,197,198]

Raman spectroscopy data show that some portion of OLC exists as almost ideal fullerene-like shells enclosed in each other (up to 6–7 shells).[119] However, the results of other characterization methods demonstrate the presence of various types of defects, which resemble the defects in graphite materials.[2,10] Figure 13.13 shows possible defects in OLC structures. The X-ray emission study of OLC combined with quantum chemical simulation for the characterization of their electronic structure led to the conclusion that the onions produced by ND annealing at the intermediate temperature (1400–1900 K) have holes in the internal shells.[171] The origin of such defects accompanying OLC formation can be explained in terms of the deficit of diamond carbon atoms in the diamond/graphite interface to form perfect fullerene-like shells during ND annealing (see Section 13.4.5). The radicals in the inner cores of OLC are well shielded by outer defect-free shells from the adsorption of reactive gases. The proposed formation of OLC with a holed structure is in a good agreement with the ESR study[110] of similar samples. Thus, 10 unpaired electrons per carbon onion were registered in ref. [110], where onions were prepared at a temperature lower than 2100 K. The accumulation of different types of defects in the curved graphite layers during ND graphitization was proposed to cause an increase in the density of states near the Fermi level of OLC produced from NDs at 1600, 1800, and 1900 K (Ultraviolet Spectroscopy [UPS] study).[134] The defects present in carbon onions can be annealed at temperatures higher then 2100 K. This annealing of defects is accompanied with the formation of bigger polygonized hollow onions. A photoemission study of potassium-intercalated polygonal

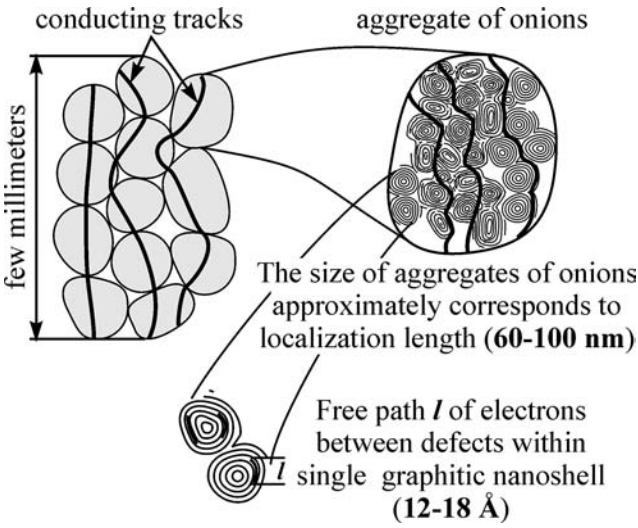

Figure 13.28 Scheme of three scales of OLC particle organization. The heavy solid lines correspond to current conduction tracks.[198]

hollow onions produced at 2140 K showed that these carbon onions behave as small graphite crystals.[194]

Data on the structure of OLC correlate with its electrical properties. Figure 13.28 summarizes the data on the conductivity of OLC. The electroresistivity of the samples demonstrates the temperature dependence typical of systems with variable hopping-length conductivity. The dimensionality of the space for current carrier movement varies between 1/2, 1, and 3/2 depending on the annealing temperature.[135] Figure 13.28 illustrates the scheme of a hierarchical arrangement of OLC forming aggregates that results in their unique electrical characteristics. OLC aggregates are obtained by annealing ND aggregates. Within the aggregates onions are linked to each other by defect graphite-like sheets and C—C bonds. Some part of the onions is represented by elongated particles with linked external graphitic layers and closed quasi-spherical shells. The conduction carrier concentration n for OLC samples was estimated within the framework of the theory of negative magnetoresistance in semiconductors in the hopping conduction region (with the proposition $n \sim nc$, where nc is the critical concentration). The parameter is estimated as $n \sim 8 \cdot 10^{21}\,\mathrm{cm}^{-3}$ for OLC prepared at 1800 K and $n \sim 3 \cdot 10^{21}\,\mathrm{cm}^{-3}$ for OLC prepared at 2140 K.[197] The free path length of electrons within OLC particles is comparable to the size of graphitic fragments within the hollow structure of a single onion ($l \sim 12 \pm 2$ Å). When their hollow structure is

annealed with the formation of hollow polygonized structures, the free path length of the electron increases to 18 ± 2 Å. The size localization length of current carriers is comparable to the size aggregates of OLC particles.

Unusual OLC properties can be used in a variety of applications. It has been shown that due to an efficient optical limiting action of OLC, it is a good candidate for photonic applications.[199] These structures are related to the interstellar dust problem, and can contribute to the large UV adsorption band at 217.5 nm wavelength.[191,200] OLC is potentially a perfect solid lubricant similar to hollow WS_2 nanoparticles. Recently Hirata et al.[201] showed that carbon onions produced by the heat treatment of diamond clusters exhibit stable low-friction coefficients both in air and in vacuum at room temperature. OLC also demonstrates high selectivity and catalytic activity in the oxidative dehydrogenation of ethyl benzene to styrene.[202] The last example demonstrates that OLC, like ND, can be incorporated into chemical reactions and, thus, an onion's surface may be functionalized allowing further incorporation in biosystems. The properties of sp^2/sp^3 nanocomposites and bucky-diamonds have not yet been properly investigated and are topics of future research.

13.8 Conclusion

Diamond graphitization is important from both theoretical and practical points of view. Graphitization of diamond may be induced by thermal treatment and reactive gases, and promoted by metal catalysts and irradiation from different sources. On the one hand, graphitization limits the temperature range and conditions where diamond can be effectively used; on the other hand, it provides the possibility to produce new nanosized carbon materials. We found that thermal annealing of NDs of size 2–5 nm produces OLC, while the annealing of micron-sized diamond produces closed curved graphite-like structures, namely, nanotubes, nanofolds, etc. Theoretical considerations based on molecular modeling using combinations of molecular mechanics, molecular dynamics, and Hartree-Fock (HF) methods allow us to propose that the formation of OLC and closed curved graphite species on a diamond surface have features of self-assembling processes, which proceed via several steps.

Due to the high surface-to-volume ratio of ND particles and their high surface area, the surface groups of ND play an important role in its physical and chemical properties. Controlled functionalization presents a powerful tool for the specific modification of properties of ND particles;

promotes ND participation in various chemical reactions; improves the interaction of ND particles with a solvent, components of a composite material, a polymer, a catalyst; and allows design of new types of biocompatible sorbents and materials. Surface groups stabilize ND surfaces and prevent ND particles from graphitization. Decomposition of surface groups results in graphitization of ND and the formation of bucky-diamonds (intermediates in the ND to OLC transformation) and eventually OLC. Due to the high stability of surface hydrogen-containing groups, the most thermally stable ND can be prepared via its surface hydrogenation.

The large difference between the rates and the kinetic parameters obtained by us (1370–1860 K) and those estimated by G. Davies and T. Evans for the temperature range 2150–2300 K indicates that there are different graphitization mechanisms operating in the "low" and "high temperature regions. Within the high-temperature region the graphitization rate-determining step in the process is detachment of a single atom from the diamond surface. Within the low-temperature region the graphitization mechanism involves a process in which carbon atoms do not completely separate from the diamond surfaces and the outer diamond planes transform progressively into graphite planes. The Debye temperature for diamond, 1910 K, appears to serve as the boundary between these regions. At and above this temperature all oscillating degrees of freedom of the diamond are excited.

Knowledge of the kinetics of ND graphitization provides the possibility to produce diamond/nanographite composites with variable ratios of diamond core and defective curved graphitic shells (sp^2/sp^3 nanocomposites) decreasing in size. The small size of curved graphitic shells, the presence of an interface between nanosized diamond cores and graphitic shells, and probably the high concentration of open graphitic edges can produce the unusual electronic properties of these composites and OLC.

The properties of OLC are poorly studied, mainly due to its low availability for experiments. Nevertheless, this material stimulates great interest. It is related to the interstellar dust problem. Due to a very efficient optical limiting action of OLC, it is a good candidate for photonic applications. OLC is a perfect solid lubricant. OLC also demonstrates high selectivity and catalytic activity in the oxidative dehydrogenation of ethyl benzene to styrene. This last example shows that OLC, like ND, can participate in chemical reactions. The onions' surface can be functionalized allowing further incorporation into biosystems. However, extensive experiments on the preparation of narrow fractions of onions and their functionalization are still required.

Acknowledgments

This work was supported in part by the Russian Foundation for Basic Research Grants No. 05-03-32995; the NATO project CBP.NR.SFPP 981051; and the cooperative grant of the Department of Education of Russian Federation and CRDF NO-008-X1. The authors would like to thank Prof. E. A. Paukshtis and Dr. A. L. Chuvilin for fruitful discussions and assistance with the FTIR spectroscopy experiments and HRTEM experiments, respectively.

References

1. J.E. Field (ed.), *The Properties of Natural and Synthetic Diamonds*, Academic Press, London, 1992.
2. H.O. Pierson, *Handbook of Carbon, Graphite, Diamond and Fullerenes. Properties, Processing and Applications*, Noyes Publications, Park Ridge, NJ, 1993.
3. J.E. Field, *The properties of natural and synthetic diamond*, Academic Press, London, 1992.
4. N.V. Novikov et al. (eds.), *Physical Properties of Diamond, Handbook*, Naukova Dumka, Kiev, 1987.
5. T. Evans, "Changes produced by high temperature treatment of diamond", in J.E. Field (ed.), *The Properties of Diamond*, Academic Press, London, 1979, pp. 403–425.
6. K.S. Uspenskaya, Yu.N. Tolmachev, and D.V. Fedoseev, "Oxidation and graphitization of diamond at low pressures", *Zh. Fiz. Khim.* 56, 495 (1982) (in Russian).
7. D.V. Fedoseev, S.P. Vnukov, V.L. Bukhovets, and B.A. Anikin, "Surface graphitization of diamond at high temperatures", *Surf. Coat. Technol.* 28, 207 (1986).
8. G. Davies, *Properties and Growth of Diamond*, INSPEC, London, 1994.
9. J.F. Prins, "Ion implantation of diamond for electronic applications", *Semicond. Sci. Technol.* 18(3), S27 (2003).
10. F. Banhart, "Irradiation effects in carbon nanostructures", *Rep. Prog. Phys.* 62, 1181 (1999).
11. Y.G. Gogotsi, A. Kailer, and K.G. Nickel, "Transformation of diamond to graphite", *Nature* 401, 663 (1999).
12. F. Banhart and P.M. Ajayan, "Carbon onions as nanoscopic pressure cells for diamond formation", *Nature* 382, 433 (1996).
13. F. Banhart, "The transformation of graphitic onions to diamond under electron irradiation", *J. Appl. Phys.* 81, 15 (1997).
14. P. Wesolowski, Y. Lyutovich, F. Banhart, H.D. Carstanjen, and H. Kronmüller, "Formation of diamond in carbon onions under MeV ion irradiation", *Appl. Phys. Lett.* 71, 1948 (1997).

15. Y. Lyutovich and F. Banhart, "Low-pressure transformation of graphite to diamond under irradiation", *Appl. Phys. Lett.* 74, 659 (1999).
16. M. Zaiser and F. Banhart, "Radiation-induced transformation of graphite to diamond", *Phys. Rev. Lett.* 79, 3680 (1997).
17. S. Evans, "Surface properties of diamond", in J.E. Field (ed.), *The Properties of Natural and Synthetic Diamond*, Academic Press, London, 1992.
18. A.L. Vereschagin "Detonation nanodiamonds", Altai State Technical University, Barnaul, Russian Federation, 2001.
19. O.A. Shenderova, V.V. Zhirnov, and D.W. Brenner, "Carbon nanostructures", *Crit. Rev. Solid State Mater. Sci.* 27(3/4), 227 (2002).
20. V.V. Danilenko, *Synthesis and Sintering of Diamond by Detonation*, Energoatomizdat, Moscow, 2003.
21. V.Yu. Dolmatov, "Detonation synthesis ultra-dispersed diamond", St. Petersburg Government University, St. Peterbursg, 2003.
22. Proceedings of the International Symposium on Detonation Nanodiamonds: Technology, Properties and Applications, St Petersburg, Russia, July 7–9, 2003. *Phys. Solid. State* 46(4) (2004).
23. Proceedings of the NATO ARW on Synthesis, Properties and Applications of Ultrananocrystalline Diamond, St. Petersburg, Russia, 7–10 June 2004. *Synthesis, Properties and Applications of Ultrananocrystalline Diamond*, D.M. Gruen. O.A. Shenderova, and A.Ya. Vul' (eds.), Kluwer Academic, Dordrecht, 2005, XI.
24. V.Y. Dolmatov, "Detonation synthesis ultradispersed diamonds: properties and applications", *Usp. Khim.* 70, 687 (2001) (in Russian).
25. V.I. Trefilov, G.I. Savvakin, V.V. Skorokhod, Y.M. Solonin, and A. Khrienko, "Specific features of ultradispersed diamond produced by the high temperature synthesis under conditions of explosion", *Dokl. Akad. Nauk SSSR* 239, 838 (1978).
26. G.I. Savvakin, Y.M. Solonin, and V.I. Trefilov, "Formation possibility and nonstoichiometric cubic phase of molybdenum carbide under high pressure shock compression", *Dokl. Akad. Nauk SSSR* 270, 92 (1983).
27. G.I. Savvakin, V.A. Serdyuk, and V.I. Trefilov, "Influence of the crystallization conditions of diamonds under high-temperature shock compression on their optical-properties", *Dokl. Akad. Nauk SSSR* 270, 329 (1983).
28. A.M. Staver, A.I. Lyamkin, N.A. Gubareva, and E.A. Petrov, "Ultradispersed diamond powders obtained with the use of explosion energy", *Fiz. Gorenya i Vzryva* 20(5), 101 (1984).
29. A.M. Staver, N.V. Gubareva, A.I. Lyamkin, and E.A. Petrov, "Ultra-disperse diamond powders made by the use of explosion energy", *Combust. Explos. Shock Waves* 20(5), 567 (1984).
30. A.I. Lyamkin, E.A. Petrov, A.P. Ershov, et al., "Production of diamonds from high explosives", *Dokl. Akad. Nauk SSSR* 302(3), 611 (1988).
31. N.R. Greiner, D.S. Phillips, J.D. Johnson, and F. Volk, "Diamonds in detonation soot", *Nature* 333, 440 (1988).
32. V.M. Titov, V.F. Anisichkin, and I.Y. Malkov, "Synthesis of ultradispersed diamond in detonation-waves", *Combust. Explos. Shock Waves* 25(3), 372 (1989).

33. A.L. Vereschagin, G.V. Sakovich, V.F. Komarov, and E.A. Petrov, "Properties of ultrafine diamond clusters from detonation synthesis", *Diamond Relat. Mater.* 3, 160 (1993).
34. V.L. Kuznetsov, A.L. Chuvilin, Yu.V. Butenko, I.L. Malkov, and V.M. Titov, "Onion-like carbon from ultra-disperse diamond", *Chem. Phys. Lett.* 222, 343 (1994).
35. V.L. Kuznetsov, A.L. Chuvilin, E.M. Moroz, V.N. Kolomiichuk, Sh.K. Shaichutdinov, Yu.V. Butenko, and I.Yu. Malkov, "Effect of explosions on the structure of detonation soots: ultradisperse diamond and onion carbon", *Carbon* 32, 873 (1994).
36. V.L. Kuznetsov, A.L. Chuvilin, Yu.V. Butenko, A.K. Gutakovskii, S.V. Stankus, and R.A. Khairulin, "Closed curved graphite-like structures formation on micron-size diamond", *Chem. Phys. Lett.* 289, 353 (1998).
37. O.A. Shenderova, Z. Hu, and D. Brenner, "Carbon family in nanoscale", in D.M. Gruen, O.A. Shenderova, and A.Ya. Vul (eds.), *Synthesis, Properties and Applications of Ultrananocrystalline Diamond*, Springer, Berlin, 2005, pp. 1–14.
38. F.P. Bundy, W.A. Bassett, M.S. Weathers, R.J. Hemley, H.K. Mao, and A.F. Goncharov, "The pressure-temperature phase and transformation diagram for carbon; updated through 1994", *Carbon* 34, 141 (1996).
39. J.A. Viecelli, S. Bastea, J.N. Glosli, and F.H. Ree,. "Phase transformations of nanometer size carbon particles in shocked hydrocarbons and explosives", *J. Chem. Phys*. 115, 2730 (2001).
40. V.V. Danilenko, "Nanocarbon Phase Diagram and conditions for detonation Nanodiamond Formation, in Synthesis, Properties and Applications of Ultrananocrystalline Diamond", (eds. D.M. Gruen, O.A. Shenderova and A.Ya. Vul), Springer, pp. 181–198 (2005).
41. V.L. Kuznetsov, A.L. Chuvilin, Yu.V. Butenko, I.Yu. Malkov, A.K. Gutakovskii, S.V. Stankus, and R.A. Khairulin, "Study of onion-like carbon (OLC) formation from ultra disperse diamond", in P. Bernuer et al. (eds.), *Science and Technology of Fullerene Materials*, vol. 359, MRS Proceedings, Material Research Society, Pittsburgh, 1995, pp. 105–110.
42. D. Tomanek and M.A. Schluter, "Growth regimes of carbon clusters", *Phys. Rev. Lett.* 67, 2331 (1991).
43. J.L. Martins, F.A. Reuse, and S.N. Khanna, "Growth and formation of fullerene clusters", *J. Cluster Sci.* 12, 513 (2001).
44. R.O. Jones, "Density functional study of carbon clusters C2n ($2 < n < 16$). I. Structure and bonding in the neutral clusters", *J. Chem. Phys.* 110, 5189 (1999).
45. G.N. Churilov, P.V. Novikov, V.E. Tarabanko, V.A. Lopatin, N.G. Vnukova, and N.V. Bulina, "On the mechanism of fullerene formation in a carbon plasma", *Carbon* 40, 891 (2002).
46. F. Fugaciu, H. Hermann, and G. Seifert, "Concentric-shell fullerenes and diamond particles: a molecular-dynamics study", *Phys. Rev. B* 60 10711 (1999).
47. N.W. Winter and F.H.Ree, "Carbon particle phase stability as a function of size", *J. Comput.-Aided Mater. Des.* 5, 279 (1998).

48. F.H. Ree, N.W. Winter, J.N. Glosli, and J.A. Viecelli, "Kinetics and thermodynamic behavior of carbon clusters under high pressure and high temperature", *Physica B* 265, 223 (1999).
49. J.E. Dahl, S.G. Liu, and R.M.K. Carlson, "Isolation and structure of higher diamondoids, nanometer-sized diamond molecules", *Science* 299, 96 (2003).
50. R.M.K. Carlson, J.E.P. Dahl, S.G. Liu, M.M. Olmstead, P.R. Buerki, and R. Cat, "Diamond molecules found in petroleum. New members of the H-terminated diamond series", in D.M. Gruen, O.A. Shenderova, and A.Ya. Vul (eds.), *Synthesis, Properties and Applications of Ultrananocrystalline Diamond*, Springer, Berlin, 2005, pp. 63–78.
51. S. Evans, "Surface properties of diamond", in J.E. Field (ed.), *The Properties of Natural and Synthetic Diamond*, Academic Press, London, 1992.
52. V.F. Loktev, V.I. Makal'skii, I.V. Stoyanova, A.V. Kalinkin, V.A. Likholobov, and V.N. Mit'kin, "Surface modification of ultradispersed diamonds", *Carbon* 29, 817 (1991).
53. T. Jiang and K. Xu, "FTIR study of ultradispersed diamond power synthesized by explosive detonation", *Carbon* 33, 1663 (1995).
54. E. Mironov, E. Petrov, and A. Koretz, "Chemical aspect of ultradispersed diamond formation", *Diamond Relat. Mater.* 12, 1472 (2003).
55. V.L. Kuznetsov, M.N. Aleksandrov, I.V. Zagoruiko, A.L. Chuvilin, E.M. Moroz, V.N. Kolomiichuk, V.A. Likholobov, P.M. Brylyakov, and G.V. Sokovich, "Study of ultra disperse diamond obtained using explosion energy", *Carbon* 29, 665 (1991).
56. F. Cataldo and A.P. Koscheev, "A study on the action of ozone and on the thermal stability of nanodiamond", *Fullerenes, Nanotubes, Carbon Nanostruct.* 11(3), 201 (2003).
57. E. Mironov, A. Koretz, and E. Petrov, "Detonation synthesis ultradispersed diamond structural properties investigation by infrared absorption", *Diamond Relat. Mater.* 11, 872 (2002).
58. Yu.V. Butenko, V.L. Kuznetsov, E.A. Paukshtis, A.I. Stadnichenko, I.N. Mazov, S.I. Moseenkov, A.I. Boronin, and S.V. Kosheev, "The thermal stability of nanodiamond surface groups. Onset of nanodiamond graphitization", *Fullerenes, Nanotubes, Carbon Nanostruct.* submitted (2005).
59. K. Iakoubovskii, M.V. Baidakova, B.H. Wouters, A. Stesmans, G.J. Adriaenssens, A.Ya. Vul', and P.J. Grobet, "Structure and defects of detonation synthesis nanodiamond", *Diamond Relat. Mater.* 9, 861 (2000).
60. H. Mutschke, J. Dorschner, Th. Henning, C. Jager, and U. Ott, "Facts and artifacts in interstellar diamond spectra", *Astrophys. J.* 454, L157 (1995).
61. W.W. Duley and V.I. Grishko, "Evolution of carbon dust in aromatic infrared emission sources: formation of nanodiamonds", *Astrophys. J.* 554, L209 (2001).
62. A.P. Koscheev, A.E. Serzhantov, S. Merchel, U. Ott, O. Guillois, and C. Reynaud, "Surface chemistry of chemically treated diamond nanograins", 34th Lunar and Planetary Science Conference, Houston, TX, The Lunar and Planetary Institute, March 17–21, 1287 (2003).
63. A.P. Jones, L.B. d'Hendecourt, S.Y. Sheu, H.C. Chang, C.L. Cheng, and H.G.M. Hill, "Surface C-H stretching features on meteoritic nanodiamonds', *Astron. Astrophys.* 416, 235 (2004).

64. V.S. Bondar and A.P. Puzyr, "Nanodiamonds for biological investigations", *Phys. Solid State* 46, 716 (2004).
65. X.Y. Xu, Y.W. Zhu, B.C. Wang, and X.Q. Shen, "Surface modification of nanodiamond in aqueous medium", *Trans. Nonferrous Met. Soc. China* 13, 1415 (2003).
66. X. Xua, Z. Yua, Y. Zhub, and B. Wang, "Effect of sodium oleate adsorption on the colloidal stability and zeta potential of detonation synthesized diamond particles in aqueous solutions", *Diamond Relat. Mater.* 14, 206 (2005).
67. T. Xu, J.Z. Zhao, and K. Xu, "The ball-bearing effect of diamond nanoparticles as an oil additive", *J. Phys. D: Appl. Phys.* 29, 2932 (1996).
68. G.A. Chiganova, V.A. Bondar, and A.S. Chiganov, "Electrophoresis of ultradispersed diamond hydrosols of and modification of its surface", *Colloid J.* 55, 182 (1993) (in Russian).
69. A.N. Alimova, N.N. Chubun, P.I. Belobrov, and V.V. Zhirnov, "Electrophoresis of nanodiamond powder for cold cathode fabrication", *J. Vac. Sci. Technol. B* 17, 715 (1999).
70. E. Maillard-Schaller, O.M. Kuettel, L. Diederich, L. Schlapbach, V.V. Zhirnov, and P.I. Belobrov, "Surface properties of nanodiamond films deposited by electrophoresis on Si(100)", *Diamond Relat. Mater.* 8, 805 (1999).
71. T. Tyler, V.V. Zhirnov, A.V. Kvit, D. Kang, and J.J. Hren, "Electron emission from diamond nanoparticles on metal tips", *Appl. Phys. Lett.* 82, 2904 (2003).
72. A.M. Affoune, B.L.V. Prasad, H. Sato, and T. Enoki, "Electrophoretic deposition of nanosized diamond particles", *Langmuir* 17, 547 (2001).
73. T. Enoki, "Diamond-to-graphite conversion in nanodiamond and the electronic properties of nanodiamond-derived carbon system", *Phys. Solid State* 46(4), 651 (2004).
74. G.L. Bilbro, "Theory of electrodeposition of diamond nanoparticles", *Diamond Relat. Mater.* 11, 1572 (2002).
75. H. Tabata, M. Fujii, and S. Hayashi, "Laser ablation of diamond nanoparticles suspended in solvent: synthesis of polyynes", *Chem. Phys. Lett.* 395, 138 (2004).
76. X. Xu, Z. Yu, Y. Zhu, and B. Wang, "Influence of surface modification adopting thermal treatments on dispersion of detonation nanodiamond", *J. Solid State Chem.* 178, 688 (2005).
77. Y. Liu, Z. Gu, J.L. Margrave, and V.N. Khabashesku, "Functionalization of nanoscale diamond powder: fluoro-, alkyl-, amino-, and amino acid-nanodiamond derivatives", *Chem. Mater.* 16, 3924 (2004).
78. V.S. Bondar and A.P. Puzyr, "Use of nanodiamond particles for rapid isolation of recombinant apoobelin from *Escherichia coli*", *Dokl Biochem.* 373(1–6),129 (2000).
79. A.P. Puzyr, V.S. Bondar, P.I. Belobrov, and A.A. Bukaemskii, "Preparation of nanodiamond-protein-δ-aluminum oxide complex", *Dokl. Russ. Acad. Sci.* 373, 408 (2000) (in Russian).
80. K.V. Purtov, V.S. Bondar, and A.P. Puzyr, "Supramolecular structure of nanodiamond particles and obelin built up on a two-dimensional plate", *Dokl. Biochem. Biophys.* 380, 339 (2001).

81. V.S. Bondar, I.O. Pozdnyakova, and A.P. Puzyr, "Applications of nanodiamonds for separation and purification of proteins", *Phys. Solid State* 46(4), 758 (2004).
82. L.-C. Lora Huang and H.-C. Chang, "Adsorption and immobilization of cytochrome c on nanodiamonds", *Langmuir* 20, 5879 (2004).
83. X.L. Kong, L.C.L. Huang, C.-M. Hsu, W.-H. Chen, C.-C. Han, and H.-C. Chang, "High-affinity capture of proteins by diamond nanoparticles for mass spectrometric analysis", *Anal. Chem.* 77, 259 (2005).
84. A.P. Puzyr, I.O. Pozdnyakova, and V.S. Bondar, "Design of a luminescent biochip with nanodiamonds and bacterial luciferase", *Phys. Solid State* 46, 761 (2004).
85. N. Kossovsky, A. Gelman, H.J. Hnatyszyn, S. Rajguru, R.L. Garrell, S. Torbati, S.S.F. Freitas, and G.-M. Chows, "Surface-modified diamond nanoparticles as antigen delivery vehicles", *Bioconjugate Chem.* 6(5), 507 (1995).
86. A.P Puzyr, S.V. Tarskikh, G.V. Makarskaya, G.A. Chiganova, I.S. Larionova, P.Y. Detkov, and V.S. Bondar, "Damaging Effect of detonation diamonds on human white and red blood cells in vitro translated", *Dokl. Biochem.* 385, 201 (2002).
87. A.P. Puzyr, D.A. Neshumayev, S.V. Tarskikh, G.V. Makarskaya, V.Y. Dolmatov, and V.S. Bondar, "Destruction of human blood cells in interaction with detonation nanodiamonds in experiments in vitro", *Diamond Relat. Mater.* 13, 2020 (2004).
88. K. Nakagawa, K. Okumura, T. Shimamura, N. Ikenaga, T. Suzuki, T. Kobayashi, M. Nishitani-Gamo, and T. Ando, "Novel selective oxidation of light alkanes using carbon dioxide. Oxidized diamond as a novel catalytic medium", *Chem. Lett.* 32, 866 (2003).
89. K. Okumura, K. Nakagawa, T. Shimamura, N.O. Ikenaga, M. Nishitani-Gamo, T. Ando, T. Kobayashi, and T. Suzuki, "Direct formation of acetaldehyde from ethane using carbon dioxide as a novel oxidant over oxidized diamond-supported catalysts", *J. Phys. Chem. B* 107, 13419 (2003).
90. K. Nakagawa, C. Kajita, N. Ikenaga, T. Suzuki, T. Kobayashi, M. Nishitani-Gamo, and T. Ando, "The role of chemisorbed oxygen on diamond surfaces for the dehydrogenation of ethane in the presence of carbon dioxide", *J. Phys. Chem. B* 107, 4048 (2003).
91. K. Nakagawa, H. Nishimoto, M. Kikuchi, S. Egashira, Y. Enoki, N. Ikenaga, T. Suzuki, M. Nishitani-Gamo, T. Kobayashi, and T. Ando, "Synthesis gas production from methane using oxidized-diamond-supported group VIII metal catalysts", *Energy Fuels* 17, 971 (2003).
92. S.B. Wang and Z.H. Zhu, "Catalytic conversion of alkanes to olefins by carbon dioxide oxidative dehydrogenation – a review", *Energy Fuels* 18, 1126 (2004).
93. K. Nakagawa, M. Nishitani-Gamo, and T. Ando, "Hydrogen production from methane for fuel cell using oxidized diamond-supported catalysts", *Int. J. Hydrogen Energy*, 30, 201 (2005).
94. H. Nishimoto, K. Nakagawa, N. Ikenaga, M. Nishitani-Gamo, T. Ando, and T. Suzuki, "Partial oxidation of methane to synthesis gas over oxidized diamond catalysts", *Appl. Catal. A-Gen.* 264, 65 (2004).

95. B.V. Spitsyn, M.N. Gradoboev, T.B. Galushko, T.A. Karpukhina, N.V. Serebryakova, I.I. Kulakova, and N.N. Melnik, "Purification and functionalization of nanodiamond", in D.M. Gruen, O.A. Shenderova, and A.Ya. Vul (eds.), *Synthesis, Properties and Applications of Ultrananocrystalline Diamond*, Springer, Berlin, 2005, p. 241.
96. V.L. Kuznetsov and Yu.V. Butenko, "Nanodiamond graphitization and properties of onion-like carbon", in D.M. Gruen, O.A. Shenderova, and A.Ya. Vul (eds.), *Synthesis, Properties and Applications of Ultrananocrystalline Diamond*, Springer, Berlin, 2005, pp. 199–216.
97. N.V. Novikov, G.P. Bogatyreva, and M.N. Voloshin, "Detonation diamonds in Ukraine", *Phys. Solid State* 46, 600 (2004).
98. I.I. Kulakova, "Surface chemistry of nanodiamonds", *Phys. Solid State* 46, 636 (2004).
99. S. Ji, T. Jiang, K. Xu, and S. Li, "FTIR study of the adsorption of water on ultradispersed diamond powder surface", *Appl. Surf. Sci.* 133, 231 (1998).
100. V.L. Kuznetsov and Yu.V. Butenko, "Synthesis and properties of nanostructured carbon materials: nanodiamond, onion-like carbon and carbon nanotubes", in Y.G. Gogotsi and I.V. Uvarova (eds.), *Nanostructured materials and coating for biomedical and sensor applications*, NATO Science Series 102, Kluwer Academic, Dordrecht, 2003, p. 187.
101. A.P. Koscheev, N.V. Zaripov, and U. Ott, "Diamond nanograins in carbon soot: does the chemistry of extracted diamonds depend on the properties of pristine soot?", 36th Lunar and Planetary Science Conference, League City, TX, The Lunar and Planetary Institute, March 14–18, 1406 (2005).
102. A. Dandekar, R.T.K. Baker, and M.A. Vannice, "Characterization of activated carbon, graphitized carbon fibers and synthetic diamond powder using TPD and DRIFTS", *Carbon* 36, 1821 (1998).
103. A.J. Gordon and R.A. Ford, *The Chemist's Companion. A Handbook of Practical Data, Techniques, and References*, John Wiley & Sons, New York, 1972.
104. Y. Otake and R.G. Jenkins, "Characterization of oxygen-containing surface complexes created on macroscopic carbon by air and nitric acid treatment", *Carbon* 31, 109 (1993).
105. G.P. Bogatyreva, M.M. Voloshin, V.G. Malogolovets, V.L. Gvyazdovskaya, and G.D. Ilnitskaya, "The effect of heat treatment on the surface condition of nanodiamond", *J. Optoelectron. Adv. Mater.* 2, 469 (2000).
106. A.S. Barnard, S.P. Russo, and I.K. Snook, "Coexistence of bucky diamond with nanodiamond and fullerene carbon phases", *Phys. Rev. B* 68, 073406 (2003).
107. J.-Y. Raty, G. Galli, C. Bostedt, T.W. van Buuren, and L.J. Terminello, "Quantum confinement and fullerene-like surface reconstructions in nanodiamonds", *Phys. Rev. Lett.* 90, 037401 (2003).
108. Yu.V. Butenko, V.L. Kuznetsov, A.L. Chuvilin, V.N. Kolomiichuk, S.V. Stankus, R.A. Khairulin, and B. Segall, "The kinetics of the graphitization of dispersed diamonds at 'low' temperatures", *J. Appl. Phys.* 88, 4380 (2000).
109. S. Tomita, M. Fujii, S. Hayashi, and K. Yamamoto, "Electron energy-loss spectroscopy of carbon onions", *Chem. Phys. Lett.* 305, 225 (1999).

110. S. Tomita, T. Sakurai, H. Ohta, M. Fujii, and S. Hayashi, "Structure and electronic properties of carbon onions", *J. Chem. Phys.* 114, 17 (2001).
111. S. Tomita, A. Burian, J.C. Dore, D. LeBolloch, M. Fujii, and S. Hayashi, "Diamond nanoparticles to carbon onions transformation: X-ray diffraction studies", *Carbon* 40, 1469 (2002).
112. O.O. Mykhaylyk, Y.M. Solonin, D.N. Batchelder, and R. Brydson, "Transformation of nanodiamond into carbon onions: a comparative study by high-resolution transmission electron microscopy, electron energy-loss spectroscopy, x-ray diffraction, small-angle x-ray scattering, and ultraviolet Raman spectroscopy", *J. Appl. Phys.* 97, 074302 (2005).
113. N.S. Xu, Jian Chen, and S.Z. Deng, "Effect of heat treatment on the properties of nano-diamond under oxygen and argon ambient", *Diamond Relat. Mater.* 11, 249 (2002).
114. A.E. Aleksenskii, M.V. Baidakova, A.Ya. Vul', V.Yu. Davydov, and Yu.A. Pevtsova, "Diamond-graphite phase transition in ultradisperse-diamond clusters", *Phys. Solid State* 39(6), 1007 (1997).
115. M.V. Baidakova, V.I. Siklitsky, and A.Y. Vul, "Ultradisperse-diamond nanoclusters. Fractal structure and diamond-graphite phase transition", *Chaos Solitons Fractals* 10, 2153 (1999).
116. B.L.V. Prasad, H. Sato, T. Enoki, Y. Hishiyama, Y. Kaburagi, A.M. Rao, K. Oshida, and M. Endo, "Heat-treatment effect on the nanosized graphite pi-electron system during diamond to graphite conversion", *Phys. Rev. B* 62, 11209 (2000).
117. J. Qian, C. Pantea, J. Huang, T.W. Zerda, and Y. Zhao, "Graphitization of diamond powders of different sizes at high pressure–high temperature", *Carbon* 42, 2691 (2004).
118. M. Yoshikawa, Y. Mori, H. Obata, M. Maegawa, G. Katagiri, H. Ishida, and A. Ishitani, "Raman scattering from nanometer-sized diamond", *Appl. Phys. Lett.* 67, 694 (1995).
119. E.D. Obraztsova, M. Fujii, S. Hayashi, V.L. Kuznetsov, Yu.V. Butenko, and A.L. Chuvilin, "Raman identification of onion-like carbon", *Carbon* 36, 821 (1998).
120. N. Wada and S.A. Solin, "Raman efficiency measurements of graphite", *Physica B* 105, 353 (1981).
121. R. Azria, Y.L. Coat, M.H. Hamou, M.N. Hedhili, S. Ustaze, M. Tronc and A. Hoffman, "Dissociative electron attachment in H^- electron stimulated desorption from hydrogenated diamond surfaces", *Surf. Sci.* 482, 324 (2001).
122. C. Goeden and G. Dollinger, "Electron stimulated desorption of negative ions: a time-of-flight experiment", *Rev. Sci. Instrum.* 73, 3058 (2002).
123. C. Goeden and G. Dollinger, "Electron-stimulated hydrogen desorption from diamond surfaces and its influence on the low-pressure synthesis of diamond", *Appl. Phys. Lett.* 81, 5027 (2002).
124. A. Laikhtman, A. Lafosse, Y. Le Coat, R. Azria, and A. Hoffman, "Clarification of oxygen bonding on diamond surfaces by low energy electron stimulated desorption and high resolution electron energy loss spectroscopy", *J. Chem. Phys.* 119, 1794 (2003).
125. L.-C. Qin and S. Iijima, "Onion-like graphitic particles produced from diamond", *Chem. Phys. Lett.* 262, 252 (1996).

126. V.V. Roddatis, V.L. Kuznetsov, Yu.V. Butenko, D.S. Su, and R. Schloegl, "Transformation of diamond nanoparticles into carbon onions under electron irradiation", *Phys. Chem. Chem. Phys.* 4, 1964 (2002).
127. B.B. Pate, "The diamond surface: atomic and electronic structure", *Surf. Sci.* 165, 83 (1986).
128. A.P. Dementjev, K.I. Maslakov, and A.V. Naumkin, "Interaction of carbon atoms with nanodiamond surface", in D.M. Gruen, O.A. Shenderova, and A.Ya. Vul (eds.), *Synthesis, Properties and Applications of Ultrananocrystalline Diamond*, Springer, Berlin, 2005, p. 253.
129. A.S. Barnard, N.A. Marks, S.P. Russo, and I.K. Snook, "Hydrogen stabilization of {111} nanodiamond", *MRS Symp. Proc.* 740, 69 (2003).
130. O.E. Anderson, B.L.V. Prasad, H. Sato, T. Enoki, Y. Hishiyama, Y. Kaburagi, M. Yoshikawa, and S. Bandow, "Structure and electronic properties of graphite nanoparticles", *Phys. Rev. B* 58, 16387 (1998).
131. J. Chen, S.Z. Deng, J. Chen, Z.X. Yu, and N.S. Xu, "Graphitization of nanodiamond powder annealed in argon ambient", *Appl. Phys. Lett.* 74, 3651 (1999).
132. A.E. Aleksenskii, M.V. Baidakova, A.Y. Vul', A.T. Dideikin, and V.I. Siklitskii, "Effect of hydrogen on the structure of ultradisperse diamond", *Phys. Solid State* 42, 1575 (2000).
133. E. Osawa, "Desintegration and purification of crude aggregates of detonation nanodiamond", in D.M. Gruen, O.A. Shenderova, and A.Ya. Vul (eds.), *Synthesis, Properties and Applications of Ultrananocrystalline Diamond*, Springer, Berlin, 2005, pp. 231–240.
134. Yu.V. Butenko, S. Krishnamurthy, A.K. Chakraborty, V.L. Kuznetsov, V.R. Dhanak, M.R.C. Hunt, and L. Šiller, "Photoemission study of onion-like carbons produced by annealing nanodiamonds", *Phys. Rev. B* 71, 075420 (2005).
135. V.L. Kuznetsov, Yu.V. Butenko, A.L. Chuvilin, A.I. Romanenko, and A.V. Okotrub, "Electrical resistivity of graphitized ultra-disperse diamond and onion-like carbon", *Chem. Phys. Lett.* 336, 397 (2001).
136. E.D. Obraztsova, S.M. Pimenov, V.I. Konov, M. Fujii, S. Hayashi, V.L. Kuznetsov, Yu.V. Butenko, A.L. Chuvilin, and E.N. Loubnin, "Raman investigation of onion-like carbon", *Mol. Mater.* 10(1–4), 249 (1998).
137. G. Davies and T. Evans, "Graphitization of diamond at zero pressure and a high pressure", *Proc. R. Soc.* 328, 413 (1972).
138. F. Bechstedt, A.A. Stekolnikov, J. Furthmuller, and P. Kackell, "Origin of the different reconstructions of diamond, Si, and Ge(111) surfaces", *Phys. Rev. Lett.* 87, 016103 (2001).
139. A. Hoffman, K. Bobrov, B. Fisgeer, H. Shechter, and M. Folman, "Annealing of ion beam amorphized diamond surfaces studied by in situ electron spectroscopy", *Diamond Relat. Mater.* 5, 76 (1996).
140. V.L. Kuznetsov, I.L. Zilberberg, Yu.V. Butenko, A.L. Chuvilin, and B. Segall, "Theoretical study of the formation of closed curved graphite-like structures during annealing of diamond surface", *J. Appl. Phys.* 86, 863 (1999).
141. A.C. Ferrari, A. Libassi, B.K. Tanner, V. Stolojan, J. Yuan, L.M. Brown, S.E. Rodil, B. Kleinsorge, and J. Robertson, "Density, sp^3 fraction, and cross-sectional structure of amorphous carbon films determined by x-ray

reflectivity and electron energy-loss spectroscopy", *Phys. Rev. B* 62, 11089 (2000).
142. R. Haerle, E. Riedo, A. Pasquarello, and A. Baldereschi, "sp^2/sp^3 hybridization ratio in amorphous carbon from C1s core-level shifts: X-ray photoelectron spectroscopy and first-principles calculation", *Phys. Rev. B* 65, 045101 (2002).
143. P.C. Lurie and J.M. Wilson, "The diamond surface. I. The structure of clean surface and the interaction with gases and metals", *Surf. Sci.* 65, 453 (1977).
144. A.V. Hamza, G.D. Kubiak, and R.H. Stulen, "Hydrogen chemisorption and the structure of the diamond C(100)-(2 × 1) surface", *Surf. Sci.* 237, 35 (1990).
145. R.E. Thomas, R.A. Rudder, R.J. Markunas, D. Huang, and M. Frenklach, "Atomic hydrogen adsorption on the reconstructed diamond (100)-(2 × 1) surface", *J. Chem. Vapor Depos.* 1, 6 (1992).
146. L.F. Sutcu, C.J. Chu, M.S. Thompson, R.H. Hauge, J.L. Margrave, and M.P. D'Evelin, "Atomic force microscopy of (100), (110) and (111) homoepitaxial diamond films", *J. Appl. Phys.* 71, 5930 (1992).
147. S. Scocov, C.S. Carmer, B. Weiner, and M. Frenklach, "Reconstruction of (100) diamond surface using molecular dynamics with combined quantum and empirical forces", *Phys. Rev. B* 49, 5662 (1994).
148. J. Ristein, "Electronic properties of diamond surfaces–blessing or curse for devices?", *Diamond Relat. Mater.* 9, 1129 (2000).
149. G. Kern, J. Hafner, J. Furthmüller, and G. Kresse, "(2 × 1) reconstruction and hydrogen-induced de-reconstruction of the diamond (100) and (111) surfaces", *Surf. Sci.* 352–354, 745 (1996).
150. K.C. Pandey, "New π-bonded chain model for Si(111)-(2 × 1) surface", *Phys. Rev. Lett.* 47, 1913 (1981).
151. G.D. Kubiak and K.W. Kolasinski, "Normally unoccupied states on C(111) (diamond) (2 × 1)–support for a relaxed π-bonded chain model", *Phys. Rev. B* 39, 1381 (1989).
152. S. Iarlori, G. Galli, F. Gygi, M. Parrinello, and E. Tosatti, "Reconstruction of the diamond (111) surface", *Phys. Rev. Lett.* 69, 2947 (1992).
153. F. Bechstedt, A.A. Stekolnikov, J. Furthmuller, and P. Kackell, "Origin of the different reconstructions of diamond, Si, and Ge(111) surfaces", *Phys. Rev. Lett.* 87, 016103 (2001).
154. R.P. Chin, J.Y. Huang, Y.R. Shen, T.J. Chuang, H. Seki, and M. Buck, "Vibrational spectra of hydrogen on diamond C(111)-(1 × 1)", *Phys. Rev. B* 45, 1522 (1992).
155. R. Stumpf and P.M. Marcus, "Relaxation of the clean and H-covered C(111) and clean Si(111)-1 × 1 surfaces", *Phys. Rev. B* 47, 16016 (1993).
156. C. Su, K.-J. Song, Y.L. Wang, H.-L. Lu, T.J. Chuang, and J.-C. Lin, "Hydrogen chemisorption and thermal desorption on the diamond C(111) surface", *J. Chem. Phys.* 107, 7543 (1997).
157. C. Su and J.-C. Lin, "Structural instability of the diamond C(111) surface induced by hydrogen chemisorption", *J. Chem. Phys.* 109, 9549 (1998).
158. Th. Schaich, J. Braun, J.P. Toennies, M. Buck, and Ch. Woll, "Structural changes accompanying the hydrogen desorption from the diamond

C(111):H(1 × 1)-surface revisited by helium atom scattering", *Surf. Sci.* 385, L958 (1997).
159. G. Kern, J. Hafner, and G. Kresse, "Atomic and electronic structure of diamond (111) surfaces: I. Reconstruction and hydrogen-induced dereconstruction of the one dangling-bond surface", *Surf. Sci.* 366, 445 (1996).
160. G. Kern, J. Hafner, and G. Kresse, "Atomic and electronic structure of diamond (111) surfaces: II. (2 × 1) and (sqr(3) × sqr(3)) reconstructions of the clean and hydrogen-covered three dangling-bond surfaces", *Surf. Sci.* 366, 464 (1996).
161. G.N. Ramachandran, "Crystal structure of diamond", *Nature* 156, 83 (1945).
162. G. Kern and J. Hafner, "Ab-initio calculations of the atomic and electronic structure of clean and hydrogenated diamond (110) surfaces", *Phys. Rev. B* 56, 4203 (1997).
163. O.A. Shenderova, D.W. Brenner, A. Omeltchenko, X. Su, and L.H. Yang, "Atomistic modeling of the fracture of polycrystalline diamond", *Phys. Rev. B* 61, 3877 (2000).
164. G. Jungnickel, D. Porezag, Th. Frauenheim, M.I. Heggie, W.R.L. Lambrecht, B. Segall, and J.C. Angus, "Graphitization effects on diamond surfaces", *Phys. Status Solidi A* 154, 109 (1996).
165. R.P. Fehlhaber and L.A. Bursill, "Nanoscale size effects on the plasmon response of diamond powder", *Philos. Mag. B* 79, 477 (1999).
166. P.W. Chen, Y.S. Ding, Q. Chen, F.L. Huang, and S.R. Yun, "Spherical nanometer-sized diamond obtained from detonation", *Diamond Relat. Mater.* 9, 1722 (2000).
167. A.L. Vereschagin and G.V. Sakovich, "Structure of detonation nanodiamonds", *Mendeleev Commun.* 1, 39 (2001).
168. S. Matsumoto and Y. Matsui, "Electron microscopic observation of diamond particles grown from the vapour phase", *J. Mater. Sci.* 18, 1785 (1983).
169. W.R.L. Lambrecht, C.H. Lee, B. Segall, J.C. Angus, Z. Li, and M. Sunkara, "Diamond nucleation by hydrogenation of the edges of graphitic precursors", *Nature* 364, 607 (1993).
170. J. Abrahamson, "The surface energies of graphite", *Carbon* 11, 337 (1973).
171. A.V. Okotrub, L.G. Bulusheva, V.L. Kuznetsov, Yu.V. Butenko, A.L. Chuvilin, and M.I. Heggie, "X-ray emission studies of valence band of nanodiamonds annealed at different temperatures", *J. Chem. Phys. A* 105, 9781 (2001).
172. J.-Y. Raty, G. Galli, C. Bostedt, T.W. van Buuren, and L.J. Terminello, "Quantum confinement and fullerene-like surface reconstructions in nanodiamonds", *Phys. Rev. Lett.* 90, 037401 (2003).
173. F. Fugaciu, H. Hermann, and G. Seifert, "Concentric-shell fullerenes and diamond particles: a molecular-dynamics study", *Phys. Rev. B* 60, 10711 (1999).
174. A.S. Barnard, S.P. Russo, and I.K. Snook, "Structural relaxation and relative stability of nanodiamond morphologies", *Diamond Relat. Mater.* 12, 1867 (2003).
175. A.J. Stone and D.J. Wales, "Theoretical studies of icosahedral C60 and some related species", *Chem. Phys. Lett.* 128, 501 (1986).

176. B.N. Davison and W. Picket, "Graphite-layer formation at a diamond (111) surface step", *Phys. Rev. B* 49, 14770 (1994).
177. C. Nebel and J. Ristein (eds.), *Thin Film Diamond: Semiconductors and Semimetals*, Academic Press, London, 2003.
178. C. Pantea, J. Qian, G.A. Voronin, and T.W. Zerda, "High pressure study of graphitization of diamond crystals", *J. Appl. Phys.* 91, 4, (2002).
179. A.P. Grigoriev, S.K. Lifshits, and P.P. Shamaev, "Method of treating diamond", US Patent 4,339,304, 1980.
180. Yu.V. Butenko, "Low temperature diamond graphitization", Ph.D. Thesis, Boreskov Institute of Catalysis, Novosibirsk, 2001 (in Russian).
181. O.P. Krivoruchko, V.I. Zaikovskii, and K.I. Zamaraev, "Formation of unusual liquid-like like Fe-C particles and dynamics of their behavior on amorphous carbon surface at 920-1170 K", *Dokl. Akad. Nauk* 329, 744 (1993).
182. M.S. Dresselhaus, G. Dresselhaus, and P.C. Eklund, *Science of Fullerenes and Carbon Nanotubes*, Academic Press, San Diego, CA, 1996.
183. T.W. Ebbesen (ed.), *Carbon nanotubes: Preparation and properties*, CRC Press, Boca Raton, FL, 1997.
184. M.S. Dresselhaus, G. Dresselhaus, and P. Avouris, *Carbon Nanotubes: Synthesis, Structure, Properties, and Applications*, Topics in Applied Physics Vol. 80, Springer, New York, 2001.
185. P. Harris, *Carbon Nanotubes and Related Structures: New Materials for the Twenty-First Century*, Cambridge University Press, Cambridge, 2001.
186. R. Saito, G. Dresselhaus, and M.S. Dresselhaus, *Physical Properties of Carbon Nanotubes*, Imperial College Press, London, 1998.
187. J. Liu, S. Fan, and H. Dai, "Recent advances in methods of forming carbon nanotubes", *MRS Bull.* 29(4), 244 (2004).
188. V.L. Kuznetsov, Yu.V. Butenko, V.I. Zaikovskii, and A.L. Chuvilin, "Carbon redistribution processes in nanocarbons", *Carbon* 42, 1057 (2004).
189. B. Palosz, E. Grzanka, C. Pantea, T.W. Zerda, Y. Wang, J. Gubicza, and T. Ungár, "Microstructure of nanocrystalline diamond powders studied by powder diffractometry", *J. Appl. Phys.* 97, 064316 (2005).
190. Jiang Qian, C. Pantea, G. Voronin, and T.W. Zerda, "Partial graphitization of diamond crystals under high-pressure and high-temperature conditions", *J. Appl. Phys.* 90, 1632 (2001).
191. W.A. de Heer and D. Ugarte, "Carbon onions produced by heat treatment of carbon soot and their relation to the 217.5 nm interstellar absorption feature", *Chem. Phys. Lett.* 207, 480 (1993).
192. D. Ugarte, "High-temperature behavior of fullerene black", *Carbon* 32, 1245 (1994).
193. M.V. Baidakova, Yu.V. Butenko, V.L. Kuznetsov, A.Ya. Vul', and M.A. Yagovkina, "X-ray diffraction study of low temperature graphitization of diamond", International Symposium, Detonation Nanodiamonds: Technology, Properties and Applications, St. Petersburg, Russia, July 7–9, 2003, p. 77, 2003.
194. M. Montalti, S. Krishnamurthy, Y. Chao, Yu.V. Butenko, V.L. Kuznetsov, V.R. Dhanak, M.R.C. Hunt, and L. Siller, "Photoemission spectroscopy of clean and potassium-intercalated carbon onions", *Phys. Rev. B* 67, 113401 (2003).

195. S. Tomita, M. Fujii, and S. Hayashi, "Optical extinction properties of carbon onions prepared from diamond nanoparticles", *Phys. Rev. B* 66, 245424 (2002).
196. S. Tomita, S. Hayashi, Y. Tsukuda, and M. Fujii, "Ultraviolet-visible absorption spectroscopy of carbon onions", *Phys. Solid State* 44, 450 (2002).
197. A.I. Romanenko, O.B. Anikeeva, A.V. Okotrub, L.G. Bulusheva, V.L. Kuznetsov, Yu.V. Butenko, A.L. Chuvilin, C. Dong, and Y. Ni, "The temperature dependence of the electrical resistivity and the negative magnetoresistance of carbon nanoparticles", *Phys. Solid State* 44, 487 (2002).
198. A.I. Romanenko, O.B. Anikeeva, A.V. Okotrub, V.L. Kuznetsov, Yu.V. Butenko, A.L. Chuvilin, C. Dong, and Y. Ni, "Temperature dependence of electroresistivity, negative and positive magnetoresistivity of carbon nanoparticles", in S. Komarneni et al. (eds.), *Nanophase and nanocomposite materials*, MRS Proc., Material Research Society, Pittsburgh, 703, 259 (2002).
199. E. Koudoumas, O. Kokkinaki, M. Konstantaki, S. Couris, S. Korovin, P. Detkov, V. Kuznetsov, S. Pimenov, and V. Pustovoi, "Onion-like carbon and diamond nanoparticles for optical limiting", *Chem. Phys. Lett.* 357, 336 (2002).
200. Ph. Lambin, L. Henrard, A.A. Lucas, and Th. Cabioc'h, "Optical properties of the carbon onions", in G. Benedek, P. Milani, and V.G. Ralchenko (eds.), *Nanostructured Carbon for Advanced Applications*, Kluwer Academic, Dordrecht, pp. 273–284, 2001.
201. A. Hirata, M. Igarashi, and T. Kaito, "Study on solid lubricant properties of carbon onions produced by heat treatment of diamond clusters or particles", *Tribol. Int.* 37, 899 (2004).
202. N. Keller, N.I. Maksimova, V.V. Roddatis, M. Schur, G. Mestl, V.L. Kuznetsov, Yu.V. Butenko, and R. Schlögl, "The catalytic use of onion-like carbon materials for Styrene synthesis by oxidative dehydrogenation of ethylbenzene", *Angew. Chem. Int. Ed.* 41, 1885 (2002).

14 Applications of Detonation Nanodiamond

Valerii Yu. Dolmatov

JSC Diamond Centre, St. Petersburg, Russia

14.1 Electrochemical Coatings

In the mid-1980s the possibility of Ultrananocrystalline diamond (UNCD) co-deposition with metals during their reduction from water solutions was discovered.[1–3] In the deposition process the suspended UNCD particles interact with the surface of the growing layer due to hydrodynamic, electrostatic, and molecular forces. Using Auger electron spectroscopy (OGE) and infrared (IR) spectroscopy methods it was found that individual UNCD particles and more often UNCD agglomerates penetrate the depositing metal film.

Special surface modification of purified UNCD makes the highly disperse suspensions stable, even in the media of strong electrolytes. UNCD is kept suspended by gassing and heat convection in the process of manufacturing metal–diamond composite electrochemical coatings (CECs). The coating is quite dense and uniform because UNCD particles are very small – tenths of a percent[6,7] – in contrast to all known fillers.[4,5]

14.1.1 Chrome Plating

At first the process of electrochemical deposition of UNCD with chrome was developed.[1,2] Later it became a very interesting target when the chrome-plating process was used to improve the wear resistance of tools and component parts.

In chrome plating with UNCD, hard chrome plating and self-regulating electrolytes (i.e., buffer) are used. The classical electrolyte content is: CrO_3, 250 g/l; H_2SO_4, 2.5 g/l; and UNCD, 15–30 g/l. It gave the best results and was the simplest to use. In the coating there is a UNCD content of 0.3–1.0% by mass. A real microhardness of 900–1000 kg/mm^2 is attained.

Dolmatov and co-workers[8,9] investigated the quality and deposition processes for CEC with diamonds of different origin: at the JSC Diamond

Centre in St. Petersburg, diamonds of static synthesis (DSS) were reduced to nanoscale dimensions of 0.1/0 (notation for the product in Russia is ASM 0.1/0), i.e., dimensions of crystals up to 100 nm.

It was found in hard chrome plating that the microhardness of the Cr–ASM coating is lower than that of the Cr–UNCD coating. In addition:

- When coated parts are dynamically loaded, the Cr–ASM coating partly flakes away, revealing the base and leading to breakdown of a part. This is explained by the low surface activity of classical diamonds and their weak bonds to the surface of the part being coated.
- In contrast to UNCD, the ASM do not positively influence such an important electrolyte parameter as dispersive ability (i.e. uniformity of the coating).
- During contact the counter-body (a conjugating part) is increasingly worn out due to the protruding cutting edges of the diamond crystal on the surface of the Cr–ASM coating.

The application of the UNCD–ASM mixed additive in the chrome-plating electrolyte gives substantially different results than in their separate applications. Table 14.1 shows the dependence of the microhardness of the Cr–UNCD–ASM coating in hard chrome-plating on the cathode current density and the percentage of two different diamonds (UNCD and ASM). A comparison of the microhardness of Cr–UNCD and Cr–ASM with the data in Table 14.1, obtained under similar conditions, shows that microhardness increases by 32% in comparison to Cr-UNCD and by 48–81% in comparison to microhardness of the coating with the mixed additives increases Cr-ASM, including practically important regions of a current density of 50–60 A/dm^2.

Table 14.2 gives the data on the wear resistance of chrome–diamond coatings depending on the content of additives in comparison to a titanium nitride coating (TiN coating thickness of 3–5 μm, wearing time 10 hours).

The use of mixed diamonds eliminates all the disadvantages of separate use and significantly improves the performance characteristics of a coated part. Further, the total value of diamond additive is relatively small and it also improves the economical factors of the process.

In 2004 the service life of hollow milling cutters (made in South Korea) with a chrome–diamond coating was compared with that of similar cutters with a TiN coating at the "Obuhovskiy Plant" (St. Petersburg). The test showed that the service life of the former was longer by a factor of 1.5–2.3 than that of the latter. In addition, the cutters with pure UNCD or

Table 14.1 **The Dependence of Microhardness of Hard Cr-UNCD-DSS Coating Against the Cathode Current Density, Quantity of Mixed Diamond Additive in the Standard Electrolyte, and Relation of UNCD and ASM (CrO_3, 250 g/l; H_2SO_4, 2.5 g/l; t = 45–47 °C)**

Cathode Current Density (A/dm^2)	Quantity of UNCD/ASM in Electrolyte (g/l)							
	0	0.1/9.9	2.5/5.0	5.0/2.5	5.0/5.0	2.5/10.0	10.0/5.0	10.0/10.0
	Microhardness of Cr-UNCD-ASM Coating (kg/mm^2)							
30	756	992	1214	1108	1073	–	1253	–
40	793	989	1306	1123	1202	–	1314	–
50	816	1033	1381	1303	1318	–	1388	–
60	858	1029	1408	1342	1481	–	1427	–
80	935	–	–	–	1368	1426	–	1538
100	1064	1244	1481	1466	1449	1782	1517	1825
120	1100	1290	1422	1393	2103	2143	1502	2289

Table 14.2 Wear Resistance of Chrome–Diamond Coatings, Measured by LTI Method (Russia), Depending on the Contents of Diamond Additive in the Standard Electrolyte (CrO_3, 250 g/l; H_2SO_4, 2.5 g/l; t = 54–56 °C, Thickness 20 μm, Wearing Time 20 h)

Quantity of Diamonds in Electrolyte (g/l) Sample Nos.			Wear (mass %)
Without additives			15.5
UNCD	1	2	–
	2	2.5	4.8
	3	5.0	3.0
	4	10.0	3.15
	5	15.0	2.1
	6	30.0	1.3
ASM	7	2.0	2.1
	8	5.0	1.5
	9	10.0	1.22
UNCD/ASM	13	2.5/2.0	1.4
	14	2.5/5.0	1.1
	15	2.5/10.0	0.83
	16	5.0/2.0	1.1
	17	5.0/5.0	1.2
	18	5.0/10.0	0.94
TiN (ordinary steel)	19		19.1
TiN (steel M42), South Korea	20		16.0

Note: Time of wearing of samples (Nos. 19 and 20), 10 h. Sample No. 19 was plated with TiN in Britain, sample No. 20 in Korea.

combined UNCD–ASM coatings worked practically equally well (though the latter is more effective by 20–25%). The plating technology of this instrument with mixed diamonds (UNCD–ASM) was developed and patented in South Korea.

14.1.2 Copper Plating

The process of copper plating was investigated on the basis of a simple acid electrolyte comprising two components: sulphuric copper and sulphuric acid.[6,9,10] When UNCD was added to the electrolyte in concentrations from 0.1 to 5.0 g/l, the polarization curves showed that UNCD did

not change their nature and mechanism of the electrode process. A standard mechanism of copper discharge and the nature of the limiting polarization phase are also not changed.

A more uniform metal distribution on the electrode demonstrates a better characterization of the throwing power of the electrolyte. It was determined that the throwing power of the electrolyte with UNCD additive increases three-fold in comparison to that of an electrolyte without additive.

UNCD significantly influences the porosity of copper coatings due to the influence of UNCD on the structure and density of deposit packing. This is related to the absorption of UNCD on the electrode surface. The addition of UNCD electrolyte reduces the number of pores from 10 pcs/cm^2 (0.1 g/l of UNCD) to total absence (5.0 g/l of UNCD). When UNCD additive was used, an iridescent oxide film appeared on all samples. This film is the protection against corrosion. When the corrosion was tested, the loss of mass was not observed. The coating is more compact and corrosion resistant, and consists of smaller crystals.

The wear of copper-coated samples deposited from the electrolyte with UNCD is smaller by a factor of 9–10 than that of samples deposited from the pure electrolyte (no UNCD).

In order to determine the properties mentioned above the following parameters for the electrolyte and electrolysis are recommended: $CuSO_4 \cdot 5\ H_2O$, 80 g/l; H_2SO_4, 100 g/l; UNCD, 2–5 g/l; room temperature, 20 ± 2 °C); cathode current density $i_k = 1$ A/dm^2.

14.1.3 Zinc Plating

In the steel zinc-plating process, alkaline zincate and weak acid chloride electrolytes have mainly been investigated.[9–12] It was experimentally determined that the optimum concentration of UNCD amounts to 10 g/l (the UNCD content in the coating is 0.7 mass %).

For the corrosion testing of Zn–UNCD coatings from the electrolyte, the following parameters appeared to be the most effective: 12 g/l ZnO, 120 g/l NaOH, and 7–10 g UNCD at a current density of 1–2 A/dm^2. These coatings result in a higher resistance to sea water (by 60–62%) than any other zinc coatings.

As UNCD concentration in an electrolyte is increased the fineness of deposited layers increases. Passivation of Zn–UNCD coatings by chromate or phosphate treatment improves the corrosion resistance (Table 14.3). Corrosion has been found on a zinc layer and there were no traces of corrosion on a steel substrate.

Table 14.3 Corrosion Resistance (Mass Loss, mg/dm^2) of Coatings in the Climate Chamber According to the State Standard GOST 9.308-85 (Russia) in Neutral Salt Fog; Electrolyte Composition (g/l) ZnO 10, NaOH 100; Organic Additives 4; UNCD 8; Thickness of the Coating 6 μm; Number of Samples of Each Type 6

Hours	60	150	200	350
Uncoated steel	127			
Pure Zn coating (made Germany, chloride in electrolyte, 7.5 μm)	40			
Cadmium coating (6 μm)	14			
Zn–UNCD coating	24			
Zn–UNCD coating with chromate treatment	–	Beginning of corrosion on 1 sample	There is no corrosion on 5 samples	
Zn–UNCD coating with phosphate treatment	–	–	–	Beginning of corrosion on 3 samples

14.1.4 Tin Plating

Tin plating is widely used in the electronic, electrotechnical, and food processing industries. Existing tin coatings have low wear and corrosion resistance, and poor throwing power of the electrolyte. The addition of UNCD significantly improves the characteristics mentioned above:[6,9,10] the porosity of a coating decreases greatly, and consequently the corrosion resistance increases while the solder spreading coefficient and specific electrical resistance remain practically unchanged. The wear resistance of such coatings increases by three times.

14.1.5 Silvering

After testing various silver electrolytes, the cyanide–thiocyanate silvering electrolyte was chosen. Different concentrations of UNCD, Ag^+,

Table 14.4 Wear Resistance of Silver–Diamond Coatings

UNCD Additive Content (g/l)	Thickness of Coating (μm)	Wearing Time (h)	Coating Mass Losses (mass %)
0	5	20	33.3
0.2	1.7	20	6.7
0.5	1.3	20	5
1.0	1.3	40	2.5
2.0	1.5	25	*not found*

and additives were investigated where the optimum current density depends on the Ag^+ content of the electrolyte.[6,7,9,10,13,14]

The data obtained on the wear resistance of silver–diamond coatings are presented in Table 14.4. The results prove that as UNCD concentration increases, the wear resistance of the coating improves. Even a coating of 1.5–2 μm in thickness can provide a practically non-wearing silver film. This offers the possibility to decrease the thickness of silver coating and improve the quality of goods in many cases, and thus the service life of goods with a UNCD–silver coating can be significantly increased.

Testing electrical contacts plated with Ag–UNCD film at various production facilities (e.g., the "Elektroapparat" factory in St. Petersburg) in high-voltage switches of type VGB-220 (220 kV, 3200 A) for 6000 on/off operations confirmed the results of laboratory tests and suitability of the developed technology for electrical machines.

14.1.6 Gold Plating

The target of applications of UNCD in gold plating is to increase wear resistance and hardness while retaining high electrophysical characteristics. Cyanic acid (citrate), cyanic alkaline, and ferriferous cyanide electrolytes have been used for gold plating.[15] The addition of 0.5 to 10 g/l UNCD results in dense fine crystal and light semi-glittering coatings containing 0.01–0.6 mass % of diamonds. These coatings have led to a five–ten-fold increase in wear resistance at high electrophysical and technological properties compared to pure gold coatings.

14.1.7 Nickel Plating

Nickel plating is widely used in tools and machinery components. According to refs. [6,16] nickel–UNCD-coated parts have a service life 20 times longer than those coated with the usual nickel plating. Their microhardness reaches 580 kg/mm^2.

Dolmatov et al.[17] used a classical nickel-plating electrolyte with the following content (g/l): $NiSO_4$, 150–200; NaCl, 10–15; $MgSO_4$, 20–30; H_3BO_3, 25–30; and with a pH of 4.8–5.2, $t = 18–20\,°C$, and current density varying from 1 to 6 A/dm^2. The results of the wearing tests are presented in Table 14.5, where it follows that a concentration of 5 g/l UNCD in electrolyte results in a 4.5–8.5 times increase in wear resistance.

14.1.8 Anode Oxidation

It was found[6,9,10,18] that when UNCD was added to the electrolyte of acid oxidation the negatively charged diamonds were directed to the anode (aluminum and its alloys) under an electromotive force effect (emf effect) and penetrated the pores formed during surface oxidation. After discharging UNCD is kept in the pores by both mechanical forces and van der Waals forces and other physical–mechanical forces. The filling is so highly packed that the weight of the oxide film increases by 2–3.5 times.

Table 14.5 Results of Wearing Tests of Ni-UNCD Coating Samples (1 cm^2, Thickness ~2 μm) (the UNCD Content in Electrolyte Amounts to 5 g/l)

Current Density (A/dm^2)	1 (without UNCD)	1 (with UNCD)	1.5 (with UNCD)
Increase in weight of nickel coating after electrolysis (before wearing) (mg)	22.7	11.0	16.0
Weight loss (mg) in wearing series in:			
3 h	15.0	0.35	2.0
4 h	0.2	0.25	0.3
3 h	0.2	0.15	0.1
2 h	1.2	0.2	0.2
Total weight loss in 12 h	16.6	0.95	2.6
Weight loss (mass %)	73.1	8.6	16.3

The wear resistance of such a film increases by 10–13 times, and the corrosion resistance and electric insulation properties also improve significantly.

Thus the use of UNCD for the preparation of anode oxide films on aluminum and its alloys results in simultaneous filling of the films with insoluble nanodiamonds directly during electrolysis and in a significant improvement of the properties of the non-metallic non-organic CEC being formed. The optimum content of UNCD in oxidization electrolyte amounts to 2–15 g/l. The filling level of a film with UNCD can be very different as it depends on the concentration of diamonds in the electrolyte and also on the temperature of the electrolyte and current load.

The presence of UNCD does not influence the film growth rate but provides its filling during electrolysis. The set of properties of oxide–diamond coatings prepared by the technology mentioned above, and its simplicity, make this method quite competitive with any known production methods for the filled oxide films.

The polarization curves for all processes described above show that the presence of UNCD simplifies metal discharge on a cathode, i.e., the curves are shifted to positive potential values. In addition, UNCD does not change the kinetic process influencing mainly the absorption phenomena. Despite the fact that the polarization curves are shifted to positive potentials, the slope of the curves (i.e., the polarization ability) is increased. This bears witness to an improvement in the dispersing ability of electrolytes. UNCD strongly facilitates the process of hydrogen secretion.

14.1.9 The Deposition of Alloys along with UNCD

The co-deposition of UNCD has been investigated along with such widely utilized alloys as Sn–Pb[19], Sn–Sb, and Ag–Sb.

The use of UNCD in the deposition of Sn–Pb alloy is very effective. As the concentration of UNCD is increased in the electrolyte (correspondingly, in the coating) and some reduction of Sn concentration in the alloy takes place, and the porosity decreases by dozens of times, the resulting coating is found to be fine-grained and dense. So at a UNCD concentration in the electrolyte of 2 g/l and a coating thickness of 15 μm, a non-porous coating may be obtained. At a UNCD concentration in the electrolyte of 0.5–2.0 g/l, the throwing power of the electrolyte increases by two times and results in a coating more uniform in thickness. More-

over, the addition of UNCD to the electrolyte does not influence the electrical conductivity and soldering ability of the coating.

If the Sb salt is also added to a tinning pyrophosphate electrolyte, the microhardness and soldering ability of the Sn–Sb–UNCD coating remain at the same level as those of the Sn–UNCD coating. However, the cathode efficiency in the alloy increases, the porosity decreases by 5–8 times, and the wear resistance increases by 2–2.5 times.

On the addition of UNCD to the silvering cyanic electrolyte which contains the Sb salt, the Sb content in the silver coating reduces by 0.7–2.0 mass %, the microhardness decreases by 20–40 kg/mm^2, but the wear resistance of the Ag–Sb–UNCD coating increases by 1.5–1.7 times.

In summary, the distinctive characteristics of the UNCD-metal coatings are that the microhardness and wear resistance increase, the micro porosity decreases or disappears, and, as a result, the pitting corrosion, reducing the coefficient of friction.

The developed technologies of metal–diamond coatings result in a decrease in electric energy and metal consumption, and the cost price of the coating therefore decreases by 15–25%.

14.2 Polymer Compositions and Antifriction Coatings

The effectiveness of UNCD and diamond blend (DB) added to polymer compositions and films utilizing polyfluoro-elastomer, perfluorating hydrocarbons (fluoro-plastics), polysiloxanes, polyisoprenes, butadiene–styrene rubber, polyurethane, polyamide, etc., as a base has been described in numerous works.[9,20–27] On the whole, such a modification increases the elastic strength characteristics and secures unique tribological properties due to the formation of a space grid of the physical and chemical bonds on the boundary of the polymer matrix and to the nanoparticles having a chemically active outer shell and high adsorption properties.

When DB is added it produces a significant decrease in the fluoroelastomer film permeability. According to the row of optimization parameters, the *copolymer of vinylidenefluoride with perfluorinepropyle ether* (*CVPE*) with different filling levels of DB (from 2 to 50 mass %) was chosen as a suitable elastomer.[22–24]

A comparative analysis of mass thermograms of the initial elastomer and its nanocomposites showed an increase in the initial thermal destruction temperature, on average, of 40 °C. The data in Table 14.6 show that

Table 14.6 Physical and Mechanical Properties of the CVPE Films (a Protective Coating)

DB (mass %)	*M* (MPa)	*P* (MPa)	*L* (%)	*l* (%)
30*	8.5	15.7	280	108
2	92.0	173.0	480	81
5	2.4	28.7	400	228
7	10.0	21.9	480	80
10	10.5	15.7	230	83
20	9.9	16.1	270	112
30	10.1	18.4	235	100
40	9.6	18.2	260	180
50	9.1	17.3	280	126

M is the stress at 100% of elongation; *P* is the rupture strength; *L* is the elongation up to the moment of rupture; *l* is the residual elongation (after unloading).
* The technical carbon T-900 only was used.

the optimum quantity of DB added amounts to 2 mass % of polymer; the stress then increases about 10-fold at 100% of elongation and the tensile strength increases as well. DB is a more active filler than carbon and more frequently used in vulcanization networks.

The physical and mechanical indexes (e.g., of SKF-26, which is the analogue of VAITON-A, USA) of the nanocomposites on the basis of DB in the process of thermal aging at 250 °C are on a level with the vulcanizing properties of the standard formula (which had not been subjected to thermal aging) or even exceed them.

The DB coatings introduced into the fluoro-elastomers (up to 20 mass %) exceed in tribological properties such known materials as DuPont's perfluorine-containing polymers, namely, Tedlar (polyvinylfluoride), Teflon (tetrafluoroethylene), and Teflon FEP (hexafluoride-co-tetrafluoroethylene). Simultaneously they also provide a wider interval of working temperatures and mechanical loads.

When adding DB of 2 mass % to SKF-32 (Kel F-5500, USA) the sliding coefficient of friction on the boundary between the metal–rubber phases drops by up to 0.007.

The developed formulas of the rubber mixtures on the basis of the fluoro-elastomers modified with DB show that the resistance to abrasive

wear improves by 1.5–2.0 times (it tends to similar values for the rubber made from the polyisoprene rubbers).

Therefore, DB is the more active among the known fillers for fluoroelastomers, it frequently provides vulcanization networks, minimal thermal aging, low coefficient of friction of the film coatings, and it increases the service life of such coatings by 25–40% in the friction units.

14.2.1 The Polyisoprene and Butadiene–Styrene Copolymer

The investigation of the modifying action of DB was demonstrated by the example widely used in Russia of the standard filled compounds on a base of polyisoprene rubber SKI-3 (Russia) and butadiene–styrene rubber SKMS-30 APK (Russia) (data have not been published).

The results of optimization of the DB dose which is added to SKI-3 along with the technical carbon (the rubbers did not contain the oil) are presented in Table 14.7. As can be seen from the table, the rubbers with DB have the a higher degree of vulcanization – the stress at 300% of elongation is 12–35% as high, while the maximum swelling index of these rubbers in the toluene is 20–30% as low. The rubbers with DB have higher strength indexes (by 10–30% as against a control) at the normal test conditions and bigger fatigue strength. DB added to the given rubber compound does not have a considerable influence on the attrition resistance. By a summary influence on the physical and mechanical indexes of the rubbers the optimal DB doses are within the range of 2–4 mass % of the rubber.

The character of the change of elongation is not consistent with the current notion that elongation increases as M_{300} is increased (usually, the elongation decreases as M_{300} is increased). This inconsistency points to a change of the molecular structure mentioned above when adding the DB.

As the DB content is increased the rubber cohesion strength increases by 1.3–2.0 times depending on the elongation ratio (from 50 to 400%). The maximum cohesive strength is reached at 7.5 mass % of DB, and at the DB content of 0.5–2.0 mass % the cohesive strength is 1.2–1.3 times as high as that of the control.

The majority of rubbers on a base of general purpose rubbers (including SKI-3) contain oil (in Russia, PN-6 oil) as a plasticizer.

The cohesive strength of oil-filled rubber compounds depends to a significant degree depends on the method of addition of DB. If DB is

Table 14.7 Physical and Mechanical Properties of Standard Filler Rubber Compounds on the Base of SKI-3 with Different Content of DB (143 °C, 20 min)

Name of Indexes	Rubbers with DB in Quantity of Mass Parts								
	0	0.5	1.0	2.0	3.0	4.0	5.0	7.5	10
Test No.	1	2	3	4	5	6	7	8	9
Stress at 300% elongation (M_{300}, MPa)	7.7	8.5	8.7	10.0	8.5	10.8	10.7	12.3	9.4
Conditional strength at elongation (P, MPa)	20.5	28.2	22.2	25.9	27.3	25.8	26.3	24.7	25.0
Elongation at rupture (L %)	520	610	530	570	600	530	550	500	570
Rupture strength (kN/m)	139	139	131	148	126	126	125	136	143
Wearability (m^3/kW h)	120	123	137	123	115	116	124	133	120
Maximum swelling index in toluene	3.97	3.09	3.25	2.92	3.02	3.02	2.75	2.87	3.26

introduced as an oil composition the cohesive strength decreases by 1.1–1.3 times. If DB is introduced in parallel with technical carbon and then oil is added, on the contrary, the cohesive strength of the rubber increases by 1.2 times.

Oil-containing rubbers with DB have a higher degree of vulcanization than the controls (the higher the conditional stress at 300% elongation, the lower the elongation). The rupture strength of the experimental rubber with DB, which had been introduced in parallel with the technical carbon, surpasses that of all other experimental rubbers by 6–22%. This parameter of the rubbers containing DB as an oil composition exceeds that of the experimental rubbers by 25–35%. With any method of adding of DB to the rubber compounds the attrition resistance drops a little.

The modifying activity of DB depends on the presence of plasticizer (oil) in the rubber compound and on the method of adding DB to the compound. It is shown that DB activity decreases when it is preliminarily combined with oil of grade PN-6.

In order to determine the influence of the rubber matrix on the modifying activity of DB, DB was added in over-recipe quantities of 2, 3, and 4 mass % to the standard rubber compound on a base of butadiene–styrene copolymer with 30% of the styrene groups (the "Russian" resin, SKMS-30 ARK) (Table 14.8). The rubber compounds with 3 and 4 mass % of DB had a cohesive strength 1.5–2.0 times as high as the control. The vulcanizations with DB are characterized by a higher degree of vulcanization at the practically equal strength indexes with the control rubber and

Table 14.8 Physical and Mechanical Properties of Standard Filled Rubber Compounds on the Base of SKMS-30 with Different Content of DB

Name of Indexes	Rubbers in Quantity of Mass Parts			
Rubber Properties (153 °C, 20 min)	**0**	**2.0**	**3.0**	**4.0**
Stress at 300% elongation (M_{300}, MPa)	7.9	8.8	7.9	11.4
Conditional strength at elongation (P, MPa)	21.0	20.3	19.5	21.5
Elongation at rupture (L %)	518	480	480	485
Rupture strength (kN/m)	71	133	135	133

their rupture strength exceeds the control rubbers by two times (Table 14.8).

Consequently, it was found that in the different rubber matrixes the modifying activity of DB develops to a different degree.

14.2.2 The Polysiloxane Polyblock Cyclolinear Copolymer

The combination of the applicability of polysiloxane polymers in wide-temperature range with high adhesive and dielectric properties allows them to be used as the basis for the creation of film-forming materials with a wide spectrum of potential applications – from protective coatings to selective permeable membranes. The disadvantage of the films is unsatisfactory mechanical properties. The solution to this problem is a controlled increase in the elastic properties at small deformations by transition to the filled compositions.

The polyblock copolymer of double-chain phenylsilsesquioxane and polydimethylsiloxane (PhSO–PDMS) was used as a polymer matrix:

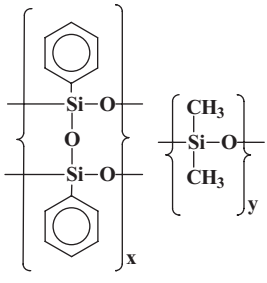

Both are produced by the Research Institute of Synthetic Rubber in St. Petersburg on an experimental and industrial scale:[25] In this work, the high dispersion silicon oxide (A-300), DB, and UNCD (from the "Diamond Centre", St. Petersburg) and glass spheres (GSph) were used. For surface modification of the preliminary annealed particles of powders, the sililization reaction was used with an equimolar sililizing mixture of Me_3SiCl:$(Me_3Si)_2NH$, where Me = —CH_3.

The use of the modified fillers in the individual states results in the growth of film strength parameters by 20–30% in the practically important deformation area (up to 100%) for conservation of the elastic

Table 14.9 The Influence of Composite Modifiers on Strength Parameters of PhSO–PDMS (T = 20 °C)

No.	Film Composition	M_{100} (MPa)	M_{300} (MPa)	P (MPa)	L (%)
1	Initial (without modifiers)	2.6	4.4	6.0	500
2	1% A-300* + 4% GSph*	3.4	5.2	5.9	400
3	2.5% GSph* + 2.5% DB	4.3	6.4	7.0	300
4	4% GSph* + 1% UNCD*	3.2	5.2	5.8	350

* Modified fillers.

properties. The obtained effect is reached at a filling level of no more than 5% by weight.

In order to obtain the maximum physical and mechanical parameters of polymers a series of films were prepared with the composite fillers. The parameters obtained for the optimized films are shown in Table 14.9.

The use of the composite fillers results in an increase of the strength parameters in the deformation interval of interest on the level of the modified homofillers, with the exception of film 3 (with DB), which is characterized by a higher increase (≈1.7 times) of the strength parameters.

14.2.3 Polyurethane Foam

The filling of polyurethane foam (PUF) with different materials is realized to improve the physical and mechanical characteristics, to decrease the cost have been used: of products, etc. The following fillers have been: DB which may be considered as modified UNCD; modified UNCD with grafted vinyl or amine surface groups; as well as the composition of DB and glass spheres (GSph).[26]

Adding a small quantity of DB (0.3% by weight, i.e., 0.12 wt.% in terms of UNCD) results in a large increase (1.5 times) of compression resistance and the PUF properties of starting and gel formation time increase. Adding UNCD modified by vinyl groups on the surface (UNCD-V) having a poor affinity for the PUF results in some decrease in the strength properties (by 10–30%). On the contrary, adding UNCD modified by amine groups on the surface (UNCD-A) having PUF affinity gives rise to an increase in all the technological and strength factors. Moreover, UNCD modified by amine groups (according to data in the dynamic diffusion method) results in more than 90% of all aggregates having sizes

from 5 to 30 nm, i.e., the modification does not remove UNCD from the nanodispersed size range.

Taking into account the previous investigations, the addition of composite fillers (DB and GSph) to PUF is quite reasonable. It was shown that the addition of about 0.1 wt.% of each active filler may be compared to 0.3 mass % of DB added. It is necessary to point out that in the case of PUF, a positive effect is observed even at smaller concentrations of an active component than in the PhSO–PDMS case.

14.2.4 Frost-Resistant Butadiene–Nitrile Rubber

Sokolova and co-qorkers[27,28] have investigated the influence of DB on rubber properties based on butadiene–nitrile rubber SKN-18, which is the most widely used material for the manufacture of frost-resistant sealing rubbers.

Adding DB to the rubber V-14 (on a base of the rubber SKN-18) was carried out by adding DB powder on surfaces of a raw rubber sheet compressed between two rolling cylinders. The DB content was up to 1 mass %. The authors have obtained a homogeneous, good quality mix, but the increase in DB content above 1 wt.% affected the agglomeration of filler particles and the separation of the mix. It was shown that adding DB does not result in a sharp change of rheological behavior of the rubber V-14 mix. As the DB content in the mix is increased up to 1 mass % the vulcanization rate increases insignificantly.

The most important properties determining the efficiency of sealing rubbers operating in cold regions are high elasticity, frost resistance, corrosion resistance and tribological characteristics. Research has shown that the addition of DB significantly increases the elongation at rupture up to 70% in comparison with the initial rubber. The values of the rupture strength are decreased by 10% over the whole DB content range. The modified rubber has a lower hardness. However, it is reasonable to note that the decrease in strength and hardness is not beyond the standard values for the initial rubber V-14. The modified rubber has a wear resistance 13% as high. DB strongly influences the decrease in the coefficient of friction (by 45–50% as compared to an unfilled rubber).[27]

In order to estimate the frost resistance of elastomers the frost-resistance coefficient after compression K_β was determined. Investigations showed that down to temperatures of −35 °C the frost-resistance coefficients of elastomers are practically equal, and the difference in the values of K_β becomes perceptible at a temperature of −40 °C.[27] This is very

important for the rubbers used in cold regions because even an insignificant increase in the frost resistance at critical temperatures (near the glass transition temperature, T_{gt}) increases the range of use of articles made from such materials. At a temperature of –50 °C the increase in the frost resistance reaches 50%.

Tests of the modified rubbers on their resistance to attack by corrosive media, where the movable elastomer sealants (oils, petroleum, and benzene) are more widely used, showed that the addition of DB (up to 1 mass %) does not change the modified rubbers' behavior compared to the base rubber. Some improvement in the resistance to carbon media, especially the benzene medium (the swelling index decreases by 20%), has been noted.[28]

It has been established that the addition of DB to rubber V-14 influences the morphology of the matrix. As a results, the layer structures formed by ultradispersed particles of DB appear there. The layers are situated between other ingredients of the rubber mix. The increase in DB content from 0.1 to 1% results in the rise of a portion of such structures. A comparison of this and the physical–mechanical tests explains the increase in elasticity of the rubber modified by DB: during deformation the macromolecules are oriented along the line of deformation, and in this case DB promotes slightly more slipping of the macromolecules relative to each other that simplifies the orientation of macromolecules along the line of loading.

So adding DB in a quantity of 0.1–0.5% leads to an improvement in the important performance characteristics: that is, a decrease in the coefficient of friction and an increase in wear resistance, elasticity, and frost resistance. Further, the investigated rubbers have low hysteresis losses during the dynamic loading regime, which means a longer service life for parts made of these rubbers. The improvement of the properties pointed out above is stipulated by the unique properties of DB, namely its higher structural activity which is realized even at a small filling level. Thus, the modification of butadiene–nitrile rubber by DB allows the creation of sealing frost-resistance rubbers with high-performance properties.

14.2.5 Rubbers Stable to Explosive Decompression

One difficult but very real problem is to develop rubbers and resin–technical articles which are stable to explosive decompression (ED) in equipment for the oil and gas industries. The mechanical behavior of

rubbers under different operational conditions including the ED effect is determined by the relaxation properties of the rubbers and also by their influence on fillers of different nature and their dispersivity on slow physical λ-processes of the relaxation resulting from the mobility of different types of physical units.

The addition of DB to the different rubbers has a considerable influence on the stability to ED.[29] This stability to ED was estimated by the appearance, by the change in mass Δm in volume ΔV of the sample, and by $\Delta m/\Delta V$ after the ED effect.

The addition of a small quantity of DB (from 0.14 to 1.67 mass %) to a series of rubbers on the base of different polymers with elastic modulus E in the range of 2.5–8.0 MPa significantly increases the rupture strength (by 20–60%) and attrition resistance (by 10–40%) of most of the rubbers tested. This is bound up with the acceleration of the slow physical λ-processes of relaxation.[26] In high-modulus rubbers ($E \geq 13$ MPa) on a "Terban" base, as DB content is increased from 0.26 to 27.1 mass %, the rupture strength also increases and, correspondingly, the λ-processes of relaxation accelerate, decreasing the time to reach the relation value of $\sigma/\sigma_0 = 0.85$ (σ/σ_0 is the relaxation of the stress at uniaxial compression, where σ_0 and σ are the initial (in 5 minutes) and current stresses at a temperature of 23 ± 3 °C, respectively).

At a DB content of 27.1 mass % the specific failure energy A_f increase sharply. It moves over the developed surface of DB and is explained by the net formation of physical and chemical bonds due to the adsorption and chemical interaction of a polymer with the functional groups on the DB surface.

The rubbers stable to ED must comply with complex conflicting requirements and be characterized by low sorption ability, sufficiently high values of elasticity, strength, and resistance to attack by media accompanying petroleum production. The base for the development of such rubbers in Russia is the hydrogenated butadiene–nitrile rubber "Terban" using the combination of DB and fillers of different nature, dispersion, and anisotropy. As a result, Sirotinkin et al.[26] have developed high-elastic materials stable to ED which contain DB in combination with other fillers.

14.2.6 Gas-flame Deposition of Polymer Coatings

The flame deposition technology of single- and multilayer polymer coatings in which UNCD is dispersed has been developed.[27]

In single-layer deposition the material for application of a coating is a mechanical mixture of polyamide powder and UNCD as well as additives of the metallic and ceramic components. The technology developed allows coatings of different thickness to be applied to friction units having different shapes and dimensions.

Double-layer metallic polymer coatings of 0.5 mass % of UNCD obtained by means of flame deposition reliably protect the bearings and rotors of submersible pumps and other components from the joint action of corrosion and wear, which enables high operating characteristics for a long time.

The use of UNCD results in an increase in density and adhesion strength of a coating with a base as well as in high adhesion of a lubricant to the frictional surface; as a result, the service life of the components increases by 1.5–2.0 times. Polymer coatings modified with UNCD are typically characterized by high antifriction properties, mechanical strength, absence of toxicity, silent operation, good machinability by cutting tools, and high resistance to attack by liquid fuel, mineral oils and grease, organic solvents, acids, and alkalis.

14.3 Polishing

UNCD is a new kind of abrasive material which is very useful for electronic microelectronics.

The state of machined surface depends on the depth of a damaged layer, roughness, optical purity, absence of defects, and integrity of the structure during finish and superfinish treatments.

High–quality smooth surfaces of optical and semiconductor materials are made using the chemical–mechanical polishing (CMP) method. The base of the CMP technology is the polishing compositions containing non-abrasive colloidal particles of the solid phase. These are the carriers of some functional groups that chemically interact with the surface under treatment.

Compared to aerosiles (colloid systems on a base of ultradispersed amorphous, spherical, modified SiO_2 particles with a size from 1 to 50 nm) as the base of the well-proved compositions for CMP, UNCD is resistant to attack by acids, alkalis, and others liquid-phase oxidants at temperatures from room temperature up to 150–200 °C.[31,32] Thus, UNCD is very compatible with active components at high temperatures for a long time. This fact revealed the possibility of creating highly productive polishing compositions. The chemical stability of UNCD also allows us to examine the possibility of regenerating nanodiamonds from the waste pol-

ishing systems that significantly improve the economic characteristics of CMP technology using UNCD.

The structural non-uniformity of near-surface carbon layers of UNCD due to denotation synthesis peculiarities forms the whole set of non-standard surface states which are active in CMP. On the surface of high–pure UNCD (e.g. UDD-TAN, "Diamond Centre", St. Petersburg) in use in CMP, there is a line of oxygen-containing functional groups with well-marked acid properties. The adsorption and ion exchange activities of UNCD may change over a wide range depending on the treatment conditions:

- the adsorption of potential determinant ions, 0.3–3.0 μ-equiv/g;
- the static exchange capacity, 0.1–3.0 μ-equiv/g;
- the density of the protonogene groups, 1–10 μg-equiv/m^2.

The addition of UNCD to the polishing compositions improves the chemical and physical–chemical aspects of the CMP process and increases the treatment effectiveness as a whole.

The cluster particles of UNCD are aggregated into complex fractional structures the sizes of which, as well as their colloid, sedimentation, and structural–mechanical properties, mainly depend upon the production method and the composition of a liquid dispersion medium. UNCD has a strong structuring influence on the liquid. For UNCD such an influence is determined at the mass portion of 0.1–0.3% being based on a change in the kinetics of ionic exchange reactions in electrolyte solutions. If UNCD is graded carefully by particle size (0.02–0.04 μm) the use of low-filled aqueous, organic, and aqueous–organic dispersions of such UNCD can result in ideal parameters for the material surfaces under treatment – surface microasperity is at the interatomic distance level.

The fractural structure of UNCD peculiar to the fractal distribution of properties in the polishing layer volume contributes to the effective distribution of local loads which occur when approaching working surfaces, e.g., a polishing tool and the material under treatment. Coarse, friable UNCD aggregates are easily disaggregated under minimum action on the suspension but they are also easily re-formed being at a quiescent state. In order to disaggregate a part of UNCD to 1.0–0.1 μm in size it is necessary to apply more energy using special dispersing and disintegrating devices. The middle-diameter aggregates (hundredths of a micron) have the mechanical properties of a solid material but their hardness and strength, and therefore abrasive quality, are lower than that of bulk

diamond. The primary UNCD particles (~10^{-3} μm) are the carriers of the major diamond properties of this material.

So, by tracing the levels of UNCD aggregation the multistep mechanism of dissipation of energy load in the polishing process can therefore be imagined: fractal structures of UNCD play the part of a peculiar damper decreasing the probability of hard, pointwise interactions between working surfaces. That protects the material under treatment from deformation and stresses in the near-surface layer.

Nevertheless, the first attempts in the 1990s to use UNCD in polishing processes did not result in its commercial use.[31–33] Plausible reason are (1) insufficient suitability of the polishing techniques for a new nanoproduct; (2) the absence of uniform quality UNCD from different producers; (3) the impossibility of using UNCD in its usual polishing form – as a dry powder.

The production technology for polycrystal micropowders is very promising for the polishing process.[34,35] Their porous particles differ in the nanostructure. Such powders are prepared by fragmenting sintered UNCD nanopowders.

In such work[36] UNCD from three main producers of the CIS were useful: JSC Diamond Centre (St. Petersburg, Russia), "ALIT Ltd" (Zhitomir, Ukraine), and (3) JSC "Sinta" (Minsk, Belarus) for powders, suspensions, and pastes.

The materials currently being exposed to polishing are presented in Table 14.10. There are two types of polishing members used: the woven one, on a base of polyester (PE), polypropylene (PP), polyamide (PA), and mixed (PE + PA); and the non-woven one, like politex, polivel, and artificial leather. The quality criterion of surface treatment was the y_{av} value being a mean square deviation of asperity heights at a definite length of the profilograph section.

It has been found that[36] when optimizing the treatment conditions and polishing tools the relief smoothing was observed to form a mirror-finish surface without macrodefects (scores and cracks) on the majority of machine tools and all materials. The polishing process is realized simultaneously with the material removal process. The removal rate depends upon the type of a machine tool and the polishing member, conditions, pretreatment, and material hardness. The removal rate changes between wide limits.

As for comparative polishing by static synthesis diamonds (monocrystals; ASM 1/0, a particle diameter of 0–1 μm in Russia), continuous rectilinear scratches are formed on the material surface and occupy the whole area of the sample and cross it in all directions.

Table 14.10 Materials for Polishing by UNCD According to the Criteria and Fields of Application

Chemical composition	Elementary: Si, Ge, W, Mo, Nb, Cu Oxides: α-Al_2O_3, SiO_2, ZrO_2 : Y_2O_3 (ZOY) Oxygen-containing: $Gd_3Ga_5O_{12}$ (GGG), $Y_3Al_5O_{12}$ (YAG), $LiNbO_3$ (LNO), MgO : Al_2O_3 ($MgAl_2O_4$), $SrTiO_3$ Fluorides: CaF_2 Carbides: SiC Nitrides: AlN, Si_3N_4 Hard solutions: groups A^2B^6, A^3B^5
Production method	Czochralski's method: Si, Ge, Nb, $LiNbO_3$, GGG, A^3B^5 Vernail's method: $MgAl_2O_4$ Kiropolus's modified method: α-Al_2O_3 Directional crystallization: YAG, CaF_2 Smelting in the cold container: ZOY Electron ray without melting pot band smelting: W, Mo Sublimation from gas phase: CdS, ZnSe CVD: ZnSe (polycrystalline) Semi-dry pressing with following caking: AlN
Structure	Crystals of cubic, hexagonal, trigonal synergies: W (100) (111), Mo (100), (101), Nb (100)g, Si (100), Ge (111); CdS (0001), ZnSe (100), GaAs (100), GaSb (100), GGG (111), YAG (111), LNO_y + 127°, $SrTiO_3$ (100) and bi-crystals, α-Al_2O_3 (0001), ZOY (100), SiC : 6H, CaF_2 (111) Polycrystals: Si, Cu, ZnSe CVD Amorphous: SiO_2 (KY-1), glass K-8 Composites: ceramics AlN
Electrical properties	Conductors: W, Mo, Nb, Cu Semiconductors: Si, Ge, type A^2B^6, A^3B^5, SiC Dielectrics: SiO_2, Si_3N_4, CaF_2, α-Al_2O_3, etc.
Application	Microelectronics Optoelectronics Acoustoelectronics Optics

The peculiarity of polishing by UNCD suspensions is that the character of scratches changes greatly (e.g., for W, Ge, α-Al_2O_3, ZOY, etc.) and scratches of different types can be observed: namely, equal in width, widening in the middle or narrowing at one of the ends, dashed- or point-viewed ones, short (many times smaller than the sample diameter), and

long (rectilineal and bow shaped). The scratches usually do not occupy all the area and there are extensive regions of small scratches without optical resolution.

There are deep scratches all along the surfaces: Ge, 0.7 nm (UNCD suspensions, "Sinta Ltd", Byelorussia); GGG, up to 6.0 nm (suspension of UNCD polycrystals (pdd) "Alit Ltd", Ukraine); AIN, 0.8 nm (UNCD suspension, sort UDD-STW, "Diamond Centre", Russia); and the large protuberance–cavity overfall (h_{max}): Ge, 19.8 nm (diamond monocrystals 0.1/0, "SAKID Ltd", St. Petersburg, Russia); W, 66 nm (diamond monocrystals 1/0); CdS, 0.9 nm (diamond monocrystals 0.25/0, "SAKID Ltd"). However, in all cases y_{av} clearly decreases sometimes as the diamond particles size is decreased from micro- to nano-sized values for Si, 10–18 nm (pdd); Ge, starting with 0.7 nm ("Sinta Ltd"); W, 0.5 nm ("Sinta Ltd"); YAG, ZOY, LNO, up to 0.7–0.8 nm (pdd). There are sections of such parts which have tenths of the y_{av} value (0.3–0.2 nm) and sometimes hundredths of a nanometer. As y_{av} does not represent the real state of the relief and the peculiarities of formation of its roughness, it is necessary to take into account the width (l) of large and small scratches and the roughness of their walls.

The polishing by UNCD of all materials whatever their hardness and other properties proceeds to form nanoscratches, the width of which, together with y_{av}, also decrease as the size of the diamond particles is decreased:

for W using
- ASM 1/0 $l = 1.7–3\,\mu m$
- UNCD, sort UDD-STW $l = 2.2\,\mu m$
- UNCD, "Sinta Ltd" $l = 0.15\,\mu m$

for CaF_2 using
- ASM 1/0 $l = 1.8\,\mu m$
- ASM 0,25/0 $l = 0.5\,\mu m$
- UNCD, "Sinta Ltd" $l = 0.1\,\mu m$.

When UNCD is useful the formation of scratches mainly takes place when pressing back the material along the surface (tangentially). The fact that l is many times as large as the particle size when polishing by UNCD suspensions ("Sinta Ltd") and UDD-STW sort ("Diamond Centre") testifies that the relief is formed under the action of both primary particles (y_{av}, h_{max}) and their aggregates.

With microabrasive polishing the dislocations are formed with the advent of local temperatures equal to the temperature of the critical plasticity: about 500 °C for Ge and 700 °C for Si. According to the data,[37,38] the polishing process of Si by abrasive particles of 0.25–0.8 μm size and smaller, taking into account the destruction anisotropy, is not accompanied by friable destruction.

Two new methods of polishing the silicon boards by UNCD are presented in ref. [39]. The first method of polishing uses the polishing tool with ultrasmall abrasive material produced by electrophoretic precipitation of UNCD on a brass rod. The dry polishing tests showed that the surface roughness of a silicon board decreases from R_a = 107 up to 4 nm after polishing for 30 minutes. The second method uses a new polishing support with self-generated porosity. When polishing with the new support using polycrystalline UNCD in an aqueous suspension it is possible to reach the desired roughness of the silicon board surface sooner than when using a PUF support. The tests showed that in the given case the roughness of the silicon board decreases from R_a = 107 up to 2 nm after polishing for 90 minutes.

For epitaxial, vapor, and lithographic processes the preparation of atomic–molecular smooth pure surfaces is possible only if nanometer-sized hard particles are used. Therefore, UNCD with a particle size of less than 1 μm fills in the niche which is not occupied by the static synthesis diamonds (namely, as the minimum, micropowders ASM 1/0). The real possibility to fractionate UNCD in a narrow enough range in production quantities (e.g., up to aggregates of 130–100 nm, 60–50 nm, and 30–20 nm in size consisting of primary particles of 3–5 nm) allows use of them purposefully in electronic and optical technologies where the lowest roughness and highest geometrical properties are needed for special articles constrcuted of expensive materials.

UNCD compositions have now been shown to result in high planarity (up to 1 μm) and to reductively form nanometric roughness from parts to units of nanometers of more than 30 crystals (semiconductors (elementary and complex), dielectrics (Si_3N_4), oxides (α-Al_2O_3, ZrO_2:Y α-SiO_2), garnets (GGG, YAG), glasses, etc.) being included in six syngonies as well as the ceramics AlN and alloys CuW, VT6, etc. In addition, the nomenclature of materials and quality of the treatment are constantly improved in reference to the universal character of the technology. It is important that UNCD compositions can be stabilized, significantly increasing useful life, and also chemically modified to impart the chemical–mechanical character to the polishing process which increases the articles' quality still further.

In order to promote UNCD distribution in electronics it is necessary to point out some urgent problems:

(1) The UNCD quality and properties depend mainly on chemical purification methods which differ significantly at different producers. Therefore, it is necessary to draw up technical documents (specifications) for UNCD coordinated between producers and consumers and recommending and regulating the fields of application depending on the properties. The unification and standardization of UNCD products according to basic consumers' characteristics are very important for the electronic techniques. Now, in the absence of that, a strong binding of a concrete consumer of UNCD to its producer should be recommended.
(2) Decrease of the cost of UNCD-containing polishing product due to decrease in the production cost of UNCD will be beneficial for their applications in electronics.
(3) The use of UNCD in electronic materials treatment (EMT) requires new (or special) equipment or, as a last resort, the modification of current polishing benches. It is necessary to develop and create special purpose tools and rigging to use UNCD.

In fact, the polishing technology of solid-state materials (not just EMT) using detonation synthesis diamonds is just starting, as it once was with static synthesis micropowders and pastes. It is at the necessary stage of creation of the industry, equipment and technology, and training of specialists of a required profile. Now it is very difficult to foresee all aspects of the further development of the direction of this scientific technology. Without doubt, one thing is that the vector of development and perfection of this direction has a positive impulse, and is directed to high technologies, as such claiming serious attention and immediate support.

Some polished compositions based on UNCD are given in a brief review[40] (see Table 14.11).

The results of polishing the materials with different hardness and plasticity are presented in Table 14.12. The data presented for the roughness values reached do not represent the possible limit. So, when polishing a melt silicon oxide by a UNCD suspension (4.5 mass %) in ethylene glycol at a tool rotating speed of 76 rpm, a load of $P = 1\,\mathrm{N/cm^2}$, and a material removal rate of 809 nm/min, the roughness level $R_{max} = 1$ nm was reached

Table 14.11 Polishing Compositions Based on UNCD

Consistency	Carrier	UNCD Content (mass %)
Suspension	Water, ethylene glycol, water solution KOH and $FeSO_4$, oil	3–5
Paste	Tallows, polymer	3–5
Solid body of given shape	Hardened rubbers (silicon, nitrile, etc.)	2–3
	Hardened resins (formaldehyde, epoxide)	2–5
	Metal (aluminum, nickel)	up to 50

Table 14.12 The Results of Polishing Different Materials by UNCD

Material	Roughness Level, R_{max} (nm)
Hard alloy	1–5
Steel	5–6
Sapphire	5–6
Quartz	0.5–1.5
Melt silicon oxide	0.5–1.0
Silicon	0.5–1.5
Sodium chloride crystal	2–3
Potassium bromide crystal	2–3

in 10 min and $R_{max} = 0.5$ nm in 15 min. When polishing the hard alloy by means of the tool made of hardened resin with UNCD of 2 mass % content at a rotating speed of 70 rpm, a load $P = 3.58$ N/cm^2 and $R_{max} \sim 4$ nm were reached in 30 min.

A separate problem is the polishing process using DB, not UNCD. In ref. [41] DB with an average statistical grain size of 30 nm was tested as a polishing material. Suspensions based on DB in organic liquids were prepared, the anticoagulant properties of which were formed by adding surface-active substances (SAS) and special stabilization methods.

The investigations of two different suspension compositions, "Sufipol-1" and "Sufipol–2" (Russia), when polishing the quartz samples with the chamois polishing tool, 200–250 mm in diameter, at a speed in the working zone of 140–180 rpm, showed the complete absence of the sctratches. The removal rate averaged 0.1–0.2 μm/h. The viscosity and density of the suspensions do not influence the quality of the surface being treated.

The quartz removal rate when using "rigid" polishing members increased by an order of magnitude.

The quality characteristics for the polished surfaces of quartz articles for the "soft" polishing members had the following values:

- surface finish, not less than 0–10 Å;[42]
- height of the surface imperfections, 3–10 Å.

For hard polishing bases the same values have been achieved by using a resin polishing member of lower hardness.

Thus, the use of DB for the preparation of suspensions for deep finish polishing is found to be perspective. In the author's view, as is DB from any producer for polishing suspension may not be suitable. The presence and quantity of incombustible impurities, UNCD content in DB, different methods of pretreatment of DB and its modification, are of great importance. Nevertheless, as DB is many times cheaper than purified UNCD, this direction seems to be very promising.

14.4 Oils and Lubricants

There are widely known lubricant compositions in which hard materials are used as antifriction additives, in particular: metal powders, graphite, molybdenum compounds, classic diamonds.[43,44] The powders of copper, silver, and molybdenum disulphide have the best antifriction properties, the maximum concentration of the powders in the oil being not more than 5 mass % and the optimal powder sizes not less than 1 μm. The use of these additives results in a decrease in the coefficient of friction and wear; and increases ultimate loads in the friction units. However, the use of the widely known compositions is limited due to the low rheological and corrosion-resistant properties as well as sedimentation stability.

The advantages of UNCD as a friction modifier are the following in comparison to other similar kinds of substances:

- the effectiveness at very low concentration in the base oil;
- the compatibility with different kinds of synthetic and mineral oils;
- the ecological safety of a carbon additive to oils compared to metallic or fluorine–carbon particles and substances.

The presence of a large quantity of superfine graphite particles and nanodiamonds in DB changes the properties of a lubricating film and the interaction character of friction surfaces. The concentration of the particles in liquid may reach 10^{14} in 1 cm^3 and 10^8–10^9 in 1 cm^2 of monolayer; the distance between separate fractal aggregates amounts to 0.1–0.5 μm.[45] The fluid viscosity, the lubricant film strength, and, as a consequence, the loading capacity of the lubricated surface increase.

UNCD, being ~50% of DB mass and having a certain cutting ability when submicrocutting, plays a very active role in running in and "healing" microdefects in mating surfaces (including newly formed ones). This process is practically stopped on reaching the actual contact area when semi-fluid or fluid lubricating regimes are realized.

The pioneering work in this field is due to a research group of the "Altai" research and production plant (Biisk, Russia) that has developed the pilot preparation technology for the additive and widely investigated and tested the new preparation under different frictional conditions.[46]

These authors proposed a lubricant composition consisting of an oil base and DB. The composition of the latter was 2.0–99.0 mass % of nonabrasive diamond and 1.0–98.0 mass % of graphite. The components relation is DB, 0.01–1.0 mass %, and the oil base – everything else.

As a base for the lubricant composition, mineral or synthetic lubricant oils and lubricant–cooling liquids may be used with DB.

The coagulation stability of DB in the oil base is provided by the fact that the size of the energy-equilibrium fractural carbon clusters does not exceed 30–60 nm. It excludes the separation of lubricating compositions for a long time (more than 6 months).

The presence of DB in the lubricating compositions results in the following:

- Small-sized carbon clusters saturate the friction surfaces filling up their imperfections and creating new (juvenile) friction surfaces. In addition, boundary friction and wear are decreased, and the formation of grips on the friction surface are excluded.

- Carbon clusters cause an increase in the lubricating composition viscosity in thin films due to the dispersion structuring, except for the "brittle" fissuring of a film at high strain rates due to stoppage fissure formation on the clusters; the leakage oil is lost through the gaps and seals are decreased.
- Carbon clusters result in a decrease in lubricating composition viscosity at low temperatures due to the lowering of the vitrification threshold of the dispersion-filled medium. As a result, the operating temperature range expands by 5–10 °C (by its inferior limit) as observed for lubricating compositions.
- Carbon clusters cause an after-effect (more than 60 hours) after the substitution of a lubricating composition by an oil base. This effect concerns the mechanically strong absorption and diffuser attachment of the carbon clusters on the friction surface.
- At high loads and maximum fluid displacement between the friction surfaces the cluster diamonds work as frictionless microbearings that increase the growth of ultimate loads which the friction couple can take without dripping. So, for steel–bronze the load is found to increase from 160 to 720 kg/cm^2 (from 16 to 72 MPa).

The DB content in the lubricating composition with a solid friction modifier depends on the character and operational duty of the device (machines, mechanisms, units) where this lubricating composition is used. So, for lubricating heavily loaded units with large sliding surfaces the DB content amounts to 0.3–1.0 mass %.

For middle-loaded mechanisms, for example, internal combustion engines (diesel and carburetor ones), the DB content in the oil composition varies from 0.01 to 0.3 mass %. Such content results in an optimal effect decreasing the friction and fuel consumption and increasing the compression and dynamic characteristics.

For low-loaded mechanisms, for example, mechanical equipment with circulation lubrication systems, the DB content in the lubricating composition amounts to 0.01–0.15 mass %.

The method of preparation for the lubricating composition with DB is technologically simple and is realized in the following way. DB produced by denotation synthesis is dewatered by vacuum drying and loaded in the preliminary mixing vessel in the required quantities to which the oil base, for example, the mineral oil, is added. After intimate mixing the mixture is forced through screen filters and magnetic separators with the help of

pumps and then through the final dispersion devices, for example, disintegrators, acoustic (supersonic) mixers, or mills, with after-filtering through fine filters to remove the large inclusions and impurities.

The running-in time for the internal combustion engine with a lubricating composition on a DB basis can be decreased from 60 to 5.5 hours; the wear of cylinder–piston parts is decreased by 1.5–2.5 times along with a decrease in the internal friction of the motor by 25–30%. Compression in the cylinders is increased by 10–17%. The optimal content of DB in the lubricating composition is 0.02–0.04 mass %.

It has been established that there is no negative influence of DB additives on the performance attributes of motor oils, the thermal–oxidative stability is not decreased, the corrosion resistance relative to non-ferrous metals and alloys is not increased, and the antifriction and wear resistance of oil characteristics are better.[33,47,48]

It has also been noted that when using DB the engine's power is increased by 4–8%, the specific fuel consumption is decreased by 3–6%, and the exhaust temperature is decreased by 2–9%.

The use of DB for modifying industrial and transmission oils decreases the coefficient of friction in transmissions and mechanisms by 20–30%, wear of friction surfaces is also decreased by 2–2.5 times, the evenness of the units' motion is improved, and the noise level of the transmission is decreased.

For use in viscous lubricants DB or UNCD is added to the base oil directly or through an intervening medium and can take part in the formation of a structural frame depending on the technique in operation. In such lubricants the presence of DB decreases the coefficient of friction by 20–30%, decreases the wear of friction couples by 1.3–3.0 times, and increases the loading capacity of joints.

DB essentially influences the majority of structural–mechanical and performance characteristics of all types of oils. In preservative oil the chemical and electrochemical corrosion of metal is reduced due to the decrease or giving up of many additives which are, as a rule, corrosion-active substances. With DB in leads and thread lubricants, the leak-proofness of joints is improved, corrosion of contact surfaces is decreased, and the shearing force and torque strength value are decreased or stabilized.

For machining operations, lubricant–cooling liquids (LCLs) on a base of mineral oils were developed. They contain DB, chlorosulphided grease, and sulphur-containing polyisobutylene.[49–51] These LCLs are shown to be effective at manual and machinery thread-cutting, drilling of holes, polishing of ferrites, etc. The use of LCLs and DB increases the service life of tools by 1.5–4.0 times, improves the cutting process due to the decrease of

cutting forces, and allows some LCLs to be given up (e.g., sulphonicfresol and oleic acid) which pollute the environment and are harmful to health.

The right choice of component content of LCL and DB allows an eight-fold increase in the run-in index of friction surfaces (in comparison to the run-in index in the pure oil).[9,49] Redkin and co-workers[50,51] have concluded the following:

(1) The addition of DB to LCLs promotes the stabilization of the cutting process and decreases the cutting moment by 20–30%.
(2) The developed LCLs are more effective for thread-cutting and drilling holes in hard-to-machine materials.
(3) The small sizes of DB particles allow the use of the developed compositions in the power LSL feed.

As shown in ref. [52] the addition of DB (1–5 mass %) in the lubricant used for machining under pressure allows a significant decrease in the coefficient of friction and an increase in the surface quality of the finished article. In addition, a significant effect may be obtained in processes of wire-drawing, calibrating, and deep drawing.

As mentioned in ref. [53] the use of DB in viscous lubricants as compared to base lubricants such as cup grease, cyatim, lithol (Russia), etc., results in an increase in the wear resistance of friction units by 1.2–3.0 times, a decrease in antifriction by 6–20%, a decrease in the level of damage by 1.2–3.0 times, and a decrease in temperature in the contact zone by 16–19%.

A significant effect is achieved when UNCD and DB are used in solid lubricants based on hydrocarbons applied to abrasive wheels when dry polishing. The developed composition as compared to a base one allows an increase in burn-resistance and a decreased roughness of work surfaces by 1–2 grades.

Commercial tests have further shown that the productivity of polishing operations is increased by 20–30%, "loading" of the abrasive surface is decreased, and the temperature of the abrasive grits and the surfaces of work parts are decreased.

14.5 Diamond Sinters and Compacts

The experience of sintering of diamond micropowders showed that the physical and mechanical properties of the sintered polycrystals become

worse as their grain is decreased. The most likely cause is the interaction of sintered diamond particles with gases in the vapor and desorbed from the particle surfaces during sintering.[54,55] It has been shown that the counterpressure value of the desorbed gases at a sintering temperature of 1600 °C and external pressure of 8 GPa becomes significant (>0.5 GPa) when sintering static synthesis diamond powder ASM 10/7 (the particle size is 7–10 μm). When sintering diamond powder with a particle size of less than 0.9 μm the counterpressure value becomes equal to the external pressure value.[56] Therefore before sintering diamond powders with a particle size of less than 5 μm in the high-pressure apparatus, their degassing along with hermetic sealing of the working chamber are necessary.[55]

The desorption of gases physically adsorbed by nanopowder surfaces is realized by thermal treatment of the formed briquettes in vacuum for 2 hours at a temperature of 500 °C and a pressure of residual gases of 10^{-3} Pa.[57] According to ref. [58], at such a temperature the physically adsorbed water and CO_2 are practically removed from the surface of the diamond nanodispersed powder. This decreases the degree of graphitization but does not exclude it completely. As the sintering temperature is increased the graphitization is supposed[55] to increase due to the chemical interaction of nanoparticles of carbonyl and hydroxyl groups chemosorbed on the surface with the carbon of a diamond core.

Chemical modification of the surface by means of annealing the powder in an inert gas medium in combination with the thermal treatment in vacuum results in the removal of carbonyl groups and a large decrease in the quantity of hydroxyl groups on the surface of diamond nanoparticles. This decreases the degree of graphitization of the powder when sintering and therefore as temperature is increased the density of sintered polycrystals is increased and results in an increase of their strength and hardness. The samples show direct proportionality in their hardness–density relationship. The maximal hardness value of the obtained samples is 28 GPa.[57]

In ref. [59] sintering UNCD with a bulk density of 0.6–0.7 g/cm^3 was investigated. Such a powder is packed to 1.52 g/cm^3 in a steel press mould under an applied pressure of 0.4 GPa. The density of a sample treated in a high-pressure apparatus consisting of an anvil with a recess at a pressure of 4.5 GPa increased to 1.83 g/cm^3, i.e., ~50% of the theoretical value of the density of diamond. As the pressure is increased to 8 GPa the sample density increases to 1.95 g/cm^3. As a result, UNCD pressing at a high initial porosity level is subjected to the impact of temperature.

The kinetics of the shrinkage of samples was investigated at three different temperatures of sintering. At 8 GPa the rapid compaction of the

material being sintered takes place within the first 3–10 s during non-isothermic heating. The density of the compacts obtained is ~2.8 g/cm^3. As the sintering time is increased the density increases slightly at 1500 °C and, on the contrary, the density of the compacts substantially decreases with higher process temperatures (2000 and 2300 °C).

The peculiarity of the compacts sintered at 8 GPa and 2300 °C for 36 s is the complete graphitization of UNCD in the "hot" zone of a sample near the heater. At the same parameters for the sintering process of 12 s of pressure and temperature action the thinner layer of the completely graphitizied material along the cylindrical surface of the obtained compact is found.

As the sintering time is increased the shrinkage rate slows down at T = 1500 °C due to the graphitization processes of UNCD taking place in the volume of the sintered compact. The formation of graphite is mainly observed along the boundaries of aggregates. The graphitization becomes visible, especially at sintering temperatures which are higher than 1000 °C. In the author's opinion[59] the high level of dispersivity of UNCD results in a low level of their thermal stability.

The data for the conditions of the sintering process and characteristics of the structural state are given in Table 14.13.

As evident from this table, during the sintering process of UNCD there are two processes: the transformation of the structural state of UNCD and the phase transition of diamond to graphite. At first non-porous aggregates of dispersed particles are formed. The first groups of the aggregates appear at P = 4.5 and 8 GPa starting from T = 1000 °C. However, at T = 1500 °C the aggregate quantity at both pressure values is ~20%. At T = 2000 °C and P = 8 GPa a new constituent – monocrystal grains – appears in the diamond grain structure. The monocrystal grains are formed on the basis of non-porous aggregates. At T = 2300 °C the monocrystal grains are a base constituent of the diamond grain structure. The average size of grains in such samples is increased compared to the samples obtained at T = 2000 °C.

In all samples tested (with the exception of the one obtained at P = 8 GPa and T = 750 °C) the diamond–graphite transition takes place (Table 14.13). Thus graphite is in the high-dispersion (disordered) state. The increase in sintering temperature (from 1000 to 2300 °C) at P = 8 GPa and during isothermic heating (at T = 2000 °C) results in an increase in the graphite content too. In the samples sintered in the temperature range of 1000–2000 °C the graphite is found to be along the boundaries of aggregates and seldom in the form of lengthy monophase inclusions. Such inclusions are often found in the samples obtained at T = 2300 °C.

Table 14.13 Characteristics of the Structural State of Initial UNCD and Compacts on Their Bases Obtained Under Different Thermobaric Treatment Conditions

Treatment Conditions			Phase Composition	Constituents of Diamond Structure					
				Polycrystal particles		Aggregates of particles		Monocrystal grains	
Test no. *P* (GPa)	T (°C)	τ (s)		Size Range	Content (%)	Size Range (Å)	Content (%)	Size Range (Å)	Content (%)
1			Initial diamond	I II	90 10				
2/4.5	1000	36	Diamond, graphite	I + II	100	–		–	
3/4.5	1500	36	Diamond, graphite	I + II	80	100–150	20		
4/8	750	36	Diamond	I + II	100	–		–	
5/8	1000	36	Diamond, graphite	I + II	100	–		–	
6/8	1500	36	Diamond, graphite	I + II	80	100–150	20	–	
7/8	2000	12	Diamond, graphite	I + II	20	100–200	70	100–300	10
8/8	2000	36	Diamond, graphite	–		100–500	70	100–500	30
9/8	2300	12	Diamond, graphite	–		100–500	20	500–1500	80

Note: I, size range of 3–50 Å; II, size range of 100–150 Å.

In the same samples there are also microareas of recrystallized graphite.

So, during thermobaric sintering of UNCD and reconstruction of the diamond grain structure the phase diamond–graphite transition takes place. Reconstruction of the structure is realized by the following elementary processes: (1) the formation of dense aggregates on the base of polycrystal grains in the initial UNCD; (2) recrystallization of diamond in the dense aggregates (monocrystallization of aggregates); and (3) recrystallization of monocrystal grains formed on the base of the aggregates.

The increase in T at constant P and τ (Table 14.13, numbers 4–6,8) and the increase in τ at constant P and T (Table 14.13, numbers 7,8) promote the more intensive formation of dense aggregates of grains and the recrystallization both in the aggregates and between monocrystal grains formed on the base of the aggregates. The degree of diamond–graphite transition is also increased.

One of the ways to counteract the influence of desorbed gases on the sintering process of diamond nanopowders is the addition of elements or compounds, so called getters, to the reaction volume to chemically fix the gases.[60]

The modification of the UNCD surface by carbon dioxide allows us unify the composition of surface functional groups that promote contact interactions between particles at the level of chemical bonds.[61] This improves the physical and mechanical properties of compacts compared to non-modified samples. The modification of UNCD by cobalt and nickel[61] allows us to replace a part of volatile oxides with low-volatile ones and, consequently, to decrease the gassing at hot pressing and to increase the density and strength of compacts.

The addition of compounds such as B_2O_3, SiO_2, CaO, or B which, when interacting with the oxides of the functional covering of UNCD particles promoted the formation of glasses, turned out to be fruitful. The addition of B_2O_3, SiO_2, CaO, or B of 1–3 mass % allowed us to decrease the sintering pressure from 7 to 5.5–6 GPa, to increase the temperature and the sintering time, as well as to slow the graphitization and recrystallization of diamond.[62]

Zvonarev et al.[63] investigated the processes of interaction of UNCD with compounds such as boric nitride and aluminum nitride having diamond-like crystal lattice forms and similar physical and chemical properties.

The peculiarities of the sintering process in the AIN UNCD system were investigated at a pressure of 3–7 GPa and temperature of 1000–

2000 °C; the samples consisted of 25 and 75 mass % and 50 and 50 mass % of UNCD and AIN respectively. The interaction process of UNCD-AIN was shown to differ significantly at different sintering temperatures. In all cases oxygen is very important (it is present in functional surface groups, gas absorbed from air, and adsorbed water) and causes the formation of corundum (α-Al_2O_3) at moderate temperatures (up to 1500 °C) and γ-Al—O—N at high temperatures (more than 1650 °C). The presence of ALN in an initial mixture influences the phase transitions in UNCD preventing the graphitization and stimulating the recrystallization of diamond.

The UNCD—α-BN system is of great importance and interest. Experiments with it were carried out at a pressure of ~7 GPa and within a temperature range from 1000 to 2000 °C. The treatment time was from 5 to 60 s. The samples contained 10 and 90 mass % of hexagonal boric nitride and UNCD, respectivey.

It has been established that for all compositions and all treatment temperatures in the area of catalytic synthesis of boric nitride there is an optimal time of thermobaric treatment. The maximal density and microhardness of samples is reached at 30–40 s. With less treatment time UNCD, α-BN, and some quantities of β-BN are found in the sinters. At the optimal treatment time the almost complete transition of α-BN into the required β-BN accompanied by the recrystallization of UNCD is observed. The increase in the sintering time (more than 40 s) results in an increase in density and microhardness of the samples. However, in this case the graphitization of UNCD can be observed and it stimulates the reverse transition of β-BN to α-BN. The dependence of density on the sintering temperature is as follows: at T = 1400 °C it amounts to 2.85 g/cm^3, and as the temperature is increased further the density decreases to 2.5 g/cm^3, and then at T = 1800 °C it increases to 2.6 g/cm^3. Further increase in temperature to 2000 °C results in an increase in density up to 3.2–3.25 g/cm^3. At that point the microhardness is 30–35 GPa. X-ray-phase analysis showed that it relates to phase transformations in boric nitride and UNCD.

There is therefore the possibility to prepare new composite materials for constructive and functional purposes with a wide range of properties by varying the composition of the primary mixture (diamond blend) and changing the UNCD surface.

14.6 Bioactivity of UNCD Particles

Nowadays there is no doubt that free radical processes are mostly responsible for cancer growth. Changes in lipid metabolism and growth

of a tumor are also tightly interlinked. The growth of the tumor is accompanied by deep disorders in the metabolism of proteins, serious changes in the intracellular production of energy, and large deviations in oxidative–reductive processes from the ordinary levels. All these processes take place due to a leak of partly reduced oxygen species (the so-called active oxygen species, AOS) out of the chain of tissue breathing and the produced AOS are responsible for disorders in the main metabolic processes involving AOS in the tumor-containing body.

Based on the leading role of radical reactions in the processes of tumor growth, inhibitors of chain radical processes are traditionally tested as anticancer chemicals, but the majority of anticancer medicines show a high level of toxicity and the search for new anticancer drugs of low toxicity is of great interest.

Currently there are two main directions leading to new anticancer substances:

(1) Investigation of the derivatives of traditional medicines.
(2) Testing of new synthetic and natural formulations.

Nowadays the second route of testing new anticancer drugs with a low toxicity is preferable.

Classical diamonds possess as a rule excellent tetrahedral crystal organization (sp^3 hybridization) showing unique physical–mechanical, thermophysical, and electric properties. At the same time, at normal conditions diamond is inert to all chemical and biochemical reagents. Diamond shows no toxicity and does not stimulate tumor growth or any changes in DNA structure. Diamonds are insoluble in all solvents. Any experience with the use of diamonds in medical practice appears to be absent.

Crystals of UNCD possess classical a chemically inert nucleus of cubic diamond having an oval or ball-like form. However, the surface of UNCD is covered with many functional groups (such as oxy, carboxy, or carbonyl fragments) responsible for hydrophilic properties[64,65] of the particles and which are harmless for living organisms. Also, each crystal of UNCD has a lot of unpaired electrons and behaves as a polyradical cluster.[66] UNCD also possesses other peculiarities in comparison to diamonds of different origin. UNCD shows unique characteristics of adsorption (1–10 mg-equivalents/m^2) and a greatly developed surface of adsorption (~450 m^2/g) in comparison to statically produced diamonds (ACM 1/0 has the same parameter equal to 13.5 m^2/g)[67]. All the above unique properties of UNCD have led us to study their biological properties. At first we found that UNCD shows its unique characteristics only in

liquid media such as aqueous, alcohol or oil. The dry powder of purified UNCD, when introduced into the media mentioned above, is not efficient. After purifying UNCD with nitric acid under excess pressure[68] the surface of the crystals does not contain any harmful contaminations. UNCD belongs to principally new anticancer substances[69–70] which may be treated as polyfunctional supramolecular structures containing on their surface such functional groups as —OH, —NH_2, —C(O)NH_2 responsible for their antiradical activity and ability to interfere in free radical processes in the cell.

Many traditionally used anticancer medicines showing antiradical effect also contain —OH and —NH_2 functional groups in their structure.

Many of the functional groups on the surface of UNCD may be responsible both for additional generation and for withdrawing excessively produced free radicals in the cell.

So, UNCD may behave as a specific regulator of radical processes in biological systems showing low toxicity ($LD_{50} > 7000$ mg/kg per os, male white rats). Their ability to regulate free radical processes is the base of the UNCD anticancer effect. The hydrophylic surface and strong adsorbing capacity of UNCD are also of great value for its medical use.

In refs. [69–70] several patients suffering from cancer in the IV grade with different localizations of the initial tumor (breast, intestine, stomach) were treated with UNCD. In all cases UNCD showed a pronounced positive effect. Treatment of the patients with UNCD extended their period of life in comparison to the predicted one.

The explanation of such an effect may be based on the results given below. It was shown that UNCD actively adsorbs pathogenic viruses and other microorganisms. All attempts to desorb microorganisms after treatment with UNCD failed. So based on the above properties of UNCD it may be used as a specific material in the case of internal toxic states.

The influence of UNCD on the period of life of Af line mice suffering from ascite Erlich carcinoma was also investigated. Each laboratory mouse was injected with $6 \cdot 10^6$ cells of ascite Erlich carcinoma. The influence of UNCD upon the level of spontaneous mutations in the mice was also estimated. Mice were chosen as a model in these experiments because the influence of different factors, e.g., radiation, is traditionally investigated on these laboratory animals and the results may be extrapolated to human beings.[9,69,70] It was also shown that 2.5–3% aqueous suspension of UNCD (a very high concentration of suspension produced by the "Diamond Centre") has no mutagenic properties in the sex cells of mice. Treatment of the mice suffering ascite Erlich carcinima with such a suspension prolonged their period of life by about 38% in comparison to the

control group. Further, mice being treated with UNCD were active up to the terminal moments of their lives.

Several patients suffering cancer in the IV stage were treated with aqueous and oil suspensions of UNCD after chemical and radio therapeutic courses. All the patients were informed about laboratory experiments with UNCD and the results achieved. Treatment of oncology patients with UNCD led to the following results:

- strong pain became much reduced or faded totally;
- the function of the intestines was restored;
- several immobile patients were able to get up and even walk;
- some blood indexes improved;
- the urea of the patients changed its color – a distinctive odor of the urea appeared and intensive excretion of toxins was observed;
- activation of the immune system took place and the patients showed a great will to live. So the effect of UNCD greatly enhances the physical state of terminally ill people.

The same effects were also registered in experiments with dogs dying of cancer. Dogs given UNCD suspension orally did not suffer strong pain (they stopped growling and whining), the function of the intestines was restored, and the immune system became stronger.

According to a private communication from Prof. E. V. Nikitin (January 20, 2003, from Lesnoy, Sverdlovskaya region), the treatment of an 81-year-old woman suffering from cancer with an aqueous suspension of UNCD for 1.5 months led not only to a better physical state of the patient but also to a total reduction of polyps on the internal walls of the urinary bladder. And according to a private communication from Prof. S. S. Krestovsky (February 4, 2003, St. Petersburg), rinsing of the mouth and throat with an aqueous suspension of UNCD led to a very rapid healing of wounds and cuts and to a very quick recovery from purulent processes in the mouth and throat. We have also shown that rinsing the mouth with an aqueous suspension of UNCD thoroughly improved the state of the patients suffering of paradontosis.[9]

The preliminary results of the anticancer effect of UNCD need systematization and elucidation of its mechanisms. Further, wider clinical tests should also be carried out. The main aim of such work is to introduce UNCD into clinical practice for treating oncology patients.

The influence of UNCD on whole blood and several fractions of blood cells has been investigated in refs. [71,72]. The influence of UNCD on

white blood cells was estimated through the intensity of generation of active oxygen species measured with the help of the chemiluminescent luminole reaction. The test of supravital colouring with a special reagent (a solution of blue tripanic) to estimate the living ability of white cells after experimental treatment with UNCD was also used. The effect of UNCD upon red blood cells was measured through the percentage of hemolyzed red cells that was estimated according the UV spectroscopic method proposed in the article.[71]

It was shown that the addition of UNCD to whole blood greatly changed the kinetics of both activated and spontaneous luminole-dependent chemiluminescence. Both the intensity of radiation (I_{max}) and the period before maximum radiation (T_{max}) are influenced by UNCD. It was also shown that UNCD led to the destruction of white cells and hemolysis of red cells during *in vitro* experiments. On the basis of these results it was concluded that UNCDs are able to damage cell membranes.

The registered growth of the level of malonic dialdehyde being the terminal product of lipid peroxydation and the level of peroxydation of proteins measured through the amount of their 2.4-dinitrophenylhydrazone derivatives after the incubation of red cells with UNCD support the idea of their destructive effect on cell membranes. But UNCD incubated with red cells in the presence of $NaNO_2$-initiating peroxy processes in red cells protects the main antioxidant enzymes (superoxide dismutase and catalase) strongly inactivated by $NaNO_2$. Under the protection of UNCD the activity of these enzymes remains on a level close to that of native red cells. According to these results, UNCD may be treated as a specific material stimulating the enzymatic antioxidant system of the cell.

The influence of UNCD on the peroxydation of lipids initiated with ferrous sulphate has also been shown in ref. [73]. The experiments were carried out in liposome suspension in a buffer solution at 37 °C in the pH region of 5.9–7.0. In these experiments the method of chemiluminescence was also used. It was shown that the effect of UNCD depended strongly on the pH of the reaction media. In acidic media (pH = 5.9) the introduction of UNCD does not influence the intensity of peroxidation of phospholipids. When pH = 6.4 a temporary activation of lipid peroxidation takes place. Under these conditions we register the growth both of I_{max} and of the total sum of luminescence equal to about 20%.

At neutral pH we see a pronounced depression of chemiluminescence. At this pH and with a concentration of ferrous sulphate equal to $1.2 \cdot 10^{-4}$ M the suspension of UNCD with concentration 0.0095 mass % inhibits peroxydation of lipids. An increase in concentration to 0.0205 mass % slowly increases the effect.

Together with UNCD, a mixture of $C_{60}:C_{70}$ fullerenes in a mass proportion of 4 : 1 and with multilayer nanotubes was also treated as a potential inhibitor of lipid peroxidation. The above-mentioned allotropic modifications of carbon opposite to UNCD in an amount of 0.0065 mass % did not effect the process of peroxidation of lipids.

Analyzing the data given above we may conclude:

(1) There are no analogies to UNCD in terms of complex action upon organisms bearing in mind its physical state as an insoluble solid powder.
(2) The use of UNCD together with chemo- and radiotherapy may become rather effective in treating cancer tumors and may help to prevent the mutagenic effect of special medicines without lowering the therapeutic effect. The use of UNCD may also help to prevent mutations in normal cells and to block the occurrence of secondary tumors during treatment with anticancer medicine.
(3) The ability of UNCD to normalize the functions of the gastro-intestinal system is without doubt.
(4) The effect of normalization of blood pressure in patients treated with UNCD was also recorded.

UNCD is also of great interest in theoretical and practical biochemistry as a new adsorbent useful for the division and purification of proteins.[74–77]

The ability of UNCD clusters to adsorb obeline is described in ref. [74]. It was shown that on being adsorbed this protein conserves its bioluminescent activity.

Obeline belongs to the row of Ca^{+2}-activated photoproteins, the so-called photoemission EF proteins that are able to produce photons on interaction with calcium ions. A set of these proteins makes up stable enzyme–substrate complexes consisting of the apoprotein molecule (in this case it is apoobeline), a substrate molecule (tcelentheazine), and molecular oxygen.[78]

It was mentioned in ref. [75] that UNCD selectively adsorbs recombinant apoobeline out of the protein extract of *E. coli*. It has been found that UNCD particles are able to adsorb active photoprotein on their surface. During adsorbtion, apoobelline preserves its ability to generate quanta of light on interaction with calcium ions. The activity of the protein in the UNCD–obeline complex measured directly after its formation comprises 40–50% of the activity of the initial protein in the solution. The reduction of the intensity of the signal and dissipation of quanta of light by the par-

ticles of UNCD incorporated into the complex are negligible according to ref. [74]. If particles of UNCD are treated as the adsorbent, the complex formed may be treated as an immobilized enzyme.

When stored at 4 °C for 24 hours the activity of obeline adsorbed on UNCD particles decreases by 7% or more.[79] During the next two weeks the output of light quanta does not change. The stabilization of activity of the protein taking place in 24 hours makes it possible to produce materials suitable for use over a long period of time. Though the activity of obeline in the stable sample of UNCD–obeline is only 35–40% of the activity of the initial protein in the solution, the level of bioluminescence provides easy registration.

Purtov et al.[74] succeeded in adjecting UNCD–obeline to the surface of aluminum foil having produced the progenitor of dimeric (planal) luminescent biochips. Knowing that aluminum is always covered with a layer of oxide unable to adsorb obeline molecules from solution and also unable to adsorb UNCD particles from its suspension, these authors created a composition of the so-called adhesive layer having a high affinity for Al_2O_3 and UNCD. Introduction of this "adhesive" layer made it possible to construct a supramolecular structure including an Al-Al_2O_3–adhesive layer–UNCD–obeline complex with a presumably uniform distribution of UNCD particles and molecules of photoprotein on the surface of the foil. Such a created supramolecular structure cannot be washed away with buffer solutions and water. The structure shows high stability and pronounced adherence to the surface of the foil.

Lyophilically dried foils with UNCD and obeline may be stored at room temperature without any reduction in the activity of obeline.

The kinetics of the luminescent reaction of obeline immobilized on the foils differs from the enzymatic reaction of the protein in solution and suspension. The difference is in the slowing down of the attenuation of the bioluminescent reaction. There may be two reasons for this effect: (1) The protein adsorbed on the foil forms a multilayer film. As a result the availability of calcium ions for obeline molecules is affected. (2) The foil may influence the kinetics of the bioluminescent reaction.

The principal possibility of using lyophylically dried foil with UNCD and obeline without using buffer systems for calcium registration in native physiological liquids was shown in experiments with human saliva.[71] So the presence of immobilized, light-radiating protein on the plane sample permitted the creation of a bioluminiscent test system for calcium registration as an alternative to the traditional methods of measuring it in the volume of the reaction mixture. The proposed method may be of great value in space. It is well known that long periods in space lead to decal-

cification of human bone tissue. But under conditions of microgravitation work with liquids is a great problem.

14.7 Other Technological Applications of UNCD Particles

A new initiating composition sensitive to low-temperature laser emission containing perchlorate of 5-hydrazinotetrazole mercury (II) and polymer polymethylvinyltetrazole involving UNCD was developed in ref. [80]. The components ratio, in mass %, is:

perchlorate of 5-hydrazinotetrazole mercury (II)	85.7–90.0
polymethylvinyltetrazole	9.5–10.0
UNCD	0.1–5.0

Laser initialization is a relatively new method for blasting explosives with a remarkable record of safety. In laser initialization a high level of insulation of an optical detonator from spurious pulses is provided by the fact that in the optical band there are no random sources with sufficient power to explode a detonator.

Light-sensitive explosives are used in fiber-optic detonators functioning under the initiating laser emission effect. Laser initialization can be successfully used for explosion welding, forming, mine blasting operations, explosively automated mechanisms in spacecraft, deep-well perforation during synthesis of UNCD, etc.

The developed composition provides for a simultaneous increase in sensitivity to the laser emission effect by 1.5–1.7 times (in comparison to the composition without UNCD) and high adhesion to a contact surface due to the strengthening of adhesion properties of a thermoplastic (polymethylvinyltetrazole). The minimum initialization energy when using UNCD reduces from 310 to 180 μJ. The delay time of initialization of the composition amounts to 11–12 μs. In order to protect architectural monuments (e.g., white Italian marble) silicate–organic coatings containing UNCD were developed and tested. The presence of UNCD inhibits the growth of the fungi and bacteria prevailing in urban media and destroying the stone structure.

To form such coatings sols based on tetraethosysilane and modified UNCD have been used. Similar sols containing UNCD can be used for modifying a surface of powder components of cements and concretes. The application of such sols can inhibit vital functions of detrimental micro-

organisms and fungi and substantially prolong the service life of concrete structures (e.g., buildings and such constructions, motorways, hydroelectric power stations, etc.).

The technology of metallization of UNCD powder with nickel to form diamond-containing capsules 0.35–1.8 μm in size has also been developed.[81] The use of such compositions on a base of metallized UNCD when making cutting disks for the treatment of jewelry allowed an increase in wear resistance, elasticity, and the rolling and cutting abilities of the disks by 1.5–1.8 times. In other work,[30] chrome–diamond coatings produced by the method of ion-plasma scattering of a composite target of Cr + 5 mass % of UNCD were shown to have a size of subgrains of 30–70 nm, nanodiamond particles forming a net along the boundaries of these subgrains.

In ref. [82] the results of an investigation on the electrochemical behavior of compacts made of different dispersivity diamond powders in aqueous electrolytes under high pressure and temperature are described to ascertain the possibility of their use as compacts in electrochemistry. Compacting UNCD has been realized at a pressure of 8 GPa and temperature of 1600 °C in vacuum conditions. Values for the specific resistance of the sintered UNCD are over the range of (1–5) × 103 ohm cm. An electrode represents a compact in the form of a tablet 8 mm in diameter and 5 mm in thickness. The results of the investigation showed that a high corrosion resistance and a wide potential area for the ideal polarizability of an electrode (from −1.3 to +1.5 V) are similar for electrodes of UNCD and micropowders of static synthesis (MA) in the background electrolyte of 0.5M H2SO4. In the background electrolyte of KCl on UNCD and MA electrodes,[82] cyclic voltameter graphs with current peaks at potentials of +0.7 and +0.64 V (direct and on the back respectively) were obtained.

The potential difference of anodic and cathodic current peaks corresponds to reversible one-electron charge transfer. So, the sintered compacts on the base of UNCD and MA powders can be used as indicating electrodes in electrochemical research. A disadvantage of UNCD and MA electrodes is their low electrocatalytic reactivity. Therefore, special attention should be concentrated on searching for methods of activation of the surface of UNCD to create highly effective electrodes for the solution of tasks in electrosynthesis and electroanalysis.

References

1. Shebalin A.I., Gubarevich V.D., Brilyakov P.M., “Production method for composite coatings on the basis of chrome”, International Application PCT/SU 88/00230 (WO 89/07668), C 25D15/00, appl. 24.08.89.

2. Shebalin A.I., Gubarevich V.D., Brylyakov P.M., Besedin V.I., Sakovich G.V., Cheremisin A.Ya., Kotov A.N., Kozlovsky S.A., Altshuller N.B., "Production method for composite coatings on the basis of chrome", Inventors certificate 1694710, USSR, C 25D15/00, 14.04.86, Bull. N44, 1991, p. 91, publ. 30.11.1991.
3. Tokyo Daiyamondo Kogu Seisakusho K.K., "Chrome-plating solution", Patent 5-10695, Japan (A), 27.04.1993 (19).
4. Burkat G.K., Dolmatov V.Yu., "Galvanic processes with the use of ultradispersed diamonds", Abstracts of All-Union Scientific-Practical Conference "*Galvanotekhnika i obrabotka poverhnosti*", Moscow, 1–3 June 1999, Moscow: D.I. Mendeleev Russian Chemical-Technical University, 1999, p. 15 (Russian edition).
5. Antropov L.I., Lebedinsky Yu.N., *Composite electrochemical coatings and materials*, Kiev: Texnika, 1986 (Russian edition).
6. Dolmatov V.Yu., Burkat G.K., "Detonation-synthesized ultradispersed diamonds as a basis of a new class of composite metal-diamond electroplated coatings", *Superhard Materials*, 2000, Vol. 22, No. 1, pp. 78–86.
7. Dolmatov V.Yu., Burkat G.K., Sabourbaev V.Yu., Salko A.E., Veretennikova M.V., "Preparation and properties of electrochemical composite coatings of precious and nonferrous metals with ultradispersed detonation-synthesized diamonds", *Superhard Materials*, 2001, Vol. 23, No. 2, pp. 49–55.
8. Dolmatov V.Yu., Fujimura T., Burkat G.K., Orlova E.A., "Preparation of wear-resistant chromium coatings containing nanodiamonds of different origins", *Superhard Materials*, 2002, Vol. No. 6, pp. 15–20.
9. Dolmatov V.Yu., *Detonation synthesis ultradispersed diamonds*, St. Petersburg: St. Petersburg State Polytechnic University, 2003 (Russian edition).
10. Burkat G.K., Dolmatov V.Yu., "Application of ultrafine-dispersed diamonds in electroplating", *Physics of the Solid State*, 2004, Vol. 46, No. 4, p. 703–710.
11. Lung B., Burkat G.K., Dolmatov V.Yu., Sabourbaev V.Yu., Production method for composite coatings on the basis of zinc, Patent 2169798, Russian Federation, Bull. No. 18 (II), 2001, p. 279, publ. 27.06.2001.
12. Burkat G.K., Dolmatov V.Yu., "Preparation and properties of electrochemical zinc-diamond coatings from zincate electrolyte", *Galvanotekhnika i obrabotka poverhnosti*, Vol. X, No. 2, 2001, pp. 35–38 (Russian edition).
13. Dolmatov V.Yu., "Experience in and prospects for non-traditional use of explosion-synthesized ultradispersed diamonds", *Superhard Materials*, 1998, Vol. 20, No. 4, pp. 70–73.
14. Baltrunene N.B., Vishomirskis R.M., Molchadsky A.M., Shebalin A.I., Electrolyte for deposition of silver coatings, Inventors certificate 1668490, USSR, C25D3/46, 15/00, appl. 10.05.1989. Bull. No. 29, 1991, p. 123, publ. 07.08.1991.
15. Lung B., Burkat G.K., Dolmatov V.Yu., Sabourbaev V.Yu., Production method for composite coatings based on gold, Patent No. 2191227, Russian Federation, C25D 3/46, publ. 20.10.2002.
16. Chukhaeva S.I., Detkov P.Ya., Tkachenko A.P., Toporov A.D., "Physicochemical properties of fractions isolated from ultradispersed diamonds", *Superhard Materials*, 1998, Vol. 20, No. 4, pp. 26–32.

17. Dolmatov V.Yu., Lung B., Burkat G.K., Sabourbaev V.Yu., Veretennikova M.V., "New generation of metal-diamond galvanic coatings on the basis of detonation synthesis ultradispersed diamonds", Abstracts of International Conference "*Materials and coatings in extreme conditions*", Katseveli, Ukraine, 2000, p. 64 (Russian edition).
18. Lung B., Burkat G.K., Dolmatov V.Yu., Production method for inorganic oxide composite coatings of aluminium and its alloys, Patent 2169800, Russian Federation, Bull. No. 18 (II), 2001, p. 279, publ. 27.06.2001.
19. Fujimura T., Dolmatov V.Yu., Burkat G.K., Orlova E.A., Veretennikova M.V., "Electrochemical codeposition of Sn-Pb-metal alloy along with detonation synthesis nanodiamonds", *Diamond and Related Materials*, 2004, Vol. 13, pp. 2226–2229.
20. Sakovich G.V., Komarov V.F., Petrov E.A. et al., "Ultradispersed diamonds and their practical using", Proceedings of V All-Union Meeting on Detonation, Krasnoyarsk, 1991, Vol. 2, pp. 272–278 (Russian edition).
21. Voznyakovskii A.P., Shelohneva L.F., Dolmatov V.Yu., Bodrova V.S., "Prospects of using of explosion synthesis technical diamond carbon for strengthening of isoprene rubbers", *Kauchuk i resina*, 1996, No. 6, p. 27 (Russian edition).
22. Dolmatov V.Yu., Voznyakovskii A.P., Levintova E.A., Composition including vinylidenefluorine-containing rubber, Patent No. 2100389 Russian Federation, CO 8L 27/16., Bull. No. 36, publ. 27.12.1997.
23. Dolmatov V.Yu., Voznyakovskii A.P., Veretennikova M.V., "Modification of polymers using detonation-synthesized ultradispersed diamonds (nanodiamonds)", *Superhard Materials*, 2001, Vol. 23, No. 6, pp. 75–78.
24. Voznyakovskii A.P., Dolmatov V.Yu., Levintova E.A., Gubarevich T.M., "Composite materials based on polyfluorinated co-polymers and explosion synthesis technical diamond carbon", Proceedings of International Conference on Rubber, Moscow, 1994, Vol. 2, pp. 80–87 (Russian edition).
25. Voznyakovskiy A.P., Dolmatov V.Yu., Veretennikova M.V., "Nanocomposites based on polyblock polysiloxane copolymers and nanodiamonds. Distribution topology features and properties", *Superhard Materials*, 2003, Vol. 25, No. 4, pp. 21–30.
26. Sirotinkin N.V., Voznyakovskii A.P., Ershova A.N., "Model of formation of three-dimensional polyurethane films modified by detonation nanodiamonds", *Physics of the Solid State*, 2004, Vol. 46, No. 4, pp. 746–747.
27. Adrianova O.A., Sokolova M.D., Popov S.N., "Application of ultradispersed diamond-graphite as a modifier of frost-resisting packing elastomers", *Kauchuk i resina*, 1999, No. 6, pp. 11–14 (Russian edition).
28. Sokolova M.D., Popov S.N., Adrianova O.A. et al., Rubber compound on the basis of butadiene-nitrile rubber, Patent No. 2129132 Russian Federation, C08 L 9/02, publ. 24.12. 1996.
29. Akopyan L.A., Zlotnikov M.N., Rumyantsev B.V., Abramova N.L., Zobina M.V., Mordvintseva T.L., "Synthesis of explosive decompression-resistant rubbers with the use of detonation carbon", *Physics of the Solid State*, 2004, Vol. 46, No. 4, pp. 742–744.

30. Vityaz' P.A., "The state of the art and prospects of detonation-synthesis nanodiamond applications in Byelorussia", *Physics of the Solid State*, 2004, Vol. 46, No. 4, pp. 606–610.
31. Gubarevich T.M., Dolmatov V.Yu., "Polishing systems on the basis of ultradispersed diamonds", *Journal Prikladnoi khimii*, 1993, Vol. 66, No. 8, pp. 1878–1881 (Russian edition).
32. Gubarevich T.M., Dolmatov V.Yu., Polishing composition for chemical-mechanical polishing, Patent No. 2082738, Russian Federation, 6 C 09 G$^1/_2$, publ. 27.06.1997.
33. Dolmatov V.Yu., "Detonation synthesis ultradispersed diamonds: properties and applications", *Russian Chemical Reviews*, 2001, Vol. 70, No. 7, pp. 607–626.
34. Kirilin K.V., Padalko V.V., "Method for the production of diamond-like material, diamond-like material and use thereof", priority date 21.07.2000.
35. Novikov N.V., Bogatyreva G.P., Voloshin M.N., Marinich M.A., Padalko V.I., Slavinsky Yu.S., "Nanostructural porous diamond powders and their surface properties", *Superhard Materials*, 2002, Vol. 24, No. 6, pp. 2–7.
36. Artyomov A.S., "Polishing nanodiamonds", *Physics of the Solid State*, 2004, Vol. 46, No. 4, pp. 687–695.
37. Stickler R., Booker Y.R., "Surface damage on abraded silicon specimens", *Philosophical Magazine*, 1963, Vol. 8, No. 89, pp. 859–876.
38. Stickler R., Booker Y.R., "Transmission electron microscope investigation of removal of mechanical polishing damage on Si and Ge by chemical polishing", *Journal of The Electrochemical Society*, 1964, Vol. 111, No. 4, pp. 485–488.
39. Kurobe T., Fujimura T., Ikeda H., "Nano-polishing of silicon wafers using ultra-dispersed diamonds", *Physics of the Solid State*, 2004, Vol. 46, No. 4, pp. 751–754.
40. Komarov V.F., "Ultradispersed diamonds in machine-building", *Tekhnika mashinostroeniya*, 1997, Vol. 4, No. 14, pp. 106–107 (Russian edition).
41. Zakharov A.A., Yuzova V.A., Eristova N.V., "Superfinished polishing of optical glass and quartz", Proceedings of "Ultradispersed materials. Preparation and properties", Krasnoyarsk: Krasnoyarsk Polytechnic Institute, 1990, pp. 170–173 (Russian edition).
42. All-Union State Standard 11141-84. Detail optical. Classes of purity of surface. Methods of control.
43. Kolisnechenko L.F., "The influence of chalcogenides of molybdenum on tribotechnical properties of lubricating materials", *Poroshkovaya metallurgiya*, Minsk, 1987, No. 11, pp. 67–71 (Russian edition).
44. Matsuo K., Maede U., Kurabashi M., Miuva M., "Additive Schmierst und Arbeitssigkeit. 5 und Kollog Esslingen", 14–16 January 1986, Bd. 2 Esslingen, 1986, pp. 5.417–5.418.
45. Lyamkin A.I., Redkin V.E., "Ultradispersed diamond-graphite and diamond powders obtained from explosives", *Nauka – proizvodstvu*, 2000, Vol. 3, No. 28, pp. 59–64 (Russian edition).
46. Sakovich G.V., Brilyakov P.M., Gubarevich T.M., Gubarevich V.D., Shebalin A.I., Privalko Yu.N., Badaev F.Z., Besedina O.A., Lubricating composition with hard modifier of friction, Application PCT/SU, 87/00249.

47. Schelkanov S.I., Kan S.V., Redkin V.E., "The influence of additives on antifriction properties of motor and transmission oils", Proceedings of "Ultradispersed materials. Preparation and properties", Krasnoyarsk: Krasnoyarsk Polytechnic Institute, 1990, pp. 173–180 (Russian edition).
48. Zakharov A.A., Redkin V.E., Staver A.M., Lyamkin A.I., Kuchma E.I., Lubricating composition, Application PCT WO 93/01261, publ. 21.01.1993.
49. Sannikov V.M., Koreibo Yu.M., "About break-in ability of ultradispersed diamond-graphite powder", Proceedings of "Ultradispersed materials. Preparation and properties", Krasnoyarsk: Krasnoyarsk Polytechnic Institute, 1990, pp. 155–161 (Russian edition).
50. Shangin A.P., Redkin V.E., Rakshin E.D., Seligeev S.V., "The use of UDP-AG in lubricant-coolant compositions for machining", Proceedings of "Ultradispersed materials. Preparation and properties", Krasnoyarsk: Krasnoyarsk Polytechnic Institute, 1990, pp. 165–170 (Russian edition).
51. Redkin V.E., Staver A.M., Shangin A.P., Lubricant-coolant for machining, Patent No. 2009186, Russian Federation, Bull No. 5, 1992, publ. 15.05.92.
52. Istomin V.N., Rakshin E.D., Akimov Yu.D., "Application of ultradispersed powder of diamond-graphite in technological lubricants for metal forming", Proceedings of "Ultradispersed materials. Preparation and properties", Krasnoyarsk: Krasnoyarsk Polytechnic Institute, 1990, pp. 161–163 (Russian edition).
53. Sakovich G.V., Komarov V.F., Petrov E.A., Brilyakov P.M., Potapov M.G., Idrisov I.G., "Ultradispersed diamonds and their practical using", Proceedings of V All-Union Meeting on Detonation, Krasnoyarsk, 5–12 August 1991, Vol. 2, pp. 272–278 (Russian edition).
54. Shulgenko A.A., Gargin V.G., Shishkin V.A., Bochechka A.A., *Polycrystalline materials based on diamond*, Kiev: Naukova dumka, 1989 (Russian edition).
55. Bochechka A.A., "Effect of degassing on the formation of polycrystals from diamond nanopowders produced by detonation and static synthesis", *Physics of the Solid State*, 2004, Vol. 46, No. 4, pp. 670–673.
56. Bochechka A.A., "Effect of desorbed gases on high-pressure sintering of diamond powders", *Superhard Materials*, 1998, Vol. 20, No. 4, pp. 8–13.
57. Shulgenko A.A., Bochechka A.A., Romanko L.A., Kytsai A.M., Gargin V.G., "Sintering behavior of vacuum-heat-treated diamond nanopowders", *Superhard Materials*, 2000, Vol. 22, No. 6, pp. 45–51.
58. Nozhkina A.V., Kolchemanov N.A., Kardanov A.A., Detkov P.Ya., "Physicochemical properties of dynamically synthesized diamonds", *Superhard Materials*, 2000, Vol. 22, No. 1, pp. 73–77.
59. Danilenko V.V., Petrusha I.A., Oleinik G.S., Danilenko N.V., "Evolution of the structure of a compact during high-pressure sintering of nanodispersed diamonds", *Superhard Materials*, 1998, Vol. 20, No. 4, pp. 49–56.
60. Shulzhenko A.A., Bochechka A.A., Gargin V.G., Romanko L.A., Tkach V.N., "Effect of gas desorption on the structure and properties of polycrystal sintered from nanometric diamond powders", *Superhard Materials*, 1998, Vol. 20, No. 4, pp. 43–48.
61. Shipilo V.B., Starchenko I.M., Gubarevich T.M., "About sintering of UDD-powders under high pressures and at high temperatures", *Poroshkovaya metallurgiya*, Minsk, 1995, No. 18, pp. 126–130 (Russian edition).

62. Shipilo V.B., Starchenko I.M., Zvonarev E.V., Senyut V.T., "Diamond-containing material on the basis of detonation synthesis powders", *Materials, technologies, tools*, 1997, Vol. 2, No. 4, pp. 61–63 (Russian edition).
63. Zvonarev E.V., Senyut V.T., Starchenko I.M., Finskaya V.M., "Peculiarities of high pressure-high temperature compacting of ultradispersed diamond powders", *Superhard Materials*, 1998, Vol. 20, No. 4, pp. 38–42.
64. Kulakova I.I., Gubarevich T.M., Dolmatov V.Yu., Rudenko A.P., "Chemical properties of detonation-synthesized ultradispersed diamond", *Superhard Materials*, 2000, Vol. 22, No. 1, pp. 42–48.
65. Vereschagin A.L., Petrova L.A., Brilyakov V.V., "Polarographic study of diamond-like carbon phase", *Superhard Materials*, 1992, Vol. 14, No. 1, pp. 13–15.
66. Nachalnaya T.A., Malogolovets V.G., Podzerei G.A., Nikitin Yu.I., Novikov N.V., Polkanov Yu.A., "Special features of structure and physico-mechanical properties of natural diamonds of Ukraine", *Superhard Materials*, 2000, Vol. 22, No. 1, pp. 33–41.
67. Barushkina T.N., Aleinikov V.G., Donster B.B., Savvakin G.I., "Chemical modification of diamond surface with ozone", Proceedings of Institute of Superhard Materials of Ukrainian Academy of Sciences, 1990, pp. 41–48 (Russian edition).
68. Dolmatov V.Yu., Suschev V.G., Marchukov V.A., Gubarevich T.M, Korgenevsky A.P., The method of isolation of synthetic ultradispersed diamonds, Patent No. 2109683, Russian Federation, 27.04.98. Chemical Abstracts, 124; 180335y.
69. Dolmatov V.Yu., Kostrova L.N., "Detonation-synthesized nanodiamonds and the possibility to develop a new generation of medicines", *Superhard Materials*, 2000, Vol. 22, No. 3, pp. 79–82.
70. Dolmatov V.Yu., Biologically active detonation synthesis ultradispersed diamonds, Patent No. 2203068, Russian Federation, A61 K 33/44, publ. 27.04.2003.
71. Puzyr A.P., Neshumayev D.A., Dolmatov V.Yu. et al., "Destruction of human cells in interaction with detonation nanodiamonds in experiments in vitro", *Diamond and Related Materials*, 2004, Vol. 13, pp. 2020–2023.
72. Puzyr A.P., Dolmatov V.Yu., Shigalei I.V. et al., "The influence of detonation nanodiamond powder on blood cells", Proceedings of NATO Advanced Research Workshop, Innovative superhard materials and sustainable coating, May 12–15, 2004, Kyiv, Ukraine.
73. Shugalei I.V., Dubyago N.P., Dolmatov V.Yu. et al., "Investigation of antioxidant activity of detonation synthesis ultradispersed diamonds by means of chemiluminescence", Proceedings of III International Conference "Carbon: fundamental problems of science, science of materials and technology", Moscow, 13–15 October 2004, Moscow State University (Russian edition).
74. Purtov K.V., Bondar V.S., Pusyr A.P., "Creation of the permolecular structure from nanodiamond particles and obeline on the two-dimensional substrate", *Reports of Academy of Sciences*, 2001, Vol. 380, No. 3, pp. 411–414 (Russian edition).

75. Bondar V.S., Puzyr A.P., "The use of nanodiamond particles for express-isolation of recombinant apoobeline from ESCHERICHIA COLI", *Reports of Academy of Sciences*, 2000, Vol. 373, No. 2, pp. 251–253 (Russian edition).
76. Bondar V.S., Pozdnyakova I.O., Puzyr A.P., "Applications of nanodiamonds for separation of and purification of proteins", *Physics of the Solid State*, 2004, Vol. 46, No. 4, pp. 758–760.
77. Puzyr A.P., Pozdnyakova I.O., Bondar V.S., "Design of a luminescence biochip with nanodiamonds and bacterial luciferase", *Physics of the Solid State*, 2004, Vol. 46, No. 4, pp. 761–763.
78. Blinks J.R., Prendergast F.G., Allen D.G., "Photoproteins as biological calcium indicators", *Pharmacological Review*, 1976, Vol. 28, No. 1, pp. 1–93.
79. Triven M., *Immobilized ferments*, Moscow: Mir, 1983 (Russian edition).
80. Iljushin M.A., Ugryumov I.A., Dolmatov V.Yu., Veretennikova M.V., Initiating explosive composition, Application for a patent No. 2004134657, Russian Federation, 23 November 2004, MKI C 01 B 11/18.
81. Novikov N.V., Bogatyreva G.P., Voloshin M.N., "Detonation diamonds in Ukraine", *Physics of the Solid State*, 2004, Vol. 46, No. 4, pp. 600–605.
82. Novoselova I.I., Fedotishina E.N., Panov E.V., Bochechka A.A., Romanko L.A., "Electrochemical properties of compacts of nano- and microdisperse diamond powders in aqueous electrolytes", *Physics of the Solid State*, 2004, Vol. 46, No. 4, pp. 748–750.

15 Nanodiamond: Designing the Bio-Platform

Varvara P. Grichko and Olga A. Shenderova

International Technology Center, Raleigh, NC, USA

Introduction

All major forms of carbon at the nanoscale – fullerenes, nanotubes, and nanodiamond (ND), the last in the forms of both particulate and films – appear to be valuable materials for biomedical applications (Freitas, 1999; 2003). Importantly, carbon nanostructures span the same length scale as bio-compounds (Fig. 15.1), ranging from subnanometer-size nucleotides, to tens and hundreds of nanometer-sized organelles and viruses, and up to micron-sized cell sizes.

In the mid 1990s it was discovered that fullerene compounds have biological activity, and their potential as therapeutic agents for the treatment of several diseases was demonstrated. As a result, a private biopharmaceutical company, *C Sixty Inc*., has been established with a primary focus on the discovery and development of novel fullerene-based therapeutics. At 7.2 Å in diameter, C_{60} is similar in size to steroid hormones and peptide alpha-helices, and, thus, fullerene compounds are ideal molecules to serve as ligands for enzymes and receptors (Wilson, 2000). Within the last few years, a number of useful fullerene-based therapeutic applications have been developed, including as antiviral agents and anticancer drugs (*www.csixty.com*) and biosensors for diagnostic applications (Anonymous, 2001); a protective agent against iron-induced oxidative stress (Lin et al., 1999); and an *in vitro* antibacterial agent (Da Ros et al., 1996).

The exploration of buckytubes in biomedical applications is also underway. Multiwall carbon nanotubes have been used for immobilization of proteins, enzymes, and oligonucleotides (Lin et al., 2004). Significant progress has been made within the last few years in an effort to overcome some of the fundamental and technical barriers toward bioapplications of carbon nanotubes, especially on issues concerning solubility in water, biocompatibility, modifications of carbon nanotubes with various biological and biologically active compounds, and both design and fabrication of biosensor prototypes (Lin et al., 2004).

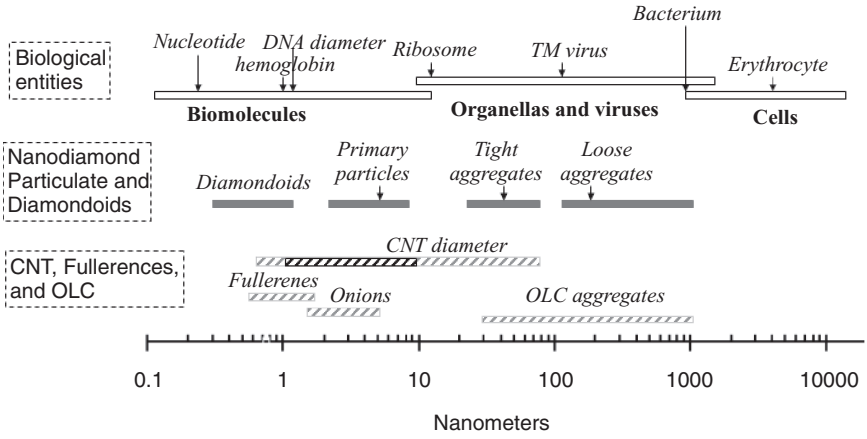

Figure 15.1 The sizes of typical bio-entities compared to those of nanocarbon structures. For nanodiamond particulate, characteristic sizes are shown for nanodiamonds of detonation origin. Arrows correspond to maxima in size distributions of nanodiamond primary particles, tightly and loosely bonded aggregates (particularly sizes of aggregates in aqua solutions). For CNTs, a range of typical SWCNT diameters (1–10 nm) is highlighted. Size range for onions corresponds to single carbon onions with low concentration of defects (maximum size up to 70 shells); onion-like carbons (OLCs) correspond to the structures obtained by annealing of nanodiamonds of detonation origin.

Nanodiamond particles and their derivatives, diamondoids and their derivatives, and ultrananocrystalline diamond (UNCD) films all have high potential in biotechnological and biomedical applications. UNCD films have been suggested to be the ideal platforms for future biochips and biosensors because of their superior mechanical, thermal, and chemical properties as compared to those of glass, silicon, and gold surfaces (Yang et al., 2002). UNCD particles had been probed in the separation of proteins (Bondar and Puzr, 2004), fabrication of integrated biochips and sensors (Puzyr et al., 2004a), and even in anticancer applications (Dolmatov, 2001).

In general, multifunctional hierarchical structures consisting of nanoparticle derivatives of organic and inorganic molecular entities began to play increasingly important roles in a variety of applications in nanobiotechnology (Niemeyer, 2001), genomics (Wengel, 2004), drug discovery (Ozkan, 2004), and nanomedicine (Freitas, 2003). For example, zero-dimensional nanostructures reported for medical applications include gold and magnetic nanoparticles, semiconductor quantum dots, a wide variety of polymer-based nanoparticles, nanoshells consisting of metals and dielectrics, and many others. Nanoparticles act as potential carries for

several classes of drugs such as anticancer agents, antihypertensive agents, immunomodulators, and hormones; and macromolecules such as nucleic acids, proteins, peptides, and antibodies. An absence of narrow fractions of nanodiamond particulate on the market hindered their biomedical applications. Recently, however, production of narrow fractions of ND (5 nm sized particle suspensions; several fractions within the 40–100 nm size range as well as fractions above 100 nm) has been achieved in research laboratories (Chapter 3 of this book and private communications). In combination with the advances in the production of high-purity particles and the fact that UNCD particles of detonation origin are relatively inexpensive (compared to fullerenes, pure carbon nanotube (CNT), and gold particles, for example), a fast growth of bioapplications of ND particulate is expected.

This chapter will be organized as follows: in the next section different approaches to the surface functionalization of ND particles, that is, the key in successful biomedical applications, will be summarized, followed by a discussion of modification of diamond surfaces with nucleic acids and proteins. After that both current and potential applications of diamond films and particles in the areas of biosensing and medicine will be addressed. The concluding section will summarize results reported on the biocompatibility of ND, the paramount property in the biomedical applications of artificial nanostructures.

15.1 Functionalization of ND with Heteroatoms and Chemical Groups

Diamond possesses a number of distinct properties that make it an attractive biotechnological material. Although natural diamond is highly hydrophobic, hydrophilic surface groups, important for bioapplications, can be generated on a diamond surface by heating to high temperature in an oxygen atmosphere and using ion bombardment and other rather aggressive treatments. ND particles synthesized by detonation have numerous oxygen-containing chemical groups on the surface and, thus, are intrinsically hydrophilic. The detonation ND particles are 4–5 nm round-shaped monocrystals that form tightly and loosely bond aggregates of about 50 nm and 100–200 nm in diameter, correspondingly. Detonation ND possesses a very large specific surface area (300–400 $m^2 g^{-1}$) (Dolmatov, 2001), which is an important factor for bioapplications. Detonation ND is likely to have a significant number of unpaired electrons that make it an efficient free radical scavenger and opens up the

opportunity for its use in medicine (Kulakova et al., 2000; Nachalnaya et al., 2000).

In general, the size, purity, and surface chemistry of detonation ND varies considerably from one manufacturer to another. The composition of the explosive mixture, coolant media, chamber size, and consequent purification of detonation soot are all important factors in the manufacture of UNCD particles with the desirable physical and chemical properties of their surface (Donnet et al., 1997). The methods of extraction and purification of ND from the detonation product may include ozone treatment, oxidation by different reagents with/without catalysts, treatment with acids, modification of the ND surface in gaseous and liquid media (Kulakova, 2004), selective inhibition of ND oxidation (Chiganov, 2004), and many others. Disaggregating of detonation ND can be achieved, for example, by its graphitization in a N_2 atmosphere at 1000 °C followed by oxidation in air at 450 °C in order to remove the surface graphite layer. In this way, the average size of ND aggregates can be reduced to 50 nm or less with a very high yield (Xu and Xue, 2004).

Dispersion efficiency and stability of colloidal solutions of ND in water is important for ND applications in nanobiotechnology and medicine, and is determined by the electrostatic, hydration, and hydrophobic (the tendency of lypophilic ND to form aggregates in an aqueous solution) interactions among the particles (Xu et al., 2005a). Within the last few years a number of new methods have been introduced to control ND solubility in water by biological and chemical modifications of the ND surface. To obtain stable suspensions of well-dispersed ND particles in water the *mechanochemical* procedure has been developed, which employs a set of different mechanical treatments (high-power sonification or vibration milling techniques) along with the application of surfactant agents (Xu et al., 2005b; 2005c). The mechanochemical modification with anionic surface modifiers increased the zeta potential and lowered the amount of hydroxyl groups and the size of individual particles (Zhu et al., 2004). The mechanochemical processes were also successfully applied for the preparation of stable highly dispersed ND suspensions in non-polar solvents (Xu et al., 2004): an oil suspension of ND particles with an average size of 55 nm was prepared and stored for 6 months without any visible signs of sedimentation.

There has been steady progress in the development of *chemical* methods of ND surface modification as well. A summary of methods of altering the ND surface chemistry with the final purpose of biofunctionalization is illustrated in Fig. 15.2. Various organic molecules can be attached to polycrystalline diamond films when under irradiation with UV

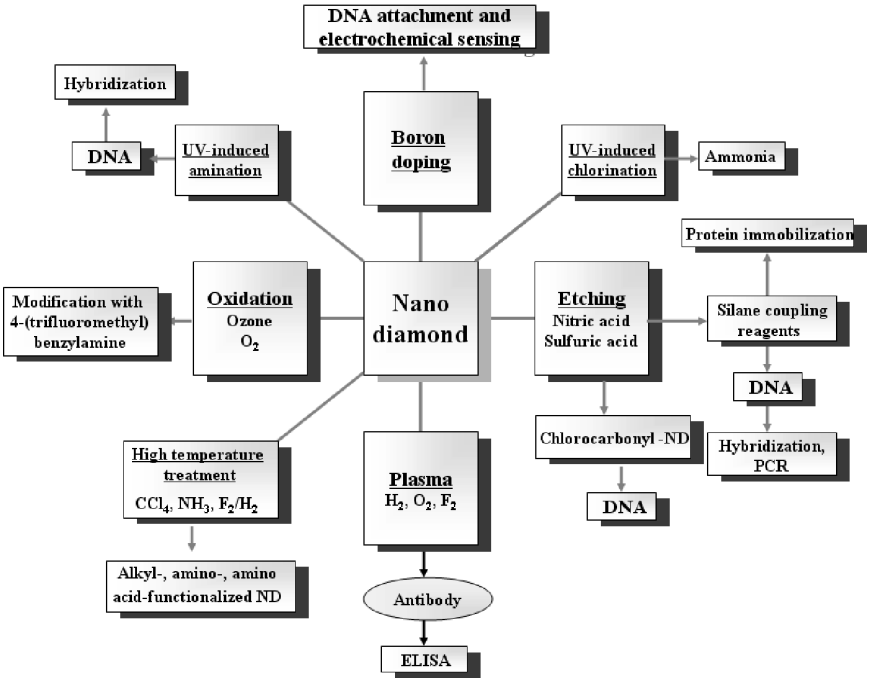

Figure 15.2 Schematic summary of approaches for alteration of nanodiamond surface groups allowing further biofunctionalization.

light. Prior to exposure to UV light the hydrogen-terminated diamond surface must be coated with a thin film of the solution containing organic molecules in order to be immobilized. By attaching molecules with specific protecting groups and removing protecting groups after the attachment, it is possible to obtain diamond surfaces functionalized with carboxyl or primary amine groups that may facilitate further steps in chemical modification of diamond surfaces such as DNA and protein immobilization (Strother et al., 2002).

To increase ND solubility in water and prepare the ND surface for biomolecule attachment, *oxidation* of the ND surface is frequently required (Fig. 15.2). Under mild conditions the diamond surface can be directly functionalized with carboxylic acids by initiating radical reactions (Tsubota et al., 2004). However, the number of carboxylic acid residues introduced on the diamond surface may be low in some cases. Indeed, oxidation of ND does not proceed easily under the mild conditions. In an aqueous slurry, ND of 4 nm size may react with ozone, though a very long time is needed in order to functionalize the surface of ND with the ketonic groups (Cataldo and Koscheev, 2003). In air ND may suddenly explode

above a temperature of 450 °C. The functionalization of NDs at elevated temperature affects both their size and surface chemistry. The weight of ND particles was reported to decline by 11.5% as a result of heating at 900 °C in an inert atmosphere (Cataldo and Koscheev, 2003). Spherical diamond powder with a particle size ranging from 150 to 600 nm can be oxidized in an oxygen atmosphere at 450–610 °C (Lee et al., 2004). The oxidized diamond powders were further successfully functionalized by reacting with 4-(trifluoromethyl)benzylamine containing the reactive amino group (Lee et al., 2005). Under certain conditions the high rate of diamond oxidation may result in an explosive process. Ida et al. (2003) have investigated the reactivity of hydrogenated diamond surfaces with peroxide radical initiators such as benzoyl peroxide, lauroyl peroxide, dicumyl peroxide, and di-*t*-butyl peroxide. With benzoyl peroxide, they detected IR peaks that were then assigned to the aromatic C—H and C═O stretching vibrations. The C═O stretching vibration was observed after the diamond was exposed to lauroyl peroxide. The areas under the peak of spectra determined with Fourier transform infrared spectroscopy (FTIR) increased with reaction time and amount of reagent. Dicumyl peroxide and di-*t*-butyl peroxide did not react with diamond surfaces. While the yield of reaction of diamond surface with radical species generated from benzoyl peroxide depends on the organic solvent used, the same functional groups were synthesized in toluene, tetrahydrofuran, N,N-dimethylformamide, cyclohexane, and hexane (Tsubota et al., 2002a). The hydroxyl groups located on the surface of diamond powders, which was treated either with sulfuric acid alone or with a mixture of sulfuric and nitric acids, can be reacted with metoxy groups of silane-coupling reagents (3-aminopropyltrimethoxysilane, 3-mercaptopropyltrimethoxysilane, or *n*-octyltrimethoxysilane) with the formation of stable modified diamonds (Tsubota et al., 2002b). The silane-modified NDs can be used for surface synthesis of DNA and protein immobilization.

The substantial increase in the number of surface C—H groups was achieved by the *gas treatment* of ND powder with H_2, plasma-ionized hydrogen, N_2, methane and air, and in vacuum at different temperatures (Jiang et al., 1996). Surface decomposition, decarbonylation, and decarboxylation were likely to be the main reactions. The H-terminated ND surfaces can be further reacted photochemically ($\lambda = 254$ nm) with long-chain ω-unsaturated amines to produce a homogeneous layer of amine groups for consequent DNA attachment (Yang et al., 2002).

ND purification and functionalization can also be carried out using gas and vapor reactive media (Fig. 15.2). The chlorinated diamond was pre-

pared by Sotowa et al. (2004) by irradiating hydrogenated diamond with UV light in the presence of elemental chlorine. The formation of chlorinated diamond was confirmed by diffuse reflectance FTIR, which revealed a strong peak corresponding to the C—Cl stretching. The researchers then treated the chlorinated diamond surface further with ammonia and found that diamond amination is a temperature-dependent process and results in the formation of NH_4^+; C═N and NH_2; and imines at room temperature, 100 °C, and 200 °C, respectively. High-temperature treatment of detonation ND with hydrogen, CCl_4, or NH_3 has been studied recently by Spitsyn et al. (2005). ND, which was annealed in hydrogen flow at 850 °C for 5 h, possessed about 1000 cal g^{-1} lower combustion heat than non-modified ND powder. Moreover, the initial dangling bonds density of ~1.16×10^{20} spin/cm^3 was reduced 1.5 times after the treatment with hydrogen. After treatment in a CCl_4/Ar mixture at 450 °C for 0.5–3 h the hydrophilicity of ND was changed significantly: the atmospheric water vapor readsorbance was at least 20 times lower than in the ND samples treated in pure Ar. After treatment in a NH_3 flow at 600 °C for 70 min the number of oxygen-containing groups had decreased and atmospheric water vapor readsorbance was four times lower than in the initial ND samples. A number of characterization methods such as chemical analysis, Raman, FTIR, electron spin resonance (ESR), and chromatomass spectrometry confirmed the possibility of extensive modification and controlled functionalization of the ND using gas treatment (in terms of hydrophilic/hydrophobic or acidic/basic ND termination) (Spitsyn et al., 2005). This prevents agglomeration of hydrophilic and hydrophobic detonation ND in polar and non-polar solvents, correspondingly.

Fluorination is another efficient method for ND chemical modification that enables a variety of applications in engineering and biological sciences (Fig. 15.2). Treatment of detonation UNCD powder (1–2 μm sized particles composed of 3.5–6.5 nm diamond nanocrystals, >97% purity) with a F_2/H_2 mixture at 150–470 °C resulted in the formation of fluorinated NDs with 8.6 at.% fluorine (Liu et al., 2004). The fluorinated ND material was then used as a precursor for preparation of alkyl-, amino-, and amino acid-functionalized NDs that showed an increased solubility in polar solvents and reduced particle agglomeration (Liu et al., 2004). Application of fluorinated ND has been found in cost-effective synthesis of diamond coatings covalently bonded to glass surfaces (Liu et al., 2005). Before that the production of diamond thin films could only be achieved by chemical vapor deposition that requires heating to 1000 °C. Liu et al. (2005) applied a silane coupling agent, 3-aminopropyltriethoxysilane, to attach fluoro-ND to the glass slide surface, which was preliminary func-

tionalized with terminal amino groups. Using atomic force microscopy (AFM), SEM, and X-ray photoelectron spectroscopy (XPS) analysis it was established that surface-bonded fluoro-ND particles were closely packed and had an average size of 10–40 nm. The fluoro-ND, which is covalently attached to the surface of the glass slide, can be further modified by chemical substitution of residual fluorine.

15.2 Modification with Nucleic Acids

Nanoparticles are valuable platforms in controlled drug delivery and can be administered via most routes to carry various therapeutics, anticancer, antiviral, antibacterial, and antihypertensive agents, immunomodulators, hormones, antibodies, proteins, peptides, and nucleic acids to isolated cells, tissues, and organs (Bala et al., 2004; Ozkan, 2004). Successful design of highly efficient drug delivery systems may solve many problems faced by present-day medical sciences.

In gene therapy, genes are delivered to the cell nucleus allowing cells to produce therapeutic proteins. Gene delivery is achieved using either viral or non-viral vectors. Viral vectors are genetically engineered adenoviruses, retroviruses, and other viruses that are very efficient when used for gene transfer *in vivo*. Methods of non-viral gene delivery, including nanoparticle carriers, represent a small fraction of all methods used for transfection *in vivo*. However, they have gradually become as popular as the viral vector-based technology. In the development of non-viral technologies, the main goal is to have a transfection method that is efficient, reproducible, non-toxic, and allows the prolonged gene expression to occur. Efficiency of targeted delivery of nanoparticles loaded with biologically active molecules is affected by many factors including particle size, surface charge, and chemistry, and mechanism of target recognition. Over the years, a number of natural and synthetic materials have been used to prepare nanoparticles, and their stability, biocompatibility, and biodegradability were investigated (Bala et al., 2004). In some cases nanocarriers protect naked DNA from nucleases while allowing DNA plasmids to pass the cell membrane and get into the nucleus (Kneuer et al., 2000; Roy et al., 2005). To optically monitor intracellular trafficking and gene transfection events Roy et al. (2005) first prepared fluorescently labeled organically modified silica nanoparticles for use in non-viral gene delivery and biophotonics applications and then showed that these nanoparticles can serve as a delivery platform with superior efficacy in targeted drug therapy and as the real-time monitoring of drug action. The highly monodispersed stable water

suspensions of the organically modified silica nanoparticles, which were labeled with the fluorescent dyes and functionalized by amino groups, were prepared using micelle chemistry. The nanoparticles efficiently bound DNA due to positively charged amino groups and protected it from digestion by DNase I. Imaging by fluorescence confocal microscopy confirmed that *in vitro* cells efficiently took up the nanoparticles in the cytoplasm, and the nanoparticles delivered DNA to the nucleus. Very recently Bejjani et al. (2005) reported the breakthrough discovery that polylactic nanoparticles enable *in vivo* gene transfer and expression with a high efficiency. Solid nanoparticles can be used to deliver drugs and biologically active molecules to any body organ including the brain, because they can cross the blood–brain barrier (Lockman et al., 2002; Koziara et al., 2003). The nanoparticles that are biodegradable in a controlled way are likely to become the carriers of choice for *in vivo* non-viral gene delivery. Surface-modified and appropriately labeled ND particles may also serve as an efficient platform for *in vivo* transfection. However, because of the very low, if any, biodegradability of ND, ND nanoparticles, when applied *in vivo*, must be of a size small enough to allow their excretion by the kidney or applied cutaneously.

Immobilization of DNA on diamond surfaces via covalent bonding has been explored intensively. For example, Ushizawa et al. (2002) first modified diamond powder with particle sizes of 1–2 μm (Fig. 15.3) by oxidation in a heated mixture of sulfuric acid and nitric acid and then converted it in chlorocarbonyl–diamond by reacting with thionyl chloride at 50 °C for 1 day. Chlorocarbonyl–diamond was then reacted with thymidine in the presence of 4-dimethylaminopyridine. The DNA was attached to the 3′-end of diamond-attached thymidine by 5′-end phosphatization. The formation of ester bonds was confirmed by diffuse reflectance FTIR spectroscopic analysis. Preparation of DNA-modified diamond films for use in hybridization has received increased attention. The chemical stability of diamond surfaces is substantially greater than that of gold or silicon surfaces (Lu et al., 2004), and the DNA molecules attached to the diamond surfaces are easily accessible to enzymes. Nanocrystalline diamond thin films covalently modified with DNA oligonucleotides following the photochemical modification of H-terminated surfaces with amine groups provide a very stable and highly selective platform for the surface hybridization reaction (Yang et al., 2002). After linking DNA to the amine groups, hybridization reactions with fluorescently tagged complementary and non-complementary oligonucleotides did not reveal any non-specific adsorption, with extremely good selectivity between matched and mismatched sequences (Yang et al., 2002). In a similar manner, hydrogen-

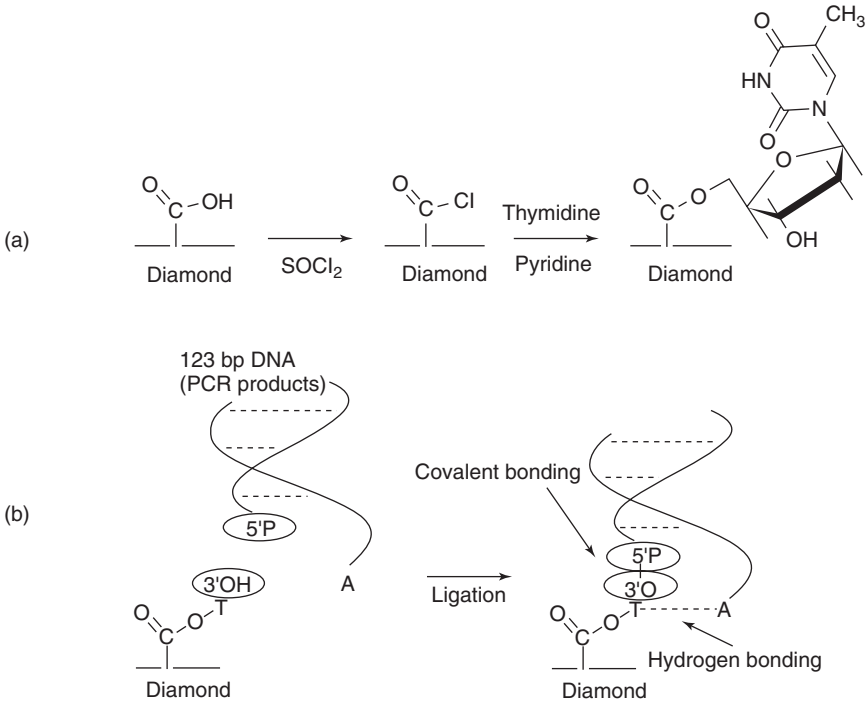

Figure 15.3 Immobilization of DNA on diamond surface. (a) thymidine-immobilized diamond powder is obtained by diamond surface carboxylation (acid treatment), followed by formation of chlorocarbonyl surface groups reacting with thymidine in anhydrous pyridine. (b) DNA-ligated diamond through thymidine ester. (From Ushizava et al., 2002, with permission.)

terminated diamond substrates were photochemically converted into amine-terminated surfaces following by linking to thiol-terminated DNA oligonucleotides reported by Knickerbocker et al. (2003). The DNA hybridization on DNA-modified polycrystalline diamond is highly specific and when compared to the hybridization on DNA-modified surfaces of crystalline silicon shows that the diamond surface exhibits superior chemical stability (Knickerbocker et al., 2003). DNA-modified diamond surfaces are particularly suitable for invasive cleavage reactions, in which introduction of target DNA to solution results in the specific cleavage of surface-bound probe oligonucleotides, permitting SNP (single nucleotide polymorphisms) detection. The sensitivity of the analysis can be improved 100 times by replacing the DNA-modified gold surface with a more stable DNA-modified diamond surface (Lu et al., 2004). CVD diamond has also found some applications for DNA immobilization. Using thymidine as a

linker molecule, the fragment of the human *PKU* gene was covalently bound to the CVD diamond film by Wenmackers et al. (2003).

Boron-doped diamond (BDD) thin films with enhanced conductivity offer a substantial advantage for use in DNA hybridization analysis. For example, Gu et al. (2004) electropolymerized a thin layer of polyaniline/poly(acrylic acid) onto the diamond surface. The carboxylic acid residues in the polymer film enhanced the electron transfer between DNA and a BDD surface and acted as the binding sites for DNA attachment. Both fluorescence microscopy and cyclic voltammograms indicated that the polymer-modified BDD did not show significant non-specific DNA adsorption, while providing a stable transduction platform for DNA detection by hybridization.

The absence of efficient technology for *in vivo* delivery of oligonucleoticles limits many therapeutic applications. For successful application *in vivo*, in most cases *in vitro* delivery platforms should be extensively modified in order to provide targeted drug delivery. The adamantane-based materials have found application in the preparation of carriers for *in vivo* nucleic acid delivery because they can be modified by using cyclodextrin/adamantane host/guest interactions to provide the particles suitable for systemic application (Pun and Davis, 2002). Transferrin-modified nanoparticles containing DNAzymes (DNA enzymes that are RNA-cleaving phosphodiester-linked DNA-based enzymes, which cleave their target mRNA in a gene-specific fashion) for targeting tumors were prepared by using conjugates of adamantane with poly(ethylene glycol) and administered to tumor-bearing nude mice by intraperitoneal bolus and infusion, intravenous bolus, and subcutaneous injection. DNAzymes packaged in polyplex formulations were concentrated and retained in tumor tissue, whereas unformulated DNAzyme was eliminated from the body within 24 hours after administration (Pun et al., 2004). In wound healing therapy, the localized delivery of growth factors is achieved by gene transfer to the wound site. Synthetic biocompatible materials prepared with a linear, beta-cyclodextrin-containing polymer and an adamantane-based crosslinking polymer are very suitable for *in vivo* gene delivery to fibroblasts via the inclusion of adenoviral vectors in the synthetic construct (Bellocq et al., 2004). Gene-deleted adenoviral vectors were originally developed as delivery vehicles for use in gene therapy trials and are currently being developed as HIV vaccines and in other medical applications.

From a different perspective, in biological materials science and in rapidly emerging angstrom-scale chemical engineering the nucleic acids are thought to find many applications in the fabrication of self-assembling,

multi-dimensional materials (Wengel, 2004). ND and diamondoid structures can be valuable candidates for crosslinking of oligonucleatides in carbon-based systems.

15.3 Interaction with Proteins

Both selective adsorption of proteins and their immobilization onto surfaces of ND particles (Fig. 15.4) may be advantageous in nanobiotechnological applications and medicine.

Fibrinogen is widely accepted as an indicator in a biocompatibility test and material-caused inflammation. The adsorption of human fibrinogen on the surface of chemical-vapor-deposited diamond has been studied by Tang et al. (1995) and was the first report on the diamond interaction with

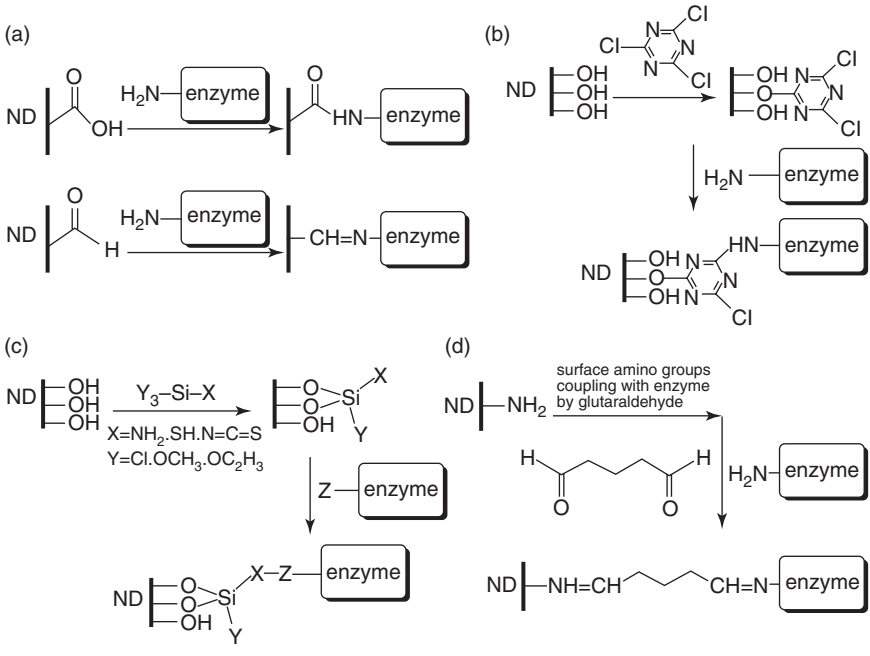

Figure 15.4 Role of hydroxyl-, carboxyl-, and amino groups in possible immobilization of proteins on nanodiamond. (a) Covalent linkage of enzyme ND surface by coupling of carboxy functionalities; (b) attachment of enzyme via 2,4,6-trichlorotriazine to ND surfaces; (c) siloxane assemblies on ND surfaces for the immobilization of enzymes, where Z is a complementary functional group for X; (d) covalent linkage of enzyme to ND surfaces by coupling of amino functionalities. (Adapted from Choi, 2004.)

a protein and its biocompatibility. The CVD diamond was found to be biologically compatible to the same extent as titanium and stainless steel.

In 1995 Kossovsky et al. demonstrated that surface-modified ND particles with a size ranging from 5 to 300 nm provided both conformational stabilization and a high degree of surface exposure to protein antigens and used them to generate antibodies. Recently Huang and Chang (2004) developed the universal procedure for protein immobilization onto the surface of 5 nm ND particles. It starts with ND particles with strong acids followed by modifying their surface with poly-L-lysine. Covalent attachment of proteins is then carried out by activating the amine-terminated ND to react with the heterobifunctional linker SSMCC followed by mixing with the protein. The researchers successfully immobilized both Alexa Fluor 488 dye and yeast cytochrome *c* using the free SH group for linkage. More information on the application of protein-modified ND in biosensing and biotechnology can be found in Section 15.5.

Hollow nanoparticles are thought to be the most suitable carriers of proteins and peptides susceptible to degradation. Many nanoparticles can be made hollow by heating at high temperature, treating with strong acids, alkali, and organic solvents, or using gentle chemical treatment to encapsulate susceptible organic molecules such as proteins, peptides, and enzymes or others inside the cavity of hollow nanoparticles (Sharma et al., 2005). ND particles produced by detonation of the mixture of trinitrotoluene and cyclomethylenetrinitramine have a tetragonal structure and according to Vereshchagin and Yurjev (2003) are hollow particles with an inner diameter of 18.94 Å and outer diameter of 25.47 Å. Yurjev et al. (2005) used synchrotron X-ray diffraction to characterize these spherical hollow detonation NDs that can be modified even further by grinding in a planetary mill.

The surface-modified NDs and diamondoids are expected to find vast application in the development of a new generation of protein delivery platforms and antigen carriers because they can be readily modified to both carry and stabilize biologically active molecules, proteins, and enzymes. In addition, these particles are rigid, biocompatible, available in different shapes, and span the subcellular size range (Fig. 15.1).

15.4 Application in Biosensors and Medicine

A biosensor (Fig. 15.5) generally comprises biomolecules sensing an analyte, e.g., DNA, antibody, receptor, or enzyme, and the electrochemical, optical, calorimetric, or piezoelectric transducer that detects an attach-

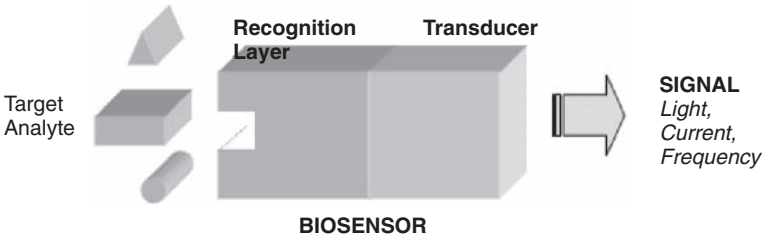

Figure 15.5 Schematic of biosensor: coupling of biorecognition with signal transduction.

ment of an analyte to the biorecognition layer (Deisingh and Thompson, 2004). The physiochemical properties that determine the analytical characteristics of biosensing devices are surface characteristics of the sensing area and its size, as well as intrinsic properties of the material. In the past few years, significant advances have been made toward the development of both biosensors and biochips for single-cell analysis, detecting of pathogens and toxins (Vo-Dinh et al., 2001), and other biological and medical applications.

Diamond films occupy a special place as an electrode material in biosensors. When made sufficiently electrically conducting by boron doping, thin-film and free-standing diamond electrodes exhibit remarkable chemical resistance to etching, a wide potential window, low background current responses, mechanical stability toward ultrasound-induced interfacial cavitation, a low stickiness in adsorption processes, and a high degree of tunability of the surface properties (reviewed by Compton et al., 2003). Tatsuma et al. (2000) have examined direct electron transfer from BDD electrodes to heme peptide and horseradish peroxidase for the application to H_2O_2 biosensors. Diamond electrodes exhibit low sensitivity to interfering agents and may become a capable H_2O_2 biosensor.

Nanocrystalline diamond films can be both a platform for biofunctionalization and serve as an electrode in biosensors based on electrochemical reactions. Different proteins can be covalently attached to the hydrogen-terminated nanocrystalline diamond films modified with amino groups and remain fully functional. Hartl et al. (2004) functionalized nanocrystalline diamond electrodes with catalase and detected a direct electron transfer between the redox centre of the enzyme and the diamond electrode. Also, the electrode was found to be sensitive to hydrogen peroxide. Hydrogenated diamond can gain surface conductivity after exposure to air and by transfer doping with C_{60} resulting in a significant rise

in two-dimensional conductivity (Strobel et al., 2004). The fully hydrogen terminated diamond surfaces are not pH sensitive but can gain this sensitivity after a mild surface oxidation by ozone (Garrido et al., 2005). The difference in DNA adsorption on the H- and O-terminated diamond surfaces may be useful in the nanofabrication of biosensors (Tachiki et al., 2003). Compared to multiwalled carbon nanotube-based electrodes, BDD electrodes exhibit less selective voltammetric responses to the different biomolecules and slower electron-transfer kinetics. BDD electrodes have no intrinsic selective response to L-ascorbic acid, and surface modification by anodic polarization is required to resolve L-ascorbic acid and dopamine (Poh et al., 2004). Highly conductive BDD electrodes are especially suited for electrochemical detection of nucleic acids in aqueous solutions. Their distinctive features are high reproducibility, small background currents at high positive potentials, and robustness under extreme conditions (Prado et al., 2002). Importantly, BDD electrodes can be used in analysis involving a heating step and ultrasonic treatment. Well-defined peaks, observed with tRNA, single- and double-stranded DNA, and 2′-deoxyguanosine 5′-monophosphate were directly assignable to the electrooxidation of deoxyguanosine monophosphate (Prado et al., 2002).

Polycrystalline diamond films deposited by microwave plasma CVD were incorporated in the design of four different glucose sensors by Troupe et al. (1998). While a diamond–platinum–glucose oxidase sensor was affected by the presence of electroactive chemicals in blood, usage of BDD as a conducting electrode in place of the platinum provided a strong and repeatable response to glucose. The sensor that was fabricated with the surface-modified diamond allowed attachment of biologically active molecules and electron transfer from glucose oxidase to the electrode. This approach received further development in a study by Loh et al. (2004). However, a 3,3′-diaminobenzidine-electropolymerized carbon nanotube-based electrode outperformed the diamond one in terms of selectivity and sensitivity. In another attempt to develop a ND-based biosensor Huang et al. (2004) immobilized polyclonal antibodies against *Salmonella typhimurium* and *Staphylococcus aureus* on nanocrystalline diamond films and evaluated the efficacy of immobilization by enzyme-linked immunosorbent assay (ELISA). The immobilization of antibodies and attachment of bacteria measured by SEM were more efficient on a surface of air plasma-treated diamond than on a surface of diamond treated preliminarily with the hydrogen plasma. The plasma-oxidized surface of ND was more hydrophilic and was terminated with hydroxyl and carbonyl groups.

Modified ND particles and films have been used in heterogeneous and electrochemical oxidation catalyses and related applications, and in electrochemical analysis (Bogatyreva et al., 2004; Song et al., 2004; Yang et al., 2005). Using the new amperometric biosensors designed with monocrystalline diamond and L- and D-amino acid oxidases, Stefan et al. (2004) conducted differential pulse voltammetric assay of L-pipecolic and D-pipecolic acids in serum samples with a low limit of detection. The impedance of the diamond film can be affected by DNA hybridization at the interface that induces a field effect in the diamond space-charge layer. By identifying a range of impedances, where the impedance is dominated by the diamond space-charge layer, and measuring the interfacial impedance, it is possible to directly monitor DNA hybridization. No DNA labeling is required. Frequency-dependent interfacial electrical properties of nanocrystalline diamond films that were covalently linked to DNA oligonucleotides were changed significantly in the presence of complementary DNA oligonucleotides, with only minimal changes due to the presence of non-complementary DNA oligonucleotides (Yang et al., 2004). The electrolyte–solution–gate field-effect transistors with H-terminated polycrystalline diamond surface were shown to be sensitive to Cl^- and Br^- and can find application in cystic fibrosis tests (Song et al., 2003). The capability for biomolecular recognition was provided to the highly sensitive field-effect transistor (Bio-FET) made of a nanocrystalline diamond thin film by linking human immunoglobulin G to the diamond surface. Electrical measurements showed that the Bio-FET responded specifically to the anti-IgG antibody (Yang and Hamers, 2004).

Puzyr et al. (2004a) have recently developed a prototype ND-based biochip for use in bioluminescent analysis. The biochip incorporates aluminum oxide film-adhesive layer-deposited ND particulate-luciferase, which retained substantial enzymatic activity.

It is also worth mentioning here that diamond sensor applications include high-sensitivity detection of charged particles such as protons and pions that are possible due to diamond's high radiation tolerance. A CVD diamond strip detector that can be used for tracking and detection of charged particles has been recently introduced on the market. Fast charged particles create charge carriers in the irradiated diamond followed by induction of an electric charge on the strips. Similarly, detonation ND and monocrystal CVD diamonds may be used for detecting both intermediate and high-energy heavy ions and in other instrumental analysis (Adam et al., 2002; Berdermann et al., 2004).

Because both carboxylated and oxidized ND exhibit a remarkably high affinity for proteins, proteins in dilute solutions can be easily captured by

NDs with a size of 100 nm, separated by centrifugation, and analyzed by matrix-assisted laser desorption/ionization time-of-flight mass spectrometry (MALDI-TOF-MS) without any need for pre-separation of the adsorbed proteins from ND (Kong et al., 2005). With the dilute mixed solution of cytochrome c, myoglobin, and albumin that preferentially adsorbs on a hydrophilic surface, the developed method offered significantly higher sensitivity than conventional MALDI-TOF-MS and had a limit of detection of 100 pM for a 1 mL sample solution. The potential of ND-assisted MALDI-TOF-MS for use in clinical proteomics was demonstrated with human blood serum analysis (Kong et al., 2005). If necessary, surfaces of ND particles can be modified to decrease non-specific protein adsorption and optimize their use for bioanalysis (Lasseter et al., 2004). Application of detonation NDs facilitated separation of *Obelia longissima* apoobelin from the recombinant *E. coli* cell extract and made possible the preparation of purified protein with a yield of up to 38% (Bondar et al., 2004).

Within the ND family, to a large extent medical applications have been developed for diamondoids. Diamondoids such as adamantane derivatives (single-molecule unit of diamond with the formula $C_{10}H_{16}$) have been used in pharmacology, clinical medicine, and biosensing (Freitas, 2003). Until recently the cholinesterase inhibitors were the only available drugs for the treatment of Alzheimer's disease, which is one of the leading causes of death for people over 65 years of age. Unfortunately, the cholinesterase inhibitors cannot stop the process of neurodegeneration and just symptomatically enhance the cognitive state to some degree (Sonkusare et al., 2005). In Alzheimer's disease, neuronal death is caused by glutamate excitotoxicity mediated through the N-methyl-D-aspartate (NMDA) receptors making them an excellent target for preventing the disease. Excitotoxicity is excessive exposure to the neurotransmitter glutamate or overstimulation of its membrane receptors, leading to neuronal injury or death. Activity of the nmDA receptor is also essential for normal neuronal function, and neuroprotective agents that fully block nmDA receptor activity will have severe side effects (Lipton, 2004). Memantine (1-amino adamantane derivative) is the potent nmDA-receptor antagonist that blocks excessive NMDA receptor activity without disrupting normal activity through its action as an uncompetitive, low-affinity, open-channel blocker. It also has beneficial effects in Parkinson's disease, stroke, epilepsy, central nervous system (CNS) trauma, amyotrophic lateral sclerosis, drug dependence, chronic pain, depression, glaucoma, and severe neuropathic pain. Memantine is available in Europe and has been recently approved for treatment of dementia in the USA. At the present time the

second-generation memantine derivatives, which take advantage of the additional modulatory sites in the NMDA receptor that could also be used for clinical intervention, are under development (Lipton, 2004; Sonkusare et al., 2005). Many adamantane derivatives possess antibacterial, antiviral, and antifungal activity (Wang et al., 1998; El-Sherbeny, 2000; Orzeszko et al., 2002; El-Emam et al., 2004). For example, 5-(I-adamantyl)-2-substituted thio-1,3,4-oxadiazoles and 5-(1-adamantyl)-3-substituted aminomethyl-1,3,4-oxadiazoline-2-thiones exhibit substantial antimicrobial activity against Gram-positive bacteria and the antiviral activity against HIV-1 significantly reducing viral replication at 2–50 $\mu g\,mL^{-1}$ concentrations (El-Emam et al., 2004). Adamantane-based drugs, namely, amantadine and tromantadine, are excreted unaltered in the urine and are not susceptible to hydroxylation (Koppel and Tenczer, 1985). In 2005, Hodek et al. discovered that adamantane, diamantane, triamantane, 2-isopropenyl-2-methyladamantane, and 3-isopropenyl-3-methyldiamantane inhibited cytochromes P450 of subfamily IIB by binding to the active site and, thus, could be potent inhibitors for hepatic oxidative drug metabolism in humans. Theoretical and experimental values of the dissociation constant of cytochrome P450 complexes with the diamondoids were in good agreement and confirmed the high potency of identified inhibitors. Bananins, the antiviral agents that possess a trioxa-adamantane moiety attached to a pyridoxal derivative, were shown to be potent inhibitors of the SARS (severe acute respiratory syndrome) coronavirus helicase and can prevent replication of animal SCV (SARS-related coronavirus) (Tanner et al., 2005). Recently, the adamantane derivatives have been identified as the potential drugs acting on the P2X(7) receptor, which is involved in signaling in many inflammatory processes (cytokine release, NO generation, cytotoxicity, killing of intracellular pathogens) (Baraldi et al., 2004; Romagnoli et al., 2005).

Because ND is not mutagenic or toxic (oral LD50 value for rats is 7 $g\,kg^{-1}$), can neutralize free radicals, and possesses a very large surface area, it was suggested that detonation ND particles may have some anti-tumor activity (Dolmatov and Kostrova, 2000; see also Chapter 13). Indeed, mice with Erlich ascetic carcinoma that were given supplements with the ND suspensions were more active and lived almost 40% longer than non-treated animals. In 2001, Dolmatov reported the results of a new medical study of the possible oral administration of water suspensions of NDs to terminally ill cancer patients. The oral administrations of ND did not result in any side effects and, moreover, were moderately beneficial in some cases.

15.5 Biocompatibility of ND

Diamond has the outstanding reputation of a chemically inert and uniquely biologically compatible material that has found a number of applications in medicine (Freitas, 2003). Diamond is biocompatible in both bulk and particulate forms. In orthopedic surgery the use of a diamond coating on the metallic components reduces generation of macrophages and improves the wearability of devices (Santavirta et al., 1999). In addition, nanocrystalline diamond films show an excellent resistance to bacterial colonization (Jakubowski et al., 2004). The diamond-like carbon coating is also very inert and particularly suitable for use in orthopedic implants. In an early, pioneering study Thomson et al. (1991) grew mouse peritoneal macrophages and fibroblasts on tissue culture plates coated with 0.4 μm of an amorphous diamond-like carbon layer and assessed the biocompatibility both biochemically and morphologically. The diamond-like carbon coating caused no adverse effects on cells in the culture. Recently diamond-like carbon films have been reexamined and it was reported that they have good biocompatibility and high corrosion resistance (Kim et al., 2005). Additional evidence of diamond biocompatibility came from Zheng et al. (2005) who fabricated nanocrystalline diamond films (NDFs) on optical glass using microwave plasma assisted CVD and used osteoblast cell cultures and platelet adhesion tests for *in vitro* evaluation of biocompatibility of NDFs. Their results indicated that the diamond films exhibit good tissue compatibility and hemocompatibility, which makes them very suitable for biomedical applications. The excellent chemical inertness and smoothness of NDFs made them a promising material for medical implants, cardiovascular surgery, and coating of artificial heart valves (Mitura et al., 1996; 1999). In 2004 Specht et al. were able to demonstrate the ordered growth of mammalian neurons on diamond. To accomplish this the researchers patterned proteins on diamond surfaces by micro-contact printing and cultured mouse cortical neurons on these substrates. The diamond biocompatibility and the suitability of neuron interfacing with the surface make this an interesting approach for implant engineering. The high biocompatibility, corrosion resistance, chemical inertness, low friction coefficient, electrical insulation, and excellent mechanical characteristics of CVD diamond suggested that diamond-coated materials may find numerous applications in medicine (Tang et al., 1995).

In biomaterials research, it is known that the biocompatibility of a bulk material is not necessarily the same as the biocompatibility of fine parti-

cles of the same material, which may penetrate inside live cells and their organelles (Freitas, 2003). The main threat to cell viability comes from possible mechanical damage to cellular organelles and membranes. Foreign intracellular particles with a diameter of 20–200 nm do not damage cells mechanically (Lu and Rosenzweig, 2000). Detonation particles possess a rounded shape, superior lubricity characteristics, hardness, and wear resistance. The fine diamond particles and diamond-like carbon coatings were always found to be very inert and non-inflammatory (Tse and Phelps, 1970; Hedenborg and Klockars, 1989; Swan et al., 1990; Grill, 2003). When Higson and Jones (1984) treated both pig and horse neutrophils with diamond crystals, no induction of peroxide and superoxide generation was observed. The interaction of leucocytes with diamonds with a size of 4–8 μm in 0.2% diamond suspension did not cause any cell damage. No increase in degranulation and production of cell motility factors, and cell death, was observed (Swan et al., 1990). Nordsletten et al. (1996) compared particles of diamond, SiC, and hydroxyapatite in serum-free cultures of human monocytes and found that all particles were phagocytozed, and monocyte morphology changed except after the ingestion of diamond. It was concluded that diamond particles were inert in a serum-free human monocyte culture, while both SiC and hydroxyapatite had a stimulatory effect comparable to that of polymethylmethacrylate. When suspensions of phagocytosable particles of diamond and SiC in hyaluronan were introduced into a canal traversing the bone implant in rabbits neither the diamond nor the SiC particles caused any decrease in bone formation. It confirmed that particles of diamond and SiC are harmless (Aspenberg et al., 1996). Human blood cells' lack of adherence to the CVD diamond substrates, and blood clotting on diamond, produced a less rough surface than blood clotting on glass (Baranauskas et al., 2004). Recent reports on possible ND-induced damage to both white and red human blood cells *in vitro* (Puzyr et al., 2002; 2004b; 2005a) raised the question about the mechanism promoting these phenomena. Prior to use, NDs are usually modified to gain high stability in water colloids (Bondar and Puzyr, 2004), and it is not clear whether bacterial contamination, unidentified impurities, defects (Shames et al., 2002), and surfactants were not the factors involved. Indeed, in those studies, the total content of non-diamond carbon, non-combustible residue, and volatile compounds reached 16% in some samples (Puzyr et al., 2002). In contrast to these observations, Dion et al. (1993) did not notice any *in vitro* hemolysis when 14% blood solutions were treated with 0.5 g cm^{-3} diamond powder produced by De Beers Industrial Diamond Division, and the early reports on crystalline diamond-induced damage to cells were never confirmed

(Freitas, 2003). Rodil et al. (2005) reported that the diamond-like coating did not have any toxic effect on human osteoblasts cells *in vitro*. Interestingly, Monteiro-Riviere et al. (2005) found that carbon nanotubes, which were grown using a microwave plasma enhanced CVD system, accumulated within cytoplasmic vacuoles of the human epidermal keratinocytes and stimulated release of the proinflammatory cytokine interleukin 8. There are no reports on site-specific intracellular accumulation of ND particles by live cells.

As was mentioned in the previous section, administration of detonation ND particles to both Erlich ascetic carcinoma mice and terminally ill cancer patients did not result in any side effects. Moreover, it was beneficial in some cases (Dolmatov and Kostrova, 2000; Dolmatov, 2001). However, 0.002–0.01% ND suspensions administered orally to white mice over the course of 3 months did cause a substantial increase in leukocyte content in the blood of animals (Puzyr et al., 2004c). The treatment did not affect the weight of the experimental mice though. Very unexpectedly, the intravenous administration of 0.3 mL of sterile colloids of 1% modified NDs in 10% glucose to rats and dogs did not result in sickness or premature death of the animals (Puzyr et al., 2005b). When 1 mL of 1% ND was administered to a dog followed by the second administration 1 week later, the ECG tests revealed substantial changes in heart activity immediately after each treatment. However, the cardiac condition became normal again within 1 day.

The safety and effectiveness of nanosystems and platforms made of NDs will fully depend on their compatibility with human organs, tissues, cells, and cellular organelles. Extensive thorough research has yet to be done to clearly establish physiological, immunological, and cytological responses of the human body to ND particles and films.

15.6 Conclusion

In this review, methods of surface modification were discussed for the development of functionalized diamond nanoparticles for biomedical applications. To be used in biomedical applications, nanoparticles must be biocompatible, non-toxic, non-detective by immune systems, and should not induce side effects. Size control of particles is a prerequisite for biomedical applications. To meet all these criteria, the diameter of particles should be less than 100 nm and their surfaces should be modified by hydrophilic moieties. Such nanoparticles are likely to avoid uptake by the reticuloendothelial system and remain in blood at a high enough concen-

tration to reach the target organs, tissues, or cells. The surface of nanoparticles has to be preliminarily modified by functional ligands with a high affinity to a disease site to achieve site-specific delivery. In many cases, nanoparticles may encapsulate and protect therapeutic agents against enzymes and hydrolysis; it is not clear yet how nanodiamond particles can satisfy this requirement.

It is obvious from the reviewed literature that both nanodiamond particulates and films have become very popular objects in biomedical research.

References

Adam W et al. (2002) Performance of irradiated CVD diamond micro-strip sensors. *Nucl. Instrum. Methods A* 476: 706–12.

Anonymous (2001) Nanotechnology in biology: The good of small things. *The Economist* Dec. 22.

Aspenberg P, Anttila A, Konttinen YT, Lappalainen R, Goodman SB, Nordsletten L, Santavirta S (1996) Benign response to particles of diamond and SiC: Bone chamber studies of new joint replacement coating materials in rabbits. *Biomaterials* 17: 807–12.

Bala I, Hariharan S, Kumar MNVR (2004) PLGA nanoparticles in drug delivery: The state of the art. *Crit. Rev. Ther. Drug* 21: 387–422.

Baraldi PG, Di Virgilio F, Romagnoli R (2004) Agonists and antagonists acting at P2X(7) receptor. *Curr. Top. Med. Chem.* 4: 1707–17.

Baranauskas V, Fontana M, Guo ZJ, Ceragioli HJ, Peterlevitz AC (2004) Analysis of the coagulation of human blood cells on diamond surfaces by atomic force microscopy. *Nanotechnology* 15: 1661–4.

Bejjani R, BenEzra D, Cohen H, Rieger J, Andrieu C, Jeanny JC, Gollomb G, Behar-Cohen F (20905) Nanoparticles for gene delivery to retinal pigment epithelial cells. *Mol. Vis.* 11: 124–132.

Bellocq NC, Kang DW, Wang XH, Jensen GS, Pun SH, Schluep T, Zepeda ML, Davis ME (2004) Synthetic biocompatible cyclodextrin-based constructs for local gene delivery to improve cutaneous wound healing. *Bioconjugate Chem.* 15: 1201–11.

Berdermann E, Ciobanu M, Connell SH, da Costa AMOD, Fernandez-Hernando L, Oh A, Sellschop JPF (2004) Charged particle detectors made of single-crystal diamond. *Phys. Status Solidi A* 201: 2521–8.

Bogatyreva GP, Marinich MA, Ishchenko EV, Gvyazdovskaya VL, Bazalii GA, Oleinik NA (2004) Application of modified nanodiamonds as catalysts of heterogeneous and electrochemical catalyses. *Phys. Solid State* 46: 738–41.

Bondar VS, Puzyr AP (2004) Nanodiamonds for biological investigations. *Phys. Solid State* 46: 716–19.

Bondar VS, Pozdnyakova IO, Puzyr AP (2004) Applications of nanodiamonds for separation and purification of proteins. *Phys. Solid State* 46: 758–60.

Cataldo F, Koscheev AP (2003) A study on the action of ozone and on the thermal stability of nanodiamond. *Fullerenes Nanotubes Carbon Nanostruct.* 11: 201–18.

Chiganov AS (2004) Selective inhibition of the oxidation of nanodiamonds for their cleaning. *Phys. Solid State* 46: 620–1.

Choi M (2004) Progress in enzyme-based biosensors using optical transducers. *Microchim. Acta* 148: 107–32.

Compton RG, Foord JS, Marken F (2003) Electroanalysis at diamond-like and doped-diamond electrodes. *Electroanalysis* 15: 1349–63.

Da Ros T, Prato M, Novello F, Maggin M, Banfi E (1996) Easy access to water-soluble fullerene derivatives via 1,3-dipolar cycloadditions of azomethine ylides to C60. *J. Org. Chem.* 61: 9070–2.

Deisingh AK, Thompson M (2004) Biosensors for the detection of bacteria. *Can. J. Microbiol* 50: 69–77.

Dion I, Lahaye M, Salmon R, Baquey C, Monties JR, Havlik P (1993) Blood hemolysis by ceramics. *Biomaterials* 14: 107–10.

Dolmatov VY (2001) Detonation synthesis ultradispersed diamonds: Properties and applications. *Usp. Khim.* 70: 687–708.

Dolmatov VY, Kostrova LN (2000) Detonation-synthesized nanodiamonds and the possibility to develop a new generation of medicines. *Superhard Mater.* 22: 79–82.

Donnet JB, Lemoigne C, Wang TK, Peng CM, Samirant M, Eckhardt A (1997) Detonation and shock synthesis of nanodiamonds B. *Soc. Chim. Fr.* 134: 875–90.

El-Emam AA, Al-Deeb OA, Al-Omar M, Lehmann J (2004) Synthesis, antimicrobial, and anti-HIV-1 activity of certain 5-(I-adamantyl)-2-substituted thio-1,3,4-oxadiazoles and 5-(1-adamantyl)-3-substituted aminomethyl-1,3,4-oxadiazoline-2-thiones. *Bioorgan. Med. Chem.* 12: 5107–13.

El-Sherbeny MA (2000) Synthesis, antitumor activity, and anti-HIV-1 testing of certain heterocyclic systems containing an adamantane nucleus. *Arch. Pharm.* 333: 323–8.

Freitas RA (1999) *Nanomedicine, Volume I: Basic Capabilities*. Austin, Texas: Landes Bioscience.

Freitas RA (2003) *Nanomedicine, Volume IIA: Biocompatibility*. Texas: Landes Bioscience.

Garrido JA, Hardl A, Kuch S, Stutzmann M, Williams OA, Jackmann RB (2005) pH sensors based on hydrogenated diamond surfaces. *Appl. Phys. Lett.* 86: Art. No. 073504, Feb. 14.

Grill A (2003) Diamond-like carbon coatings as biocompatible materials–An overview. *Diamond Relat. Mater.* 12: 166–70.

Gu HR, Su XD, Loh KP (2004) Conductive polymer-modified boron-doped diamond for DNA hybridization analysis. *Chem. Phys. Lett.* 388: 483–7.

Hartl A, Schmich E, Garrido JA, Hernando J, Catharino SCR, Walter S, Feulner P, Kromka A, Steinmuller D, Stutzmann M (2004) Protein-modified nanocrystalline diamond thin films for biosensor applications. *Nature Mater.* 3: 736–42.

Hedenborg M, Klockars M (1989) Quartz-dust-induced production of reactive oxygen metabolites by human-granulocytes. *Lung* 167: 23–32.

Higson FK, Jones OTG (1984) Oxygen radical production by horse and pig neutrophils induced by a range of crystals. *J. Rheumatol.* 11: 735–40.

Hodek P, Borek-Dohalska L, Sopko B, Sulc M, Smrcek S, Hudecek J, Janku J, Stiborova M (2005) Structural requirements for inhibitors of cytochromes P4502B: Assessment of the enzyme interaction with diamondoids. *J. Enzym. Inhib.* 20: 25–33.

Huang LCL, Chang HC (2004) Adsorption and immobilization of cytochrome c on nanodiamonds. *Langmuir* 20: 5879–84.

Huang TS, Tzeng Y, Liu YK, Chen YK, Walker KR, Guntupalli R, Liu C (2004) Immobilization of antibodies and bacterial binding on nanodiamond and carbon nanotubes for biosensor applications. *Diamond Relat. Mater.* 13: 1098–102.

Ida S, Tsubota T, Hirabayashi O, Nagata M, Matsumoto Y, Fujishima A (2003) Chemical reaction of hydrogenated diamond surface with peroxide radical initiators. *Diamond Relat. Mater.* 12: 601–5.

Jakubowski W, Bartosz G, Niedzielski P, Szymanski W, Walkowiak B (2004) Nanocrystalline diamond surface is resistant to bacterial colonization. *Diamond Relat. Mater.* 13: 1761–3.

Jiang TL, Xu K, Ji SF (1996) FTIR studies on the spectral changes of the surface functional groups of ultradispersed diamond powder synthesized by explosive detonation after treatment in hydrogen, nitrogen, methane and air at different temperatures. *J. Chem. Soc. Faraday Trans.* 92: 3401–6.

Kim HG, Ahn SH, Kim JG, Park SJ, Lee KR (2005) Electrochemical behavior of diamond-like carbon films for biomedical applications. *Thin Solid Films* 475: 291–7.

Kneuer C, Sameti M, Bakowsky U, Schiestel T, Schirra H, Schmidt H, Lehr CM (2000) A nonviral DNA delivery system based on surface modified silica-nanoparticles can efficiently transfect cells in vitro. *Bioconjugate Chem.* 11: 926–32.

Knickerbocker T, Strother T, Schwartz MP, Russell JN, Butler J, Smith LM, Hamers RJ (2003) DNA-modified diamond surfaces. *Langmuir* 19: 1938–42.

Kong XL, Huang LCL, Hsu CM, Chen WH, Han CC, Chang HC (2005) High-affinity capture of proteins by diamond nanoparticles for mass spectrometric analysis. *Anal. Chem.* 77: 259–65.

Koppel C, Tenczer J (1985) A revision of the metabolic disposition of amantadine. *Biomed. Mass Spectrom.* 12: 499–501.

Kossovsky N, Gelman A, Hnatyszyn HJ, Rajguru S, Garrell RI, Torbati S, Freitas SSF, Chow GM (1995) Surface-modified diamond nanoparticles as antigen delivery vehicles. *Bioconjugate Chem.* 6: 507–11.

Koziara JM, Lockman PR, Allen DD, Mumper RJ (2003) In situ blood-brain barrier transport of nanoparticles. *Pharm. Res.* 20: 1772–8.

Kulakova II (2004) Surface chemistry of nanodiamonds. *Phys. Solid State* 46: 636–43.

Kulakova II, Gubarevich TM, Dolmatov VY, Rudenko AP (2000) Chemical properties of detonation-synthesized ultradispersed diamond. *Superhard Mater.* 22: 42–8.

Lasseter TL, Clare BH, Abbott NL, Hamers RJ (2004) Covalently modified silicon and diamond surfaces: Resistance to nonspecific protein adsorption and optimization for biosensing. *J. Am. Chem. Soc.* 126: 10220–1.

Lee JK, Anderson MW, Gray FA, John P, Lee JY, Baik YJ, Eun KY (2004) Oxidation of CVD diamond powders. *Diamond Relat. Mater.* 13: 1070–4.

Lee JK, Anderson MW, Gray FA, John P, Lee JY (2005) Reactions of amines with CVD diamond nanopowders. *Diamond Relat. Mater.* 14: 675–8.

Lin AM, Lin AMY, Chyi BY, Wang SD, Yu HH, Kanakamma PP, Luh TY, Chou CK, Ho LT (1999) Carboxyfullerene prevents iron-induced oxidative stress in rat brain, *J. Neurochem.* 72: 1634–40.

Lin Y, Taylor S, Li HP, Fernando KAS, Qu LW, Wang W, Gu LR, Zhou B, Sun YP (2004) Advances toward bioapplications of carbon nanotubes. *J. Mater. Chem.* 14: 527–41.

Lipton SA (2004) Paradigm shift in NMDA receptor antagonist drug development: Molecular mechanism of uncompetitive inhibition by memantine in the treatment of Alzheimer's disease and other neurologic disorders. *J. Alzheimer's Dis.* 6: S61–74.

Liu Y, Gu ZN, Margrave JL, Khabashesku VN (2004) Functionalization of nanoscale diamond powder: Fluoro-, alkyl-, amino-, and amino acid-nanodiamond derivatives. *Chem. Mater.* 16: 3924–30.

Liu Y, Khabashesku VN, Halas NJ (2005) Fluorinated nanodiamond as a wet chemistry precursor for diamond coatings covalently bonded to glass surface. *J. Am. Chem. Soc.* 127: 3712–13.

Lockman PR, Mumper RJ, Khan MA, Allen DD (2002) Nanoparticle technology for drug delivery across the blood-brain barrier. *Drug Dev. Ind. Pharm.* 28: 1–13.

Loh KP, Zhao SL, De Zhang W (2004) Diamond and carbon nanotube glucose sensors based on electropolymerization. *Diamond Relat. Mater.* 13: 1075–9.

Lu JZ, Rosenzweig Z (2000) Nanoscale fluorescent sensors for intracellular analysis. *Fresenius J. Anal. Chem.* 366: 569–75.

Lu MC, Knickerbocker T, Cai W, Yang WS, Hamers RJ, Smith LM (2004) Invasive cleavage reactions on DNA-modified diamond surfaces. *Biopolymers* 73: 606–13.

Mitura S, Niedzielski P, Jachowicz D, Langer M, Marciniak J, Stanishevsky A, Tochitsky E, Louda P, Couvrat P, Denis M, Lourdin P (1996) Influence of carbon coatings origin on the properties important for biomedical application. *Diamond Relat. Mater.* 5: 1185–8.

Mitura S, Mitura A, Niedzielski P, Couvrat P (1999) Nanocrystalline diamond coatings. *Chaos Solitons Fractals* 10: 2165–76.

Monteiro-Riviere NA, Nemanich RJ, Inman AO, Wang YYY, Riviere JE (2005) Multi-walled carbon nanotube interactions with human epidermal keratinocytes. *Toxicol. Lett.* 155: 377–84.

Nachalnaya TA, Malogolovets VG, Podzerei GA, Nikitin YI, Novikov NV, Polkanov YA (2000) Special features of structure and physico-mechanical properties of natural diamonds of Ukraine. *Superhard Mater.* 22: 33–41.

Niemeyer CM (2001) Nanoparticles, proteins, and nucleic acids: Biotechnology meets materials science. *Angew. Chem. Int. Ed.* 40: 4128–58.

Nordsletten L, Hogasen AKM, Konttinen YT, Santavirta S, Aspenberg P, Aasen AO (1996) Human monocytes stimulation by particles of hydroxyapatite, silicon carbide and diamond: In vitro studies of new prosthesis coatings. *Biomaterials* 17: 1521–7.

Orzeszko A, Kaminska B, Starosciak BJ (2002) Synthesis and antimicrobial activity of new adamantane derivatives III. *Farmaco*. 57: 619–24.

Ozkan M (2004) Quantum dots and other nanoparticles: What can they offer to drug discovery? *Drug Discovery Today* 9: 1065–71.

Poh WC, Loh KP, De Zhang W, Triparthy S (2004) Biosensing properties of diamond and carbon nanotubes. *Langmuir* 20: 5484–92.

Prado C, Flechsig GU, Grundler P, Foord JS, Marken F, Compton RG (2002) Electrochemical analysis of nucleic acids at boron-doped diamond electrodes. *Analyst*. 127: 329–32.

Pun SH, Davis ME (2002) Development of a nonviral gene delivery vehicle for systemic application. *Bioconjugate Chem.* 13: 630–9.

Pun SH, Tack F, Bellocq NC, Cheng JJ, Grubbs BH, Jensen GS, Davis ME, Brewster M, Janicot M, Janssens B, Floren W, Bakker A (2004) Targeted delivery of RNA-cleaving DNA enzyme (DNAzyme) to tumor tissue by transferrin-modified, cyclodextrin-based particles. *Cancer Biol. Ther.* 3: 641–50.

Puzyr AP, Tarskikn SV, Makarskaya GV, Chiganova GA, Larionava IS, Detkov PY, Bondar VS (2002) Damaging effect of detonation diamonds on human white and red blood cells *in vitro*. *Biochem. Biophys. Mol. Biol.* 385: 21–4.

Puzyr AP, Pozdnyakova IO, Bondar VS (2004a) Design of a luminescent biochip with nanodiamonds and bacterial luciferase. *Phys. Solid State* 46: 761–3.

Puzyr AP, Neshumayev DA, Tarskikh SV, Makarskaya GV, Dolmatov VY, Bondar VS (2004b) Destruction of human blood cells in interaction with detonation nanodiamonds in experiments *in vitro*. *Diamond Relat. Mater.* 13: 2020–3.

Puzyr AP, Bondar VS, Selimhanova ZY, Tyan AG, Bortnikov EV, Injevatkin EV (2004c) Dynamics of the selected physiological responses in laboratory mice under the prolonged oral administration of nanodiamond suspentions. *Siberian Med. Obozr.* 4: 19–23.

Puzyr AP, Neshumaev DA, Tarskikh SV, Makarskaya GV, Dolmatov VY, Bondar VS (2005a) Destruction of human blood cells upon interaction with detonation nanodiamonds in experiments *in vitro*. *Biofizika* 50: 101–6.

Puzyr AP, Bortnikov EV, Skobelev NN, Tyan AG, Manashev GG, Bondar VS (2005b) A possibility of using of intravenous administration of sterile colloids of modified nanodiamonds. S*iberian Med. Obozr.* 1: 20–24.

Rodil SE, Olivares R, Arzate H (2005) In vitro cytotoxicity of amorphous carbon films. *Biomed. Mater. Eng.* 15: 101–12.

Romagnoli R, Baraldi PG, Di Virgilio F (2005) Recent progress in the discovery of antagonists acting at P2X(7) receptor. *Expert Opin. Ther. Pat.* 15: 271–87.

Roy I, Ohulchanskyy Y, Bharali DJ, Pudavar HE, Mistretta RA, Kaur N, Prasad PN (2005) Optical tracking of organically modified silica nanoparticles as DNA carriers: A nonviral, nanomedicine approach for gene delivery. 102: 279–84.

Santavirta S, Takagi M, Gomez-Barrena E, Nevalainen J, Lassus J, Salo J, Konttinen YT (1999) Studies of host response to orthopedic implants and biomaterials. *J. Long-Term Eff. Med.* 9: 67–76.

Shames AI, Panich AM, Kempinski W, Alexenskii AE, Baidakova MV, Dideikin AT, Osipov VY, Siklitski VI, Osawa E, Ozawa M, Vul AY (2002) Defects and

impurities in nanodiamonds: EPR, NMR and TEM study. *J. Phys. Chem. Solids* 63: 1993–2001.

Sharma RK, Das S, Maitra A (2005) Enzymes in the cavity of hollow silica nanoparticles. *J. Colloid Interf. Sci.* 284: 358–61.

Shenderova OA, Zhirnov VV, Brenner DW (2002) Carbon nanostructures. *Crit. Rev. Solid State* 27: 227–356.

Song KS, Sakai T, Kanazawa H, Araki Y, Umezawa H, Tachiki M, Kawarada H (2003) Cl-sensitive biosensor used electrolyte-solution-gate diamond FETs. *Biosens. Bioelectron.* 19: 137–40.

Song KS, Degawa M, Nakamura Y, Kanazawa H, Umezawa H, Kawarada H (2004) Surface-modified diamond field-effect transistors for enzyme-immobilized biosensors. *Jpn. J. Appl. Phys.* 243: L814–17.

Sonkusare SK, Kaul CL, Ramarao P (2005) Dementia of Alzheimer's disease and other neurodegenerative disorders–Memantine, a new hope. *Pharmacol. Res.* 51: 1–17.

Sotowa KI, Amamoto T, Sobana A, Kusakabe K, Imato T (2004) Effect of treatment temperature on the amination of chlorinated diamond. *Diamond Relat. Mater.* 13: 145–50.

Specht CG, Williams OA, Jackman RB, Schoepfer R (2004) Ordered growth of neurons on diamond. *Biomaterials* 25: 4073–8.

Spitsyn B et al. (2005) Purification and modification of nanodiamond. In *Ultra-nanocrystalline Diamond: Synthesis, Properties and Applications* (Gruen D, Vul A, Shenderova OA, eds.). NATO Science Series,. Berlin: Springer, pp. 241–53.

Stefan RI, Nejem RM, van Staden JF, Aboul-Enein HY (2004) New amperometric biosensors based on diamond paste for the assay of L- and D-pipecolic acids in serum samples. *Prep. Biochem. Biotech.* 34: 135–43.

Strobel P, Riedel M, Ristein J, Ley L (2004) Surface transfer doping of diamond. *Nature* 430: 439–41.

Strother T, Knickerbocker T, Russell JN, Butler JE, Smith LM, Hamers RJ (2002) Photochemical functionalization of diamond films. *Langmuir* 18: 968–71.

Swan A, Dularay B, Dieppe P (1990) A comparison of the effects of urate, hydroxyapatite and diamond crystals on polymorphonuclear cells–Relationship of mediator release to the surface-area and adsorptive capacity of different particles. *J. Rheumatol.* 17: 1346–52.

Tachiki M, Kaibara Y, Sumikawa Y, Shigeno M, Banno T, Song KS, Umezawa H, Kawarada H (2003) Diamond nanofabrication and characterization for biosensing application. *Phys. Status Solidi A* 199: 39–43.

Tang L, Tsai C, Gerberich WW, Kruckeberg L, Kania DR (1995) Biocompatibility of chemical-vapor-deposited diamond. *Biomaterials* 16: 483–8.

Tanner JA, Zheng BJ, Zhou J, Watt RM, Jiang JQ, Wong KL, Lin YP, Lu LY, He ML, Kung HF, Kesel AJ, Huang JD (2005) The adamantane-derived bananins are potent inhibitors of the helicase activities and replication of SARS coronavirus. *Chem. Biol.* 12: 303–11.

Tatsuma T, Mori H, Fujishima A (2000) Electron transfer from diamond electrodes to heme peptide and peroxidase. *Anal. Chem.* 72: 2919–24.

Thomson LA, Law FC, Rushton N, Franks J (1991) Biocompatibility of diamond-like carbon coating. *Biomaterials* 12: 37–40.

Troupe CE, Drummond IC, Graham C, Grice J, John P, Wilson JIB, Jubber MG, Morrison NA (1998) Diamond-based glucose sensors. *Diamond Relat. Mater.* 7: 575–80.

Tse Rl, Phelps P (1970) Polymorphonuclear leukocyte motility in-vitro. 5. Release of chemotactic activity following phagocytosis of calcium pyrophosphate crystals, diamond dust, and urate crystals. *J. Lab. Clin. Med.* 76: 403–15.

Tsubota T, Hirabayashi O, Ida S, Nagaoka S, Nagata M, Matsumoto Y (2002a) Abstraction of hydrogen atoms on diamond surface using benzoyl peroxide as a radical initiator. *Diamond Relat. Mater.* 11: 1374–8.

Tsubota T, Ida S, Hirabayashi O, Nagaoka S, Nagayama S, Nagata M, Matsumoto Y (2002b) Surface reforming of the oxidized diamond surface with silane coupling reagents. *J. Ceram. Soc. Jpn* 110: 904–10.

Tsubota T, Tanii S, Ida S, Nagata M, Matsumoto Y (2004) Chemical modification of diamond surface with various carboxylic acids by radical reaction in liquid phase. *Diamond Relat. Mater.* 13: 1093–7.

Ushizawa K, Sato Y, Mitsumori T, Machinami T, Ueda T, Ando T (2002) Covalent immobilization of DNA on diamond and its verification by diffuse reflectance infrared spectroscopy. *Chem. Phys. Lett.* 351: 105–8.

Vereshchagin AL, Yurjev GS (2003) Structure of detonation diamond nanoparticles. *Inorg. Mater.* 39: 247–53.

Vo-Dinh T, Cullum BM, Stokes DL (2001) Nanosensors and biochips: Frontiers in biomolecular diagnostics. *Sensors Actuators B (Chem.)* 74: 2–11.

Wang JJ, Chern YT, Liu TY, Chi CW (1998) In vitro and in vivo growth inhibition of cancer cells by adamantylmaleimide derivatives. *Anticancer Drug Des.* 13: 779–96.

Wengel J (2004) Nucleic acid nanotechnology – Towards Angstrom-scale engineering. *Org. Biomol. Chem.* 2: 277–80.

Wenmackers S, Haenen K, Nesladek M, Wagner P, Michiels L, vandeVen M, Ameloot M (2003) Covalent immobilization of DNA on CVD diamond films. *Phys. Status Solidi A* 199: 44–8.

Wilson SR (2000) Biological aspects of fullerenes. In *Fullerenes: Chemistry, Physics, and Technology* (Kadish KM, Ruoff RS, eds.). New York: John Wiley & Sons.

Xu K, Xue QJ (2004) A new method for deaggregation of nanodiamond from explosive detonation: Graphitization-oxidation method. *Phys. Solid State* 46: 649–50.

Xu XY, Yu ZM, Zhu YM, Wang BC (2004) Dispersion and stability of nanodiamond in clean oil. *Mater. Sci. Forum* 471: 779–83.

Xu XY, Yu ZM, Zhu YM, Wang BC (2005a) Effect of sodium oleate adsorption on the colloidal stability and zeta potential of detonation synthesized diamond particles in aqueous solutions. *Diamond Relat. Mater.* 14: 206–12.

Xu XY, Zhu YW, Wang BC, Yu ZM, Xie SZ (2005b) Mechanochemical dispersion of nanodiamond aggregates in aqueous media. *J. Mater. Sci. Technol.* 21: 109–12.

Xu XY, Yu ZM, Zhu YW, Wang BC (2005c) Influence of surface modification adopting thermal treatments on dispersion of detonation nanodiamond. *J. Solid State Chem.* 178: 688–93.

Yang WS, Hamers RJ (2004) Fabrication and characterization of a biologically sensitive field-effect transistor using a nanocrystalline diamond thin film. *Appl. Phys. Lett.* 85: 3626–28.

Yang WS, Auciello O, Butler JE, Cai W, Carlisle JA, Gerbi J, Gruen DM, Knickerbocker T, Lasseter TL, Russell JN, Smith LM, Hamers RJ (2002) DNA-modified nanocrystalline diamond thin-films as stable, biologically active substrates. *Nature Mater.* 1: 253–7.

Yang WS, Butler JE, Russell JN, Hamers RJ (2004) Interfacial electrical properties of DNA-modified diamond thin films: Intrinsic response and hybridization-induced field effects. *Langmuir* 20: 6778–87.

Yang WS, Baker SE, Butler JE, Lee CS, Russell JN, Shang L, Sun B, Hamers RJ (2005) Electrically addressable biomolecular functionalization of conductive nanocrystalline diamond thin films. *Chem. Mater.* 17: 938–40.

Yurjev GS, Vereshagin AL, Korchagin MA (2005) Structural study of detonation nanodiamonds. *Diamond Relat. Mater.* 14: 192–5.

Zheng CL, Qi R, Yang WB (2005) MPACVD nanocrystalline diamond for biomedical applications. *High Performance Ceram.* 280–283: 1595–8.

Zhu YW, Shen XQ, Wang BC, Xu XY, Feng ZJ (2004) Chemical mechanical modification of nanodiamond in an aqueous system. *Phys. Solid State* 46: 681–4.

16 History of Russian Patents on Detonation Nanodiamonds

Igor L. Petrov

New Technologies, Chelyabinsk, Russia

Olga A. Shenderova

International Technology Center, Raleigh, NC, USA

Introduction

The popularity of detonation nanodiamonds (DNDs) as objects of research is growing very rapidly.[1] Accordingly, the number of DND-related patents filed all over the world grew noticeably in the last few years. The aim of writing a chapter on the history of Russian patents on DNDs is two-fold. First, there was a burst of patent applications in the former USSR at the end of the 1980s and the beginning of the 1990s. Due to instabilities in the economy of the Russian Federation in the late 1990s many of the issued patents were not maintained so became public knowledge. The discoveries published in these works are valuable for the more rapid development of the field of DND; from this perspective it is worthwhile to recall these findings. Second, according to US patent laws, if the invention has been described in a printed publication *anywhere in the world*, a patent cannot be obtained.[2] Thus in order to assist potential inventors in the USA and other countries in finding "prior art" published in the *Russian Patent Bulletin*,[3] but not easily accessible to non-Russian native speakers, the present chapter was compiled to include all Russian patents related to the DND field filed before 2000, to the best of our knowledge.

There is also a difference that should be pointed out in the terminology for a document issued to inventors before and after the collapse of the USSR in 1991. In the former USSR the rights for an invention were owned by the State, and the document issued to the inventor was called "Avtorskoe Svidetelstvo" (Author's Certificate). Since 1991, the issued document has been called a patent of the Russian Federation and the rules for the assignment of rights became similar to those, for example, in the USA.

According to US classification, patents filed on DND in the USA are related to a class of so called *utility patents*, that "may be granted to anyone who invents or discovers any new and useful process, machine, article of manufacture, or composition of matter, or any new and useful improvement thereof".[2] Keeping in mind this definition as well as for the convenience of the readers to analyze the provided information, we grouped patents on DND into four categories according to their claims or as called in Russian patents "formula of an invention": **method of DND synthesis**, **post-synthesis DND treatments**, **composition of matter** (DND), and DND **applications** (including **composition of matter for applications**). US patents filed by the inventors of the former USSR and Russia are also included in the review (as well as one Bulgarian patent). It should be noted that DND production was started by companies in Japan and China by the mid 1990s,[4] thus a similar analysis of the patents from these countries for the purposes outlined above should also be done. The present work, however, does not extend the analysis of the patent literature beyond Russian and US sources.

16.1 Patents on Methods of DND Synthesis

As described in Chapter 10 by V. Danilenko, one of the "first wave" of inventors of DND synthesis, the history of DND synthesis started in 1963 in the All-Union Research Institute of Technical Physics (VNIITF, Snezhinsk, Chelyabinsk region). The experiments on explosions were conducted in an explosion chamber with the charge encased in a water medium to suppress graphitization and reduce the unloading rate of the detonation products.[5] As a result of hundreds of experiments conducted between 1963 and 1965, the effect of the explosion conditions, and the composition and configuration of charges on ultradispersed diamond synthesis, were revealed.[5] Unfortunately, the results of the experiments were highly classified and were not published until the late 1980s,[6, 7] when this research topic became very popular. In 1986 the largest part of the reports of 1963 was provided by VNIITF to other research centers working on the synthesis of diamond and particularly on DND.[8] In 1986–1988 experiments using large mass detonation charges were performed by Danilenko at VNIITF.[5] DND systematic research (and production) at VNIITF, Snezhinsk was renewed in 1989 under the leadership of L. I. Filatov. Within a short period of time, the production of 50 kg of DND per month had been implemented in the laboratory (practically an industrial-scale production).[8]

As described in Chapter 10, at the beginning of the 1980s DND synthesis was rediscovered at two other USSR scientific centers, the Institute of Hydrodynamics of AN SSR and the Institute for Material Science Problems, Ukraine. The patent[9] filed in 1979 indicates that the work on synthesis of ultradispersed diamond (UDD, as the material was called in the USSR) directly from carbon-containing explosives during their detonation was started even earlier in the late 1970s by G. Savvakin and colleagues. UDD was experimentally observed after detonation of carbon-containing explosives (trotyl, hexogen, and others) at negative oxygen balance during rapid water quenching of the detonation products. Contrarily, relatively slow cooling of detonation products did not result in UDD formation.[118] One of the early works where DND was described is that by Vlasova et al.[10] The work by Savvakin and Trefilov[10] describes a very high yield of DND in detonation soot (up to 85 wt.%) in the process of synthesis using water cooling. Interestingly, the existence of DND within the 1.5–3 nm size range is reported. This work also reports using a wide variation of composition TNT/hexogen (5–70 wt.%) explosive charge that is one of the claims in several patents. In the experiments of the scientists from the Institute of Hydrodynamics, Novosibirsk, the cooling of the detonation product to preserve the DND formed during detonation was implemented using a gaseous medium inert toward carbon, the so-called "dry" cooling, namely using gases CO_2,[11] air,[15] vacuum (>0.89 kPa),[16] CO, N_2, C_3H_8, C_4H_{10}, argon, helium, and others.[4,5,12–16] As cooling media, gases from the previous explosion (mixture of CO_2, CO, and N_2) can also be used.[15] References on different methods of DND synthesis published since 1988 can be found in ref. [1]. DND as an industrial product has been produced since 1983 at the Research-and-Production Center "Altai",[4] where a method of dry cooling of the detonation products was implemented.[11] In 1989 the USSR government issued a decree to increase the production scale at Altai from 10 to 75 million, and ultimately up to 250 million carats of DND per year.[4] By 1993 Altai produced more than 25 million carats (more than 5 tonnes).[4] By the end of the 1980s, the DND produced at Altai had been widely used in various technical applications.[4,13,17,18] According to ref. [4], the major consumer of DND was the machine-building industry, where DND had been used for co-deposition in chrome galvanic coatings. This process had been applied at more than 200 machine-building factories in the former USSR. According to ref. [10], by the beginning of the 1990s, in the Ukraine DND had also been reduced to practice in such applications as lubricants, metallic coating composites, DND compacts, polymer composites, and others. Thus it is important to emphasize that the patent-protected dry method of

DND synthesis was implemented at an industrial scale in the former USSR by the late 1980s and the beginning of the 1990s.

The patents claiming a method of synthesis are summarized in Table 16.1.[9,11,19–39] The most recent patent on synthesis is ref. [40]. Most of the patents in this class detail the use of specific cooling media, mostly the gaseous ones. The first patent on a dry method of synthesis was filed in 1982[11] by scientists from the Institute of Hydrodynamics of AN SSSR who rediscovered DND synthesis from carbon-containing explosives with a negative oxygen balance. Scientists from this institute collaborated with researchers from NPC Altai on the industrialization of DND synthesis with academician Sakovich as leader of this activity. This was followed by a variety of patents from the Altai group on variations of the gaseous cooling media,[17–20,23,28,33] with the addition of liquid and solid cooling envelopes around the charge.[21,22,24] The patent from VNIITF, Snezinsk[26] describes the use of ice cooling media applied around the charge. Several patents describe the effective constructions of a detonation chamber.[25–27] There is a very instructive example of the practical realization of the patent [27] by V. Danilenko and co-authors. By that time, in 1989, Danilenko had left VNIITF, Snezhinsk and continued his carrier at the Institute for Material Science Problems, Ukraine. Based on the patent related to the detonation chamber of a special construction, large-scale technology for producing UDD (charges 10 kg from RDX/TNT 60/40%, water cooling, UDD yield 8–10% and UDD concentration in soot 60–75%, particles size 4–6 nm) was implemented at the commercial plant of the "ALIT" company (Zhitomir, Ukraine). The main part of the plant was an explosion chamber 100 m^3 in volume with water cooling of the UDD designed by Danilenko.[27]

Regarding US-filed patents by Russian researchers at the beginning of the 1990s (5,482,695, 5,861,349, and 5,916,955), these are methods of synthesis with modifications to the previously patented general methods on dry synthesis with an objective of obtaining diamond-containing product with a high concentration of amorphous and graphite phases for specific applications (mostly in lubricants and polishing compounds).[29,31,37] To achieve these specific compositions, described in a patent by Staver and colleagues who worked at that time in the Krasnoyarsk State Technical University,[29] various CO_2 content cooling gas media regulate the cooling rate and therefore the amount of diamond phase in the total carbon content. The authors report that at a CO_2 content in excess of 60% (neutral gas–the balance at 1 atm pressure) the amount of DND in the carbon phase composition exceeds 38%. The patent [29] also claims a popular composition of carbon-containing explosives as a

mixture of TNT/RDX between 40–60 and 60–40 wt.%. The authors from Altai[31] suggested a method for regulating the diamond/non-diamond carbon composition by producing explosive detonation in an atmosphere of 0.1–6.0 vol.% oxygen and inert gas–the rest, in the presence of ultra-dispersed carbon phase in the atmosphere at certain concentrations. The same authors, in another patent [37], suggest regulating the cooling of the detonation product at a rate in the range of 200 to 6000 °C/minute, in the atmosphere consisting of a gaseous medium, formed by blasting an initial charge of the explosive in the closed space prior to the detonating step. In another US patent (5,353,708) filed by Bulgarian researchers, water cooling media as well as spatial arrangement of different types of explosives within a charge are claimed.

Probably there is still a wide range of possibilities for improvements to the existing methods of synthesis, as for example, in ref. [39] where as a cooling liquid a variety of organosols had been suggested, resulting in suspensions of DNDs with very high concentrations extracted from the chamber, as well as DND fractions with primary grain sizes half those typically reported at 4 nm.

As can be seen from Table 16.1, due to the lack of communication in 1960–1990 in the former USSR, the inventive steps claimed in different patents may be disputable; there are overlaps in the claims of some of the patents from one side, and partial disclosure of knowledge in the open literature before the patent priority dates, from the other side (including, for example, widely cited ref. [41], where charge compositions were described). An analysis of the patent literature on DND synthesis also demonstrates that this material can gain new and unusual properties if some of the methods from Table 16.1 not currently in use are implemented in practice.

16.2 Patents on Post-Synthesis Treatments

DND purification is an expensive and complex process (Chapter 11). Different purification methods have been used mostly based on the liquid phase oxidation of detonation soot. More specifically, the following soot oxidation technologies have been used at major DND production centers: at VNIITF (1963–1966), a mixture of H_2SO_4 + KNO_3:[5] at VNIITF (1990–2000), a mixture of chromic anhydrid and sulfuric acid;[58] at SPC Altai, a mixture of H_2SO_4 + HNO_3;[5] at "ALIT" company (based on the technology of the Ukrainian Institute of Superhard Materials), a mixture of H_2SO_4 + Cr_2O_3.[5] At the end of the 1980s, the technology for UDD

Table 16.1 Patents on Synthesis of Detonation Nanodiamonds

Patent No., Ref.	Priority/ Issue Dates	Essence of the Claims
845378 [9]	1979.10.05/	Diamond powder synthesis using carbon-containing explosives as a source of carbon at negative oxygen balance; additions of catalysts
1165007 [11]	1982.01.07/	DND synthesis in a chamber using CO_2 atmosphere as cooling media
1534819 [19]	1984.06.26/	DND synthesis using gas inert to carbon at elevated pressure as cooling media
1538321 [20]	1985.06.06/	Explosion of pressed charge in the mix of inert gas and air at elevated pressure
1658557 [21]	1985.08.15/ 1991.02.22	DND synthesis using air/mechanical foam as cooling media at atmospheric pressure
1570222 [22]	1987.02.08/ 1990.01.27	DND synthesis using solid coat as cooling media from coolants such as oxalate ammonia, sodium hydrocarbonate, calcium carbonate, sodium chloride, water, and others
1578999 [23]	1988.07.19/	Description of mass of the charge as a function of the chamber volume and pressure of the detonation product (for a synthesis with multiple repeating explosions)
1623107 [24]	1989.06.14/	DND synthesis using water coating around the charge and atmospheric or elevated pressure in the chamber before detonation; for increased DND yield, organic viscous additives in water coating are used
1826958 [25]	1990.08.20/ 1993.07.07	Truncated conical shape of the charge in DND synthesis for increase yield of DND
US Patent 5,353,708 [26]	1990.11.9/ 1994.11.11	Use of water cooling media; location of the explosives in a “hard” or “soft” shell with radial–axial control of the detonation process from its center to its periphery or vice versa, correspondingly
1813293 [27]	1991.5.12/	Detonation chamber of a special construction using a central fixed cylinder and two cylinders adjusted from both sides that can move along rails during explosion to damp the detonation wave

Table 16.1 Patents on Synthesis of Detonation Nanodiamonds (cont'd)

Patent No., Ref.	Priority/ Issue Dates	Essence of the Claims
1833593 [28]	1991.07.02/	Using ice as cooling media is suggested. In the example, content of diamond phase after purification is more than 98.5%
US Patent 5,482,695 [29]	1991.7.3/ 1996.1.9	Method for producing a diamond/graphite composition (Table 16.3) in cooling media containing a neutral gas (can be Ar or N_2); CO_2 (40–60 vol.%) and free O_2 not exceeding 2 vol.%. Using as carbon-containing explosives a mixture of TNT/RDX between 40–60 and 60–40 wt.%
2051092 [30]	1991.12.25/ 1995.12.27	Method for producing diamond-containing composition (Table 16.3) by producing explosive detonation in atmosphere of 0.1–6.0 vol.% oxygen and inert to carbon gas – the rest, in the presence of ultradispersed carbon phase in the atmosphere at concentration 0.01–0.15 kg/m^3
US Patent 5,861,349 [31]	1991.12.25/ 1999.01.19	Same as in 2051092 with emphasis that DND is not formed from the ulradispersed carbon initially dispersed in the chamber atmosphere; listed group of explosives
2049723 [32]	1992.05.19/ 1995.12.10	Detonation process in the presence of drops or streams of liquid (e.g., distilled water, 40% aqueous solution of ethanol, kerosene, 30% aqueous solution of glycerin)
2036835 [33]	1992.09.01/ 1995.06.09	At the moment of blasting of explosive charge with negative oxygen balance in blasting sealed chamber, its space is sprayed with water at specific mass-to-explosive-charge mass ratio
2041166 [34]	1993.04.02/ 1995.08.09	Detonation of explosives applying electrical current through the shock wave during explosion. To achieve high temperatures during detonation, it is suggested to use octagon, hexogen, aluminum nitrate, magnum, bensothreefuroksin. Heating of charge before the explosion

Table 16.1 Patents on Synthesis of Detonation Nanodiamonds (cont'd)

Patent No., Ref.	Priority/ Issue Dates	Essence of the Claims
2094370 [35]	1993.10.19/ 1997.10.27	Annealing of nanodiamond in vacuum or inert atmosphere resulting in production of onion-like carbon
2041165 [36]	1993.12.02/ 1995.09.08	Diamond–carbon material produced by detonating an explosive with a negative oxygen balance in a confined volume in a medium inert to carbon at a cooling rate of detonation products varying from 200 to 6000 °C/min
US Patent 5,916,955 [37]	1993.12.02/ 1999.01.29	As in 2041165; also claimed on the atmosphere consisting of a gaseous medium, formed by blasting an initial charge of the explosive in the closed space prior to the detonating step
2078661 [38]	1995.01.20/ 1997.05.10	Claimed specific housing of the detonation chamber making it more efficient and convenient for operation
2128625 [39]	1995.11.14/ 1999.04.10	Blasting in water shell of trotyl-hexogen explosive composition with equal weight additives of orthoboric acid and $Al(OH)_3$; boiling of solid explosion products in mixture of acids. Diamond yield is increased. The composition affects temperature and pressure in the region of diamond stability on carbon phase diagram

purification by using nitric acid under pressure was developed at the Special Technical Design Office (SKTB) "Tekhnolog" (St. Petersburg), where a continuous-operation unit was constructed.[42] It should be noted that for some applications (coatings, lubrications), a mixture of DND and non-diamond carbon is used (e.g., detonation soot without extraction of DND).

Table 16.2 contains a list of the patents related to soot purification and DND extraction. Mostly oxidizing agent content, temperature, pressure conditions, as well as duration of the treatment, are claimed. There are also descriptions on how to accelerate DND sedimentation for the purpose of DND extraction from a water suspension,[51] using electric

Table 16.2 Patents on Post-synthesis Treatment of the Product of Detonation

Patent No., Ref.	Priority/ Issue Dates	Essence of the Claims
1770271 [43]	1984.06.13/ 1992.06.22	Treatment of detonation soot using sulfuric acid containing free serum anhydride and nitric acid or nitrate of alkaline metal or ammonia at heating
1828067 [44]	1986.03.25/ 1992.10.13	Treatment of detonation soot using water solution of 40–90% nitric acid at high temperature and pressure
1480306 [45]	1986.06.09/	Diamond powder purification consisting of heating up to 110–120 °C followed by treatment in sulfuric acid and an oxidizer (manganese anhydride)
1540195 [46]	1988.01.25/	Diamond powder purification using concentrated sulfuric acid and manganese anhydride
1614354 [47]	1988.07.19/ 10.01.96	The process of DND extraction consists of DND coagulation by treating its water suspensions with an electric field
1658558 [48]	1988.07.19/ 1991.02.22	DND purification using water solution of 5–30% of hydrogen peroxide at high temperature and pressure
1794888 [49]	1988.07.19/ 1993.02.05	Treatment of the wet soot (60–90% water) with the mix of anhydride (SO_3), nitric acid, and sulfuric acid
1770272 [50]	1988.07.19/ 1992.06.22	Purification from metallic impurities and non-diamond carbon. First DND is treated with nitric acid with concentration 5–20 wt.% at 50–100 °C, separation of wet residue followed by treatment similar to 1794888
1792915 [51]	1988.07.19/ 1993.7.02	In order to accelerate DND sedimentation for the purpose of DND extraction from water suspension, heat treatment at high pressure for 5–15 min is suggested

Table 16.2 Patents on Post-synthesis Treatment of the Product of Detonation (cont'd)

Patent No., Ref.	Priority/ Issue Dates	Essence of the Claims
1830883 [52]	1988.07.19/ 1992.10.13	Use of two connected purification reactors: soot is first treated by a mix of oleum and nitric acid at 160 °C; the mix flows to another reactor heated to a higher temperature. Quality of purification and yield of the process are increased
1538430 [53]	1987.09.29/ 15.09.89	Method of deep purification of DND. DND suspension is treated using strong-acid cation exchange in H form and then using strong-acid anion exchange in OH form
1815933 [54]	1990.07.27/ 1996.06.20	Treatment of diamond suspension by electric field in inter-electrode space isolated from ion-exchange selective diaphragm. Useful for DND cleaning from soluble and adsorbed impurities in an aqueous suspension
2019500 [55]	1990.08.10/ 1994.09.15	For extraction of DND from suspension, DND suspension is heated and separation is carried out using flow ultrafiltration under pressure
1819851 [56]	1991.01.02/ 1992.12.10	Soot treatment with H_2O_2, mineral acid (nitric or others), salt of metal of variable valence (Fe(FeSO4), Cu, and others), water. High temperatures and pressures are applied
2019502 [57]	1991.01.09/ 1994.09.15	Construction of device and method of using ozone–air mixture for oxidizing graphite
2077476 [58]	1991.03.21 1997.04.20	Soot is treated with concentrated sulfuric acid and chromic anhydride. The mixture is heated
2004491 [59]	1991.07.02/ 1993.12.15	Soot treatment in air at 300–550 °C in the presence of boron anhydride
2081821 [60]	1995.01.11/ 1997.06.20	Initially soot is washed and dried. Then dry mixture is treated by oxidation mixture of nitric acid and sulfuric acid

Table 16.2 Patents on Post-synthesis Treatment of the Product of Detonation (cont'd)

Patent No., Ref.	Priority/ Issue Dates	Essence of the Claims
2083490 [61]	1995.04.10/ 1997.10.07	Isolation of DND from aqueous suspension using pneumatic heated high-pressure nozzle for water evaporation by heating and subsequent separation of dry product from gaseous heat carrier
2109683 [62]	1996.03.05/ 1998.04.27	Soot is treated in two steps with aqueous solution of nitric acid, at elevated pressure. Content of recovered diamonds in purified product is 98.2–98.3, that of oxidized forms of carbon is 0.7–0.8%, and that of incombustible residue is 0.9–1.0%
2132816 [63]	1997.11.10/ 1999.10.07	Diamond-containing blend (5 wt.%) suspension is treated in high-pressure apparatus in the presence of potassium nitrate at high temperature. Then cooled, washed, and dried. Content of impurities in treated diamond does not exceed 1 wt.%
2168462 [64]	1999.04.05/ 2001.03.20	Soot containing about 40 wt.% of diamonds and the rest in the form of non-diamond carbon and metal impurities are placed on the pan of an electric furnace, heated at a certain thermal budget, and oxidized by air oxygen. Diamond yield amounts to 38.5–39.1 wt.% of initial substance; content of non-diamond carbon is 0.1–0.8 wt.%

fields in the process of purification,[47,54,65–67] and DND drying from water suspension.[61]

An important subclass of patents on the post-synthesis treatment of DND is surface modification of purified DND, such as methods of modification for improved sedimentation stability of DND.[68,69] It should be noted that patents filed during the last few years in the Russian Federation are often filed under Patent Cooperation Treaty (PCT) status. An extensive bibliography of the earlier publications related to the gas phase

and liquid phase methods of DND surface modification is provided in the books in refs. [5] and [1].

16.3 Patents on Composition of Matter

A primary goal of a patent is to provide protection from unlicensed use of a proprietary method of synthesis/treatment of DND. Where it is possible it makes sense to protect the final DND product that bears specific features based on the method of synthesis/treatment. While a "passport" of DND material has not been finalized (although the importance of the international standardization of the DND product is widely recognized), the following characteristics can be considered in order to specify DND produced by different vendors: carbon phase composition obtained, for example, by the X-ray diffraction (XRD) method; lattice constant; monocrystallite size; specific surface area; elemental composition (in terms of content of incombustible impurities as well as elemental gas phase composition in terms of C—N—H—O content); the nature and content of the surface groups. Such characteristics as average aggregate size in a specific solvent, zeta potential in a specific pH range, possibly Fourier transform infrared (FTIR) and XRD spectra themselves, can in principle be claimed as a "signature" of the product. However, after decades of study of the properties of DND material, a wide variety of properties had been described as a prior art in the open literature so that probably only a combination of the specific characteristics can distinguish a product sufficiently to be patentable.

Protecting a composition of DND was the objective of the patents [29–32,36,37,70] (Table 16.3). As described in Section 16.1, methods of synthesis were developed to create a product with a high concentration of non-diamond carbon content for antifrictional and polishing applications.[29–31,36,37] As described in the patent [29], a primary object is to provide diamond-containing compositions by selecting a proper ratio between diamond/non-diamond carbon content with high content of the latter in order to create a highly dispersed nanomaterial which, due to its dumping properties, creates a specific tribo-mechanical effect favorable for the treatment of hard surfaces. In the patent [29] the carbon composition consists of diamond (4–12 nm grains) and graphite (20–100 nm grains) in a specific ratio; the principal abrasive effect is exerted by the diamond component, but during movement of the carbon composition over a surface being machined, the diamond grains are embedded in the superficial layer consisting of larger graphite grains so that the graphite

Table 16.3 Patents on Composition of Matter (DND)

Patent No., Ref.	Priority/ Issue Dates	Essence of the Claims
US Patent 5,482,695 [29]	1991.7.3/ 1996.1.9	Diamond/graphite composition with diamond being 18–38 wt.% and graphite being 62–82 wt.% produced by the process described in ref. [29] (Table 16.1)
2051092 [30]	1991.12.25/ 1995.12.27	Diamond-containing substance of rounded shape with the following characteristics: – contains 70–90 wt.% diamond of cubical modification and the rest contains the amorphous phase (according to XRD data); – composition (wt.%): [C] 78–90; [H] 0.8–1.2; [N] 1.5–4.5, and [O] the rest; – the size of the coherent scattering region, specific surface area, surface functional groups and their occupancy, number of carbon atoms with non-compensated bonds, and parameter of crystal lattice of the substance are also claimed
US Patent 5,861,349 [31]	1991.12.25 –based on 2051092/ 1999.01.19	Diamond-containing substance of rounded or irregular shape with the following characteristics: (1) Elemental composition (wt.%): [C] 75–90; [H] 0.8–1.5; [N] 0.6–4.5 and [O] the rest; carbon phase composition is same as in 2051092, carbon atoms with non-compensated bonds; close to 2051092 specific surface area, surface functional groups, and their occupancy; specific porosity is added (2) Another specific porosity than in (1) (3) In addition to (1) crystal lattice parameter listed
2049723 [32]	1992.05.19/ 1995.12.10	Compositions of condensed liquid (e.g., distilled water, 40% aqueous solution of ethanol, kerosene, 30% aqueous solution of glycerin) with high concentration of DND (fractions: less 1.5 nm and ~4 nm) (see Table 16.1 on the process)

Table 16.3 Patents on Composition of Matter (DND) (cont'd)

Patent No., Ref.	Priority/ Issue Dates	Essence of the Claims
2041165 [36]	1993.2.12/ 1995.09.08	Diamond–carbon substance containing diamond cubic phase 30–75 wt.%, XRD–amorphous carbon phase 10–15 wt.%; crystalline carbon, the balance; composition, (wt.%): [C] 84–89; [H] 0.3–1.1; [N] 3.1–4.3, and [O] 2.0–7.1, incombustible impurities, up to 5.0 wt.%; surface contains methyl, carboxyl, quinine, lactones, ether, and aldehyde functional groups
US Patent 5,916,955 [37]	1993.2.12– based on 2041165/ 1999.01.29	(1) Diamond bearing material as in 2041165, except non-combustible impurities 2–5 wt.%; in addition, specific surface area 218–600 m^2/g (2) As in (1) plus specific weight (3) As in (2) plus predominant methyl functional groups (4) Compositions of (1) in lubricating oil, polytetrafluorethene (5) Composition of (3) plus rubber (6) Particle structure: diamond nucleus, surrounded by amorphous phase of carbon, the latter disposed between diamond phase and non-diamond crystalline phases
2046094 [70]	1993.05.26/ 1995.10.20	The material comprises various elements, their ratios being as follows (wt.%): 65–80 [C]; 0.6–3.3 [H]; 1.4–3.4 [N]; 13.3–33.[O]; carbon comprises 60–92 wt.% ulradispersed diamond and 8–40 wt.% non-diamond carbon forms. The material has improved absorption and ion-exchange properties

modification serves as a dumping layer preventing high impact loads on the diamond component, reducing possible charging of the machined surface, and improving heat-conducting properties. To achieve this effect the authors recommend the use of a diamond content of 18–38 wt.%. Vereschagin et al.[30,31] cover the use of a diamond-containing substance

with 70–90 wt.% of diamond phase and the rest, the so-called XRD amorphous carbon phase if one considers the carbon phase content. The XRD pattern of the material demonstrates specific features for a non-diamond carbon. It should be notid that for well-purified DND such features are absent. Also, in order to distinguish their material, the authors claim an elemental composition (not mentioning incombustible impurity content), specific surface area, surface functional groups and their occupancy; specific porosity and lattice parameter (as a separate claim); and other characteristics. While the claimed elemental composition in terms of C—N—HO content overlaps with compositions of DND produced by other methods,[18,71–75] the combination of these characteristics with the phase content of carbon and other specific features allow this material to be well distinguished from DND produced by other methods. In a similar fashion, patents [36,37] detail the compositions of detonation soot (so a high content of incombustible impurities is added to the elemental composition); in addition the patents claim specific applications of their product. The elemental composition of DND is also claimed in the patent [70], distinguished from the previously discussed patents by the high concentration of oxygen in the elemental composition and higher diamond phase content in the carbon phase composition. The patent [32] covers compositions of condensed liquid (e.g., distilled water, 40% aqueous solution of ethanol, kerosene, 30% aqueous solution of glycerin) with a high concentration of DND.

16.4 Patents on Applications

While the three classes of patents on DNDs discussed above are mostly filed by DND producers, the inventions of DND applications are accessible to a wide research community (and to the general public).[77–117] This is demonstrated by descriptions of the patents given in Table 16.4. The topics range from traditional polishing applications in galvanic coatings and lubricants, to such exotic applications as ski grease,[95] biologically active agents,[115] and in cosmetic compositions for improved skin elasticity.[117]

It is important to emphasize that, as described in Section 16.1, very well-developed applications including those implemented in USSR factories existed by the end of 1980s and beginning of the 1990s.[17,18,76] According to ref. [18], significant improvement of the properties of electroplated Ni, Cr, Cu, and electroless Cu coatings co-deposited with DND on different instruments was demonstrated; and improved properties of a variety of lubricating oils with DND additives was also discussed.

Table 16.4 Patents on Applications, DND-Containing Product for Specific Applications, as well as Patents from the Previous Tables Where Specific Applications Are Described as Practical Examples

Patent No., Ref.	Priority/ Issue Dates	Essence of the Claims
1694710 [77]	1986.4.14/ 1991.11.30	Use of nanodiamond 1–10 nm in size for electroplated chromium compositions. Method of diamond synthesis is not discussed
1770350 [78]	1988.07.19/ 1992.10.23	Addition of DND to lubricating oil for improved antifriction properties and robustness of engines and mechanisms. Oil contains mineral oil and 0.1–1 mass % of addition of mix of ultradispersed diamond, graphite, and amorphous carbon. Content of diamond and non-diamond carbon components vary between 30 : 70 and 99 : 1
2026892 [79]	1990.06.05/ 1995.01.20	Composition for electrometallurgy (g/l): nickel chloride, or iron chloride, or cobalt chloride 300; boric acid 40; amorphous boron 10–40; ultradispersed carbon condensate 2–140. The latter (wt.-%): carbyne 2–5; graphite 1–15; non-crystalline carbon 3–50, and diamond – the rest
1791376 [80]	1990.07.09/ 1993.01.30	Process of producing superhard diamond ceramics. Compact structure made out of diamond powder including DND, by high pressure; anti-friction electrolyte is added before the compaction followed by a sequence of treatments
2006362 [81]	1990.08.28/ 1994.01.30	Material has sintered intermetallic compounds of copper with zinc and tin and DND powder at mass %: 48–88 of CuZn; 0.5–3 of CuSn: 1.5–4 of CuZnSn; 5–50 of diamond
1756806 [82]	1990.10.31/ 1992.8.23	Method of thermoluminescence is demonstrated as useful method for diagnostics of genesis of diamond powders. Sample is heated at 5–20 °C/s and its lighting is monitored. Ratio between thermal luminescence in diapasons 110–230 and 130–350 °C DND is specific for diamond of different origin. For DND ratio is >1.8

Table 16.4 Patents on Applications, DND-Containing Product for Specific Applications, as well as Patents from the Previous Tables Where Specific Applications Are Described as Practical Examples (cont'd)

Patent No., Ref.	Priority/ Issue Dates	Essence of the Claims
1781271 [83]	1991.1.12/ 1992.12.15	Abrasive suspension containing ultradispersed diamond–graphite powder with particles sizes 4–12 nm where diamond content is 16–40 mass %. Abrasive suspension content: DND–graphite powder 5–50 wt.%, stabilizing surface-active chemical 3–5%, organic component – the rest
2030449 [84]	1991.04.26/ 1995.03.10	Lubricant containing,, (wt.%): sulfur 10–15; molybdenum disulfide 10–20; indene coumarone resin 5–7; DND powder or detonation soot powder 1–15; and stearic acid – the rest
2042711 [85]	1991.04.30/ 1995.08.27	Proposed oil contains (mass %): polyoxyethylene glycol ether of fatty alcohols of C_{10}–C_{16} fraction 1–2: ultradisperse graphite–diamond powder (60–80% of graphite) 0.3–0.8; synthetic fatty acids 0.3–0.8; mineral oil – the balance
US Patent 5,482,695 [29]	1991.7.3/ 1996.1.9	Applications of the diamond/graphite composition as friction modifiers' lubricating compositions; an antifriction additive to the composition of the working layer of a magnetic storage medium; composition for pencil manufacture; as a pigment for letterpress and offset ink; superfinishing in polishing
2007967 [86]	1991.10.01/ 1994.02.28	Stomatologic drill comprises stem and head with cutting teeth having a coating; the coating penetrates into the structure of the head because the coating contains a dispersed phase of ultradispersed diamonds

Table 16.4 Patents on Applications, DND-Containing Product for Specific Applications, as well as Patents from the Previous Tables Where Specific Applications Are Described as Practical Examples (cont'd)

Patent No., Ref.	Priority/ Issue Dates	Essence of the Claims
US Patent 5,158,695 [87]	1991.11.29/ 1992.11.27	Antifriction material comprising sintered intermetallides of copper with zinc and tin; and ultradispersed diamond powder with grain size below 0.1 micrometers, the antifriction material having the following composition (mass %): CuZn 48–88, CuSn 0.5–3, CuZnSn 1.5–4, diamond 5.0–50
2001718 [88]	1991.12.11/ 1993.10.30	Process related to powder metallurgy by adding DND to metal powders followed by hot pressing. Dispersion hardening of aluminum has been demonstrated. Best properties of the composite were demonstrated at 1.5–2.5 wt.% of DND. Mechanochemical activation of DND to remove non-diamond outer shell before compacting was suggested
2094371 [89]	1991.12.20/ 1997.10.27	Suspension with high sedimentation stability containing (g/l): the DND, 40–70; stearox, 8–10; silicon dioxide, 8–10; and water, up to 1 liter. Demonstrated in examples as addition to electrolytes and resulting electroplated product; as an addition agent for polishing pastes
2051092 [30] 5,861,349 [31]	1991.12.25/ 1995.12.27	Demonstrated by example improvements on additions to lubricating oil; chrome galvanic coatings; as a material for chromatography
2048573 [91]	1992.01.03/ 1995.11.20	Electrochemically plated nickel with improved microhardness with electrolyte composition (mass %): boron 0.2–3.2; ultradispersed diamond powder 0.1–2.6; the balance – nickel

Table 16.4 Patents on Applications, DND-Containing Product for Specific Applications, as well as Patents from the Previous Tables Where Specific Applications Are Described as Practical Examples (cont'd)

Patent No., Ref.	Priority/ Issue Dates	Essence of the Claims
2005758 [92]	1992.04.20/ 15.01.94	Abrasive composite: DND–graphite powder having 10–99 wt.% diamond and a surface active polymer, where abrasive composition (wt.%): 1–30 DND and graphite powder; 0.2–20 sulfanilic acid-based iminofuran resin and water – the balance
2054456 [93]	1992.05.15/ 1996.02.20	The antifriction additive comprises (wt.%): soot (with 40–60% DND) 0.2–0.5 in relation to DND; 0.01–0.05 vinyl succinimide, and the petroleum oil – the balance
2009186 [94]	1992.05.15/ 1994.03.15	Lubricating and coolant liquid contains (mass %): sulfurized polyisobutylene 5–15, chlorsulfonated fat 2–5, DND–graphite powder 1–5 (DND 10–50%, graphite 50–90%), mineral oil – the rest
2039783 [95]	1992.06.11/ 1995.07.20	Ski grease has (vol.%): paraffin 85–99.3; additions with temperature and metal conductivity 0.7–15. Grease has an ultradispersed addition – a mixture of graphite and diamond (0.5–10 vol.%) or nickel
2059022 [96]	1992.08.14/ 1996.04.27	In the process of electrochemical plating from chromium plating electrolyte with DND, coating is periodically subjected to X-ray structural analysis to monitor morphology and therefore quality of DND deposition within the coating
2058359 [98]	1993.04.05/ 1996.04.20	Polishing paste (wt.%): paraffin 30–35; wax 3–5, DND powder, chrome oxide 20–50; and triethanolamine oleate – the rest. Mixed mass is cooled and poured in forms. Paste is used for complex-pattern article and metallic tool polishing

Table 16.4 Patents on Applications, DND-Containing Product for Specific Applications, as well as Patents from the Previous Tables Where Specific Applications Are Described as Practical Examples (cont'd)

Patent No., Ref.	Priority/ Issue Dates	Essence of the Claims
2082738 [99]	1993.05.26/ 1997.06.27	Polishing aqueous–organic base has additionally 0.1–15% of DND with size 2–20 nm, density of surface adsorption-active centers of acid nature 1–20 mcg-equiv./mg and electrolytes at amount 1–20% of the base mass
2079532 [100]	1993.11.29/ 1997.05.20	Polishing paste consists of DND (grain size is 2–12 nm) as abrasive and organic base consisting of organosilicon liquid, oleic acid, and wax at the following composition (wt.%): DND 2–15; oleic acid 5–25; wax 3–15; and organosilicon liquid – the balance
2041165 [36] 5,916,955 [37]	1993.12.02/ 1995.09.08	Demonstrated by example improvements at additions of DND–graphite material to rubbers; lubricating oil; polytetrafluorethene
2100389 [101]	1994.09.30/ 1997.12.27	Production of abrasion-resistant materials (wt.%): fluorovinylidene-containing rubber; vulcanizing agent 4–6; triallyl isociscurate 2–4; vulcanization activator 4–6; and DND-containing carbon, 5–15
2107115 [102]	1995.06.23/ 1998.03.20	Electrolyte contains chromium trioxide, sulfuric acid, potassium fluosilicate, barium sulfate, and diamond-containing mixture including ultradispersed diamonds introduced into electrolyte in the amount of 40–60%
2093495 [103] US patent 6,083,614 [105]	1995.09.27/ 1997.10.20 1996.9.27/ 2000.07.4	A method of producing a nanoporous body containing nanodiamond and having a desired shape, comprising the steps of forming an intermediate body having the desired shape of nanodiamond particles having a maximum size of 10 nm, exposing this body to a gaseous hydrocarbon at a temperature exceeding the decomposition temperature for the hydrocarbons. Uses of such a body described

Table 16.4 Patents on Applications, DND-Containing Product for Specific Applications, as well as Patents from the Previous Tables Where Specific Applications Are Described as Practical Examples (cont'd)

Patent No., Ref.	Priority/ Issue Dates	Essence of the Claims
2088689 [104]	1996.02.06/ 1997.08.27	Ultrasonic dispersing of submicroparticles in electrolyte to the state of fine metastable colloid for applying metal-based composite coatings with dispersed phase. Improved properties of metal coatings (Cr, Cu, Ni) at addition of DND by the method is demonstrated
2137242 [106]	1997.12.23/ 1999.09.1	Given material is produced from particles of diamond (including DND) intercoupled by means of graphite-like carbon matrix (the content of the matrix not exceeding 35 mass %). Result: improved emission properties for planar emitters of large areas
2150154 [107]	1998.11.18/ 2000.05.27	Emitter is manufactured from material homogeneous by composition and carrying grains of diamond intercoupled by means of graphite-like carbon with specifically patterned surface
2174138 [109]	1999.04.21/ 2001.09.27	Paste comprises abrasive (DND with purity of at least 98%, dispersity of 400–500 m^2/g, and primary particle size of 3.5–6.0 nm), organic substrate (glycerol), and surfactant (oleic acid) in wt.%: DND, 14–15; oleic acid, 2–5; and glycerol, the balance
2163921 [110]	1999.05.12/ 2001.03.10	Lubricant comprises (wt.%): DND–graphite powder, 0.2–5; highly dispersed metal salt, 2–15; soapy plastic lubricant, up to 100. Highly dispersed salt includes tin sulfate, copper sulfate, barium sulfate, lead sulfate, and barium sulfide
2172238 [111]	1999.07.28/ 2001.08.20	Binder contains copper, tin, nickel, aluminum, and additionally ultradispersed diamond

Table 16.4 Patents on Applications, DND-Containing Product for Specific Applications, as well as Patents from the Previous Tables Where Specific Applications Are Described as Practical Examples (cont'd)

Patent No., Ref.	Priority/ Issue Dates	Essence of the Claims
2169798 [112]	2000.02.21/ 2001.06.27	Method of electrochemical deposition from galvanizing electrolyte containing DND 0.001 to 0.120 μm in the amount of 0.5 to 30 g/l. Demonstrated improved anticorrosive properties of coats; facilitated procedure of production
2169800 [113]	2000.02.21/ 2001.06.27	Methods of production of composite coats by anode oxidizing of aluminum and its alloys; oxidizing in electrolyte containing DND, 0.001 to 0.120 um in size in the amount of 0.05 to 56 g/l. Demonstrated enhanced hardness and wear resistance; improved antifriction properties
2191227 [114]	2000.10.05/ 2002.10.20	Electroplating and electroforming of gold-base coatings. Gold-plating electrolyte containing DND 0.001 to 0.120 um in the amount of 0.1–35 g/l. Demonstrated enhanced wear resistance

16.5 Conclusion

The history of DND discovery is rather complicated: the material has been rediscovered several times (see also Chapter 10). It seems that commercialization of the product with related intellectual property protection follows a similar "complicated" fashion. A rather impressive "detonation nanodiamond empire" existed at the late 1980s in the former USSR according to the patent publications reviewed in the current chapter as well as a vast number of publications in USSR scientific journals that are not discussed in the chapter, and yet to be revealed. SPC Altai produced more than 25 million carats of DND by 1993,[4] an amount comparable to the annual production volume of nanodiamonds produced by the shock wave compression of graphite (DuPont method). Different aspects of DND synthesis, treatment, and applications are presented in a quite impressive portfolio of about 90 patents filed in the former USSR and

Russian Federation. Since DND in the former USSR was mostly oriented to the internal market, most of the patents at that time were filed only in the USSR; some of them were classified. This period of rapid development of DND production and commercialization was interrupted by the collapse of the USSR followed by economic stagnation in the newly formed countries. Many patents filed during the 1990s were abandoned by the end of the decade due to the simple fact of maintenance fees. Consequently, there exists an information "gap" between the findings of the 1980s and recent discoveries. Within the last few years, scientific and commercial interest in this material has developed worldwide, thus it is valuable to recall the vast experience and knowledge developed more than a decade and a half ago. It would be valuable to perform an analysis of scientific publications dating back to this period in a similar fashion to the analysis in the current chapter. We hope that the information summarized here will help avoid the reinvention of applications for this nanomaterial that were born four decades ago.

It is important to emphasize once again that there is no single detonation nanodiamond existing as a technological material on the market. DNDs produced by different vendors demonstrate specific properties such as size of primary particles, lattice constant, elemental composition, composition of surface functional groups, different ability to oxidation in air, ability to sintering, and a variety of other properties. Thus different categories of DNDs exist on the market; at the same time, these features help to protect DNDs synthesized by a specific method from unauthorized production and commercialization.

Acknowledgments

The authors are very grateful to Vycheslav Danilenko, Valerii Dolmatov, Sergey Gordeev, Irina Larionova, Alexei Lyamkin, Gary McGuire, Vladimir Padalko, Euvgenii Petrov, Alexei Puzur, and Dmytro Savvakin for valuable discussions during the compilation of this chapter.

References*

1. Vul A., Dolmatov V., Shenderova O. (Eds.), *Detonation Nanodiamonds and Related Materials,* Bibliography Index, First Issue. "FIZINTEL", St. Petersburg, 2003.

* In the references related to the patents, the index SU is related to the Author's Certificates granted by the Patent Department of the USSR, and the index RU is related to the patents granted by the Patent Agency of the Russian Federation.

2. General information concerning USA patents: http://www.uspto.gov/web/offices/pac/doc/general/index.html#patent.
3. Rospatent: http://www.fips.ru/ruptoen/index.htm.
4. Vereschagin A.L. *Properties of Detonation Nanodiamonds*, Barnaul State Technical University Altay Region, 2005 (in Russian).
5. Danilenko, V.V., *Synthesis and Sintering of Diamonds by Explosion*, Energoatoizdat, Moscow, 2003 (in Russian).
6. Volkov K.V., Danilenko V.V., Elin V.I., Sanina S.E., Timofeeva T.P., Krupnikov K.K., Sanin I.V., Synthesis of diamond and dense modifications of boron nitrite by dynamic method, explosion, shock, protection. *Inf. Byull.* No. 17, Inst. Geofiz. Sib. Otd. Acad. Nauk USSR, Novosibirsk, 1987.
7. Volkov K.V., Danilenko V.V., Elin V.I., Diamond synthesis from detonation carbon, *Fiz. Gorenya Vzryva*, Vol. 26, No. 3, pp. 123–125 (1990).
8. Timofeev V.T., Detkov P.Ya., Filin V.P., Diamonds from explosive material.s, *Atom*, No. 1, 2006 (in press).
9. Savvakin G.I., Trefilov V.I., Zaika, N.I., Method of manufacturing of ultradispersed diamond and boron nitride powders, Institute for Material Science Problems, Ukraine, SU **845378**, filed 1979.10.05.
10. Savvakin G.I., Trefilov V.I., Formation of structure and properties of ultradispersed diamonds at detonation in different media of explosion materials with negative oxygen balance, *Dokl. Akad. Nauk SSR*, Vol. 321, No. 1, p. 99 (1991); Vlasova M.V., Kakazei N.G., Savvakin G.I., Some properties of ultradispersed diamond obtained by high-temperature explosive synthesis, *Inorg. Mater.*, Vol. 15, No. 7, pp. 1020–1021 (1979).
11. Staver A.M., Lyamkin A.I., Gubareva N.I., Petrov E.A., Method of diamond synthesis, SU **1165007**, filed 1.07.1982.
12. Staver A.M., Lyamkin A.I., Gubareva N.A., Petrov E.A., Ultradisperse diamond powders produced by explosion, *Fiz. Gorenya Vzryva*, Vol. 20, No. 5, pp. 100–103 (1984).
13. Lyamkin A.I., Petrov E.A., Ershov A.P., Sakovich G.V., Staver A.M., Titov V.M.. Production of diamond from explosives,. *Dokl. Acad. Nauk SSR*, Vol. 302, No. 3, pp. 611–613 (1988).
14. Titov V.M., Anisichkin V.P., Mal'kov I.Yu., A study of ultradispersed diamond synthesis by detonation waves, *Fiz. Gorenya Vzryva*, Vol. 25, No. 3, pp. 117–126 (1989).
15. Staver, Lyamkin A.I., Production of ultradispersed diamonds from explosive materials,n *Ultradispersed materials. Synthesis and Properties*, Inter-institutes Proceedings, Krasnoyarsk, 1990, pp. 3–22; Staver, Lyamkin A.I. and Kuzmin I., Experimental study of gaseous products of detonation of condensed explosives in different atmospheres, *Ibid.*, pp. 23–28.
16. Petrov E.A., Sakovich G.V., Brylykov P.M., Conditions for preserving diamonds when produced by explosion, *Dokl. Acad. Nauk SSR*, Vol. 313, p. 862 (1990).
17. Collection of Reports of the 5th All-Union Meeting on Detonation, Krasnoyarsk, State Technical University, Russia, August 5–12, 1991 (in Russian).

18. Sakovitch G.V., Brylyakov P.M., Verestchagin A.L., Komarov V.F., Gubarevitch V.D., Production of diamond clusters by explosion and their application, *Zh. Vses. Khim. Obschestva*, Vol. 35, No. 5, pp. 600–602 (1990).
19. Petrov E.A., Molokeev V.A., Shebalin A.I., Sakovich G.V., Method of diamnd synthesis, SU **1534819**, filed 1984.06.26.
20. Petrov E.A., Molokeev V.A., Brulykov P.M., Komarov V.F., Sakovich G.V., Method of diamond synthesis in a detonation wave, SU **1538321**, filed 1985.06.06.
21. Petrov E.A., Molokeev V.A., Brulykov P.M., Komarov V.F., Sakovich G.V., Smirnov B.V., Kozurev N.V., Vereschagin A.L., Method of diamond synthesis, SU **1658557** from 1991.02.22, filed 1985.08.15.
22. Petrov E.A., Kalashnikova G.S., Brulykov P.M., Sakovich G.V., Method of diamond synthesis, SU **1570222** from 1990.01.27, filed 1987.02.08.
23. Kozurev N.V., Petrov E.A., Leontiev B.P., Brulykov P.M., Sakovich G.V., Smirnov B.V., Method of detonation diamond synthesis, SU **1578999**, filed 1988.07.19.
24. Petrov E.A., Kalashnikova G.S., Brulykov P.M., Kozurev N.B., SU **1623107**, filed 1989.06.14.
25. Kozurev N.B., Balyasov C.E., Kazakov A.A., Lihteckaya N.G., Charge for the detonation explosives for detonation synthesis of diamond, RU **1826958** from 1993.07.07, filed 1990.08.20.
26. Stavrev S.Y., Lazarov S.B., Stoev K.L., Markov L.G., Ivanov V.I., Method for production of ultradispersed diamond, US **5,353,708** 1994, filed: Nov. 09, 1990 [BG].
27. Danilenko V.V., Trefilov, V., Danilenko V.N., Detonation chamber for synthesis of superhard materials, SU **1813293**, filed 1991.05.12.
28. Litvinov B.V., Samulov S.M., Averin A.N., Filatov L.I., Detkov P.Y., Kramskoy Y.E., Oleynik V.S., Emelyanov U.E., Method of synthesis of superhard synthetic materials, SU **1833593**, filed 1991.07.02.
29. Guschin V.A., Zakharov A.A., Lyamkin A.I., Staver A.M., Carbon composition production process, US Patent **5,482,695**, Jan. 9, 1996, PCT filed 1991.07.03.
30. Vereschagin A.L., Petrov E.A., Sakovich G.V., Komarov V.F., Klimov A.V., Kozyrev N.V., Diamond-containing material and its production technology, RU **2051092** from 27.12.95, filed 1991.12.25.
31. Vereschagin A.L., Petrov E.A., Sakovich G.V., Komarov V.F., Klimov A.V., Kozyrev N.V., Synthetic diamond-containing material and method of obtaining it, US Patent **5,861,349**, Jan. 19, 1999, 1991.12.25.
32. Korobov D.Yu., Korobov Yu.A., A nanodiamond-containing composition and its production, Russian Patent **2049723**, filed 1992.05.19.
33. Misonochnikov Al., Rumyncev B.V., Method of production of ultradispersed diamond, RU **2036835** from 1995.06.09, filed 1992.09.01.
34. Anisichkin V.F., Dolgushin D.S., Petrov E.A., Klimov A.V., Komarov V.F., Sakovich G.V., SU **2041166** from 1995.08.09, filed 1993.04.02.
35. Titov V.M., Mal'kov I.Yu., Kuznetsov V.L., Chuvilin A.L., A way of producing onion carbon, RU **2094370** from 1997.10.27, filed 1993.10.19.

36. Vereschagin A.L., Petrov E.A., Sakovich G.V., Komarov V.F., Klimov A.V., Kozyrev N.V., Diamond-carbon material and method for producing thereof, RU **2041165**, 09.08.1995; filed 1993.02.12.
37. Vereschagin A.L., Petrov E.A., Sakovich G.V., Komarov V.F., Klimov A.V., Kozyrev N.V., Diamond-carbon material and method for producing thereof, US Patent **5,916,955** from 1999.01.29, filed 1993.02.12.
38. Averin A.N., Filatov L.I., Alekseev A.V., Filin V.P., Lobojko B.G., Detkov P.Ja., Chamber for explosive treatment of materials, RU **2078661**, 1997.05.10, filed 1995.01.20.
39. Lin E.E., Dubitskii G.A., Zjulkova T.V., Mazanov V.A., Sirenko A.V., Sukharenko V.I., Method of producing polycrystalline diamond, RU **2128625**, from 1999.04.10, filed 1995.11.14.
40. Dolmatov V.Ju., Veretennikova M., Method of preparing nanodiamonds, RU **2230702**, from 2004.06.20, filed 2003.02.06.
41. Greiner N.R., Philips D.S., Johnson J.D., Volk F., Diamonds in detonation soot, *Nature*, Vol. 333, pp. 440–442 (1988).
42. Dolmatov, V.Y., Ultradisperse diamonds of detonation synthesis: production, properties and applications, St. Petersburg, State Politechnical University, 2003.
43. Shebalin A.I., Molokeev V.A., Sakovich G.V., Taranenko G.S., Lushnikova N.I., Petrov E.A., Method of purification of diamond from graphite, SU **1770271** from 1992.06.22, filed 1984.06.13.
44. Dolmatov V.Yu., Suschev V.G., Aleksandrov M.M., Sakovich G.V., Vishnevskij E.N., Pyaterikov V.F., Sataev P.P., Komarov V.F., Brylyakov P.M., Shitenkov N.V., A way of separating synthetic nanodiamonds, SU **1828067** from 13.10.92, filed 1986.03.25.
45. Institute of Superhard Materials AN Ukraine SSR, Method of purification of diamond powder, SU **1480306**, filed 1986.06.09.
46. Institute of Superhard Materials AN Ukraine SSR, SU **1540195**, filed 1988.01.25.
47. Brylyakov P.M., Sataev P.P., Gubarevich T.M., Ladonina A.K., Bruleva N.G., Pavlov A.M., Dimidova M.A., Method of purification of ultradisperesed diamonds, SU **1794888** from 1993.02.05, filed 1988.07.19.
48. Ovcharenko A.G., Gubarevich T.M., Sataev P.P., Brylyakov P.M., A technology for removal of nanodiamonds from stable aqueous suspensions, RU **1614354** from 10.01.96, filed 1988.07.19.
49. Gubarevich T.M., Larionova I.S., Kostyukova N.M., Sataev P.P., Brylyakov P.M., Dolmatov V.Yu., Suschev V.T., Aleksandrov M.M., A technology for purification of diamond powder from surface impurities, SU **1658558** from 22.02.91, filed 1988.07.19.
50. Gubarevich T.M., Larionova I.S., Kostyukova N.M., Ryzhko G.A., Turitsyna O.F., Pleskach L.I., Sataev P.P., A diamond purification technology, SU **1770272** from 22.06.92, filed 1988.07.19.
51. Ovcharenko A.G., Brylyakov P.M., Sataev P.P., Gubarevich T.M., A technology for removal of nanodiamonds from stable aqueous suspensions, RU **1792915** from 7.02.93, filed 1988.07.19.
52. Gubarevich T.M., Larionova I.S., Ryzhko GA, Kostyukova N.M., Sataev P.P., Purification of diamond-containing mixtures, SU **1830883** from 10.13.92, filed 1988.07.19.

53. Gubarevich T.M., Kostyukova N.M., Sataev P.P., Larionova I.S., Brylyakov P.M., A way of purifying nanodiamonds, SU **1538430** from 15.09.89, filed 1987.09.29.
54. Ovcharenko A.G., Ignatchenko A.V., Sataev R.R., Bryljakov P.M., Method of ultradispersed diamond cleaning, RU **1815933** from 1996.06.20, filed 1990.07.27.
55. Ovcharenko A.G., Gubarevich T.M., Sataev P.P., Brylyakov P.M., Ovcharenko A.G., Gubarevich T.M., Sataev P.P., Brylyakov P.M., Ovcharenko A.G., Sataev P.P., Solohina A.B., Ignatchenko A.V., A nanodiamond separation technology, RU **2019500** from 15.09.94, filed 1990.08.10.
56. Gubarevich T.M., Larionova I.S., Sataev P.P., Dolmatov V.Yu., Pyaterikov V.F., A technology for purification of nanodiamonds from non-diamond carbon, Avt. Svid. USSR **1819851** from 12.10.92, filed 1991.01.02.
57. Pavlov E.V., Skrjabin J.A., Method for removal of impurities of non-diamond carbon and device for its realization, RU **2019502** from 1994.09.15, filed 1991.01.09.
58. Filatov L.I., Chuhaeva S.I., Detkov P.Ya., A technology for nanodiamond purification, Russian Patent **2077476** from 20.04.97, filed 1991.03.21.
59. Chiganov A.S., Chiganova G.A., Tushko Yu.M., Staver A.M., Purification of detonation diamond, Russian Patent **2004491** from 15.12.93, filed 1991.07.02.
60. Eryomenko N.K., Obraztsova I.I., Efimov O.A., Korobov Yu.A., Safonov Yu.N., Sidorin Yu.Yu., A technology for nanodiamond separation, RU **2081821** from 20.06.97, filed 1995.01.11.
61. Vasilishin M.S., Bratilov B.I., Petrov E.A., Svetlov S.A., A way of nanodiamond removal from an aqueous suspension, Russian Patent **2083490** from 10.07.97, filed 1995.04.10.
62. Dolmatov V.Y., Sushchev V.G., Marchukov V.A., Gubarevich T.M., Korzhenevskii A.P., Method for recovering synthetic ultradispersed diamonds, RU **2109683** from 1998.04.27, filed 1996.03.05.
63. Kovrigin S.A., Migin A.N., Uvarov S.V., A way of separating nanodiamond from non-diamond carbon, Russian Patent **2132816** from 10.07.99, filed 1997.11.10.
64. Larionova I.S., Molostov I.N., Kulagina L.S., Komarov V.F., Method of cleaning of synthetic ultradispersed powder, RU **2168462** from 2001.03.20, filed 1999.04.05.
65. Korzenevskii A.P., Gubarevich T.M., Gamanovich T.M., Dolmatov V.Y., Method of extraction of synthetic diamonds, Byelorussia Patent **4321** from 22.10.2001.
66. Korzenevskii A.P., Gubarevich T.M., Gamanovich T.M., Dolmatov V.Y., Method of purification of ultradispersed diamonds from impurities, Byelorussia Patent **4533** from 2002.02.25.
67. Gordeev S.K., Korchagina C.B., Zukova N.A., Dolmatov V.Y., Method of purification of ultradispersed diamonds, RU **2244679** from 21.02.2005, filed 2002.02.21.
68. Puzur A.P., Bondar B.C., Method of obtaining of nanodiamonds with increased colloidal stability, RU **2252192** from 2005.05.20, filed 2003.06.26.

69. Puzur A.P., Bondar B.C., Method of treatment of nanodiamonds, RU **2258671** from 2005.08.20, filed 2003.09.17.
70. Gubarevich T.M., Dolmatov V.Y., Pjaterikov V.F., Marchukov V.A., Sushchev V.G., Synthetic hydrocarbon diamond-containing material, RU **2046094** from 1995.10.20, filed 1993.05.26.
71. Petrova L.A., Vereschagin A.L., Novoselov V.V., Bryliakov P.M., Shein N.V., Composition analysis of surface groups in diamond like carbon phase, *Superhard Mater.*, Vol. 4, pp. 3–5 (1989).
72. Gubarevich T.M., Kostukova H.M., Sataev P.P., Fomina L.B., Investigation of micro-impurities composition of ultradispersed diamond, *Superhard Mater.*, Vol. 5, pp. 30–35 (1991).
73. Vereshchagin A.L., Sakovich G.V., Brylyakov P.M., Zolotukhina I.I., Petrova L.A., Novoselov N.N., Structure of the diamond-like phase of carbon made by explosive synthesis, *Dokl. Akad. Nauk SSSR*, Vol. 314, p. 866 (1990).
74. Vereshchagin A.L., Sakovich G.V., Petrova L.A., Novoselov N.N., Brylyakov P.M., Study of the chemical composition of the surface of ultradispersed diamond synthesized by detonation, *Dokl. Akad. Nauk SSSR*, Vol. 315, p. 104 (1990).
75. Vereshchagin A.L., Sakovich G.V., Komarov V.F., Petrov E.A., Properties of ultrafine diamond clusters from detonation synthesis, *Diamond Relat. Mater.*, Vol. 3, pp. 160–162 (1993).
76. Sakovich G.V., Komarov V.F., Petrov E.A., Bryilyakov P.M., Potapov M.G., Idrisov I.G., Ultra disperse diamonds and its practical application, Proceedings of V All-Union Workshop on Detonation, Krasnoyarsk), Vol. 2, pp. 272–278 (1991).
77. Shebalin A.I., Gubarevich V.D., Privalko Y.N., Brylykov P.M., Besedin V.I., Sakovich G.V., Cheremisin A.Y., Kotov A.N., Kozlovskii S.A., Altshuller N.B., Method of processing of chrome composite coatings, SU **1694710** from 1991, filed 1986.4.14.
78. Shebalin A.I., Privalko U.N., Sakovich G.V., Porohov V.S., Molokeev B.A., Petrov E.A., Brulyakov P.M., Samsonov B.V., Dorfman V.P., Lifontov B.C., Staver A.M., Korobov U.A., Lubricating oil, SU **1770350** from 1992.10.23, filed 1988.07.19.
79. Guslienko J.A., Luchka M.V., Savvakin G.I., Burda M.I., Composition for preparing composition electrolytical coatings on the basis of iron group metals, RU **2026892** from 1995.01.20, filed 1990.06.05.
80. Lapin V., Dubickii G.A., Andreev V.G., Method of production of polycrystalline diamond material, SU **1791376** from 1993.01.30, filed 1990.07.09.
81. Jashchenko N.K., Ogorodnik V.V., Friction surface antifriction material, RU **2006362** from 1994.01.30, filed 1990.08.28.
82. Kashkarov L.L., Fisenko A.V., Breysov O.S., Tacii V.F., Method of diagnostics of diamond powders obtained at high pressures, SU **1756806** from 1992.08.23, filed 1990.10.31.
83. Zaharov A.A., Red'kin V.E., Staver A.M., An abrasive diamond suspension, Russian Patent **1781271** from 15.12.92, filed 1991.01.18.
84. Baranov A.I., Brost I.I., Bryljakov P.M., Kirdjakin A.A., Morozov V.A., Potapov M.G., Sakovich G.V., Kigel' S.G., Antifriction lubricant for abrasive working of materials, RU **2030449** from 1995.03.10, filed 1991.04.26.

85. Zakharov A.A., Kuchma E.I., Staver A.M., Juzova V.A., Sharova O.N., Industrial oil, RU **2042711** from 1995.08.27, filed 1991.04.30.
86. Vinokur V.S., Ignashin J.P., Utjashev R.A., Shakirov N.K., Shvetsov M.A., Dental drill, RU **2007967** from 1994.02.28, filed 1991.10.01.
87. Yashchenko N.K., Ogorodnik V.V., Diamond-based antifriction material, US Patent **5,158,695**, 1992.11.27, filed 1991.11.29.
88. Kozharskij S.P., Komarov V.F., Potapov M.G., Petrov E.A., Sakovich G.V., Shalyuta V.N., A way of producing a nanodiamond-strengthened material, Russian Patent **2001718** from 30.10.1993, filed 1991.12.11.
89. Zalyaliev M.M., Nadeeva F.I., Xabibullin I.G., A modified nanodiamond suspension, Russian Patent **2094371** from 1997.10.27, filed 1991.12.20.
90. Kovalev V.V., Petrov E.A., Antifrictional material, RU **2005741** filed 1992.01.03.
91. Dertjag L.A., Kukoz F.I., Kudryvseva L.I., Sysoev G.N., Composition electrochemical plating, RU **2048573** from 1995.11.20, filed 1992.01.03.
92. Martonik M.V., Primacheva L.G., Red'kin V.E., Staver A.M., A grinding and polishing composition, Russian Patent **2005758** from 15.01.94, filed 1992.04.20.
93. Nikitin E.V., Slyusarev S.Ya., Filippova E.V., Danilov A.I., Skryabin Yu.A., An antifriction additive, Russian Patent **2054456** from 20.02.1996, filed 1992.05.15.
94. Red'kin V.E., Staver A.M., Shangin A.P., A liquid cooling lubricant for mechanical treatment of metals. Russian Patent **2009186** from 15.03.94, filed 1992.05.15.
95. Andreev V.V., Tkachenko I.B., Ski grease, RU **2039783** from 1995.07.20, filed 1992.06.11.
96. Dolgopolov V.I., Zajtseva T.N., Korytnikov A.V., Nikitin E.V., Sljusarev S.J., Skrjabin J.A., Chromium-diamond coatings electroplating method, RU **2059022** from 1996.04.27, filed 1992.08.14.
97. Komarov V.F., Sakovich G.V., Petrov E.A., Klimov A.V., Kostukov S.I., Baraboshkin K.S., Composition for superfinishing treatment of material surface, RU **2034889** from 1995.05.10, filed 1993.04.02.
98. Martonik M.V., Red'kin V.E., Staver A.M., A polishing paste, Russian Patent **2058359** from 20.04.96, filed 1993.04.05.
99. Dolmatov V.Y., Gubarevich T.M., Polish composition for chemical-mechanical polishing, RU **2082738** from 1997.06.27, filed 1993.05.26.
100. Martonik M.V., Red'kin V.E., Staver A.M., Polishing paste, RU **2079532** from 1997.05.20, filed 1993.11.29.
101. Levintova E.A., Voznyakovskii A.P., Dolmatov V.Y., Kabakova I.I., Gubarevich T.M., Composition comprising fluorovinylidene-containing rubber, RU **2100389** from 1997.12.27, filed 1994.09.30.
102. Nikitin E.V., Korytnikov A.V, Breusov O.N., Zajtseva T.N., Sljusarev S.J., Grishchuk N.B., Electrolyte for deposition of chromium-diamond coatings, RU **2107115** from 1998.03.20, filed 1995.06.23.
103. Gordeev S.K., Zukov S.G., Belobrov P.I., Smolyninov A.N., Dikov Y.P., Method of preparing carbon material, RU **2093495** from 1997.10.20, filed 1995.09.27.

104. Oparin E.M., Method of preparing electrolyte for applying metal-based composite coatings, RU **2088689** from 1997.08.27, filed 1996.02.06.
105. Gordeev S., Zhukov S., Belobrov P., Smolianinov A., Dikov I., Method of producing a composite, more precisely a nanoporous body and a nanoporous body produced thereby, US **6,083,614** from 2000.07.04, filed 1996.09.27.
106. Gordeev S.K. , Ral'chenko V.G., Negodaev M.A., Karabutov A.V., Belobrov P.I., Material on basis of diamond with low threshold of field emission of electrons, RU **2137242** from 1999.09.10, filed 1997.12.23.
107. Gordeev S.K., Ral'chenko V.G., Negodaev M.A., Karabutov A.V., Belobrov P.I., Field emitter of electrons and a method of its fabrication, RU **2150154** from 2000.05.27, filed 1998.11.18.
108. Gordeev S.K., Ral'chenko V.G., Negodaev M.A., Karabutov A.V., Belobrov P.I., Field emitter of electrons and a method of its fabrication, Ukranian patent **42119** filed 1998.11.18
109. Nikitin E.V., Prahnin P.I., Volchkov V.M., Superfinish polishing diamond past, RU **2174138** from 2001.09.27, filed 1999.04.21.
110. Shchelkanov S.I., Red'kin V.E., Dokshanin S.G. , Terent'ev V.F., Ljamkin A.I., Plastic lubricant, RU **2163921** from 2001.03.10, filed 1999.05.12.
111. Potapov V.A., Poljakov L.A., Nikitin E.V., Binder based on copper to produce diamond tool, RU **2172238** from 2001.08.20.
112. Lung B., Burkat G.K., Dolmatov V.Ju., Saburbaev V.Ju., Method of production of composite zinc-based coats, RU **2169798** from 2001.06.27, filed 2000.02.21.
113. Lung B., Burkat G.K., Dolmatov V.Ju., Method of production of oxide composite coat on aluminium and its alloys, RU **2169800** from 2001.06.27, filed 2000.02.21.
114. Lung B., Burkat G.K., Dolmatov V.Ju., Saburbaev V.Ju., Process for applying composition type gold-base coatings, RU **2191227** from 2002.10.20, filed 2000.10.05.
115. Dolmatov V.Ju., Biologically active ultradispersed diamond of detonation synthesis, RU **2203068** from 2003.04.27, filed 2001.04.12.
116. Gerasimenko V.F., Kolegov L.E., Mazanov V.A., Method of production of alloyed ultradispersed diamonds, RU **2202514** from 2003.04.20, filed 2002.01.09.
117. Lunkin V.V., Cosmetic composition, RU **2257889** from 2005.08.10, filed 2004.06.18.
118. Savvakin D., Private communications, 2005.